LECTURE NOTES
IN PHYSICS

A. Loiseau · P. Launois
P. Petit · S. Roche
J.-P. Salvetat
(Eds.)

Understanding Carbon Nanotubes

From Basics to Application

Springer

Lecture Notes in Physics

Editorial Board

R. Beig, Wien, Austria
W. Beiglböck, Heidelberg, Germany
W. Domcke, Garching, Germany
B.-G. Englert, Singapore
U. Frisch, Nice, France
P. Hänggi, Augsburg, Germany
G. Hasinger, Garching, Germany
K. Hepp, Zürich, Switzerland
W. Hillebrandt, Garching, Germany
D. Imboden, Zürich, Switzerland
R. L. Jaffe, Cambridge, MA, USA
R. Lipowsky, Golm, Germany
H. v. Löhneysen, Karlsruhe, Germany
I. Ojima, Kyoto, Japan
D. Sornette, Nice, France, and Zürich, Switzerland
S. Theisen, Golm, Germany
W. Weise, Garching, Germany
J. Wess, München, Germany
J. Zittartz, Köln, Germany

The Lecture Notes in Physics

The series Lecture Notes in Physics (LNP), founded in 1969, reports new developments in physics research and teaching – quickly and informally, but with a high quality and the explicit aim to summarize and communicate current knowledge in an accessible way. Books published in this series are conceived as bridging material between advanced graduate textbooks and the forefront of research to serve the following purposes:

• to be a compact and modern up-to-date source of reference on a well-defined topic;
• to serve as an accessible introduction to the field to postgraduate students and nonspecialist researchers from related areas;
• to be a source of advanced teaching material for specialized seminars, courses and schools.

Both monographs and multi-author volumes will be considered for publication. Edited volumes should, however, consist of a very limited number of contributions only. Proceedings will not be considered for LNP.

Volumes published in LNP are disseminated both in print and in electronic formats, the electronic archive is available at springerlink.com. The series content is indexed, abstracted and referenced by many abstracting and information services, bibliographic networks, subscription agencies, library networks, and consortia.

Proposals should be sent to a member of the Editorial Board, or directly to the managing editor at Springer:

Dr. Christian Caron
Springer Heidelberg
Physics Editorial Department I
Tiergartenstrasse 17
69121 Heidelberg/Germany
christian.caron@springer.com

A. Loiseau P. Launois P. Petit
S. Roche J.-P. Salvetat (Eds.)

Understanding Carbon Nanotubes

From Basics to Applications

Springer

Editors

Annick Loiseau
Laboratoire d'Etude des
Microstructures (LEM)
UMR 104 CNRS-ONERA
BP 72
Avenue de la Division Leclerc
92322 Châtillon, France
E-mail: annick.loiseau@onera.fr

Pascale Launois
Laboratoire de Physique des
Solides (LPS)
UMR 8502 CNRS-Université Paris Sud
Bât. 510
91405 Orsay Cedex, France
E-mail: launois@lps.u-psud.fr

Pierre Petit
Institut Charles Sadron
UPR 22 CNRS
6 rue Boussingault
67083 Strasbourg, France
E-mail: petit@ics.u-strasbg.fr

Stephan Roche
Commissariat à l'Energie Atomique
DSM/DRFMC/SPSMS
17 avenue des Martyrs
38054 Grenoble, France
E-mail: stephan.roche@cea.fr

Jean-Paul Salvetat
Centre de Recherche sur la
Matiére Divisée (CRMD)
UMR 6619 CNRS-Université d'Orléans
1B rue de la Férollerie
45071 Orléans Cedex 2, France
E-mail: salvetat@cnrs-orleans.fr

A. Loiseau et al., *Understanding Carbon Nanotubes*, Lect. Notes Phys. 677 (Springer, Berlin Heidelberg 2006), DOI 10.1007/b10971390

Library of Congress Control Number: 2006921041

ISSN 0075-8450
ISBN-10 3-540-26922-3 Springer Berlin Heidelberg New York
ISBN-13 978-3-540-26922-9 Springer Berlin Heidelberg New York

This work is subject to copyright. All rights are reserved, whether the whole or part of the material is concerned, specifically the rights of translation, reprinting, reuse of illustrations, recitation, broadcasting, reproduction on microfilm or in any other way, and storage in data banks. Duplication of this publication or parts thereof is permitted only under the provisions of the German Copyright Law of September 9, 1965, in its current version, and permission for use must always be obtained from Springer. Violations are liable for prosecution under the German Copyright Law.

Springer is a part of Springer Science+Business Media
springer.com
© Springer-Verlag Berlin Heidelberg 2006
Printed in The Netherlands

The use of general descriptive names, registered names, trademarks, etc. in this publication does not imply, even in the absence of a specific statement, that such names are exempt from the relevant protective laws and regulations and therefore free for general use.

Typesetting: by the authors and techbooks using a Springer LaTeX macro package
Cover design: *design & production* GmbH, Heidelberg

Printed on acid-free paper SPIN: 10971390 57/techbooks 5 4 3 2 1 0

Preface

Carbon nanotubes were identified for the first time in 1991 by Sumio Iijima at the NEC Research Laboratory, using high resolution transmission electron microscopy, while studying the soot made from by-products obtained during the synthesis of fullerenes by the electric arc discharge method. In this soot, Iijima clearly observed the so-called multiwalled nanotubes, molecular carbon tubes with diameters in the nanometer range, consisting of carbon atoms arranged in a seamless graphitic structure rolled up to form concentric cylinders. Two years later, single-wall carbon nanotubes were synthesized by adding metal particles to the carbon electrodes.

An electric arc produced between two carbon electrodes at different chemical potentials has actually been used as a tool to produce carbon structures for more than forty years. This method was originally developed in 1960 by R. Bacon for the synthesis of carbon whiskers. Although carbon nanotubes were probably produced in these experiments, their observation has only been made possible with the technical improvements of electron microscopy. The discovery of carbon nanotubes has provided unique one-dimensional structures that interconnect different physical length scales (from the nanometer up to the millimeter), and has opened new pathways toward the development of nanoscience, as envisioned by Richard Feynman in his seminal talk held at the Annual American Physical Society Meeting in 1959 (R.P. Feynman, 'There's Plenty of Room at the Bottom'). Research on carbon nanotubes has been strongly dependent on the progress of nanotechnology research, which in turn has been sustained owing to the spectacular unrivaled properties of these objects.

Carbon nanotubes and graphite, which are the most stable forms of carbon, share the same sp^2 bonding structure. This results in extremely stable covalent bonds between carbon atom nearest neighbors. Carbon nanotube properties are, in addition, determined by distinctive topological characteristics: their curvature, which gives some sp^3 character to the C–C bond, and their one-dimensional, seamless cylindrical structure. The richness and diversity of the properties of carbon nanotubes (mechanical, electronic, thermal,

and chemical) lie in this blend of singularities, and have naturally led the scientific community to focus on these objects, both from an academic point of view and for their potential applications.

Carbon nanotubes may well prove important in a wide range of applications, such as high performance composite materials, field emission displays, and nanoelectronic devices. However, to witness such a revolution, decisive progress is needed in the fields of controlled synthesis, manipulation and integration into conventional or disruptive technologies. Thirty years have been necessary for developing integrated circuits on Si chip-based semiconductors, and there probably still remains a long way to go for nanotube-based applications to penetrate the mass market. It may also be that carbon nanotubes will never reach the hall of fame of big market materials for economic reasons. Whatever the outcome, research efforts are never wasted as, citing Bergson, 'Si nous retirons un avantage immédiat de l'objet fabriqué, comme pourrait le faire un animal intelligent, si même cet avantage est tout ce que l'inventeur recherchait, il est peu de choses en comparaison des idées nouvelles, des sentiments nouveaux que l'invention peut faire surgir de tous côtés, comme si elle avait pour effet essentiel de nous hausser au-dessus de nous même et, par là, d'élargir notre horizon' (Henri Bergson, L'évolution créatrice).[1]

More than ten years after the discovery of carbon nanotubes, we felt it was necessary to establish the foundations as well as the state of the art on the accumulated knowledge concerning carbon nanotube science, and to examine in detail the potential for innovative applications. This was one of the aims of the thematic School held in 2003 at Aussois (France), organized by the French Research Group (GDR 'Nanotubes mono et multiéléments')[2] with financial support from the French CNRS, and from where this book is issued.

This book is not the usual proceeding of a School, which collect and place side by side the contributions of the lecturers. It has been conceived, designed, and written with strong emphasis on pedagogy, to be suitable as an introduction to the field for beginners, students or as a reference textbook for researchers and engineers in physics, chemistry, and material sciences. Where relevant, some description of possible applications has been provided. Each

[1] 'Though we derive an immediate advantage from the thing made, as an intelligent animal might do, and though this advantage be all the inventor sought, it is a slight matter compared with the new ideas and new feelings that the invention may give rise to in every direction, as if the essential part of the effect were to raise us above ourselves and enlarge our horizon' (Henri Bergson, Creative evolution)

[2] GDRs are research groups created and financially supported by the CNRS (Centre National de la Recherche Scientifique). This GDR focused on fostering national collaborations between researchers working in the field of carbon nanotubes, but coming from materials science, physics, chemistry, life science, medicine, pharmacy, and even astrophysics. Particular effort is paid to training and exchanges of researchers. In 2004, this research group was extended to the rest of Europe and it is now becoming international, as the GDR-I 'Science and applications of nanotubes' (NanoI)

chapter has been co-written as a joint effort by several lecturers of the School, all scientists chosen for their demonstrated international expertise and pedagogical abilities. All of them have made major research contributions to the field of carbon nanotube science.

The book is organized as follows: Chap. 1 is a general introduction to the structure of nanotubes, referring to other forms of carbon; synthesis techniques and discussion on the formation and growth of nanotubes are presented in Chap. 2, with reference to carbon fibers; two chapters then examine the means to experimentally investigate and describe their structural and spectroscopic properties (Chaps. 3 and 5); Chap. 4 addresses the essentials of electronic structure of carbon nanotubes, as well as electron emission aspects, and provides the basics for understanding the vibrational (phonon) properties (Chap. 5). Electronic transport properties (Chap. 6) are covered from classical conduction to ballistic transport, disorder and interference effects, thermal aspects and nanotube-based field effect transistor devices; mechanical properties are discussed in Chap. 7, for both nanotube-based materials and individual objects; Chap. 8 focuses on the chemical properties of nanotubes, based on the specific surface reactivity of carbon-based structures. Each chapter is divided into two parts, a pedagogical presentation of the fundamental concepts either in physics, chemistry or material science, followed by a section entirely devoted to the specific relevance of these concepts to carbon nanotubes.

To summarize, the diversity of topics and special care to pedagogy are the main characteristics of the book. It aims to give a general overview of a multidisciplinary new science, as well as allowing the readers to deepen their knowledge in fundamental concepts of prime importance for the understanding of nanotube properties and perspectives for applications.

This book is the result of a joint and collective effort from many contributors that have participated in this project with fantastic enthusiasm, dedicating a lot of time to working together in order to produce a single volume with a high level of scientific and pedagogical coherence. Edward Mc Rae deserves particular acknowledgment for his strong support to improving the written quality of the text. Chris Ewels is also warmly thanked for his help.

We wish you pleasant reading, and hope that this book will prove both useful and informative.

Paris (France)
October 2005

Annick Loiseau
Pascale Launois
Pierre Petit
Stephan Roche
Jean-Paul Salvetat

Contents

1 Polymorphism and Structure of Carbons
P. Delhaès, J.P. Issi, S. Bonnamy and P. Launois 1
1.1 Historical Introduction 1
1.2 Polymorphism of Crystalline Phases 5
1.3 Non-Crystalline Carbons 13
1.4 Transport Properties 24
1.5 Doped Carbons and Parent Materials 37
1.6 Conclusion 42
References 43

2 Synthesis Methods and Growth Mechanisms
A. Loiseau, X. Blase, J.-Ch. Charlier, P. Gadelle, C. Journet, Ch. Laurent and A. Peigney 49
2.1 Introduction 49
2.2 High-Temperature Methods for the Synthesis of Carbon and Boron Nitride MWNTs and SWNTs 51
2.3 Catalytic CVD Growth of Filamentous Carbon 63
2.4 Synthesis of MWNT and SWNT via Medium-Temperature Routes . . 77
2.5 Nucleation and Growth of C-SWNT 92
2.6 Growth Mechanisms for Carbon Nanotubes: Numerical Modelling . . 106
2.7 $B_xC_yN_z$ Composite Nanotubes 119
References 122

3 Structural Analysis by Elastic Scattering Techniques
Ph. Lambin, A. Loiseau, M. Monthioux and J. Thibault 131
3.1 Basic Theories 131
3.2 Analysis of Graphene-Based Structures with HREM 152
3.3 Analysis of Nanotube Structures with Diffraction and HREM 164
3.4 Analysis of the Nanotube Structure with STM 190
References 195

4 Electronic Structure
F. Ducastelle, X. Blase, J.-M. Bonard, J.-Ch. Charlier and P. Petit 199
4.1 Electronic Structure: Generalities 199
4.2 Electronic Properties of Carbon Nanotubes 217
4.3 Non-Carbon Nanotubes 227
4.4 Monitoring the Electronic Structure of SWNTs by Intercalation and Charge Transfer 236
4.5 Field Emission 248
References 271

5 Spectroscopies on Carbon Nanotubes
J.-L. Sauvajol, E. Anglaret, S. Rols and O. Stephan 277
5.1 Vibrational Spectroscopies 277
5.2 Electron Energy-Loss Spectroscopy 290
5.3 Raman Spectroscopy of Carbon Nanotubes 302
5.4 Applications of EELS to Nanotubes 322
References 331

6 Transport Properties
S. Roche, E. Akkermans, O. Chauvet, F. Hekking, J.-P. Issi, R. Martel, G. Montambaux and Ph. Poncharal 335
6.1 Quantum Transport in Low-dimensional Materials 335
6.2 Quantum Transport in Disordered Conductors 357
6.3 An Interaction Effect: the Density-of-States Anomaly 375
6.4 Theory of Quantum Transport in Nanotubes 377
6.5 Measurement Techniques 396
6.6 The Case of Carbon Nanotube 406
6.7 Experimental Studies of Transport in Nanotubes and Electronic Devices 408
6.8 Transport in Nanotube Based Composites 419
6.9 Thermal Transport in Carbon Nanotubes 423
References 432

7 Mechanical Properties of Individual Nanotubes and Composites
J.-P. Salvetat, G. Désarmot, C. Gauthier and P. Poulin 439
7.1 Mechanical Properties of Materials, Basic Notions 439
7.2 Mechanical Properties of a Single Nanotube 449
7.3 Reinforcing Composite Materials with Nanotubes 459
References 488

8 Surface Properties, Porosity, Chemical and Electrochemical Applications
F. Béguin, E. Flahaut, A. Linares-Solano and J. Pinson 495
8.1 Surface Area, Porosity and Reactivity of Porous Carbons 495

8.2 Surface Functionality, Chemical
and Electrochemical Reactivity of Carbons 513
8.3 Filling of CNTs and In-Situ Chemistry 524
8.4 Electrochemical Energy Storage using Carbon Nanotubes 530
References 543

Index 551

List of Contributors

Eric Anglaret
Laboratoire des colloïdes, Verres et Nanomatériaux (LCVN)
UMR 5587 CNRS-UM2
Université Montpellier II
Place Eugène Bataillon
34095 Montpellier Cedex 5, France
eric@gdpc.univ-montp2.fr

François Béguin
Centre de Recherche sur la Matière Divisée (CRMD)
UMR 6619 CNRS-Université d'Orléans
1B rue de la Férollerie
45071 Orléans Cedex 2, France
beguin@cnrs-orleans.fr

Xavier Blase
Laboratoire de Physique de la Matière Condensée et Nanostructures (PMCN)
UMR 5586 CNRS-Université Lyon I
43 bld du 11 novembre 1918
69622 Villeurbanne, France
xblase@lpmcn.univ-lyon1.fr

Sylvie Bonnamy
Centre de Recherche sur la Matière Divisée (CRMD)
UMR 6619 CNRS-Université d'Orléans
1B rue de la Férollerie
45071 Orléans Cedex 2, France
bonnamy@cnrs-orleans.fr

Jean-Christophe Charlier
Unité de Physico-Chimie et de Physique des Matériaux (PCPM)
Université Catholique de Louvain (UCL)
Place Croix du Sud, 1
(Bâtiment Boltzmann)
1348 Louvain-la-Neuve, Belgium
charlier@pcpm.ucl.ac.be

Olivier Chauvet
Institut des Matériaux Jean Rouxel (IMN)
UMR 6502 CNRS – Université de Nantes
2 rue de la Houssinière
44322 Nantes, France
chauvet@cnrs-imn.fr

Pierre Delhaès
Centre de Recherche Paul Pascal (CRPP)
UPR 8641 CNRS
Université Bordeaux I
Avenue Albert Schweitzer
33600 Pessac, France
delhaes@crpp-bordeaux.cnrs.fr

François Ducastelle
Laboratoire d'Etude des Microstructures (LEM)
UMR 104 CNRS-ONERA
BP 72
Avenue de la Division Leclerc
92322 Châtillon, France
Francois.Ducastelle@onera.fr

Emmanuel Flahaut
Centre Inter universitaire de Recherche et d'Ingénierie des Matériaux (CIRIMAT)
UMR 5085 CNRS-Université Paul Sabatier
118 Route de Narbonne
Bâtiment 2R1
31062 TOULOUSE Cedex 04, France
flahaut@chimie.ups-tlse.fr

Patrice Gadelle
Laboratoire de Thermodynamique et Physico-Chimie Métallurgiques (LTPCM)
UMR 5614 CNRS-INPG-UJF
ENSEEG
BP 75
38402 Saint Martin d'Hères, France
Patrice.Gadelle@ltpcm.inpg.fr

Catherine Gauthier
Groupe d'Etude de Métallurgie Physique et de Physique des Matériaux
(GEMPPM)
UMR 5510 CNRS-INSA Lyon
7 avenue Capelle
69621 Villeurbanne cedex, France
Catherine.Gauthier@insa-lyon.fr

Frank Hekking
Laboratoire de Physique et Modélisation des Milieux Condensés (LPMMC)
UMR 5493 CNRS-UJF
25 avenue des Martyrs
38042 Grenoble Cedex, France
hekking@grenoble.cnrs.fr

Jean-Paul Issi
Unité de Physico-Chimie et de Physique des Matériaux (PCPM)
Université Catholique de Louvain (UCL)
Place Croix du Sud, 1
(Bâtiment Boltzmann)
1348 Louvain-la-Neuve, Belgium
issi@pcpm.ucl.ac.be

Catherine Journet
Laboratoire de Physique de la Matière Condensée et Nanostructures
(PMCN)
UMR 5586 CNRS-Université Lyon I
43 boulevard du 11 novembre 1918
69622 Villeurbanne, France
cjournet@lpmcn.univ-lyon1.fr

Philippe Lambin
Facultés Universitaires Notre-Dame de la Paix (FUNDP)
Département de Physique
61 Rue de Bruxelles
5000 Namur, Belgium
philippe.lambin@fundp.ac.be

Pascale Launois
Laboratoire de Physique des Solides (LPS)
UMR 8502 CNRS-Université Paris Sud
Bât. 510
91405 Orsay Cedex, France
launois@lps.u-psud.fr

Christophe Laurent
Centre Inter universitaire de Recherche et d'Ingénierie des Matériaux (CIRIMAT)

UMR 5085 CNRS-Université Paul Sabatier
118 Route de Narbonne
Bâtiment 2R1
31062 TOULOUSE Cedex 04, France
laurent@chimie.ups-tlse.fr

Angel Linares-Solano
Departamento de Química Inorgánica
Universidad de Alicante
Apartado 99
03080, Alicante, Spain
linares@ua.es

Annick Loiseau
Laboratoire d'Etude des Microstructures (LEM)
UMR 104 CNRS-ONERA
BP 72
Avenue de la Division Leclerc
92322 Châtillon, France
annick.loiseau@onera.fr

Gilles Montambaux
Laboratoire de Physique des Solides (LPS)
UMR 8502 CNRS-Université Paris Sud
Bât. 510
91405 Orsay Cedex, France
montambaux@lps.fr

Marc Monthioux
Centre d'Elaboration des Matériaux et d'Etudes Structurales (CEMES)
UPR 8011 CNRS
BP 94347
29 rue Jeanne Marvig
31055 Toulouse Cedex 4, France
marc.monthioux@cemes.fr

Alain Peigney
Centre Inter universitaire de Recherche et d'Ingénierie des Matériaux (CIRIMAT)
UMR 5085 CNRS-Université Paul Sabatier
118 Route de Narbonne
Bâtiment 2R1
31062 TOULOUSE Cedex 04, France
peigney@chimie.ups-tlse.fr

Pierre Petit
Institut Charles Sadron
UPR 22 CNRS
6 rue Boussingault
67083 Strasbourg, France
Petit@ics.u-strasbg.fr

Jean Pinson
Alchimer
15 rue du Buisson aux Fraises
91300 Massy, France
jean.pinson@alchimer.com

Philippe Poncharal
Laboratoire des colloïdes, Verres et Nanomatériaux (LCVN)
UMR 5587 CNRS-UM2
Université Montpellier II
Place Eugène Bataillon
34095 Montpellier Cedex 5, France
Poncharal@gdpc.univ-montp2.fr

Philippe Poulin
Centre de Recherche Paul Pascal (CRPP)
UPR 8641 CNRS
Université Bordeaux I
Avenue Albert Schweitzer
33600 Pessac, France
poulin@crpp-bordeaux.cnrs.fr

Stephan Roche
Commissariat à l'Energie Atomique (CEA)
DSM/DRFMC/SPSMS
17 rue des Martyrs
38054 Grenoble, France
stephan.roche@cea.fr

Stéphane Rols
Laboratoire des colloïdes, Verres et Nanomatériaux (LCVN)
UMR 5587 CNRS-UM2
Université Montpellier II
Place Eugène Bataillon
34095 Montpellier Cedex 5, France
rols@gdpc.univ-montp2.fr

Jean-Paul Salvetat
Centre de Recherche sur la Matière Divisée (CRMD)
UMR 6619 CNRS-Université d'Orléans
1B rue de la Férollerie
45071 Orléans Cedex 2, France
salvetat@cnrs-orleans.fr

Jean-Louis Sauvajol
Laboratoire des colloïdes, Verres et Nanomatériaux (LCVN)
UMR 5587 CNRS-UM2
Université Montpellier II
Place Eugène Bataillon
34095 Montpellier Cedex 5, France
sauva@gdpc.univ-montp2.fr

Odile Stephan
Laboratoire de Physique des Solides (LPS)
UMR 8502 CNRS-Université Paris Sud
Bât. 510
91405 Orsay Cedex, France
stephan@lps.u-psud.fr

Jany Thibault
Commissariat à l'Energie Atomique (CEA)
DRFMC
17 rue des Martyrs
38054 Grenoble, France
jthibault@cea.fr

1

Polymorphism and Structure of Carbons

P. Delhaès, J.P. Issi, S. Bonnamy and P. Launois

Abstract. In this chapter, our purpose is to introduce carbon materials, situating the nanotubes inside this *polymorphic zoo*. We aim at giving the reader the basic notions on carbon materials structural and physical properties, necessary for the understanding of the following chapters. The introductory section gives a historical background about the peculiar carbon element and the numerous carbon materials which have been identified up to now. Then in a second part a classical thermodynamic approach is presented to describe the crystalline and non-crystalline forms of carbon, up to fullerenes and nanotubes. It is shown that the choice of the processing ways, including the crucial role played by the temperature, is fundamental to control the final type of material. In particular the different processes to prepare non-crystalline graphitic carbons are described in Sect. 1.3. Based on the texture symmetries different types of classical carbon materials are presented in relation with their numerous industrial applications. Then a general introduction is given concerning mainly the transport properties of the crystalline forms, including the intercalation compounds, but also their 'avatars' as pregraphitic carbons. In a final part, this panorama, which is going from the classical forms to the more molecular ones including nanotubes, is completed by the presentation of similar compounds. Starting from neighboring elements in the periodic classification we show that doped carbons and parent compounds present a similar polymorphism which enlarges this general introduction.

1.1 Historical Introduction

1.1.1 A Short Story of Carbon

Carbon is a singular element in the periodic table. It is not one of the most abundant on the earth and in the universe, around 0.20% in weight inside the terrestrial environment only, but it is fundamental for the living world. As pointed out by Primo Levi [1] it can bind itself, or to other light atoms, without a great expense of energy, giving rise to the organic chemistry and therefore to the biochemistry and the miracle of life on earth. Our interest extends also to the characteristics and properties of carbon as a solid and

P. Delhaès et al.: *Polymorphism and Structure of Carbons*, Lect. Notes Phys. **677**, 1–47 (2006)
www.springerlink.com
© Springer-Verlag Berlin Heidelberg 2006

subsequently as a material. We will present a short introduction about the natural and artificial forms of carbon. We will show that they have been used for human activity for a long time and that they are fundamental tools from astronomy to geology research areas.

– *The natural carbons as witnesses of the universe and earth histories.* Inorganic species and in particular carbonaceous ones are found in extraterrestrial environments as for example presolar grains in meteorites as diamond particles, and carbon type aggregates in interstellar dusts [2]. These astrophysical observations are noteworthy for elucidating the origin and the evolution of the solar system.

On earth the carbonaceous matter is relatively wide spread, in particular inside metamorphic rocks. It results from the transformation of organic matter under temperature and pressure effects. This diagenesis process gives birth to the family of kerogens and then, depending of these natural constraints, to natural gas, liquid or solid phases [3]. This progressive maturation is clearly dependent of the geological evolution and allows a geophysical approach powerful in petrology. In particular the presence of coal, graphite and diamond mines in different parts of the world gives a signature of these events.

– *The artificial carbons as a memory of the human evolution.* Acquaintance with coal would be synchronous with that of domestic fire; in prehistoric ages coal was used by man as a pigment to decorate the walls of his caves. During the Antiquity the most advanced civilizations have started to use different forms of artificial and natural carbons for their developments [4]. Two interesting examples are, firstly in the middle East, the discovery of carbon in metallurgy as reducing element to prepare metals or alloys from natural oxides (copper then iron), secondly in Egypt the use of active carbons to purify a liquid, water in general, or for medical purposes. During the middle age, Chinese have invented the black powder mixture containing coal, sulphur and saltpeter used for fireworks. Then this mixture was used on the whole planet for military applications around the fifteenth century. This is an outstanding example of alchemy, a science developed by the Arabs who gathered and developed ideas from the West (Greek heritage) and from Asian civilizations. Before the chemistry age, this knowledge was transferred to western Europe, where the discovery of the ultimate components of matter was elucidated with the advent of the atomistic concept.

1.1.2 The Carbon Element

The chemical background of the sixteenth and seventeenth centuries evolved at first time timidly, then with more and more boldness, until the advent of modern chemistry with Antoine Laurent Lavoisier at the end of the eighteenth century. In his memoir on combustion, Lavoisier clearly emphasizes the effect of carbon and all carbonaceous materials on air and he develops a theory of combustion which makes obsolete the so called phlogistic model [5]. All

these researches lead him to propose a system of nomenclature for chemistry described in his textbook published in 1789 'Traité élémentaire de chimie présenté dans un ordre nouveau et d'après les découvertes modernes'.

As reproduced in Fig. 1.1, the new classification of the elements is compared with the old one; the word 'carbon' is appearing in the middle of the table on which we can notice that real elements are mixed with other miscellaneous things. The development of this new and rational nomenclature was due to the efforts of many of his contemporaries, with in particular the creation of the chemical symbols necessary to represent the chemical reactions. But it was only one century later that the final classification of elements, proposed by Igor Mendeleev, was accepted by the whole chemists.

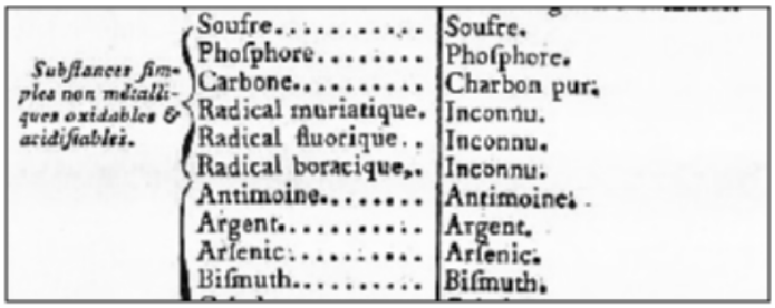


Fig. 1.1. Partial copy of the table of simple substances proposed by A.L. Lavoisier in 1789 [5]

During the nineteenth century an identification of the different forms of solid carbon progressively emerged with the diamonds and graphites as natural products. This progress has been associated with the concept of polymorphism which seems to appear for the first time in Mistscherlich's papers in 1822 [6]. Nowadays, a polymorphic system is providing two or more different crystalline environments in which the properties of a particular entity with different morphologies may be studied and compared. It must be noticed that the term allotropy is used in a similar manner but with a thermodynamic sense (see Sect. 1.2). To summarize the situation the best way is to cite Le Chatelier's book 'Leçons sur le Carbone' written one century ago [7], where the following statement is given 'Le carbone non combiné se présente sous des formes très curieuses: carbone amorphe, graphite et diamant' – 'uncombined carbon is found under very inquiring forms: amorphous carbon, graphite and diamond' (lesson 2, page 35). Soon after the discovery of the X-Ray diffraction in 1912, these two fundamental crystal structures i.e. cubic diamond and hexagonal graphite were identified (Bernal's work in 1922; see the atomic structures presented in Fig. 1.2).

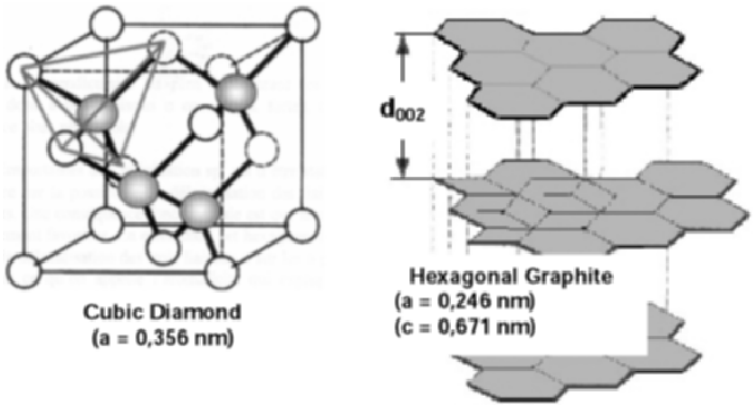


Fig. 1.2. Classical X-ray structures, at room temperature and under atmospheric pressure, of cubic diamond and hexagonal graphite (note the distance between graphitic planes $d_{002} = 0.335$ nm is equal to c/2)

1.1.3 New Forms

After the second world war, in the middle of the last century, further tremendous progress in the science of carbon has lead to unexpected and fascinating discoveries. The so called amorphous carbons, already quoted by Le Chatellier, were intensively studied as demonstrated by the numerous publications on the subject (see Sect. 1.3). Other forms of carbons have been evidenced which are extending this curious atomic polymorphism. One dimensional, chain-like polymers of carbon atoms were noticed by Russian scientists in the sixties and called carbynes, as recently described in a review paper [8]. In 1985, the discovery of a large family of spherical closed cage carbon molecules called fullerenes, including the basic molecule C_{60}, has added new excitements [9]. Then the latest discovery, so far, is a curved form of graphene (graphene refers to an atomic layer of graphite): by accurate transmission electron microscopy (TEM) a tubular form of carbon, called single-walled nanotube (SWNT) has been seen by Iijima, Bethune and co-workers in 1993 [10, 11]. It must be noticed that several nanotubular forms made with rolled sheets of graphene have been evidenced several times before this ultimate monolayer form came on, as early as in 1953 [12], but also in 1991, on the basis of precise electron microscopy analyses, leading to a strong renewal of interest in the field [13]. In general, these hollow tubular multisheet morphologies are called multiwalled nanotubes (MWNT). From these discoveries it turns out that a convenient classification scheme will be useful to understand all these forms and to predict new ones [15].

1.1.4 Basic Concepts: Orbital Hybridizations and Coordination Number

The advent of quantum mechanics at the beginning of the twentieth century has been the novel paradigm to understand the chemical bonding between atoms. It has been shown that the phenomenon of electronic hybridization can lead to several types of covalent bonding. Without going into any details, the linear combination of s and p atomic orbitals leads either to σ-type orbital (with a cylindrical symmetry along the internuclear axis) or a π-type orbital (with a nodal plane including the molecular axis). The orbital hybridization allows us to introduce two essential parameters for classifying the different forms ($1s^2$, $2s^2$, $2p^2$ electrons) as presented in Table 1.1. The relevant parameters are respectively the coordination number of a given atom ($z = 2, 3, 4$) and the lattice dimensionality ($D = 1, 2$ or 3) within the associated topological approach. For the fullerenes and nanotubes, because of the surface curvature, a rehybridization process including a certain amount of σ character in a π-type orbital changes both its chemical and physical characteristics [14].

Table 1.1. Schematic classification of the different forms of carbon

Crystalline Form	Diamonds	Graphites	Carbynes*	Fullerenes, Nanotubes
Hybridization	sp^3	sp^2	sp^1	$sp^{2+\epsilon}$
Coordinance z	4	3	2	3
Physical dimensionality D	3	2	1	0 and 1
Bond length (Å)	1.54	1.40	1.21	1.33 to 1.40
Bond energy (eV/mole)	15	25	35	> 25

* Also mixed sp^1 and sp^3 hybridizations (α form)

The energy of the chemical bonding is always high, indicating a strong cohesive energy and valuable structural properties; a simple type bonding allows us to characterize the structural, mechanical and thermal properties, whereas the presence of π orbitals will be crucial for electronic and magnetic properties.

1.2 Polymorphism of Crystalline Phases

1.2.1 Thermodynamic Stability and Associated Phase Diagram

The various allotropic forms of elemental carbon are known as thermodynamically stable and metastable phases. Based on a phenomenological approach, the point is to define a coherent phase diagram, and then to control the reaction dynamics between the phases over a wide range of temperature and pressure (T and P), including the reaction conditions [14].

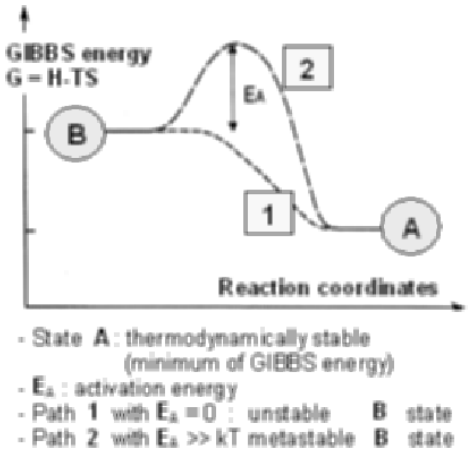


Fig. 1.3. Schematic representation of the Gibbs energy change —ΔG— between a thermodynamically stable state A and a metastable one B, where E_A is the involved activation energy (from Delhaès [15])

A stable thermodynamic state is associated with the absolute minimum of Gibbs free energy ($G = H - TS$, where H and S are respectively the enthalpy and the entropy state functions) expressed as a function of P and T in the absence of any chemical reaction. The existence of a local minimum will induce the possibility of a metastable state. The probability of a phase transformation is determined by the Gibbs free energy difference ΔG between the two considered states and the possible thermodynamic paths between them (see Fig. 1.3). Two main types of situations are observed depending of the activation energy (E_A) involved in the process. Firstly the phase transformation between two thermodynamic states is governed by the absence of any sizable activation energy (path 1 on Fig. 1.3), state B will be an unstable state, difficult to observe. Secondly, if E_A is larger than the thermal energy ($\mathrm{k}T$), this energy barrier will create a local minimum on the energy surface leading to the presence of a quenched kinetic state (path 2 on Fig. 1.3). This second situation is favored in presence of large binding energies and high associated cohesion energy as found in solid carbons (see Table 1.1). A large amount of activation energy is necessary, i.e. high temperatures and high pressures are essential to initiate a phase transition, which can be modified thanks to the presence of a catalyst. Indeed the activation energy can be lowered with a transition metal used as a catalyst, which modifies the kinetics but not the final state in principle. This approach is largely used to prepare the different forms of carbon and in particular nanotubes (see Chap. 2).

The thermodynamic phase diagram of the carbon element has been established after several decades of experimental works [16], as presented in Fig. 1.4. This (T,P) general presentation is representative of the different allotropic forms. Firstly the stable thermodynamic phase under ambient conditions is

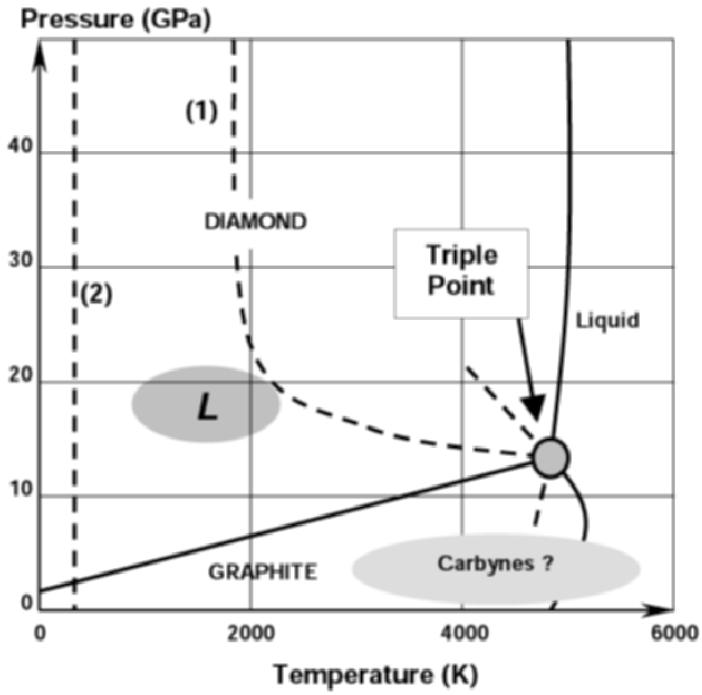


Fig. 1.4. Thermodynamic phase diagram of the carbon element. *Solid lines* represent equilibrium phase boundaries and *dotted lines* the kinetic transformations; L is for Lonsdaleite phase (adapted from Bundy et al. [16])

the hexagonal graphite (with the existence of a polytype, a rhombohedral variety under metastable conditions). Secondly the cubic diamond phase is stable under high pressures and only metastable at room temperature under atmospheric conditions; an hexagonal phase known as Lonsdaleite is found under specific conditions (see Fig. 1.4). Thirdly the carbyne phase should exist at high temperature, below the melting line of graphite.

This phase diagram presents several salient features:

- The transition line, at equilibrium, between the graphite and diamond stable regions runs from 1.7 GPa at zero Kelvin to the graphite-diamond-liquid triple point I at 12 GPa/5000 K.
- A classical triple point should exist at a lower pressure with the coexistence of solid, liquid and gas (not presented here) phases with the possible presence of two liquid phases, as predicted by molecular dynamics simulations [17], which is an additional complication.
- The dotted line 1 represents the graphite-diamond kinetic transformation under shock compression and quench cycles; it should be noticed that catalytic phase transformations are also real processes.

– The melting line of diamond runs at high P and T, above the triple point I with a positive slope, associated with the research of other possible novel phases.

To finish this presentation it is noteworthy to point out that all the phase transformations are considered as theoretically reversible. Under this frame it does not appear evident to include in the same diagram the new molecular carbon phases, fullerenes and nanotubes which are not classical extended solids but can form themselves crystalline structures.

1.2.2 Theoretical Approaches and New Predicted Phases

A topological classification of the allotropic forms of solid carbons is based on the coordination number (z) and the spatial occupation of the coordinated sites. We will divide them in two classes either with a constant z, three- or four-fold coordinated sites as in diamonds and graphites, or a combination of them, as developed elsewhere [15].

During the last decade theoretical models have been developed to predict new forms of carbon and related materials with specific properties [18]. These models are based on the calculation of the excess of cohesion energy at zero Kelvin, i.e. the enthalpy, using an equation of state for an isotropic solid phase. One essential parameter is the bulk modulus B_0, defined as

$$B_0 = -V_0 \left(\frac{\mathrm{d}P}{\mathrm{d}T} \right)_{T \to 0} \tag{1.1}$$

A useful semi-empirical expression has been proposed by Cohen [18]:

$$B_0 = \frac{Nc}{4}(1972 - 220\lambda)d^{-3.5} \tag{1.2}$$

where Nc is the average coordination number of the compound considered, d the average bond length λ is an ionization factor which is zero for pure carbons. It is clear from this relation (1.2) that short bond lengths d associated with a large bond energy (see Table 1.1) are the best for getting a large compressibility factor and consequently a high cohesion energy. Indeed the highest density of strong covalent bonds will lead to super hard compounds associated with low compressibility factors. Diamond is such material and the quest for ultra-hard compounds has been the motor for this research together with the dream to combine the metallic characteristic of graphite with the hardness of diamond. A few examples are quoted in the followings:

– *Fourfold coordinated structures*: it has been calculated that as a function of the unit cell volume, five different metastable phases could be expected [19]; in particular a simple cubic phase and a body centered cubic structure (called H6) have been predicted [20] but not found experimentally.

– *Triply coordinated structures*: new metastable phases have been proposed, which consist entirely of threefold coordinated atoms in a rigid three-dimensional lattice; for example, an original structure was suggested by Hoffmann et al. [20], which consists of buckled layers of carbon chains joined by bonds parallel to the c-axis; this type of phase is supposed to be metallic because of the presence of π electrons [21] but nobody has been able to prepare such phase so far.
– *Exotic structures with variable coordination numbers*: an alternative approach has been to predict new forms of carbons with $z = 2$ and 3 or 3 and 4. These (2–3) carbon nets would present an intermediary between carbynes and graphenes with rings containing a variable number of carbons and planar structures [22]. Alternatively (4–3) connected nets with trigonal and tetragonal atoms would give an intermediary valency between graphite and diamond [23]. One interesting example results from the polymerization of C_{60} under pressure (see next paragraph), where a crystal structure considered as a mixture of sp^2 and sp^3 orbitals has been published [24]. In spite of several attempts, no effective syntheses have been realized and the description of these virtual forms will not be pursued here.

1.2.3 Structures on Curved Surfaces

In the new molecular phases such as fullerenes and nanotubes, the importance of the surface energy is large, including the edge of finite graphene sheets that contain dangling bonds. The total cohesion energy can be decreased by curving the sheets and forming closed structures as spheres and cylinders, playing with the number of carbon atoms involved in an aromatic ring.

A topological classification for curved surfaces, in non-Euclidian geometry, as proposed by Schwarz [25] a long time ago, allows us to classify these surface varieties. A simple approach is to define a mean and a gaussian curvatures (H and K) proportional to the inverse of a length and a surface, respectively. As proposed by Mackay and Terrones [26], the following geometrical shapes may exist:

– $K > 0$ (spheres) as fullerenes
– $K = 0$ (planes or cylinders if $H = 0$), as nanotubes
– $K < 0$ (saddle): 'Schwarzites'.

As presented in Fig. 1.5, these different forms exist or have been proposed in the case of the graphene type structure presenting a negative gaussian structure. This curvature is made possible by introducing seven or eight member rings in addition to the usual six member for planar surfaces. The same holds for a positive curvature owing to a five member ring (case of C_{60}). In fact these negatively curved carbon networks belong to the class of periodic minimal surfaces and they have been called 'Schwarzites' [25]. In spite of different attempts, these big unit cells (see one example in Fig. 1.5), which are also considered as possible metastable phases, have not been observed experimentally [26].

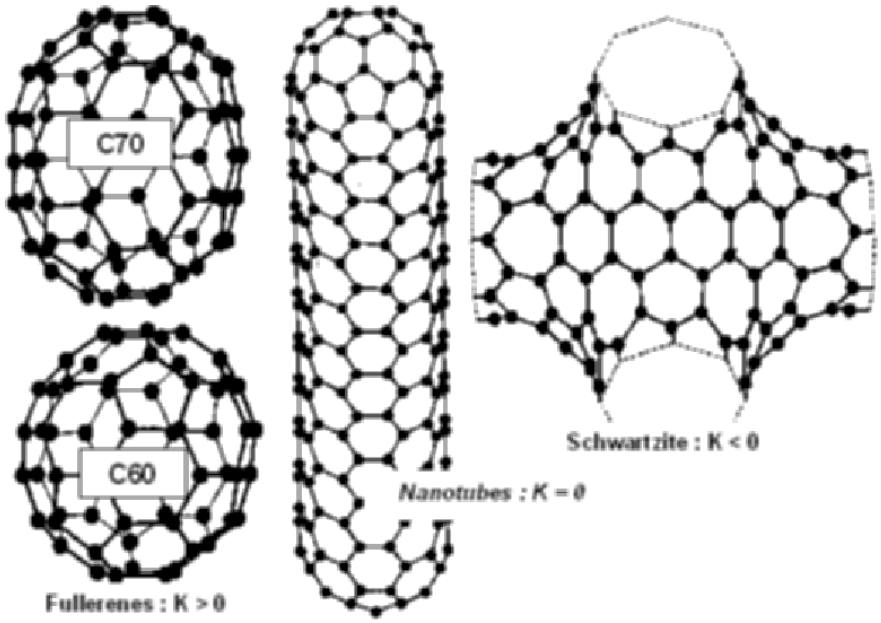


Fig. 1.5. Examples of curved graphene varieties classified through their gaussian curvature K, as defined in the text (from [15])

At the opposite, following the discovery of C_{60} in 1985 [9], many studies have concerned these molecular forms called 'fullerenes'. The sixty carbon atoms form a truncated icosahedron, a platonic polyhedron which obeys Euler's theorem considering that the pentagons should be isolated [27]. Because of its high molecular symmetry C_{60} has attracted a large interest both in chemistry and physics. Two points have to be mentioned here; firstly larger molecular weight fullerenes have been isolated (C_{70},C_{76},C_{78},C_{82}, ...), up to multi-shell onion like nanoparticles, which are the intermediate towards the classical carbon soots. Secondly, by combined pressure-temperature treatments of C_{60}, several interesting crystalline phases have been characterized [28,29]. As presented in Fig. 1.6, a tentative (P, T) phase diagram has been established, based on several works; under pressure a dimer phase is prepared but trimers and oligomers are also obtained and they give birth respectively to chain like, planar and three-dimensional structures; orthorhombic (O), tetragonal (T) and rhombohedral (R) phases have been identified. Among these new phases, we can notice the claim for a room temperature ferromagnetic state in the rhombohedral state [30], as indicated in the phase diagram (Fig. 1.6). Indeed this research field is surely one of the most promising for discovering interesting properties on new metastable phases with the quest for super hard materials under very high pressures [31].

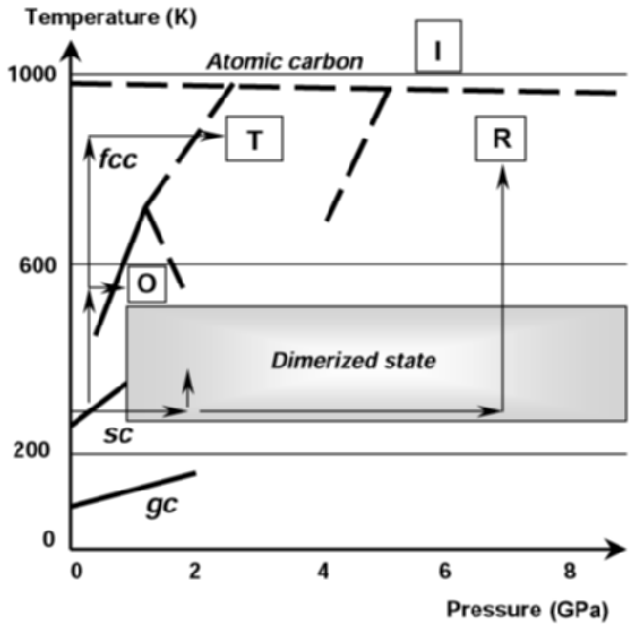


Fig. 1.6. (P,T) phase diagram of pressure polymerized phases of C_{60}; the arrows show P and T paths starting from the C_{60} glass (gc), simple cubic (sc) or face-centred cubic (fcc) phases respectively (adapted from [28])

1.2.4 Carbon Nanotubes: Structures and Defects

The crucial role of the carbon orbital hybridization and coordination number has been introduced in Sect. 1.1.4. Infinite single-walled nanotubes are seamless cylinders at the surface of which carbon atoms are organized in a honeycomb lattice. Their coordination number is three ($z = 3$) and the surface curvature induces some s-p hybridization. Moreover, carbon nanotubes (NT) are one dimensional systems which present specific, original structure-properties relations, that will be the subject of Chaps. 4 to 8. Our aim now is thus to give the reader the basic notions on carbon nanotubes geometrical properties.

SWNTs can be ideally constructed starting from a graphene sheet, and rolling it. This construction allows one to characterize the NT structure with a pair (n,m) of integers. These indices define the so-called 'chiral vector':

$$\overrightarrow{C} = n\overrightarrow{a_1} + m\overrightarrow{a_2} \tag{1.3}$$

which joins two crystallographically equivalent sites of the nanotube on the graphene sheet, $(\overrightarrow{a_1}, \overrightarrow{a_2})$ being the graphene basis [32] where $a = |\overrightarrow{a_1}| = |\overrightarrow{a_2}| \approx$

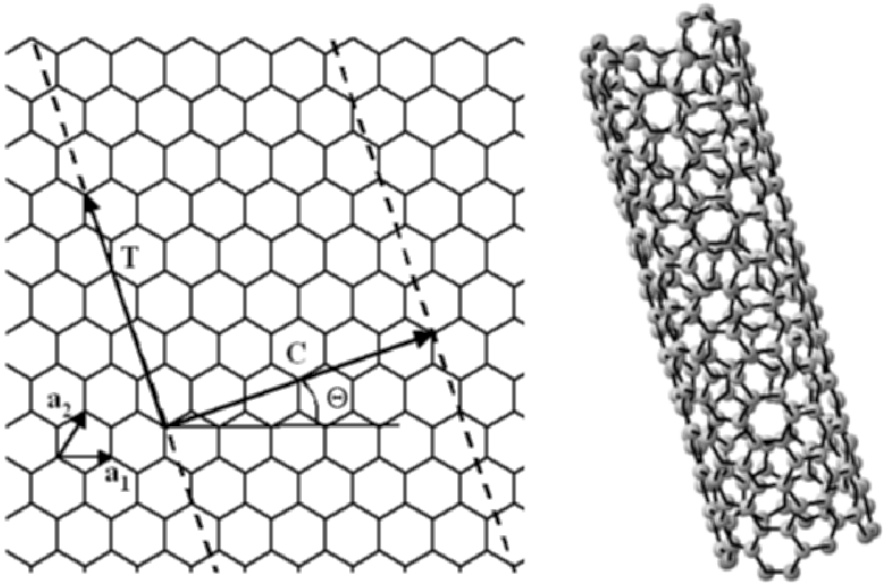


Fig. 1.7. *Left*: the principle of nanotube construction from a graphene sheet. *Right*: example of a nanotube

2.49 Å. The nanotube is obtained by cutting a ribbon of perpendicular basis $\overrightarrow{C}$ in the sheet and by rolling it up, as is shown in Fig. 1.7 [33,34]. One easily demonstrates [35] that the tube circumference writes:

$$C = |\overrightarrow{C}| = a\sqrt{n^2 + m^2 + nm} \tag{1.4}$$

and that its period along the long axis is:

$$T = a\sqrt{t_1^2 + t_2^2 + t_1 t_2} \tag{1.5}$$

with $t_1 = -(2m+n)/d_R$ and $t_2 = (2n+m)/d_R$, d_R being the greatest common divisor of $(2m+n)$ and $(2n+m)$. The hexagons orientation on the tube surface is characterized by the angle θ, named the 'chiral angle':

$$\theta = \arctan(\sqrt{3}m/(2n+m)) \tag{1.6}$$

In summary, nanotube structural characteristics are all deduced from n and m values. Due to the six-fold symmetry of graphene, these values can be restricted to $-\frac{n}{2} < m \leq n$. All tubes are chiral except the (n,n) 'armchair' tubes ($\theta = 30°$) and the $(n,0)$ 'zig-zag' tubes ($\theta = 0°$). The electronic structure of nanotubes is strongly dependent of their diameter and chiral angle, as will be shown in Chap. 4.

Single-walled nanotubes are rarely found as isolated specimens. They usually assemble in bundles [36] to minimize their energy through van der Waals

interactions. Nanotube diameters are rather homogeneous within a bundle. However, they often present a wide distribution of chiral angles [37] except for some specific production methods [38]. Nanotubes can also be obtained as multiwalled nanotubes, which are concentric SWNTs. The interlayer tubule is about 3.4 Å, that is almost the inter-sheet distance in hexagonal graphite (see Fig. 1.1). The periods of each tubule of a MWNT can be commensurate or not, the second case being the more frequent.

Furthermore, real NTs are far from being exempt of numerous local defects. Carbon atoms can form a pentagon instead of a hexagon, as was found in fullerene molecules inducing locally a positive curvature. Such defects are thus involved in cap nanotube closure whereas heptagons will induce a negative curvature. Appropriate associations of pentagons and heptagons allow one to connect tubules of different diameter and/or chiral angles [39,40] and to obtain electronic junctions. A peculiar combination of pentagons and heptagons, the typical Stone-Wales defect [41], is of strong interest also because it is involved in nanotube formation processes [42] and because it plays a special role with respect to mechanical properties [43], as it will be discussed in Chaps. 2 and 7.

Finally, to end this introduction about NT structure, one should mention that other carbon nano-objects have also been found to exist since the discovery of cylindrical carbon nanotubes – our school case. One may cite for instance different morphologies such as the scrolled MWNTs [44], MWNTs and SWNTs with polygonal cross sections [45–48], nanocones [48], nanohorns [49], coils [50] and even torii [51].

1.3 Non-Crystalline Carbons

1.3.1 Definitions

As already identified one century ago [7], the non-crystalline forms are existing when the involved atoms in the solid are bonded by either sp^2 or sp^3 orbitals or even a mixture of them (see Table 1.1). In such a case no long-range spatial order is detected but the local atomic arrangement presents different forms. As demonstrated by numerous authors, different structural types are found which are very dependent of the processing way. A phenomenological classification has been proposed, based on the choice of the pristine phase and the technical supply of the excess free energy, involving both chemical reactions and physical parameters as temperature or pressure [52]. Different metastable non-crystalline phases are obtained which are different from those already described as allotropes (see Sect. 1.3.2). In that case, the excess free enthalpy is mainly due to the increase of the entropy term. These materials, also called pseudo-polymorphic carbons, present specific structural and physical properties. At first glance they are divided in two main sub-classes, depending of the experimental conditions, amorphous diamond-like carbons

similar to a glass and involving essentially fourfold coordinated atoms or variable microcrystalline compounds constituted with π-type orbitals [53]. The vast majority of non-crystalline carbons falls in the category of pregraphitic types involving more or less developed aromatic systems which are considered as the basic structural units (BSU) [54]. Usually the standard way, starting from a natural or an artificial organic precursor implies the heating process under an inert atmosphere to prevent any oxidation or combustion. This thermal evolution is characterized by the highest treatment temperature (HTT) which is a very convenient parameter to define the evolutionary stage of a pregraphitic carbon. Usually the following different steps are recognized [54]: the pyrolysis of the organic matter below 1000°C, then the primary and secondary carbonizations between 700−1000° and 2000°C, where all the other hetero-elements as hydrogen, nitrogen and oxygen have been eliminated, and finally the graphitization stage, between 2000° and 3000°C, where in principle the long range organization of hexagonal graphite should be reached. It is noteworthy that by heating around 3000°C the three-dimensional crystalline state of the graphite, which is the thermodynamic stable phase (see the phase diagram Fig. 1.4), is obtained in the case of so-called graphitizing or soft carbons. It appears however that non-graphitizing or hard carbons are recognized when a topological layered disordered state is still present after this HTT process. This different behavior is related with the type of organic precursor involving in particular its chemical composition [54].

1.3.2 Textures Symmetries in Carbon Materials

These non-crystalline forms of carbon are indeed multi-scale materials which need to be described at different levels. The first one is the atomic level because the carbon atoms can present several coordination numbers (see Table 1.1), which imply different local symmetries, in particular the planar one when aromatic systems which are very stable are involved. Usually, different textures are described that we summarize now. At the end of the primary carbonization, condensed poly-aromatic units are formed, so-called BSU. Then during the secondary carbonization, a more or less developed coalescence of these units occurs forming nanoscale crystallites defined by their mean in-plane size (L_a) and stacking thickness (L_c) of these turbostratic (non-planar) sheets, characterized by the mean interlayer distance d_{002} which is larger than in graphite. At a larger scale which can reach the micrometer or even the millimeter range, the local molecular ordering (LMO) is related with the lamellar arrangements of these turbostratic planes. The development of this long-range order is strongly connected with the chemical composition of the precursors and the nature of the initial phase; in particular the presence of an intermediary fluid phase which behaves as a liquid crystal is observed: this is the carbonaceous mesophase [55]. A huge variety of morphologies are obtained following either a plastic or liquid precursor, or even a gaseous one [56]. All these morphologies are issued from the self-associations (LMO) of

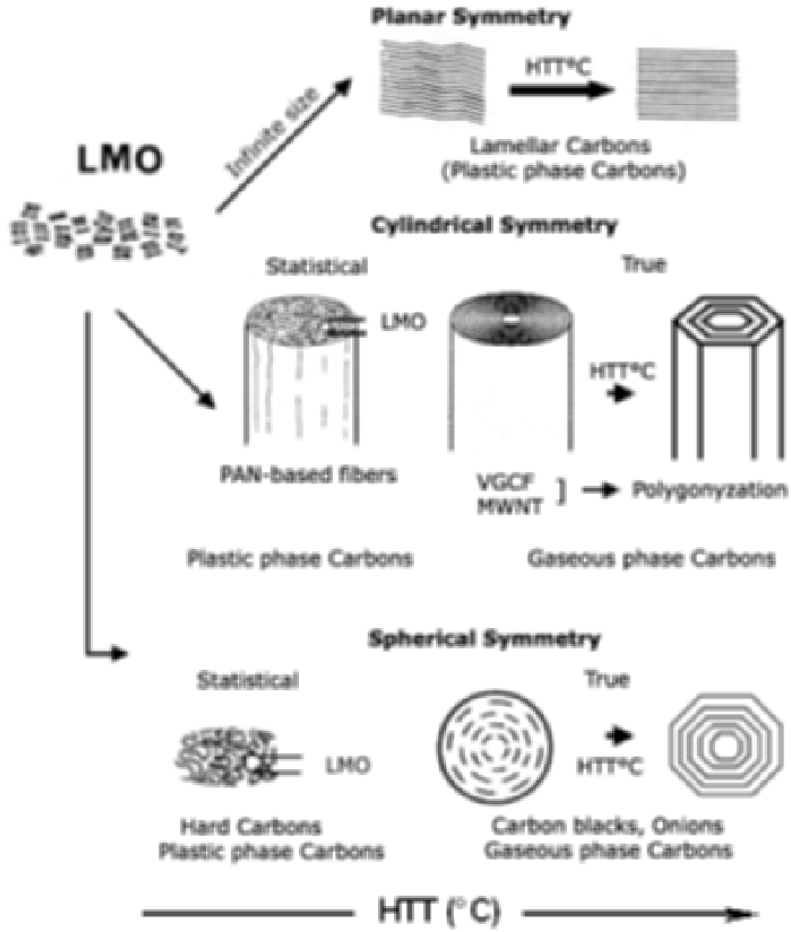


Fig. 1.8. Textures of typical carbon materials based on the preferred orientation of basic structural units (BSU) and local molecular order (LMO) and evoluting under HTT (adapted from Inagaki [57])

nano-entities (BSU) differently arranged in space [57], as presented in Fig. 1.8, where the symmetry argument is leading to the formation of carbon textures at different scales. To characterize these materials several structural techniques have been developed and used. They are statistical ones as X-ray scattering and the topological techniques as optical microscopy under polarized light or scanning tunneling microscopy (STM). Scanning electron microscopy (SEM) for micro textures and joined to transmission electron microscopy (TEM), including electron diffraction for nano-textures [56] are also powerful tools.

1.3.3 Textures Resulting in Plastic or Liquid Phases

Such processes correspond to thermal conversion of various precursors such as kerogens, coals, oil derivatives (refinery residues), asphaltenes, tars, pitches, actually described as organic macromolecules. Being thermally activated, they depend on temperature, pressure and time; they start from room temperature to 2000°C (primary then secondary carbonization) or more, and the involved kinetics spreads over several hours. In nature, coalification temperature never exceeds 1000°C due to the geothermal gradient, which is pressure dependent and extends over geological times. During this process, the carbon precursor transformations occur at first through the macromolecule breakage leading to the formation of nanometric aromatic units [55,56]. These elemental units were evidenced in precursors by X-ray diffraction (so-called WAXS, SAD, μD, ...) as well as by imaging techniques (HRTEM, STM, ...) and consist of stacks of polyaromatic molecules piled-up by two to three entities, less than 1 nm in diameter and with an interlayer spacing ranging from 0.50 to 0.36 nm. An illustration (high resolution (002) Bragg reflection obtained from dark-field TEM image) is given in Fig. 1.9a and insert, where BSU seen edge-on appear as bright dots, homogeneously dispersed at random in the precursor. Molecular mechanics calculations [58] determined that the more stable face to face aromatic molecules association is got with at least the size of coronene (Fig. 1.9b) and dicoronene, they represent the smallest possible polyaromatic brick of aromatic layer stacks. On the other hand, the largest size values given by TEM for BSU never exceed diekacoronene. Furthermore, chemical models based on the concept of colloids indicate that BSU edges are saturated by various side chains (aliphatic, ...) or functional groups depending on the precursor elemental composition, thus increasing their steric hindrance. At that stage the representation of the organic matter is consistent with a highly viscous liquid or a gel in which the continuous phase is formed by alkyl chains cross-linked via the BSU. During further thermal evolution, hydrocarbons release as volatiles, thus aromatic units self-associate into locally oriented orientations (LMO) or liquid crystals of various domain sizes (from 5 nm up to 50 µm) related to the precursor composition [55].

– *Lamellar carbons and films*
  During primary carbonization of precursors devoid of cross-linker atoms, liquid crystals, known as Brooks and Taylor mesophase spheres, demix [59]. In this peculiar phase, BSU have a columnar arrangement. With thermal treatment, the mesophase spheres coalesce up to solidification, and the material is thus made of oriented anisotropic domains (under the form of anisotropic bands in optical microscopy), where aromatic layers are oriented in parallel over large domains limited by disclinations randomly distributed. Such a large LMO which has a statistical planar symmetry will provide lamellar carbons (such as pitch-based materials) when they are deposited on a planar substrate (Fig. 1.10a) [54].

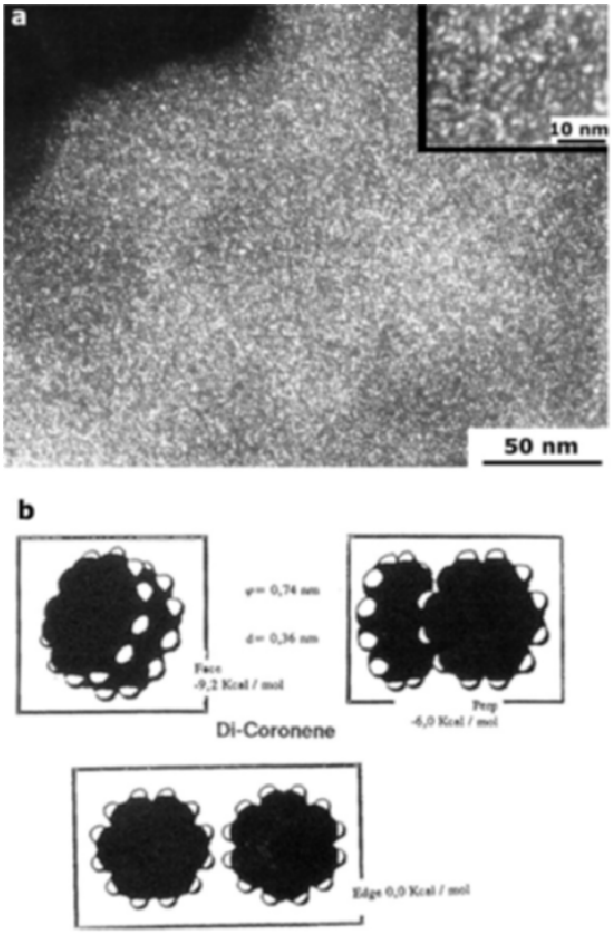


Fig. 1.9. (**a**) TEM imaging of BSU (002 dark field technique), each bright dot is a BSU seen edge on [56]. (**b**) Sketches of dicoronene [58]

– *Porous bulk carbons*
In the case of precursors, such as oil heavy products, asphaltenes, kerogens, coals, ..., the size of the liquid-crystal phases occurring during carbonization decreases with an increasing amount of cross-linking atoms, mainly oxygen, in the materials. They appear as mesophase spheres of decreasing ordering and size (of about 1 µm down to 200 nm) or oriented volumes limited by digitized contours (from 200 down to 5 nm) [60]. This association of BSU into LMO is favored by the bubbles due to volatile release. LMO diameter, determined by the size of the liquid crystals, delimits the pore diameter in the solid state after carbonization (Fig. 1.10b). The more cross-linked the materials are the smaller are the pore sizes. This process leads thus to porous carbons which present a statistical spherical symmetry at

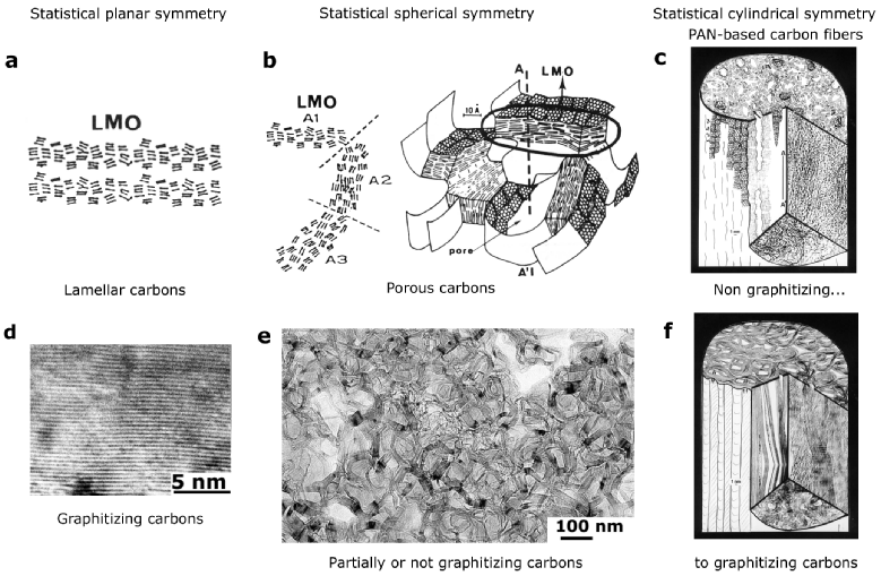


Fig. 1.10. Drawings and photographs of oriented textures with different statistical symmetries for examples of graphitizing or non-graphitizing carbons

the microscale in the microporous carbons (asphaltenes and oil derivatives) and at the nanoscale in the case of nanoporous ones as for hard carbons.

– *Carbon fibers*
When the thermal conversion of an organic filament is performed under uniaxial stress, a statistical cylindrical symmetry is produced leading to carbon fibers. Different types of precursors are used [61] as coal or petroleum pitches in isotropic or mesophasic phases, cellulosic natural matter or artificial one as polyacrylonitrile (PAN). In general the LMO and pores are elongated parallel to the fiber axis (Fig. 1.10c). Here the pore size also decreases with LMO, from pitch-based to PAN-based fibers. Only PAN-based carbon fiber synthesis and characteristics will be shortly described here because they represent more than 90 per cent of the manufacturing processes. As other organic carbonaceous matter, PAN-based fiber synthesis takes place in plastic phase. At first a precursor made of acrylonitrile associated with various co-monomers is polymerized and wet-spun under tension. Cyclization leads to a ladder polymer which is oriented along the fiber axis. The stabilization step, performed under warm air between 200 and 300°C still under stretching, corresponds to oxygen fixation (cross-linking), preventing melting and responsible for giving after graphitization treatment a non-graphitizing microporous carbon. The carbonization step is done in continuity with stabilization but without stretching and under nitrogen allowing to obtain high tensile strength fibers. The stabilization and carbonization steps are marked at first by aromatization, where BSU are formed, then by formation of the carbon skeleton (rigidification) which corresponds to self-associations of BSU into LMO. LMO occurrence corresponds to the maximum of dehydrogenation, after that the BSU edges are only saturated with CH aromatics, oxygen and nitrogen insuring a certain flexibility to aromatic layers and deleting their coalescence into continuous layers. During further carbonization, nitrogen is eliminated by the Watt mechanism, which creates lateral bonding [62]. The model of high tensile strength (HTS) fibers (Fig. 1.10c), based on nanostructural values measured on longitudinal and transversal thin sections, corresponds to that of a porous carbon to which stretching was applied along the fiber axis. LMO are arranged in strongly distorted and entangled sheets including pores elongated along this axis. Since the radius of curvature of the crumpled layer stacks is very small and the sheets made of BSU are very defective, the lateral cohesion is strong. Hence the tensile strength is high and Young's modulus E is relatively low (see Subsect. 1.3.5 for typical values). High modulus (HM) PAN-based fibers (Fig. 1.10f) are obtained from HTS ones after heat-treatment at or above 2000°C under nitrogen. After thermal treatment curvatures of the layers are maintained instead of polygonization due to the presence of stable disclinations, so the carbon is non-graphitizing, i.e. there is no occurrence of a three dimensional order. BSU contained in LMO coalesced into distorted continuous layer stacks. The entangled sheets,

parallel to the fiber axis, are oriented at random and bound from place to place by their defective areas (Fig. 1.10f). Since the sheets are better organized, have less defects, and therefore less lateral bonding and cohesion, their tensile strength decreases. But since the stacking order and the diameter (L_a) measured along the fiber axis increase, the fibrous orientation improves and Young's modulus increases (see paragraph 1.3.5).

– *Graphitization step*
For the materials sketched in Fig. 1.10, the end of thermal conversion to pure carbon (end of carbonization) is marked by the annealing of all defects present between BSU inside each LMO. It provides at first distorted and wrinkled aromatic layers and then at about 2000°C dewrinkled and flat layers. As a result the pores become polyhedral with flat faces (Fig. 1.10e). All the carbonaceous materials follow the same graphitization process but the final degree of graphitization reached at 3000°C is predetermined entirely by the size of the LMO acquired during the carbonization step. At 2000°C all carbons are still turbostratic, i.e. they are finite two-dimensional crystals; during further heat-treatment in the range 2000–3000°C, the lamellar carbons having statistical planar symmetry (Fig. 1.10d) are able to progressively graphitize approaching three-dimensional crystalline order of graphite. This transformation is not due to the growth of localized crystallites. It is a statistically homogeneous process [63] progressing with thermal treatment with an increasing probability P of finding a pair of graphitic carbon layer stacked as in hexagonal graphite (see Fig. 1.2). When P is equal to one, three-dimensional order is achieved as observed by the decrease of the mean interlayer distance d_{002} which is reaching the single-crystal value. This is evidenced by a sudden plasticity change from fragile to ductile during mechanical tests at high temperature (Fig. 1.11) [64]. When the LMO are less and less extended, i.e. when the symmetries of textures are reduced from planar to spherical and cylindrical ones (Fig. 1.10b and c), due to the geometrical constraints, the reorganization remains limited without getting perfect 3D order, and the graphitizability progressively decreases ($0 < P < 1$). This leads to partially graphitizing carbons [56] (oil derivatives carbons, pitch-based carbon fibers for example) down to turbostratic non graphitizing carbons (hard carbons such as glassy carbons or even PAN-based fibers). P is directly connected to the thickness of the carbon layer stack (L_c) determined through ($00l$) Bragg reflections [65].

1.3.4 Textures Resulting of Process in Gaseous or Vapor Phases

– *Pyrocarbons and pyrographites* [66–68]
Pyrocarbons are bulk carbon deposits obtained by dehydrogenation of a gaseous hydrocarbon (mainly CH_4) on a hot planar substrate (chemical vapor deposition or CVD). Such deposits are usually employed to densify porous materials such as fibrous preformed by infiltration (chemical vapor infiltration or

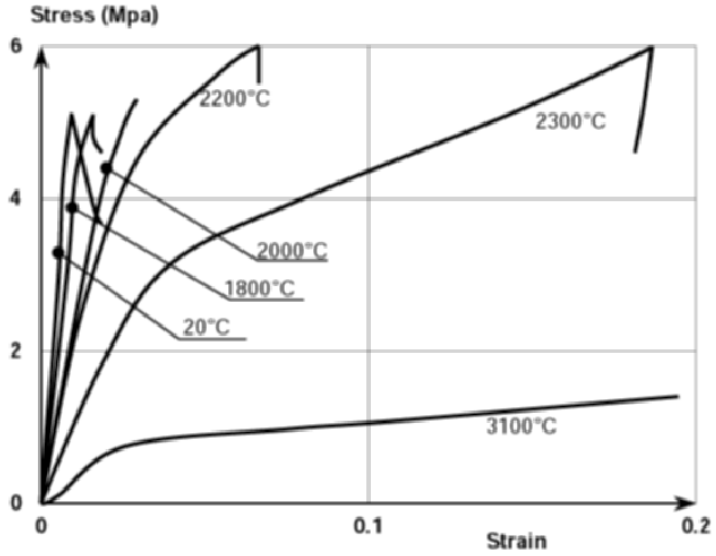


Fig. 1.11. Stress-strain curves obtained from tensile measurements on ex-mesophase fibers measured at different temperatures [64]

CVI), so as to make carbon/carbon composites. The deposition temperature ranges from 900 up to 2000°C; at high temperatures and under high pressure an highly oriented pyrographite can be directly prepared (HOPG) which is a mosaic of single crystals [69]. As a rule in pyrocarbons, the carbon layers tend to deposit more or less parallel to the substrate surface. They are usually classified by their increasing crystallite misorientation. As observed in the liquid phase, the better oriented pyrocarbons have a statistical planar symmetry providing lamellar graphitizing carbons such as so-called rough laminar ones (RL Pyc). The optical phase shift is large indicating a good orientation of the layers as verified by TEM experiments [70]. As in the liquid phase when misorientation of the layers increases, pores of decreasing size are produced ending as nanopores of spherical statistical symmetry. These pyrocarbons, called smooth laminar or isotropic, are optically more or less isotropic and they behave as hard carbons. Since the path from planar to spherical symmetry depends on layer misorientation, the classification of pyrocarbons is usually based on misorientation measurements at different scales. Various ways are used to measure it, based either on the determination of the value of the phase shift, or of the extinction angle by rotation of one of the polarizers or at the nanometer range on the value of the opening of the 002 diffraction arc which increases with the BSU misorientation [70]. As in the plastic phase, the graphitizability of pyrocarbons decreases progressively from rough laminar (where $P_{max} = 0.8$) through intermediate textures (where P ranges from 0.7 to 0.2) down to isotropic one ($P = 0$). The heterogeneous nucleation and growth of pyrocarbons is a complicated process since many reactions occur

in competition [68]. Homogeneous reactions are produced in the gas phase providing larger associations of carbon atoms as the residence time increases. This is the maturation effect (from C2 to C3...C6 and polyaromatic hydrocarbons, the PAHs). Simultaneously heterogeneous reactions at the contact with the substrate are produced, they are not well known but fundamental, for lack of surface studies at the nanoscale. The only experimental certainty is the fact that pyrocarbons are never the result of entirely homogeneous reactions. Any nano-rugosity or the presence of peculiar active sites on the substrate locally changes the nature of deposited pyrocarbons [66]. Different models have been proposed and are currently examined to explain the formation of rough laminar pyrocarbons, the best one for applications including thermal and electrical conductivities and also mechanical behavior [67].

– *Vapor-Grown Carbon Filaments (VGCFs)* [61]
VGCFs are obtained by decomposition of hydrocarbons such as benzene or methane at temperatures around 1100°C over catalytic metal particles. These catalytically grown filaments have been known for a long time [71, 72] with their diameter controlled in the range from 10 nm to more than few 100 µm by playing on the growth conditions. Indeed the VGCFs formation results of a two-step growth: at first a catalytic decomposition of hydrocarbons leads to a thin-walled hollow core, either single-walled or multiwalled nanotubes, then thermal decomposition of hydrocarbons allows thickening by deposit of a kind of rough laminar pyrocarbon layers surrounding the VGCF core. Consequently the VGCF graphitization behavior is similar to that of graphitizable carbons, i.e. they polygonize so they acquire a polyhedral cross section after HTT above 2500°C.

– *Carbon blacks* [73]
They are produced in the gas phase by incomplete decomposition of hydrocarbons in various technological processes [74]. All products are made of elemental units (BSU) associated in a statistical spherical symmetry but similarly to pyrocarbons and plastic phase carbons. The diameter of the spheres varies in the same range as the LMO previously described, i.e. from micrometer to nanometer sizes. The largest spheres suspended in a gas are isolated (thermal blacks) or self-associated following all possible fractal dimensions [75]. As other types of carbons, they become polyhedral by heat treatment above 2000°C and their graphitizability decreases with their diameter from partial graphitization ($P < 1$) down to $P = 0$ for the smallest non-graphitizing carbon blacks.

1.3.5 Relation between Textures and Mechanical Properties

As shown above, one of characteristics of carbon materials is a wide variety of textures with different morphologies, which are known to govern the physical properties [61]. It is well justified to ask why carbon materials are so much

diversified. The reason is that a single crystal of graphite shows a maximum of anisotropy with a maximum of stiffness in the (001) plane due to the short C-C bond length of 0.142 nm (versus 0.154 nm for diamond) and easy (001) glides due to van der Waals spacing (see Fig. 1.2). The anisotropy of elastic constants is a consequence of this structural factor and therefore controls the mechanical properties [76]; Young's modulus in graphitic planes is $E_{//} = 1036\,\mathrm{GPa}$ and perpendicular to them only $E_{\perp} = 36\,\mathrm{GPa}$ (corresponding to the C_{11} and C_{33} components of the elastic tensor), the associated tensile strengths are respectively $\sigma_{//} = 100\,\mathrm{GPa}$ and $\sigma_{\perp} = 0.7\,\mathrm{GPa}$. So all carbons will present intermediate values which range inside these extrema since they are built with similar elemental units; their three-dimensional arrangements are infinitely variable leading to carbon textures scaling from macroscopic to nanometer scales. Anytime when texture favors planar development, the in-plane values of graphite will be approached. When the symmetry decreases from planar to statistically planar, from cylindrical to statistically cylindrical down to spherical, the in-plane properties of graphite degrade towards those of the graphite perpendicular direction. In the case of mechanical properties for planar symmetry textures, they decrease from highly oriented pyrolytic graphite (HOPG) to the non-graphitizing glassy carbons. For fibers, Young's modulus was demonstrated to depend on on aromatic layers (or BSU) preferred orientation along the fiber axis. Its value is thus limited by the graphite in-plane value. Hence the products closest to true cylindrical symmetry (VGCFs, pitch-based fibers) have also the highest values as compared to PAN-based carbon fibers [77]. In addition, products prepared or heat treated (HTT$\geq 2000^{\circ}$C) are also favored by improving the modulus from high tensile strength (HTS) to high modulus (HM) for PAN-based fibers and pitch-based fibers. A classical way to compare the different types of fibers is to represent a figure of merit where the fiber tensile strength is plotted versus Young's modulus (Fig. 1.12) with the possible elongation length as underlying parameter. A similar trend is found for electrical resistivities and thermal conductivities (see next section) because all the physical properties depend on the size and orientation of the BSU building blocks. Correspondingly, numerous industrial applications are based on the properties described above since lamellar and cylindrical symmetries are often used for example as arc or electrochemical electrodes, also for electrical conductors and thermal heat sinks. The good tribological properties associated with lamellar products (pyrocarbons) in composites are used in brakes (for race cars, airplanes) whereas the properties in the perpendicular direction are exploited as thermal or electrical insulator (in space shuttle, missiles, launchers etc). Pure spherical symmetry provides insulating powders in thermal exchangers and furnaces, or dispersed in an insulating matrix, typically a polymer, as used in tires [73].

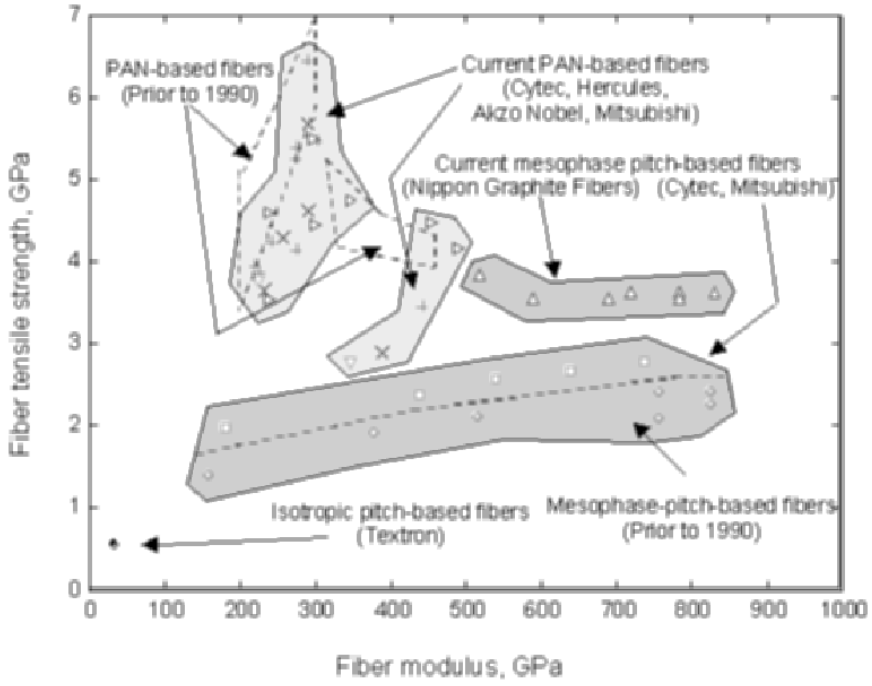


Fig. 1.12. Mechanical properties of commercial ex PAN-based and ex mesophase pitch based carbon fibers prior to 1990 and compared to selected current fibers (the trade names are given into the brackets; adapted from Eddie [77])

1.4 Transport Properties

1.4.1 Introduction

The various pristine carbon allotropes cover a wide range of electronic properties from insulators like diamond to semimetallic conduction, as is the case for highly oriented pyrolytic graphite (HOPG) (Fig. 1.13). Moreover, if we consider intercalation compounds of graphite with electron donors or acceptors as guest molecules, a complete metallic behavior is even observed. One may get a first insight into these properties by considering the chemical orbital concept of hybridization which exhibits either σ or π character in carbon compounds. The σ bonding and antibonding orbitals create a full valence band and an empty conduction band separated by a large energy gap. Without π electrons, the material is an insulator, as illustrated by diamond which presents a large band gap of nearly 7 eV. However, when π electrons are present, the valence and conduction bands, due to this new hybridization, fill the gap left by the σ bands. When the carbon structure has one π electron per carbon atom, the Fermi level is then positioned where the two π electronic bands are in contact. This electronic model describes the graphite family, including most

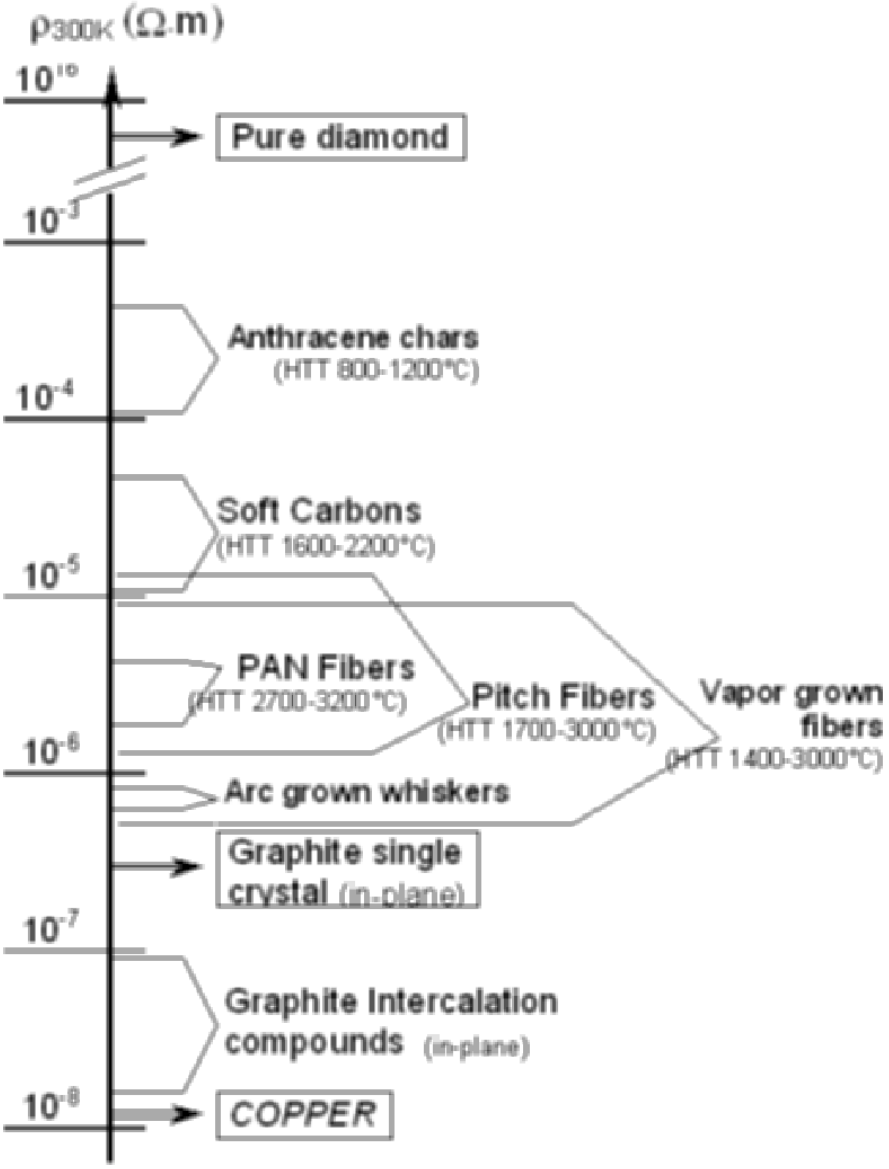


Fig. 1.13. Orders of magnitude of the room-temperature electrical resistivities of various forms of carbons and graphites compared to that of copper. The heat treatment temperature (HTT) range is indicated in brackets. The range of resistivities for graphite intercalation compounds showing their conductivity enhancement for HOPG in-plane value is presented [79]

intercalation compounds, which are considered as highly anisotropic electrical conductors because of their lamellar structure [78].

For this reason most physical properties of graphites are highly anisotropic and, in principle, should be described by tensors. However, when this anisotropy is very high, e.g. exceeding two or three orders of magnitude, they could be considered as quasi two-dimensional systems (2D) and their properties can be described by two scalars, one in-plane figure and the other out-of-plane. This simplifies to a great extent the interpretation of the experimental observations as we develop in the followings. The anisotropy is different according to both the property and the temperature considered. As regards transport properties, on the one hand the anisotropy may be extremely high, as is the case for the electrical conductivity of acceptor intercalation compounds, where it may exceed in some cases six orders of magnitude. On the other hand, the thermoelectric power does present a small anisotropy, as well as the low temperature lattice thermal conductivity. By increasing the temperature this anisotropy increases to exceed two orders of magnitude around room temperature.

The physical properties of carbons and graphites are particularly sensitive to structural perfection as already presented in Sect. 1.3 for the mechanical properties. Controlling their defect structure enables to tailor these physical properties at the desired level; as a corollary, the analysis of the physical properties of a given sample allows to gain insight into the defects in various carbons and graphites. This is particularly true also for the transport properties such as the electrical resistivity and the magnetoresistance, the thermal conductivity and the thermoelectric power (Subsects. 1.4.2, 1.4.3, 1.4.4). Thus, these properties may be used as additional tools to characterize these materials at the macroscopic scale yielding useful information about their structure and texture.

Since the electrical resistivity is very sensitive to lattice defects, the results of its measurement are delicate to analyze quantitatively in carbons and graphites. This is also the case for the thermoelectric power. In principle, magnetoresistance measurements probe the mobilities, thus is essentially sensitive to the scattering mechanism. The analysis of thermal conductivity measurements yield information about lattice defects and about other phonon scattering events. It allows one to determine directly an essential parameter in graphites, the associated in-plane coherence length.

Also, many papers have been published the last two decades on the transport properties of carbons and graphites in general [78, 81] and on their intercalation compounds [80, 82] and others are dealing with the particular case of carbon fibers [61, 79, 83] and carbon nanotubes [84]. In Chap. 6 of this book, we discuss in some detail the thermal conductivity and the thermoelectric power of carbon nanotubes.

1.4.2 Electrical Resistivity and Magnetoresistance

Conduction and Transmission

For macroscopic samples at temperatures which are not too low, electrical transport in a solid is generally diffusive. In the semi-classical picture, electrons are accelerated by the applied electric field, within a certain distance, the mean free path, and after experiencing a collision with a scattering center, loose memory of their initial state, are again accelerated by the electric field, and so on ... The mean free path, a few interatomic distances for metals at room temperature, being much shorter than the sample dimensions, a single electron does not travel from one side of the sample to the other, as it is the case for ballistic motion. The regime of charge transport depends thus on some critical lengths. We will define below three of them which are important to understand, even qualitatively, charge carrier propagation in carbons and graphites at low temperatures [85]:

- *the elastic mean free path* ℓ_e, which is directly related to the time of flight between two elastic collisions, is due to scattering by static defects, such as impurities, vacancies, dislocations, grain boundaries, ... Through these collisions, electrons exchange momentum but retain their phase memory.
- *the phase-coherence length* L_ϕ, which is the distance traveled by electrons before their initial phase memory is destroyed. Generally the phase coherence length corresponds to the inelastic mean free path.
- *the Fermi wavelength*, which is related to the kinetic energy of electrons at the Fermi level, is almost temperature insensitive for metals. However, the characteristic wavelength of carriers for semiconductors and semimetals, in presence of a non degenerate electronic gas, may vary widely with temperature. Thus for carbons and graphites the two last characteristic lengths are temperature sensitive.

For samples with dimensions much higher than the characteristic lengths described above, inelastic electron-phonon collisions are dominant at high temperatures and the phase memory of electrons is lost together with their change of momentum after collision. Diffusive motion dominates as illustrated by Ohm's law, which in its simplest form reads:

$$\boldsymbol{J} = \sigma \boldsymbol{E} \tag{1.7}$$

where $\boldsymbol{J}$ is the current density, σ the electrical resistivity second rank tensor (usually treated as a scalar) and $\boldsymbol{E}$ the applied electric field.

When the temperature is lowered, the probability for electron-phonon collisions decreases leading to an increase of the inelastic mean free path, which eventually becomes much larger than the elastic mean free path. Since electrons exchange momentum but do not lose their phase memory through elastic collisions, interferences may show up in the electronic system generating weak localization effects [86]. These effects, which depend on the dimensionality of

the system, occur even in macroscopic samples, as is the case for bulk carbons and graphites at low temperatures [78, 87]. When, as is the case for carbon nanotubes, the sample has dimensions comparable to the phase coherence length, additional quantum effects such as universal conductance fluctuations may show up in the presence of a magnetic field [88]. In a defect-free sample, when the elastic mean free path exceeds the dimensions of the sample, the charge carriers propagate ballistically from one end of the sample to the other without experiencing collisions. The charge carrier propagation is then directly related to the quantum probability of transmission across the global potential of the sample.

Hence, the mechanisms responsible for charge transport properties depend critically on the temperature and the geometrical dimensions of the samples as compared to a few characteristic lengths associated to the charge carriers. These will be discussed in length in Chap. 6 of this book, but it is worth to recall them briefly here, since they had an important impact on the transport properties of carbons and graphites these last decades. This is certainly true for the case of nanotubes, but also for bulk carbons and graphites where quantum transport and quantum effects were found to show up in the early eighties [89, 90].

Zero-Field Resistivity

Since the scalar electrical conductivity, σ, depends on the carrier density, N, and their mobility, μ:

$$\sigma = qN\mu \tag{1.8}$$

we should consider the effect of defects on these two parameters. On one hand, the electrical resistivity depends strongly on impurities which modify the carrier density, such as doping impurities or intercalated species, and, at low temperatures magnetic impurities. Intercalation by means of acceptor or donor species may increase drastically the electrical conductivity [84, 85]. On the other hand, the low temperature electrical resistivity, i.e. the residual resistivity, depends almost exclusively on the static lattice defects which are the dominant scatterers for charge carriers at low temperature decreasing the mobility of the latter. In Fig. 1.13 we present the order of magnitude of the room-temperature electrical resistivities of various forms of carbons and graphites. The heat treatment temperature (HTT) range is indicated in brackets. The range of resistivities for graphite intercalation compounds showing the conductivity enhancement for HOPG in-plane resulting from intercalation is also presented. In Fig. 1.14, the temperature variation of the electrical resistivity of various forms of carbons is shown.

The temperature dependence of the electrical resistivity of pristine carbons and graphites is very sensitive to lattice defects. The resistivity decreases with increasing structural perfection during the graphitization process. One may see from Figs. 1.13 and 1.14 that increasing the heat treatment temperature

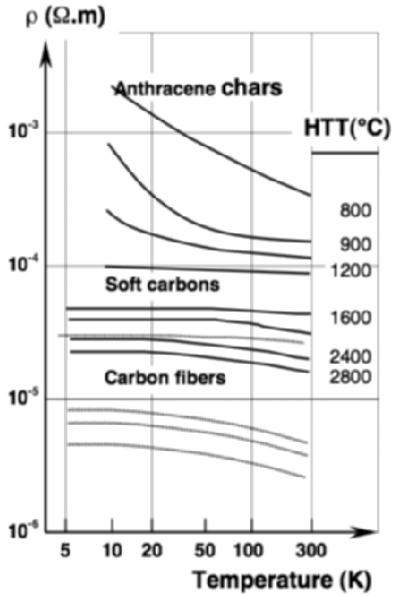


Fig. 1.14. Temperature variations in logarithmic scale of the electrical resistivity of typical forms of carbons [80]

(HTT), i.e. improving sample perfection, has a drastic effect on the electrical resistivity. It is generally observed that the differences between various samples within one class of carbon-based materials are more dependent on the heat treatment temperature than they are between various classes for samples heat treated at approximately the same temperature. The general trend of the electrical resistivity behavior may be sketched in the following way [61]. Samples which present the highest structural perfection exhibit resistivities which do not exceed a few $10^{-6}\,\Omega\,\mathrm{m}$ and which may be described by Klein's semimetallic graphite band model [91]. Around room temperature, electrons and holes are scattered by phonons, as in metallic conductors, as well as by static lattice defects. But, contrary to the case of metals, the carrier mobilities as well as the carrier densities are defect and temperature-sensitive in semimetallic compounds. However, while the mobilities increase with decreasing temperature due to the decreasing phonon density, the number of thermally activated electronic carriers decreases with decreasing temperature, as is the case for semiconductors. For a semimetal like graphite, where the electronic structure is presented in Fig. 1.15 together with the Brillouin zone and the Fermi surface, owing to their very small densities, the number of electronic carriers is very sensitive to both defects and temperature. Since the effect of lattice defects on the carrier densities cannot be quantitatively determined, it is generally not possible to predict whether the resistivity will increase or decrease with temperature. This is different from the situation in metals,

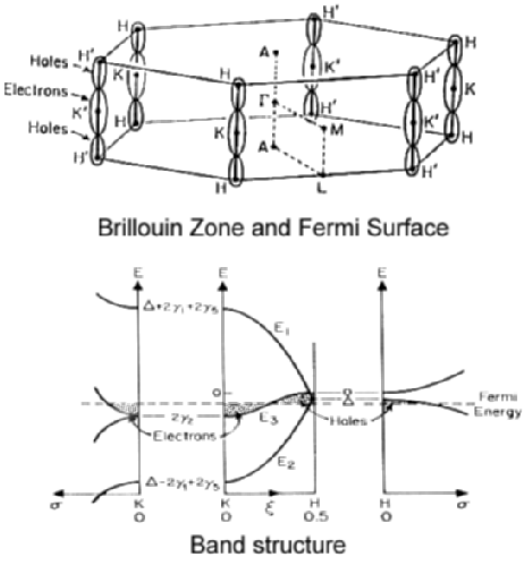


Fig. 1.15. Slonczewski-Weiss-McClure model, issued from tight binding approximation, with the Brillouin zone, Fermi surface and the dispersion relationship for charge carriers at Fermi energy in ideal single crystal of graphite [80]

where the carrier densities are very large and insensitive to temperature and consequently only the mobility varies with temperature. Partially carbonized samples exhibit resistivities higher than $10^{-4}\,\Omega\,\mathrm{m}$, which generally increase when the temperature is lowered. Between these two extreme cases, we find samples that present an intermediate behavior with electrical resistivities both less HTT and temperature sensitive.

In order to illustrate the effect of lattice perfection on the electrical resistivity, we present in Fig. 1.16 the room-temperature electrical resistivity ($\rho_{300\,\mathrm{K}}$) of a series of pitch-derived carbon fibers as a function of in-plane coherence length which is the planar crystallite size (L_a): the resistivity increases when L_a decreases, i.e. when the samples are more disordered and finally they suffer a strong localization regime [79, 92].

For solids with one dominant type of charge carriers such as metals and semiconductors in the extrinsic temperature range, the measurement of the electrical resistivity and Hall effect allows to determine the charge carrier density and mobility. By contrast, in graphite where there are two types of carriers (Fig. 1.15), electrons and holes, we need to measure four parameters to have access to the mobilities and charge carrier densities. If we add the fact that the carrier densities are very small compared to metals, and, as a consequence, that these densities are very sensitive to temperature the interpretation of electrical-resistivity measurements are significantly complicated.

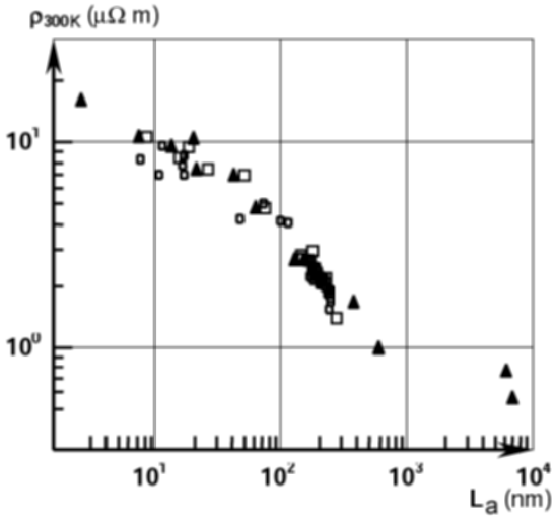


Fig. 1.16. Room-temperature electrical resistivity ($\rho_{300\,\mathrm{K}}$) of selected pitch-derived carbon fibers as a function of in-plane coherence length (L_a). The resistivity decreases when L_a increases, i.e. when the samples are less disordered under graphitization process [79, 92]

Magnetoresistance

When a transverse magnetic field is applied to a conductor carrying an electrical current, an increase in resistance is generally observed due to the effect of the Lorentz force on the charge carriers. This effect is called 'positive transverse magnetoresistance'. The fractional change in the resistance caused by the application of an external magnetic field is expressed by:

$$\frac{\Delta\rho}{\rho_0} = \frac{\rho_H - \rho_0}{\rho_0} \tag{1.9}$$

where ρ_H and ρ_0 are the electrical resistivities with and without a magnetic field, respectively. For low magnetic fields, this positive magnetoresistance depends essentially on the carrier mobilities. However, negative magnetoresistances, i.e. decreases in resistivities with increasing magnetic fields, have been first observed in pregraphitic carbons by Mrozowski and Chaberski [93] and later on in other forms of carbon. These include poorly graphitized bulk carbons, as pyrocarbons, PAN-based fibers [94, 95], pitch-derived fibers [96] and vapor-grown fibers [97]. It was found that this negative magnetoresistance confirms the occurrence of 2D weak-localization effects in carbon materials [86]. In addition, the sign and the magnitude of the magnetoresistance was closely related to the microstructure of the sample [81,96]. We present in Fig. 1.17 the results obtained by Bright [96] at 4.2 K for the transverse magnetoresistance of ex-mesophase pitch carbon fibers heat-treated at temperatures ranging from

Sample	HTT	$\rho_{4.2K}$
	°C	μΩ m
A	3000	3.8
B	3000	5.1
C	3000	7.0
F	3000	6.6
G	2500	6.8
E	2000	9.2
D	1700	12.5

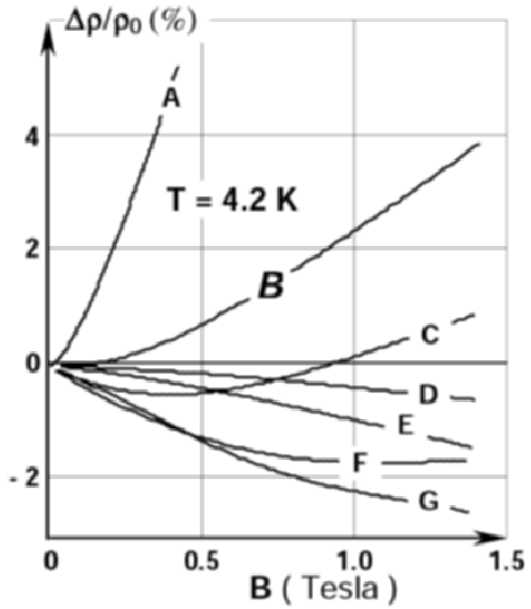


Fig. 1.17. Transverse magnetoresistance for a series of ex-mesophase pitch carbon fibers heat treated at different temperatures ranging from 1700°C (sample D) to 3000° (samples A, B, C, F). Samples A, B, C and F, which were heat treated at the same temperature, exhibit different residual resistivities (measured at 4.2 K): 3.8, 5.1, 7.0 and 6.6 μΩ m respectively and a change from negative to positive magnetoresistance [96]

1700°C (sample D) to 3000°C. The four samples A, B, C and F which were all heat-treated at 3000°C, exhibit different residual resistivities; we note that higher residual resistivities correspond to higher structural disorder (samples G and E were heat treated at 2500°C and 2000°C respectively). Highly graphitized fibers, i.e. those heat treated at the highest temperatures, present large positive magnetoresistances, as expected from high mobility charge carriers. This explains why samples A and B which exhibit the lowest residual resistivities exhibit also large positive magnetoresistances, even at low magnetic fields. With increasing disorder, a negative magnetoresistance appears at low

temperature, where the magnitude and the temperature range at which it shows up increase as the relative fraction of turbostratic planes (i.e. the probability P of finding a pair of graphitic carbon layers is decreasing) increases also in the material [92]. The results obtained, which are presented in Fig. 1.17, were later confirmed by Bayot et al. [90] and Nysten et al. [98], who found the same qualitative behavior on different samples of pitch-derived carbon fibers.

1.4.3 Thermal Conductivity

– *Conduction mechanisms*
In metallic solids heat is generally carried by the charge carriers, while in electrical insulators such as diamond heat is exclusively carried by the quantized lattice vibrations, the phonons. In graphites, owing to the small density of charge carriers, associated with a relatively large in-plane lattice thermal conductivity due to the strong covalent bonds, heat is almost exclusively carried by the phonons, except at very low temperatures, where both contributions may be observed [61]. This last situation prevails for the case for graphite intercalation compounds in a wide temperature range [82]. The total thermal conductivity is then the sum of the electronic, κ_{e}, and lattice, κ_{L}, contributions:

$$\kappa = \kappa_{\mathrm{e}} + \kappa_{\mathrm{L}} \tag{1.10}$$

In Chap. 6, we present the order of magnitude of the thermal conductivity of carbons and graphites at room temperature compared to that of copper and polymeric materials.

– *Lattice conduction*
Although less pronounced than for the electrical conductivity, the lattice thermal conductivity of graphites is highly anisotropic and the anisotropy is higher around room temperature as observed by comparing the temperature variation of the thermal conductivity of HOPG in-plane and out-of-plane. In Fig. 1.18 we present the temperature variation of the thermal conductivity of various carbon fibers heat treated at different temperatures. It may be seen that the higher the HTT, the larger is the thermal conductivity.

The thermal-conductivity measurements which have been performed below room temperature on carbons and graphites have allowed to determine the in-plane coherence length (Fig. 1.17) and yield information about point defects [83]. They have also enabled to compare between shear moduli (C_{44}) of the elastic tensor [76]. It was shown that the phonon mean free path for boundary scattering is almost equal to the in-plane coherence length as determined by x-ray diffraction or TEM. Thermal conductivity measurements allow then to determine this parameter, especially for high L_a values where x-ray techniques are inadequate. One may also deduce from thermal conductivity measurements that the concentration of point defects, such as impurities and vacancies, decreases with graphitization, in agreement with other observations. As for electrical resistivity (see Sect. 1.4.2), the interpretation

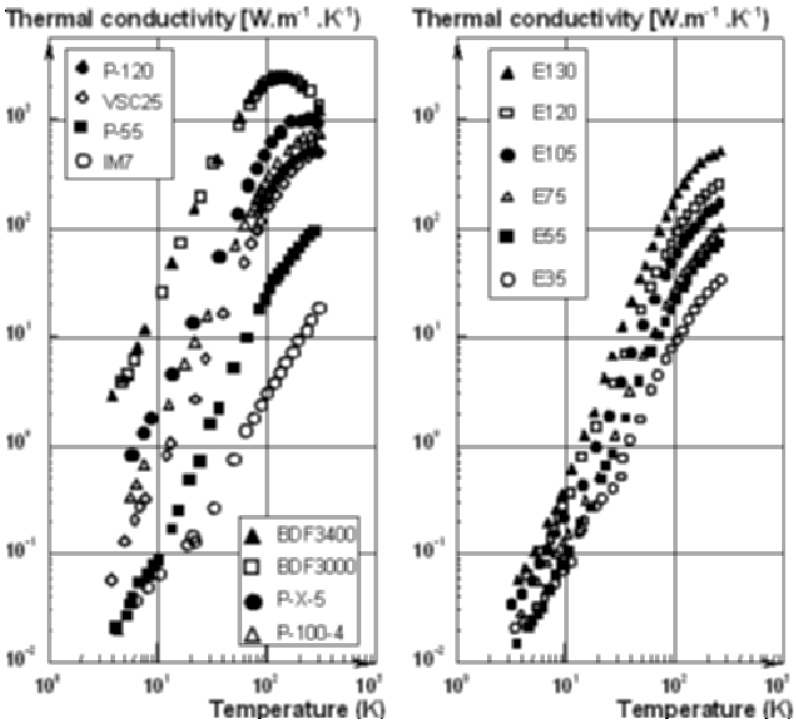


Fig. 1.18. Comparison at logarithmic scales of the temperature variations of the thermal conductivity of pristine carbon fibers of various origins and precursors. Since scattering below room temperature is mainly on the crystallite boundaries, the phonon mean free path at low temperatures, i.e. below the maximum of the thermal conductivity versus temperature curve is temperature insensitive and mainly determined by the crystallite size. Note that some VGCF and BDF(ex-benzene) of good crystalline perfection show a maximum below room temperature. For decreasing lattice perfection the maximum is shifted to higher temperatures [79]

of thermal-conductivity data presents an overall view over the entire sample. This is in contrast to microscopic imaging techniques which only probe a tiny portion of the sample.

A simple picture may be used to understand how lattice conduction operates in graphite in-plane, assuming that it is a quasi 2D system around room temperature. The atoms may be represented by a 2D array of balls and springs where a vibration at one end of the system will be transmitted via the springs to the other end. The carbon atoms having small masses which experience strong covalent interatomic forces (see Debye model), the vibrational motion is effectively transmitted and a high lattice thermal conductivity is observed. Static defects and atomic vibrations will cause a perturbation in the regular arrangement of the atoms which will tend to impede the heat flow, by generating scattering events which limit the thermal conductivity. The lattice

thermal conductivity may be expressed by means of the Debye relation

$$\kappa_{\mathrm{g}} = (1/3).C.\ell.v \tag{1.11}$$

where C is the lattice specific heat per unit volume characterized by the Debye temperature [61], v is an average phonon velocity, and ℓ their mean free path. This mean free path is related to the phonon relaxation time, τ through the relation $\ell = v\tau$.

Diamond, in-plane highly oriented pyrolytic graphite (HOPG) in-plane and vapor-deposited carbon fibers (VGCF) heat treated at 3000°C, may present room-temperature heat conductivities exceeding 2000 $\mathrm{Wm^{-1}K^{-1}}$. The thermal conductivity of various forms of less ordered carbons may vary widely, about two or more orders of magnitude, according to their microstructure [83]. At low temperature (Fig. 1.18), the lattice thermal conductivity is mainly limited by phonon-boundary scattering and is directly related to the in-plane coherence length, L_{a} in this case, the phonon mean free path is temperature insensitive. Since the velocity of sound is almost temperature insensitive, the temperature dependence of the thermal conductivity follows that of the specific heat. In that case, the larger the crystallites size the higher the thermal conductivity. Well above the maximum, phonon scattering is due to an intrinsic mechanism: the phonon-phonon umklapp processes, and the thermal conductivity should be the same for different samples of the crystalline material.

Around the thermal-conductivity maximum, the interaction of phonons with point defects (small scale defects) will be the dominating scattering process. The position and the magnitude of the thermal-conductivity maximum will thus depend on the competition between the various scattering processes (boundary, point defect, phonon, ...). So, for different samples of the same material the position and magnitude of the maximum will depend on the density of point defects and L_{a}, since phonon-phonon interactions are assumed to be constant. Thus, by measuring the low-temperature thermal conductivity, one may gather information about the in-plane coherence length and point defects which are related with the mean interlayer spacing [84]. This shows also that by adjusting the texture of carbon fibers, one may control their thermal conductivity to a desired value as already indicated for the mechanical properties.

– *Effect of intercalation*

As a result of charge transfer, intercalation by donors or acceptor species increases the carrier density and reduces, to a lesser extent, the electronic mobility. The net result is thus an increase in electrical conductivity. According to the Wiedemann-Franz relation, one should expect a corresponding increase in the electronic thermal conductivity in intercalation compounds. Also, because of lattice defects introduced by intercalation, the lattice thermal conductivity should decrease: this is what is observed experimentally [82]. Intercalation decreases the total thermal conductivity at high temperature and increases it

at low temperature with respect to that of the pristine material. As for the pristine material, the interpretation of the low-temperature lattice thermal conductivity allows the estimation of the size of the large scale defects and the concentration of point defects [82].

1.4.4 Thermoelectric Power

The thermoelectric power (TEP) or Seebeck coefficient, S, is the potential difference generated by an applied unit temperature difference across an electrical conductor. The main mechanism for TEP generation, the diffusion thermoelectric power, is due to the diffusion of charge carriers from hot to cold caused by the redistribution of their energies caused by the temperature gradient. The charge carriers accumulating at the cold end of the sample give rise to the thermoelectric voltage. This potential difference tends to counterbalance the flow of diffusing carriers until a steady state is reached. It is also shown that, for a given group of charge carriers, the TEP is very sensitive to the scattering processes at the Fermi energy and moreover, as is the case for HOPG, when there is more than one type of carriers, the total thermoelectric power is obtained by considering the different groups of carriers with partial thermoelectric powers that contribute to the total thermoelectric power as electromotive forces working in parallel.

As a typical example, we present in Fig. 1.19 the temperature variation of the thermoelectric power of a graphite single crystal [99]. In Fig. 1.20 the room temperature TEP ($S_{300\mathrm{K}}$) of pitch-derived carbon fibers is shown as a function

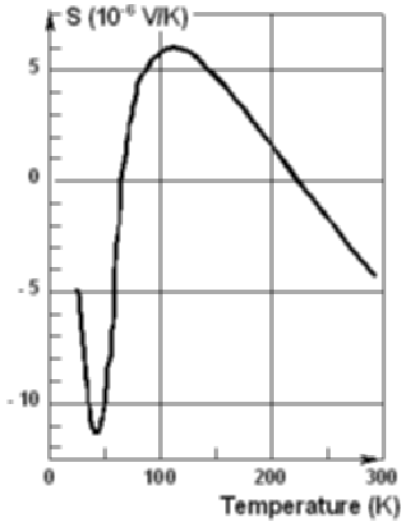


Fig. 1.19. Temperature variations of the thermoelectric power of a graphite single crystal [99]

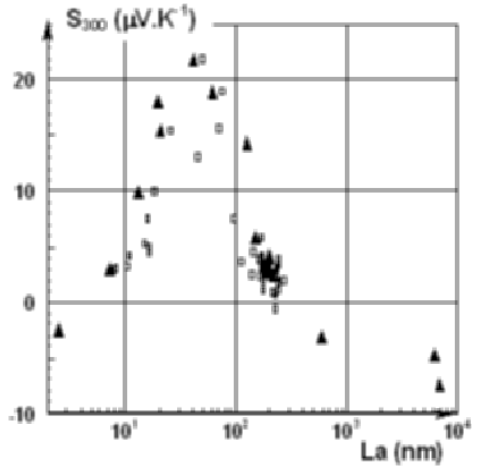


Fig. 1.20. Room temperature thermoelectric power ($S_{300\,\mathrm{K}}$) of pitch-derived carbon fibers as a function of in-plane coherence length (L_a) [79]

of in-plane coherence length (L_a) [83]. In Chap. 6 of this book, we discuss in some detail the thermoelectric power (TEP) of carbon nanotubes and show that the interpretation of the TEP results obtained for carbon materials is a complicated task.

1.4.5 Relation between Structure and Transport Properties

Since the mechanical, electrical and thermal properties are structure-sensitive, one should expect a relation between these properties. It was shown indeed that this is the case. Both electrical and thermal properties are related to the elastic modulus and, as a corollary, there is also a relation between the thermal conductivity and the electrical resistivity [83]. So, for the same precursor, once the electrical resistivity is determined, the thermal conductivity may be calculated, avoiding thus delicate and time-consuming thermal-conductivity measurement and also giving a general assessment relative to the mechanical properties (see Sect. 1.3.5).

1.5 Doped Carbons and Parent Materials

During the last years novel compounds based on boron, nitrogen and carbon and sometimes other atoms, have been predicted and in some cases synthesized [100]. The light boron and nitrogen atoms which are on the same line of Mendeleev's table as carbon can be threefold-coordinated or fourfold-coordinated and the polymorphism observed for pure solid carbons is extended. It can be noticed that with silicon, which is in the same row as carbon

in the classification of elements, only single bonds are present and fourfold-coordinated compounds as silicon carbide exist. For light atoms, one can consider three groups of materials: doped graphitic lattices, diamond lattices and parent materials presenting analogous 2D or a 3D structures. One should also mention here other compounds of interest with respect to nanotubes, such as dichalcogenides of transition metals MX_2 as for example lamellar MoS_2 and WS_2, which can form analogs of graphene-type curved shapes.

1.5.1 Doped Carbons and Solid Solutions

Small quantities of boron and nitrogen can be introduced at substitutional position in the graphite and the diamond lattices. In cubic diamond, which is a large gap semiconductor, p- or n-type extrinsic semiconductors are obtained. In the case of graphite at thermodynamic equilibrium, up to 2.3% of atomic boron can be introduced but only a very small amount of nitrogen. However using classical CVD (chemical vapor deposition) larger amounts are stabilized inside a so-called pyrocarbon [101] as shown on the ternary phase diagram between these three elements (Fig. 1.21). It is interesting to note that all these metastable disordered solid solutions are located on the left side of the isoelectric vertical line between an sp^2 carbon and the boron nitride because it is almost impossible to stabilize a substitutional nitrogen above 1000°C. As explained from the electronic structure of graphite (see Sect. 1.4) these boron-doped pyrocarbons or carbon black particles present either a metallic or a semiconducting character [102–104].

1.5.2 Parent Materials

Following the topological arguments already used for pure allotropic carbons (see Sect. 1.2), a sketch of the principal series of known ceramic materials is

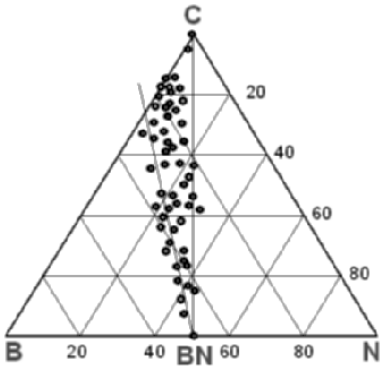


Fig. 1.21. Ternary compositional (C,B,N) diagram of pyrocarbons and analogs [102, 103]

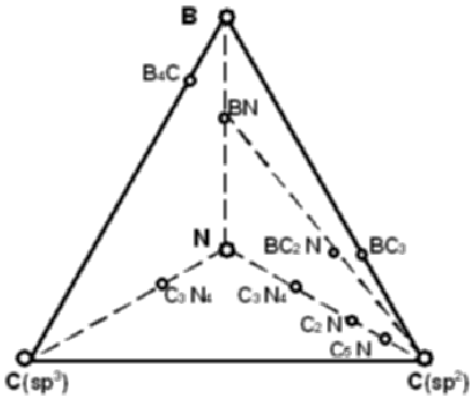


Fig. 1.22. Quaternary compositional (C sp^2, C sp^3, B and N) diagram and the main identified binary and ternary compounds [15]

presented in Fig. 1.22 in a quaternary compositional diagram. All the usual phases with a coordination number z equal to 3 or 4 are presented, associated or not with π bonds and rather 2D or 3D structures. Among the presented binary and ternary compounds several of them are resulting from a theoretical approach as developed in particular from Cohen's model on bulk modulus and cohesive energy [18]. These theoretical and experimental works have been developed to discover new phases which should be harder than cubic diamond. We will present only a few typical cases which are significant to illustrate this rich similar polymorphism.

- *Boron nitride* (BN): this binary compound is isoelectronic with 'C2' molecules and it presents a similar thermodynamic phase diagram (Fig. 1.23). An hexagonal lamellar structure which is thermodynamically stable and a 3D cubic phase, including a wurtzite with an hexagonal symmetry, are present [105]. It is interesting to note that cubic BN was the first artificial phase synthesized in laboratory under very high pressure, which does not exist in the nature [106]. As we will see in the next paragraph single-walled nanotubes of BN have been also synthesized. A general comment would be that the structural varieties of BN are very similar to those of carbon but their electronic properties are different. All the allotropic forms of BN are insulators because they do not own a π delocalized electronic system.
- *Carbon Nitrides* (C_3N or C_3N_4); this is an outstanding example of prediction for new polymorphs which present interesting mechanical properties. By analogy with the β-phase of silicon nitride (β-Si_3N_4) such lightweight material could be envisaged [105]. Indeed in 1996 Teter and Hemley [107] have proposed five stable or metastable phases of C_3N_4 presented in Fig. 1.24. Since that time different experimental works have been initiated to create these compounds, so far only one or two phases have been identified in very small quantities as for example the β-hexagonal one [108, 109].

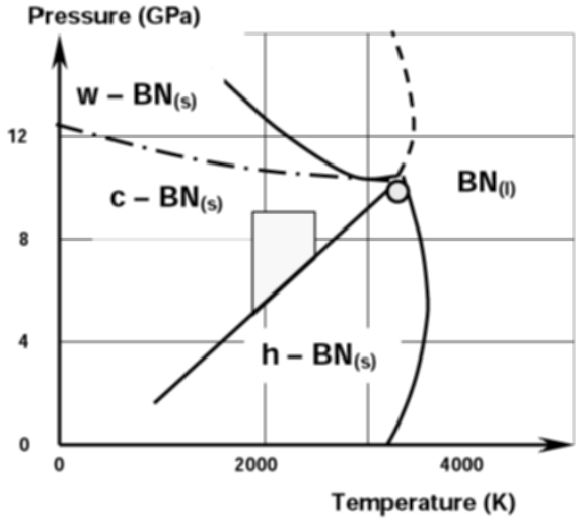


Fig. 1.23. Thermodynamic phase diagram of boron nitride (adapted from Riedel [105])

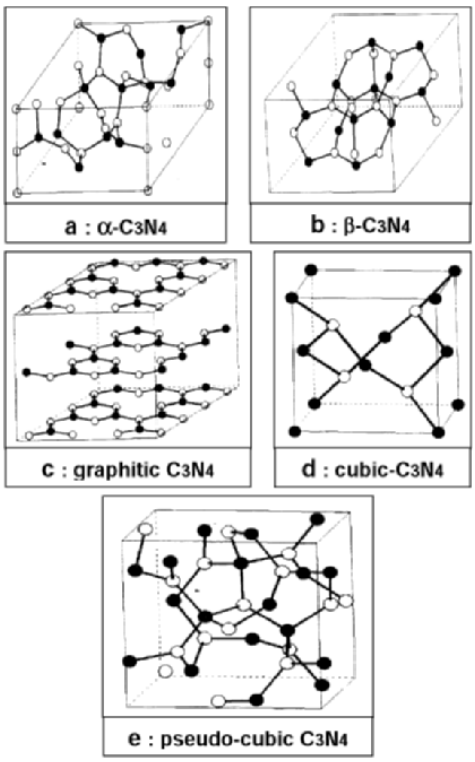


Fig. 1.24. Representation of the different predicted phases: (**a**) α-C_3N_4, (**b**) β-C_3N_4, (**c**) graphite like, (**d**) pseudo-cubic, (**e**) cubic structure C_3N_4 (dark points represent nitrogen and white points carbon atoms), adapted from Teter and Hemley [107]

– *Ternary compounds*, as for example the heterodiamond BC_2N [108], have also been predicted but the experimental achievements are rather scarce because the chemistry paths are difficult to control.

To conclude this part it turns out that the research for novel low compressional superhard solids, with a large bulk modulus B_0 (see eq. 1.2), in light covalent solids is a difficult task which needs improved synthetic ways [110].

1.5.3 Heterofullerenes and Heteronanotubes

– *Heterofullerenes*
Doping fullerenes by replacing one or several carbon atoms by N or B has been done mainly on C_{60} molecule where it is crucial to keep the truncated icosahedral structure. Regarding theoretical studies on stable structures of heterofullerenes, the quantum molecular-dynamics calculations have shown the possibility to synthesize $C_{59}N$ and $C_{59}B$, $C_{58}N_2$ and $C_{58}B_2$ [111] or for example $C_{12}B_{24}N_{24}$ [112]. The experimental successes are rather scarce: boron heterofullerene $C_{59}B$ has been prepared [113] and the most convincing result is the synthesis of the anion $C_{59}N$ and its stable dimer $(C_{59}N)_2$ [114]. The fundamental point to consider is the chemical reactivity of this molecular form of carbon [115] which can be functionalized and polymerized, forming endohedral fullerenes or even charge transfer salts, as in intercalation compounds of graphite (see Sect. 1.4.1), but giving rise to interesting superconductors [27]. These peculiar molecular materials are outside the main purpose of this chapter but they are valuable molecular models for considering the nanotube chemistry.

– *Heteronanotubes*
In inorganic materials as graphite, one can define rather stable layers, where atoms are linked by chemical bonds, while interlayer interactions are much weaker van der Waals interactions. For BN compounds, a layer consists of a single sheet of alternating B and N atoms (Fig. 1.25a), while for MX_2 compounds, it is formed of atom sheet sandwiches, as is illustrated in Fig. 1.25b for the 2H-trigonal prismatic coordination-polytype of WS_2. It can be argued that nanoparticles of such compounds are unstable because of unsatisfied chemical bonds on the layers borders, and that under appropriate conditions, this can lead to the formation of inorganic fullerenes and nanotubes [116]. And indeed, only one year after the discovery of carbon MWNTs, tungsten disulfide MWNTs was reported [117]. Since then, numerous MX_2 MWNTs have been synthesized [118] for X = S or Se and M = W, Mo, Nb, Hf, etc. Boron nitride MWNTs [119] have also been produced in 1995, and SWNTs (see e.g. [120]) can also be obtained now; it can be added that doping of carbon nanotubes in particular with boron is currently developed as for pyrocarbons to modify the electronic behavior (see Fig. 1.21).

In brief, the field of inorganic nanotubes is currently in strong development. Their physical or chemical properties are not yet as well studied as

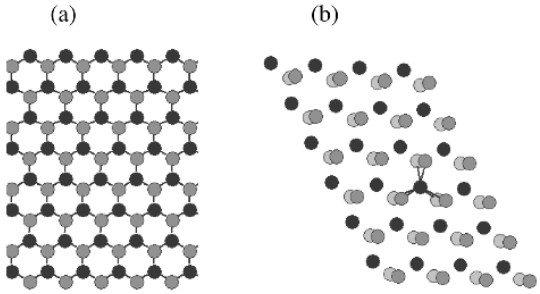


Fig. 1.25. Structure of a layer of: (a) hexagonal BN, (b) 2H-polytype WS_2; in (**a**) black and grey circles represent boron and nitrogen, respectively; in (**b**) the WS_2 layer is formed of three atomic sheets, the tungsten one is surrounded by two outer sulphur sheets (black and grey circles respectively)

those of carbon nanotubes. As for their structure, it can be described by two indices (n,m), like for carbon nanotubes. A difference between carbon and inorganic nanotubes concerns the nature of defects, in particular at the closure of the tubes. In contrast to carbon nanotubes, BN nanotubes can not be closed by pentagons (see Sect. 1.2.4) because BB and NN bonds are energetically unfavorable with respect to the BN bond (see also Fig. 1.21 on doped pyrocarbons). BN nanotube closure is ensured through B_2N_2 rhomb. In MX_2 compound, the point defects responsible for local curvature at tube end could be triangular and rhombohedral defects centered on atomic vacancies [121]. Finally it should be pointed out that deeper investigations have to be carried out for a better knowledge of these nano-objects.

1.6 Conclusion

In this chapter we have shown that the versatility of carbon in terms of chemical bonding is associated with the hybridization quantum effect of σ and π orbitals. Associated with a macroscopic approach in classical thermodynamics the phase diagram and the involved stable and metastable states of crystalline solid carbons have been presented. Then, following an historical approach, it was pointed out that the discovery of curved conjugated structures, namely fullerenes and nanotubes, has modified our vision of carbon, introducing a novel topological approach.

Because of the possibility of different degrees of coordination for the atom's first neighbors, a large variety of predicted phases, including doped carbons and parent compounds, have been theoretically calculated. These virtual phases should present interesting properties such as hardness for diamond type structures, or combined eventually with an electrical conduction in presence of 1D or 2D π delocalized systems. These numerous predicted metastable phases need improved synthetic ways to be materialized but different recent

results demonstrate their potentiality in particular with the synthesis of similar materials. Indeed the development of dedicated chemical methods which have not been described here, is a key parameter to create new molecular varieties as already known with non-crystalline forms of carbon.

These non-crystalline forms of graphitic compounds are hierarchical materials with several characteristic lengths. Besides the atomic scale which is related to the type of involved chemical bonding, different morphologies are present associated with different symmetry elements acting at a mesoscopic scale. In particular we describe the different textures based on the self-assembly of the polyaromatic units (BSU) and their collective preferred orientation controlled by selected processes. These different morphologies known as films like pyrocarbons, carbon fibers and carbon blacks are relevant for many applications and are still subject of further developments. To explain these facts we establish the relationship between the different morphologies and textures and, on the one hand the mechanical properties, and on the other hand the electrical and thermal transport properties.

Finally this introduction locates the place of nanotubes, SWNT as well as MWNT, inside the carbon 'zoo' with their geometrical specificity as nanofilaments. They have to be considered, especially for the SWNT, as the ultimate form of solid carbon with the rolling of a graphene sheet, where their surface characteristics and associated voids are essential. Indeed, as for other nanostructured form of carbon, this is the combination of surface characteristics and bulk properties which leads to specific behaviors interesting for applications as presented in the following chapters.

Acknowledgements

A. Oberlin, P. Lauginie and M. Trinquecoste are acknowledged for interesting discussions, comments and help in different parts of this chapter.

References

1. P. Levi: *The periodic table* (Schoken books, New York 1984)
2. F. Robert: In *Carbon molecules and materials*, ed by R. Setton, P. Bernier and S. Lefrant (Taylor and Francis, London 2002)
3. J.F. Newton: *Man and the chemical elements* (Ch. Griffin and company LTD, London 1953)
4. H.M. Leicester and H.S. Klickstein: *A source book in chemistry 1400-1900* (McGraw Hill book company, New York 1952)
5. A.L. Lavoisier: *Traité élémentaire de chimie* (Suchet libraire, Paris 1789)
6. E. Mitscherlich: Ann. Chem. Physique **19**, 350 (1822) and ib. **24**, 264 (1823)
7. H. Le Chatelier: *Leçons sur le carbone* (Dunod et Pinat, Paris 1908)
8. Y.P. Kudryavtsev, S.E. Evsyukov, M.B. Guseva, V.G. Babaev and V.V. Khvostov: In *Chemistry and Physics of Carbon*, vol 25, ed by P.A. Thrower (Marcel Dekker Inc., New-York 1996)

9. H.W. Kroto, J.P. Heath, S.C. O'Brien, R.F. Curl and R.E. Smalley: Nature **318**, 162 (1985)
10. S. Iijima and T. Ichibashi: Nature **363**, 603 (1993)
11. D.S. Bethune, C.H. Klang, M.S. de Vries, G. Gorman, R. Savoy, J. Vazquez and R. Beyers: Nature **365**, 605 (1993)
12. W.R. Davis, R.J. Slawson and G.R. Rigby: Nature **171**, 756 (1953)
13. S. Iijima: Nature **354**, 56 (1991)
14. R.C. Haddon: Acc. Chem. Res. **25**, 127 (1992)
15. P. Delhaès: In *Carbon molecules and materials*, ed by R. Setton, P. Bernier and S. Lefrant (Taylor and Francis, 2002)
16. F.P. Bundy, W.A. Bassett, M.S. Weathers, R.J. Hemley, H.K. Mao and A.F. Goncharov: Carbon **34**, 141(1996)
17. C.J. Wu, J.N. Glosli, G. Galli and F.H. Ree: Phys. Rev. Lett. **99**, 135701 (2002)
18. M.L. Cohen: Solid State Comm. **92**, 45 (1994)
19. M.T. Yin and M.L. Cohen: Phys. Rev. Lett. **50**, 2006 (1983)
20. R. Hoffmann, T. Hugbanks and M. Kertesz: J. Am. Chem. Soc. **105**, 4831 (1983)
21. A.Y. Liu and M.L. Cohen: Phys. Rev. B **45**, 4579 (1992)
22. R.L. Baughman, H. Eckhardt and M. Kertesz: J. Chem. Phys. **87**, 6687 (1987)
23. K.M. Merz, R. Hofmann and A.T. Balaban: J. Am. Chem. Soc. **109**, 6742 (1987)
24. V.D. Blank, B.A. Kulnitsky, Y.V. Tatyanin and O.M. Zhigalina: Carbon **37**, 549 (1999)
25. H.A. Schwarz: *Gesammelte Mathematische Abhandlungen* (Springer-Verlag, 1890)
26. A.L. Mackay and H. Terrones: Nature **352**, 762 (1991)
27. M.S. Dresselhaus, G. Dresselhaus and P.C. Ecklund: *Science of fullerenes and carbon nanotubes* (Academic Press, 1995)
28. V.A. Davydov, L.S. Kashevarova, A.V. Rakhmanina, V.M. Enyavin, R. Céolin, H. Szwarc, H. Hallouchi and V. Agafonov: Phys. Rev. B **61**, 11936 (2000)
29. B. Sundqvist: Advances in Physics **48**, 1 (1999)
30. T.L. Makarova, B. Sundqvist, R. Hohne et al.: Nature **413**, 716 (2001)
31. W.L. Mao, H. Mao, P.J. Eng et al.: Science **302**, 425 (2003)
32. The conventional basis chosen in crystallography for a graphene sheet is a basis $(\boldsymbol{a_1}, \boldsymbol{a_2})$ where the angle between the vectors is 120° [33]. The angle between reciprocal vectors $\boldsymbol{a_1^*}$ and $\boldsymbol{a_2^*}$ is thus 60°, which allows one to use the well known $(h, k, l = -h - k)$ notation: the wave-vectors are equivalent for circular permutations of the h, k, l indices which describe three-fold rotations. However the basis which is the most frequently used in nanotube literature is the one with $(\boldsymbol{a_1}, \boldsymbol{a_2})$=60° [34], that we choose in this book.
33. N. Hamada, S.I. Sawada and A. Oshiyama: Phys. Rev. Lett. **68**, 1579 (1992)
34. D.H. Robertson, D.W. Brenner and J.W. Mintmire: Phys. Rev. B **45**, 12592 (1992)
35. R. Saito, G. Dresselhaus and M. Dresselhaus: *Physical properties of carbon nanotubes* (Imperial college press, 1998)
36. A. Thess, R. Lee, P. Nikolaev et al.: Science **273**, 483 (1996)
37. L. Henrard, A. Loiseau, C. Journet and P. Bernier: Eur. Phys. J. B **27**, 661 (2000)
38. J.F. Colomer, L. Henrard, P. Launois, et al.: Chem. Comm. **22**, 2592 (2004)

39. B.I. Dunlapp: Phys. Rev. B **46**, 1933 (1992)
40. Ph. Lambin, A. Fonseca, J.P. Vigneron et al.: Chem. Phys. Lett. **245**, 85 (1995)
41. A.J. Stone and D.J. Wales: Chem. Phys. Lett. **128**, 501 (1986)
42. A. Maiti, C.J. Brabec and J. Bernholc: Phys. Rev. B **55**, 6097 (1997)
43. M.B. Nardelli, B.I. Yacobson and J. Bernholc: Phys. Rev. B **57**, 4277 (1998)
44. W. Ruland, A.K. Schaper, H. Hou and A. Greiner: Carbon **41**, 423 (2003)
45. M. Liu and J.M. Cowley: Ultramicroscopy **53**, 333 (1994)
46. J. Tang, L.C. Qin, T. Sasaki et al.: Phys. Rev. Lett. **85**, 1887 (2000)
47. S. Rols, I.N. Goncharenko, R. Almairac et al.: Phys. Rev. B **64**, 153401 (2001)
48. M. Endo, K. Takeuchi, S. Igarashi, et al.: J. Phys. Chem. Solids **54**, 1841 (1993)
49. S. Iijima, M. Yudasaka, R. Yamada et al.: Chem. Phys. Lett. **309**, 165 (1999)
50. L.P. Biró, S.D. Lazarescu, P.A. Thiry et al.: Europh. Lett. **50**, 494 (2000)
51. J. Li, H. Dai, J.H. Hafner et al.: Nature **385**, 780 (1997)
52. P. Delhaès and F. Carmona: In *Chemistry and Physics of Carbon*, vol 17, ed by P.L. Walker and P.A. Thrower (Marcel Dekker Inc., 1981) pp 89–174
53. J. Robertson: Graphite and precursors. In *World of Carbon*, vol 1, ed by P. Delhaès (Gordon and Breach science publishers, 2001) pp 249–273
54. A. Oberlin and S. Bonnamy: Graphite and precursors. In *World of Carbon*, vol 1, ed by P. Delhaès (Gordon and Breach science publishers, 2001) pp 199–220
55. A. Oberlin, S. Bonnamy and P.G. Rouxhet: Colloidal and supramolecular aspects of carbon. In *Chemistry and physics of carbon*, vol 26, ed by P.A. Thrower, L.R. Radovic (Marcel Dekker Inc., New York 1999) pp 1–48
56. A. Oberlin: High resolution TEM studies of carbonisation and graphitisation. In *Chemistry and physics of carbon*, vol 22, ed by P.A. Thrower (Marcel Dekker Inc., New York 1989) pp 1–143
57. M. Inagaki: *New carbons, control of structure and functions* (Elsevier science Ltd., Oxford 2000)
58. E.R. Vorpagel and J.G. Lavin: Carbon **30**, 1033 (1992)
59. J.D. Brooks and G.H. Taylor: In *Chemistry and Physics of carbon*, vol 4, ed by P.L. Walker Jr (Marcel Dekker Inc., New-York 1968) pp 243–286
60. S. Bonnamy: Carbon **37**, 1691 and **37**, 1707 (1999)
61. M.S. Dresselhaus, G. Dresselhaus, K. Sigihara, I.L. Spain and H.A. Goldberg: In *Graphite fibers and filaments*, Springer series in materials science vol 5 (Springer-Verlag, 1988)
62. A. Oberlin and M. Guigon: In *Fibre reinforcements for composite materials*, ed by A.R. Bunsell (Elsevier Science Publishing, Amsterdam 1988) pp 149–210
63. M. Monthioux: In *Carbon, molecules and materials*, chap 4, ed by R. Setton, P. Bernier and S. Lefrant (Taylor and Francis, 2002)
64. A. Oberlin, S. Bonnamy and K. Lafdi: In *Carbon fibers*, 3rd ed, ed by J-B. Donnet, T.K. Wang, J.C. Peng and S. Rebouillat (Marcel Dekker Inc., New-York 1998) pp 85–160
65. M. Monthioux, A. Oberlin, X. Bourrat and R. Boulet: Carbon **20**, 167 (1982)
66. A. Oberlin: Carbon **40**, 7 (2002)
67. P. Delhaès: Carbon **40**, 641 (2002)
68. H.M. Huttinger: Fibers and composites 4. In *World of carbon*, vol 2, ed by P. Delhaès (Taylor and Francis, 2003) pp 75–86
69. A.W. Moore: In *Chemistry and physics of carbon*, vol 17, ed by P.L. Walker, P.A. Thrower (Marcel Dekker Inc., 1981) pp 233–286
70. X. Bourrat: Fibers and composites 8. In *World of carbon*, vol 2, ed by P. Delhaès (Taylor and Francis, 2003) pp 159–187

71. A. Oberlin, M. Endo and T. Koyama: J. Cryst. Growth **32**, 335 (1976)
72. G.C. Tibbetts: J. Cryst. Growth **66**, 632 (1984)
73. J.-B. Donnet and A. Voet: *Carbon blacks* (Marcel Dekker Inc. inc., 1976)
74. J. Lahaye and G. Prado: In *Chemistry and Physics of carbons*, vol 14, ed by P.L. Walker and P.A. Thrower (Marcel Dekker Inc., New-York 1978) pp 167–200
75. X. Bourrat and A. Oberlin: Carbon **26**, 100 (1988)
76. B.T. Kelly: *Physics of Graphite* (Applied Science Publishers, London,1981)
77. D.D. Eddie: Fibers and composites 2. In *World of carbon*, vol 2, ed by P. Delhaès (Taylor and Francis, 2003) pp 24–46
78. I.L. Spain: Electronic Transport Properties of Graphite, Carbons, and Related Materials. In *Chemistry and Physics of Carbon*, vol 13, ed. P.L. Walker Jr. and P.A. Thrower (Marcel Dekker Inc., New York 1981)
79. J.-P. Issi and B. Nysten: In *Carbon Fiber*, ed by J-B. Donnet, S. Rebouillat, T.K. Wang, J.C.M. Peng (Marcel Dekker Inc., New-York 1998)
80. M.S. Dresselhaus and G. Dresselhaus: Adv. Phys. **30**, 139 (1981)
81. J.P. Issi: In *World of Carbon*, vol 1, ed by P. Delhaès (Gordon and Breach, 2000) pp 45–70
82. J.P. Issi: In *Graphite Intercalation Compounds II, Springer Series in Materials Science*, vol 18, ed by H. Zabel, S.A. Solin (Springer-Verlag, Berlin 1992)
83. J-P. Issi: In *World of Carbon*, vol 2. 'Fibers and composites' p. 47 ed by P. Delhaès (Gordon and Breach, 2003)
84. J.-P. Issi and J.-C. Charlier: In *Science and technology of carbon nanotubes*, ed by K. Tanaka (Elsevier, London 1998)
85. J.C. Charlier and J.P. Issi: Appl. Phys. A **66**, 1 (1998)
86. G. Bergmann: Phys. Rev. B **28**, 2914 (1983)
87. L. Piraux: J. Mater. Res. **5**, 1285 (1990)
88. L. Langer, V. Bayot, E. Grivei et al.: Phys. Rev. Lett. **76**, 479 (1996)
89. L. Piraux L., J.-P. Issi, J.-P. Michenaud, E. McRae and J.-F. Marêché: Solid State Comm. **56**, 567 (1985)
90. V. Bayot, L. Piraux, J.-P. Michenaud and J.-P. Issi: Phys Rev B **40**, 3514 (1989)
91. C.A. Klein: J. Appl. Phys. **35**, 2947 (1964)
92. B. Nysten: Ph. D Thesis, Université Catholique de Louvain, Louvain-la-Neuve (1991) (in french)
93. S. Mrozowski and A. Chaberski: Phys. Rev. **104**, 74 (1956)
94. D. Robson, F.Y.I. Assabghy and D.J.E. Ingram: J. Phys. D: Appl. Phys. **5**, 169 (1972)
95. D. Robson, F.Y.I. Assabghy, E.G. Cooper and D.J.E. Ingram, J. Phys. D: Appl. Phys. **6**, 1822 (1973).
96. A.A. Bright and L.S. Singer: Carbon **17**, 59 (1979)
97. M. Endo, Y. Hishiyama and T. Koyama, J. Phys. D: Appl. Phys. **15**, 353 (1982)
98. B. Nysten, J.-P. Issi, R. Barton, et al.: J. Phys. D: Applied Physics **24**, 714 (1991)
99. T. Takezawa, T. Tsuzuku, A. Ono and Y. Hishiyama: Phil. Mag. **19**, 623 (1969)
100. D.M. Teter: MRS Bulletin (1998) p 22
101. A. Marchand: In *Chemistry and Physics of Carbon*, vol 7, ed by P.L. Walker (Marcel Dekker Inc., 1971) pp 155–189
102. L. Fillippozi, A. Derre, J. Conard et al.: Carbon **33**, 1747 (1995)
103. B. Ottaviani, A. Derre, E. Grivei et al.: Mater. Chem. **8**, 197 (1998)

104. B. Maquin, J.-M. Goyeneche, A. Derre et al.: J. Phys.: Appl. Phys. **33**, 8 (2000)
105. R. Riedel: Adv. Mater. **6**, 549 (1994)
106. G. Demazeau: In *Carbon, molecules and materials*, Chap. 13, 481 ed by R. Setton, P. Bernier and S. Lefrant (Taylor and Francis, 2002)
107. D.M. Teter and R.J. Hemley: Science **271**, 5355 (1996)
108. Y. Tateyama, T. Ogitsu, K. Kusakabe et al.: Phys. Rev. B **55**, R10161 (1997)
109. L.W. Yin, Y. Bando, M.-S. Li, Y.-X. Liu and Y.-X. Qi: Adv. Mater. **15**, 1840 (2003)
110. M. Kawaguchi: Adv. Mater. **9**, 615 (1997)
111. N. Kurita, K. Kobayashi, H. Kumahora and K. Tago: Phys. Rev. B **48**, 4850 (1993)
112. J.R. Bowser, D.A. Jelski and T.F. George: Inorg. Chem. **31**, 154 (1992)
113. H.F. Muhr, R. Nesper, B. Schnyder and R. Lotz: Chem. Phys. Lett. **249**, 399 (1996)
114. J.C. Hummelen, B. Knight, J. Pavlovitch, R. Gonzalez and F. Wudl: Science **269**, 1554 (1995)
115. V.I. Sokolov: Russian chemical bulletin **42**, 1 (1992)
116. M.S. Dresselhaus, G. Dresselhaus and Ph. Avouris: *Carbon Nanotubes, Synthesis, Structure, Properties and Applications* (Springer-Verlag, Berlin 2001)
117. R. Tenne, L. Margulis, M. Genut and G. Hodes: Nature **360**, 444 (1992)
118. C.N.R. Rao and N. Nath: Dalton Trans. 1 (2003)
119. N.G. Chopra, R.J. Luyken, K. Cherrey, V.H. Crespi, M.L. Cohen, S.G. Louis and A. Zettl: Science **269**, 966 (1995)
120. R.S. Lee, J. Gavillet, M. Lamy de la Chapelle, A. Loiseau, J.-L. Cochon, D. Pigache, J. Thibault and R. Willaime: Phys. Rev. B **64**, 121405 (2001)
121. R. Tenne, M. Homyonfer and Y. Feldman: Chem. Mater. **10**, 3225 (1998)

2

Synthesis Methods and Growth Mechanisms

A. Loiseau, X. Blase, J.-Ch. Charlier, P. Gadelle, C. Journet, Ch. Laurent and A. Peigney

Abstract. In this chapter, our purpose is to present how carbon nanotubes are synthesized and how their formation and growth can be studied, understood and modeled. We give an overview of the different synthesis methods, which can be classified into two main categories according to the synthesis temperature. We include a review of the CVD synthesis of carbon filaments, as an introduction to that of nanotubes.

2.1 Introduction

The identification of what we call carbon nanotubes today is dated from 1991 due to the work of S. Iijima. However the story of their synthesis is a sequence of serendipities in the expansion of synthesis routes to C_{60} molecules and to carbon fibers which merits to be evoked in this introduction in order to explain the organization of this chapter.

The C_{60} molecule was discovered in 1985 by Kroto, Smalley and coworkers [1] with an original synthesis setup which consists of ablating a graphite target with an energetic pulsed laser. However, the full expansion of the synthesis and the research on fullerenes did not truly begin until the mass production of these materials was invented by Krätschmer and Huffman in 1990 [2]. The principle of this synthesis route was ingeniously simple and cheap since it consisted in establishing an electric arc between two electrodes made in graphite under an helium atmosphere. Therefore, it was popularized immediately and research groups all over the world built carbon-arc fullerene generators and started to investigate the C_{60} molecules.

This could have been the happy end of the success story. In fact, the publication by Krätschmer and Huffman was only its beginning. It soon turned out that there were other cage structures to be found in the soot produced by the electric arc, like C_{70}, which looks a bit like a rugby ball. Even more interesting, when the carbon arc power supply was changed to direct current instead of alternating current, strange filamentous structures could be found

A. Loiseau et al.: *Synthesis Methods and Growth Mechanisms*, Lect. Notes Phys. **677**, 49–130 (2006)
www.springerlink.com
© Springer-Verlag Berlin Heidelberg 2006

in one of the electrode deposits. Nobody cared about this deposit until S. Iijima looked at it in his high-resolution transmission electron microscope in 1991 [3]. He observed and identified tubular structures entirely made of perfectly crystallized carbon and named them nanotubes, referring to their diameters, which were only a few nanometers. The structure of these objects attracted immediately a general attention of the research community so that the publication of S. Iijima can be considered as a true breakpoint in the history of carbon.

This is even more remarkable since tubular carbon structures turn out not to have been observed for the first time in 1991. Indeed, such structures have been known since at least the 60's and the work by Bacon [4] under the generic name of filaments or carbon fibers. They were at the beginning an undesired by-product in industrial chemical processes. The diameter of the filaments is typically less than 100 nm and can be as small as a few nm as attested by the observations of M. Endo in transmission electron microscopy in the seventies [5]. The thinner filaments were therefore very close to the present nanotubes. However, their observation did not attract so much attention because at that time there was no way to study and to use objects so small in size. This context was completely changed in the nineties and explains the expansion of the research after the observations of S. Iijima. But there is even more. Catalytic chemical vapor deposition (CCVD) processes, which are the synthesis route to filamentous carbon par excellence, have then been adapted to the synthesis of carbon nanotubes and are now able to produce mm-long single-walled nanotubes. Because of their flexibility and their facility to be scaled up, they are promising candidates to become the major way for synthesizing in a controlled way carbon nanotubes.

Several methods have been devised to synthesize carbon nanotubes (CNT) since 1991. Very generally, they can be classified into two main categories depending on whether they are running at high or at medium temperatures. High-temperature routes are, as the electric-arc method, based on the vaporization of a graphite target whereas medium-temperature routes are based on CCVD processes. They are successively described in this chapter (Sect. 2.2 and Sect. 2.4) with for the latter an introductory section giving the reader the basic notions of CCVD growth of filamentous carbon (Sect. 2.3). The panorama of high-temperature methods is completed by a presentation of their use and their adaptation to the synthesis of parent BN nanotubes.

Sections 2.5 and 2.6 are devoted to the formation and growth mechanisms of these objects. Since all their properties are directly related to the atomic structure of the tube, it is essential to understand what controls nanotube size, the number of shells, the helicity and the structure during the synthesis. A thorough understanding of the formation mechanisms for these nanotubular carbon systems is crucial to design procedures for controlling the growth conditions to obtain more practical structures which might be directly available for applications. Section 2.5 focuses on carbon single-walled nanotubes (C-SWNTs) and aims at understanding why this kind of nanotubes – in

contrast to carbon multiwalled nanotubes (C-MWNTs) – can only be produced with the help of a metallic catalyst whatever the synthesis process. It presents a comprehensive and phenomenological analysis of their formation and growth based on different experimental investigations either done in-situ during the synthesis or performed on the synthesis products after the synthesis. Section 2.6 presents the numerical simulations of the growth mechanisms of C-MWNTs and SWNTs using ab initio and semi-empirical methods. In the final section (Sect. 2.7), this panorama is completed by the analysis of growth of $B_xC_yN_z$ nanotubes and the numerical simulations performed for these parent objects.

2.2 High-Temperature Methods for the Synthesis of Carbon and Boron Nitride MWNTs and SWNTs

2.2.1 Generalities on High Temperature Methods

High-temperature methods are directly issued from the historical carbon-arc process invented by Krätschmer and Huffman in 1990 [2] for the production of fullerenes. They all involve sublimating graphite in a reduced atmosphere or rare (inert) gases, brought to temperatures above 3200°C – that is the sublimation temperature of graphite – and condensing the resulting vapor under a high temperature gradient. What differentiates the various processes is the method used for sublimating graphite. This can be an electric arc formed between two electrodes made in graphite, an ablation induced by a pulsed laser or a vaporization induced by a solar or a continuous laser beam. These processes are described in detail in the following sections.

2.2.2 The Electric Arc Discharge Technique

In his initial experiment, S. Iijima [3] used a DC arc discharge in argon consisting of a set of carbon electrodes. The discharge temperature was in the range of 2000–3000°C at nominal conditions of 100 A and 20 V. This apparatus produced multiwalled nanotubes in the soot. Later, single-walled carbon nanotubes were grown with the same set-up by adding to the electrodes suitable catalyst particles, e.g. of Fe, Co, Ni or rare-earth metals.

Principle and Description

This method is a slightly modified version of the method used for fullerene production. An arc discharge is generated between two graphite electrodes placed face to face in the machine's principal airtight chamber (Fig. 2.1) under a partial pressure of helium or argon (typically 600 mbar). The electrical discharge that results brings the temperature up to 6000 °C. This is hot enough for

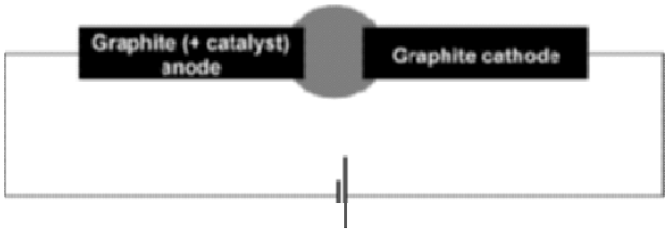


Fig. 2.1. Principle of the electric arc discharge technique

the carbon contained in the graphite to sublimate – that is, transform from a solid state to gaseous one without turning into a liquid first. During sublimation, pressure runs very high, ejecting carbon atoms from the solid and forming a plasma. These atoms head toward colder zones within the chamber, allowing a nanotube deposit to accumulate on the cathode. The type of nanotube that is formed depends crucially upon the presence of metal catalysts. If small amounts of transition metals such as Fe, Co, Ni or Y are introduced in the target graphite, then single-walled carbon nanotubes are the dominant product. In the absence of such catalysts, the formation of multiwalled carbon nanotubes is favored.

In-Situ Diagnoses

In-situ diagnostics during growth of carbon nanotubes is quite difficult to carry out in an electric-arc apparatus. However methodologies for determining the temperature in the arc process for SWNTs production have been investigated by a few groups.

Generally, a lens, located about 30 or 40 cm from the center of the arc chamber, collects light through a window in the side of the chamber. The lens focuses an image of the arc on a focal plane at which an optical fiber is located. The fiber then transfers the light from a particular spot on the image to a spectrometer. This spectrometer is used to analyze radiation emitted during the arc discharge from catalyst atomic lines, ion lines, and from C_2 Swan bands.

S. Farhat and co-workers estimated temperature dependencies and electron density distribution from these spectral lines [6]. They obtained excitation temperatures assuming Boltzmann equilibrium among the various excited states, as well as relative equilibrium concentrations of ions and atoms. Measurements taken with single catalysts and with the yttrium/nickel mixture indicated that when nickel was the only catalyst present, the inferred temperature was significantly higher, about 10000 K, than when yttrium was present, about 3000 K. As the argon/helium mixture was varied they saw a maximum of the temperature near the center of the arc for 60% argon. Further work needs to be done to explain this behavior.

H. Lange and co-workers [7] find temperatures within 3500–6500 K and C_2 column densities within $(0.5-6)\times10^{15}\,\mathrm{cm}^{-2}$ depending upon the arc current and plasma coordinates.

Synthesis of Either SWNTs or MWNTs

Two kinds of syntheses can be performed with this method.

Evaporation of Pure Graphite

In this case, two kinds of products are formed in the reactor: a deposit which grows on the end of the cathode during the arc process [3] and soot on the reactor walls. The flocky-to-crumbly soot contains fullerenes, amorphous carbon, some graphitic sheets but no nanotubes. The deposit consists of a hard grey outer shell and a soft fibrous black core [8]. Various microscopic observations have shown that the outer hard shell is formed of nanoparticles and MWNTs fused together whereas the core contains about one-third polyhedral graphitic nanoparticles and two-thirds MWNTs [9]. The MWNTs consist of a few to a few tens of graphitic sheets which are concentrically rolled up around each other with a constant separation between the layers nearly equal to that of the graphite layer spacing (0.34 nm). Their inner diameter varies between 1 nm up to 3 nm and their outer diameter ranges from 2 nm up to 25 nm depending on the number of concentric layers. Generally their length is not more than 1 µm but some exceeding 1 µm have been observed. The perfectness of the crystallinity of the layers and of their stacking observed in high resolution electron microscopy (HRTEM) (Fig. 2.2) is striking. Each concentric layer is seen as a set of two dark lines symmetrically located with respect to the tube axis as explained in Chap. 3. The great majority of the MWNTs have closed caps by insertion of pentagonal defects into the hexagonal network, as also explained in this chapter.

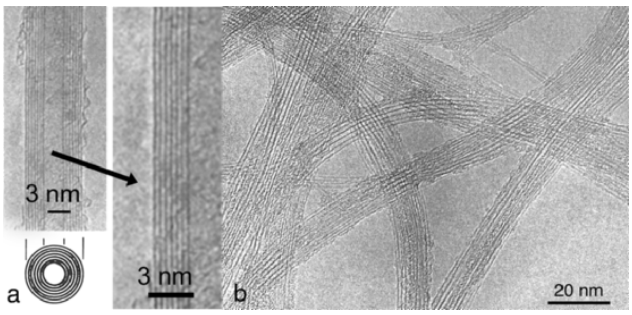


Fig. 2.2. High resolution transmission microscopy images of nanotubes produced by the electric arc method: (**a**) A multiwalled nanotube with a magnification showing details of the layer structure (adapted from [3]); (**b**) set of single-walled nanotubes assembled into ropes (the synthesis procedure is described in [20])

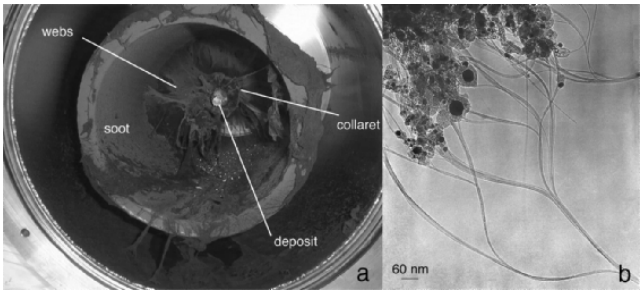


Fig. 2.3. (**a**) View of the reactor after synthesis where one can distinguish the various products obtained when using a mixture of carbon and catalysts; (**b**) TEM image of the collaret containing bundles of SWNTs mixed with catalyst metallic particles and different graphitic structures

Co-vaporization of Graphite and Metal

By drilling a hole in the center of the anode and filling it with a mixture of a metal catalyst and graphite powders, another element is introduced and co-evaporated with the carbon during the arc discharge process. As a consequence the macroscopic and the microscopic structure of the formed products changes [10]. As with pure graphite, a deposit grows at the surface of the cathode (Fig. 2.3a). This deposit contains MWNTs, empty or filled graphitic nanoparticles, and round spherical metallic particles when obtained with the majority of the tested elements [11–25]. Sometimes the MWNTs observed in the deposit are found to be filled [25–27]. Under certain conditions, a collaret similar to a soft belt is formed around the hard shell of the deposit [11–20]. In this collaret, amorphous carbon, spherical metallic nanoparticles, a few graphitic sheets, and a high density of SWNTs are found (Fig. 2.3b).

Single-walled nanotubes can be isolated or organized in bundles consisting of a few to a few tens of single tubes stuck together in a triangular lattice and more or less covered with fullerene/soot material. Figure 2.2b shows an example of bundles observed in HRTEM. Each bundle is imaged as a set of fringes parallel to their axis as explained in Chap. 3. The majority of the tubes have a diameter between 1.2 and 1.4 nm and lengths reaching up to several microns.

However no collaret is formed with some elements [10–14, 16–18, 21–25]. Growing from the cathode to the reactor walls and decorating the chamber are also found some kinds of 'spider webs'. These structures, containing fullerenes, amorphous carbon, some graphitic sheets, and a low density of SWNTs are obtained when using mixtures of Co or Ni [11–20]. In some cases, webs might not appear [10–14,16–19,21–25]. The soot can vary from crumbly to spongy in appearance and is formed of the same structures as those found in the webs. Depending on the element co-evaporated, it can contain SWNTs [10–20,23,28] or short SWNTs radially growing from catalytic particles like 'sea urchins'

[11, 24, 29] or MWNTs with a good portion of their length filled with metal [13,14,22] or no nanotubes at all [11,13,17,19,21]. The quantity and quality of the nanotubes obtained this way depend mainly on the metal/carbon mixture. A lot of elements and mixtures of elements have been tested by various authors and it is noted that the above-described results can vary significantly from one author to another even though the elements used are the same. This is not surprising since the experimental conditions depend on various parameters such as the metal concentration [10–29], the inert-gas pressure, the nature of the gas [30], the current, and the geometry of the system.

2.2.3 Laser Ablation

Historically, pioneer production of fullerenes was obtained with a laser ablation technique [1]. In this process, a quartz tube was heated to about 1200 °C in a furnace. Within the furnace, an argon flow at sub-atmospheric pressure was maintained. The tube contained a block of compressed graphite. By the use of intense pulsed laser irradiation, the graphite was vaporized and fullerenes were formed in the condensed soot. Later, the same technique was used to produce carbon nanotubes [33].

Principle and Description

The laser ablation technique is rather similar to the arc method as it also consists of sublimating graphite in a reduced atmosphere of rare gases and has been proven to lead to very similar structures to those obtained by the arc method: fullerenes, SWNTs or MWNTs with the same crystalline quality, onions, etc.

Ablation of a graphite target with a focused laser beam is realized in an inert atmosphere at low pressure (Fig. 2.4). Two kinds of methods were developed and they used either a pulsed laser [33,34] or a continuous laser [35]. The main difference between both lasers is that the pulsed laser demands a much higher light intensity (100 kW/cm^2 compared with 12 W/cm^2). In the pulsed laser configuration, a Nd-YAG laser pulse evaporates a solid target of

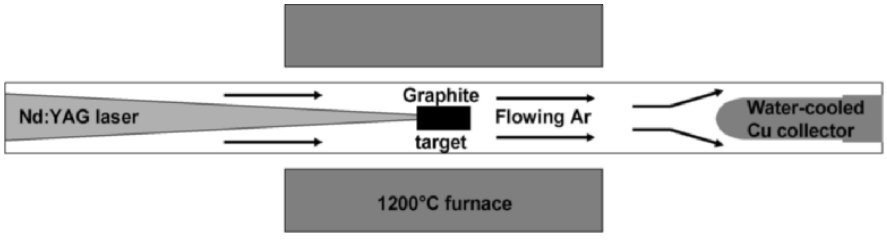


Fig. 2.4. Principle of the laser ablation technique, after [34]

graphite (or graphite and catalyst) into a background gas which is gently flowing through a quartz tube inside a high temperature oven. The laser converts the composite solid material into small aggregates which can only recombine if placed in an external furnace heated to 800°C minimum [36]. The role of the furnace is to create a temperature gradient suitable for the formation and growth of long nanotubes [37]. In the continuous laser configuration a 2-kW continuous-wave CO_2 laser is focused on the target, heating it up to 3000–3500 K. The target is placed vertically and an inert gas (He, Ar, N_2) is flowing from the bottom to the top of the reactor chamber. During the vaporization process the flowing argon gas sweeps the produced soot inside the quartz tube. In this case, carbon nanotubes can be formed without the help of an additional furnace. Indeed, in contrast to the pulsed laser configuration, the flowing gas is heated in the vicinity of the target up to the temperature reached at the surface illuminated by the laser as shown by Foutel-Richard [38] and Dorval et al. [39].

In both cases, the nanotubes nucleate in the vapor phase, coalesce, get carried away by the flowing argon and condense downstream on the water-cooled copper collector. The felt-like material, when scraped off the wall, contains MWNTs or SWNTs depending on the experimental conditions. As with the electric arc method, MWNTs are obtained when using a pure graphite target and SWNTs when the target is a mixture of graphite and metallic catalysts such as Ni-Co or Ni-Y mixtures [35,40]. Nanotubes are accompanied by amorphous carbon, metal particles, and onions as in electric arc techniques. Many purification methods have been developed to extract high yield samples of SWNTs and MWNTs.

The main differences with the arc method are:

- The material is submitted to a laser ablation instead of an arc discharge.
- No tube of reasonable length has ever been synthesized without some catalyzing particles. This implies that a certain local anisotropy is necessary to grow a nanotube.
- Particles are collected through a carrier gas on a cool plate far from the target. A secondary heating is usually added.

In-situ Diagnoses

Formation and growth mechanisms of carbon nanotubes during the laser ablation process are being more and more frequently investigated [39,41–44]. In this part, we will distinguish pulsed laser from continuous laser vaporizations.

Pulsed-Laser Vaporization

Pulsed-laser vaporization with nanosecond lasers is especially amenable to diagnostic investigations. The vaporizing pulse lasts only 10 ns and SWNT growth then can occur undisturbed from further excitation, even for single

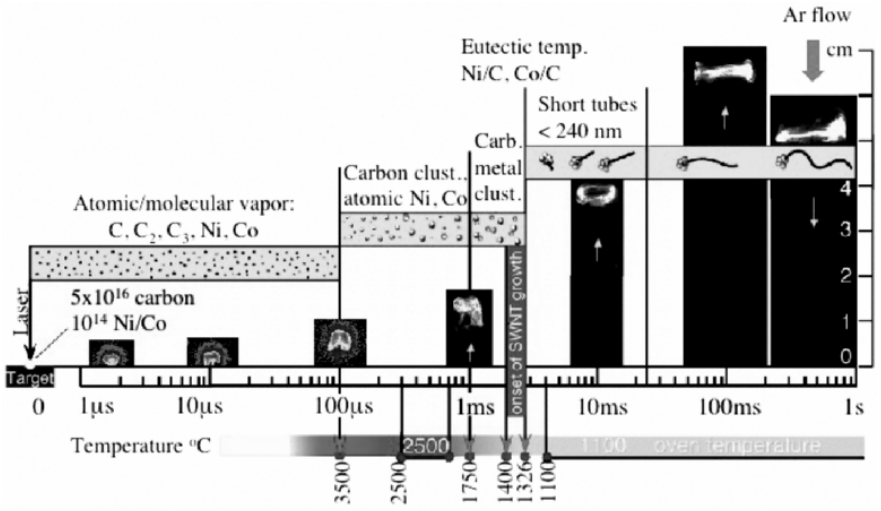


Fig. 2.5. A compendium of the results from Puretzky et al. [41, 42], which shows actual images of the ablation plume vs. time (log scale), the species detected spectroscopically from the plasma emission or laser-induced luminescence spectra, plume temperatures measured through blackbody emission above the oven temperature, and lengths measured from arrested-growth experiments

laser ablation events. D. B. Geohegan's group at ORNL has developed a set of unique diagnostics including spectroscopic gated-ICCD imaging, ion probe measurements and several optical spectroscopic methods to monitor the laser ablation of graphite for the synthesis of nanotubes [41, 42]. Results of these studies are summarized in Fig. 2.5.

Spectroscopic measurements of the luminous laser plasma are made at early times after Nd:YAG laser ablation (<200 μs) and after long-pulse CO_2 laser ablation at room temperature. However, these measurements are limited to times while the ablated material is still quite hot. It is found that carbon converts to clusters very early (∼0.2 ms), at a temperature below 3500°C, the catalyst converts to clusters much later (2 ms) and at a much lower temperature below 1750°C and after 2 ms only carbon nanotubes can be detected. The key finding of these measurements is that the atomic and molecular species appear to feed the formation of clusters within the first 2 ms. The temperature range 1400–1300°C is found to correspond to the onset of nanotube growth. It roughly corresponds to the eutectic temperature of Ni–C and of Co–C systems [45]. The majority of nanotube growth occurs for times >2 ms and can exceed tens of ms. Therefore, the feedstock for the majority of nanotube growth is small carbonaceous clusters, or larger aggregates of these clusters (and not atomic or molecular species).

These main conclusions regarding plume composition versus time are confirmed by Kokai et al. [46] and Arepalli et al. [43] who used a similar time-

resolved imaging and spectroscopy approach based on in-situ measurements of laser-induced emission and scattering from the propagating plume.

These results are also confirmed by De Boer et al. [47] who performed in-situ laser-induced fluorescence monitoring the atomic Ni density in the near-target region and showing that the majority of Ni atoms stay in the vapor phase for several milliseconds after ablation.

Finally the necessity of using an external furnace for creating the suitable temperature gradient has been shown by black-body emission spectroscopy measurements [37].

Continuous Laser Vaporization

A dedicated reactor has been developed [38,40,48] to investigate the gas phases during carbon nanotube formation by a complete set of optical diagnoses: laser-induced fluorescence (LIF), laser-induced incandescence (LII), coherent anti-Stokes Raman Scattering (CARS), and emission spectroscopy [39]. The temperature gradient above the target has been determined by measuring by CARS the temperature of the flowing gas [39, 40]. Three distinct spatial regions of cooling are derived from a fast cooling above 2000 K in the first 3 mm above the vaporized target (region 1), a moderate cooling up to 7 mm where the gas temperature reaches 1600 K (region 2), and then a long plateau of temperature at about 1000 K (region 3). LII imaging yields a map of the density of the hot carbonaceous flow and revealed drastic spatial changes due to the presence of catalysts.

These observations are confirmed by gas phase LIF and spontaneous emission of Co, Ni, and C_2. The C_2 radical is well detected as in pulse-laser set-up and its existence is found to be restricted to region 1. The transition between regions 1 and 2 at a temperature about 2000 K corresponds to the drop of C_2 concentration in the gas phase. As in pulse-laser experiments, metal vapors remain present at much lower temperatures and disappear at the end of region 2 only. Region 2 at temperatures between 2000 and 1600 K is associated with the condensation of metal vapors into liquid metal particles. This condensation influences the process of carbon coalescence because the spatial profiles of C_2 and soot concentrations are markedly different with and without catalysts. Dissolution of carbon in liquid metal particles may explain this key observation. It is therefore suggested that at this location, growth of carbon nanotubes starts.

2.2.4 Vaporization Induced by a Solar Beam

In 1993, being aware of the interest of the solar method, the Smalley [49] and A. Lewandowski [50] teams in the USA and groups from University of Montpellier and the Institute for Material Science and Process Engineering (IMP-CNRS) in Odeillo (France) [51] demonstrated that fullerenes could be produced by sublimation of graphite using highly concentrated sunlight from a solar furnace.

Principle and Description

This method, which can be compared with continuous laser vaporization, uses a solar furnace to focus the sunlight on a graphite sample and vaporize carbon. The soot is then condensed in a cold dark zone of the reactor.

At the solar furnace from Odeillo (France) [51], the sunlight is collected by a flat tracking mirror and is reflected towards a parabolic mirror which focuses the solar radiation directly on the graphite target. The target is placed at the center of an experimental chamber which is first evacuated and then swept by helium or argon. Under clear-sky conditions, temperatures of around 3000 K can be reached at the 2-kW set-up of the solar station and the evaporation process can start. With this reactor, evaporation of graphite is possible and gives a small amount of soot. This soot, which contains fullerenes, is collected in a filter on the water-cooled surface of the chamber. Until 1998, this process was only used to produce fullerenes. However, with an improved setup, the same team [52, 53] demonstrated that they could form nanotubes using the solar energy. Just by changing the target composition and adjusting the experimental conditions, carbon nanotubes can be produced with exactly the same experimental setup. The target, a graphite crucible, is filled with a mixture of graphite powder and metallic catalysts and placed in a graphite pipe heated at its top by the sunlight (Fig. 2.6). The evaporated material is drawn immediately through the graphite pipe, which acts as a thermal screen by reducing radiative losses. On its walls the produced soot material is in the form of rubbery sheets which can be collected. Especially nickel/cobalt and nickel/yttrium in the graphite – target mixtures result in the formation of soot containing carbon nanotubes. Depending on the pressure and flow conditions, either bamboo-like MWNTs, or MWNTs and SWNTs together, or only SWNTs in the form of long bundles can be found. Additionally, the

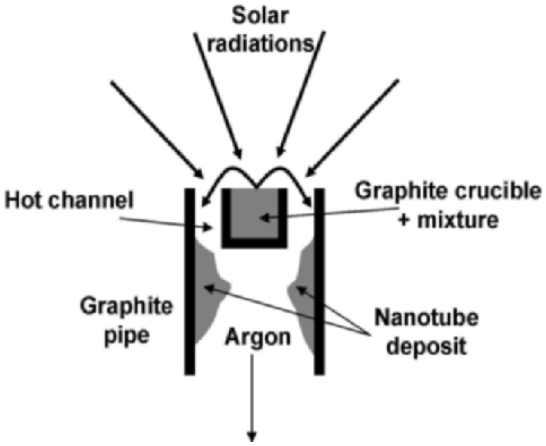


Fig. 2.6. Principle of the solar furnace technique

nanotubes are accompanied by amorphous carbon and metal nanoparticles. The diameter distribution of the SWNTs lies in the range of 1.2 to 1.5 nm and the sample purity can be as good as that produced by the laser methods. The solar process can lead to production rates of 100 mg per each run (per hour) if the weather conditions allow to keep the temperature during the experiment at 3000 K.

In-situ Diagnoses and Simulation of the Synthesis

Diagnostic data have been obtained by pyrometry and emission spectroscopy during the production of carbon nanotubes with a solar reactor [54]. In relation with these measurements, a numerical simulation of the vaporization has also been done. The results point out some common behavior with electric arc or laser ablation, especially concerning the great influence of the cooling rate of vapors on the structure and yield of nanostructured carbon material. The best nanotubes yield is found for a cooling speed of 1000 K/ms, while a medium yield is obtained at 100 K/ms and no nanotubes at all at 50 K/ms. It is also found that the change of catalyst induces differences in the diameter of SWNT and change of both length and diameter of the bundles. It is finally assumed that the key parameter is the temperature at which the SWNTs are formed. This temperature range can be related to the sublimation temperature of the target and to the eutectic temperature of Ni–C and Co–C systems which is about 1300–1350°C [45].

2.2.5 Upscaling

Since their discovery, carbon nanotubes have promised the development of a wide range of applications but commercial development has been constrained by the lack of a reliable large-scale manufacturing process. The availability of carbon nanotubes in commercial quantities, of consistent quality and at an accessible price will unlock the potential for a wide range of industrial applications. In this section, we discuss the possibilities of upscaling the three main methods described before.

– The carbon arc-discharge method is the most common and perhaps easiest way to produce carbon nanotubes as it is rather simple to undertake. It generally produces large quantities of a mixture of components which requires a purification treatment for separating nanotubes from the soot and the catalytic metals present in the crude product. The nanotubes produced have a very good structural quality. The main limitation of this technique is related to the carbon flow rate which is limited by the electrode erosion. It has been shown that the nanotube yield decreases linearly with electrode diameter increase [31]. Despite this problem, some start-up companies have taken up the challenge of upscaling this technique and they supply bulk quantities of arc-grown carbon nanotubes [32].

– Laser ablation produces a small amount of clean nanotubes and because of their good quality, scientists are trying to upscale this method. However, though promising, the results are not yet as good as for the arc-discharge method. Scaling up is possible, but the technique is rather expensive due to the laser and the large amount of power required. Finally a decisive advantage of these methods lies in their suitability for in-situ diagnostics.
– Improvement in the production rate of the solar technique can be envisaged by adapting the experimental set-up to a more powerful 1 MW facility at the Odeillo station. For the production of carbon nanotubes with high purity, the temperature of the carbon vapor must be very high (3100°C). With a 1000-kW furnace, targets 100 times larger than those currently used could be heated to such high temperatures. The prototype of a reactor able to withstand such intense power has been developed at the solar furnace in Odeillo and is currently being tested at a power of 50 kW [55]. It has already provided very promising results.

2.2.6 Synthesis of Heteroatomic Nanotubes

For the synthesis of heteroatomic nanotubes (mainly BN and BCN), many methods were inspired by carbon nanotubes: arc discharge, laser ablation, pyrolysis, CVD techniques, etc. But making an equivalent production (thin tubes over the micron scale, ropes, quantity higher than what is needed for electron microscopy observations) remained a challenge until very recent years. In this part, we will discuss the synthesis of BN and BCN nanotubes by arc discharge and laser ablation methods only.

Pure BN MWNT and SWNT

Arc Discharge

The main difficulty for synthesizing boron nitride (BN) nanotubes with an arc discharge lies in the insulating character of h-BN which prevents one from simply replacing graphite electrodes by hexagonal BN (h-BN) ones. Therefore different kinds of electrodes have been successively tried, which should both be electrically conducting and contain B and/or N. The first synthesis of BN multiwalled nanotubes was done in an arc discharge using a hollow tungsten electrode filled with h-BN [56]. A route to the successful arc-discharge synthesis of pure BN multiwalled and single-walled nanotubes was found by A. Loiseau et al. in 1996 [57]. The carbon-free plasma was established between electrodes made of hafnium diboride (HfB_2), which is a metallic compound having a high temperature melting point, in a nitrogen atmosphere. At the same time, Terrones et al. obtained nanotubes and encapsulated polyhedral particles by arcing a mixture of h-BN and of tantalum in a nitrogen atmosphere [58]. Later, Y. Saito and M. Maida used ZrB_2 electrodes instead of HfB_2 [59]. Recently, J. Cumings and A. Zettl claimed they could produce macroscopic amounts of

pure BN nanotubes by arc discharge in nitrogen gas using boron electrodes containing 1 atomic percent each of nickel and cobalt [60].

This arc discharge technique, even if realized under different conditions, always leads to the formation of BN nanotubes in very low yields and made of very few layers including single- and double-layer tubes, as identified by high-resolution transmission-electron microscopy. Electron-energy-loss spectroscopy shows that boron and nitrogen are present in a one-to-one ratio approximately. The most frequently observed terminations are empty and flat, with layers perpendicular to the tube axis, in a square shape as explained in detail in next chapter.

Laser Ablation

With laser ablation, the first pure BN multiwalled nanotubes were obtained by laser heating of c-BN micro-crystals at high nitrogen pressure (5–15 GPa) [61], and later, by using excimer laser ablation at 1200 °C [62,63]. In 2001, Lee et al. succeeded in synthesizing bulk quantities of pure BN SWNTs without using a metal catalyst [64] by heating and decomposing a h-BN target with a CO_2 continuous laser under a nitrogen pressure of one bar. A vast majority of these nanotubes had a zig-zag configuration and were organized in crystalline bundles. The end of the BN SWNTs showed encapsulated boron nanoparticles, suggesting that BN SWNTs grow via a root-based mechanism from the reaction of these boron particles with nitrogen.

B–C–N Nanotubes

B–C–N nanotubes have been synthesized using laser ablation of C/B/N mixed targets [69] and arc discharge experiments with graphite cathodes and different kinds of anodes: B/C inside graphite anode in nitrogen atmosphere [65], BC_4N anode in helium atmosphere [66], BCN anodes [67], and HfB_2 anode in nitrogen atmosphere [68].

These B–C–N nanotubes are all multiwalled. Elemental profiles obtained by spatially resolved electron-energy-loss spectroscopy (see Chap. 5) reveal a strong phase separation between BN layers and carbon layers along the radial direction. Most of these tubes have a sandwich structure with carbon layers both in the center and at the periphery, separated by a few BN layers [68]. These segregations reflect the tendency to phase separation between graphite and h-BN observed in the B–C–N phase diagram [70].

2.2.7 Conclusion

In conclusion, high-temperature methods have been known to produce high quality nanotubes, particularly the single-walled variety, and in relatively large quantities. Depending on the experimental conditions, it is possible to selectively grow SWNTs or MWNTs. Owing to their high structural quality, these nanotubes have been instrumental in many fundamental studies of transport, nano-optics, etc.

2.3 Catalytic CVD Growth of Filamentous Carbon

Catalytic Chemical Vapor Deposition (CVD) processes make possible the growth of carbon filaments of various sizes and shapes at low temperature ($\leq 1000°C$) from carbon-containing gaseous compounds which decompose catalytically on transition-metal particles [71–73]. The word *catalytic* is used here to emphasize the role of metallic particles serving as decomposition sites as well as growth germs. We use *filament* here as a generic name for a large family of elongated structures of diameters less than 100 nm, which obviously includes nanotubes at the top of the structural-order scale. Some authors prefer to distinguish filaments from nanotubes, and use *filament* to describe stacked cone-shaped graphene layers; others use the term *nanofibers* instead of filaments.

Formation of filamentous carbon by catalytic decomposition of gases has been intensively studied for 50 years (soon after the introduction of the TEM) because of its detrimental effect during important industrial chemical processes such as steam reforming [72]. This detail is more than anecdotal: the approach used by specialists of catalysis to study carbon growth is based on thermodynamic and kinetic analysis of CVD, with the goal of determining growth rates as a function of various parameters. Material scientists, on the other hand, have been more interested in filament properties, seeking the best way to tailor the filament structure [73]. Many studies have been based on TEM observations after growth without any details on thermodynamics and reaction kinetics. This difference in the scientific approach is even more pronounced in the CNT community, and only rarely has the thermodynamic and kinetic approach been applied to CNT growth [74–76].

Carbon filaments are in some sense ancestors of Iijima's multiwalled carbon nanotubes and it is obvious that the huge amount of research performed in this field (before and after 1991) is useful to the CNT community. We thus find it appropriate to introduce CVD growth of nanotubes by starting with that of carbon filaments, insisting on the thermodynamics and kinetics of the formation mechanism. The chemical reactions involved in the production of carbon (such as the disproportionation of CO, see 2.3.1) would be infinitely slow or would produce non-filamentary carbon (by decomposition of hydrocarbons) without small particles of metal like Fe, Co or Ni. These metals are considered as catalysts because they are often recovered without any chemical change after the growth reaction. Nevertheless, it has recently been shown that nanoparticle morphology may change during the growth reaction due to high atomic mobility at the surface or because of a solid-liquid phase transition. For the same reasons it happens that elongated nanoparticles are found trapped and melted inside filament cores during growth. Atomic impurities of metals may also be incorporated in the filament structure during growth. Moreover, metals can be changed into carbides by the gaseous reactants and some authors consider that carbon filaments are the result of carbide decomposition (see 2.3.1). Others consider that filaments precipitate directly

from carbon atoms dissolved in the metal, and it has been suggested that the (low temperature) solid-liquid transition evoked above is induced by carbon dissolution in the metal network. Catalytic growth of carbon is thus not just a surface phenomenon but a definitely more complicated one, and much work remains to be carried out before a complete understanding of the process is achieved. The long-term goal is to produce carbon filaments (and nanotubes) at will, with controlled morphology and therefore with defined properties. To do so, we need to understand the thermodynamics and kinetics of specific CVD reactions and the role of the catalytic particle.

2.3.1 Thermodynamics of Carbon CVD

CVD growth relies on the capability to provide the atoms needed to form the solid deposit (here carbon filaments) from a gas source that decomposes under the action of temperature. The first important point is thus to examine the thermodynamics of the gas decomposition reaction, i.e., first to determine if the reaction is possible or not at the desired working temperature and then secondly to measure the equilibrium constants, which are compared to those for the formation of graphite. Analysis of deviations from graphite equilibrium gives useful information on the filament growth process [77]. We first describe herein two important reactions that have been thoroughly studied because of their industrial interest: decomposition of hydrocarbons, particularly of methane, and disproportionation of CO.

Decomposition of Hydrocarbons

Except for methane and other light paraffins, hydrocarbons (C_nH_m) have a positive value of the Gibbs function of formation $\Delta_f G^\circ$, i.e., variation of the Gibbs free energy ($G = H - TS$) of the system that occurs during the formation reaction from graphite and hydrogen, at all temperatures under standard-state conditions. Variation of the Gibbs function during the decomposition reaction of hydrocarbons into graphite and hydrogen under standard-state conditions (partial pressures are fixed at 1 bar) is opposite ($\Delta_r G^\circ = -\Delta_f G^\circ$) and the decomposition is therefore thermodynamically possible at all temperatures. $\Delta_f G^\circ$ is a measure of how far the standard-state is from equilibrium according to the following reaction:

$$C_nH_{m(gas)} \Leftrightarrow nC_{graphite} + m/2\ H_2.$$

The relationship between the Gibbs function of reaction at any moment in time ($\Delta_r G$) and the standard-state Gibbs function of reaction ($\Delta_r G^\circ$) is described by the following equation,

$$\Delta_r G = \Delta_r G^\circ + RT \ln Q\ ,$$

where R is the ideal gas constant and Q the reaction quotient at that moment in time. At equilibrium, $\Delta_r G = 0$ and $Q = K$, the equilibrium constant. Partial pressures of H_2 and of C_nH_m, $P(H_2)$ and $P(C_nH_m)$ (in bars), verify $K = P(H_2)^{m/2}/P(C_nH_m)$ and $RT \ln K = -\Delta_r G^\circ = \Delta_f G^\circ(C_nH_m)$. K and $\Delta_f G^\circ(C_nH_m)$ both depend on the temperature.

In the case of acetylene, which is often used in nanotube growth, $\Delta_f G^\circ(C_2H_2) = 225.31 - 0.054\,T$ (kJ mol^{-1}) and so $P(H_2)/P(C_2H_2) = \exp(27098/T - 6.5)$, decreasing when the temperature increases but still as high as 1151 at 2000 K. The decomposition of acetylene is therefore thermodynamically almost total at usual temperatures and is controlled by kinetics. Similar results are found with the other unsaturated hydrocarbons.

By contrast, methane has a negative standard-state Gibbs function of formation below 825 K. Therefore methane does not decompose easily. Using values given in [78], we can calculate, under a total pressure of 1 bar, the equilibrium pressures by solving the system $K = \exp[\Delta_f G^\circ(CH_4)/RT]$, $K = P(H_2)^2/P(CH_4)$ and $P(H_2) + P(CH_4) = 1$ (Table 2.1).

Table 2.1. Gibbs function of formation and H_2 equilibrium pressure for the decomposition reaction of methane

T(K)	600	700	800	900	1000	1100	1200
$\Delta_f G^\circ(CH_4)$ (kJ mol^{-1})	−22.851	−12.596	−2.057	8.685	19.572	30.562	41.624
$P(H_2)_{equilibrium}$ (bar)	0.096	0.286	0.565	0.800	0.920	0.967	0.985

Disproportionation of Carbon Monoxide ($2CO \rightarrow C + CO_2$)

$\Delta_r G^\circ = \Delta_f G^\circ(CO_2) - 2\Delta_f G^\circ(CO) = -170.7 + 0.1746\,T$ is negative (and therefore the reaction is thermodynamically favorable) for temperatures lower than 978 K. Table 2.2 gives $P(CO_2)$ at different temperatures under 1 bar of total pressure:

As in the case of methane decomposition, a mixture containing a lower amount of product than the equilibrium pressure is thermodynamically unstable and may deposit graphite. As seen in 2.3.1, this reaction is favored by high temperature for methane decomposition whereas the disproportionation of CO is favored by low temperature for which the kinetics are usually slow. CO is often chosen as the carbon source because of the opposite effects of thermodynamics and kinetics.

Table 2.2. CO_2 equilibrium pressure for the disproportionation reaction of carbon monoxide

T(K)	600	700	800	900	1000	1100	1200	1300
$P(CO_2)_{equilibrium}$ (bar)	0.9987	0.9846	0.907	0.67	0.305	0.082	0.02	0.006

Thermodynamic Effects of Carbon Polymorphism

The Gibbs function of formation is established from graphite which is the reference state for carbon. When carbon is deposited in a form other than that of graphite, the above-given changes of the Gibbs function must be corrected by the Gibbs function of formation of the form considered and the above-calculated equilibria are modified. For instance, at 900 K, $\Delta_r G^\circ$(diamond) = 5.54 kJ mol^{-1} and the calculated value for $P(CO_2)$ at the equilibrium with CO and diamond is 0.56 bar (under a total pressure of 1 bar) instead of 0.67 bar with CO and graphite.

Though the filamentary form of carbon is closer to graphite than to diamond, its Gibbs function differs from that of graphite. Its value depends on the geometrical arrangement (more or less perfect) of carbon layers and may (slightly) vary from one sample to another (Fig. 2.7). It can be measured from the composition of gaseous mixtures at the equilibrium with filamentary carbon (or other solid carbon materials). Rostrup-Nielsen [79] obtained in this way Gibbs functions as high as 24 kJ mol^{-1} for nanofibers from CO or CH_4 decomposition over nickel catalysts. He interpreted these results by assuming that 'structural disorder' leads to higher surface energies than in graphite, and gave evidence of a relation between the Gibbs function of the nanofibers and the sizes of the nickel particles located inside the nanofibers. Tibbetts and Alstrup considered the elastic-energy effect due to curvature of filament graphite planes as an important contribution to the deviation from graphite equilibrium [77, 80]. Tibbetts demonstrated that it was energetically favorable for the fiber to precipitate with graphite basal planes parallel to the exterior planes, arranged around a hollow core, thus forming a wide-diameter ($\sim$1 μm) multiwalled tube.

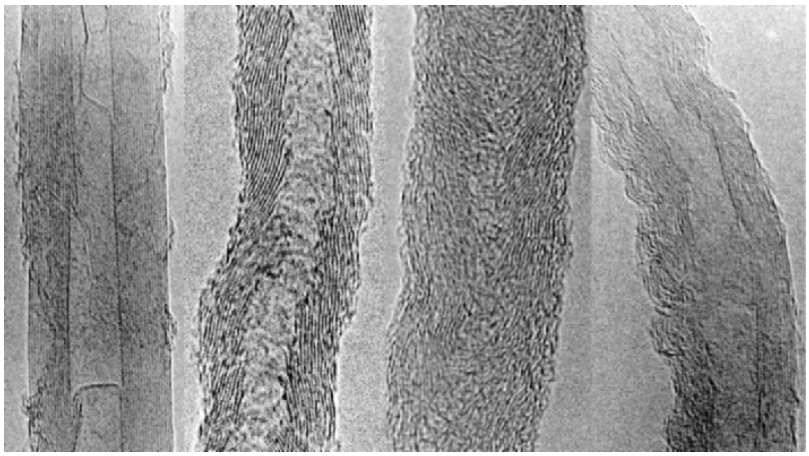


Fig. 2.7. High-resolution transmission electron micrograph (HRTEM) of various carbon filaments (by courtesy of T. Cacciaguerra)

Formation of Carbides as a Cause of Deviation from Equilibrium

De Bokx et al. [81] obtained results similar to those reported by Rostrup-Nielsen on deviations from equilibrium calculated from graphite data, but disagreed with the interpretation. Using nickel or iron catalyst for the decomposition of CH_4 or CO in the temperature range 650–1000 K, they gave evidence of formation of an intermediate carbide phase according to the following equilibrium:

$CH_4 + 3Ni \Leftrightarrow Ni_3C + 2H_2$ or $2CO + 3Ni \Leftrightarrow Ni_3C + CO_2$ (or similar with Fe) followed by $Ni_3C \rightarrow 3Ni + C$ or $Fe_3C \rightarrow 3Fe + C$.

They concluded their work stating that 'The process in which filamentous carbon is formed should not be referred to as catalytic. It concerns a heterogeneous reaction with a decomposition product'.

2.3.2 Kinetics and Mechanisms of Filament Growth

The *Dissolution-Extrusion* Mechanism

The kinetics of filamentary growth was extensively studied by Baker et al. [71, 82, 83]. They observed the growth of filaments from acetylene under the controlled atmosphere of a modified transmission electron microscope and measured the growth rate in situ over Ni, Fe, Co and Cr particles. The growth rate was inversely proportional to the diameter of the particles observed at the filament tips, which suggested a diffusion process. They demonstrated that the activation energy of the growth had the same value as the activation energy of carbon diffusion inside the catalyst, which could therefore be the limiting stage in the process. Figure 2.8 (where $2CO \rightarrow C + CO_2$ can be replaced by $C_nH_m \rightarrow nC + (m/2)H_2$) pictures the four stages of the 'tip-growth' dissolution-extrusion mechanism:

1. diffusion (in the gas phase) of reactive species (CO or C_nH_m) to the catalytic surface
2. gas-solid process: surface adsorption, followed by reaction between adsorbed species (Langmuir-Hinshelwood mechanism) or between an adsorbed species and a gaseous molecule (Eley-Rideal mechanism), both leading to carbon atoms
3. diffusion of carbon atoms through the catalyst particles to extrusion sites
4. segregation and bonding of carbon atoms into carbon layers

The same stages are supposed to occur in the 'root-growth' dissolution-extrusion mechanism when the particle remains stuck to its support [84, 85]. In experiments of Melechko et al. [86], changing the C_2H_2 partial pressure in a $NH_3 + C_2H_2$ mixture modified the growth mechanism from tip-growth to root-growth. They considered that the initial orientation of growth depended

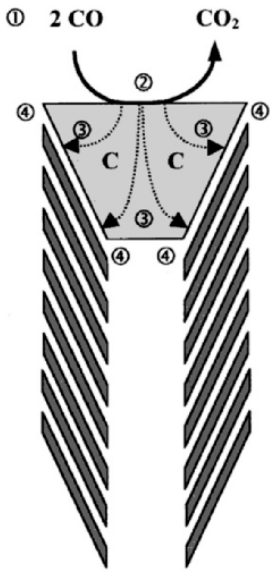


Fig. 2.8. Schematic illustration of truncated conical filament growth following the dissolution-extrusion model proposed by Baker et al. Stages 1–4 are described in the text

on the relative concentration of carbon at the different locations of the particle, which originated in different rates of carbon formation. Changing the composition of the gaseous mixture could change the order of these rates. Rates of filamentous carbon production from gas phases have been measured and analyzed by many authors in the framework of the dissolution-extrusion mechanism. One important point is to determine what is the driving force for the bulk diffusion of carbon. Baker et al. [83] suggested it was the temperature gradient created by the heat generated by the catalytic reaction, whereas Rostrup-Nielsen and Trim [87] supposed it was a carbon concentration gradient induced by different carbon activities at the filament-metal interface and the area where the decomposition occurs. Audier and coworkers compared carbon deposition rates from CO–CO_2 and CH_4–H_2 mixtures over FeNi and FeCo alloys [88,89]. For gas-mixture compositions not too far from thermodynamic equilibrium, the rate of carbon deposition depended on the deviation from equilibrium irrespective of the nature of the reactant gas (CO or CH_4). This strongly supports the idea that the rate-limiting step is the bulk diffusion of carbon driven by an isothermal gradient with local equilibrium at both metal-carbon and metal-gas interfaces. (A more detailed description is given below in 2.3.2). Snoeck et al. studied CH_4 cracking over a Ni catalyst and also proposed a growth mechanism in which the diffusion of carbon originates from a concentration gradient; the reasoning is based on thermodynamics arguments on different solubilities of carbon at the metal-carbon and metal

gas interfaces [90]. Another approach involved an intermediate carbide layer which can explain both the deviation from graphite equilibrium (see 2.3.1) and the driving force by a difference of carbon solubilities in the metal and in the surface carbide [77]. Moreover, carbides play a role in kinetics during the activation step (by fragmentation) of massive catalysts [91,92] and during the deactivation step (by poisoning) [93,94].

Quantitative Kinetic Study of Carbon Deposition from CO over a Supported Fe-Co Catalyst

Disproportionation of CO on iron-cobalt alloys was thoroughly studied by Audier et al. [88] and more recently by Pinheiro et al. [95,96]. Binary alloys were chosen because of their larger stability range vs. carbiding and oxidizing reactions. A kinetic study is thus easier to perform with these catalytic alloys than with pure metals. This example shows that a simple kinetic approach can be applied to a real case and furnish valuable information.

Rates of disproportionation from different $CO+CO_2$ mixtures over aluminosilicate supported FeCo particles were measured around 800 K. Plots against time typically exhibited two regions: a rapid (a few minutes) increase, followed by a slow decrease. The intermediate maximum rates were considered as representative of steady states of the reaction. Following Pinheiro et al. [95] we calculate the kinetic law of carbon growth starting from the assumption that carbon diffusion in the catalytic particle (step 3 in the dissolution-extrusion model) is the limiting step. The disproportionation reaction is then at equilibrium:

$$2CO \Leftrightarrow C(\text{dissolved at the metal-gas interface}) + CO_2$$

According to the Law of Mass Action, $K = P_{CO_2}(P_{CO})^{-2}\ a_{C,\text{metal}-\text{gas}}$, with $a_{C,\text{metal}-\text{gas}}$ the thermodynamical activity of the dissolved carbon at the metal-gas interface, which can be written as γx_{mg}, with γ the activity coefficient under the same conditions and x_{mg} the atomic fraction of dissolved carbon at the metal-gas interface. Supposing carbon extrusion from the catalyst is not limiting (step 4 of the model), carbon that is dissolved near its interface of extrusion can be in equilibrium with filamentary carbon and have the same activity: $a_{C,\text{filamentary}} = \gamma x_{mf}$, x_{mf} being the atomic fraction of dissolved carbon at the metal-filament interface.

Diffusion of carbon proceeds through the metal particle owing to the carbon concentration gradient $(x_{mf} - x_{mg})/V_m$, where V_m is the metal atomic volume. Considering a one-dimensional flow, the diffusion current density is given by Fick's law: $J = -D\ \mathrm{d}C_C/\mathrm{d}l$ where D is the diffusion coefficient of carbon in the metal and $\mathrm{d}C_C/\mathrm{d}l$ the concentration gradient.

Thus, $J = -D\ (x_{mf}\text{-}x_{mg})/V_m L = D(LV_m\gamma)^{-1}(K(P_{CO})^2(P_{CO_2})^{-1} - a_{C,\text{filamentary}})$ where L is the diffusion length. The rate of carbon deposition is the product of J by the total surface S of the catalyst. Maximal experimental rates are plotted against $K(P_{CO})^2/(P_{CO_2})$ on Figs. 2.9 and 2.10. Their

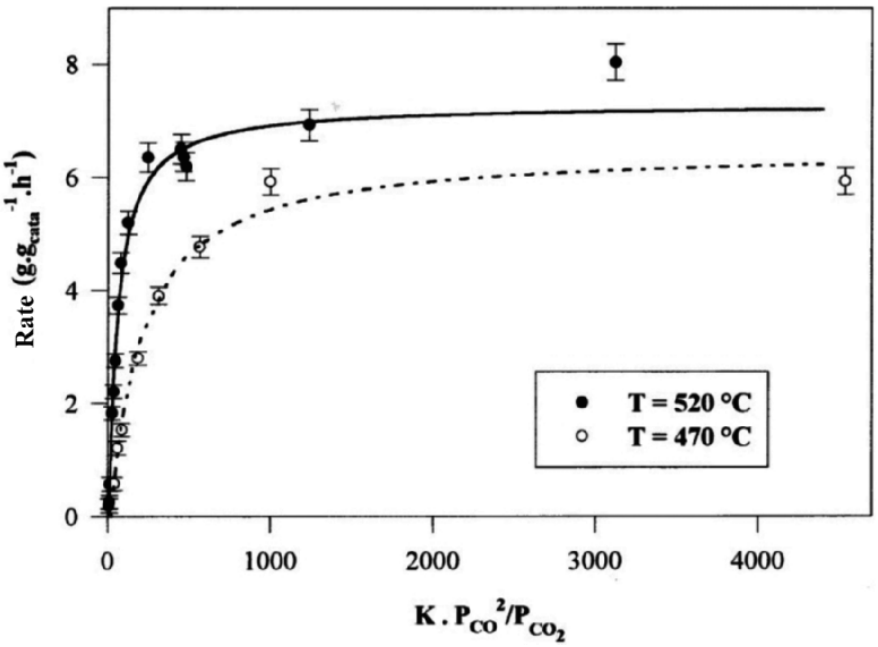


Fig. 2.9. Maximal rates of deposition vs $(P_{\mathrm{CO}})^2/(P_{\mathrm{CO_2}})$

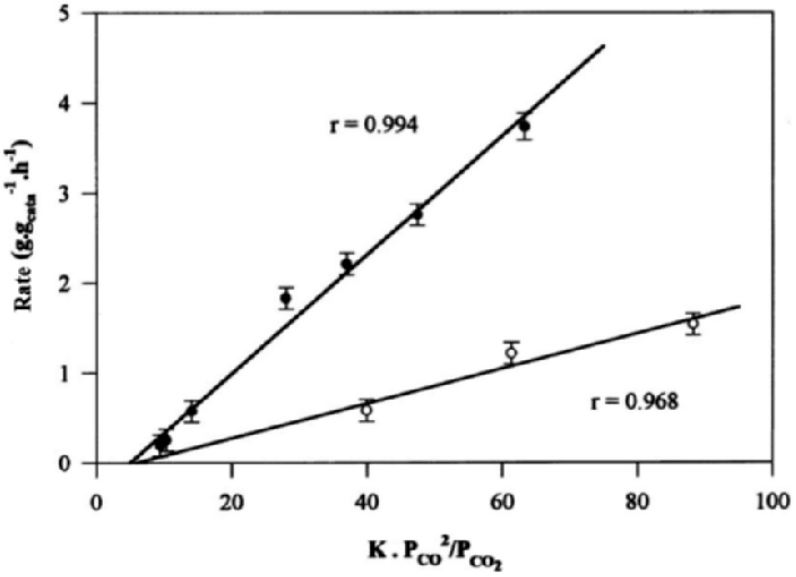


Fig. 2.10. Enlargement of Fig. 2.9 for 'weak' values of $(P_{\mathrm{CO}})^2/(P_{\mathrm{CO_2}})$

linear parts can be considered as domains where rates of deposition are limited by diffusion inside the catalyst particles in agreement with the calculation.

The intercept with the $K(P_{CO})^2/(P_{CO_2})$-axis gives $a_{C,filamentary}$ at the considered temperatures, which leads to the Gibbs function of formation $\Delta_f G^\circ = RT \ln a_{C,filamentary}$. Taking into account the uncertainties, the following values (in kJ mol^{-1}) are obtained: $8.5 \leq \Delta_f G^\circ(\text{filaments}) \leq 12.8$ at 470°C and $7.2 \leq \Delta_f G^\circ(\text{filaments}) \leq 11.8$ at 520°C. Note that at higher values of $(P_{CO})^2/(P_{CO_2})$, diffusion in the gaseous phase becomes limiting.

These results are corroborated by a more extensive study of how maximum rates vary with temperature. In the rate law $DS(LV_m\gamma)^{-1}(K(P_{CO})^2 (P_{CO_2})^{-1} - a_{C,filamentary})$, four factors are temperature-dependent: D, γ, K and $a_{C,filamentary}$. Nevertheless, $a_{C,filamentary}$ varies slowly with T, γ vs. T can be taken from the literature and the (known) variation of K can be balanced by keeping constant the expression $K(P_{CO})^2(P_{CO_2})^{-1}$ (sometimes named carbon activity in the gas phase). Moreover, the constancy with temperature of the two geometric parameters S (active area of the catalyst) and L (length of diffusion), which both depend on the dimensions of the catalyst particles (by fragmentation or coalescence) must be checked. Hence, the rate varies as the D/γ ratio: D and γ are proportional to $\exp(-E/RT)$ where E is a (constant) energy of activation, therefore the logarithm of the rate should be linear when plotted against T^{-1} and the slope gives the activation energy of D/γ. After such a treatment, the measured rates for temperatures from 498 to 548°C look roughly linear (Fig. 2.11) and the activation energy lies between 168 and 183 kJ mol^{-1} which is consistent with usually observed values.

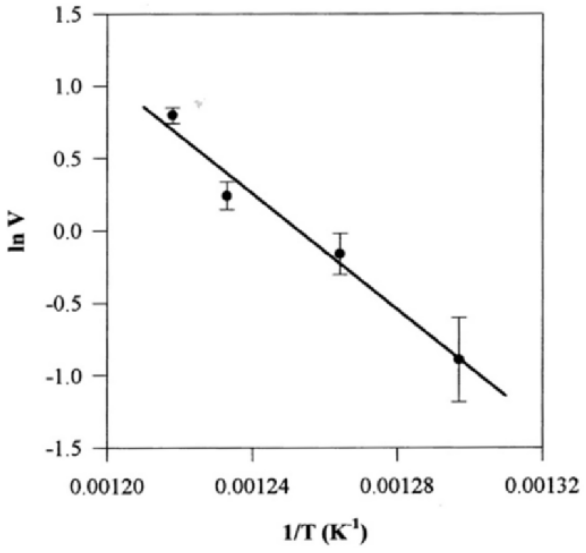


Fig. 2.11. Logarithm of the maximum rates vs. T^{-1}

2.3.3 Influence of the Morphology and Physical State of the Catalytic Particle

Catalytically grown filaments exhibit various diameters, shapes and microtextures depending on the microscopic details of the growth process. Since the filament structure greatly influences the properties, it is important to control the growth process and thus to understand why some filaments grow tubular while others are of the cup-stacked type; why some grow straight while others are helix-shaped [97]. Numerous factors have a potential influence on the process selectivity: the reaction temperature, the reactant composition, the material supporting catalytic particles, and the morphology and physical state of the catalytic particles. Unfortunately all these parameters cannot be varied independently one by one so that it is difficult to extract a clear phase diagram from the huge number of reported results. We choose here to focus on the catalytic particle and we review a number of studies which aimed at correlating the characteristics of the filament to those of its germ.

Structure of Filaments Grown from Solid Crystalline Particles

A correlation between the crystallographic orientation of carbon and catalytic metal in filaments was demonstrated by Audier, Coulon, and Oberlin [98,99]. They established by HRTEM that truncated-conical catalyst particles made of different metal alloys were oriented with respect to the filament axis, the orientation being dependent only on the crystallographic system of the alloy and not on its composition. 'In the case of all the metal composites prepared from alloys of bcc structure, the metal particle is a single crystal with a [100] axis parallel to the axis of the carbon tube, and the basal faces of the truncated cone, which appear free of carbon, are (100) faces.' For fcc FeCo alloys, the [110] axis coincided with the filament axis and the metal-gas interface was (111). It was indeed well known from surface science that the reactivity of catalytic metals depends on crystallographic orientation. For example, graphite epitaxial growth on nickel is more favorable on (111) faces [100]. It was thus tempting to conclude that growth proceeds by dissolution of carbon through some facets and extrusion from others that have a stronger affinity for graphite and so govern the geometric alignment of the platelets in the filaments. This was justified theoretically in the case of Ni particles by extended Hückel molecular-orbital calculations [101]. Graphite epitaxy is stronger with the (111) and (311) faces of Ni than with the (100) and (110) faces consistent with geometrical arrangements where some faces are carbon-covered and others are not. Yang and Chen observed that (100) faces are the most abundant at the metal-gas interface for filaments grown on nickel [101].

The role of epitaxy in the nucleation and growth of graphitic filaments by decomposition of 1,3-butadiene on nickel/Al_2O_3 has been analyzed in detail by Zaikovskii et al. [102]. Depending on the reaction temperature, cup-stacked or tubular filaments were grown according to the different mechanisms and catalyst structures. They confirmed that (111) flat faces offer epitaxial sites

for (002) planes of graphite, and suggest that steps of (100) planes of nickel particles can favor formation of nanotubes at high temperature. In the case of filaments grown from Pd particles, no preferred orientation of the Pd planes with respect to graphite (002) was found [103]. Growth can occur without true epitaxy and shape only seems to have an influence on filament morphology. Kiselev et al. [104] observed that in the case of anisotropic multifaceted nickel particles, catalytic activity is not homogeneous and the extrusion velocity vector, a concept introduced by Amelinckx et al. to explain growth of helicoidal tubular filaments [97], is not constant, which induces topological defects in the filament structure. They confirmed that facets incorporating carbon are (100) and (110). Different facets are found at the metal-carbon interface.

So it follows that filament morphology is governed to a large extent by particle shape and crystallographic structure, and we find in the literature a variety of filament microtextures. Murayama and Maeda reported synthesis of filaments made by the stacking of flat graphene layers arising from facets of the catalytic iron-containing particle (Fig. 2.12) [105]. Many authors have observed filaments with carbon layers at various inclination angles to the conical particle surface. Rodriguez et al. explained this apparent inclination by a faceting of the lateral surface of conical particles (see Fig. 2.13) [106]. Since adsorbed gases can modify the shape of supported nanoparticles [107], it may be that variation in the gas composition modifies filament morphology. For example, modification of particle faceting might explain the result of Nolan [108], confirmed by Pinheiro et al. [109], that adding H_2 to CO in the 500–600°C range leads to filaments where carbon layers are inclined to the filament axis (Fig. 2.13), whereas the absence of H_2 leads to nanotubes (Fig. 2.14).

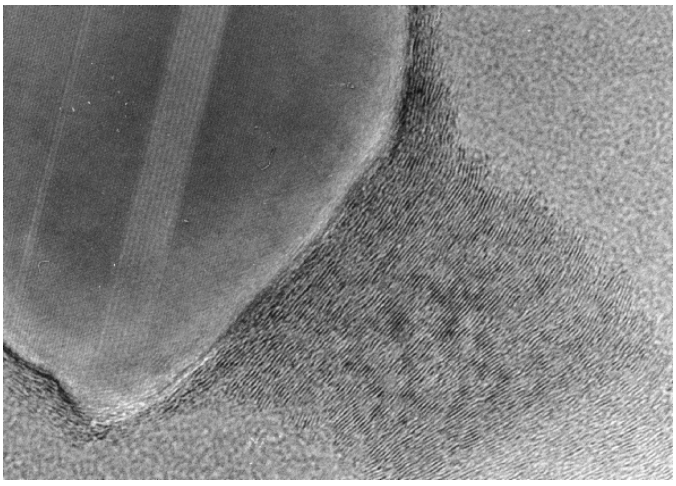


Fig. 2.12. HRTEM of a nanofiber synthesized from a CO + H_2 mixture over Fe particles

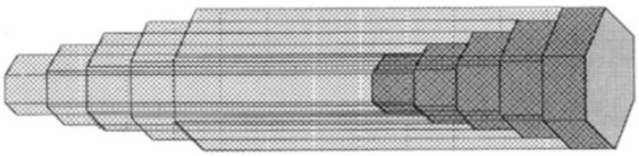


Fig. 2.13. Particle faceting according to Rodriguez [106]

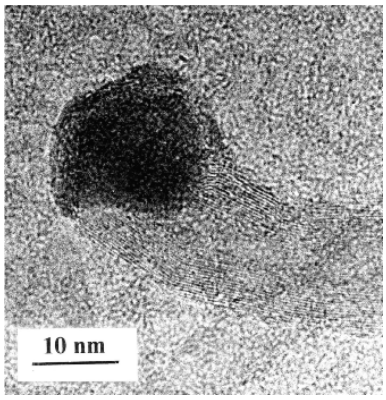


Fig. 2.14. HRTEM of a MWNT based on CO disproportionation over MgO-supported Co

Growth of Filaments from Liquid Particles

So far we have discussed growth mechanisms supposing the particles were solid since the growth temperature was well below the melting point of the catalytic metal. This assumption is reasonable in the case of big particles ($\geq$10 nm in diameter) but is questionable when dealing with nanometer-sized germs.

Tibbetts and Balogh showed recently that filaments can be grown from melted iron particles when the reaction temperature is above the iron/graphite eutectic [110]. In fact, filament growth from melted particles dates back to the 70s when Koyama discovered that carbon fibers could be grown from benzene between 1150 and 1290°C using hydrogen as a carrier gas [111]. These so-called vapor-grown-carbon-fibers (VGCF) have diameters larger than one micrometer and lengths longer than one millimeter (sometimes several centimeters). Oberlin et al. established that the growth resulted from a two-stage mechanism: catalytic growth of a 'precursor' filament first occurs (thinner than 100 nanometers) and then thickening proceeds via the deposition of pyrolytic carbon layers [5]. Melting of the catalyst nanoparticles explains the unusual length of the precursor [110, 112] because it enhances the decomposition of hydrocarbons at the particle surface and/or the diffusion of carbon through or over the melted nanoparticle. In the case of VGCF, the growth temperature is lower than the eutectic temperature in the Fe-C system (1150°C) but

surface tension lowers the melting point of small particles [112]. More accurate HRTEM observations [113–115] evidenced later that precursors were MWNT with cylindrical carbon layers (Fig. 2.15).

The growth mechanism of these precursor nanotubes has been proposed by Baker [82,85], Oberlin et al. [5] and Tibbetts [80]. The model adopted the concepts of the vapor-liquid-solid (VLS) dissolution-extrusion-like model first introduced by Wagner and Ellis [116,117] in the sixties to explain the growth of silicon whiskers. In the VLS model, growth occurs by precipitation from a super-saturated catalytic liquid droplet located at the top of the filament, into which carbon atoms are preferentially absorbed from the vapor phase. From the resulting super-saturated liquid, the solute continuously precipitates, generally in the form of faceted cylinders (VLS-silicon whiskers [116]) or tubular structures [80]. According to Oberlin et al. [5], carbon (as individual atoms or not) diffuses over the catalyst surface until it reaches a coalescence site (first, the contact circular line between the particle and its support, then the previously-formed carbon layers).

Melting of the catalytic particle was the ground for interpretation of sequential growth of nanofilaments over FeNi at 1080°C [118]. Li and co-workers studied the influence of pressure on the growth of nanotubes which were produced from acetylene decomposition at 750°C over supposedly liquid Fe particles [119]: whereas cylindrical layers were obtained with a low acetylene pressure (0.6 torr), inclined layers and bamboo-like occlusions occurred at higher pressures, the distance between two occlusions decreasing upon increasing the pressure. Krivoruchko and Zaikovski [120] suggested that iron nanoparticles

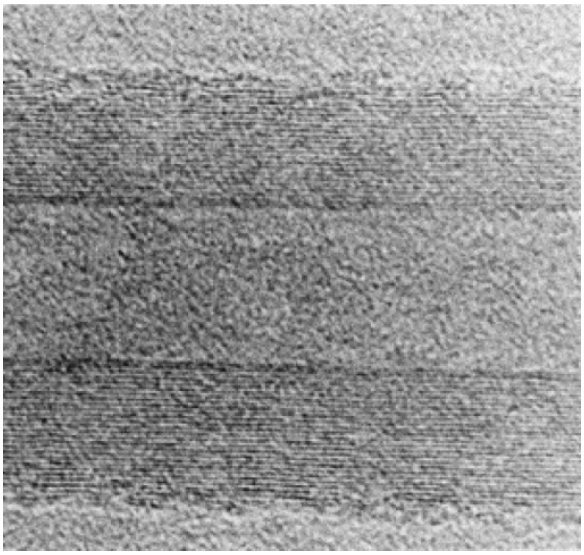


Fig. 2.15. Nanotubular precursor of a VGCF

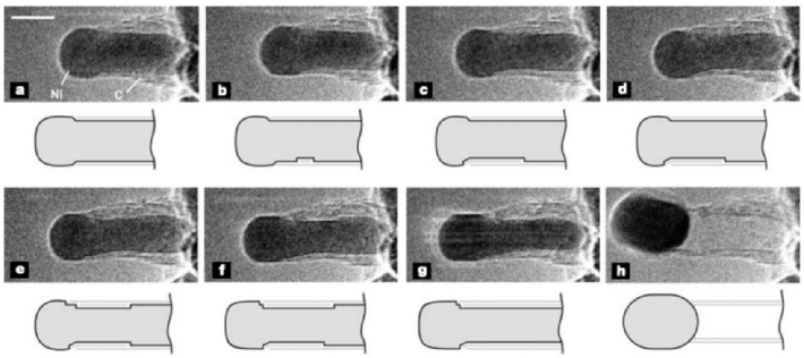


Fig. 2.16. Image sequence of a growing nanofiber illustrating the Ni particle dynamic behavior (from Helveg et al. [122])

are liquid at 700°C when oversaturated by carbon and Kukovitsky et al. discussed dissolution-extrusion involving Ni particles in the solid state at 700°C and in the liquid state at 800°C [121]. A voluminous theoretical literature is devoted to this topic, which will be considered again in SWNT growth.

Dynamics and Restructuring of Catalytic Nanoparticles During Growth

Although the importance of the particle state is well recognized, most observations have been done a posteriori so it is difficult to ascertain what really happens during growth. Helveg et al. [122] recently studied the growth of nanofibers in situ using time-resolved high-resolution TEM. They showed that the nanoparticle shape is modified dynamically during the growth, which has important consequences on the nanofiber morphology (see Fig. 2.16). The authors proposed a growth mechanism involving only surface diffusion. They checked that the core of the particles remained solid and that only surface diffusion modified its shape.

It is interesting to re-examine the morphology of nanocrystals located at the filament root in the light of these new results: the conical particles shown in many cases may well have been formed by stretching during the first layer growth, as suggested recently by X. Chen et al. [123]. Bamboo-structured filaments may also be the result of an extension-retraction mechanism without going through a liquid state. Another recent work on growth of nanofilaments on Pd nanoparticles suggests that a consumption of the catalytic metal occurs during the growth in addition to a modification of the particle shape [124]. Nanoparticles can therefore modify their shape rapidly without going through a solid-liquid phase transition. The carbon growth mechanism depends in fact on the particle dynamics which can be modified by various parameters such as temperature, gas pressure and metal composition. CVD growth using small catalytic nanoparticles is thus a fascinating domain where in-situ experiments

coupled with thermodynamic and kinetics studies will bring a wealth of new results in the near future.

2.4 Synthesis of MWNT and SWNT via Medium-Temperature Routes

2.4.1 From Carbon Nanofibres to Carbon Nanotubes by CCVD

We have seen in the previous section that the catalytic chemical vapor deposition (CCVD) methods are efficient to produce carbon filaments. These filaments, which are not necessarily hollow, even with fishbone-type or bamboo type structure, are often named carbon nanofibers when they have a small diameter (< 100 nm). But single- or multiwalled carbon nanotubes (SWNT and MWNT respectively) are hollow and made up of one or several concentric graphene layers as described by Iijima [3]. Many works have been conducted first to adapt the CCVD methods to the synthesis of MWNT, and then also to the synthesis of SWNT. Besides the wall structure, the second particularity of CNT among other carbon filaments is their diameter which is much smaller, no more than a few nanometers for SWNT. Considering the previously described formation mechanisms in which each filament is generated from one catalytic particle, located either at the base or at the tip of the filament, the first aim in order to synthesize CNT, particularly SWNT, has been to decrease the size of the catalytic particles. The second aim has been to adjust the conditions of the reaction, often by modifying the value of the physical parameters or the nature of the reacting gas.

The synthesis of nanometer-sized metal particles has been widely studied. But their use as efficient catalytic agents to synthesize CNT supposes to prevent their coalescence during the heating up to the decomposition temperature of carbonaceous gases (600–1100°C). Thus, many ways have been explored in order to obtain nanometer-sized metal particles at these high temperatures. Refractory metals could be used because they are less prone to coalesce than other metals. However, although it has been shown that Mo nanoparticles can catalyze the formation of CNT [125], it has been widely evidenced that Co, Fe, Ni nanoparticles, alone or associated with Mo, V or W, are much more active. The formation or deposition of metal nanoparticles on finely divided and/or highly porous powders, which is often used in heterogeneous catalysis, can be efficient but only when the reaction temperature is not too high [126–129]. Another way is to generate the metal nanoparticles in-situ inside the reactor, preferentially at the reacting temperature, either from an organometallic precursor [130–134] or from a solid, by the selective reduction of an oxide solid solution [135–140] or of an oxide compound [141]. The use of moderate temperatures (600–800°C), employing carbonaceous gases which easily decompose, as CO or certain hydrocarbons, also prevents a too pronounced coalescence of

catalytic nanoparticles [142, 143]. A very rapid heating of the catalyst to the reaction temperature can be also an alternative way [127].

Depending on the maximal temperature permitted to avoid or limit the coalescence of the catalytic particles, the carbonaceous gas can be either CO or hydrocarbons (CH_4, C_2H_2, C_2H_4, C_6H_6, ...). Generally, the carbonaceous gas is mixed with an inert gas (Ar, He or N_2) or with H_2 that allows to act on the hydrodynamic parameters or/and to modify the thermodynamic conditions. The reaction temperature must be adjusted to assure thermodynamic conditions favorable for the decomposition of the carbonaceous gas, i.e., for instance, not too high for CO and not too low for CH_4, but also to avoid the deposition of pyrolytic carbon on the CNT. However, it will be shown that, if MWNT are easily synthesized at rather low temperatures (600–800°C), a higher temperature (1000–1100°C) is generally preferred to synthesize SWNT. Often, it is useful to operate at atmospheric pressure but, in some cases, lower or higher pressures have been proved to be essential [132, 144]. The gas flow must also be adjusted as a function of the quantity of catalyst, taking into account the reaction yield and the necessity to supply each catalytic particle with carbon. Most often, the reaction is conducted with a horizontal tubular furnace fitted with a silica glass tube supplying a controlled flow of the gas mixture. Either the catalyst material is put as a bed on a plate in the middle of the reactor or is generated in-situ from an organometallic precursor. In this latter case, another furnace, operating at low temperature, can be used to sublimate or vaporize the organic precursor. The furnace and the reactor can be vertical, when the catalyst is introduced in the form of a spray or when a fluidized bed of a catalyst powder is used.

Thus, a lot of strategies have been used to adapt the CCVD methods to the synthesis of CNT. All the parameters, related either to the catalyst or to the reaction conditions, are important and may interact. So, each method must be considered as a whole and, for a given type of CNT (SWNT, small or large diameter MWNT), their efficiency can be evaluated as a function of the quantity and quality of the products. However, depending on the works, the characterization of the produced CNT may be minimal with only a few TEM or SEM images, sometimes without any elementary analysis of carbon or of the catalytic element(s), or can include several methods as, for instance, high-resolution transmission electron microscopy (HRTEM), Raman spectroscopy, evaluation of reactivity by thermogravimetry analysis or temperature-programmed oxidation, or specific-surface-area measurements. In the following sections, we will briefly describe a selection of synthesis works representative of the large variety of methods used for the different types of CNT. The particular cases of local grow and template synthesis of CNT will also be presented.

2.4.2 Synthesis of Carbon Multiwalled Nanotubes (MWNT) by CCVD

Synthesis of MWNT Using Supported Catalysts

Previous to the report by Iijima [3] of the structure of MWNT, several authors [5, 82, 145] described the CCVD synthesis of carbon filaments, some of which, being not larger than a few tens of nanometers in diameter, probably were MWNT. But after Iijima's paper [3], Yacaman et al. [146] were the first, in 1993, to report the catalytic growth of the so-called carbon microtubules with fullerene structure, by decomposition at 700°C of C_2H_2 diluted in N_2 on graphite-supported Fe particles. The sample contains many other forms of carbon such as bamboo-shaped nanofibers, nanocapsules or nanoparticles, showing the poor selectivity of the method.

Later on, keeping C_2H_2-N_2 mixtures as the reacting gas, B. Nagy and his team, at Namur, have worked to optimize the preparation of metal nanoparticles on porous oxide supports [142, 147, 148]. Impregnation or ion-exchange or sol-gel methods routes, using metal-salt solutions and silica gels, zeolites, alumina or alumina-silica as substrates, are followed by air calcination and sometimes pre-reduction in H_2/N_2 at 500°C and then treatment at 600–700°C in C_2H_2/N_2. The quantity and the characteristics of MWNT depend on catalytic materials and reaction parameters. In some cases, some filaments are helical or covered by disordered carbon. They showed that Fe, Co or Fe-Co alloys are better than Ni or Cu and that a lower temperature favors a lowering of the quantity of disordered carbon deposit but also a lower crystallinity of the CNT [142]. With Co on zeolite, bundles of SWNT were obtained besides MWNT [147]. A better selectivity was obtained using a sol-gel preparation or alumina-silica substrates [148]. Chen et al. [149, 150] obtained MWNT (Fig. 2.17) by generating the metal nanoparticles in-situ by the selective reduction of $Mg_{0.6}Ni_{0.4}O$. Using CO/He, MWNT with a cylindrical structure

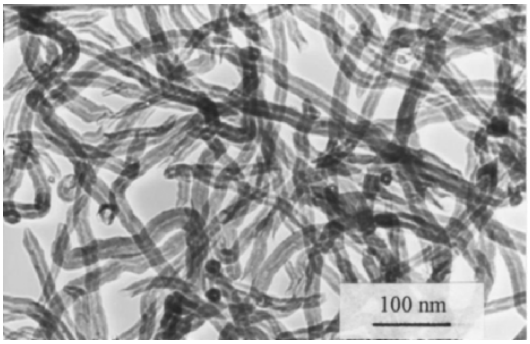


Fig. 2.17. Typical low resolution TEM image of MWNT synthesized by CCVD over supported catalysts [149]. Reproduced from P. Chen, X. Wu, J. Lin, H. Li, and K. L. Tan: Carbon **38**, 139 (2000), copyright 2000 with permission from Elsevier

were formed from Ni particles whereas CH_4/He produces carbon nanofibers with a conical structure. This method and the one using $Mg_{1-x}Co_xO$ solid solutions [137] were adapted by Soneda et al. and Delpeux et al. [151,152]. With Co, C_2H_2 as hydrocarbon instead of CH_4 and a low temperature (600°C), 10–15 walls MWNT were obtained in great quantity (400 mass.% of the catalyst material). As reported by Flahaut et al. [137], the MgO substrate is then easily removed by dissolution in hydrochloric acid. Sun et al. [144] prepared 40 nm diameter Co-Ni particles by ionic exchange on zeolites, air calcination (500°C) and reduction (H_2/N_2, 500°C). The reaction (820°C) with C_2H_2/N_2 at a pressure of only 160 Torr led to very straight MWNT. Ning et al. [141] prepared a Mo rich (50 wt.%) Co-Mo-Mg oxide catalyst based on the very well crystallized $MgMo_2O_7$ compound. Very large quantities of bundles of MWNT (1500 mass. % of the catalyst material), about 10 nm in diameter, were obtained by decomposition of CH_4 on this catalyst, showing the great influence of Mo.

Synthesis of MWNT Using Catalytic Particles Formed in-situ from an Organometallic Precursor

With ferrocene vapor as Fe source and a CH_4/H_2 gas mixture (80 kPa, 900–1100°C), Qin et al. [153] obtained quite well graphitized MWNT embedded in disordered carbon. Using a two stage furnace (200°C, 900°C), Sen et al. [154] showed that if metallocene vapors (Fe, Co, Ni) carried by Ar/H_2 produce a mixture of MWNT and onion-like structures, the addition of C_6H_6 leads to high yields of MWNT whose thickness depends on the metallocene content. At higher temperatures (400°C, 1100°C), with a high gas flow (1000 sccm Ar or Ar/C_2H_2), large or very large quantities of bundles of aligned MWNT are synthesized [155]. The alignment of the NTC and the density of the bundle increases with the C_2H_2 flow.

Synthesis of MWNT Aligned in Bundles

By spin-coating of a Fe nitrate solution on Al or SiO_2 substrate and heating up to 650–750°C under vacuum, Emmeneger et al. [156] obtained Fe clusters whose average diameter and density is controlled by the nitrate solution concentration and the temperature. The decomposition of C_2H_2 highly diluted in N_2 (2/98) at 0.5 bar and 630–750°C led to well aligned MWNT (10–15 µm length – Fig. 2.18). The cluster diameter and density determined the diameter and density of the MWNT. Terrones et al. [157] prepared laser-etched thin films of cobalt on SiO_2 on which well aligned MWNT (30–80 walls) were synthesized by pyrolysis of 2-amino-4.6-dichloro-s-triazine under Ar flow at 950°C. The growth of CNT, perpendicularly to the substrate surface, occurred only in the etched areas, catalyzed by cobalt particles (< 50 nm) which condensed and crystallized in these areas. Wei et al. [158] showed that pillars

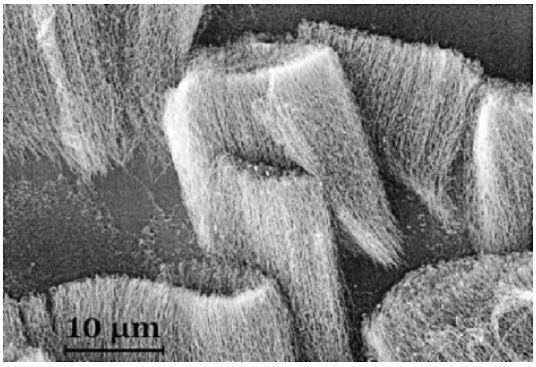


Fig. 2.18. SEM image of well-aligned CNT synthesized by thermal CCVD over Fe clusters supported on an aluminium substrate [156]. Reproduced from C. Emmenegger, P. Mauron, A. Zuttel, C. Nutzenadel, A. Schneuwly, R. Gallay, and L. Schlapbach: Appl. Surf. Sci. **162–163**, 452 (2000)

of densely packed MWNT grow on Ni thin films deposited on Si/SiO_2 substrates when exposed to a prevaporized xylene/ferrocene mixture carried by Ar. The authors proposed that the catalytically active species are Fe particles preferentially deposited on circular microcracks of the Ni films.

Localized Synthesis of Oriented MWNT

Many authors have developed methods to locally synthesize carbon filaments, densely packed on large areas and vertically aligned on Si/SiO_2 substrates, especially for application to field-emission displays. Although the authors generally call these filaments nanotubes, it seems that they often are bamboo-shaped filaments. Lee et al. [159–161] prepared Ni, Co or Fe particles by etching a metal thin film with a dilute HF solution, followed by a thermal treatment in NH_3 at 850–900°C. Vertically-aligned bamboo-shaped carbon filaments (80–120 nm in diameter, about 20 µm in length) were obtained by thermal CCVD of C_2H_2 at the same temperature. The filament diameter and growth rate were controlled by the parameters (flow and dwell time) of both NH_3 and C_2H_2 treatments. Ago et al. [162] synthesized Co particles (average diameter 4 nm) by a reverse micelle method. After a pretreatment in $H_2S/H_2/N_2$ at 400°C in order to activate and sulfurize Co nanoparticles, vertical filaments which seem to be true MWNT with a cylindrical structure were grown at 800–900°C in C_2H_2/N_2. Such oriented and well-crystallized MWNT were also synthesized by Andrews et al. [163, 164] at 675°C using vapours issue from a ferrocene/xylene mixture carried by an Ar/H_2 flow.

Plasma-enhanced CCVD methods (PE-CCVD), with sometimes the assistance of a hot filament or microwave have also been studied, mainly in order to improve the alignment and orientation of the carbon filaments. Ren et al. [165] used as catalyst a Ni thin film (16–60 nm) etched by an NH_3 plasma

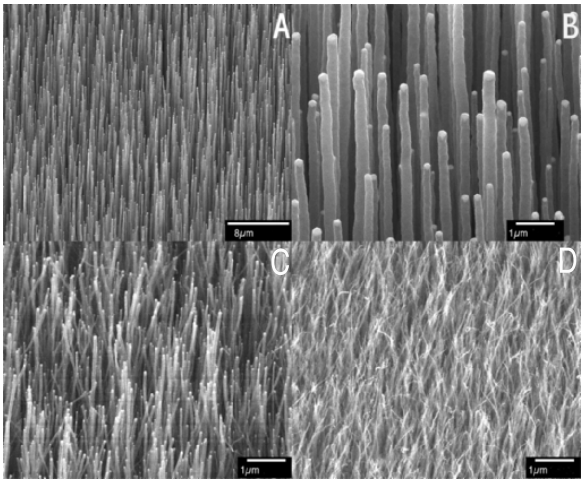


Fig. 2.19. SEM images of large arrays of well-aligned CNT synthesized by plasma-enhanced hot filament CCVD; (**A, B**) large diameter (250 nm) CNT which are very rigid and very well aligned; (**C-D**) thinner CNT (65 and 20 nm in diameter, respectively) showing that the alignment of CNT gradually decreases with their diameter reproduced [165]. Reproduced from Z. F. Ren, Z. P. Huang, J. W. Xu, J. H. Wang, P. Bush, M. P. Siegel, and P. N. Provencio: Science (Washington, D. C.) **282**, 1105 (1998), copyright American Society for the Advancement of Science

which was then exposed to a C_2H_2/ NH_3 plasma (1–10 Torr) in the presence of a hot filament, the temperature of samples being estimated at 666°C. The MWNT were very well aligned perpendicularly to the substrate when their density (quantity for a given surface area of substrate) is sufficient. Moreover, the larger is the diameter of the MWNT, the higher are their rigidity and their alignment (Fig. 2.19). Ho et al. and Wang et al. [166–168] generated Fe, Co or Ni particles by etching continuous or micro-patterned thin films (5–100 nm) with an H_2 plasma, which appears much more efficient than H_2 gas. The PE-CCVD was performed with C_2H_2/H_2 plasma (1–1.2 Torr, radio-frequency power of 100 W). The alignment of carbon filaments, which seem to be true MWNT, is more or less pronounced, depending on their density on the substrate. Cui et al. [169] used a PE-CCVD system assisted by microwave, firstly at 660–1000°C with a NH_3 plasma to etch a Fe thin film (10 nm) to obtained 100–200 nm particles, and then with a CH_4/NH_3 plasma to depose well aligned bamboo-shaped carbon filaments. The characteristics of the deposit depend essentially on the etching temperature and on the CH_4/NH_3 ratio.

Conclusions

Many CCVD methods have been developed to prepare MWNT and most of them use Fe, Co or alloy nanoparticles as catalyst, only a few using Ni

nanoparticles which seem to be less active. Among the different forms of the catalytic materials, the use of nanoparticles supported on powders is probably more selective. This can be optimized by varying the nature, the specific surface area and the porosity of the substrate. After the CNT synthesis, the elimination of the substrate without damage to the CNT can be a problem and thus, substances such as MgO which are easily dissolved by non-oxidative acids are preferable. The generation of catalytic particles in-situ in the reactor from vapors of organometallic precursors seems to be less selective, but presents the advantage to avoid the step of the substrate elimination and is also easier to be adapted for a continuous production. Many gases may be used for the carbon supply, particularly C_2H_2 or CO which decompose at low temperatures. However, a better crystallinity of the MWNT is obtained when higher synthesis temperatures are used. The characteristics of the MWNT are more or less adjustable by the process parameters but the control of the MWNT diameter is clearly related to that of the nanoparticle diameter. The nature and the proportion of other forms of carbon, which are considered as impurities, are a direct function of two mutually dependent process parameters, the nature of the carbonaceous gas and reactor temperature. The alignment of MWNT into bundles, more ore less packed, is easily obtained when great quantities are deposed on a limited area of substrate. For application to field-emission displays, carbon filaments, densely packed on large areas and vertically aligned on Si/SiO_2 substrates, can be synthesized either by thermal CCVD or by plasma assisted CCVD (without or with hot filament or microwave). Plasma treatments of metal thin films are very efficient to obtain metal particles. The nature of the carbon filaments (MWNT or bamboo-shaped filaments), their dimensional characteristics and density on the substrate are adjustable both by the characteristics and density of the metal particles and also by the carbon deposition parameters. The alignment of the filaments perpendicularly to the substrate clearly increases with their density on the substrate and with their diameter.

2.4.3 Synthesis of Carbon Single-Walled Nanotubes (SWNT) by CCVD

Methods Using Catalytic Particles Formed in-situ from an Organometallic Precursor

The CCVD synthesis of SWNT using an organometallic precursor for the catalytic nanoparticles requires the modification of the parameters used for the synthesis of MWNT. Satishkumar et al. [133] used the same reactor and same parameters than Rao et al. [155] except for a lower temperature in the first furnace (350°C instead 400°C) in which the metallocene (or the mixture of metallocenes) are sublimated, probably in order to lower the metallocene vapor partial pressure in the C_2H_2(5 vol.%)/Ar flow, and thus to reduce the size of the metal nanoparticles generated in the second furnace, at 1100°C.

They also used vapours of $Fe(CO)_5$ carried by C_2H_2 and then mixed with Ar. SWNT (1–1.5 nm in diameter) were obtained, most of them being covered by disordered carbon. The SWNT quantity is higher with Fe or Co as catalyst and the SWNT seem cleaner with a Fe/Co mixture. Ci et al. [131] used ferrocene sublimated at very low temperature and carried by Ar mixed with very few C_2H_2 (< 1 vol.%). The obtained SWNT (0.3–1.8 nm in diameter) come individually or in small-diameter bundles, cleaner than the previous ones [133] but the samples contain a lot of carbon capsules formed around Fe particles. Cheng et al. [130, 170] used ferrocene vapours carried by a flow of H_2/C_6H_6 to which some thiophene vapours were also added. The obtained samples consist of long and wide ropes or ribbons formed of bundles of SWNT (1–3 nm in diameter), representing about 60 wt.% of the whole sample, about 10–12 wt.% of Fe and some disordered carbon deposits. It appears that the sulphur supply considerably raises the proportion of SWNT. Wei et al. and Zhu et al. [134, 171] used a vertical reactor (1200°C, 1 atm) at the top of which a solution of n-hexane, ferrocene and thiophene carried by H_2 is introduced. Very long strands (> 10 cm) of well-organised bundles of SWNT were produced. Nikolaev et al. [132] developed the so-called 'HiPco' method, which is continuous and consists of the supply of two flows, a cold $Fe(CO)_5/CO$ mixture flow and a pre-heated CO flow, giving 2–10 ppm of $Fe(CO)_5$ in the final flow. The influence of both the reactor temperature (800–1200°C) and pressure (1–10 atm) on the yield and characteristics of SWNT showed that the higher yield (44 wt.% of SWNT) and lowest diameters with a narrowest diameter distribution (0.6–1.3 nm) were obtained with the highest temperature and pressure (1200°C, 10 atm). Most SWNT are in bundles, regularly covered by many nanoparticles (Fig. 2.20), which are removed by combining gas and acid oxidations [172, 173].

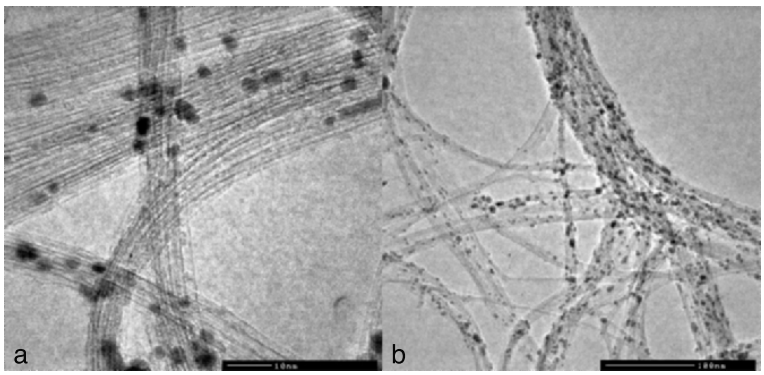


Fig. 2.20. High (**a**) and low (**b**) magnification TEM images of products obtained by the 'HiPco' method showing that the SWNT are free of disordered carbon and decorated with catalytic Fe nanoparticles [132]. Reproduced from P. Nikolaev, M. J. Bronikowski, R. K. Bradley, F. Rohmund, D. T. Colbert, K. A. Smith and R. E. Smalley, Chem. Phys. Lett. **313**, 91 (1999), copyright 1999 with permission from Elsevier

Methods Using Supported Catalytic Nanoparticles

Supported metal nanoparticles can be generated in-situ, at a high temperature, by the selective reduction of an oxide solid solution [174]. When the reducing gas mixture contains a hydrocarbon, CNT are simultaneously synthesized owing to the high catalytic activity of the metal nanoparticles (0.5–5 nm in diameter) which are located at the oxide grain surface [139, 140, 175, 176]. Indeed, these native metal particles are small enough to immediately catalyze the formation of SWNT. The first work on this method was reported in 1997 by Peigney et al. [140] who used a CH_4/H_2 gas mixture to reduce $Al_{2(1-x)}Fe_{2x}O_3$ powders at 1070°C. The optimization of the characteristics of the solid solution and the parameters of the reaction was conducted by Laurent et al. [139] and Peigney et al. [175, 176] using both macroscopic parameters and a microscopic characterization. The obtained CNT are mainly SWNT and double-walled nanotubes (DWNT), individual or gathered in small-diameter bundles (Fig. 2.21), without carbon nanofibers nor disordered carbon, the undesirable carbon form being essentially capsules surrounding Fe_3C particles. This method was then extended using $Mg_{1-x}M_xAl_2O_4$ (M = Fe, Co, Ni) powders as starting material, showing that, in this system, Co is the most efficient and mainly catalyzes the formation of SWNT [138]. The quantity of CNT was increased by using CoFe instead of Co [136] or a ceramic foam instead of a bed of oxide powder [177]. Flahaut et al. [137] and Bacsa et al. [135] showed that the use of a $Mg_{1-x}Co_xO$ powder ($x \leq 0.1$) gives SWNT and DWNT which can be easily separated by the dissolution of MgO in a non-oxidative acid solution such as 1 mol/l HCl, which does not damage the CNT. The obtained samples present a very high specific surface area (> 800 m^2/g) because the CNT are mainly individual [135, 178]. An improvement of this method was reported in 2001 by Tang et al. [179] using a MgO-based powder with a higher specific surface area in which both Co and Mo elements are added during the oxide synthesis. The optimum Co/Mo ratio was determined to be 2/1 which corresponds to the minimum of the D/G Raman bands ratio. In this case, CNT are supposed to be essentially SWNT, mainly gathered in bundles, and the reaction yield, calculated from the total weight of catalytic material, is 114 wt.%, much higher than without Mo addition (only 11 wt.%).

Another way to obtain supported nanometer-sized metal particles is to impregnate a substrate with one or several metallic salt solutions, to conduct a heat treatment in an oxidative atmosphere which gives pre-formed supported oxide particles and then to reduce them in-situ in the reactor under the action, at high temperature, of the carbonaceous gas and sometimes H_2. This method can be efficient to preserve the nanometer size of the particles because they are less prone to coalesce under heating in the oxide form than in the metal form. The very first synthesis of SWNT by a CCVD method was reported by Dai et al. [125], using Mo particles supported on a highly divided Al_2O_3 powder and pure CO at 1200°C. Small quantities of individual SWNT (1–5 nm in diameter) were obtained. Hafner et al. [128] used Fe/Mo (9/1)

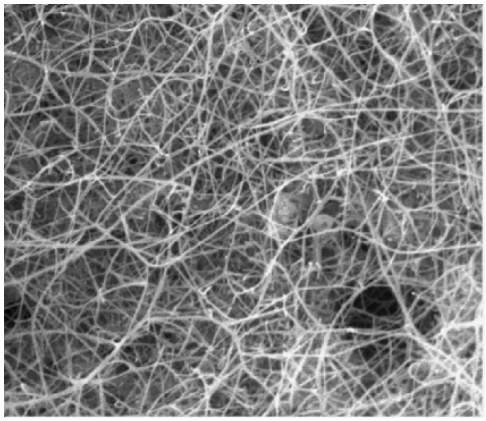


Fig. 2.21. SEM image of CNT (SWNT and DWNT), individual or gathered in small diameter bundles, upon the MgO substrate, synthesized by decomposition of CH_4 over Co nanoparticles which are generated in-situ by the selective reduction of a $Mg_{0.95}Co_{0.05}O$ oxide solid solution [135, 137]. CNT can be easily separated by the dissolution of MgO in a non-oxidative acidic solution which does not damage the CNT

on a Al_2O_3 powder and, at 700–850°C, either CO or C_2H_4 and obtained much higher quantities of CNT than with Mo alone. The CNT consist of a mixture of SWNT and DWNT, the proportion of the latter being larger (70%) with C_2H_4, for 850°C. The main undesirable carbon form being capsules surrounding catalytic particles, the author conducted energy calculations showing that a CNT is more stable than a capsule for a diameter not larger than 3 nm. Cassell et al. [126] also used Fe, FeMo or FeRu on a mixed substrate (δ, γ-) Al_2O_3-SiO_2 and CH_4 at 900°C. They reported a spacing effect of SiO_2 and an increase of the proportion of SWNT in the sample with Mo which they interpreted as a an aromatisation effect of the hydrocarbon. Colomer et al. [127] using Fe, Co, Ni or binary systems on Al_2O_3 or SiO_2 and C_2H_4/N_2 at 1080°C showed that the Al_2O_3 substrate and Co or Fe (or mixed) are to be preferred. They obtained SWNT either essentially individual (1.6–6 nm in diameter) or in bundles (NTC diameter of 0.7 nm). Possibly, in the latter case, the SWNT which compose one bundle grew together radially from a large catalytic particle. Harutyunyan et al. [129], using Fe or Fe/Mo on Al_2O_3 and CH_4/Ar at 680–900°C, compared the efficiency of the catalytic materials without and with a pre-reduction treatment. They showed that the pre-reduction treatment (H_2/He, 500°C, 10–20 h) allows to obtain almost as much SWNT at only 680°C as obtained with non pre-reduced materials at 900°C. Maruyama et al. [180] reported a low-cost method using C_2H_5OH vapours at 600–900°C and a low pressure (5 Torr), with Fe/Co on a zeolite substrate. The authors claimed that they obtained very pure SWNT (Fig. 2.22), the high quality being a consequence of the etching effect of OH radicals

attacking carbon atoms with a dangling bond. For optimized temperatures, the Raman spectra show well-defined RBM bands and very low D/G band ratios (Fig. 2.23) which confirm the high quality of the SWNT.

Some authors reduced the pre-formed supported particles before the introduction of the catalytic material in the CNT synthesis reactor. Kitiyanan et al. [143, 181] prepared a catalytic material by impregnation of a SiO_2 substrate with Co and Mo salt solutions, calcination in air at 500°C which allows the crystallisation of the $CoMoO_4$ compound and pre-reduction in H_2 at 500°C. The CNT synthesis reaction was then performed at 700°C in a CO/He (1/1) gas mixture. The products contain essentially SWNT ($d \simeq 1$ nm) with only little disordered carbon and without MWNT, showing that the association of Co and Mo with an optimized ratio (1/2) gives a high selectivity. The influence of Mo was studied by Herrera et al. [182] who claimed that the pre-reduction treatment reduces only the Co-based compounds that do not combine with Mo. Co molybdate-like species are reduced in-situ in the reactor, leading to metallic Co and Mo carbide. An interesting work on the influence of the diameter of the catalytic particles on the characteristics of CNT was conducted by Cheung et al. [183]. Three classes of Fe nanoparticles, supported on oxidized Si, with narrow diameter distributions centered respectively around 3, 9 and 13 nm were prepared by thermal decomposition of $Fe(CO)_5$. By the treatment of these catalysts in C_2H_4 or CH_4 at 800–1000°C, CNT were obtained with about the same diameter as the initial catalytic clusters. However, 3-nm clusters produced a mixture of SWNT and DWNT and larger diameter clusters produced SWNTS with a lot of DWNT and MWNT (9-nm clusters) and only MWNT (13-nm clusters). These results show that the CNT diameter can be tailored by the size of catalytic particle but also

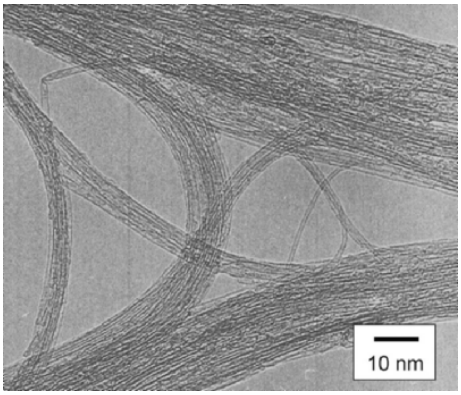


Fig. 2.22. TEM image of 'as grown' SWNT synthesized by decomposition of ethanol over Fe/Co mixtures embedded in zeolite at 800°C [180]. Reproduced from S. Maruyama, R. Kojima, Y. Miyauchi, S. Chiashi, and M. Kohno: Chemical Physics Letters **360**, 229 (2002), copyright 2002 with permission from Elsevier

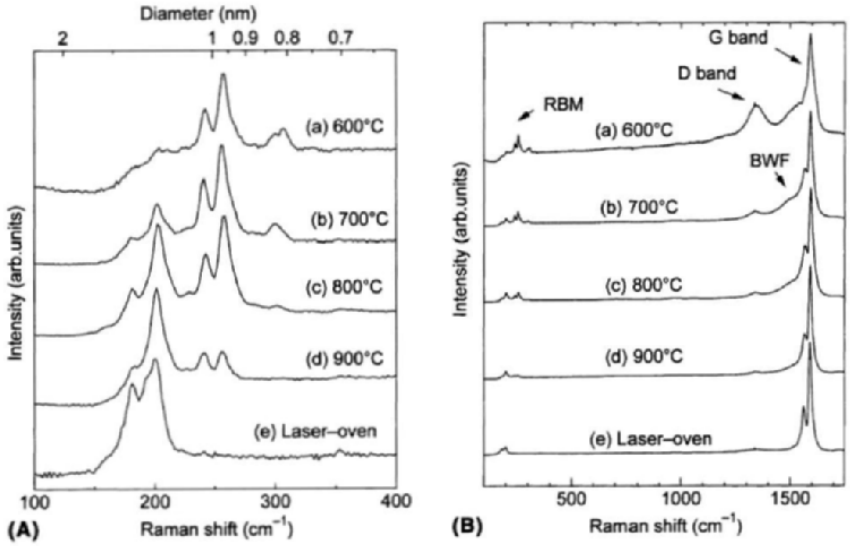


Fig. 2.23. Raman spectra ($\lambda = 488\,\text{nm}$) of 'as grown' SWNT synthesized by decomposition of ethanol over Fe/Co mixtures embedded in zeolite at various temperatures. (**A**) low frequency range showing well defined RBM bands; (**B**) large range spectra showing the very low D/B band ratios [180]. Reproduced from S. Maruyama, R. Kojima, Y. Miyauchi, S. Chiashi, and M. Kohno: Chemical Physics Letters **360**, 229 (2002), copyright 2002 with permission from Elsevier

confirm that sufficiently small catalytic particles ($< 3\,\text{nm}$) must be preferred to synthesize SWNT by CCVD methods.

Synthesis of Carbon Double-Walled Nanotubes (DWNT)

The synthesis of double-walled nanotubes (DWNT) has been researched by some authors, owing to their particular characteristics, intermediate between SWNT and MWNT. Most SWNT samples synthesized by CCVD also contain a more or less high proportion of DWNT [135,137,184,185] and thus, the synthesis parameters can be adapted to obtain a large proportion of DWNT. Ren et al. [186] used ferrocene and thiophene vapors in CH_4/H_2 at 1100°C and obtained CNT samples with about 70% DWNT (1.6–2.9 nm in diameter), often in bundles, with some disordered carbon deposit. Flahaut et al. [187] adapted the method of Tang et al. [179] using a Co- and Mo-containing MgO-based oxide and obtained CNT samples with about 80% DWNT either individual or in small bundles (Fig. 2.24), without any disordered carbon deposit, and with a yield of 13 wt.%, calculated from the weight of the starting catalytic material.

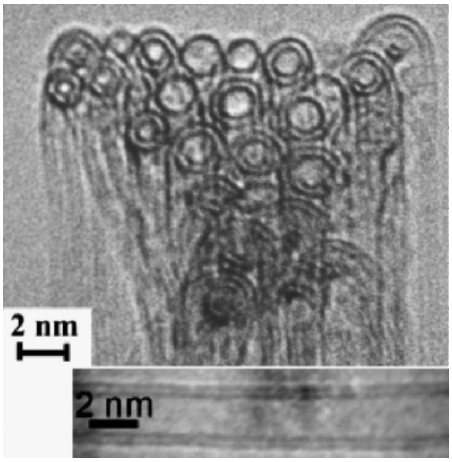


Fig. 2.24. HRTEM images of a bundle of DWNT and of an individual DWNT synthesized by decomposition of CH_4 over Co nanoparticles which are generated in-situ by the selective reduction of a MgO-based oxide solid solution containing additions of Mo oxide [187]. Reproduced from E. Flahaut, R. Bacsa, A. Peigney, and C. Laurent: Chemical Communications, 1443 (2003), by permission of The Royal Society of Chemistry

Localized Synthesis of Carbon SWNT

Because the CNT manipulation is very difficult and can cause some damages which may modify their electronic properties, many researches are attempting to locally synthesize CNT in-situ on a preformed electronic substrate. Kong et al. [188] patterned silicon wafers, by a lift off process, with micrometer scale islands of catalytic material made of alumina nanoparticles impregnated by Fe and Mo salt solutions. CNT, many being SWNT (1–3 nm in diameter, tens of micrometers in length) were grown by CCVD with CH_4 at 1000°C during 10 min, some of them bridging the metallic islands. Franklin et al. [189] prepared Co, Mo and Al precursors of oxide and printed this material on the top of Si towers. After calcination at 500°C during 12 h, the CCVD is conducted at 900°C in CH_4 during 20 min giving numerous SWNT bridging the Si towers (Fig. 2.25). It seems that one of the key points of the method was the use of a bulk amount of conditioning catalyst which was placed upstream of the patterned substrate.

2.4.4 Template Synthesis of Carbon Nanotubes

Porous materials, particularly those with cylindrical pores can be used as template to deposit carbon, without any catalysis step, which corresponds to chemical vapor deposition (CVD) methods sometimes with the help of a catalytic particle (CCVD methods). Che et al. [190] used a commercial alumina membrane (60 µm thick, pores 200 nm in diameter) and obtained, by

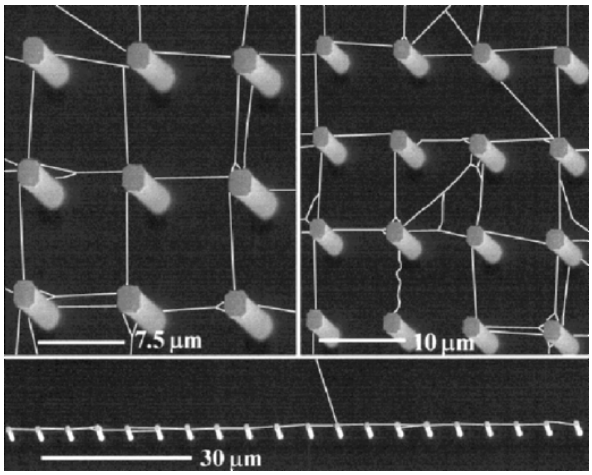


Fig. 2.25. SEM images of networks of suspended SWNT grown from silicon towers by the enhanced CCVD method described by Franklin et al. [189]. Reproduced from N. R. Franklin, and H. Dai: Adv. Mater. (Weinheim, Ger.) **12**, 890 (2000)

pyrolysis of C_2H_4 or pyrene (in a Ar flow) at 900°C, very well aligned carbon filaments which can either be hollow (nanotubular form – Fig. 2.25) or not (nanofibers) as a function of the deposition time (10 and 40 min, respectively). When the pores are impregnated with Co or Fe salts which give metal particles after calcination and then reduction in the reactor, the deposition process (here CCVD) yields carbon fibers which can grow out of the pores and fuse together in bundles. Heating the carbon nanofibers at 500°C during 36 h is sufficient to obtain a well-graphitized structure. Jeong et al. [191] prepared an alumina porous membrane (200 µm thick, pores of 80 nm in diameter) by a controlled anodic oxidation of Al, and performed an electrolytic deposition of Co and a pre-reduction (H_2/Ar, 500°C). The CCVD deposit was made from a $C_2H_2/H_2/N_2$ gas mixture at 650°C (40 min) and produced graphitized MWNT which grew out of the pores. The sonication of the obtained material allows the cutting of the MWNT to lengths between 50 and 400 µm. Xie et al. [192] prepared mesoporous SiO_2 (pore diameter 30 µm) by a sol-gel method, and impregnated it with Fe nitrate. After calcination and pre-reduction (H_2/N_2, 550°C), well graphitized MWNT (around 30 nm in diameter) were obtained by CCVD from the decomposition of C_2H_2 at 700°C. The template method is efficient to synthesize open MWNT with a narrow distribution of diameter, very well aligned into the pores or more or less aligned when they grow outside the pores. The CCVD method is preferred when a good crystallinity of the MWNT is desired. The template method can also be used to synthesize SWNT. Tang et al. [193] obtained tripropylamine embedded in 0.73 nm channels of microporous aluminophosphate crystals which decomposed, by pyrolysis at 350–450°C, to give a monodimensional carbon

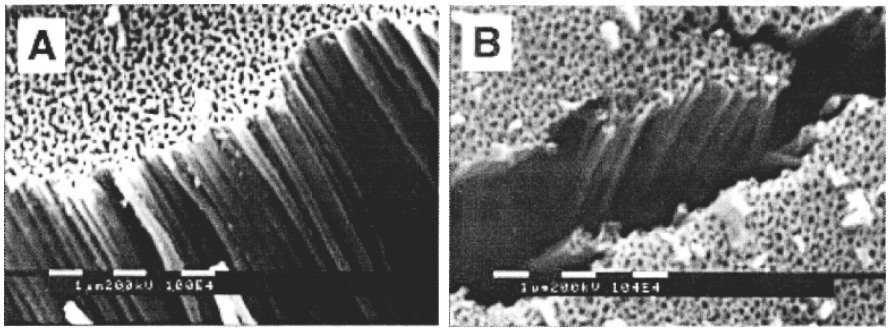


Fig. 2.26. SEM images of CNT obtained by chemical vapor deposition of carbon (CVD, without catalyst) on the walls of pores of an alumina membrane, using ethylene (**A**) and pyrene (**B**), during 10 min at 900°C. The template membranes have been dissolved in concentrated HF [190]. Reproduced with permission from G. Che, B. B. Lakshmi, C. R. Martin, E. R. Fisher, and R. S. Ruoff: Chem. Mater. **10**, 260 (1998), copyright 1998 American Chemical Society

deposit. A treatment at 500–800°C converted the deposit into crystallized SWNT with very small diameter (< 0.7 nm).

2.4.5 Conclusions

The results on the synthesis of CNT by CCVD methods have been published very recently, mainly from 1997 onwards. The key parameters of a successful method are of two kinds. Firstly, the parameters related to the starting material (i.e. the metal source and/or substrate) that aim at controlling the formation of the catalytic metal nanoparticles with the appropriate diameter. Indeed, MWNT can be obtained preferentially to nanofibers, and SWNT (or DWNT) can be obtained preferentially to MWNT by decreasing the size of the catalytic particles (generally Fe, Co) and stabilizing their size at the high temperature of the reactor. Secondly the parameters related to the carbon deposition reaction, which include the appropriate choice of the carbonaceous gas, of the auxiliary gas(es), of the proportion and flow of the gases, of the reaction temperature and pressure.

SWNT are efficiently prepared by CCVD using nanometric catalytic particles which can be either formed in-situ from an organometallic precursor in a gas flow or supported on a solid substrate material. In the first case, Fe particles are generally preferred and are formed from vapors of ferrocene or $Fe(CO)_5$. These syntheses are conducted at relatively high temperatures (1100–1200°C) with C_2H_2 or C_6H_6 and it seems that some supply of sulphur is beneficial. Using $Fe(CO)_5$ and CO at 10 atm and 1200°C, the HiPco method produces good quality SWNT by a continuous process. Many ways have been studied to prepare nanoparticles (generally Fe, Co or alloy) on an oxide substrate, which are sufficiently stable to act as catalyst at high temperatures.

They can be generated in-situ, in the reactor, by selective reduction of an oxide solid solution, or pre-formed ex-situ as oxide particles which are reduced into metal during the reaction, or prepared in the metal form before the reaction. The addition of Mo containing species during the preparation of the catalyst is determinant to increase both the selectivity and the SWNT yield. Among the substrates, MgO is preferable because it can be easily removed with non-oxidative acids. CH_4, which decomposes at high temperatures, generally mixed with H_2, notably to avoid the formation of disordered carbon, is often preferred. The temperature of the reactor is chosen according to the nature and partial pressures of the carbonaceous and auxiliary gases. It has not yet been demonstrated that samples containing 100% SWNT can be prepared by CCVD. In comparison with SWNT produced by arc-discharge or laser ablation, CCVD SWNT samples have a larger distribution in diameter but their Raman spectroscopy spectra can nonetheless present a very small D band, which is characteristic of a very small amount of disordered carbon or defects, and often show very well-defined RBM modes, which is characteristic of populations with a well-defined diameter. Because many parameters are adjustable in the CCVD method, the characteristics of CNT (SWNT or DWNT, diameter) are also adjustable.

CCVD methods are promising because they are of low cost, they can be upscaled in continuous processes by multiple technical solutions, they involve a number of parameters which can be optimized to adjust the selectivity towards the synthesis of SWNT, DWNT or MWNT, with small or large diameters. Moreover, the CCVD allows the localized and/or oriented growth of CNT. Until recently, CVD methods generally resulted in poor quality SWNTs or MWNTs. However the quality of the tubes produced in this way is becoming better and better, so that they are now used in transport devices as NT produced through high temperature routes.

2.5 Nucleation and Growth of C-SWNT

2.5.1 Summary of the Synthesis Conditions of C–SWNT: Similarities and Differences of the Different Synthesis Methods

We have seen in the previous sections that C–SWNTs can be produced via both high temperature routes and CCVD processes. In spite of obvious differences, all synthesis conditions have in common the involvement of a metal catalyst. In the high-temperature-evaporation based routes, carbon and metallic elements (Co, Ni, Y, La, ...) are vaporized at temperatures above 3000 K and then condensed at lower temperatures in an inert gas (He, Ar) flow and single-walled nanotubes are believed to form at about 1500 K. In particular, the use of a pulsed laser in the laser-ablation method requires to place the reactor in an oven heated to at least 1300 K to obtain significant yields in SWNT. The CCVD based routes use the decomposition of an hydrocarbon

gas (methane, ethylene, ...) or of CO at the surface of catalytic particles (Fe, Co, Ni) which are either supported on a substrate or synthesized in-situ from a solid or liquid precursor and sprayed in the furnace heated at temperatures between 750 and 1200°C.

The analogies between these fairly different methods are actually remarkable: First, the morphologies of the SWNTs produced by the different techniques are very similar. In each case, SWNTs can be found isolated or self-assembled in crystalline bundles, their diameter varying from 0.7 to 5 nm. These correlations suggest that a common mechanism could explain the growth of SWNTS. Second, for all synthesis techniques, catalysts such as Ni, Co, Fe, Y, La or mixtures of these elements are necessary to obtain SWNTs. Several questions then arise concerning the role played by the temperature and the metallic catalyst: is the catalyst active at the atomic level or as a cluster, in a liquid or a solid state and through which catalytic reaction processes?

In nanotubes, carbon has a structure which is not very different from its most stable structure at equilibrium, i.e. graphite. Nanotubes can therefore be considered as particular sp^2 carbon structures. As for carbon fibers, understanding their formation requires an analysis of the transformation paths of carbon from the vapor to the solid state which themselves depend on the phase transformations involved in the catalyst-carbon systems. From an experimental point of view two types of methods are used. Structural determinations and chemical analyses of the synthesis products are made ex situ after the synthesis using local or global probes whereas in situ diagnostics in evaporation-based synthesis reactors are now becoming available [39, 43]. Among the techniques used in post-synthesis analyses, transmission electron microscopy plays a major role since it is the only technique able to provide structural and chemical informations [197]. In situ diagnostics inspect the temperature, nature of species issued from the target vaporization, time evolution of the matter aggregation after the initial vaporization (see Sect. 2.2). It is worth mentioning that there is no specific diagnostic, until now, able to identify the nanotube onset in high-temperature processes and therefore to identify directly the role played by metal atoms. From a theoretical point of view, thermodynamic treatments at the mesoscopic level [198, 200] as well as atomistic modelizations (starting from ab initio or empirical interatomic potentials) [201, 202] have been developed.

Although the situation is not completely clear yet, some realistic scenarios begin to emerge from these different approaches [204]. In the following, we shall focus on the phenomenological models of nucleation and growth which can be deduced from microscopic analyses of the nanotubes and their catalysts in TEM [205] and from in-situ diagnostics data, with a particular emphasis on the growth of nanotube bundles in the evaporation-based routes. The next section (Sect. 2.6) is devoted to atomistic simulations of growth mechanisms using ab initio or empirical interatomic potentials.

2.5.2 Towards a General Phenomenological Model of Nucleation and Growth

Analysis of the Link Between Catalyst Particles and SWNTs

Samples generally consist of a mixture of metallic particles and of an entangled network of nanotubes, isolated or assembled into bundles. Observations have been directed, in a first step, to the identification of the relationships between particles and bundles. The entangled nature of nanotube networks makes these observations very difficult, since it is in general not possible to find the tube ends as mentioned in the first experimental investigations [34]. However, recent detailed high-resolution transmission electron microscopy (HRTEM) analyses indicate that, actually, whatever the synthesis process [34,48,127,132,196,218], SWNT nucleate and grow from the catalytic particles [202]. Figures 2.27–2.28 show different examples of SWNT ends observed in samples produced by different high and medium temperature techniques. In all cases, it is found that the nanotubes are attached by one end to small (5–20 nm in diameter) metallic particles although differences in the size of the particles, in the number of tubes per rope and in the crystallinity of the tubes are evident. The situation where the nanotubes are short ($\leq$400 nm) is of particular interest since both tube ends can be observed simultaneously, which is quite impossible for long tubes because of their entanglement. In those cases (Fig. 2.28 and Fig. 2.27c), it is clearly seen that one tube end is attached to the particle and the other is closed and empty. The situation shown in Fig. 2.28b, where numerous bundles corresponding to several tens of SWNTs emerge radially from a given particle, is called a sea urchin structure and has been observed for different catalysts [24, 52, 194, 207, 208]. Finally, very short tubes corresponding to bundle embryos or nuclei have been clearly identified and different situations are seen in Fig. 2.28c–e. Figure 2.28c shows a bundle embryo whereas in Fig. 2.28d,e a single nanotube is emerging from the particle.

It results from these observations that there are basically two situations. In the first case the tube growth is *perpendicular* to the surface of the particle. This is the general situation encountered in the evaporation-based route, where the particles are fairly large (5–20 nm) (Fig. 2.27a, d, e, f and Fig. 2.28a, b) (see also [209]) but it is sometimes observed in CCVD samples as well (see Fig. 2.27b) [127, 196]. In this growth mode, the tubes are most frequently arranged in bundles (see Fig. 2.27a, b, d) but single tubes emerging perpendicularly from the surface of the particles can also be observed as in Fig. 2.28d. In such cases, the diameters of the tube are not correlated with the size of the particle. In the second case, the growth is *tangential*; the particles are generally smaller (1–5 nm) and are found encapsulated at the tip of the tubes (Fig. 2.27c and Fig. 2.28e), thus determining their diameter. Many other examples can be found in the literature as for instance in [125]. This growth process has, to our knowledge, only be observed in the CCVD methods.

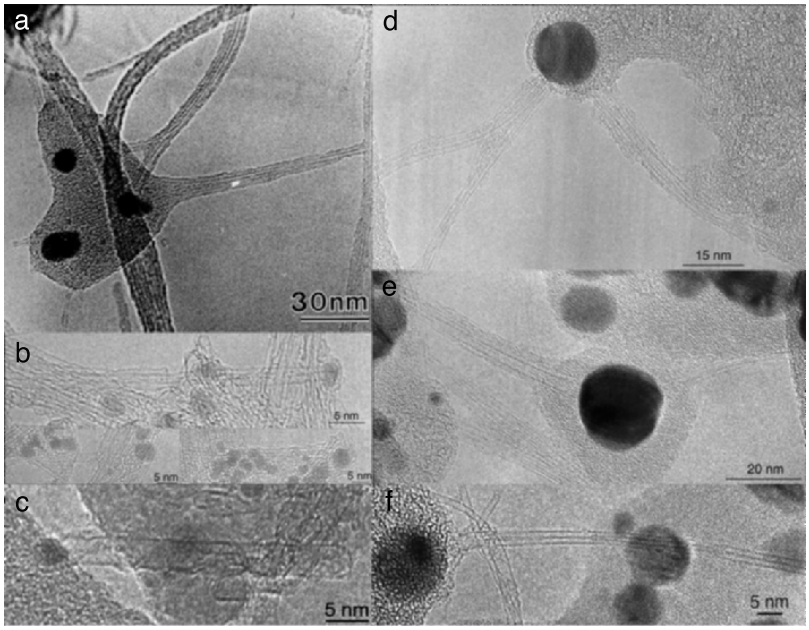


Fig. 2.27. HRTEM images (Jeol 4000FX, Cs = 3.2 mm) of long SWNT ropes emanating from metallic particles synthesized by various methods: (**a**) electric arc discharge described in [20] with a Ni-Y catalyst where the Y/Ni ratio is equal to 0.2, (**b**) HiPco CCVD process described in [132], (**c**) CCVD procedure described in [127,196]. (**d**) pulsed-laser ablation described in [34], (**e**) and (**f**) continuous laser vaporization described in [48]. Note that in (a) the particle size is much smaller than in the other cases and that the ropes contain a reduced number of tubes. When the particle is large (d, e), two ropes or more can emerge from it. Futhermore, it is frequently observed, as it can be seen in (a), that bundles issued from distinct particles attract each other according to a branching process and form a composite rope [218]. Finally, note that in (c) the diameter of the tube is related to that of the particule in contrast with the situations shown in the other cases

Phenomenological Model of Nucleation and Growth

The tangential growth process, observed for CCVD SWNTs, should be similar to that put forward to explain the growth of vapor-grown carbon filaments from liquid particles which is based on the VLS model (see Sect. 2.3 and Fig. 2.29a) [80,85]: the nanotubes can be considered in this case as ultimately small carbon filaments (Fig. 2.29b) [125]. The process, sketched in Fig. 2.29, involves a chemisorption and decomposition of the carbonaceous gas at the surface of the particle, the dissolution and the diffusion of carbon within the particle and its segregation and graphitization parallely to the surface of the particle, once the particle gets saturated in carbon. A carbon cap (called yarmulke) is formed on the top of the catalytic particle which decreases the

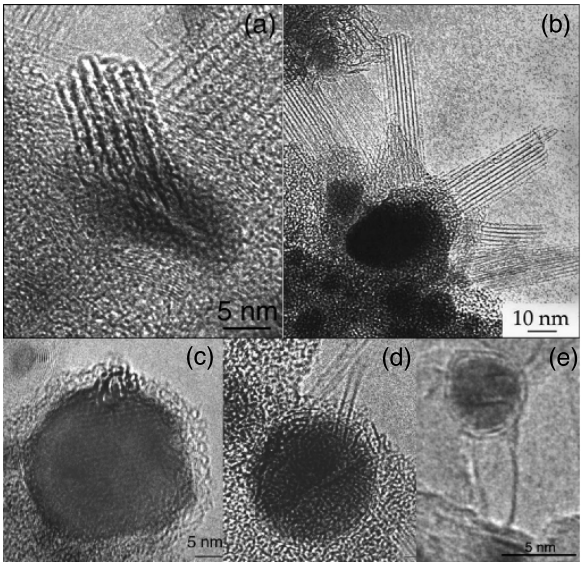


Fig. 2.28. HRTEM images of different short ropes attached to the metallic particles. Samples are synthesized with the electric arc and with a Ni-Y catalyst where the Y/Ni ratio is equal to 0.5 in (a, b, c, d) and by the CCVD process described in [127, 196] in (e). In (**a**) the rope is strongly inclined with respect the electron beam whereas in (**b**) different ropes are emerging radially from the particle in different spatial directions reminding to a sea-urchin hence the name given to these morphologies. In (**c**–**e**), the nanotubes are seen as elongated caps having a length between 3 and 5 nm. The image (c) shows embryos of a SWNT bundle. In other cases only one nanotube is emerging from the particle whose size is not correlated to that of the tube in the case (e). It is worth noticing that in this particular case, the graphitic walls of the tube are tangent to the surface of the particle whereas in the other cases, the tubular sheets are perpendicular to the particle surface

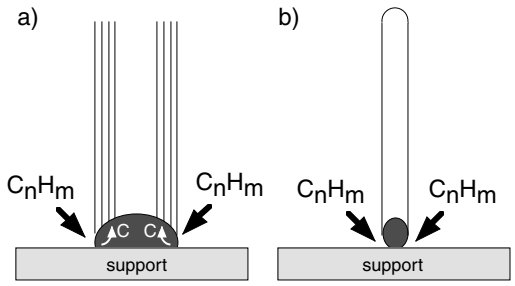


Fig. 2.29. (**a**) Simplified schema for the formation of carbon filaments obtained from CCVD methods [80, 85] and its adaptation to the formation of SWNT growing tangentially to the surface of the particle in (**b**)) [125]

surface energy. Then, either the carbon shell continues to grow and covers the particle, deactivating it and forming a carbon capsule, or the cap lifts up, forming the cylindrical form of a SWNT, or a second cap is formed under the first one before their lift up, forming a DWNT. The carbon concentration gradient between the surface and the bulk of the particle ensures the continuity of the process as long as the temperature and gas supply, at a rate avoiding catalyst poisoning, are maintained [220]. The diameter of the tube emerging from the graphitization process is naturally determined by the size of the particle which, during the growth, can either be rejected at the tip or be kept at the foot of the tube and attached to the support.

Such a process, however, fails to account for the situation, typical of the vaporization routes, where the growth is perpendicular to the particle. Different alternative models have been tentatively proposed in recent years. First, a direct formation process in the gas phase has been considered [34]: catalyst acts through aggregates reduced to a few atoms located at the tip of the nanotube, either preventing its closure by scooting around and stabilizing the reactive dangling bonds or leading the tip to remain chemically active [203] or stabilizing structural defects and acting as attraction sites for carbon adatoms [210]. This model will be discussed in detail in Sect. 2.6. Other models involve the growth from a liquid metallic particle, the SWNT nucleation step being a highly debated issue. It has been suggested, in particular, that preformed fullerenes could play the role of nucleation seeds [211].

On the basis of the TEM observations described above, a simple model has been developed, which adopts the concepts of the so-called VLS (vapor-liquid-solid) model introduced for explaining the growth of silicon whiskers [116]. The adaptation of the VLS approach to the growth of SWNTs was first proposed by Saito et al [24,206,207], in order to explain the formation of sea-urchin-like structures. It was then extended to the formation of both individual SWNTs and SWNTs bundles, which are emerging perpendicularly from the particle [197, 202]. In this type of model, the growth of nanotubes is believed to proceed via solvation of carbon vapor into metal clusters, followed by the precipitation of carbon excess in the form of nanotubes. The mechanism is based on the ability of metals such as Ni or Co to dissolve carbon when liquid and to almost completely segregate upon solidification, therefore allowing graphitization of carbon at temperatures as low as 1500 K [45, 204]. These properties can be directly deduced from the thermodynamic phase diagrams of Ni (Co) – C systems recalled in Fig. 2.30 [45]. Figure 2.31 presents a simplified sketch of the proposed scenario. The first step (Fig. 2.31a) of the process is the formation of a liquid nanoparticle of metal supersaturated with carbon. These nanoparticles originate from condensation of the metal plasma/vapor in the moderate temperature zone of vaporization based reactors. Upon cooling, the solubility limit of carbon decreases and carbon atoms segregate towards the surface where they precipitate. The second step (Fig. 2.31b, c) is the formation of nanotube nuclei at the surface of the particle which is competing with the formation of a graphitic sheet wetting the surface of the particle. The

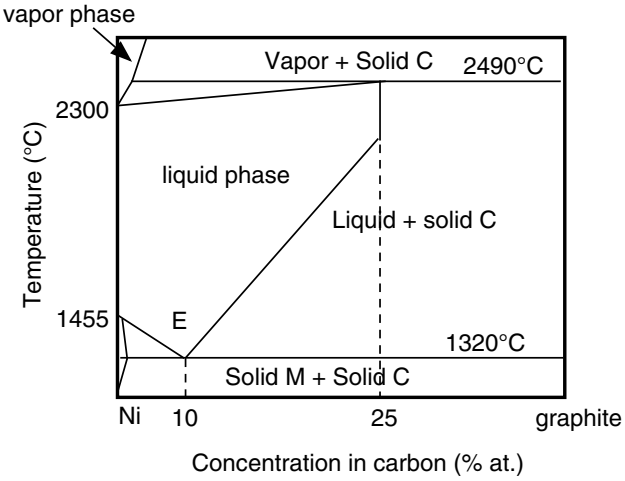


Fig. 2.30. Schematic phase diagram of the C-Ni system adapted from [45]. The C-Co diagram is quite similar

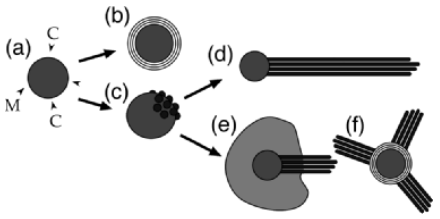


Fig. 2.31. Scenario derived from the VLS model, for the nucleation and growth of SWNT

last step (Fig. 2.31d, e, f) is the nanotube growth which is likely to proceed by a progressive incorporation of carbon at the interface particle – nanotube. This scenario, which implies a root growth mechanism, is supported by the different TEM observations presented above, for the nucleation step at least, and by ab initio calculations [202] (see Sect. 2.6). Furthermore, in-situ diagnostics performed in laser methods [39, 42–44] and solar furnaces [54] (see Sect. 2.2) provide information consistent with the first step. We discuss below in more detail these different steps with particular attention to the nucleation which is the most crucial step.

Particle Formation and Carbon Segregation

The presence of metal atomic vapors and of C_2 molecules is attested by the in-situ diagnostics [39, 42, 43, 54] done in continuous and pulsed vaporization reactors. As expected from thermodynamic data (Fig. 2.30), carbon condenses first, about 100 μs after vaporization. In pulsed laser reactors, the

signal corresponding to the metallic vapor disappears ten times later than the C_2 signal. Because of the high quenching rate, expected to be 105–106 K/s in continuous laser reactor [39] and solar furnace [44], carbon condenses in a low density amorphous state. Neither graphite nor diamond crystallites have been detected in the synthesis products. From in situ measurements [39, 42], metal condenses below 2300 –2000°C resulting in the formation of liquid particles (Fig. 2.31a). The nanoparticle size is determined by parameters such as temperature gradients, gas pressure and flow, etc. [38, 40, 212]. At this stage, these particles can dissolve a substantial amount of carbon, up to 25 at. % at 2000°C as indicated by the phase diagrams (Fig. 2.30) and probably much more, up to 50–60 % [213], when the particles are very small. Phase diagrams (Fig. 2.30) also indicate that the solubility limit drastically decreases down to a few at. % as the temperature is falling down to the eutectic temperature (T = 1400°C), where the metal solidifies. The solidification gives rise to a phase separation between an almost pure metallic phase and a solid pure carbon phase. The phase separation proceeds by a segregation of carbon towards the surface of the metallic particle because of two combined effects: the drastic difference of energy of the respective surface tensions of metals and carbon [204] and the reduced particle size. This phenomenon of surface segregation has been confirmed by ab initio calculations done in the Co–C system [197, 202].

Nucleation

Once expelled, carbon crystallizes at the surface of the particle according to two competing transformation paths (Fig. 2.31b, c), which lead either to graphene sheets wrapping the particle and wetting its surface or to SWNTs nuclei with graphitic walls perpendicular to the surface, that is, non wetting it. Since equilibrium surface energy arguments play in favor of the first configuration [204], it has to be assumed that the SWNTs nuclei result from a particular surface process, for which the graphene sheet becomes unstable. As explained above, the segregation force increases upon cooling and is maximum close to the solidification. If the segregation velocity is low, carbon can be progressively and gently extruded in such a way that carbon atoms get organized by surface and bulk diffusion in the most stable configuration, that is, the graphene sheet. On the contrary, when the segregation velocity is high, the carbon flux is too rapid to permit, by diffusion, progressive incorporation of atoms at the edges of a graphene layer and because of this conflict surface instabilities occur.

The precise nature of these instabilities is for the moment a debated issue, discussed in detail in [204]. One can imagine dynamic instabilities as those involved in the formation of dendrites in solidification processes [214] or quasi-static instabilities similar to those involved in crystal growth produced by molecular beam epitaxy deposition [215]. The latter analogy is very appealing indeed if one replaces the deposition flux by a segregating carbon flux. The equivalent of a layer-by-layer growth (or Frank-van der Merwe process) would

be here the formation of graphene sheets whereas the formation of islands (Volmer-Weber or Stranski-Krastanov processes) would be equivalent to the growth of nanotubes (for details see [204]). The limit of these analogies lies in the difference in scales compared to the length and the diameter of the nanotubes: macroscopic size of the dendrites in the first scale, nanometer height of the islands in the second case. In all cases, the instability is governed by two control parameters: one is the surface energy and the other can be, depending on the system in turn, a kinetic energy as in dendritic solidification, a concentration gradient, or elastic and chemical energies which determine the wetting properties of the surface. In our case, the carbon surface tension is clearly one parameter, whereas the second one should be related to the chemical nature of the catalyst and to the kinetic conditions of cooling. In particular, the surface layer of the catalyst should have a particular structure and chemistry in such a way that its energy becomes unfavorable to the wetting of the graphene sheet, which is a condition required for the SWNT nucleation. We will see, in Sect. 2.5.3, how this condition is achieved in the case of the Ni-RE catalyst (RE: rare earth element). Finally, since the nucleation of bundles can occur, the instability should be cooperative in order to explain the collective formation of an assembly of nanotubes. Recent observations done on bundles produced by CCVD [216] methods indicate that, for small bundles, all the tubes have the same helicity, attesting for a cooperative nucleation process.

Growth and End of the Growth

Once the nanotube nuclei are formed, growth should proceed through further incorporation of carbon. Carbon initially dissolved in the particle should continue to condensate at the root but this is not sufficient to produce long (one micron ore more) SWNTs bundles [197]. For instance, a nanoparticle of 15 nm in diameter and containing initially 50 at.%C can give rise to either one SWNT of one micrometer long or to a bundle of ten SWNTs of 100 nm each [197]. Another source is therefore necessary which is naturally the density of the remaining amorphous carbon. The incorporation of this carbon can follow the dissolution process based on a concentration gradient within the particle and invoked in the growth of filaments in CCVD methods or can directly be incorporated at the root of the nanotubes. This root growth process is also confirmed by atomistic simulations as shown in Sect. 2.6.

In order to achieve long nanotubes (Fig. 2.31d), the growth should therefore continue for a sufficiently long time, as attested by in situ diagnostics, which indicate growth times longer than tens of ms, and post-synthesis annealing experiments [42], until local temperatures are too low, leading to the solidification of the nanoparticles. These conditions define a kind of stationary regime where the kinetics of incorporation of carbon in the tube walls is compatible with the cooling kinetics and the carbon supply. These constraints certainly explain the necessity of using in the pulsed laser reactor an oven heated to around 1500 K, that is to a temperature close to the metal

solidification temperature [34,36]. Such an oven is not necessary in continuous vaporisation methods [35,37,39,52], since in this case the carrier gas is heated in the vicinity of the target and acts as a local furnace, as shown by in-situ measurements (Sect. 2.2).

Different morphologies can arise, which are sketched in Fig. 2.31e, f, when the local conditions have been perturbed in such a way that the growth has stopped. According to the root growth process, looking at the feet of the nanotubes provides information on the end of the growth, and how this has been perturbed, before to stop. The remaining carbon, which was immediately available for the growth, can partly condense into amorphous carbon flakes embedding the particle (an example can be seen in Fig. 2.27) or into a few graphitic layers wrapping the particle and building a buffer layer between the nanotubes and the particle (examples can be seen in Fig. 2.28). The former case (Fig. 2.31e) suggests a rapid decay of the local temperature whereas the latter situation (Fig. 2.31f) signifies the occurrence of a bifurcation from the nanotube growth towards the continuous layers growth. This bifurcation is an additional proof that nanotubes and graphitic layers do not occur for the same local conditions of carbon segregation [219]. Different morphologies can thus emerge from the same particle provided that the local experimental conditions suited for their growth are successively achieved.

2.5.3 Microscopic Approach of the Nucleation for a Particular Family of Catalyst: the Case of the Ni-RE Catalysts

Experimental Procedure

The nucleation step, discussed in the previous section, has been investigated in detail for Ni-RE (RE = Y, Ce, La) catalysts by examining the structure and the composition of the particles linked to the different SWNTs morphologies. We focus on this particular class of catalysts since they are preferentially used in continuous vaporization routes such as the arc discharge method [20] and the continuous laser reactor [35, 40]. It has indeed been recognized that the highest SWNT production rate is achieved when a small amount of a rare earth element such as Y is added to the transition-metal catalyst. To study the influence of the RE addition on the SWNT formation, different rare-earth elements – Y, Ce, La – with different compositions (from 0 to 100%) have been tested. SWNTs were synthesized by the arc discharge method with the conditions given in [20].

SWNTs Morphologies and Catalyst Composition

As a general result, identical results have been found for the three RE tested. The yield in nanotubes is extremely sensitive to the anode composition. The SWNT production rate has been found to be maximum for a nominal anode RE/Ni ratio between 0.2 and 0.5 and to drastically decrease by a factor up

to ten out of this composition range. Furthermore two kinds of tube morphologies have been observed, in various proportions depending on the anode composition: long ropes as in Fig. 2.27a, or sea-urchin-like structures as in Fig. 2.28b. Pure Ni produces long ropes only (in low yield) whereas pure RE produced sea-urchin structures only. For intermediate anode compositions, both types of tubes are observed in a proportion related to the amount of RE . X-ray analysis of the composition of the particles has shown that long ropes are always linked to particles whose composition RE/Ni is lower than 11 at.% whereas particles of sea-urchin-like structures have a composition RE/Ni larger than 15 at.% [197]. As a reference, the composition of the particles which are not linked to SWNTs is completely random. Finally, this relationship between particle composition and SWNTs morphologies is found whatever the nominal RE/Ni anode ratio.

Particle Analyses

It results from this first analysis that the particle structure and composition are crucial parameters to be identified for explaining the differences observed between the SWNT morphologies. Chemical maps, chemical profiles and high resolution images have been recorded in TEM by combining HRTEM and EELS on numerous particles linked either to long ropes or to sea-urchin-like structures. In the case of long ropes, chemical maps shown in Fig. 2.32 reveal that the core of the particle is pure Ni whereas the surface is partially RE enriched. Line-scan profiles extracted along a section of the particle [219] provide a clear quantitative evidence of the spatial anticorrelation between Ni and RE. The RE metal is not uniformly distributed at the surface but is concentrated in thin platelets which are clearly recognized in HRTEM images since they display a dot pattern different from the core (Fig. 2.32a, b). These differences reveal that the compositional variation has a structural counterpart. Analyses of the different patterns have revealed that the core has the fcc structure of nickel whereas the platelets have the structure of the carbide REC_2 [204]. Furthermore, platelets have been found to display two important features: their thickness is in general restricted to 2–3 atomic layers and they are always oriented with their (110) plane parallel to the surface.

The identification of the surface platelets is very crucial and provides the key of the SWNT nucleation. Indeed, their presence has been found to be directly related to the nucleation of SWNTs since a direct link between the ropes and the platelets has been frequently observed, as attested in the example shown in Fig. 2.33 (see also examples in [204]). The platelet is lying at the top of the particle in the plane of projection and hence imaged by a fringe contrast. The feets of the SWNTs of the rope are clearly attached at the surface of the platelet.

The particles linked to sea-urchins are different. The same carbides are observed at the surface but now they cover uniformly the surface as a thin shell (2–3 layer thick) encapsulating the particle [219]. Furthermore, the core

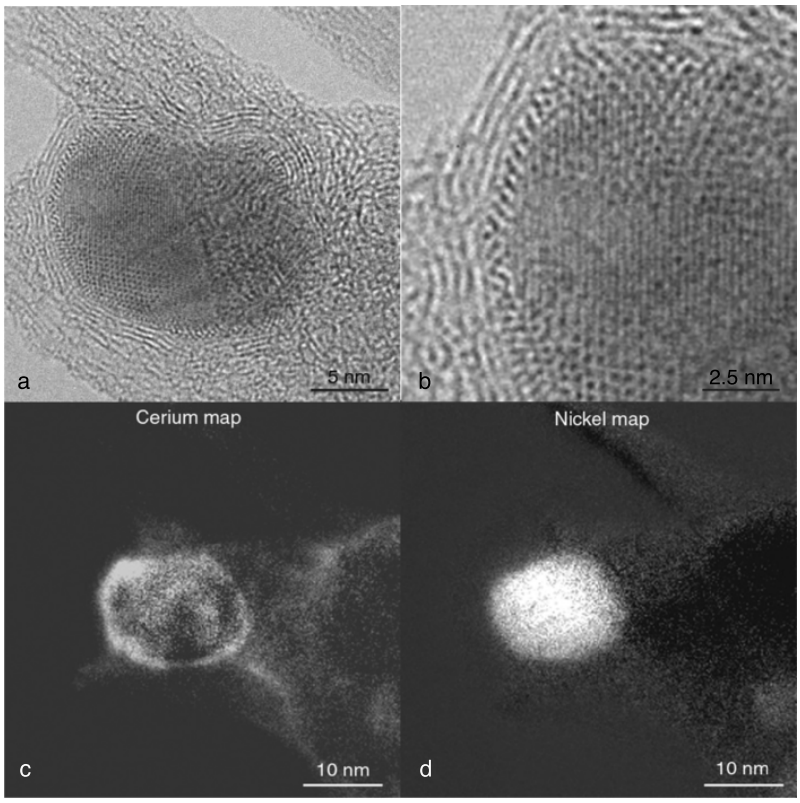


Fig. 2.32. (**a**) HRTEM image of a particle with an enlargement in **b**. (**c**) Ce, (**d**) Ni chemical maps (EFTEM images at Ce-N4,5 edge and Ni- M2,3 edge, Jeol 3010 equipped with a Gatan energy filter (GIF) operating at 300kV) of a particle linked to long SWNT ropes in the case of a Ni-Ce catalyst. Ce and C are mostly located at the surface of the particle whereas Ni is located in the core of the particle. Furthermore, location of Ce and C is correlated with the observation, in the HRTEM image, of a strong white dot contrast which is not seen in the bulk of the particle and which is the evidence that the surface has a different crystalline structure than the bulk, adapted from [204]

is now a complex Ni-RE-C compound such as the RE/NiC_2 compound or the REC_2 carbide itself when the catalyst is 100 % RE [[197, 208]. This total higher RE concentration is fully consistent with EDX analyses. In addition the core is frequently microcrystalline, which was not the case of pure Ni cores, suggesting rapid solidification due to rapid cooling conditions.

Nucleation Model: The Catalytic Role of Rare Earth Elements

The results presented above can be summarized as follows: the nanotube nucleation is directly linked to the presence of REC_2 carbide at the surface of

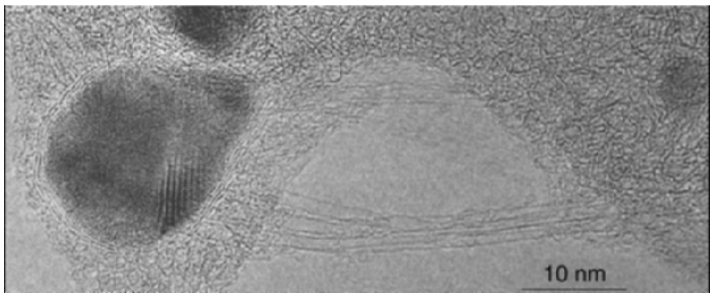


Fig. 2.33. HRTEM images illustrating the link between the carbide at the particle surface and the roots of the long ropes. The carbide platelet is lying at the top of the particle and seen with a fringe contrast, adapted from [204]

the particle, the number of nanotubes emerging from it being directly related to the covering of the particle by the carbide layers. Furthermore, the length of the tube is linked to the presence of RE in the core: when present, the length remains below 100 nm whereas in the other case there is no limitation in the length, nanotubes can achieve.

To understand the role of the RE in the nucleation, one has first to explain the formation of the surface carbide. This results from the combination of two properties of the RE metals: their abilities to form a stable carbide, with melting temperatures higher than that of Ni (for example, the melting temperature of YC_2 is equal to 2415°C) and their low surface energy which is about ten times lower than that of carbon. This second effect induces a co-segregation of C and RE at the particle surface at temperatures higher than the solidification point of the particle. Once at the surface, because of the first effect, RE and C self assemble to form a chemically ordered surface layer, which is likely to be seen as a raft floating at the surface of the particle. More precisely, since the carbide layer is experimentally found to always have the (110) orientation, the chemical ordering of the surface layer should resemble the chemical ordering of the (110) plane of the carbide. This plane consists of a regular pattern of carbon pairs and of RE atoms [204]. It is striking that the carbon pair spacing, equal to 0.12–0.13 nm, is very close to the first neighbor distance in the graphene structure. This peculiarity strongly suggests that the carbon pairs can serve as nucleation sites for a graphitic network perpendicular to the surface. This would be the starting point for the formation of SWNT nuclei.

Furthermore, the presence of RE atoms mixed with the carbon pairs is thought to help stabilizing SWNT nuclei due to a third property of RE, which is its ability to transfer electrons to carbon. This effect has been studied by simulations using a tight-binding modeling of C–C interactions combined with Monte Carlo simulations [204]. These calculations have shown that when the number of electrons is increased, which mimics a charge transfer, the graphene sheet is destabilized in favor of configurations involving pentagons

and heptagons. These defects introduce local curvatures which are necessary for building a SWNT nucleus linked by the foot to the surface [201, 209]. Therefore, it can be inferred from these simulations that charge transfer effect of RE plays in favor of the formation of a SWNT nucleus instead of a graphene layer.

In summary, the carbide surface layer can be seen as a diffuse carbon-rich interface between Ni and graphitic carbon where strong metal-carbon bonds are involved which modify the properties of the surface of Ni in such a way to avoid the wetting of graphene layers. RE carbides are thus found to play an important role in the parameters controlling the surface instability responsible for the SWNT nucleation.

The arguments put forward above make clear that the density of nucleation sites is directly determined by the RE concentration of the particle. A low concentration gives rise to a partial carbide covering and to a few number of SWNTs assembled into a rope. This corresponds to the first SWNT morphology. On the contrary, a high concentration provides a complete surface covering by the carbide and an isotropic distribution of nucleation sites which results in the sea-urchin structure.

Let us now discuss the difference in length between long ropes and sea-urchin structures. As said previously, growth stops when the particle solidifies or when the carbon source is exhausted. If the growth proceeds by the incorporation of carbon via a dissolution-precipitation process, the presence of a continuous carbide layer at the surface, at high concentration of RE, can act as a poison to the dissolution process since the layer is saturated in carbon. The carbon initially dissolved in the particle is therefore the only feeding source for growth. In addition, the observation that RE rich particles are microcrystalline, indicates a solidification in a high temperature gradient. Since in situ temperature measurements indicate that higher the temperature higher the local temperature gradient [39], RE rich particles are likely to solidify at higher temperature than Ni. At such temperature, due to the corresponding high temperature gradient, the residence time of the particle at temperatures suitable for the growth has been very short. In Ni rich particles, on the contrary, longer residence time can be achieved resulting in extended growth. Both effects, poisoning and rapid solidification, may explain why tubes of sea-urchins remain short whereas, at low RE concentration, long tubes are observed.

2.5.4 Conclusion

The general conclusion from microscopic observations is that, whatever the synthesis technique and the tube morphology, SWNTs nucleate and grow from catalyst particles. Depending on the synthesis technique, the tubes are observed to grow parallel or perpendicular to the surface of the particle. In the former case, observed in CCVD synthesis techniques, the diameter of the tube is correlated to that of the particle which is trapped at the tip

of the tube, whereas in the latter case, mostly found in vaporization-based synthesis techniques, there is no correlation between the diameter of the tube and that of the particle.

Phenomenological models of nucleation and growth have been discussed with particular emphasis on the perpendicular growth of nanotube bundles since in that case the classical models of growth working for carbon filaments can not be applied as they do for the parallel growth situation. There is now strong experimental evidence in favor of a root-growth process where carbon, dissolved at high temperature in catalytic particles, segregates at the surface at lower temperature and forms tubes via a nucleation and growth process. Particular attention has been paid to the nucleation step where the main problem is to understand why carbon does not always form graphene sheets wrapping the particles. This competition necessarily involves a surface instability where one control parameter is the low surface tension of carbon compared to metal transition.

The origin of this instability has been studied in detail for a particular class of catalyst Ni-RE (RE = Y, Ce, La) in order to understand why some addition of the RE drastically increase the production yield. Whereas Ni has the property to dissolve carbon in the liquid state and to reject it in the solid state allowing the graphitization of carbon at temperatures as low as 1400 K, RE is found to be a co-catalyst of Ni playing the role of a surfactant. It co-segregates with C at the surface of the particle and forms a chemically ordered surface layer which mimics the structure of the REC_2 carbide. This chemical modification of the surface of Ni certainly inhibits its wetting by a graphene sheet and therefore contributes to the nucleation process and to control it. Many questions remain however open such as for instance the extension of the surface arguments identified for the Ni-RE class to other classes of catalyst (transition-metal mixtures for instance), the nature of the parameter controlling the tube helicity and its diameter.

2.6 Growth Mechanisms for Carbon Nanotubes: Numerical Modelling

2.6.1 Introduction

In the following, we will address from a theoretical point of view, the growth of multiwalled and single-walled carbon nanotubes. One of our objectives will be to show that presently available simulation techniques (semi-empirical and ab initio) can provide quantitative understanding not only of the stability, but also of the dynamics of the growth of carbon nanotube systems. We will try to summarize the microscopic insight obtained from these theoretical simulations, which will allow us to isolate the essential physics and to propose good models for multi-shell and single-shell nanotube growth, and to analyze a possible consensus for certain models based on experimental data.

2.6.2 Open- or Close-Ended Growth for Multiwalled Nanotubes

Assuming first that the tube remains closed during growth, the longitudinal growth of the tube occurs by the continuous incorporation of small carbon clusters (C_2 dimers). This C_2 absorption process is assisted by the presence of pentagonal defects at the tube end, allowing bond-switching in order to reconstruct the cap topology [221, 222]. Such a mechanism implies the use of the Stone-Wales mechanism to bring the pentagons of the tip to their canonical positions at each C_2 absorption. This model explains the growth of tubes at relatively low temperatures (∼1100°C), and assumes that growth is nucleated at active sites of a vapor-grown carbon fiber of about 1000 Å diameter. Within such a lower temperature regime, the closed-tube approach is favorable compared to the open one, because any dangling bonds that might participate in an open tube growth mechanism would be unstable. However, many observations regarding the structure of the carbon tubes produced by the arc method (temperatures reaching 4000°C) cannot be explained within such a model. For instance, the present model fails to explain multilayer tube growth and how the inside shells grow often to a different length compared with the outer ones [223]. In addition, at these high temperatures, nanotube growth and the graphitization of the thickening deposits occur simultaneously, so that all the coaxial nanotubes grow at once, suggesting that open nanotube growth may be favored.

In the second assumption, the nanotubes are open during the growth process and carbon atoms are added at their open ends [223, 224]. If the nanotube has a random chirality, the adsorption of a C_2 dimer at the active dangling-bond edge site will add one hexagon to the open end (see Fig. 2.34).

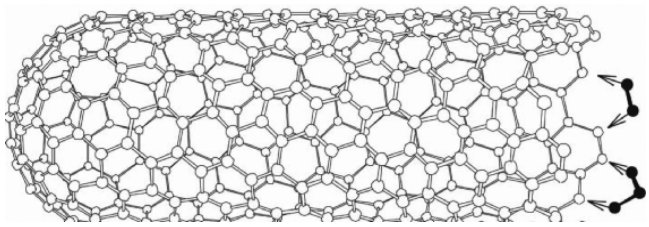


Fig. 2.34. Growth mechanism of a carbon nanotube (white ball-and-stick atomic structure) at an open end by the absorption of C_2 dimers and C_3 trimers (*in black*), respectively [222]

The sequential addition of C_2 dimers will result in the continuous growth of chiral nanotubes. However, for achiral edges, C_3 trimers are sometimes required in order to continue adding hexagons, and not forming pentagons. The introduction of pentagons leads to positive curvature which would start a capping of the nanotube and would terminate the growth (see Fig. 2.35). However, the introduction of a heptagon leads to changes in nanotube size

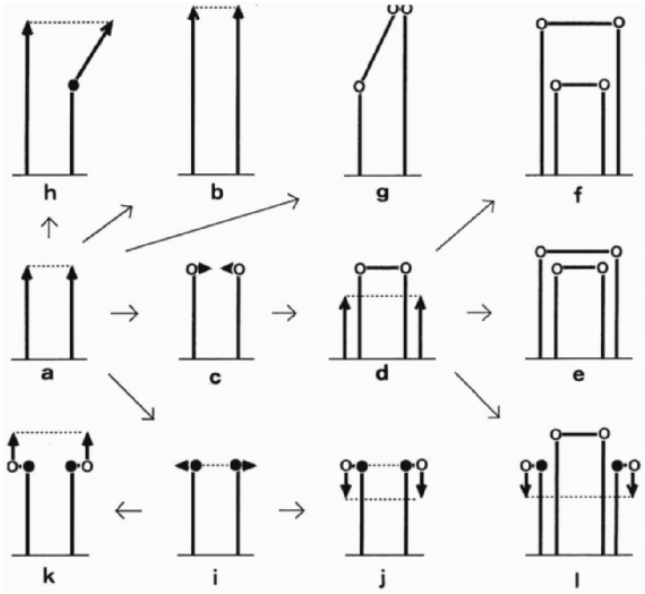


Fig. 2.35. Model for the open-end growth of the nanotube. (**Top**) The tube ends are open while growing by accumulating carbon atoms at the tube peripheries in the carbon arc. Once the tube is closed, there will be no more growth on that tube but new tube shells start to grow on the side-walls. (**Middle**) Schematic representation of a kink-site on the tube end periphery. Supplying two carbon atoms (○) to it, the kink advances and thus the tube grows. But the supply of one carbon atom results in a pentagon which transforms the tube to a cone shape. (**Bottom**) Evolution of carbon nanotube terminations based on the open-end tube growth. Arrows represent passes for the evolution. Arrow heads represents terminations of the tubes and also growth directions. Open and solid circles represents locations of pentagons and heptagons, respectively [225] (see text)

and orientation (see Fig. 2.35). Thus, the introduction of heptagon-pentagon pairs can produce a variety of tubular structures, as is frequently observed experimentally.

This model is thus a simple scenario where all the growing layers of a tube remain open during growth and grow in the axial direction by the addition of carbon clusters to the network at the open ends to form hexagonal rings [224]. Closure of the layer is caused by the nucleation of pentagonal rings due to local perturbations in growth conditions or due to the competition between different stable structures. Thickening of the tubes occurs by layer growth on already grown inner-layer templates and the large growth anisotropy results from the vastly different rates of growth at the high-energy open endshaving dangling bonds in comparison to growth on the unreactive basal planes (see top part of Fig. 2.35). Bottom part of Fig. 2.35 is a summary of various possibilities of growth as revealed by the diversity of observed capping morphologies. The

open-end tube is the starting form (nucleus) as represented in (a). A successive supply of hexagons on the tube periphery results in a longer tube as illustrated in (b). Enclosure of this tube can be completed by introducing six pentagons to form a polygonal cap (c). Open circles represent locations of pentagons. Once the tube is enclosed, there will no more growth on that tube. A second tube, however, can be nucleated on the first tube side-wall and eventually cover it, as illustrated in (d) and (e) or even over-shoot it, as in (f). The formation of a single pentagon on the tube periphery triggers the transformation of the cylindrical tube to a cone shape (g). Similarly, the introduction of a single heptagon into a tube periphery changes the tube into a cone shape (h).The latter growth may be interrupted soon by transforming into another form because an expanding periphery will cost too much free energy to stabilize dangling bonds. It is emphasized here that controlling the formation of pentagons and heptagons is a crucial factor in the growth of carbon nanotubes. A final branch in the variations of tube morphologies concerns the semi-toroidal tube ends. This growth is characterized by the coupling of a pentagon and a heptagon. Insertion of the pentagon-heptagon (5–7) pair into a hexagon network does not affect the sheet at all topologically. To realize this growth process, first a set of six heptagons is formed on a periphery of the open-tube (i). The circular brim then expands in the directions indicated by arrows. Solid circles represent locations of the heptagons. In the next step, a set of six pentagons is formed on the periphery of the brim, which makes the brim turn around by 180°, as illustrated in (j). An alternative structure is shown in (k), in which a slightly thicker tube is extended in the original tube direction, yielding a structure which has actually not yet been observed. Finally, it should be emphasized that an open-end tube can choose various passes or their combinations. One example is shown in (l), in which the first shell grows as a normal tube but the second tube follows a semi-toroidal tube end.

An electric field ($\sim 10^8$ V cm^{-1}) was also suggested as being the cause for the stability of open ended nanotubes during the arc discharge [223]. Because of the high temperature of the particles in the plasma of the arc discharge, many of the species in the gas phase are expected to be charged, thereby screening the electrodes. Thus the potential energy drop associated with the electrodes is expected to occur over a distance of 1 μm or less, causing very high electric fields. Later experiments and simulations confirmed that the electric field is in fact neither a necessary nor a sufficient condition for the growth of carbon nanotubes [226, 227]. Electric fields at nanotube tips have been found to be inadequate in magnitude to stabilize the open ends of tubes, even in small diameter nanotubes (for larger tubes, the field effect drops drastically).

2.6.3 'Lip-lip' Interaction Model for Multiwalled Nanotube Growth

Additional carbon atoms (spot-weld), bridging the dangling bonds between shells of a multilayered structure, have also been proposed for the stabilization

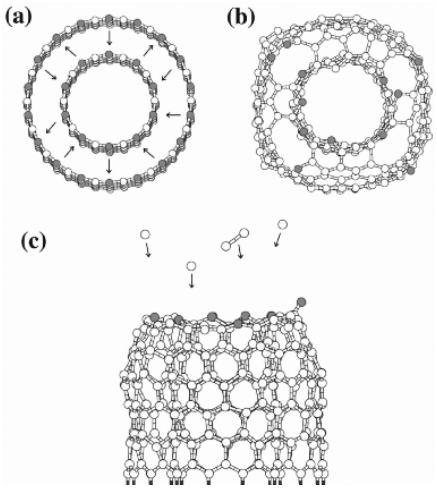


Fig. 2.36. Creation (**a**) and stabilization (**b**) of a double-walled (10,0)@(18,0) nanotube open edge by 'lip-lip' interactions at ∼3000 K. The notation (10,0)@(18,0) means that a (10,0) nanotube is contained within an (18,0) nanotube. The direct incorporation (**c**) of extra single carbon atoms and a dimer with thermal velocity into the fluctuating network of the growing edge of the nanotube is also illustrated [228,229]. The present system contains 336 carbon atoms (*large white spheres*) and 28 hydrogen atoms (*small dark gray spheres*) used to passivate the dangling bonds on one side of the cluster (*bottom*). The other low coordinated carbon atoms (*dangling bonds*) are represented as light gray spheres on the top of the structure

of the open growing edge of multishelled tubes [33]. For multiwalled species, it is quite likely that the presence of the outer walls should stabilize the innermost wall, keeping it open for continued growth. Static *tight-binding* calculations performed on multilayered structures where the growing edge is stabilized by bridging carbon adatoms, show that such a mechanism could prolong the lifetime of the open structure [33].

Quantum molecular-dynamics simulations were also performed to understand the growth process of multiwalled carbon nanotubes [228, 229]. Within such calculations, the topmost atoms (dangling bonds) of the inner and outer edges of a bilayer tube rapidly move towards each other, forming several bonds to bridge the gap between the adjacent edges, thus verifying the assumption that atomic bridges could keep the growing edge of a nanotube open without the need of 'spot-weld' adatoms (Fig. 2.36). At about 3000 K (a typical experimental growth temperature), the 'lip-lip' interactions stabilize the open-ended bilayer structure and inhibit the spontaneous dome closure of the inner tube as observed in the simulations of single-shell tubes. These calculations also show that this end geometry is highly active chemically, and easily accommodates incoming carbon clusters, supporting a model of growth by chemisorption from the vapor phase.

In the 'lip-lip' interaction model, the strong covalent bonds which connect the exposed edges of adjacent walls are also found to be highly favorable energetically within ab initio static calculations [230]. In the latter work, the open-ended growth is stabilized by the 'lip-lip' interactions, involving rearrangement of the carbon bonds, leading to significant changes in the growing edge morphology. However, using classical three-body potentials, the role of the 'lip-lip' interactions is suggested to be relegated to facilitate tube closure by mediating the transfer of atoms between the inner and outer shells [231].

Successful synthesis of multiwalled nanotubes raises the question why the growth of such tubular structures often prevail over their more stable spherical fullerene counterpart [230]. It is furthermore intriguing that these nanotubes are very long, largely defect-free, and (unless grown in the presence of a metal catalyst) always have multiple walls. The 'lip-lip' model explains that the sustained growth of defect-free multiwalled carbon nanotubes is closely linked to efficiently preventing the formation of pentagon defects which would cause a premature dome closure. The fluctuating dangling bond network present at the nanotube growing edge will also help topological defects to heal out, yielding tubes with low defect concentrations. With nonzero probability, two pentagon defects will eventually occur simultaneously at the growing edge of two adjacent walls, initiating a double-dome closure. As this probability is rather low, carbon nanotubes tend to grow long, reaching length to diameter rations on the order of 10^3–10^4.

Semi-toroidal end shapes for multiwalled nanotubes are sometimes observed experimentally [225, 232]. The tube, shown in Fig. 2.37a does not have a simple double-sheet structure, but rather consists of six semi-toroidal shells. The lattice images turn around at the end of the tube, so that an even number of lattice fringes is always observed. Another example is shown in Fig. 2.34b, in which some of the inner tubes are capped with a common carbon tip structure, but outer shells form semi-toroidal terminations. Such a semi-toroidal termination is extremely informative and supports the model of growth by 'lip-lip' interactions for multiwalled nanotubes.

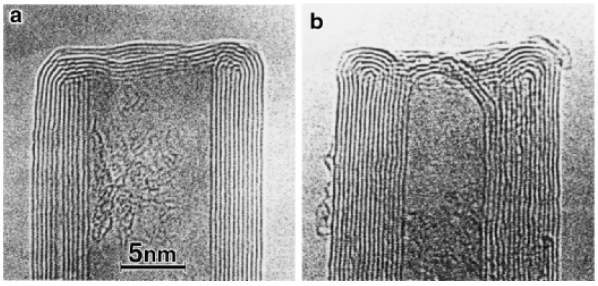


Fig. 2.37. Transmission electron micrographs of the semi-toroidal termination of multiwalled tubes, which consists of six graphitic shells (**a**). A similar semi-toroidal termination, where three inside tube shells are capped (**b**) [225]

2.6.4 Is Uncatalyzed Growth Possible for Single-walled Nanotubes ?

The growth of single-shell nanotubes, which have a narrow diameter distribution (0.7–2 nm), differs from that of multishell tubes insofar as catalysts are necessary for their formation. This experimental fact is consequently an indirect proof of the existence of covalent lip-lip interactions which are postulated to be indispensable in a *pure carbon atmosphere* and imply that all nanotubes should have multiple walls. Single-walled tubes with unsaturated carbon dangling bonds at the growing edge are prone to be etched away in the aggressive atmosphere that is operative under typical synthesis conditions, which again explains the absence of single-walled tubes in a pure carbon environment.

There have been several works based on classical, semi-empirical and quantum molecular-dynamics simulations attempting to understand the growth process of single-shell tubes [228, 229, 233–235]. Most importantly, these studies have tried to look at the critical factors that determine the kinetics of open-ended tube growth, as well as studies that determine the relative stability of local-energy minimum structures that contain six-, five-, and seven-membered carbon rings in the lattice. Classical molecular dynamics simulations show that wide tubes which are initially open can continue to grow straight and maintain an all-hexagonal structure [234, 235]. However, tubes narrower than a critical diameter, estimated to be about $\sim$3 nm, readily nucleate curved, pentagonal structures that lead to tube closure with further addition of carbon atoms, thus inhibiting further growth. Continued carbon deposition on the top of a closed tube yields a highly disordered cap structure, where only a finite number of carbon atoms can be incorporated, implying that uncatalyzed defect-free growth cannot occur on single-shell tubes.

First-principles molecular-dynamics simulations [228] show that the open end of single-walled nanotubes closes spontaneously, at experimental temperatures (2000 K–3000 K), into a graphitic dome with no residual dangling bonds (see Fig. 2.38). Similar self-closing processes should also occur for other nanotubes in the same diameter range, as is the case for most single-walled nanotubes synthesized so far. The reactivity of closed nanotube tips was also found to be considerably reduced compared to that of open end nanotubes. It is therefore unlikely that single-walled nanotubes could grow by sustained incorporation of C atoms on the closed hemifullerene-like tip. This is in agreement with the theoretical finding that C atoms are not incorporated into C_{60} [236].

2.6.5 Catalytic Growth Mechanisms for Single-Wall Nanotubes

All these classical and quantum simulations, described above, may explain why single-walled nanotubes do not grow in the absence of transition metal catalysts. However, the role played by these metal atoms in determining the growth has been inaccessible to direct observation and is therefore a highly

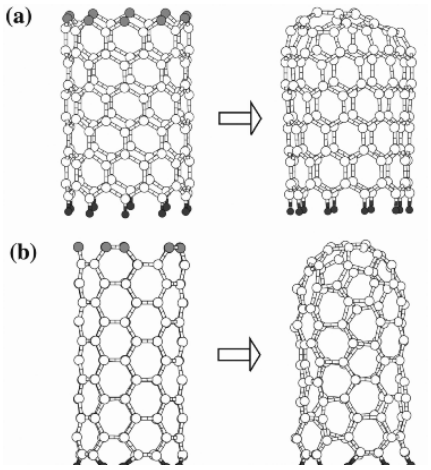


Fig. 2.38. Spontaneous closure of two single-walled nanotubes: (**a**) (10,0) zigzag tube and (**b**) (5,5) armchair tube. Both nanotubes have a fully reconstructed closed-end configuration with no residual dangling bonds [228, 229]. The present systems contains 120 carbon atoms (*large white spheres*) and 10 hydrogen atoms (*small dark grey spheres*) used to passivate the dangling bonds on one side of the two clusters (*bottom*). The other low coordinated carbon atoms (*dangling bonds*) are represented as light grey spheres on the top of the structure

debated issue. Plausible suggestions include metal atoms initially decorating the dangling bonds of an open fullerene cluster, thus preventing it from closing.

One of the first assumption proposed in the literature [34] was that, in high-temperature routes, one or a few metal atoms sit at the open end of a precursor fullerene cluster, which will be determining the uniform diameter of the tubes (the optimum diameter being determined by the competition between the strain energy due to curvature of the graphene sheet and the dangling bond energy of the open edge. The role of the metal catalyst is to prevent carbon pentagons from forming by 'scooting' around the growing edge (see Fig. 2.39).

Static ab initio calculations have investigated this scooter model and have shown that a Co or Ni atom is strongly bound but still very mobile at the growing edge [237]. However, the metal atom locally inhibits the formation of pentagons that would initiate dome closure. In addition, in a concerted exchange mechanism, the metal catalyst assists incoming carbon atoms in the formation of carbon hexagons, thus increasing the tube length. With a non-vanishing concentration of metal atoms in the atmosphere, several catalyst atoms will eventually aggregate at the tube edge, where they will coalesce. The adsorption energy per metal atom is found to decrease with increasing size of the adsorbed cluster [237]. The ability of metal clusters to anneal defects is thus expected to decrease with their increasing size, since they will gradually become unreactive and less mobile. Eventually, when the size of the

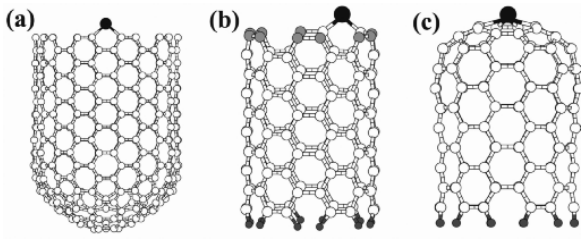


Fig. 2.39. (**a**) View of a (10,10) armchair nanotube (*white ball-and-stick atomic structure*) with a Ni (or Co) atom (*large black sphere*) chemisorbed onto the open edge [34]. The metal catalyst keeps the tube open by 'scooting' around the open edge, insuring that any pentagons or other high energy local structures are rearranged to hexagons. The tube shown has 310 C atoms. (**b**) Catalytic growth of a (6,6) armchair single-walled nanotube. The metal catalyst atom cannot prevent the formation of pentagons, leading to tube closure (**c**) at experimental temperatures (1500 K) [203]. The present systems contains 1 cobalt atom (*large black sphere*), 120 carbon atoms (*white spheres*) and 12 hydrogen atoms (*small dark grey spheres*) used to passivate the dangling bonds on one side of the two clusters (*bottom*). The other low coordinated carbon atoms (*dangling bonds*) are represented as light *grey spheres* on the top of the structure (*left*)

metal cluster reaches some critical size (related to the diameter of the nanotube), the adsorption energy of the cluster will decrease to such a level that it will peel off from the edge. In the absence of the catalyst at the tube edge, defects can no longer be annealed efficiently, thus initiating tube closure. This mechanism was consistent with first experimental observations that no 'observable' metal particles were detected on the grown tubes [34]. Although the scooter model was initially investigated using static ab initio calculations [237], first-principles molecular-dynamics simulations were also performed [203] in order to study the growth of single-walled tubes within a scheme where crucial dynamical effects are explored by allowing the system to evolve free of constraints at the experimental temperature (Fig. 2.39b). Within such a simulation at 1500 K, the metal catalyst atom is found to help the open end of the single-shell tube close into a graphitic network which incorporates the catalyst atom (see Fig. 2.39c). However, the cobalt-carbon chemical bonds are frequently breaking and reforming at experimental temperatures, providing the necessary pathway for carbon incorporation, leading to a closed-end catalytic growth mechanism.

This model, where the Co or Ni catalyst keeps a high degree of chemical activity on the nanotube growth edge, clearly differs from the uncatalyzed growth mechanism of a single-walled nanotube discussed above, which instantaneously closes into an chemically-inert carbon dome. The model, depicted in Fig. 2.39b, supports the growth by chemisorption from the vapor phase, according to the so-called vapour-liquid-solid (VLS) model, as proposed long ago for carbon filaments by Baker [82,85], Oberlin et al. [5], and Tibbetts [80].

Although the VLS model initially has been a macroscopic model based on the fluid nature of the metal particle which helps to dissolve carbon from the vapor phase and to precipitate carbon on the walls, the catalytic growth model for the single-walled nanotubes considered here can be seen as its analogue, with the only difference being that the catalytic particle is reduced to one or a few metal atoms. In terms of this analogy, the quantum aspects of a few metal atoms at the growing edge of the single-shell tube has to be taken into account. In the catalytic growth of single-shell nanotubes, it is no longer the 'fluid nature' of the metal cluster (VLS model), but the chemical interactions between the Co or Ni $3d$ electrons and the π carbon electrons, that make possible a rapid incorporation of carbon atoms from the plasma. The cobalt $3d$ states increase the DOS near the Fermi level, thus enhancing the chemical reactivity of the Co-rich nanotube tip [203].

The observation of SWNTs produced in CCVD by preformed catalytic particles [125], which are encapsulated at the tip (Fig. 2.27) and thus are closely correlated with the tube diameter size (from 1 to 5 nm), demonstrates the validity of the VLS model on a nanometer scale, as already described in Sect. 2.5, Fig. 2.29. Such configurations are not found for high temperature routes, since actual observations show that nanotubes have grown from particles with no correlation between particle size and tube diameter. Since tube tips, especially for long tubes, cannot be easily observed, it cannot be excluded that the growth could also proceed from a very small particle located at the tip as in the CCVD situation. Precisely because of the enhancement of the chemical activity due to the presence of metal catalyst particles at the experimental growth temperature, the Co–C bonds are frequently reopened and the excess of cobalt could be ejected from the nanotube tip, making its observation impossible.

The presence of any remaining metal catalyst atoms at the free nanotube tip in high temperature routes (even in very small undetectable amounts) can therefore not be excluded. The presence of such ultra-small catalyst particles, which is certainly not easy to establish experimentally, should strongly influence the field emission properties of these single-shell tubes [238] and could explain some field-emission patterns observed at the nanotube tip. Magnetic susceptibility measurements and magnetic STM could be used to investigate the presence of metal catalysts at the nanotube tip, as such experimental techniques are sensitive to tiny amounts of magnetic transition metals. At this stage, a better experimental characterization method for the atomic structure of single-walled nanotube tips is required.

2.6.6 Root Growth Mechanism for Single-Wall Nanotubes

We now turn to the phenomenological model, presented in Sect. 2.5, Fig. 2.31, which accounts for the situation obseved in high-temperature routes where nanotubes are found to nucleate from large particles and to grow from the root. We briefly summarize this model. Carbon and metal atoms, issued from the

vaporization of the target, condense and form alloy particles. As these particles are cooled, carbon atoms, dissolved in the particle, segregate onto the surface, because the solubility of the surface decreases with decreasing temperature. As the system is cooled, soot is formed. The sizes of the soot particles are several tens of nm wide, and are identified by TEM observations as embedded metal clusters surrounded by a coating of a few graphitic layers. Some singularities at the surface structure or atomic compositions may catalyze the formation of single-walled tubes, thereby providing another mechanism for the growth of single-walled carbon nanotubes. After the formation of the tube nuclei, carbon is supplied from the core of the particle to the root of the tubes, which grow longer maintaining hollow capped tips. Addition of carbon atoms (or dimers) from the gas phase at the tube tips (opposite side) also probably helps the growth.

Many single-shell nanotubes are observed to coexist with catalytic particles and often appear to be sticking out of the particle surfaces. One end of the tubule is thus free, the other one being embedded in the particle, which often has a size exceeding the nanotube diameter by well over one order of magnitude.

Classical molecular-dynamics simulations [201] reveal a possible atomistic picture for this root-growth mode for single-walled tubes. According to the model, carbon atoms precipitate from the metal particle, migrate to the tube base, and are incorporated into the nanotube network, thereby leading to defect-free growth. More recent classical molecular dynamics calculations, using empirical potentials for C–C bonds [239, 240] aim at simulating the nucleation step in order to show how carbon atoms segregate at the surface of the metallic particle and self-organize to built a nanotube nucleus.

To go beyond this classical approach, the metal-carbon segregation process was investigated at the atomic level using quantum molecular dynamics [202, 204]. A 153 atom mixed Co–C cluster was created by extracting a sphere 1.3 nm in diameter from a hexagonal close-packed (HCP) Co structure, and by replacing randomly 2/3 of the Co atoms by C atoms (Fig. 2.40). The mixed cluster was then heated up to 2000 K. After a thermalisation period of 5 ps at 2000 K (Fig. 2.40a), the temperature was gradually decreased to 1500 K using a thermal gradient of 100 K/ps. After 5 ps at 1500 K, most of the C atoms (about 80%) segregate to the surface of the cluster, while the Co atoms migrate to its center (Fig. 2.40b). The C atoms at the surface move very quickly and form a network composed of connected linear chains and some aromatic rings. The creation of an hexagon connected with two pentagons is remarkable (Fig. 2.40c) and can be considered as a first stage of the nucleation process. The theoretical investigation of the nucleation pathway for single-walled nanotubes on a metal surface has recently been studied by a series of ab initio total energy calculations [209]. Incorporation of pentagons at an early stage of nucleation was found to be energetically favorable as they reduce the number of dangling bonds and facilitate curvature of the structure and bonding to the metal. In addition, the nucleation of a closed cap or a

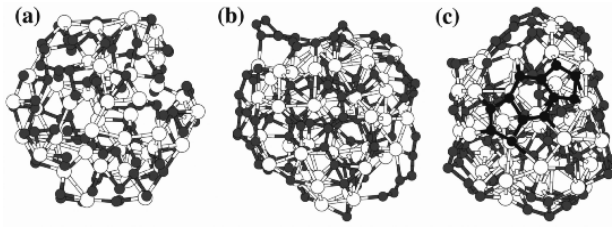


Fig. 2.40. Segregation process in a cluster containing 51 Co atoms (*big white spheres*) and 102 C atoms (*small gray spheres*) when the temperature drops from 2000K to 1500 K. (**a**) The cluster is first heated up to 2000 K, leading to random positions of Co and C within the sphere volume. (**b**) The temperature is gradually decreased to 1500 K. C atoms segregate to the surface while Co atoms migrate to the center. **c** Carbon linear chains and aromatic rings (*in black*) are created at the surface of the cluster. Total simulation time: 25 ps

capped SWNT at the metal surface is overwhelmingly favored compared to any structure with dangling bonds or to fullerenes.

When the nucleation has started, modeling the migration of carbon atoms at the surface of a catalyst particle and their incorporation to the SWNT base have also been performed using quantum molecular dynamics [202, 204]. Figure 8 represents a SWNT closed at one end by half a C_{60} molecule while the reactive open part is deposited on a double layer of HCP cobalt, satisfying most of the dangling bonds (Fig. 2.41a). Twenty carbon atoms have been added to the surface of the metal particle in order to observe a migration process to the root of the nanotube. The global system is then heated up to 1500 K. After 15ps of simulation, 5 carbon atoms had diffused to the tube base and were incorporated in the nanotube body (Fig. 2.41b). Even if the time scale of such simulations prevents us from studying the further evolution of the root growth, this incorporation as well as the absence of formation of a closed fullerene-like molecule suggest that this root growth mechanism is a good candidate to explain the emergence of carbon nanotubes from large metal catalyst particle. Our QMD simulation shows that the role of the catalyst is not only to stabilize the forming tube, but also to provide fluctuating Co–C bonds in the middle of which new carbon atoms are easily incorporated.

In summary, we have provided experimental and theoretical arguments in favor of a root-growth mechanism for single-walled nanotubes. Since the QMD simulations are extremely time and memory consuming, such technique cannot really be used in a systematic manner to increase the length and time scales and to vary relevant parameters. Simplified models using tight-binding potentials are currently under development to undertake appropriate large scale simulations [204, 241].

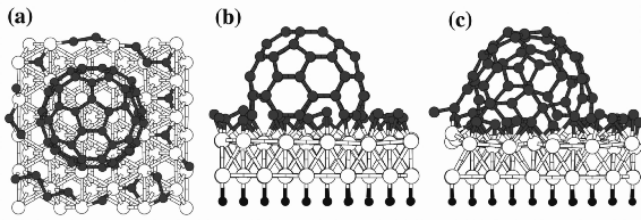


Fig. 2.41. Root growth mechanism for SWNTs extruded from large catalytic nanoparticles. A small (6,6) nanotube portion capped by a perfect fullerene-like hemisphere is placed on a slab of HCP Co, with 20 additional isolated carbon atoms on the particle surface. The model contains 74 carbon atoms (*small gray spheres*), 59 cobalt atom (*big white sphere*), and 30 hydrogen atoms (*small black spheres at the bottom*) terminating the metal particle in order to satisfy the dangling bonds. Hydrogen atoms and the last layer of Co are kept fixed during the simulation. Top (**a**) and side (**b**) views of the starting configuration at 0 K. (**c**) Incorporation in the honeycomb network of the nanotube root of 5 extra carbon atoms which have diffused on the nanoparticle surface at 1500 K. Total simulation time: 15 ps

2.6.7 Conclusion

Since their discovery in 1991, great progress has been made in the understanding of carbon nanotube growth. There has been a constant fruitful interplay between theoretical calculations and experimental measurements which has enhanced our insight into the formation processes of these ultimate carbon fibers.

Several mechanisms, as described above, have been proposed to account for the growth mechanisms of single-walled and multiwalled carbon nanotubes with or without the presence of any catalyst. The key role played by the metal catalyst is crucial for understanding the growth of single-shell tubes at the microscopic level. However, the actual role of the metal or alloy is not yet completely solved, although experimental observations and numerical simulations converge to plausible scenarios depending on the synthesis route. Ab initio calculations have been very successful and helpful to simulate and to understand different processes. They are however inadequate to simulate the whole nucleation process. Empirical methods appear to be relatively suited for simulating the growth but fail to describe the nucleation. At the present stage, semi-empirical simulations are the most promising ones.

Probably the most intriguing problem is to understand the microscopic mechanism and optimum conditions for the formation of well-designed single-walled nanotubes. Although it has been argued that the armchair nanotube structure is favored energetically [34], experimental conditions under which these tubules would be grown with good control are not yet well known. Nonetheless, as more experimental data become available to correlate the atomic structure and the synthesis conditions, and more is known about the growth at the atomic level, it is hoped that controlled growth of single-walled

carbon nanotubes with designed structures will be achieved soon. In addition, with further experimental confirmation of their unique properties, there will be a great incentive to develop industrial-scale production methods.

2.7 $B_xC_yN_z$ Composite Nanotubes

We now turn to the case of composite $B_xC_yN_z$ nanotubes. As compared to the carbon case, there has been much less work devoted to understanding at the microscopic level their growth mechanisms. An additional complexity is added by the presence of several atomic species and the related 'chemical frustrations'. Further, while good empirical or tight-binding parameters exist for carbon, the problem of charge transfer between species render the use of empirical approachs more difficult.

2.7.1 $B_xC_yN_z$ Nanotubes

While the experimental techniques developed for their synthesis have been described in Sect. 2.2, it is important to recall here briefly that such synthesis approaches can be divided into two families: the high-temperature techniques, including arc discharge [65–68] and laser ablation [69] and the medium-temperature ones, such as CVD [242, 243] or thermal decomposition of molecular precursors [244,245]. In addition to these synthesis routes, a substitution reaction on preformed carbon nanotubes has been proposed [246–248].

The importance of synthesis temperature becomes even more crucial in the case of composite $B_xC_yN_z$ nanotubes because of the tendency towards segregation into pure carbon or BN domains. Such a segregation is driven by thermodynamics as it has been shown indeed that B–N and C–C bonds are more stable than C–N or C–B ones [249, 250]. We note however that the segregation in domains means the diffusion of atoms during the growth process (we assume here that the source of B, C and N atoms is rather uniform). As a result, the topology of synthesized $B_xC_yN_z$ nanotubes will depend on the competition between thermodynamics and kinetics.

At low temperature, the growth is kinetically driven and the diffusion is limited. The systems obtained are relatively homogeneous at a few-bond-length scale. This can be inferred from the electronic properties of $B_xC_yN_z$ systems synthesized by CVD or substitution reactions, which appear to be photoluminescent with a band gap ranging between 1–3 eV [243, 251, 252]. The analysis of the electronic properties (see Chap. 4) shows that such band gaps can only be explained in the limit of very homogeneous systems.

At high temperature, thermodynamics is the main factor and one observe systems with segregated pure BN or carbon domains. The segregation can take place either within a single tube wall, leading to the formation of dots or metal/insulator C/BN junctions [253], or the segregation can be complete,

namely one observe, in the case of MWs systems, pure carbon tubes concentric with pure BN tubes [68, 248].

2.7.2 B-Doped Nanotubes

The limiting case of B-doped nanotubes, with a boron content equivalent to 1 % in the body, is quite surprising. It has been shown that B-doped nanotubes synthesized by arc-discharge tend to be much longer than their pure cabon analog [66, 254]. Further, they exhibit an improved crystallinity and seem to be *s*elected towards the zigzag helicity [255].

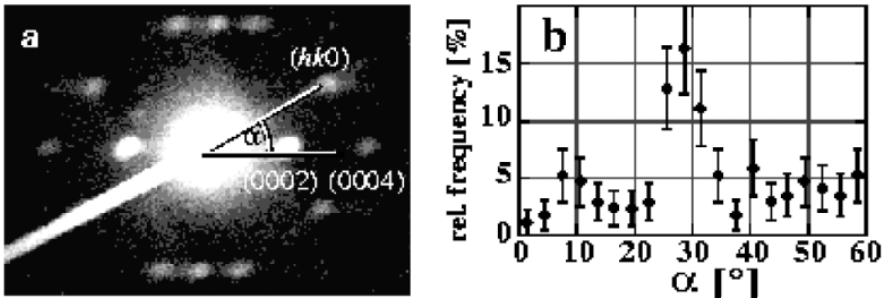


Fig. 2.42. (*Left*) Electron diffraction pattern of a B-doped tube (*Right*) Statistical analysis of the angular distribution of the *hk0* reflections. The value $\alpha = 30\,\mathrm{deg}$ corresponds to the zigzag geometry [255]

Such an increase in nanotube length has been explained on the basis of ab initio [255] and tight-binding [256] total energy and molecular-dynamics simulations. It has been shown that in the case of zig-zag tubes, boron atoms can behave as surfactant during the open-end growth of the nanotubes. One therefore can explain that a small amount of B atoms can greatly influence the growth process. The presence of B atoms on the tube lips was further shown to reduce the probability of final closure of the tubes onto closed caps. Indeed, as a charge transfer from B to C destabilizes any B–B bonding by electrostatic repulsion, such disfavored bonds were seen to re-open spontaneously at synthesis temperature (1500–2000 K). Such retarded closure can be invoked to explain the exceptional length of B-doped tubes.

The surfactant mechanism could only be evidenced for zigzag tubes. For armchair geometries, B atoms tend to sink into the carbon tube body. This observation provides some understanding on why the long B-doped nanotubes were observed to be mainly of the zigzag type. Such an helicity selection proposes a first route towards the synthesis of carbon nanotubes with well-defined geometrical, and thus electronic, properties.

Concerning the body of the tube, total-energy calculations [250] and STS experiments [257] tend to favor the model of segregated islands of pure BC_3-

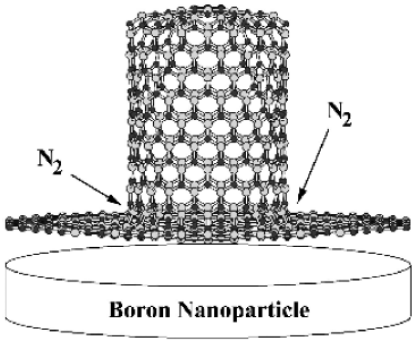


Fig. 2.43. Symbolic representation of a root-growth mechanism assisted by B-droplets [64]

like domains. Ab initio DFT simulations show that B atoms can gain as much as 0.5 eV/atom by segregating. Again, the existence of segregation in B-doped systems should strongly depend on the synthesis conditions.

2.7.3 BN Tubes

We close this review on the growth mechanisms of nanotubes by the important case of pure BN systems. There are several specific features in the topology of BN tubes that differ significantly from the carbon case. A puzzling observation is that BN nanotubes tend to have a reduced number of layers. This was evidenced in the case of uncatalyzed arc-discharge growth techniques with the presence of a large number of bi-layer and even mono-layer nanotubes [57, 58]. Further, single-walled BN tubes have been grown with 'catalyst-free' CVD [258] and laser-ablation [64] techniques. The absence of metal catalyst does not, however, rule out some catalytic effect. It has been suggested [64] that the liquid boron droplets observed in laser-assisted growth may play the role of the metallic droplet in the root-mechanism growth of SW nanotubes (see Fig. 2.43). Further, the role of Hf or Ta in early arc discharge experiments (used to render the electrode conductive) is still unclear [57, 58].

Another intriguing observation is the selection of chirality towards the zigzag geometry observed for laser-ablation grown single-walled BN tubes [64]. On the basis of ab initio MD simulations [259], the importance of maintaining a local 1/1 BN stoichiometry was emphasized as local unbalance would lead to amorphous system. In particular, in the case of open-end growth, pure boron (or N) lips present in the case of zigzag tubes was shown to lead to amorphization, supporting the idea that the growth of SW zigzag BN tubes reported in Ref. [64] is based on a root-growth approach.

We note finally that the cost associated with the formation of homo-polar B–B or N–N bonds leads to the formation of rather flat BN tips, a fact that

can be explained by the presence of squares in the final cap of the tube [57, 58, 258–260].

References

1. H.W. Kroto, J.R. Heath, S.C. O'Brien, R.F. Curl, R.E. Smalley: Nature **318**, 216 (1985)
2. W. Krätschmer, L.D. Lamb, K. Fostiropoulos, D.R. Huffman: Nature **347**, 354 (1990)
3. S. Iijima: Nature **354**, 56 (1991)
4. R. Bacon: Appl. Phys. Lett. **31**, 283 (1960)
5. A. Oberlin, M. Endo, T. Koyama: J. Cryst. Growth **32**, 335 (1976)
6. S. Farhat, I. Hinkov, C.D. Scott: Journal Nanosci. Nanotech. **4**, 377 (2004)
7. H. Lange, K. Saidane, M. Razafinimanana, A. Gleizes: J. Phys. D: Appl. Phys. **32**, 1024 (1999)
8. T.W. Ebbesen, P.M. Ajayan: Nature **358**, 220 (1992)
9. T.W. Ebbesen: Annu. Rev. Mater. Sci. **24**, 235 (1994)
10. S. Iijima, T. Ichihashi: Nature **363**, 603 (1993)
11. W.K. Maser, P. Bernier, J.M. Lambert et al: Synth. Met. **81**, 243 (1996)
12. C.H. Kiang, W.A. Goddard III, R. Beyers, D.S. Bethune: Carbon **33**, 903 (1995)
13. P.M. Ajayan J.M. Lambert, P. Bernier, L. Barbedette, C. Colliex, J.M. Planeix: Chem. Phys. Lett. 215, 509 (1993)
14. J.M. Lambert, P.M. Ajayan, P. Bernier: Synth. Met. **70**, 1475 (1995)
15. C.H. Kiang, W.A. Goddard III, R. Beyers, J.R. Salem, D.S. Bethune: J. Phys. Chem. **98**, 6612 (1994)
16. D.S. Bethune, C.H. Kiang, M.S. de Vries, G. Gorman, R. Savoy, J. Vazquez, R. Beyers: Nature **363**, 605 (1993)
17. S. Seraphin: in *Proceedings of the Symposium on 'Recent Advances in the Chemistry and Physics of Fullerenes and Related Materials'* ed by K.M. Kadish and R.S. Ruoff (The Electrochemical Society Inc., 1994)
18. S. Seraphin, D. Zhou: Appl. Phys. Lett. **64**, 2087 (1994)
19. J.M. Lambert, P.M. Ajayan, P. Bernier, J.M. Planeix, V. Brotons, B. Coq, J. Castaing: Chem. Phys. Lett. **226**, 364 (1994)
20. C. Journet, W.K. Maser, P. Bernier et al: Nature **388**, 756 (1997)
21. X. Lin, K. Wang, V.P. Dravid, R.P.H. Chang, J.B. Ketterson: Phys. Lett. **64**, 181 (1994)
22. P.M. Ajayan, C. Colliex, J.M. Lambert, P. Bernier, L. Barbedette, M. Tence, O. Stéphan: Phys. Rev. Lett. **72**, 1722 (1994)
23. S. Seraphin, D. Zhou, J. Jiao, M.A. Minke, S. Wang, T. Yadav, J.C. Withers: Chem. Phys. Lett. **217**, 191 (1994)
24. Y. Saito, K. Kawabata, M. Okuda: J. Phys. Chem. **99**, 16076 (1995)
25. A. Loiseau, H. Pascard: Chem. Phys. Lett. **256**, 246 (1996)
26. C. Guerret-Piécourt, Y. Le Bouar, A. Loiseau, H. Pascard: Nature **372**, 761 (1994)
27. M. Ata, A.J. Hudson, K. Yamaura, K. Kurihara: J. Appl. Phys. **4207** (1995)
28. C.H. Kiang, W.A. Goddard III, R. Beyers, J.R. Salem, D.S. Bethune: J. Phys. Chem. Solids **57**, 35 (1996)

29. S. Subramoney, R.S. Ruoff, D.C. Lorents, R. Malhotra: Nature **366**, 637 (1993)
30. X. Zhao, M. Ohkohchi, M. Wang, S. Iijima, T. Ichihashi, Y. Ando: Carbon **35**, 775 (1997)
31. L.P.F. Chibante, A. Thess, J.M. Alford, M.D. Diener, R.E. Smalley: J. Phys. Chem. **97**, 8696 (1993)
32. – SES Research, www.sesres.com
    – Nanocarblab (NCL), www.nanocarblab.com
    – Nanoledge, www.nanoledge.com
    – Materials and Electrochemical Research (MER, www.opus1.com/ mercorp
    – Carbon Solutions, www.carbonsolution.com
33. T. Guo, P. Nikolaev, A.G. Rinzler, D. Tomanek, D.T. Colbert, R. E. Smalley: J. Phys. Chem. **99**, 10694 (1995)
34. A. Thess, R. Lee, P. Nikolaev, H. Dai, P. Petit, J. Robert, C. Xu, Y. Hee, S.G. Kim, A.G. Rinzler, D.T. Colbert, G.E. Scuseria, D. Tomnek, J.E. Fischer, R. Smalley: Science **273**, 483 (1996)
35. W.K. Maser, E. Munoz, R.E. Smalley, A.M. Benito, M.T. Martinez, G.F. de la Fuente, Y. Maniette, E. Anglaret, J.-L. Sauvajol: Chem. Phys. Lett. **292**, 587 (1998); E. Munoz, W. Maser, A.M. Benito, M.T. Martinez, G.F. de la Fuente, A. Righi, J.-L. Sauvajol, E. Anglaret, Y. Maniette: Appl. Phys. A **70**, 145 (2000)
36. S. Bandow, A. Asaka, Y. Saito, A.M. Rao, L. Grigorian, E. Richter, P.C. Ecklund: Phys. Rev. Lett. **80**, 3779 (1998)
37. T. Ishigaki, S. Suzuki, H. Kataura, W. Krätschmer, Y. Achiba: Appl. Phys. A **70**, 121 (2000)
38. A. Foutel-Richard: PhD thesis, Conservatoire National des Arts et Métiers, Paris (2003)
39. N. Dorval, A. Foutel-Richard, M. Cau, A. Loiseau, B. Attal-Trétout, J.L. Cochon, D. Pigache, P. Bouchardy, V. Krüger, K.P. Geigle: J. Nanosc. and Nanotech. **4**, 450 (2004)
40. M. Castignolles, A. Foutel-Richard, A. Mavel, J.-L. Cochon, D. Pigache, A. Loiseau, P. Bernier: In *Electronic Properties of Novel Materials Science and Technology of Molecular Nanostructures* ed by H. Kuzmany, J. Fink, M. Mehring, S. Roth, (American Institute of Physics, 2002)
41. A.A. Puretzky, D.B. Geohegan, X. Fan, S.J. Pennycook: Appl. Phys. Lett. **76**, 182, (2000); A.A. Puretzky, D.B. Geohegan, X. Fan, S.J. Pennycook: Appl. Phys. A **70**, 153, (2000)
42. A.A. Puretzky, H. Schittenhelm, X. Fan, M.J. Lance, L.F. Allard, Jr., D.B. Geohegan: Phys. Rev. B **65**, 245425 (2002)
43. S. Arepalli, P. Nikolaev, W. Holmes, C.D. Scott: Appl. Phys. A. **70**, 125 (2000); C.D. Scott, S. Arepalli, P. Nikolaev, R.E. Smalley: Appl. Phys. A **72**, 573 (2001)
44. F. Kokai, K. Takahashi, M. Yudasaka, R. Yamada, T. Ichihashi, S. Iijima: J. Phys. Chem. B **103**, 4346 (1999); F. Kokai, D. Kasuya, K. Takahashi, M. Yudasaka, S. Iijima,: Appl. Phys. A **73**, 40 (2001)
45. T.B. Massalski (ed): *Binary of phase alloys diagrams* (ASM International,1990)
46. F. Kokai, K. Takahashi, M. Yudasaka, S. Iijima: J. Phys.Chem. B **104**, 6777 (2000)
47. G. De Boer, S. Arepalli, W. Holmes, P. Nikolaev, C. Range, C. Scott: J. Appl. Phys. **89**, 5760 (2001)

48. J.-L. Cochon, J. Gavillet, M. Lamy de la Chapelle, A. Loiseau, M. Ory, D. Pigache: in *Electronic Properties of Novel Materials Science and Technology of Molecular Nanostructures* ed by H. Kuzmany, J. Fink, M. Mehring, S. Roth, (American Institute of Physics, 1999), p 237
49. L.P.F. Chibante, A. Thess, J.M. Alford, M.D. Diener, R.E. Smalley: J. Phys. Chem. **97**, 8696 (1993)
50. C.L. Fields, J.R. Pitts, M.J. Hale, C. Bingham, A. Lewandowski, D.E. King: J. Phys. Chem. **97**, 8701 (1993)
51. D. Laplaze, P. Bernier, L. Barbedette, J.-M. Lambert, G. Flamant, M. Lebrun, A. Brunelle, S. Della-Negra. C. R. Acad. Sci. **318**, 733 (1994)
52. D. Laplaze, P. Bernier, W.K. Maser, G. Flamant, T. Guillard, A. Loiseau: Carbon **36**, 685 (1998)
53. T. Guillard, S. Cetout, L. Alvarez, J.-L. Sauvajol, E. Anglaret, P. Bernier, G. Flamant, D. Laplaze: Eur. Phys. J. B **5**, 251 (1999)
54. D. Laplaze, L. Alvarez, T. Guillard, J.M. Badie, G. Flamant: Carbon **40**, 1621 (2002)
55. G. Flamant, D. Luxembourg, J.F. Robert, D. Laplaze: Solar Energy **77**, 73 (2004)
56. N.G. Chopra, R.J. Luyken, K. Cherrey, V.H. Crespi, M.L. Cohen, S.G. Louie, A. Zettl: Science **269**, 966 (1995)
57. A. Loiseau, H. Pascard, F. Willaime, N. Demoncy, G. Hug, Phys. Rev. Lett. **76** 4737 (1996)
58. M. Terrones, W.K. Hsu, H. Terrones, J.P. Zhang, S. Ramosa, J.P. Hare, R. Castillo, K. Prassides, A.K. Cheetham, H.W. Kroto, D.R.M. Walton: Chem. Phys. Lett, **259**, 568 (1996)
59. Y. Saito, M. Maida: J. of Phys. Chem A **103**, 10, 1291 (1999)
60. J. Cumings, A. Zettl: Chem. Phys. Let. **316**, 211 (2000)
61. D. Golberg, Y. Bando, M. Eremets, K. Takemura, K. Kurashima, H. Yusa: Appl. Phys. Lett. **69**, 2045 (1996)
62. D.P. Yu, X.S. Sun, C.S. Lee, I. Bello, S.T. Lee, H.D. Gu, K.M. Leung, G.W. Zhou, Z.F. Dong, Z. Zhang: Appl. Phys. Lett. **72**, 1966 (1998)
63. G.W. Zhou, Z. Zhang, Z.G. Bai, D.P. Yu: Sol. St. Com. **109**, 555 (1999)
64. R.S. Lee, J. Gavillet, M. Lamy de la Chapelle, A. Loiseau, J.-L. Cochon, D. Pigache, J. Thibault, F. Willaime: Phys. Rev. B **64**, 121405 (2001)
65. O. Stephan, P.M. Ajayan, C. Colliex, P. Redlich, J.M. Lambert, P. Bernier, P. Lefin: Science **266**, 1683 (1994)
66. P. Redlich, J. Loeffler, P.M. Ajayan, J. Bill, F. Aldinger, M. Rühle: Chem. Phys. Lett. **260**, 465 (1996)
67. Z. Weng-Sieh, K. Cherrey, N.G. Chopra, X. Blase, Y. Miyamoto, A. Rubio, M.L. Cohen, S.G. Louie, A. Zettl, R. Gronsky: Phys. Rev. B **51**, 11229 (1995)
68. K. Suenaga, C. Colliex, N. Demoncy, A. Loiseau, H. Pascard, F. Willaime: Science **278**, 653 (1997)
69. Y. Zhang, H. Gu, K. Suenaga, S. Iijima: Chem. Phys. Lett. **279**, 264 (1997)
70. K. Suenaga, F. Willaime, A. Loiseau, C. Colliex: Applied Phys. A **68**, 301 (1999)
71. R.T.K. Baker, P.S. Harris: The formation of filamentous carbon. In: *Chemistry and Physics of Carbon*, 14, ed by P.L. Walker Jr. and P.A. Thrower (Marcel Dekker, 1978) pp 83–165
72. K.P. De Jong, J.W. Geus: Catal. Rev.-Sci. Eng. **42**, 481 (2000)

73. N.M. Rodriguez: J. Mater. Res. **8**, 3233 (1993)
74. P.E. Nolan, D.C. Lynch, A.H. Cutler: J. Phys. Chem. B **102**, 4165 (1998)
75. M. Pérez-Cabero, E. Romeo, C. Royo, A. Monzón, A. Guerrero-Ruíz, I. Rodríguez-Ramos: J. Catal. **224**, 197 (2004)
76. J. Wei, E. Iglesia: J. Catal. **224**, 370 (2004)
77. I. Alstrup: J. Catal. **109**, 241 (1988)
78. I. Barin, Thermochemical data of pure substances, VCH (1989)
79. J.R. Rostrup-Nielsen: J. Catal. **27**, 343 (1972)
80. G.G. Tibbetts: J. Cryst. Growth **66**, 632 (1984)
81. P.K. De Bokx, A.J.H.M. Kock, E. Boellaard, W. Klop, J.W. Geus: J. Catal. **96**, 454 (1985)
82. R.T.K. Baker, M.A. Barber, P.S. Harris, F.S. Feates, R.J. Waite: J. Catal. **26**, 51 (1972)
83. R.T.K. Baker, P.S. Harris, R.B. Thomas, R.J. Waite: J. Catal. **30**, 86 (1973)
84. R.T.K. Baker: Electron microscopy studies of the catalytic growth of carbon filaments. In: *Carbon Fibers Filaments and Composites*, ed by J.L. Figueiredo, C.A. Bernardo, R.T.K. Baker, and K.J. Hüttinger (Kluwer 1989) pp 405–440
85. R.T.K. Baker: Carbon **27**, 315 (1989)
86. A.V. Melechko, V.I. Merkolov, D.H. Lowndes, M.A. Guillorn, M.L. Simpson: Chem. Phys. Lett. **356**, 527 (2002)
87. J.R. Rostrup-Nielsen, D.L. Trim: J. Catal. **48**, 155 (1977)
88. M. Audier, M. Coulon, L. Bonnetain: Carbon **21**, 105 (1983)
89. M. Audier, M. Coulon: Carbon **23**, 317 (1985)
90. J.-W. Snoeck, G.F. Froment, M. Fowles: J. Catal. **169**, 240 (1997)
91. A. Sacco Jr, F.W.A.H. Geurts, G.A. Jablonski, S. Lee, R.A. Gately: J. Catal. **119**, 322 (1989)
92. G.A. Jablonski, F.W.A.H. Geurts, A. Sacco Jr, R.R. Biderman: Carbon **30**, 87 (1992)
93. J.P. Pinheiro, P. Gadelle: J. Phys. Chem. Solids **62**, 1015 (2001)
94. J.P. Pinheiro, P. Gadelle, C. Jeandey, J.L. Oddou: J. Phys. Chem. Solids **62**, 1023 (2001)
95. J.P. Pinheiro: Croissance catalytique sous CO de carbone filamentaire et nanotubulaire. PhD thesis, Université Joseph Fourier (Grenoble1) (1999)
96. J.P. Pinheiro, S. Herreyre, P. Gadelle: Carbon'97, 23rd biennial conference on carbon, Extended abstracts, pp 340–341
97. S. Amelinckx, X.B. Zhang, D. Bernaerts, X.F. Zhang, V. Ivanov, J.B. Nagy: Science **265**, 635 (1994)
98. M. Audier, M. Coulon, A. Oberlin: Carbon **18**, 73–76 (1980)
99. M. Audier, A. Oberlin, M. Coulon: Journal of Crystal Growth **55**, 549 (1981)
100. H.E. Grenga, K.R. Lawless: J. Appl. Phys. **43**, 1508 (1972)
101. R.T. Yang, J.P. Chen: J. Catal. **115**, 52–64 (1989)
102. V.I. Zaikovskii, V.V. Chesnokov, R.A. Buyanov: Kinetics and Catalysis **42**, 813 (2001), (translated from Kinetika i Kataliz)
103. H. Terrones, T. Hayashi, M. Muñoz-Navia et al: Chem. Phys. Lett. **343**, 241 (2001)
104. N.A. Kiselev, J.L. Hutchison, A.P. Moravsky, E.V. Rakova, E.V. Dreval, C.J.D. Hetherington, D.N. Zakharov, J. Sloan, R.O. Loutfy: Carbon **42**, 149 (2004)
105. H. Murayama, T. Maeda: Nature **345**, 791 (1990)
106. N.M. Rodriguez, A. Chambers, R.T.K. Baker: Langmuir **11**, 3862 (1995)

107. P.L. Hansen, J.B. Wagner, S. Helveg, J.R. Rostrup-Nielsen, B.S. Clausen, H. Topsøe: Science **295**, 2053 (2002)
108. P.E. Nolan, M.J. Schabel, D.C. Lynch, A.H. Cutler: Carbon **33**, 79 (1995)
109. P. Pinheiro, M.C. Schouler, P. Gadelle, M. Mermoux, E. Dooryhée: Carbon **38**, 1469 (2000)
110. G.G. Tibbetts, M.P. Balogh: Carbon **37**, 241 (1999)
111. T. Koyama: Carbon **10**, 757 (1972)
112. F. Benissad, P. Gadelle, M. Coulon, L. Bonnetain: Carbon **26**, 425 (1988)
113. M. Endo, K. Takeuchi, K. Kobori, K. Takahashi, H.W. Kroto, A. Sarkar: Carbon **33**, 873 (1995)
114. Ph. Serp, J.L. Figueiredo: Carbon **34**, 1452 (1996)
115. Q.T. Le, M.C. Schouler, J. Garden, P. Gadelle: Carbon **37**, 505 (1999)
116. R.S. Wagner, W.C. Ellis: Appl. Phys. Lett. **4**, 89 (1964)
117. R.S. Wagner, W.C. Ellis: Trans. Met. Soc. AIME **233**, 1053 (1965)
118. V. Jourdain, H. Kanzow, M. Castignolles, A. Loiseau, P. Bernier: Chem. Phys. Lett. **364**, 27 (2002)
119. W.Z. Li, J.G. Wen, Y. Tu, Z.F. Ren: Appl. Phys. A **73**, 259 (2001)
120. O.P. Krivoruchko, V.I. Zaikovski: Kinetics and Catalysis **39**, 561 (1998) (translated from Kinetika i Kataliz)
121. E.E. Kukovitsky, S.G. L'vov, N.A. Sainov, V.A. Shustov, L.A. Chernozatonskii: Chem. Phys. Lett. **355**, 497 (2002)
122. S. Helveg, C. López-Cartes, J. Sehested, P.L. Hansen, B.S. Clausen, J.R. Rostrup-Nielsen, F. Abild-Pedersen, J.K. Nørskov: Nature **427**, 426 (2004)
123. X. Chen, R. Wang, J. Xu, D. Yu: Micron **35**, 455 (2004)
124. Y. Breton, R. Fleurier, J.-P. Salvetat, A.-L. Thomann, M. Verstraete, J.-C. Charlier: App. Phys. Lett. **85**, 5376 (2004)
125. H. Dai, A.G. Rinzler, P. Nikolaev, A. Thess, D.T. Colbert, R.E. Smalley: Chem. Phys. Lett. **260**, 471 (1996)
126. A.M. Cassell, J.A. Raymakers, J. Kong, H. Dai: J. Phys. Chem. B **103**, 6484 (1999)
127. J.F. Colomer, G. Bister, I. Willems, Z. Konya, A. Fonseca, J.B. Nagy, G. Van Tendeloo: Chem. Commun. (Cambridge), 1343 (1999)
128. J.H., M.J. Bronikowski, B.R. Azamian, P. Nikolaev, A.G. Rinzler, D.T. Colbert, K.A. Smith, R.E. Smalley: Chem. Phys. Lett. **296**, 195 (1998)
129. A.R. Harutyunyan, B.K. Pradhan, U.J. Kim, G. Chen, P.C. Eklund: Nano Letters **2**, 525 (2002)
130. H.M. Cheng, F. Li, G. Su, H.Y. Pan, L.L. He, X. Sun, M.S. Dresselhaus: Appl. Phys. Lett. **72**, 3282 (1998)
131. L. Ci, S. Xie, D. Tang, X. Yan, Y. Li, Z. Liu, X. Zou, W. Zhou, G. Wang: Chem. Phys. Lett. **349**, 191 (2001)
132. P. Nikolaev, M.J. Bronikowski, R.K. Bradley, F. Rohmund, D.T. Colbert, K.A. Smith, R.E. Smalley: Chem. Phys. Lett. **313**, 91 (1999)
133. B.C. Satishkumar, A. Govindaraj, R. Sen, C.N.R. Rao: Chem. Phys. Lett. **293**, 47 (1998)
134. H.W. Zhu, C.L. Xu, D.H. Wu, B.Q. Wei, R. Vajtai, P.M. Ajayan: Science **296**, 884 (2002)
135. R.R. Bacsa, C. Laurent, A. Peigney, W.S. Bacsa, T. Vaugien, A. Rousset: Chem. Phys. Lett. **323**, 566 (2000)
136. E. Flahaut, A. Govindaraj, A. Peigney, C. Laurent, A. Rousset, C.N.R. Rao: Chem. Phys. Lett. **300**, 236 (1999)

137. E. Flahaut, A. Peigney, C. Laurent, A. Rousset: J. Mater. Chem. **10**, 249 (2000)
138. A. Govindaraj, E. Flahaut, C. Laurent, A. Peigney, A. Rousset, C.N.R. Rao: J. Mater. Res. **14**, 2567 (1999)
139. C. Laurent, A. Peigney, A. Rousset: J. Mater. Chem. **8**, 1263 (1998)
140. A. Peigney, C. Laurent, F. Dobigeon, A. Rousset: J. Mater. Res. **12**, 613 (1997)
141. Y.S. Ning, X.B. Zhang, Y.W. Wang, Y.L. Sun, L.H. Shen, X.F. Yang, G. Van Tendeloo: Chemical Physics Letters **366**, 555 (2002)
142. V. Ivanov, J.B. Nagy, P. Lambin, A. Lucas, X.B. Zhang, X.F. Zhang, D. Bernaerts, G. Van Tendeloo, S. Amelinckx: Chem. Phys. Lett. **223**, 329 (1994)
143. B. Kitiyanan, W.E. Alvarez, J.H. Harwell, D.E. Resasco: Chem. Phys. Lett. **317**, 497 (2000)
144. L.F. Sun, J.M. Mao, Z.W. Pan, B.H. Chang, W.Y. Zhou, G. Wang, L.X. Qian, S.S. Xie: Appl. Phys. Lett. **74**, 644 (1999)
145. F. Benissad, P. Gadelle, M. Coulon, L. Bonnetain: Carbon **26**, 61 (1988)
146. M.J. Yacaman, M.M. Yoshida, L. Rendon, J.G. Santiesteban: Appl. Phys. Lett. **62**, 657 (1993)
147. A. Fonseca, K. Hernadi, P. Piedigrosso, J.F. Colomer, K. Mukhopadhyay, R. Doome, S. Lazarescu, L.P. Biro, P. Lambin, P.A. Thiry, D. Bernaerts, J.B. Nagy: Appl. Phys. A: Mater. Sci. Process. A **67**, 11 (1998)
148. A. Kukovecz, Z. Konya, N. Nagaraju, I. Willems, A. Tamasi, A. Fonseca, J.B. Nagy, I. Kiricsi: Phys. Chem. Chem. Phys. **2**, 3071 (2000)
149. P. Chen, X. Wu, J. Lin, H. Li, K.L. Tan: Carbon **38**, 139 (2000)
150. P. Chen, H.B. Zhang, G.D. Lin, Q. Hong, K.R. Tsai: Carbon **35**, 1495 (1997)
151. S. Delpeux, K. Szostak, E. Frackowiak, S. Bonnamy, F. Beguin: Journal of Nanosc. and Nanotech. **2**, 481 (2002)
152. Y. Soneda, L. Duclaux, F. Beguin: Carbon **40**, 965 (2002)
153. L.C. Qin: J. Mater. Sci. Lett. **16**, 457 (1997)
154. R. Sen, A. Govindaraj, C.N.R. Rao: Chem. Phys. Lett. **267**, 276 (1996)
155. C.N.R. Rao, R. Sen, B.C. Satishkumar, A. Govindaraj: Chem. Commun., 1525 (1998)
156. C. Emmenegger, P. Mauron, A. Zuttel, C. Nutzenadel, A. Schneuwly, R. Gallay, L. Schlapbach: Appl. Surf. Sci. **162-163**, 452 (2000)
157. M. Terrones, N. Grobert, J.P. Zhang, H. Terrones, J. Olivares, W.K. Hsu, J.P. Hare, A.K. Cheetham, H.W. Kroto, D.R.M. Walton: Chem. Phys. Lett. **285**, 299 (1998)
158. B.Q. Wei, Z.J. Zhang, P.M. Ajayan, G. Ramanath: Carbon **40**, 47 (2002b)
159. C.J. Lee, S.C. Lyu, Y. R. Cho, J.H. Lee, K.I. Cho: Chem. Phys. Lett. **341**, 245 (2001)
160. C.J. Lee, J. Park: Carbon **39**, 1891 (2001)
161. C.J. Lee, J. Park, S.Y. Kang, J.H. Lee: Chem. Phys. Lett. **326**, 175 (2000)
162. H. Ago, T. Komatsu, S. Ohshima, Y. Kuriki, M. Yumura: Appl. Phys. Lett. **77**, 79 (2000)
163. R. Andrews, D. Jacques, A.M. Rao, F. Derbyshire, D. Qian, X. Fan, E.C. Dickey, J. Chen: Chem. Phys. Lett. **303**, 467 (1999)
164. A.M. Rao, D. Jacques, R.C. Haddon, W. Zhu, C. Bower, S. Jin: Appl. Phys. Lett. **76**, 3813 (2000)
165. Z.F. Ren, Z.P. Huang, J.W. Xu, J.H. Wang, P. Bush, M.P. Siegel, P.N. Provencio: Science **282**, 1105 (1998)
166. G.W. Ho, A.T.S. Wee, J. Lin, W.C. Tjiu: Thin Solid Films **388**, 73 (2001)

167. H. Wang, J. Lin, C.H.A. Huan, P. Dong, J. He, S.H. Tang, W.K. Eng, T.L.J. Thong: Applied Surface Science **181**, 248 (2001)
168. Y.H. Wang, J. Lin, C.H.A. Huan, G.S. Chen: Appl. Phys. Lett. **79**, 680 (2001)
169. H. Cui, O. Zhou, B.R. Stoner: J. Appl. Phys. **88**, 6072 (2000)
170. H.M. Cheng, F. Li, X. Sun, S.D.M. Brown, M.A. Pimenta, A. Marucci, G. Dresselhaus, M.S. Dresselhaus: Chem. Phys. Lett. **289**, 602 (1998)
171. B. Wei, R. Vajtai, Y.Y. Choi, P.M. Ajayan, H. Zhu, C. Xu, D. Wu: Nano Letters **2**, 1105 (2002)
172. I.W. Chiang, B.E. Brinson, A.Y. Huang, P.A. Willis, M.J. Bronikowski, J.L. Margrave, R.E. Smalley, R.H. Hauge: J. of Phys. Chem. B **105**, 8297 (2001)
173. W. Zhou, Y.H. Ooi, R. Russo, P. Papanek, D.E. Luzi, J. E. Fischer, M.J. Bronikowski, P.A. Willis, R.E. Smalley: Chem. Phys. Lett. **350**, 6 (2001)
174. X. Devaux, C. Laurent, A. Rousset: Nanostruct. Mater. **2**, 339 (1993)
175. A. Peigney, C. Laurent, O. Dumortier, A. Fousset: J. Eur. Ceram. Soc. **18**, 1995 (1998)
176. A. Peigney, C. Laurent, A. Rousset: J. Mater. Chem. **9**, 1167 (1999)
177. S. Rul, C. Laurent, A. Peigney, A. Rousset: J. Eur. Ceram. Soc. **23**, 1233 (2003)
178. A. Peigney, C. Laurent, E. Flahaut, R.R. Bacsa, A. Rousset: Carbon **39**, 507 (2001)
179. S. Tang, Z. Zhong, Z. Xiong, L. Sun, L. Liu, J. Lin, Z.X. Shen, K.L. Tan: Chem. Phys. Lett. **350**, 19 (2001)
180. S. Maruyama, R. Kojima, Y. Miyauchi, S. Chiashi, M. Kohno: Chemical Physics Letters **360**, 229 (2002)
181. W.E. Alvarez, B. Kitiyanan, A. Borgna, D.E. Resasco: Carbon **39**, 547 (2001)
182. J.E. Herrera, L. Balzano, A. Borgna, W.E. Alvarez, D.E. Resasco: Journal of Catalysis **204**, 129 (2001)
183. C.L. Cheung, A. Kurtz, H. Park, C.M. Lieber: Journal of Physical Chemistry B **106**, 2429 (2002)
184. P. Coquay, A. Peigney, E. De Grave, R.E. Vandenberghe, C. Laurent: J. Phys. Chem. B **106**, 13199 (2002)
185. E. Flahaut, A. Peigney, C. Laurent: J. Nanosci. Nanotech. **3**, 151 (2003)
186. W. Ren, F. Li, J. Chen, S. Bai, H.-M. Cheng: Chem. Phys. Lett. **359**, 196 (2002)
187. E. Flahaut, R. Bacsa, A. Peigney, C. Laurent: Chemical Communications, 1442 (2003)
188. J. Kong, H.T. Soh, A.M. Cassell, C.F. Quate, H. Dai: Nature **395**, 878 (1998)
189. N.R. Franklin, H. Dai: Adv. Mater. **12**, 890 (2000)
190. G. Che, B.B. Lakshmi, C.R. Martin, E.R. Fisher, R.S. Ruoff: Chem. Mater. **10**, 260 (1998)
191. S.-H. Jeong, O.-J. Lee, K.-H. Lee, S.H. Oh, C.-G. Park: Chemistry of Materials **14**, 1859 (2002)
192. S.S. Xie, B.H. Chang, W.Z. Li, Z.W. Pan, L.F. Sun, J.M. Mao, X.H. Chen, L.X. Qian, W.Y. Zhou: Adv. Mater. **11**, 1135 (1999)
193. Z.K. Tang, H.D. Sun, J. Wang, J. Chen, G. Li: Bull. Mater. Sci. **22**, 329 (1999)
194. L. Alvarez, T. Guillard, J.-L. Sauvajol, G. Flamant, D. Laplaze: App. Phys. A **70**, 169 (2000)
195. H.M. Cheng, F. Li Su, G. Pan, H.Y. Pan, L.L. He, X. Sun, M.S. Dresselhaus: Appl. Phys. Lett. **2**, 3282(1998)
196. J.-F. Colomer, C. Stéphan, S. Lefrant, G. Van Tendeloo, I. Willems, Z. Konya, A. Fonseca, C. Laurent, J.B. Nagy: Chem. Phys. Lett. **317**, 83 (2000)

197. J. Gavillet, A. Loiseau, F. Ducastelle, S. Thair, P. Bernier, O. Stéphan, J. Thibault, J.-Ch. Charlier: Carbon **40**, 1649 (2002)
198. H. Kanzow, A. Ding: Phys. Rev. B **60** (1999) 11 180; H. Kanzow, C. Lenski, A. Ding: Phys. Rev. B **63**, 125402 (2001)
199. V.L. Kusnetzov, A.N. Usoltseva, A.L. Chuvillin, E.D. Obratzova, J.-M. Bonard: Phys. Rev. B **64**, 235401(2001)
200. A. Gorbunov, O. Jost, W. Pompe, A. Graff: Carbon **40**, 113 (2002)
201. A. Maiti, C.J. Brabec, J. Bernholc: Phys. Rev. B **55**, 6097 (1997)
202. J. Gavillet, A. Loiseau, C. Journet, F. Willaime, F. Ducastelle, J.-Ch. Charlier: Phys. Rev. Lett. **87**, 275504 (2001)
203. J.-Ch. Charlier, G.-M. Rignanese, X. Blase, De Vita, R. Car: unpublished (2003)
204. J. Gavillet, J. Thibault, O. Stéphan, H. Amara, A. Loiseau, Ch. Bichara, J.-P. Gaspard, F. Ducastelle: J. Nanosc. and Nanotech. **4**, 346 (2004)
205. A. Loiseau, F. Willaime: Appl. Surface Science **164**, 227 (2000)
206. Y. Saito, M. Okuda, N. Fujimoto, T. Yoshikawa, M. Tomita, T. Hayashi: Jpn. J. Appl. Phys. 1 **33**, L526 (1994)
207. Y. Saito, M. Okuda, N. Fujimoto, T. Yoshikawa, M. Tomita, T. Hayashi: Jpn J. Appl. Phys. **33**, 526 (1994); Y. Saito: Carbon **33**, 979 (1995)
208. D. Zhou, S. Seraphin, S. Wang: Appl. Phys. Lett.**65**, 1593 (1994)
209. X. Fan, R. Buczko, A.A. Puretzky, D.B. Geohegan, J.Y. Howe, S.T. Pantelides, S.J. Pennycook: Phys. Rev. Lett. **90**, 145501 (2003)
210. A.N. Andriotis, M. Menon, G.E. Froudakis: Phys. Rev. Lett. **85**, 3193 (2000)
211. H. Kataura, Y. Kumazawa, Y. Maniwa, Y. Ohtsuka, R. Sen, S. Suzuki, Y. Achiba: Carbon **38**, 1691(2000)
212. O. Jost, A.A. Gorbunov, J. Mšller, W. Pompe, A. Graff, R. Friedlein, X. Liu, M.S. Golden, J . Fink: Chem. Phys. Lett. **339**, 297 (2001); O. Jost, A.A. Gorbunov, J. Mšller, W. Pompe, X. Liu, P. Georgi, L. Dunsch, M.S. Golden, J. Fink: J. Phys. Chem. B **106**, 2875 (2002)
213. A. Gorbunov, O. Jost, W. Pompe, A. Graff: Appl. Surface Science **197–198**, 563 (2002)
214. J.S. Langer: Rev. Mod. Phys. **52**, 1 (1980)
215. A. Zangwill: *Physics at surfaces*, (Cambridge University Press 1998)
216. J.-F. Colomer, L. Henrard, Ph. Lambin, G. Van Tendeloo: Phys. Rev. B **64**, 125425 (2001); Eur. Phys. J. B **27**, 111 (2002)
217. A. Loiseau, N. Demoncy, O. Stéphan, C. Colliex, H. Pascard: In *Science and Applications of Nanotubes*, ed by Tomanek and Enbody (Kluwer Academic/Plenum Publishers, New York 2000)
218. L. Henrard, A. Loiseau, C. Journet, P. Bernier: Eur. Phys. J. B **13**, 661 (2000)
219. A. Loiseau, J. Gavillet, F. Ducastelle, J. Thibault, O. Stéphan, P. Bernier, S. Thair: C. R. Physique **4**, 967 (2003)
220. J.B. Nagy, G. Bister, A. Fonseca, D. Mehn, Z. Konya, I. Kiricsi, Z.E. Horvath, L.P. Biro: J. Nanosci. Nanotech. **4**, 326 (2004)
221. M. Endo, H.W. Kroto: J. Phys. Chem. **96**, 6941 (1992)
222. R. Saito, M. Fujita, G. Dresselhaus, M.S. Dresselhaus: Mater. Sci. Eng. B**19**, 185 (1993)
223. R.E. Smalley: Mater. Sci. Eng. B**19**, 1 (1993)
224. S. Iijima, T. Ichihashi, Y. Ando: Nature **356**, 776 (1992)
225. S. Iijima: Mater. Sci. Eng. B**19**, 172 (1993)

226. A. Maiti, C.J. Brabec, C.M. Roland, J. Bernholc: Phys. Rev. Lett. **73**, 2468 (1994)
227. L. Lou, P. Nordlander, R.E. Smalley: Phys. Rev. B **52**, 1429 (1995)
228. J.-C. Charlier, A. De Vita, X. Blase, R. Car: Science **275**, 646 (1997)
229. J.-C. Charlier, X. Blase, A. De Vita, R. Car: Appl.Phys. A **68**, 267 (1999)
230. Y.-K. Kwon, Y.H. Lee, S.-G. Kim, P. Jund, D. Tománek, R.E. Smalley: Phys. Rev. Lett. **79**, 2065 (1997)
231. M. Buongiorno Nardelli, C. Brabec, A. Maiti, C. Roland, J. Bernholc: Phys. Rev. Lett. **80**, 313 (1998)
232. S. Iijima: MRS Bulletin **19**, 43 (1994)
233. D.H. Robertson, D.H. Brenner, J.W. Mintmire: Phys. Rev. B **45**, 12592 (1992)
234. A. Maiti, C.J. Brabec, C.M. Roland, J. Bernholc: Phys. Rev. B **52**, 14850 (1995)
235. C.J. Brabec, A. Maiti, C. Roland, J. Bernholc: Chem. Phys. Lett. **236**, 150 (1995)
236. B.R. Eggen, M.I. Heggie, G. Jungnickel, C.D. Latham, R. Jones, P.R. Briddon: Science **272**, 87 (1996)
237. Y.H. Lee, S.-G. Kim, P. Jund, D. Tománek: Phys. Rev. Lett. **78**, 2393 (1997)
238. D.L. Carroll, P. Redlich, P.M. Ajayan, J.-C. Charlier, X. Blase, A. De Vita, R. Car: Phys. Rev. Lett. **78**, 2811 (1997)
239. Y. Shibuta, S. Maruyama: Chem. Phys. Lett. **382**, 381 (2003)
240. F. Ding, K. Bolton, A. Rosén: J. Chem. Phys. **121**, 2775 (2004)
241. H. Amara: PhD Thesis, Université Paris 6 (2005)
242. J. Yu et al: Appl. Phys. Lett. **77**, 1949 (2000)
243. D. Goldberg et al: Chem. Phys. Lett. **359**, 220 (2002)
244. M. Terrones et al: Chem. Phys. Lett. **257**, 576 (1996)
245. R. Sen et al: Chem. Phys. Lett. **287**, 671 (1998)
246. W. Han et al: Appl. Phys. Lett. **73**, 3085 (1998)
247. D. Golberg et al: Chem. Phys. Lett. **308**, 337 (1999)
248. D. Golberg et al: Appl. Phys. Lett. **82**, 1275 (2003)
249. A.Y. Liu et al: Phys. Rev. B **39**, 1760 (1988)
250. X. Blase et al: Appl. Phys. A **68**, 293–300 (1999); ibid., Comp. Mat. Sci. **17**, 107–114 (2000)
251. M.O. Watanabe, S. Itoh, T. Sasaki, K. Mizushima: Phys. Rev. Lett. **77**, 187 (1996); Erratum, Phys. Rev. Lett. **77**, 2846 (1996); Y. Chen, J.C. Barnard, R.E. Palmer, M.O. Watanabe, T. Sasaki: Phys. Rev. Lett. **83**, 2406 (1999)
252. X.D. Bai, E.G. Wang, J. Yu, H. Yang: Appl. Phys. Lett. **77**, 67 (2000); J. Yu, J. Ahn, S.F. Yoon, Q. Zhang, Rusli et al: Appl. Phys. Lett. **77**, 1949 (2000)
253. X. Blase et al: Appl. Phys. Lett. **70**, 197 (1997)
254. D.L. Carroll et al: Carbon **36**, 753 (1998)
255. X. Blase et al: Phys. Rev. Lett. **83**, 5078–5081 (1999)
256. E. Hernández et al: J. Chem. Phys. **113**, 3814 (2000)
257. D.L. Carroll et al: Phys. Rev. Lett. **81**, 2332–2335 (1998)
258. E. Bengu et al: Phys. Rev. lett. **86**, 2385 (2001)
259. X. Blase et al: Phys. Rev. Lett. **80**, 1666 (1998)
260. K.M. Rogers et al: Chem. Phys. Lett. **332**, 43 (2000)

3

Structural Analysis by Elastic Scattering Techniques

Ph. Lambin, A. Loiseau, M. Monthioux and J. Thibault

Abstract. Much of our knowledge on the atomic structure of a material system comes from experiments based on the interaction of radiation with the atoms. The present chapter is devoted to *elastic* interactions of radiations in a broad sense – electromagnetic waves and particles (electrons or neutrons) – with matter. Each elementary interaction process is called a scattering. An elastic scattering process can only modify the direction of the wave vector of the radiation, not its energy. A well-known example is the Rayleigh scattering on an electromagnetic wave by a polarizable object, which must be small on the wavelength scale. Then, the incident wave excites an electric dipole in the object, which oscillates in time with the frequency ω of the incident electric field and radiates a wave in all the directions. This radiated wave is the scattered radiation.

Diffraction takes place when a wave is coherently scattered by many centers. Maxima of interferences arising in certain directions between the many scattered waves are linked to the spatial distribution of the diffusion centers. In transmission electron microscopy (TEM), electrons are diffracted by the electrostatic potential of the atoms. The transmitted electrons are used to construct an image of the scattering potential. In scanning tunneling microscopy (STM), electrons are elastically scattered by the potential barrier between a sharp tip and the surface of the sample. The tunneling current going across the barrier gives an information on the surface electronic density of states. All these techniques are reviewed in Sect. 3.1, and are illustrated with examples taken from graphene-based materials (Sect. 3.2) and nanotubes (Sect. 3.3).

3.1 Basic Theories

3.1.1 Kinematic Theory of Diffraction

The principle of diffraction is that waves scattered from a collection of scattering centers interfere constructively in some directions. If one wants to gain information on the microscopic structure of a piece of matter from diffraction, the scattering objects must be the molecules, the atoms, or the nuclei of the atoms from which the sample is made of. It is therefore important to

Ph. Lambin et al.: *Structural Analysis by Elastic Scattering Techniques*, Lect. Notes Phys. **677**, 131–198 (2006)
www.springerlink.com
© Springer-Verlag Berlin Heidelberg 2006

work with radiations that have a wavelength of the order of or smaller than the interatomic distances. For electromagnetic waves, this means X-rays. For non-relativistic particles with energy E_0, the wavelength is given by the de Broglie relation, $\lambda = h/\sqrt{2mE_0}$. Thermal neutrons ($E_0 = 25\,\mathrm{meV}$) for instance have $\lambda = 0.182\,\mathrm{nm}$. Electrons of 50 eV energy have about the same wavelength, but they are strongly inelastically scattered when traveling into a solid. These low-energy electrons are suitable for backscattering experiments, such as LEED which is surface diffraction. In transmission experiments, one has to work with electrons in the 100 keV range. For these high-energy electrons, the relativistic expression of the de Broglie wavelength must be used, $\lambda = h/\sqrt{2m_0E_0(1 + E_0/2m_0c^2)}$ with m_0 the electron mass at rest.

X-rays

The Thomson scattering of an electromagnetic radiation by free electrons [1] is the basis of X-ray diffraction. A plane wave of high-frequency can induce electron oscillations, though with a very small efficiency, and has no influence on the dynamics of the more massive nuclei. Due to the Coulomb force $-e\boldsymbol{E}$, an electromagnetic plane wave interacts with an electron gas of density $n = n(\boldsymbol{r})$ by inducing a current density wave

$$\boldsymbol{j}_{\,\mathrm{ind}}(\boldsymbol{r},t) = -e\,n\,\boldsymbol{v} = i\,\frac{ne^2}{m_0\omega}\boldsymbol{E}_0\mathrm{e}^{\mathrm{i}\boldsymbol{k}_0.\boldsymbol{r}-\mathrm{i}\omega t} \tag{3.1}$$

where $-e$ and m_0 are the electron charge and mass, $\boldsymbol{E}_0$ is the amplitude of the electric field, $\boldsymbol{k}_0$ is the incident wave vector and $\omega = k_0\,c$ is the angular frequency. The vector potential generated at coordinate $\boldsymbol{r}$ and time t by this current density is

$$\begin{aligned}\boldsymbol{A}(\boldsymbol{r},t) &= \frac{\mu_0}{4\pi}\int\frac{\boldsymbol{j}_{\,\mathrm{ind}}(\boldsymbol{r}',t-|\boldsymbol{r}'-\boldsymbol{r}|/c)}{|\boldsymbol{r}'-\boldsymbol{r}|}\,\mathrm{d}^3r' \\ &= \frac{\mu_0}{4\pi}\,\frac{ie^2}{m_0\omega}\int\frac{n(\boldsymbol{r}')\,\mathrm{e}^{\mathrm{i}\boldsymbol{k}_0.\boldsymbol{r}'+\mathrm{i}\omega|\boldsymbol{r}'-\boldsymbol{r}|/c}}{|\boldsymbol{r}'-\boldsymbol{r}|}\,\mathrm{d}^3r'\,\boldsymbol{E}_0\,\mathrm{e}^{-\mathrm{i}\omega t}\end{aligned} \tag{3.2}$$

where the integral runs over the volume of the sample. In the far field, that is to say at a distance r large compared to the dimensions of the sample ($|\boldsymbol{r}| \gg |\boldsymbol{r}'|$), $|\boldsymbol{r}'-\boldsymbol{r}|$ can be replaced by $|\boldsymbol{r}|$ in the denominator of (3.2) (zeroth order approximation) and by $r - \boldsymbol{r}'.\boldsymbol{r}/r$ in the argument of the exponential (first-order approximation). The result of these approximations is that the vector potential behaves asymptotically like a spherical wave, $\boldsymbol{A}(\boldsymbol{r},t) \approx \boldsymbol{A}_0\mathrm{e}^{\mathrm{i}k_0r-\mathrm{i}\omega t}/r$ whose amplitude is a Fourier transform of the charge density $n(\boldsymbol{r})$

$$\boldsymbol{A}_0 = \frac{\mu_0}{4\pi}\,\frac{ie^2}{m_0\omega}\int n(\boldsymbol{r}')\mathrm{e}^{\mathrm{i}\boldsymbol{q}.\boldsymbol{r}'}\mathrm{d}^3r'\boldsymbol{E}_0 \tag{3.3}$$

where $\boldsymbol{k} = k_0\boldsymbol{r}/r$ is the wave vector in the direction of observation and $\boldsymbol{q} = \boldsymbol{k}_0 - \boldsymbol{k}$ is the scattering wave vector (see Fig. 3.1).

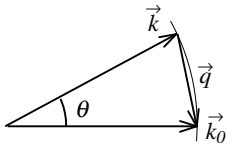


Fig. 3.1. Definition of the incident wave vector $\boldsymbol{k}_0$, the wave vector of the scattered wave $\boldsymbol{k}$, the scattering wave vector $\boldsymbol{q}$, and the scattering angle θ

The differential scattering cross-section is defined as the ratio between the power radiated in a infinitely small solid angle $\mathrm{d}\Omega$ around the direction $\boldsymbol{k}$ and the power per unit area transported by the incident wave. For the case of unpolarized incident wave, it reads

$$\frac{\mathrm{d}\sigma}{\mathrm{d}\Omega} = \omega^2 \frac{|\boldsymbol{A}_0 \cdot \boldsymbol{k}|^2}{|\boldsymbol{E}_0 \cdot \boldsymbol{k}_0|^2} = \left| \int n(\boldsymbol{r}) \mathrm{e}^{\mathrm{i}\boldsymbol{q}\cdot\boldsymbol{r}} \mathrm{d}^3 r \right|^2 r_\mathrm{e}^2 \frac{1+\cos^2\theta}{2} \tag{3.4}$$

where $r_\mathrm{e} = e^2/4\pi\epsilon_0 m_0 c^2$ is the 'classical radius' of the electron (2.8×10^{-15} m) and θ is the scattering angle (see Fig. 3.1).

Assuming that $n(\boldsymbol{r}) = \sum_j n_j(\boldsymbol{r} - \boldsymbol{r_j})$ is a sum of electron densities over atomic cells leads to

$$\frac{\mathrm{d}\sigma}{\mathrm{d}\Omega} \propto \left| \sum_j f_j(q) \mathrm{e}^{\mathrm{i}\boldsymbol{q}\cdot\boldsymbol{r}_j} \right|^2 \tag{3.5}$$

where

$$f_j(q) = r_\mathrm{e} \int_\mathrm{atom} n_j(\boldsymbol{r}) \mathrm{e}^{\mathrm{i}\boldsymbol{q}\cdot\boldsymbol{r}} \mathrm{d}^3 r \tag{3.6}$$

Equation (3.5), which discards the slowly varying function $(1 + \cos^2\theta)/2$, is the central result of the kinematic theory of diffraction. It expresses the diffraction cross section as the square modulus of a coherent sum (scattering structure) of atomic scattering factors f_j. The atomic scattering factor for X-rays is proportional to the Fourier transform of the electron density of the atoms. It is generally evaluated for free atoms (see Fig. 3.2).

Electrons

In quantum mechanics, the scattered wavefunction deduced from the first-Born approximation [2] is a spherical wave at large distance from the scattering center, $f(\boldsymbol{q})\,\mathrm{e}^{\mathrm{i}k_0 r}/r$, where k_0 is the de Broglie wave vector of the incident particles. The amplitude of the spherical wave is

$$f(\boldsymbol{q}) = -\frac{m}{2\pi\hbar^2} \int \mathrm{e}^{\mathrm{i}\boldsymbol{q}\cdot\boldsymbol{r}} U(\boldsymbol{r})\, \mathrm{d}^3 r \tag{3.7}$$

where U is the scattering energy potential, and $\boldsymbol{q}$ has the same meaning as in Fig. 3.1. For the electron–atom interaction, $U = -eV$ where V is the atomic

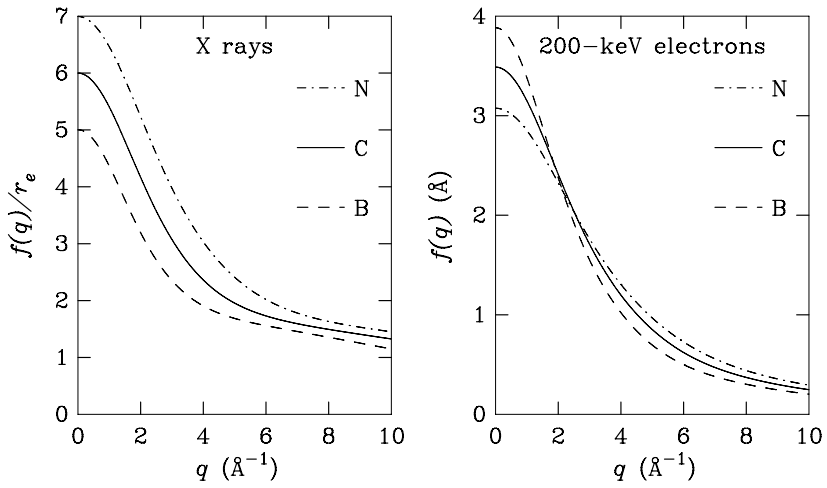


Fig. 3.2. Atomic scattering factors $f(q)$ for X-rays (*left*) and 200-keV electrons (*right*) for B, C, and N atoms [3]

electrostatic potential (nucleus plus electron screening). The differential cross section takes the same expression as in (3.5), with

$$f_j(q) = a_0 \left(1 + \frac{E_0}{m_0 c^2}\right) \frac{2\epsilon_0}{e\, a_0^2} \int_{\text{atom}} V_j(\boldsymbol{r}) \mathrm{e}^{\mathrm{i}\boldsymbol{q}\cdot\boldsymbol{r}} \mathrm{d}^3 r \ . \tag{3.8}$$

The factor $(1+\frac{E_0}{m_0 c^2})$ where E_0 is the electron energy is the relativistic correction m/m_0 to the electron mass. A graph of the electron scattering factor of B, C and N is shown in Fig. 3.2. Since the length unit is the Bohr radius a_0, the electron scattering power is 10^8 times larger than for X-rays. Thanks to this, a single nanotube can diffract the electron beam in a detectable way, whereas X-rays and neutrons demand a macroscopic amount of nanotubes. The electron scattering factor for light elements such as C is nevertheless small enough to validate the first Born approximation for nanotubes composed of up to a few tens of layers (see below).

Neutrons

With neutron, the relevant interaction in a non-magnetic material is the nuclear interaction, which is so short ranged compared with the neutron wavelength that it can be approximated by a Dirac delta function. In these conditions, one readily deduces from (3.7) that the resulting scattering factor is a (complex) constant, $f(\boldsymbol{q}) = -b$, called the neutron nuclear scattering length [4]. It depends on the isotope. The average value for natural carbon is $|\bar{b}| = 6.648 \times 10^{-15}$ m. This scattering factor is of the same order of magnitude as for X-rays ($f(0) = 6r_\mathrm{e} = 15.6 \times 10^{-15}$ m). The advantage of neutrons over

X-rays is that the constant nuclear scattering factor does not attenuate the intensity for large scattering wave vectors[1]. Neutron-diffraction profiles with q as large as $20\,\text{Å}^{-1}$ can be measured.

In general, a given element has a few stable isotopes which occupy the lattice sites with probabilities equal to their relative abundances. The neutron scattering length depends on the isotope, which means that its value fluctuates in the lattice around the average value $\overline{b}$. This fluctuation gives rise to incoherent scattering, very much like the blue sky is the result of incoherent Rayleigh scattering of the solar light by air density fluctuations. Like with the blue sky, the incoherent neutron scattering cross section is isotropic and adds a continuous background to the diffraction pattern; it is proportional to $\overline{|b-\overline{b}|^2}$. In the case of carbon, the ratio between the incoherent and coherent scattering cross sections is 0.0018, which is very small.

3.1.2 Transmission of Fast Electrons through a Crystalline Film

The interpretation of images obtained by transmission electron microscopy demands to go beyond the simple kinematic theory of diffraction. In fact, it is an extremely difficult problem to treat the interaction of the electrons with the atoms of the sample as a cascade of single-scattering events. It is much easier to consider that the electrons are scattered by the electrostatic potential of the sample as a whole, which leads to a continuous change of phase and amplitude of their wave functions as they go through the specimen [5]. To do so, we consider a slice of a crystalline material, upon which a monokinetic electron beam arrives at normal incidence (z direction) with energy E_0 (a few hundreds of keV). Above the film (see Fig. 3.3), the electron wavefunction is the plane wave $\Psi_0 = \mathrm{e}^{\mathrm{i}k_0 z}$, where k_0 is the de Broglie wave vector. We only consider elastic interactions of the electrons with the crystalline medium so that the energy E_0 is conserved. Since the crystal possesses a translational symmetry in directions $\boldsymbol{\rho}$ parallel to the surface, the momentum parallel to the surface is also conserved to within a two-dimensional reciprocal vector $\boldsymbol{g}$ of the crystal film. This means that the wavefunction elastically transmitted through the film can be decomposed in a series of plane waves

$$\Psi = \sum_{\boldsymbol{g}} A_{\boldsymbol{g}}\, \mathrm{e}^{\mathrm{i}\boldsymbol{g}\cdot\boldsymbol{\rho}+\mathrm{i}k' z} \tag{3.9}$$

with $\hbar^2(g^2+k'^2)/2m = E_0$, m being the relativistic mass of the electron. At high energy, a simplification arises from the fact that $k_0 \gg g$, which allows us to replace k' by k_0. The beams corresponding to the set of $\boldsymbol{g}$ vectors will compose the diffraction pattern of the crystal film, the intensity of the spots being proportional to the squared amplitude $|A_{\boldsymbol{g}}|^2$.

[1] This is not true for nuclei having a magnetic moment, which give additional scattering characterized by a q-dependent scattering factor. This discussion does not include either the attenuation brought about by the Debye-Waller factor, which accounts for the thermal vibration of the atoms (see (3.62) in Sect. 3.3.2).

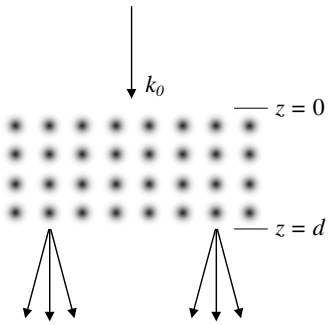


Fig. 3.3. Diffraction of a plane wave by a crystalline film

It will be interesting to write the electron wavefunction everywhere in space in the form of a product:

$$\Psi = \psi(\boldsymbol{\rho}, z)\ \mathrm{e}^{\mathrm{i}k_0 z} \tag{3.10}$$

where

$$\psi(\boldsymbol{\rho}, 0) = 1 \tag{3.11}$$

on the entrance face $z = 0$ of the film due to the assumed normal incidence of the plane wave. The kinetic operator T acting on such a product yields

$$T\Psi = -\frac{\hbar^2}{2m}\left[\nabla_t^2\psi(\boldsymbol{\rho}, z) - k_0^2\psi(\boldsymbol{\rho}, z) + 2\mathrm{i}k_0\frac{\partial\psi(\boldsymbol{\rho}, z)}{\partial z} + \frac{\partial^2\psi(\boldsymbol{\rho}, z)}{\partial z^2}\right]\mathrm{e}^{\mathrm{i}k_0 z} \tag{3.12}$$

where ∇_t^2 is the two-dimensional Laplacian. The wavefunction $\psi(\boldsymbol{\rho}, z)$ is assumed to vary with z on a length scale much longer than the electron de Broglie wavelength $2\pi/k_0$. The expression obtained below shows that this hypothesis is indeed true. This slow variation allows us to neglect the term $\partial^2\psi/\partial z^2$ compared to $k_0^2\psi$. The Schrödinger equation for the energy E_0 then simplifies into

$$i\,\frac{2E_0}{k_0}\,\frac{\partial\psi(\boldsymbol{\rho}, z)}{\partial z} = H\psi(\boldsymbol{\rho}, z) \tag{3.13}$$

where $H = -(\hbar^2/2m)\nabla_t^2 - eV(\boldsymbol{\rho}, z)$, with V the electrostatic potential felt by the incident electrons in the crystalline film. V is the potential of the nucleus screened by the crystal electron distribution. The last equation resembles the time-dependent Schrödinger equation with time $t = \hbar k_0 z/2E_0$.

We now introduce the columnar approximation, which consists in averaging the electrostatic potential $V(\boldsymbol{\rho}, z)$ along the z direction, by introducing the projected potential $V_\mathrm{p}(\boldsymbol{\rho}) = (1/d)\int_0^d V(\boldsymbol{\rho}, z)\,dz$, where d is the thickness of the film. Substituting

$$H_\mathrm{p} = -(\hbar^2/2m)\nabla_t^2 - eV_\mathrm{p}(\boldsymbol{\rho}) \tag{3.14}$$

for H in (3.13) leads to a simpler problem of wave propagation, for the Hamiltonian is now independent of 'time'. A formal solution of the Schrödinger equation is then

$$\psi(\boldsymbol{\rho}, z) = U(0; z)\psi(\boldsymbol{\rho}, 0) \tag{3.15}$$

where $U(0; z) = \exp[-\mathrm{i}(H_\mathrm{p}/2E_0)k_0 z]$ is the evolution operator that propagates the wavefunction from the entrance face $z = 0$ of the film up to the coordinate z inside the film.

When the thickness z is small enough, the evolution operator can be approximated by $U(0; z) \approx 1 - \mathrm{i}(H_\mathrm{p}/2E_0)k_0 z$. Inserting that expression into the right-hand side of (3.15) leads to

$$\psi(\boldsymbol{\rho}, z) \approx 1 + \mathrm{i}\,\sigma V_\mathrm{p}(\boldsymbol{\rho})z, \quad \sigma = ek_0/2E_0 \tag{3.16}$$

because $\psi(\boldsymbol{\rho}, 0) = 1$ (see (3.11)) and, for the same reason, $H_\mathrm{p}\,\psi(\boldsymbol{\rho}, 0) = -eV_\mathrm{p}(\boldsymbol{\rho})$. At the same level of approximation, (3.16) can also be rewritten as $\psi(\boldsymbol{\rho}, z) \approx \exp[\mathrm{i}\,\sigma V_\mathrm{p}(\boldsymbol{\rho})z]$, which means that the sample is changing the *phase* of the transmitted wavefunction, without causing a change in the amplitude. In microscopy terminology, such a sample is called a 'phase object'. Here, the phase variation is supposed to be small, and (3.16) is known as the *weak phase object* approximation, which we will return to for the specific case of carbon materials.

A practical way to deal with the formal solution (3.15) is to develop the evolution operator in the basis set of the eigenfunctions $\phi_n(\boldsymbol{\rho})$ of the two-dimensional Hamiltonian (3.14), defined by $H_\mathrm{p}\,\phi_n = E_n\phi_n$. In so doing, one obtains

$$\psi(\boldsymbol{\rho}, z) = \sum_n C_n \mathrm{e}^{-\mathrm{i}\gamma_n z}\phi_n(\boldsymbol{\rho}) \tag{3.17}$$

with $\gamma_n = (E_n/2E_0)k_0$. In that expression, $C_n = \langle\phi_n|\psi(0)\rangle$ are the so-called excitation coefficients. Due to the two-dimensional crystalline periodicity, $\phi_n(\boldsymbol{\rho})$ is a Bloch function. With the uniform boundary condition (3.11), all the C_n coefficients vanish except those associated with Bloch functions computed at the Γ point of the first-Brillouin zone and which are totally symmetrical with respect to the symmetry elements of the unit cell (Γ_1 representation). This is of course a simplification inherent in the assumed normal incidence. C_n represents the average value of the Bloch function $\phi_n(\boldsymbol{\rho})$ in a surface unit cell. Very localized states have an excitation coefficient close to 0.

In the case of a monoatomic film viewed along a high-symmetry axis (such as [001] in a cubic crystal), the two-dimensional potential energy $-eV_\mathrm{p}(\boldsymbol{\rho})$ of a projected column of atoms has only very few Γ_1 bound states. The lowest bound state, with energy E_1, has very small dispersion in reciprocal space and possesses the s symmetry. The binding energy of this s state increases with increasing atomic number (see Table 3.1). Its small dispersion indicates that the wavefunction $\phi_1(\boldsymbol{\rho})$ is well localized at the center of the atomic columns (like an atomic core state), and is close to zero between the columns. Another Γ_1 state exists above or close to the zero of energy (see Table 3.1) and, for

Table 3.1. Wavefunction parameters for a few elements at 200 keV [6]. The simple hexagonal form of graphite means AAA stacking

Film	γ_1 (Å^{-1})	C_1^2	γ_2 (Å^{-1})	C_2^2	$2\pi/(\gamma_2 - \gamma_1)$ (nm)
gr(001) s. hex	−0.0132	0.852	+0.0091	0.138	28.0
Al(001) fcc	−0.0201	0.611	0.0003	0.385	30.7
Cu(001) fcc	−0.0574	0.259	−0.0020	0.735	11.3
Au(001) fcc	−0.179	0.078	−0.008	0.897	3.7

most of the elements except the heaviest ones, it is sufficient to work with these two Bloch states only. In this approximation, one obtains

$$\psi(\boldsymbol{\rho}, z) = C_1 \mathrm{e}^{-\mathrm{i}\gamma_1 z}\phi_1(\boldsymbol{\rho}) + C_2 \mathrm{e}^{-\mathrm{i}\gamma_2 z}\phi_2(\boldsymbol{\rho}) \tag{3.18}$$

The intensity transmitted through the thickness d of the film follows by taking the square modulus of that last expression and setting $z = d$

$$I(\boldsymbol{\rho}) = 1 - 2C_1\phi_1(\boldsymbol{\rho})[1 - C_1\phi_1(\boldsymbol{\rho})][1 - \cos(\gamma_2 - \gamma_1)d] \tag{3.19}$$

taking into account that, at this level of approximation, $C_1\phi_1(\boldsymbol{\rho}) + C_2\phi_2(\boldsymbol{\rho}) = 1$ (see (3.11)).

According to (3.19), the intensity is channelled by the factor $C_1\phi_1(\boldsymbol{\rho})[1 - C_1\phi_1(\boldsymbol{\rho})]$ which strongly peaks at the center of the atomic columns (see Fig. 3.4). This characteristics gives rise to the atomic resolution of the microscope, which however is affected by the instrumental transfer function (see

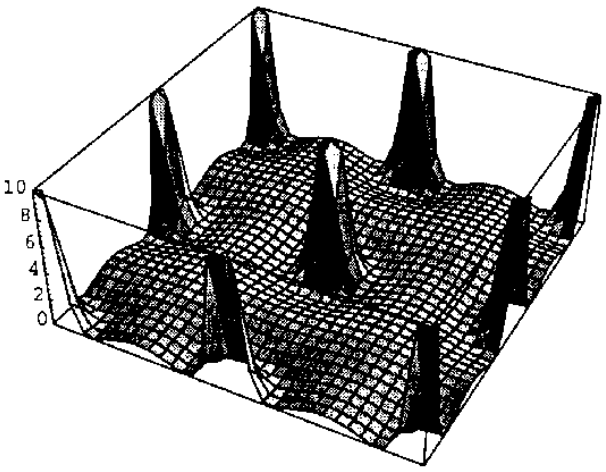


Fig. 3.4. Electron intensity transmitted through a Cu(001) film computed for the best possible contrast, which is realized when $\cos(\gamma_2 - \gamma_1)d = -1$ in (3.19). The incident energy is 200 keV, the intensity is represented against $\boldsymbol{\rho}$ in a face-centered square cell [6]

(3.25) below). As a function of thickness, there is an oscillation of intensity, with the wavelength $2\pi/(\gamma_2 - \gamma_1)$. When this wavelength is much larger than the sample thickness d, the cosine function in (3.19) can be approximated by $1 - [(\gamma_2 - \gamma_1)d]^2/2$, a parabolic dependence of the intensity on d is obtained, in agreement with the intensity deduced from the weak phase object approximation (3.16). The validation of this approximation is therefore defined by the condition $(\gamma_2 - \gamma_1)d \ll 1$.

Coming back to (3.9), the amplitude of the diffracted beams is obtained by two-dimensional Fourier transformation of the transmitted wave function. According to (3.17), one simply has to develop the periodic Bloch functions $\phi_n(\boldsymbol{\rho})$ in Fourier series, $\sum_{\boldsymbol{g}} C_{n,\boldsymbol{g}}\, \mathrm{e}^{\mathrm{i}\boldsymbol{g}\cdot\boldsymbol{\rho}}$, and insert the result of this development in (3.10). This transformation can be then identified with (3.9), leading to the following expression of the amplitude of the diffracted beams:

$$A_{\boldsymbol{g}} = \sum_n C_n C_{n,\boldsymbol{g}} \mathrm{e}^{-\mathrm{i}\gamma_n d} \tag{3.20}$$

The intensity of the diffracted $\boldsymbol{g}$ beam is $|A_{\boldsymbol{g}}|^2$. For the central beam ($\boldsymbol{g} = 0$), it is a simple property of the Fourier series that $C_{n,0}$ identifies with the excitation coefficient C_n owing to (3.11). With the two-wave approximation, the intensity of the central beam is therefore

$$|A_0|^2 = 1 - 2C_1^2(1 - C_1^2)[1 - \cos(\gamma_2 - \gamma_1)d] \tag{3.21}$$

when the normalization relation $C_1^2 + C_2^2 = 1$ is used. The intensity of the central beam follows the same oscillatory behavior versus thickness as the intensity of the wavefunction (see (3.19)).

The variation of intensity of the central beam across a graphitic slab is shown in Fig. 3.5 for three layer stackings: the normal Bernal arrangement of graphite (ABAB), the simple hexagonal stacking (AAA), and the rhombohedral structure (ABC). In the first case, there are three columns per surface unit cell, one with density corresponding to 1 atom per layer and two columns with density 0.5. In the simple hexagonal structure, there are two columns with density 1. In the rhombohedral geometry, all the columns have the same density 2/3. In the latter two cases, there is one period of oscillation of the intensity (equation (3.21) with $2\pi/(\gamma_2 - \gamma_1) = 28$ and 13.7 nm for the AAA and ABC stackings, respectively, at 200 keV incident energy) because all the columns are the identical. For the Bernal graphite, the two kinds of columns give rise to two periods of oscillations, one long period (54 nm) with large amplitude and one short period (18 nm) with small amplitude. The amplitude of the intensity oscillations is smaller in the case of rhombohedral graphite because the bound state is more delocalized over the unit cell ($C_1^2 = 0.98$) than in the simple hexagonal structure ($C_1^2 = 0.85$).

As mentioned above, the validation of the weak phase object approximation demands a sample thickness much smaller than the period of oscillation of the transmitted intensity. It can be concluded from Fig. 3.5 that this approximation works for graphite when the thickness does not exceed ∼5 nm

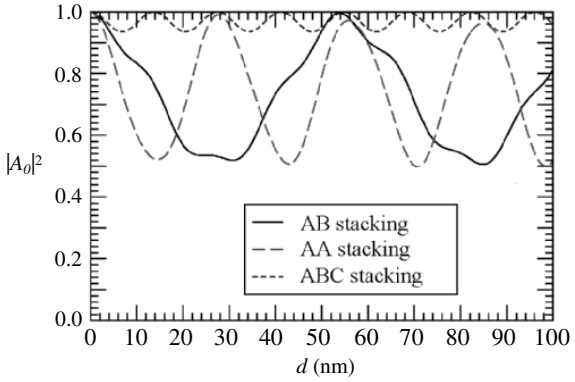


Fig. 3.5. Intensity $|A_0|^2$ of the central beam through a graphitic (001) slab as a function of thickness for three atomic-layer stackings: ABAB (usual hexagonal form), AAA (simple hexagonal), and ABC (rhombohedral). The incident energy is 200 keV (by courtesy of C. Barreteau)

with 200 keV electrons, which corresponds to 15 layers. When (3.16) is valid, the amplitude of the diffracted beams can be obtained by two-dimensional Fourier transformation of the projected potential, $V_\mathrm{p}(\boldsymbol{\rho}) = \sum_{\boldsymbol{g}} V_{\boldsymbol{g}}\, \mathrm{e}^{\mathrm{i}\boldsymbol{g}\cdot\boldsymbol{\rho}}$. This development gives

$$A_{\boldsymbol{g}} = \delta_{\boldsymbol{g},0} + \mathrm{i}\,(eV_{\boldsymbol{g}}/2E_0)\,k_0 d + O(d^2) = \delta_{\boldsymbol{g},0} + \mathrm{i}\,\sigma d\,V_{\boldsymbol{g}} + O(d^2) \qquad (3.22)$$

where $O(d^2)$ means that terms of order larger or equal to d^2 are omitted. This last expression is essentially consistent with the kinematical theory. The amplitude of the diffracted beam associated with a two-dimensional reciprocal lattice vector $\boldsymbol{g} \neq 0$ is found proportional to the Fourier transform of the projected potential of the surface unit cell times the thickness of the sample. This is indeed what (3.8) predicts for a two-dimensional scattering vector $\boldsymbol{q} = \boldsymbol{g}$ (Ewald's sphere approximated by a plane) when the potential V is assumed to be uniform over the thickness d of the sample.

It is generally admitted that the kinematical theory is valid when the sample thickness d is much smaller than the so-called extinction distance $\xi_{\boldsymbol{g}}$ for all the Bragg beams. This parameter represents the distance after which the wave intensity is totally transferred by elastic scattering from the forward beam to the diffracted beam $\boldsymbol{g}$ in the exact Bragg orientation. It is given by $\xi_{\boldsymbol{g}} = \lambda E_0/|eV_{\boldsymbol{g}}|$ with $\lambda = 2\pi/k_0$ the electron wavelength. The condition $d \ll \xi_{\boldsymbol{g}}$ is precisely what validates (3.22).

3.1.3 HREM Imaging

According to the Abbe linear theory of image formation, the image amplitude is the inverse Fourier transform of the diffraction pattern amplitude. In

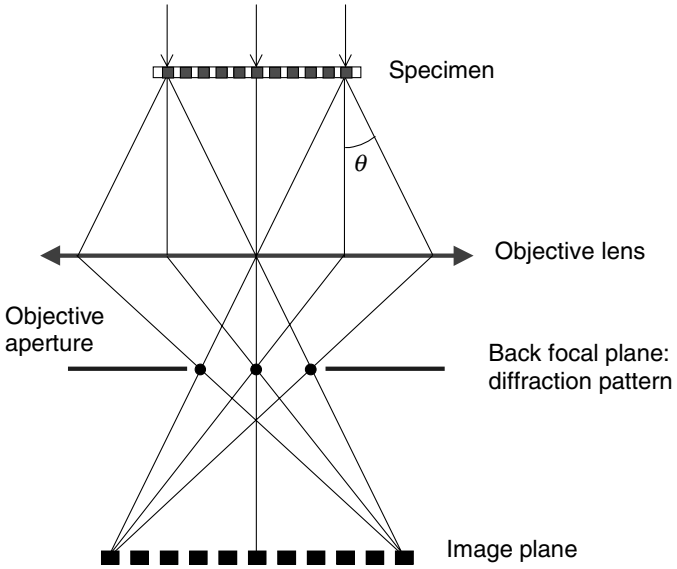


Fig. 3.6. Principles of the image construction in a transmission electron microscope

a transmission electron microscope schematized in Fig. 3.6, the electromagnetic objective lens receives the diffracted beams from sample (see (3.9)). The diffracted beams are focused on a set of spots in the back focal plane of the lens where they form the diffraction pattern of the crystal. In turn, these spots act as sources of spherical waves, which will be used to form an image.

In practice not all the diffracted beams are taking part in the image reconstruction[2]. Bright- or dark-field images correspond to imaging modes where, respectively, the transmitted or a diffracted beam is selected by the objective aperture. In this case, the image contrast is governed by the beam intensity $|A_0|^2$ or $|A_{\boldsymbol{g}}|^2$. In the high-resolution electron microscope (HREM) mode, the transmitted and some diffracted beams are allowed to interfere, by choosing an appropriate objective aperture. In this case, the phase of the different beams also controls the contrast in the reconstructed image. Since the HREM imaging is a two-step process (transfer of electrons across the specimen and microscope transfer function), the different steps will be described via simulations to sustain the main ideas developed in the previous paragraphs. In particular, the conditions under which the weak phase object approximation can be used for carboneous materials will be explored. HREM imaging of a widely used catalyst Ni will be emphasized for comparison. The reader is invited to refer to some general references on HREM [7–11].

[2]Due to the high energy incident electrons, the electron diffraction pattern results from a planar cut of the sample reciprocal space, and reversely the image is the projection of the sample along the electron beam direction. Nevertheless, images are sensitive to lens aberrations unlike diffraction patterns, as explained in this section.

HREM: A Phase Contrast Imaging Mode

The wave function at the exit face of the sample results from the interference of the diffracted beams with the transmitted beam, and is calculated owing the knowledge of the projected electrostatic potential $V_\mathrm{p}(\boldsymbol{\rho})$. The projected potentials for one graphene sheet viewed perpendicularly, for graphite viewed along [001] and [210][3], and for a Ni crystal viewed along [110] are shown in Fig. 3.7. The calculated mean inner projected potential, which corresponds to the zero order term V_0 in the Fourier series of V_p, see (3.22), varies from 4.4 V (for one sheet of graphene in a 1.3 nm thick vacuum slice), to 9 V (for a 0.7 nm thick slice of graphite) and to 7.2 V (for a 0.25 nm thick slice of Ni). For an average potential of 10 V, the weak phase object condition (3.16) $\sigma V_\mathrm{p} z \ll 1$ demands a sample thickness $d = z$ far less than 11 nm at 100 kV ($\sigma = 0.009\,\mathrm{V}^{-1}\,\mathrm{nm}^{-1}$), 14 nm at 200 kV ($\sigma = 0.0073\,\mathrm{V}^{-1}\,\mathrm{nm}^{-1}$), and 16 nm at 400 kV ($\sigma = 0.0062\,\mathrm{V}^{-1}\,\mathrm{nm}^{-1}$).

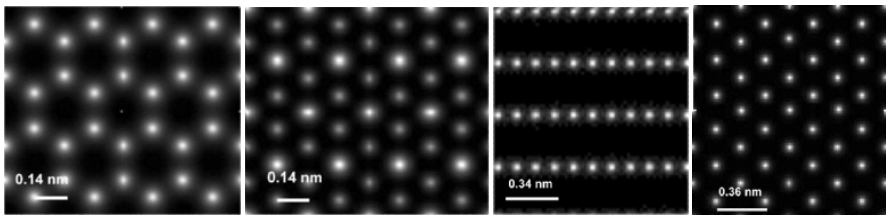


Fig. 3.7. *From left to right*: projected potential for graphene in a 1.3 nm thick vacuum slice, for graphite(001) over 0.7 nm, for graphite(210) over 0.24 nm, and for Ni(011) over 0.25 nm. In the case of graphite(210) the smallest distance between the atomic columns is 0.123 nm

Once the periodic potential is known, the modulus $a_{\boldsymbol{g}}$ and phase $\varphi_{\boldsymbol{g}}$ of the amplitudes $A_{\boldsymbol{g}} = a_{\boldsymbol{g}}\,\mathrm{e}^{\mathrm{i}\varphi_{\boldsymbol{g}}}$ of the transmitted and diffracted beams can be calculated. The Bloch wave approach (3.18) shows that, if the crystal is oriented in such a way that dense atomic columns are parallel to the electron beam, thus generally only two Bloch states are contributing to the wave function, one being confined on atomic column. An optical approach, called 'multislice method', has been developed [12], which is widely used especially when large cells (containing for instance extended defects) are studied. In this latter approach, the specimen is cut into thin slices of thickness z_i where (i) the phase object approximation applies and (ii) a propagation in vacuum is assumed between two slices. The resulting wave function at the exit of the $(\mathrm{i}+1)^{\mathrm{th}}$ slice is

[3] We used here three Miller indices related to the unit vectors $\boldsymbol{a}_1$, $\boldsymbol{a}_2$, and $\boldsymbol{c}$ with $\gamma = (\boldsymbol{a}_1, \boldsymbol{a}_2) = 120^\circ$. This basis is not that usually chosen for nanotubes, where the angle between the two $\boldsymbol{a}_1$ and $\boldsymbol{a}_2$ unit vectors of the graphene sheet is 60°, as discussed in Sect. 2.4 in Chap. 1.

$$\psi_{i+1}(\boldsymbol{\rho}) = \psi_i(\boldsymbol{\rho})\, q(\boldsymbol{\rho}) \otimes p_i(\rho) \tag{3.23}$$

where $q(\boldsymbol{\rho}) = \mathrm{e}^{\mathrm{i}\sigma V_\mathrm{p}(\boldsymbol{\rho})z_i}$ is the wave function transmission factor and $p_i(\rho) = -\mathrm{i}/\lambda z_i \exp(\mathrm{i}\pi\rho^2/\lambda z_i)$ is the propagation function. $\otimes$ indicates a convolution product. The exit wave function is then deduced from N iterations of (3.23) to account for the total thickness of the sample.

The variation of amplitudes $a_{\boldsymbol{g}}$ and phases $\varphi_{\boldsymbol{g}}$ of the transmitted and diffracted beams are shown in Fig. 3.8 for graphite(001) and graphite(210), and Ni(110) with 400 keV electrons. Since graphene is the low thickness limit of graphite, graphene is the true weak phase object with $\varphi_{\boldsymbol{g}} - \varphi_0 = \pi/2$ and $a_{\boldsymbol{g}} \ll a_0$. In the graphite(001) case, the 100 diffracted beam corresponding to a spatial frequency $u = g/2\pi = 1/0.214\,\mathrm{nm}^{-1}$ oscillates slowly with thickness (with a Pendellösung distance[4] larger than 70 nm), unlike the 110 beam ($u = 1/0.1235\,\mathrm{nm}^{-1}$) which oscillates with a 20 nm extinction distance. This is the reason why the transmitted beam has two frequencies as already shown in Fig. 3.5. The same behavior occurs on the phase variation. The main point is that graphite can no longer be considered as a weak phase object as soon as the thickness becomes larger than 10 nm (at 400 kV), and this is more restrictive for Ni as seen from amplitudes and phases variations in Ni(110), where the phase varies strongly as thickness increases. All the simulations were made using the EMS code by P. Stadelmann [13].

The exit wave function is a complex function and thus can be written as $\psi(\boldsymbol{\rho}, d) = A(\boldsymbol{\rho}, d)\, \exp[i\Phi(\boldsymbol{\rho}, d)]$, where A^2 is the wave function intensity in the exit plane of the specimen of thickness d, and Φ is the phase shift between the entrance and exit sides of the sample. Both A^2 and Φ variations with d are shown in Fig. 3.9 for graphene, graphite viewed along [001], and Ni viewed along [011]. In the graphene case (with only one slice by definition), A^2 remains around 1 and $\Phi \approx 0$. As a consequence $\psi(\boldsymbol{\rho}, d) = 1 + \mathrm{i}\Phi$ where the imaginary factor i accounts for the phase shift $\varphi_{\boldsymbol{g}} - \varphi_0 = \pi/2$ between the transmitted and the diffracted electrons. As expected for a weak phase object, the wave function intensity is $I = 1 + \Phi^2$, thus the contrast is nearly zero[5].

Considering the evolution of the intensity for graphite viewed along 001, as far as the thickness remains lower than 10 nm, the intensity maxima are positioned on the atomic columns with a weight proportional to V_p^2 but for a larger thickness, A^2 reflects only the positions of the doubled columns in the ABAB hexagonal sequence. A rapid phase variation is associated with this behavior, which essentially comes from the fact that, in projection, the atomic columns are only 0.142 nm distant. This behavior is linked to the relative weight of the Bloch states according to (3.18) and is enhanced at a lower accelerating voltage. In the Ni case, the atoms are heavier but their distance in the [110] projection is about 0.2 nm so that the A^2 and Φ variations with thickness follow the channeling behavior up to 5 nm. The phase strongly

[4] Corresponding to the extinction distance in Laüe conditions.

[5] Contrast $= (I_{max} - I_{min})/\langle I \rangle$ where $\langle I \rangle$ is the image mean intensity.

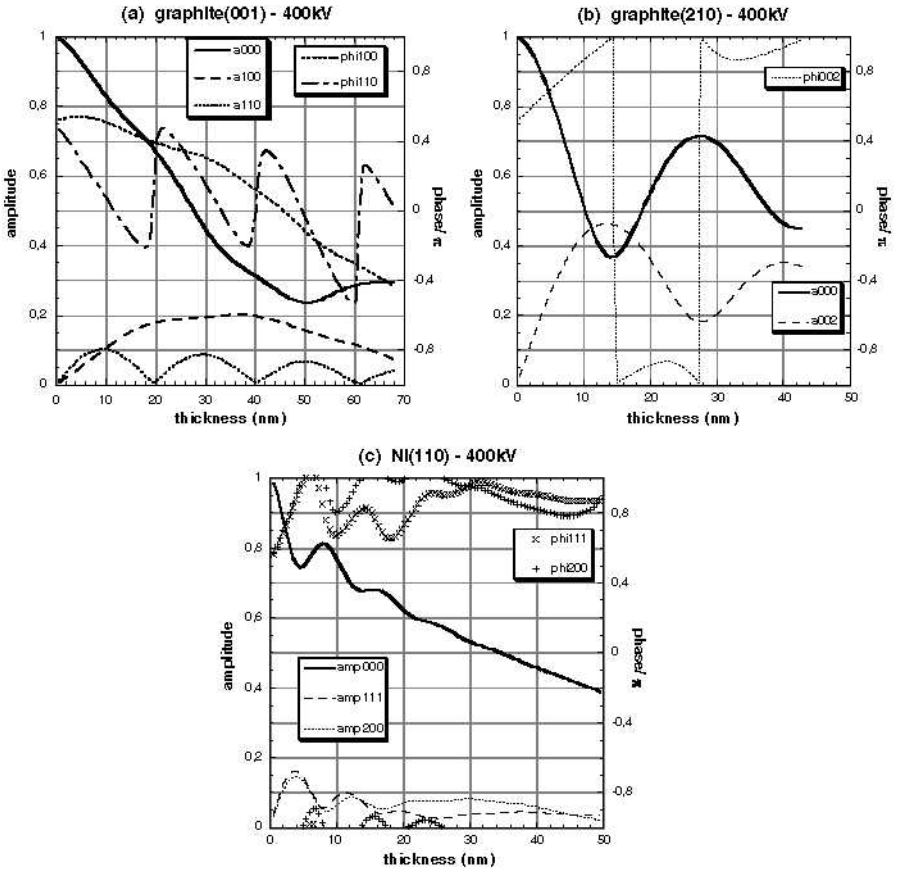


Fig. 3.8. Amplitude and phase variations with thickness of 400 keV electrons transmitted or diffracted by **(a)** graphite viewed along [001], **(b)** graphite viewed along [210], and **(c)** Ni viewed along [110]. A graphene sheet is the limit case of graphite when the thickness tends to zero. This is the illustrative case of a weak phase object

oscillates only at the column positions. As a conclusion, the exit wave function does not necessarily reflect the atomic positions and this information will be even more blurred by the microscope aberrations.

Transfer Function: HREM Images of Graphene, Graphite and Ni Catalyst

The wave function is strongly affected by the electron microscope optical aberrations, which influence both the phase and the amplitude of the electron beams. On the one hand, geometrical aberrations introduce a supplementary phase shift $\chi_{\boldsymbol{g}}$, depending on the spatial frequencies $u = g/2\pi$ of the diffracted beams, and the so-called coherent transfer function describes the effect of

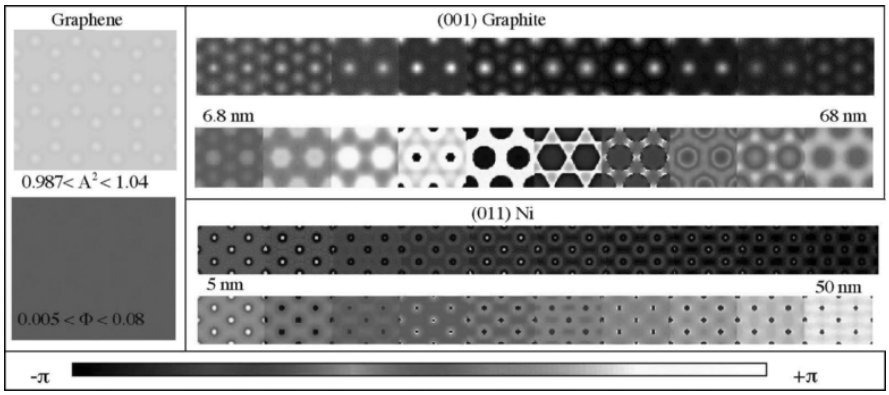


Fig. 3.9. Intensity and phase of the exit wave function (400 kV) for graphene, graphite viewed along [001], and Ni viewed along [011]. In the last two cases the variations of A^2 and Φ with thickness are shown

angular and/or field aberrations. On the other hand, the loss of coherence in the incident beam, due to chromatic aberrations and beam divergence, introduces strong dumping in the amplitude of the coherent transfer function.

For simplicity, only two main angular aberration contributions to $\chi_{\boldsymbol{g}}$ will be considered here, one is due to the defocus (proportional to the square θ^2 of the scattering angle, where $\theta \approx g\lambda/2\pi$ for high-energy electrons, see Fig. 3.1) and the other to the spherical aberration (proportional to θ^4):

$$\chi_{\boldsymbol{g}} \equiv \chi(g/2\pi) = -2\pi[C\mathrm{s}\,\lambda^3(g/2\pi)^4/4 + \Delta z\lambda(g/2\pi)^2/2] \tag{3.24}$$

where Cs is the spherical aberration coefficient and is generally fixed for a given microscope, and Δz is the defocus and can be adjusted experimentally[6]. It has to be noticed that $\chi_{\boldsymbol{g}}$ exhibits the cylindrical symmetry, which will be broken if misalignment, astigmatism or coma are present for instance. Thus the image wave function of a crystal (see (3.9)) is affected according to

$$\Psi' = \sum_{\boldsymbol{g}} \mathrm{e}^{+\mathrm{i}\chi_{\boldsymbol{g}}}\, A_{\boldsymbol{g}}\, \mathrm{e}^{\mathrm{i}\boldsymbol{g}.\boldsymbol{\rho}+\mathrm{i}k_0 z} = \psi'(\boldsymbol{\rho}, d)\, \mathrm{e}^{\mathrm{i}k_0 z} \tag{3.25}$$

For a weak phase object, the influence of the aberrations can easily be calculated through the Abbe linear theory. Using the expression (3.22) of the diffracted amplitudes $A_{\boldsymbol{g}}$, the weak phase object wave function, modified in the fully coherent case, becomes

$$\psi'(\boldsymbol{\rho}, d) = 1 + \mathrm{i}\,\sigma d \sum_{\boldsymbol{g}} \mathrm{e}^{+\mathrm{i}\chi_{\boldsymbol{g}}}\, V_{\boldsymbol{g}}\, \mathrm{e}^{\mathrm{i}\boldsymbol{g}.\boldsymbol{\rho}} = 1 + \mathrm{i}\,\sigma d\, \mathrm{TF}^{-1}[\mathrm{e}^{\chi_{\boldsymbol{g}}}.\mathrm{TF}(V_\mathrm{p})]\ , \tag{3.26}$$

[6] In the following, negative defocus is assigned to underfocus, by contrast to EMS where underfocus is assigned to positive value.

where TF means 2-D Fourier transform. This expression leads to an image intensity (neglecting second order terms)

$$I'(\boldsymbol{\rho}, d) = \psi'(\boldsymbol{\rho}, d)\psi'(\boldsymbol{\rho}, d)^* = 1 + \sigma d\, \mathrm{TF}^{-1}[-2 \sin \chi(u).\mathrm{TF}(V_\mathrm{p})] \; . \tag{3.27}$$

In the linear transfer theory, $T(u) = -2 \sin \chi(u)$ is called the coherent contrast transfer function for a weak phase object, where $u = g/2\pi$ is a spatial frequency. In these notations, the intensity I' can also be written as a convolution product

$$I'(\boldsymbol{\rho}, d) = 1 + \sigma d\, V_\mathrm{p}(\boldsymbol{\rho}) \otimes h(\boldsymbol{\rho}) \tag{3.28}$$

where $h(\boldsymbol{\rho}) = \mathrm{TF}^{-1}[-2 \sin \chi(u)]$ is the point spread function of the microscope. As a consequence, the contrast is proportional to the specimen projected potential $V_\mathrm{p}(\boldsymbol{\rho})$ convoluted by the impulse response $h(\boldsymbol{\rho})$. Considering the expression of $T(u)$, an optimal focus exits, called Scherzer focus, $\Delta z_s = -1.2\sqrt{C\mathrm{s}\,\lambda}$ where the transferred spatial frequency band is the largest one. Figure 3.10 shows the transfer functions $T(u)$ for different defocusing distances for a 400 kV electron microscope with $C\mathrm{s} = 1.05\,\mathrm{mm}$. The Scherzer focus is $\Delta z_s = -50\,\mathrm{nm}$. It is clear that the contrast of the $3\,\mathrm{nm}^{-1}$ spatial frequency corresponding to $c/2$ graphite interplanar distance depends on the defocus: it is positive at zero defocus, negative for $-50\,\mathrm{nm}$ defocii, and is close to zero at $-75\,\mathrm{nm}$.

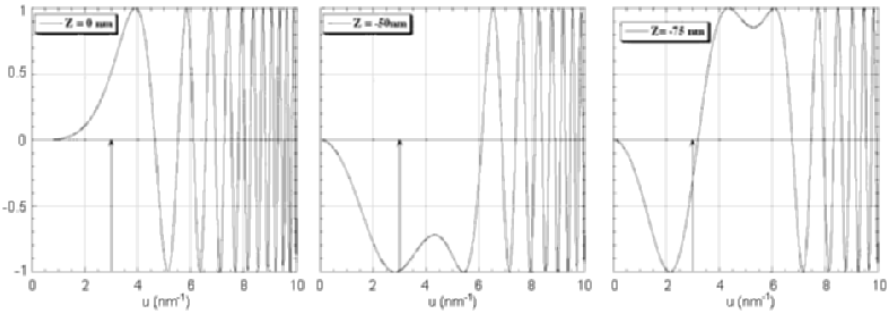


Fig. 3.10. Coherent transfer functions for three underfocii **(a)** $\Delta z = 0\,\mathrm{nm}$, **(b)** $\Delta z = -50\,\mathrm{nm}$, and **(c)** $\Delta z = -75\,\mathrm{nm}$. The spatial frequency corresponding to $u = 2/c = 3\,\mathrm{nm}^{-1}$ is outlined by an arrow

One key parameter for a microscope is the point resolution, defined as the reciprocal of the first zero of the transfer function $T(u)$ at Scherzer defocus

$$R_\mathrm{p} = 0.64\,(C\mathrm{s}\,\lambda^3)^{1/4} = 0.49\,\sqrt{|\Delta z_s|^3/C\mathrm{s}} \; . \tag{3.29}$$

In practice, one always deals with partially coherent illumination. The lateral or spatial coherence is fixed by the divergence of the incident beam, while

the longitudinal or temporal coherence is governed by non monochromaticity and electronic instabilities. The effect can be easily estimated assuming an incoherent Gaussian effective source illuminating an object in kinematical conditions [14]. Therefore, the combined effect of partial coherencies leads for weak phase object to a contrast transfer function

$$T(u) = \Theta(u)\, G_1(u)\, G_2(u)\, [-2 \sin \chi(u)] \tag{3.30}$$

where $\Theta(u)$ is the objective aperture function, which selects a given interval of spatial frequencies. $G_1(u)$ is due to the defocus spread linked to the chromatic aberration and accounts for temporal partial coherence

$$G_1(u) = \exp(-\pi^2 \lambda^2 \delta^2 u^4/2) \tag{3.31}$$

$$\delta = C\mathrm{c}\, \sqrt{(\Delta V/V)^2 + (\Delta E/E)^2 + 2(\Delta I/I)^2} \tag{3.32}$$

where $C\mathrm{c}$ is the chromatic aberration coefficient, and $\Delta V/V$, $\Delta E/E$, $\Delta I/I$ are the electron energy spread, the high voltage and objective current instabilities, respectively. $G_1(u)$ introduces a cut-off frequency, which is an other important key parameter: the information limit, defined as the frequency where the amplitude contrast is reduced by a factor of e. The corresponding resolution limit is then given by $R_i = \sqrt{\pi \delta \lambda/2}$. $G_2(u)$ is due to the beam divergence and accounts for spatial partial coherence:

$$G_2(u) = \exp[-\pi^2 \alpha^2 u^2 (C\mathrm{s}\, \lambda^2 u^2 + \Delta z)^2] \tag{3.33}$$

where α is the semi-divergence angle of the incident beam. It has to be noticed that $G_2(u)$ depends also upon the image defocus Δz. Figure 3.11 shows the point spread function $h(\boldsymbol{\rho}) = \mathrm{TF}^{-1}[T(u)]$ for different defocusing distances taking the spatial coherence into account. In the linear theory of image formation, the intensity is proportional to the convolution of $V_\mathrm{p}(\boldsymbol{\rho})$ with $h(\boldsymbol{\rho})$, as mentioned above. It can be easily seen that the 'color' of the atoms depends on $h(\boldsymbol{\rho})$: at $\Delta z = 0\,\mathrm{nm}$, the atoms or the areas of high projected potential are imaged in white, whereas at Scherzer defocus $\Delta z = -50\,\mathrm{nm}$, the reverse is true as already mentioned from the fully coherent transfer function behavior.

The influence of the microscope can be well simulated and the images of graphene, graphite and Ni will be shown as function of the two main experimental parameters, namely thickness and defocus. The conditions are 400 keV electrons, $C\mathrm{s} = 1\,\mathrm{mm}$, defocus spread $\delta = 8\,\mathrm{nm}$, semi-divergence angle $\alpha = 0.5\,\mathrm{mrad}$, and a $20\,\mathrm{nm}^{-1}$ objective aperture function $\Theta(u)$. Since graphene is only one carbon sheet, image simulations are just shown as function of defocus. Figure 3.12 shows the very low contrast expected from such an object whatever the focusing distance. The two main points are that firstly the atoms cannot be resolved by the microscope and secondly the contrast is mainly linked to the holes in the structure and oscillates with defocus: the holes appear black and white regularly. For instance, at a 20 nm underfocus, the areas with the denser potential are imaged in white according to Figs. 3.10

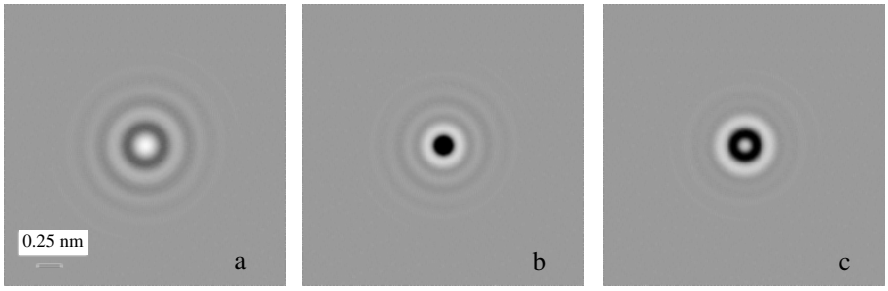


Fig. 3.11. Point spread functions $h(\boldsymbol{\rho})$ for $\Delta z = 0$ **(a)**, -50 **(b)**, -75 nm **(c)** in the case of a 400 kV electron microscope with $C\mathrm{s} = 1\,\mathrm{mm}$

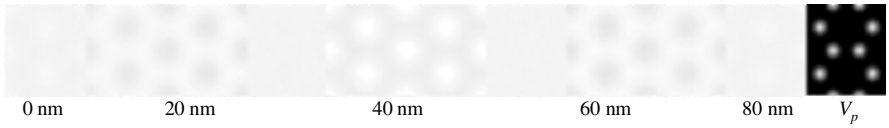


Fig. 3.12. Graphene image simulation for an underfocus series. The contrast is very low (<0.03) and the projected potential is shown on the right-hand side (400 kV, $C\mathrm{s} = 1\,\mathrm{mm}$, $\delta = 8\,\mathrm{nm}$, $\alpha = 0.5\,\mathrm{mrad}$)

and 3.11, consequently the holes appear black. The reverse is true for a 50 nm underfocus and so on.

In the cases of graphite and nickel, focus-thickness maps (Figs. 3.13 and 3.14) reveal that the contrast strongly varies with experimental conditions, which reflects the facts that, firstly the amplitude and phase of the diffracted beams vary with thickness (as shown in Fig. 3.8) and, secondly, in the linear theory the transfer function varies periodically with focus. For graphite, in both [001] and [210] projections (Figs. 3.13a and 3.13b), the contrast of individual atomic columns is hardly visible in the chosen experimental conditions. From the [210] projection map, it is clear that the knowledge of atomic plane 'black or white color' is of the main importance for a reliable determination of the layer number in a multi-wall nanotube. The fringe contrast results from the interference between the three 002, $00\overline{2}$, and transmitted beams. As long as the weak phase object condition is fulfilled ($d \ll 10\,\mathrm{nm}$) the fringe contrast is governed by the contrast transfer function $T(u) = -2\sin\chi(u)$. In agreement with Fig. 3.9, the atomic planes are white at 0 nm defocus and dark at Scherzer focus, whereas at -75 nm the d_{002} fringe contrast vanishes. As soon as the weak phase object condition fails, the contrast depends also on the thickness as attested by the variation of the low contrast zones: fringes with a $c/4$ interplanar distance may appear ($\Delta z = -75\,\mathrm{nm}$ and $d = 8.5\,\mathrm{nm}$), which could lead to misinterpretation.

For nickel in [110] projection, each atomic column is also revealed black or white, depending on the experimental conditions. Nevertheless, around

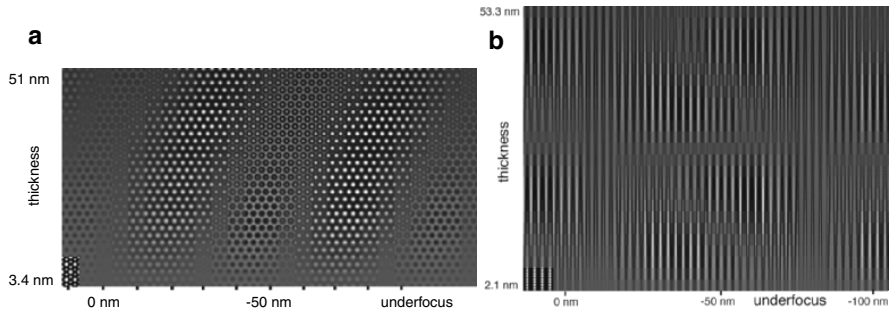


Fig. 3.13. HREM image simulations for **(a)** graphite(001) and **(b)** graphite(210) as a function of defocus Δz and thickness (400 kV, Cs = 1 mm). The projected potential is drawn at the bottom left

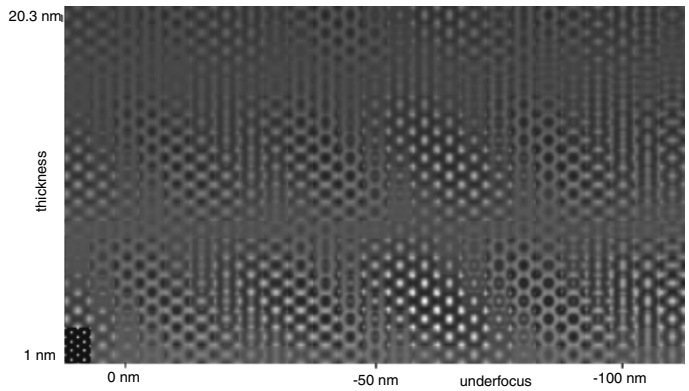


Fig. 3.14. HREM image simulation of Ni(110) (400 kV, Cs = 1 mm). The projected potential is shown in the frame bottom left

Scherzer focus as previously expected from the point spread function and for very thin samples where the phase object approximation is valid, the atoms are imaged in 'black' in other words the white dots are related to holes in the projected structure.

3.1.4 Scanning Tunneling Microscopy

In a scanning tunneling microscope (STM), an atomically sharp and conducting tip is brought at a fraction of a nanometer above a conducting sample surface. A bias potential V, typically 0.1–1 V, is applied between tip and sample. Because of the small separation distance, a tunnel current of the order of 1nA sets up across the tip-sample gap. In the most commonly used setup of the STM, called the topographic mode, the tip mechanically scans the sample surface (in the (x, y) plane) by piezo actuators, while a feedback loop controls the height of the tip above the sample (z coordinate of the tip) in such a way

as to maintain the tunnel current at a constant, preselected value. The STM $z(x, y)$ topographic image is then constructed from the voltages applied to the piezoelectric devices that pilot the tip.

The simplest description of the STM principles is based on one-dimensional (1D) tunneling theory. When an electron of energy E_0 is incident on a rectangular potential barrier of height U and width Δ, the transmission probability is

$$T = \exp(-2\kappa\Delta) \ , \ \kappa = \sqrt{2m(U - E_0)/\hbar^2} \ . \tag{3.34}$$

This expression is valid at the asymptotic limit of vanishing transmission. In an STM, one of the electrodes is not planar, but is a sharp tip. Due to the exponential dependence of the tunneling probability on the distance, most of the tunnel current flows in a narrow channel between the tip apex and the sample. The typical minimum half width at half maximum of the tunneling channel realized with a sharp tip is 0.1–0.2 nm [15, 16].

Any quantitative interpretation of STM data demands to go beyond the 1D tunnel barrier. The simplest, still approximate, approach of the full 3D tunneling problem consists in treating the tip-sample interaction as a small perturbation. Consider at this end an occupied electronic state of the tip, α, and an unoccupied state of the sample, β, and introduce at time $t = 0$ a stationary, weak coupling interaction v between the two electrodes. Time-dependent perturbation theory then shows that, for large t, the probability for an electron to go from α to β vanishes unless the two states lie exactly at the same energy:

$$P_{\alpha\to\beta}(t) \sim \frac{2\pi}{\hbar} |\langle\alpha|v|\beta\rangle|^2 \delta(E_\beta - E_\alpha) \ . \tag{3.35}$$

Provided there is an external wire enabling the circulation of the transferred electrons, a stationary current sets up across the gap between tip (t) and sample (s). This current is the time derivative of the transfer probability (3.35), multiplied by the electron charge. The total current is the sum over all states, labeled by their energy E, multiplied by the difference between the Fermi distributions $f(E)$ on both sides of the junction:

$$I = \frac{-2\pi e}{\hbar} \int_{-\infty}^{+\infty} dE \ [f_{\rm t}(E) - f_s(E)] \sum_{\alpha,\beta} |\langle\alpha|v|\beta\rangle|^2 \delta(E - E_\alpha)\delta(E - E_\beta) \ . \tag{3.36}$$

At zero degree, assuming a rigid shift of the electronic levels of the tip generated by the contact potential (difference $\delta E_F = E_F^t - E_f^s$ between the Fermi energies of the separated electrodes) and the tip bias V, this expression reduces to

$$I = (2\pi)^2 \ \frac{e}{\hbar} \int_{E_F - eV}^{E_F} dE \ \sum_{\alpha,\beta} |\langle\alpha|v|\beta\rangle|^2 \delta(E - E_\alpha + \delta E_F + eV)\delta(E - E_\beta) \ . \tag{3.37}$$

In the well-known Tersoff-Hamann theory [17], the Bardeen approximation is used to evaluate the coupling matrix elements $\langle\alpha|v|\beta\rangle$. Furthermore, the tip wavefunction is usually assumed to be a spherical wave, localized at the center of curvature $\boldsymbol{r}_0$ of the tip apex. The main result of this theory is that the tunneling current is a convolution of the tip density of states $n_{\rm t}(E)$ with the local density of states of the sample $\rho_s(E, \boldsymbol{r}_0)$ *at the tip location*,

$$I \propto \int_{E_F - eV}^{E_F} n_{\rm t}(E - \delta E_F - eV)\, \rho_s(E, \boldsymbol{r}_0)\, dE \ . \tag{3.38}$$

The local density of states of the sample can be computed by standard band-structure techniques, including 'ab-initio' methods. This quantity decreases exponentially with the distance from the sample surface, implying an exponential decay of the tunneling current with increasing tip-sample distance.

Within a tight-binding approach, it is possible to derive a slightly different form of the tunnel current, which can easily be evaluated on the computer, even for complex and non crystalline samples. In tight-binding, the electronic states of the tip and sample are written as linear combinations of atomic orbitals located at the corresponding atomic sites i and j:

$$|\alpha\rangle = \sum_{i\in t} \chi_i^\alpha |\eta_i\rangle \ , \ |\beta\rangle = \sum_{j\in s} \psi_j^\beta |\theta_j\rangle \ . \tag{3.39}$$

For simplicity, one has assumed that there was one orbital per atom. For applications to nanotubes presented in Sect. 3.4, this will be the carbon π orbital. Inserting these LCAO expressions in (3.37) leads to [18]

$$I = (2\pi)^2 \, \frac{e}{h} \int_{E_F - eV}^{E_F} dE \sum_{i,i'\in t} \sum_{j,j'\in s} v_{ij} v^*_{i'j'} n^t_{ii'}(E - \delta E_F - eV) n^s_{jj'}(E) \tag{3.40}$$

where $v_{ij} = \langle\eta_i|v|\theta_j\rangle$ is the tip-sample coupling element between two atomic orbitals. In (3.40),

$$n^s_{jj'}(E) = \sum_\beta \psi_j^{\beta *} \delta(E - E_\beta) \psi_{j'}^\beta = (-1/\pi)\ {\rm Im}\ G^s_{jj'}(E + {\rm i}0^+) \tag{3.41}$$

with $G^s_{jj'}(z)$ a Green function element of the sample for the complex energy z. A similar expression is defined for the tip. The *diagonal* elements $n^t_{ii}(E)$ and $n^s_{jj}(E)$ are the local densities of states on sites i and j of the tip and sample, respectively. If, for the sake of illustration, one considers just one coupling element between the ending atom of the tip and a single atom of the sample – the one closest to the tip, the double summation in (3.40) reduces to a single term with diagonal elements n^t_{ii} and n^s_{jj}, namely the unperturbed local densities of states on the two coupled atoms. The current is then a convolution product of these two densities of states over the bias window, multiplied by $|v_{ij}|^2$. This resembles the Tersoff-Hamann result (3.38), except that the densities of states are computed on their own atomic sites. Here, the quantity that decreases exponentially with the distance is the tip-sample coupling interaction v_{ij}.

3.2 Analysis of Graphene-Based Structures with HREM

This section will provide examples and explanations on the observed different structures of graphene-based objects, when investigated by some of the basic modes of the transmission electron microscopy (electron diffraction, lattice fringe imaging, and dark-field imaging). Further information may be found in review articles such as [19, 20].

3.2.1 Electron Diffraction

Because of the specificity of graphene-based materials, which present a continuum in the possible structures from 2D (turbostratic polyaromatic carbon[7], often called turbostratic graphite) to 3D (genuine ABABAB graphite), electron diffraction patterns display specific features that material scientists may not be always familiar with. Beside considering the theoretical aspects presented in the previous section, understanding such features can be made graphically by considering the reciprocal image of a single graphene[8] (Fig. 3.15), then by figuring out what happens to it when several graphenes are associated as flat stacks, and what the intersect of such a reciprocal image by the reciprocal image of the incident electron wave – i.e., the Ewald sphere – looks like.

Figure 3.16 illustrates this. The real object sketched in this figure corresponds to a quite frequent situation for polyaromatic carbon materials since it may correspond to anisotropic polyaromatic carbon films (such as those obtained from chemical vapor deposition of carbonization of polymer thin films for instance), or more generally to a pore wall portion in many kind of polyaromatic carbon materials with isotropic, porous texture.

An important consequence of the elongated shape of the reciprocal nodes (helped with the very large diameter of the Ewald sphere) is that the reciprocal rods could intercept the Ewald sphere surface in orientation situations where regular – i.e., dimensionless – reciprocal nodes for large 3D structures would not. In other words, beam scattering (i.e., diffraction) may occur even though graphene stacks are not tilted relative to the electron beam or tilted from angles that differ from the otherwise requested related Bragg angles. That is why, for instance, the traces of both the 10 and 11 reciprocal cylinders are always seen on the electron diffraction patterns, despite that the related Bragg angles are quite different. Such an effect is named the interference error.

Unlike regular isotropically structured materials, diffraction patterns taken from an anisotropic polyaromatic carbon object appear quite different depending on their orientation relative to the electron beam. Figure 3.17a illustrates this for an object whose graphenes are oriented edge-on, i.e., nearly parallel

[7] In a turbostratic polyaromatic carbon, there is no coherence relationship between successive stacked graphenes, but the stacking periodicity.

[8] The unit vectors of graphite are used throughout this section, see note 3.

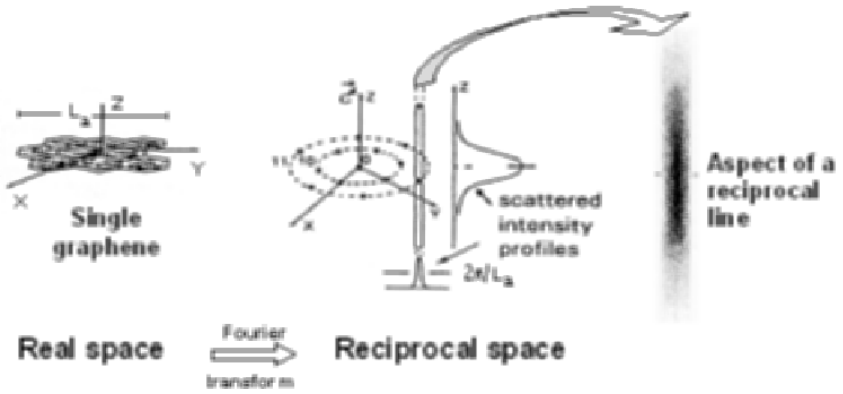


Fig. 3.15. Building the reciprocal image of a single graphene. With respect to the rules leading the reciprocal space, the reciprocal nodes the image is made up with are elongated in the c^* axis direction into nearly infinite reciprocal rods due to the fact that the related dimension of the real object (single graphene) is merely restricted to that of a single atom. Beside, the reciprocal rods are displayed as two sets of six whose Miller indices are 10 and 11 respectively. Each set exhibits the hexagonal symmetry, as the only symmetry feature present in the graphene lattice. The half width of the transversal intensity profile is as narrower as the extent of the graphene is larger (modified from [21])

to the electron beam, and Fig. 3.17b illustrates the same object lying flat, i.e., with graphenes oriented perpendicular to the electron beam.

Hence, the electron diffraction pattern from any polyaromatic carbon material can be understood by considering a combination of the latter and/or of the intermediate situations (i.e., oblique orientations, giving rise to diffraction patterns such as those worn by plane P_3^* in Fig. 3.16). For instance, carbon micro-fibers such as those prepared from spinning and subsequent carbonization of pitches or polyacrylonitrile-based polymers, or concentric-type multi-wall nanotubes all end up with graphenes oriented parallel to the fiber axis. The related reciprocal images of the latter are all the same and can be figured by rotating the reciprocal image of Fig. 3.16 around the $A^*A'^*$ axis, assuming that $A^*A'^*$ is parallel to the fiber axis. The related diffraction patterns of the whole objects are all similar, despite the major textural discrepancies which can exist depending on the fiber cross section (e.g. random, concentric, radial, etc., display of graphenes). Diffraction patterns obtained when the electron beam is perpendicular to the fiber axis mostly resemble that given in Fig. 3.17a, added with that of Fig. 3.17b and of all possible intermediate diffraction patterns in between (Fig. 3.18a). On the other hand, diffraction patterns obtained when the electron beam is parallel to the fiber axis mostly resemble that given in Fig. 3.17b, however with two major discrepancies. One is the occurrence of the 002 ring (possibly along with higher order $00l$ circles) together with the 10 and 11 rings (and possibly along with higher order hk

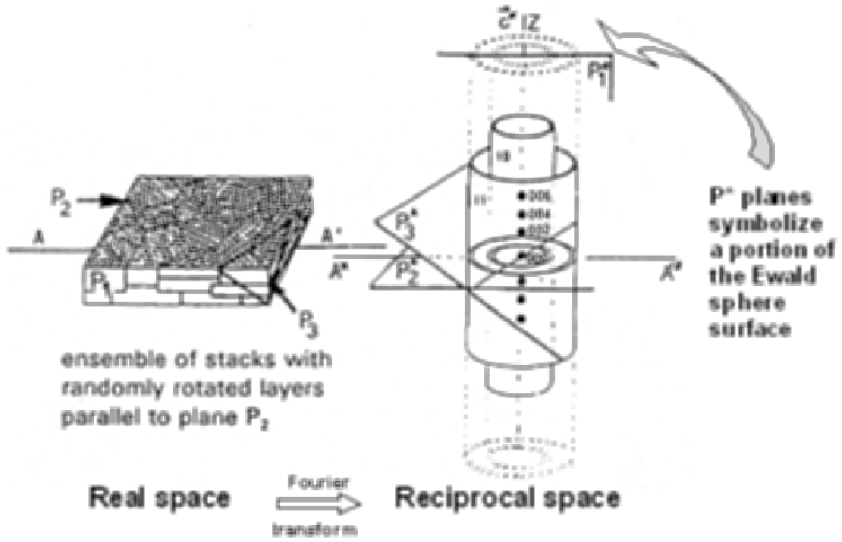


Fig. 3.16. Building the reciprocal image of an anisotropic, polycrystalline, polyaromatic carbon material made up with many graphene stacks. All graphenes, whatever the stacks they belong to, are parallel. Graphenes within each stack are superimposed incoherently, i.e., neighboring graphenes are randomly rotated with respect to each other, thus corresponding to the so-called turbostratic structure. Stacks are also laterally associated to each other incoherently, via grain boundaries. Each stack therefore is an independent bi-dimensional crystallite. The reciprocal image of the whole is built up with the addition of each reciprocal image for each graphene as sketched in Fig. 3.15. Due to the large number of randomly rotated but parallel graphenes, reciprocal rods are gathered into reciprocal cylinders 10 and 11, respectively. Other reciprocal elements appear, as $00l$ dots dispatched along the c^* axis due to the stacking periodicity, with the value of l increasing with the number of graphenes in the stack. The Ewald sphere surface portion intersecting the reciprocal image is approximated to a plane due to the very large $2\pi/\lambda$ radius of curvature of it, as opposed to X-ray for instance (adapted from [21])

circles). The other is the asymmetrical shape of the intensity profiles of the latter (Fig. 3.17c). Such an asymmetry of hk rings is typical of turbostratic structure) and is a common feature for electron diffraction patterns of most polyaromatic carbons, with the exception of some specific situations such as that illustrated in Fig. 3.17b. Figure 3.18b explains how such an asymmetrical intensity profile (band profile) is reached in the case of fiber cross sections.

On the other hand, polyaromatic carbon materials such as carbon blacks, glassy carbons, coals, etc, whose the overall texture is isotropic, exhibit similar diffraction patterns whatever the orientation relative to the electron beam and the inner texture (concentric, radial, random ...). A typical electron diffraction pattern is shown in Fig. 3.17c, in which hk circles exhibit asymmetrical intensity profiles for reasons similar to that described in Fig. 3.18b. The

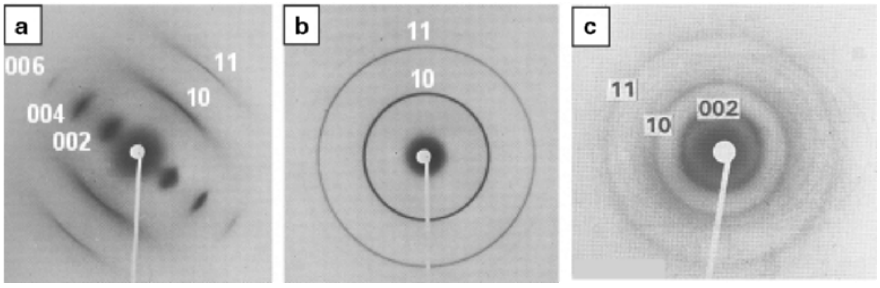


Fig. 3.17. Examples of electron diffraction patterns obtained from various polyaromatic carbon materials. **(a)** relates to Fig. 3.16, when the graphene orientation is parallel to the electron beam, so that the electron diffraction pattern is that contained in plane P_1^*. Both hk and $00l$ reciprocal elements are visible, as lines and dots respectively. **(b)** relates to Fig. 3.16, when the graphene orientation is perpendicular to the electron beam, so that the electron diffraction pattern is that contained in plane P_2^*. Only hk reciprocal elements are visible, as circles with symmetrical intensity profiles in the radial direction. **(c)** correspond to the diffraction pattern of a polyaromatic carbon material whose overall texture is so that it is made up with many ensembles of graphene stacks similar to that sketched in Fig. 3.16 but randomly displayed following all possible orientations. Both hk and $00l$ (here 002 only) reciprocal elements are visible, as circles. $00l$ circles exhibit a symmetrical intensity profile in the radial direction, while hk circles exhibit an asymmetrical intensity profile (band profile)

patterns resemble that of fiber cross sections as sketched on Fig. 3.18b, though with slight discrepancies regarding the position of the respective intensity maxima of the hk bands [20].

Though turbostratic is the most common structure for polyaromatic solids, graphitization is sometimes possible, mainly upon high temperature treatments ($>\sim$2500°C), for some of them. Since the graphitization event is progressive and results in an increasing number of graphene pairs achieving the AB stacking sequence of graphite, consequences on the electron diffraction patterns are a steadily sharpening and discretization of the reciprocal elements (rod or circle) with the occurrence of hkl reflections (such as 101 and 112, see Fig. 3.18a), accounting for the expansion of the coherent scattering volumes and the occurrence of the 3D structure of genuine graphite, respectively [19–21].

Hence, considering electron diffraction patterns may be of great help in determining the inner texture (isotropy, or type of anisotropy), structure (turbostratic, graphitic or partially graphitic), and nanotexture (perfection of graphenes within stacks) of graphene-based materials. However, possibilities of misinterpretations are numerous. The following listing is intended to help avoiding the most common mistakes, as often encountered in the published literature:

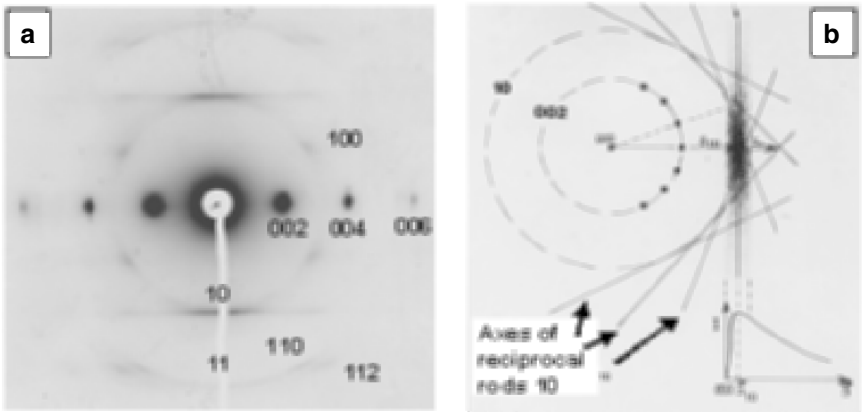


Fig. 3.18. (a) Electron diffraction pattern typical of a polyaromatic carbon fibrous texture in which all the graphenes are parallel to the fiber axis [22], and oriented so that the latter is perpendicular to the electron beam. Reciprocal elements such as 100, 110, and 112 occurred because the material was partially graphitized, and otherwise would be absent for a genuine turbostratic structure. **(b)** Construction of the electron diffraction pattern for an anisotropic fiber cross section, so that all the graphenes are oriented parallel to the electron beam, though according to a revolution symmetry. The electron diffraction pattern is obtained by adding all the patterns corresponding to Fig. 3.17a while rotating it around the pattern center (000 reciprocal node). Only the 002 and 10 circles and the reciprocal rod axes are sketched for clarity. The sum of the rotating reciprocal rods are responsible for the asymmetry of the resulting intensity profile. (Adapted from [20])

- 11 is not the second order of 10 (otherwise it should be labeled 20 and located at twice the 10 to 000 distance from the origin).
- A dotted pattern does not necessarily indicate a graphitized structure. It could merely reveal the contribution of large though turbostratic polyaromatic crystals. The only doubtless proof for actual graphitization is the occurrence of hkl reflections other than $00l$ and $hk0$.
- The absence of hkl reflections other than 10(0) or 11(0) does not necessarily points towards a turbostratic structure. The occurrence of the relevant reflections such as 101 or 112 could be prevented by the combination of specific material anisotropy and orientation relative to the electron beam (e.g. a graphite crystal lying flat).
- The absence of the 101 reflection for a randomly oriented, polycrystalline, polyaromatic solid does not necessarily indicate a turbostratic structure with no coherence relationship between successive graphene layers. Indeed, stacking faults in genuine graphite (i.e., ABC instead of ABAB stacking sequences) induce the broadening of this reflection [23]. *A contrario*, the 112 reflection remains sharp. Therefore, the doubtless witness for actual

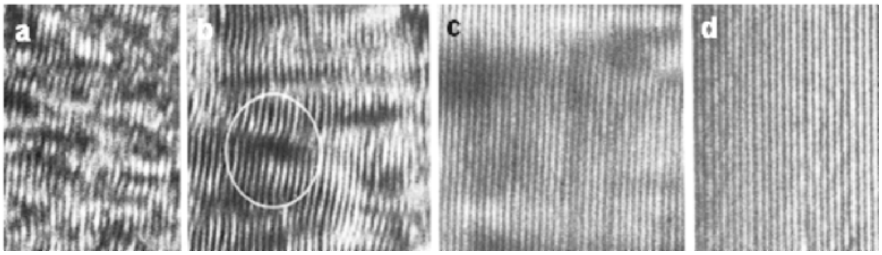


Fig. 3.19. Typical example of the removal of structural defects upon heat-treatment from **(a)** ∼1200°C to **(d)** ∼2800°C within a pore wall of a graphitizable carbon material. This overall behavior is the same whether the material is graphitizable or not, although the latter comes with some variations in the final values of the nanotexture parameters (see Fig. 3.20). The circled feature is an example of a Bragg fringe, which is discussed later on. The scale is given by the interfringe spacing, equal to 0.344 nm in (a), and to 0.335 nm in (d)

graphitization (with possible stacking faults) is the presence of the 112 reflection.

3.2.2 Lattice Fringe Imaging

Regular carbonization processes usually yield porous carbons (e.g. coals, carbonized polymers such as glassy carbons ...), whose average pore size basically depends on the intrinsic graphitizability of the material, from nanometer to micrometer (see Chap. I), while the graphene degree of perfection within the stacks making the pore walls depends on conditions such as temperature, time, pressure, catalytic activity ... In-plane (e.g. disclinations, such as those due to pentagons or heptagons replacing hexagons into the lattice) or out-of-plane (e.g. sp^3 carbon atoms, gathered into grain boundaries) structural defects induce a variable amount of distortions, which all are able to progressively heal along with a temperature treatment up to 2500°C and beyond (Fig. 3.19) whatever the graphitizability of the material. Indeed, the occurrence of stiff, perfect graphenes does not mean that the latter are stacked according to the graphite structure and may be still turbostratically stacked as well. Actually, graphenes from a graphitizable material reach the state of long range apparent perfection before acquiring the graphite stacking sequence [19, 20].

The so-called nanotexture describes the state and evolution of the graphenes within graphene ensembles, using parameters such as L_1, L_2, N, and β [19, 20] (Fig. 3.20), whose values are directly obtained from the 002 lattice fringe images (see the basics of this imaging mode in Sect. 3.1.3), i.e., visualizing graphenes seen edge on. Such values are quite important to know for directly relating to most of the physical properties of the material (see Chap. I). For this reason, though omitted in most of the published papers, nanotexture parameters should be provided for describing multi-wall nanotubes, as

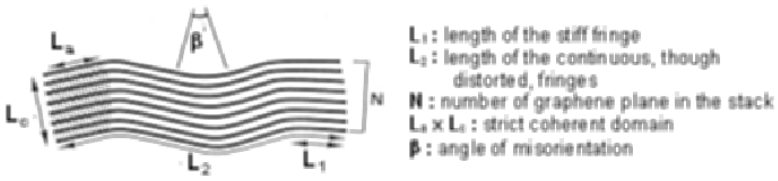


Fig. 3.20. Definition of the various parameters used to describe the nanotexture of polyaromatic carbon materials. L_1, L_2, N, and β are directly measured on the micrographs. L_1 is ideally equal to L_a, i.e., the average width of the coherent domain as calculated from X-ray diffraction. Same for N, ideally equal to L_c/d_{002}. (adapted from [19, 20]). However, due to several reasons, values from TEM and XRD exhibit variable discrepancies [24]

an important clue to distinguish between MWNTs within the same type (e.g. concentric texture).

Another specificity of graphene-based carbon materials is the difficulty to find out the actual texture from the projected image of it as a lattice fringe mode TEM micrograph. Such a difficulty does not exist for regular crystallized materials, in which atomic planes generally cannot bend the same way, which makes all the difference. Carbon materials are more or less porous, more or less anisotropic, and often built with nanosized graphene stacks associated into somehow flexible sheets, and both superposition and projection effects applied to such features result in unproper conditions for such a reconstruction (Fig. 3.21). Many serious scientists have fallen into the trap, illustrated by Fig. 3.21, and as a result, have proposed or supported texture models that are unrealistic, generally for allowing too many dangling bonds thereby making the modeled texture unlikely from an energetic point of view. For instance, any ribbon-like (or basket-like, etc.) model such as that sketched in Fig. 3.21d found in literature is misleading, whatever the material it is supposed to apply to (e.g. carbon fiber, glassy carbon ...).

3.2.3 Dark-Field Imaging

Among other use, such a mode is useful to reveal anisotropy features, specifically for materials where the low structural organization (e.g. with a low grade nanotexture, such as for 'basic structural units' BSU-made carbon materials – see Chap. I) and/or the imaging conditions (e.g. the specimen is not a weak phase object, due to over-thickness) prevent lattice fringes to show up when using the regular high-resolution mode. To operate this mode, starting from Fig. 3.6 the objective aperture opening has to be reduced so that the only beam passing through it is the direct (i.e., non scattered) beam (Fig. 3.22a). Then, the incident beam is tilted with the appropriate direction and angle so that a selected diffracted beam passes through the aperture instead (Fig. 3.22b).

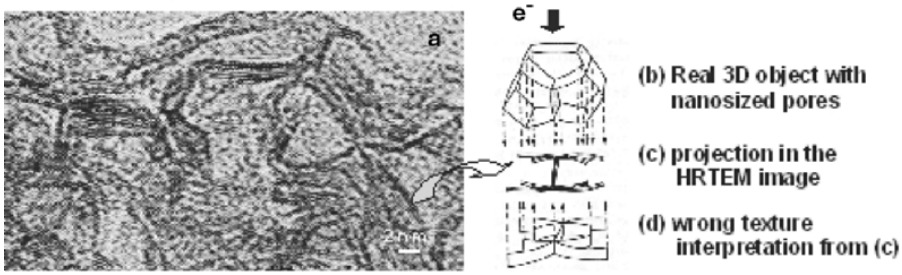


Fig. 3.21. (a) Lattice fringe image of carbonized saccharose heat-treated at 2800°C. The actual texture of it is close to that of a crumpled sheet of paper or, alternatively, that of a sponge, with pore size in the nanometer range, and whose pore walls are made of less than ∼10 stacked graphenes. **(b)** is a sketch of three adjacent pores. Though not represented for easier drawing, walls are also present at the back and at the front of the pores, so that the pores are closed. **(c)** is the projected, lattice fringe image of (b), taking into account that pore walls (i.e. graphene stacks) that are not under the Bragg angle (i.e., coarsely edge-on) cannot be seen. **(d)** is a wrong model of carbonized saccharose that could be deduced from lattice fringe images such as the image in (c). Adapted from [20]

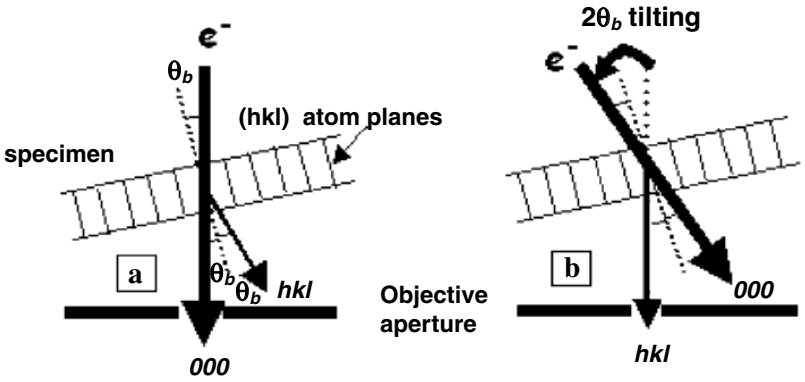


Fig. 3.22. Sketch of the way to operate dark-field imaging. The objective lens is not drawn for convenience, only its back focal plane is, where the objective aperture is located. **(a)** Contrasted bright-field mode, where every scattered beam but the direct beam passes through the aperture opening and builds the image. **(b)** Dark-field mode, where tilting the incident beam from the scattering angle $\theta = 2\theta_b$ allows the diffracted beam hkl to pass through the aperture and build the image. The image will show bright areas over a dark background (since no scattered beams come from the background). Every bright area corresponds to an area of the material where (hkl) planes are oriented so that they make an angle θ_b (= Bragg angle) relative to the incident beam (i.e., approximately oriented edge-on). (Adapted from [25])

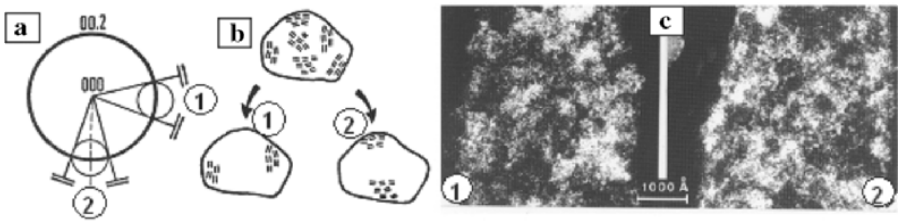


Fig. 3.23. **(a)** Two orthogonal positions of the objective aperture relative to the 002 ring from the diffraction pattern. **(b)** Sketch explaining the bright-island contrast found in the actual dark-field images in (c), starting from a material exhibiting areas of local molecular orientation. **(c)** Two 002 dark-field images from the same specimen area, as respectively obtained from positions 1 and 2 of the objective aperture, as sketched in (a). Bright domains are made of bright dots, each dot standing for one BSU (see Chap. I). BSUs within a single bright domain exhibit similar orientation (i.e., S-N in position 1 dark-field image, E-W in position 2 dark-field image). (Adapted from [26, 27])

Since this imaging mode does not involve any interference between several beams (except for Moirés, see below) the incident beam may be incoherent without affecting the image quality (amplitude contrast imaging). The main limitation regarding the resolution R, comes from the aperture opening β, according to the Abbe relation $R = 0.61\,\lambda/\beta$ where R is also called the Airy disc (i.e., the reciprocal image) of the objective aperture. Practically, using 'reasonable' aperture size (i.e., still allowing feasible aperture centering, astigmatism correction, etc.), resolution as good as $\sim$0.7 nm can be obtained (see Sect. 3.1.3), which is quite convenient for many of the problems addressed[9]. Most often, dark-field images are built using 002 diffracted beams, because of the convenient correspondence with the 002 lattice fringe images, and because 002 scattered beams are by far the most intense of the available diffracted beams of polyaromatic carbons. However, a single image is generally not sufficient to reconstruct and ascertain the material texture, and combination of at least two images corresponding to two different (e.g. orthogonal) azimuth directions is needed (Fig. 3.23a), thereby exploring azimuthally the reciprocal space. A first example of such a use of dark-field imaging is given in Fig. 3.23b, which corresponds to the early state (i.e., within the primary carbonization) of isotropically porous carbon materials such as glassy carbons, saccharose cokes, coals, polymer chars, pitch cokes, etc. Though bulkily isotropic and still dense so far, local anisotropies occur prefiguring the future pore walls. Such anisotropies are due to local preferred orientations of primary subnanometric, polyaromatic entities [26, 27] such as BSUs (see Chap. I). Size of the anisotropic areas and future graphitizability are interdependent.

[9]This value means that only coherent domains larger than 0.7 nm will appear with their real size, while smaller coherent domains will appear as 0.7 nm bright spots.

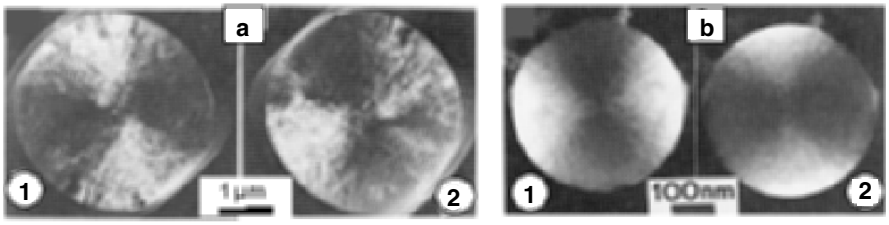


Fig. 3.24. Orthogonal 002 dark-field images of two types of polyaromatic carbon spherulites. Positions 1 and 2 refer to Fig. 3.23a. **(a)** The fact that quadrants (approximately) S-N then E-W light up for position 1 then 2 respectively indicates a radial texture. **(b)** The fact that quadrants E-W then S-N light up for position 1 then 2 respectively indicates a concentric texture. (Gathered from [28] and [29])

With respect to Fig. 3.23c, a material exhibiting graphene stacks with no preferred orientation will provide two undifferentiated images, with bright dots uniformly spread-out.

Dark-field imaging is also useful to reveal inner textures. Figure 3.24 provides two examples. Though morphologies are alike (i.e. spherical), inner textures are quite different, as revealed by the way quadrants light up when dark-field images are obtained using the same positions 1 and 2 as sketched in Fig. 3.23a, thank to a previous calibration. Figure 3.24a images a polyaromatic carbon spherulite such as obtained from high pressure carbonization of polyethylene [28] in which graphenes are displayed according to a radial texture. Figure 3.24b images a polyaromatic carbon spherulite – so-called carbon black – such as obtained from thermal-oxidative decomposition of liquid hydrocarbons [20,29], in which graphenes are displayed according to a concentric texture.

A last example of the use of azimuthal exploration of reciprocal space in the 002 dark-field imaging mode is given in Fig. 3.25. The material imaged in Fig. 3.25b is a cross section (Fig. 3.25a) of a thin pyrolytic carbon film obtained from thermal cracking of methane (chemical vapor deposition process). Deposition has proceeded from left to right. Though the whole deposit is anisotropic with most of the graphene stacks oriented parallel to deposition surface, the first $\sim$30 nm are obviously much more anisotropic than the subsequent deposit, indicating the topological but temporary influence of the substrate surface state (whose roughness was in the range of order of natural light wave length [30]).

While imaging a graphene-based material using 002 dark-field mode, bright areas representing the graphene stacks seen edge-on may exhibit more or less developed, aperiodic, dark fringes oriented perpendicular to the stacking direction. No specific examples are provided here, but the same phenomenon also appears in contrasted bright-field mode (or even lattice fringe mode, i.e., a mode where an objective aperture is present in the back focal plane of the objective lens, see Fig. 3.19 for instance). In both modes, the same

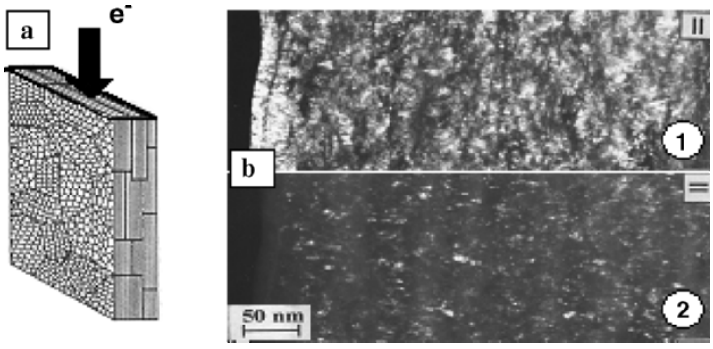


Fig. 3.25. Orthogonal 002 dark-field images of a thin pyrolytic carbon film. **(a)** Sketch of the overall orientation of the graphene stacks relative to the electron beam. **(b)** Demonstration of the anisotropy of the deposit. Positions 1 and 2 refer to Fig. 3.23a. An obvious differentiation is visible for position 1, where the deposit appears fully bright over ∼30 nm (*left*), while the remaining part of the deposit exhibits bright (prevalent) and dark contrasts. For position 2, the formerly fully bright area appears fully dark, while the remaining part of the deposit exhibits dark (prevalent) and bright contrasts. Comparison between positions 1 and 2 reveals that the first ∼30 nm are a dense deposit where all the graphene stacks are parallel to the deposition surface, while the remaining part of the deposit is made of elongated pores, with the elongation direction also parallel to the deposition surface

areas will appear dark. They are induced by slight deviations of the graphene planes relative to the Bragg angle, and are therefore called Bragg fringes. Portions of graphene stacks which are right under the Bragg angle are those which appear dark due to the fact that much of the scattered intensity is dispatched in high order reflections (004, 006, 008 . . .) which are not admitted in the objective aperture opening. On the other hand, portions of the graphene stacks which exhibit slight deviations relative to the Bragg angle will scatter the incident beam due to the interference error effect (see Sect. 3.2.1), and will show up in both modes. The highly scattering areas therefore exhibit a lack of intensity when the image is built. Bragg fringes are as more developed as the nanotexture (see Sect. 3.2.2) improves since they lengthen with the number N of graphene planes (see Figs. 3.19a-c). They are therefore a marker for the nanotexture state. However, interestingly, once the material is graphitized or at least exhibits a perfect nanotexture involving a high N value, on the one hand the interference error effect becomes limited, on the other hand the graphene stack reacts as a whole block whose deformability is much lower. This means that the graphene stack orientation with respect to the incident electron beam has to be equal to the Bragg angle and that local deformations over a nanometer range along the stack are no longer possible, with the consequence that Bragg fringes cannot occur anymore (Fig. 3.19d).

Finally, a full use of dark-field imaging may also include radial – in addition to azimuthal – exploration of the reciprocal space. In such an imaging mode, the $2\theta_b$ tilting angle (see Fig. 3.22) of the incident beam is varied so that the images reveal other graphene orientations than edge-on (as for 002 dark-field imaging). Specifically, another interesting orientation to reveal is when graphene stacks are perpendicular to the incident beam, i.e. lying flat. In that case, relevant scattered beams to built the image with are the $hk(l)$ beams (typically 10(0) or 11(0)). Considering a stack of turbostratically ordered graphenes, all of them act as superimposed but independent honeycomb lattices with identical periodic features, though slightly rotated relative to each other. This is the real situation where Moiré phenomena may occur. Moirés actually result from the interference between two beams which are scattered following the same angle but not exactly the same direction (azimuth), so that they are mutually coherent and in phase relation. When bidimensional coherent domains (= turbostratically stacked graphenes) are small, corresponding to low value nanotexture parameters, such as in a ∼1600°C-carbonized sublimation-deposited carbon film, Moirés appear as short, parallel fringes (Fig. 3.26a). As soon as the average coherent domain size expands, e.g. by increasing carbonization treatment, Moirés reveal them (Figs. 3.26b and c). Ultimately, when graphitization has occurred, there is no longer any possible Moiré pattern, except when two graphite crystals superimpose, which is quite seldom considering the huge N value that graphite crystals usually exhibit, relative to the low specimen thickness requested to maintain electron transparency.



Fig. 3.26. 11(0) dark-field images of a thin carbon film seen 'flat', along with increasing nanotexture values resulting from increasing carbonization temperature. **(a)** ∼1600°C, Moirés come from superimposed single graphenes gathered into small stacks. **(b)** ∼2300°C, Moirés reveal superimposed coherent domains. **(c)** ∼2600°C, Moirés become hardly possible. **(d)** 2800°C. Moirés cannot occur anymore due to crystal size (combined from [31] and [32])

Hence, dark-field imaging is a quite powerful mode. It is able to reveal anisotropy, provide coherent domain size range, identify texture type, and even image single molecules (such as BSUs in a pitch) whose scattered beam would otherwise be so faint that imaging them in bright-field mode is impossible [33]. In this case, each molecule is represented by a bright dot, the size of which

is that of the Airy disc (see beginning of the current section) if the actual molecule size is equal or below the latter. Then, for a uniform dispersion of the molecules within the material, the specimen may look like an amorphous material, since imaged features are alike. Notwithstanding, microscopists are resourceful people, and various means can be used to distinguish the two cases, such as recording several images while performing a through-focus series. If bright dots are actual molecules, they merely will become underfocused. If they are not, they will be replaced by other dots, still sharp.

3.3 Analysis of Nanotube Structures with Diffraction and HREM

3.3.1 HREM Imaging of Nanotubes

Provided suitable (i.e., sufficient spatial resolution) and controlled experimental conditions, HREM images supported by image simulations can provide reliable information about geometrical features of nanotubes such as diameter, number of layers, and helicity. The fact that NTs can be generally considered as phase objects greatly facilitates the interpretations (Sect. 3.1.3). In the following, we will describe the information, which can be extracted from HREM images obtained with two different microscopes, working both at the same tension (400 kV): the first one has a 'standard' point resolution of 0.23 nm determined by (3.29) with a spherical aberration coefficient Cs equal to 3.2 mm and a Scherzer focus $\Delta z_s = -90$ nm, whereas the second one has a point resolution equal to 0.17 nm (Cs = 1.05 mm) with a Scherzer focus of -50 nm. Even in the latter case, as explained above (Sect. 3.1.3), the point resolution is not sufficient enough for imaging atom positions of the honeycomb lattice since the C-C distance is equal to 0.142 nm. The 0.17 nm resolution makes it possible to image the holes of the lattice, i.e. the rhombic lattice related to this network, whereas with a 0.23 nm resolution, only stacking of graphite (002) planes can be resolved.

Single-Walled Nanotubes

Since it is made with one rolled atomic layer, a SWNT is an ideal weak phase object for electrons if it is viewed in a longitudinal projection: the mean inner projected potential remains small, even close to the edges. This might be no longer the case when the tube is viewed through an axial projection. In the following, the study of both situations will be presented through the analysis of only two nanotube configurations, namely the $(10, 10)$ armchair and the $(30, 0)$ zigzag carbon tubes, sketched in Figs. 3.27a, b respectively. The results can be easily extended to any other configuration.

In a longitudinal projection of the two different SWNTs, the projected potential is slightly higher at the edges (Fig. 3.27) which define two lines

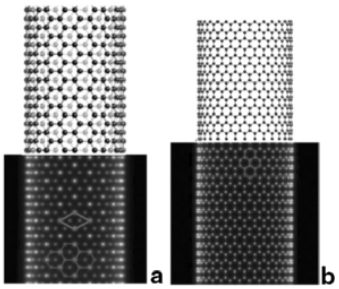


Fig. 3.27. Longitudinal projection of **(a)** $(10, 10)$ armchair and **(b)** $(30, 0)$ zigzag carbon SWNTs together with their associated projected potential

of maximum atomic density. If the microscope has a low point resolution, these two lines only contribute to the image contrast, making it possible to extract information such as tube diameter and length. However, careful examination of the HREM image simulations of the armchair and zigzag SWNTs (Figs. 3.28a,b) shows that the image varies rapidly with the TEM defocus. There is a narrow range of defocus around Scherzer where, at each tube edge, the line of high atomic density is imaged by only one dark fringe, otherwise the contrast spreads out laterally giving rise to multiple dark and white fringes. These variations with the focus mean that the contrast, as expected from a weak phase object, is dominated by the convolution of the high projected potential areas with the point spread function of the microscope (see (3.28)). In the present case, this convolution gives rise to the occurrence of focus dependent fringes, called Fresnel fringes. It should be pointed out that, even at Scherzer focus where the maximum in atomic density at the edge of the tube corresponds exactly to the black fringe, the precise measurement of the tube diameter cannot be directly determined from the intensity minimum location: it is slightly larger. Fresnel fringes occurrence along the tube image may therefore induce deep misinterpretation in terms of layer number and tube diameter, and experimentally one has to search, by varying the focus, for the finest contrast condition which corresponds to the Scherzer focus. Experimental examples in Figs. 3.28c, d illustrate the contrast difference between Scherzer condition (c) and a strong defocusing (d).

If the resolution of the microscope is better than 0.2 nm (Fig. 3.29a), normal and tangential parts to the electron beam both contribute to the image. As far as edges are concerned, the Fresnel-fringe effect is attenuated providing a more accurate diameter measurement at Scherzer focus. Normal parts of the tube do provide images of the rhombic cell from which additional structural information such as helicity can be also extracted. The contrast of the rhombic cell is very low, highly focus dependent and periodic, as for graphene imaging as attested by Fig. 3.12. Therefore, the helicity can only be determined in some favorable cases [34,35]. In particular, zigzag tube imaging is a special case where a unique feature appears at the tube edge: it is made of strong dark

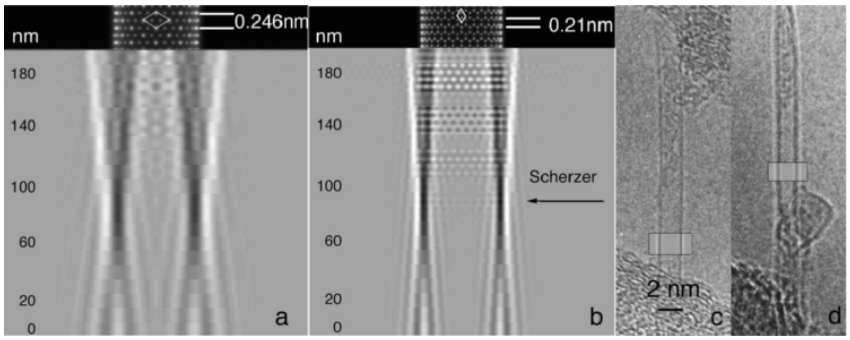


Fig. 3.28. (a) and **(b)** HREM simulated focus series respectively for the SWNTs shown in Figs. 3.27 a and b. (400 kV, $Cs = 3.2$ mm). NB: Image contrast in these simulations has been largely enhanced for visibility. The projected potential is shown at the top of each focus series accompanied with the rhombic cell outlined. **(c)** and **(d)** Experimental images for the same microscope, respectively at Scherzer defocus (−90 nm) and at a large underfocus (−180 nm). Corresponding simulations are shown in insets

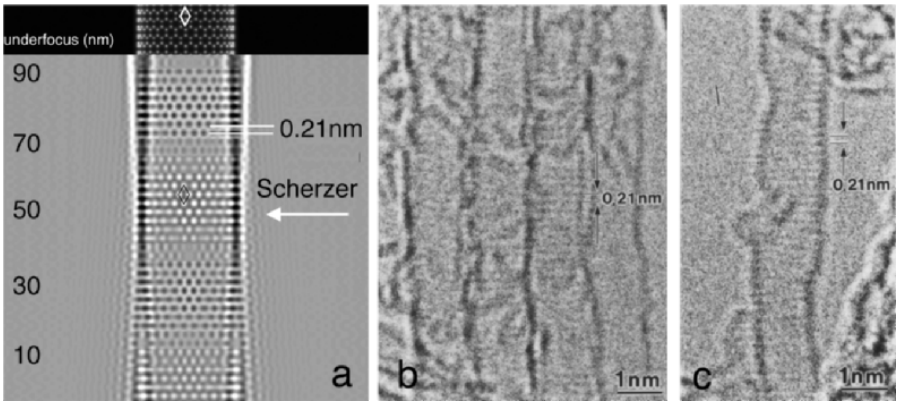


Fig. 3.29. (a) HREM simulated focus series of zigzag $(30, 0)$ tube (400 kV, $Cs = 1.05$ mm, point resolution 0.17 nm). **(b)** and **(c)** experimental images [34]

elongated dots whose spacing is $d_{10} = 0.214$ nm (Fig. 3.29a). In addition, 10 fringes perpendicular to the tube axis appear in the tube interior. Figures 3.29b and c show experimental images of such peculiar contrast obtained on SWNT images where d_{10} fringes are imaged together with elongated dark dots along the tube edge. Experimentally, this dark dot feature is easily identified, since (i) it is visible in a wide focus range as shown on simulations (Fig. 3.29a), and (ii) unlike 10 fringes, it occurs at the edges of the tube where the contrast is high. These special features have been used to determine the zigzag character of BN single-walled nanotubes [35]. As shown in [36], the contrast along and

around the tube in a longitudinal projection may be strongly perturbed if the tube axis is not lying strictly perpendicular to the electron beam. Furthermore the contrast becomes asymmetrical from one edge to the other and one of the two edge fringes may become also dotted. Thus this point is of main importance for structural interpretation.

Since many SWNTs are long and often curved or bent, a portion may be viewed along their axis, providing an image of the tube section. This may be an ideal case to measure the tube diameter. Nevertheless, since this tube portion may have a large thickness in projection, it can no longer be considered as a true phase object. In this case the contrast, which is affected by the Fresnel fringes depends on the 'apparent' thickness of the tube portion parallel to the beam as shown by image simulations in Fig. 3.30. Scherzer defocus is the only experimental condition where the projected atomic potential is imaged by a black circle whose diameter can be reliably linked to the tube diameter. This condition is for instance fulfilled in the top image of Fig. 3.30b and not in the bottom image of Fig. 3.30b. It must be noticed that, under some focus and thickness conditions ($\Delta z = -180\,\mathrm{nm}$ and $d = 20\,\mathrm{nm}$) a SWNT may appear as multi-walled!

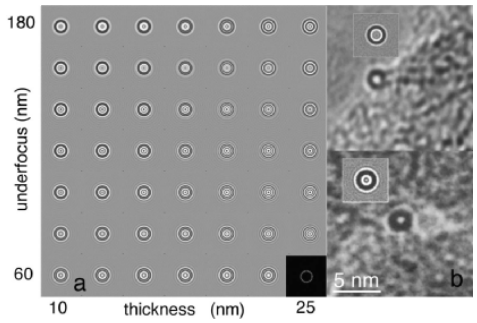


Fig. 3.30. (a) Calculated focus-thickness map (400 kV, $Cs = 3.2\,\mathrm{nm}$) of $(15, 15)$ SWNT in axial view. **(b)** Experimental images and simulations in the insets for comparison (top image: thickness $d = 15\,\mathrm{nm}$ and $\Delta z = -40\,\mathrm{nm}$, bottom image: $d = 25$ nm and $\Delta z = -60\,\mathrm{nm}$)

Multiwalled Nanotubes

The first HREM images of carbon MWNTs are due to Iijima [37] (Fig. 3.31a). Similar images obtained for BN MWNTs are shown Fig. 3.31b [38]. These images, which correspond to tubes viewed in longitudinal projections, have been proved to provide a direct determination of the layer number and diameter: in the present imaging conditions, each dark line is attributed to one layer. We will examine in the following under which conditions such information can be retrieved.

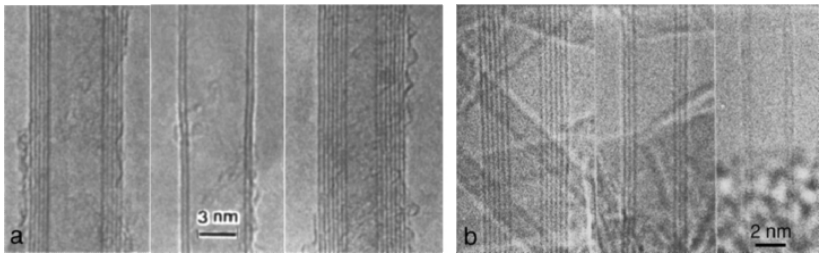


Fig. 3.31. Images of different MWNTs of **(a)** carbon (adapted from [37]) and **(b)** BN. CNTs (a) have respectively 5, 2 and 7 layers whereas BN tubes (b) have 6, 3 and 2 layers

The determination of the wall number is not straightforward and simulations help in understanding the interpretation of the image contrast. This is illustrated by considering a carbon MWNT made of four zigzag C layers, viewed in a longitudinal projection, whose projected potential is shown in Fig. 3.32a and whose images are simulated for two microscopes (Fig. 3.32b, c). This MWNT can still be considered as a weak phase object in a longitudinal projection. The tangential parts of the MWNT give a fringe contrast similar to the one of graphite viewed along [210], i.e. in prismatic orientation (see Fig. 3.7). Since the contrast arises from the interference of 002 and $00\overline{2}$ diffracted beams with the transmitted beam, as mentioned in Sect. 3.1.3, and it is governed by $T(u) = -2\sin\chi(u)$. For instance, the contrast in Fig. 3.32c faithfully follows the $1/d_{002}$ spatial frequency transfer given in Fig. 3.10. However, because of the lateral finite size of the object, Fresnel fringes occur and give rise to artifact-like fringes. As a consequence, the number of fringes can be reliably counted only for Scherzer defocus where the highest potential areas,

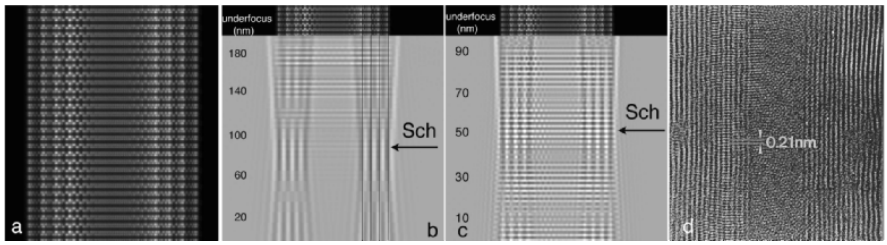


Fig. 3.32. (a) Longitudinal projection of the atomic potential of the zigzag MWNT (30,0)@(39,0)@(48,0)@(57,0). **(b)** and **(c)** Underfocus series calculated respectively for 400 kV, $Cs = 3.2$ mm, and for 400 kV, $Cs = 1$ mm, where the layer contrast is white for zero defocus, dark at Scherzer (Sch), and vanishes at 0.5 Sch and 1.5 Sch according to the sign of the $1/d_{20}$ transfer (see Fig. 3.10). The apparent number of layers is only reliable at Scherzer focus. The diameter of the four tubes is outlined. **(d)** Experimental HREM of a MWNT containing some zigzag layers and exhibiting 20 fringes normal to the tube axis, fingerprint of their zigzag character [39, 40]

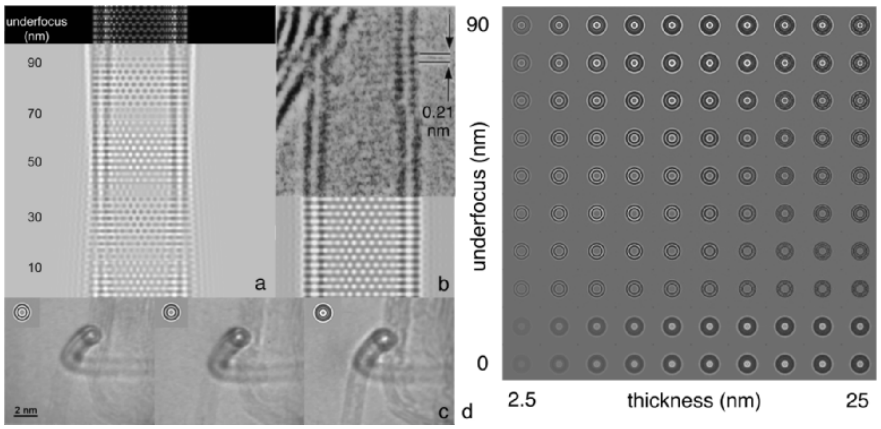


Fig. 3.33. (a) HREM underfocus series simulations (400 kV, $Cs = 1$ mm) of a $(30, 0)@(39, 0)$ carbon DWNT. **(b)** Comparison between experimental images and simulations (200 kV-FEG) shows that the (02) planes can be imaged (adapted from [41]). **(c)** Experimental focus series of a bent DWNT: the portion of the tube seen edge-on is imaged around the Scherzer focus by two thin black concentric rings and at large underfocus by only one large dark ring suggesting that the tube could be single-walled. (courtesy E. Flahaut). Simulations in insets correspond respectively to $\Delta z = -50$ nm, -70 nm, -90 nm and a projected thickness of about 8 nm. **(d)** Simulated focus-thickness map of the DWNT in axial projection

i.e., the layers, are imaged as black lines with the thinnest width. Experimentally, this condition must be fulfilled as they are in the examples in Fig. 3.31. The tube on the left in Fig. 3.31b is superimposed with two other highly defocused tubes where the Fresnel fringe effect is very pronounced. In the case of zigzag tubes and when the microscope resolution is adequate (Fig. 3.32c), simulations show that characteristic elongated black dots are present at the edge like for SWNTs. Furthermore the fringe contrast associated with the (20) plane is enhanced with respect to the SWNT case and can now be easily detected in the interior of the tube, as observed experimentally (Fig. 3.32d). Nevertheless, if the helicity of the layers is spread, the superposition of the different oriented rhombic cells results in a blurred contrast in the interior of the tube, impeding any helicity analysis. In such cases, the solution is to study diffraction patterns as described in Sect. 3.3.2.

Since double-walled tubes (DWNT) are expected to have special properties, their observation and structural characterization is of great interest. Figure 3.33 shows both experimental images and simulations of longitudinal and axial projections of a DWNT made of two zigzag layers. Basically, HREM images of a longitudinal projection exhibit the same features as in the case of MWNTs but the risk of misinterpretation is higher since the Fresnel-fringe effect is more pronounced and can induce a 100% error on the tube number far from Scherzer focus. As predicted by the simulations (Fig. 3.33a), the

zigzag character (dark spots at the edges) may be seen on experimental images (Fig. 3.33b). The simulated images (Fig. 3.33d) of axial projections pointed out once more the difficulty for extracting a reliable layer number. This is illustrated in Fig. 3.33c by the experimental focus series of a DWNT bent in such a way that a portion is exactly viewed edge-on.

Bundles of Single-Walled Nanotubes

SWNTs are often found arranged in bundles in a more or less close-packed stacking, depending on the diameter dispersion. The main parameters one would like to know are the individual tube diameter distribution, their helicity and the tube number within a bundle. As for MWNTs, the bundle can be observed either in a longitudinal or an axial projection. Different information can be extracted that we will analyze successively by considering in a first step the ideal structure of a bundle lattice sketched in Fig. 3.34a. The longitudinal projection is analyzed first. Depending on the electron beam direction with respect to the bundle lattice, fringes with different interplanar distances, i.e., d_{20} or d_{11},[10] of the tube network can be imaged and measured. First evidence of different longitudinal projections has been published by Thess et al. (1996) by rotating a bundle around its axis in order to image successively 11 and 20 fringes. However these interplanar distances being linked to the bundle lattice parameter a, one has only access to mean tube parameters: the mean diameter $\langle d_t \rangle$ and the mean intertube shortest distance $\langle d_{vdW} \rangle$ with $a = \langle d_t \rangle + \langle d_{vdW} \rangle$. Accordingly, at least two different longitudinal projections are required to determine the two unknown parameters. Otherwise, one generally assumes that d_{vdW} is governed by Van der Waals interaction between adjacent tubes as in graphite or MWNTs leading to $\langle d_{vdW} \rangle = 0.32\,\mathrm{nm}$.

HREM simulations of a bundle in the longitudinal $\langle 11 \rangle$ and $\langle 20 \rangle$ projections for different bundle thicknesses (i.e., diameters) and different defocii are shown in Figs. 3.34b, . It is clear that the images are not directly related to the SWNT atomic structure but to that of the bundle network. It has to be noticed that the contrast feature is not strongly thickness dependent but is sensitive to the projection axis. For the $\langle 11 \rangle$ projection (Fig. 3.34b), the images reveal the ordered structure of the bundle lattice: the contrast consists of periodic fringes with d_{11} spacing. Except at very low defocus, the fringes are dark and located at the highest atomic density as seen from the projected potential map providing an easy measure of d_{11}. In $\langle 20 \rangle$ projection (Fig. 3.34c), the contrast interpretation is less straightforward due to the fact that in this projection, the bundle does not exhibit as dense projected potential areas as along $\langle 11 \rangle$. As a result, at large defocus, the contrast consists of wide dark fringes with a spacing d_{20}, located on the rows of maximum potential density. Around Scherzer focus, the contrast consists of two alternating white and

[10] Miller indices refer to the centered rectangular bundle cell defined by the unit vectors $\boldsymbol{a}$ and $\boldsymbol{b}$ shown in Fig. 3.34a. In this section, directions with respect to this rectangular cell are denoted by two indices in angular brackets.

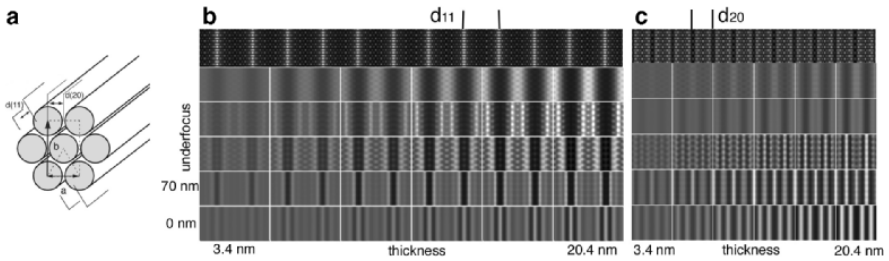


Fig. 3.34. (a) Scheme of an well-ordered bundle. The section shows the periodic tube lattice where units vectors $\boldsymbol{a}$ and $\boldsymbol{b}$ and (20) and (11) planes are indicated. HREM focus-thickness map simulations for a bundle viewed along $\langle 11 \rangle$ **(b)** and $\langle 20 \rangle$ **(c)** (400 kV, Cs = 3.2 mm), The corresponding projected potentials of the bundle are shown at the top of each map. Note that the thickness is in fact the bundle diameter. (10, 10) tubes have been used in the simulations

more or less grey fringes located on the rows of minimum potential density, each kind of fringes being spaced by d_{20}.

Different experimental situations of longitudinal projections are shown in Fig. 3.35. Figure 3.35a is a clear example of $\langle 11 \rangle$ projection at Scherzer defocus whereas Fig. 3.35b corresponds to a larger defocus revealing an internal contrast between the dark fringes, in agreement with simulations. This internal contrast is intrinsic to the coherent electron scattering along $\langle 11 \rangle$ and has to be distinguished from a contrast which might arise from some filling. Figure 3.35c is a typical example of a $\langle 20 \rangle$ projection showing the complex contrast features at a -140 nm defocus. d_{20} can only be extracted provided a careful analysis of this feature. It has to be pointed out that periodic fringes are the fingerprint of the periodic arrangement built by the tubes within the bundle and do not correspond to the individual tube image. When there is no periodic arrangement, images of bundle is the incoherent superposition of individual images leading to complex and disordered set of lines (Figs. 3.35d and e). Nevertheless, if the number of superimposed tubes is relatively low in such a way that the individual images are not blurred, then the distance d_{vdW} between tubes can be measured (Fig. 3.35d).

The lattice fringe contrast and the interfringe distance are often found to change periodically along one bundle as illustrated in Fig. 3.36. Such periodic sequence of fringe spacings is the signature of a bundle twisted around its axis as attested by the simulation performed by A.L. Hamon [42] (inset of Fig. 3.36). A period of 60 nm is often observed [43] corresponding to a twist angle equal to 1°/nm. This twist characteristic is useful, since an accurate measure of geometrical parameters can be extracted from different lattice distances. As far as helicity is studied from longitudinal projections, careful analysis of different image simulations leads to the conclusions that determining the helicity of tubes assembled in bundle required severe conditions: unique helicity, unique rotational orientation of the tubes, and observation in

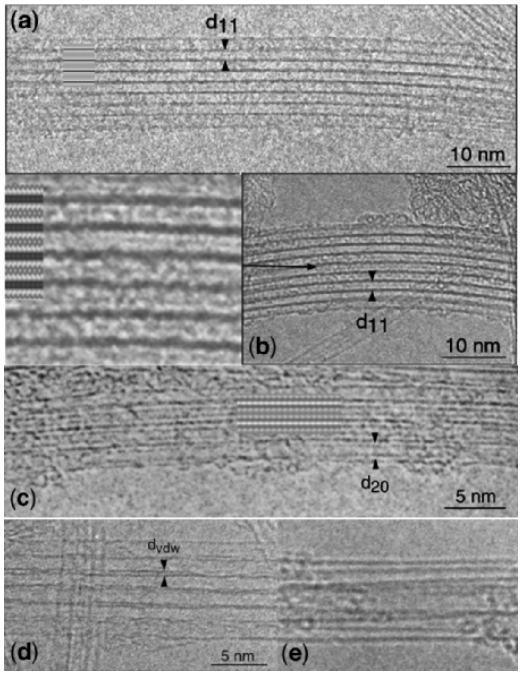


Fig. 3.35. (c) HREM experimental images of bundles (400 kV, $Cs = 3.2$ mm). **(a)** $\langle 11 \rangle$ projection view at Scherzer defocus revealing the d_{11} interplanar distance; in the inset, the corresponding simulated image for a thickness $d = 17$ nm . **(b)** $\langle 11 \rangle$ projection view with an enlargement on the left hand side accompanied with the corresponding simulation for $\Delta z = -150$ nm and $d = 17$ nm. Fine structure observed between the large dark fringes are intrinsic to the bundle and are not due to any kind of filling. c) $\langle 20 \rangle$ projection with corresponding simulation with $\Delta z = -140$ nm and $d = 17$ nm where the dominant features are white fringes d_{20} spaced, with in between two fainter grey lines. **(d)** The bundle is reduced to a row of tubes imaged individually in such a way to reveal in the intertube distance d_{vdW}. **(e)** In the bundle, the tubes are not periodically arranged so that the image is the incoherent superposition of tube individual images. In the simulations, the thickness d is estimated from the apparent bundle diameter in the images assuming a circular cross section

$\langle 11 \rangle$ projection with a very high resolution electron microscope. As for the case of MWNTs, diffraction technique is the appropriate way to handle this problem.

Similarly to SWNTs or MWNTs, bundles may be also viewed along their axis [44, 45]. In these observation conditions, tube and bundle diameter, tube lattice periodicity, tube section shape may be determined from TEM images. The general view (Fig. 3.37) attests that bundles are frequently bent so that at some place a segment can be viewed edge-on (black arrow). It can be inferred from the local curvature radius that the height range of the edge-on

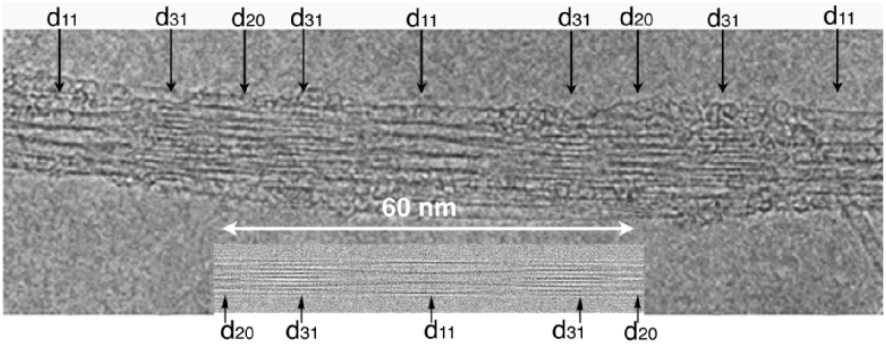


Fig. 3.36. (a) Experimental image of a twisted bundle (400 kV, Cs = 3.2 m). The twist results in the appearance of periodic sequences of differently spaced fringes along the bundle axis. Here two periods can be seen corresponding to a total rotation of the bundle of 120° and to a twist angle of 1°/nm and to a 60 nm period. The interplanar distances are indicated for the different fringe spacings. **(b)** Simulation of a bundle made of 7 (10, 10) SWNTs assembled according to Fig. 3.34a and twisted by 1°/nm: agreement with experiment is remarkable (adapted from [42])

segment is about 10 nm to 50 nm. According to the focus-thickness map of simulated axial views (Fig. 3.38a), the contrast is highly sensitive to experimental conditions. At large defocus, the contrast only reflects the bundle lattice and consists of periodic white dots located at the tube center on an almost uniform dark background. At low defocus, the contrast is a periodic pattern of dark rings, whose diameter fits the actual tube diameter only at Scherzer focus. In addition, different kinds of contrast fine structure can appear and are intrinsic to the hexagonal lattice structure, and must not be mistaken for some special structure of the bundle such as intercalation, tube filling or faceting. Some of these contrast features are well recognized in the experimental focus series of images shown in Figs. 3.38b, c, d. The appearance of a white dot hexagonal pattern surrounding a dark ring is clearly seen at low defocus (Fig. 3.38b) as well as the appearance of a strong centered dot on a dark background at large defocus (Fig. 3.38d). In between, around Scherzer focus, the image displays the finest contrast (Fig. 3.38c) from which the tube diameter can be measured. This condition is also suitable for an accurate analysis of the diameter dispersion. In some cases, dark rings within a bundle are observed to display a six-fold symmetry and it is tempting to interpret this contrast as being due to an intrinsic tube faceting. As proved in Fig. 3.39, this contrast only appears at some defocus and as supported also by simulations, a slight focus change makes it disappear and restores the actual cylindrical symmetry. If the tubes were really faceted, the six-fold contrast would persist at any focus, thus one image at a single focus is not sufficient for a reliable analysis of bundle section shape.

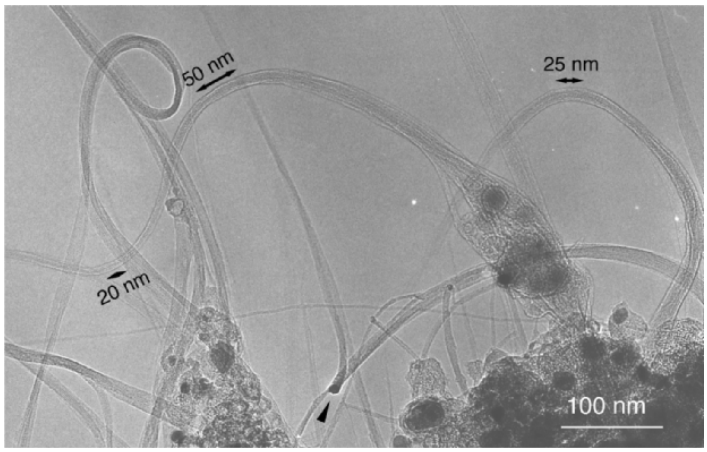


Fig. 3.37. Low magnification image of arc-grown bundles of SWNTs showing their flexibility. The *black arrow* indicates a bundle segment seen edge-on. Due to local curvature, the expected heights of segments which can be viewed along the bundle axis are indicated

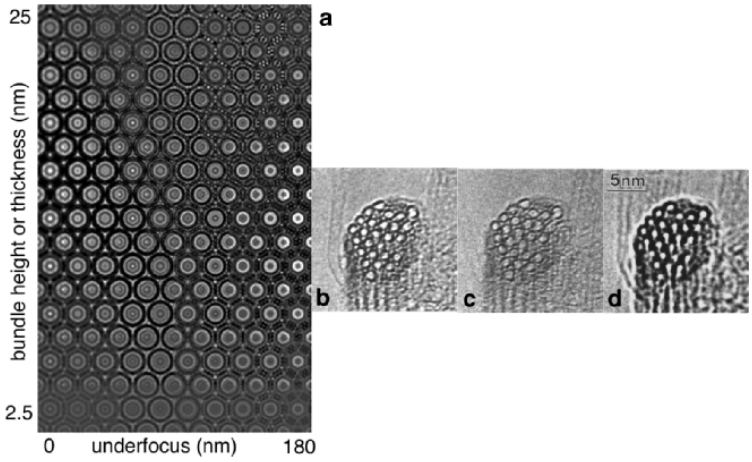


Fig. 3.38. (a) Simulated focus-thickness map of a $(10, 10)$ tube bundle viewed along its axis (400 kV, $Cs = 3.2$ mm). **(b, c, d)** Experimental focus series of a bundle axis view, respectively for $\Delta z = -30$ nm, -80 nm, and -180 nm, the bundle height or thickness is 10 nm. The relative contrast of experimental images has been kept all along the recording procedure and is in fully agreement with the simulations

Large bundles result frequently from the branching of smaller bundles (Fig. 3.40a) [46]. Interestingly, axial observations permit a detailed analysis of the branching process which shows that the final bundle is made of differently oriented networks where twin relationships between sub-bundles often occur

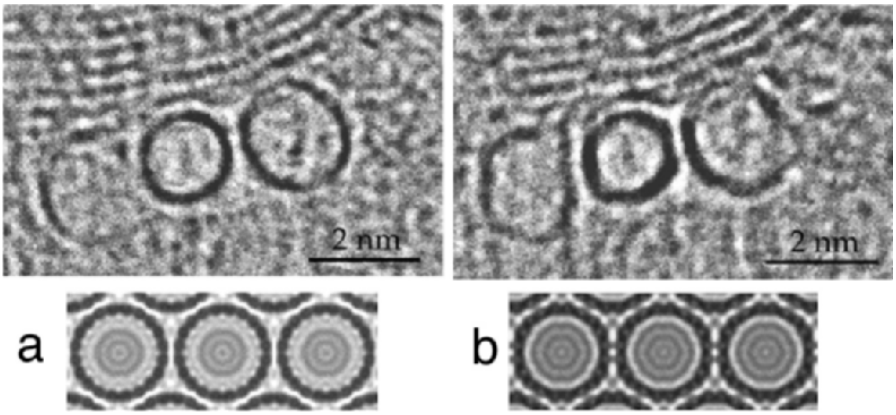


Fig. 3.39. Images of a bundle made of three tubes and the corresponding simulations recorded at two different defocii (400 kV, Cs = 1 mm). **(a)** Scherzer focus −50 nm and **(b)** $\Delta z = -30$ nm. In (b) a six-fold symmetry appears both in experiment and simulation, which is clearly not related to tube faceting

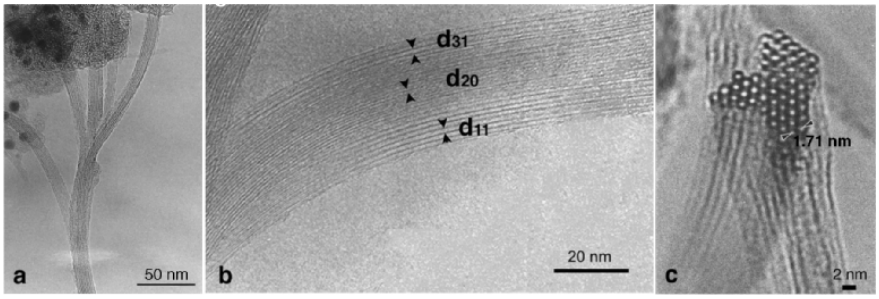


Fig. 3.40. Examples of bundle branching. **(a)** Low magnification view of a branching of 5 sub-bundles. **(b)** Longitudinal HREM image of a composite bundle resulting from the branching of three bundles differently oriented as revealed by the 11, 31, and 20 fringe spacings. **(c)** Section like view showing also that three bundles are linked together with different orientation relationship leading to three domains. In one sub-bundle, the white dots are slightly elongated meaning that it is not strictly viewed edge-on. Due to this branching process, large bundles are generally polycrystalline. The single crystalline sub-bundles can be considered as primary bundles [46]

(Fig. 3.40c). In a longitudinal projection, the branching is revealed by different lattice distances appearing along the section of a large bundle (Fig. 3.40b).

In summary, the first interest of bundle axial views is to provide an immediate information on the tube number and of the tube arrangement. More detailed measurement can only be achieved under a careful control of acquisition conditions such as focus and bundle orientation. The occurrence of fine structures in the contrast makes it difficult to analyze reliably filled nanotubes such as peapods.

Analysis of Defects

The crystallinity of the graphene layers strongly depends on the synthesis techniques or post-synthesis treatments. The high-temperature route leads to an almost perfect periodic honeycomb lattice, whereas in the catalytic CVD low-temperature route, defects are present along the tube body and some multi-wall nanotube obtained by this technique may present different graphitization degrees as in carbon fibers (see Sect. 3.2). In the following, we focus on defects appearing in SWNTs grown at high temperature only.

In a graphene layer, topological defects are made from five and seven atom rings, which change the local curvature of the nanotube such as in a tube closure, as described in Chap. 1. These defects must also fulfill chemical bond conditions, which are different in carbon where only C-C bonds exist and in BN where B-B or N-N bonds are forbidden. This supplementary condition leads to different characteristic shapes at the tube tips. It is generally assumed that tube closure is insured in carbon nanotubes by six pentagonal C rings, whereas due to chemical frustration in BN tubes three four-membered rings are necessary. HREM cannot image directly the atomic structure of these defects. Nevertheless, the analysis of curvature changes (sign and angle) induced by these defects can help their identification as illustrated in Figs. 3.41 and 3.42 for respectively C and BN MWNTs and SWNTs. Numerous HREM observations lead to the conclusions that carbon nanotube tips are either hemispheric or conical (symmetrical or distorted) consistently with the presence of six pentagons (Fig. 3.41). On the other side, BN tips display most often characteristic flat caps in accordance with the energetical most favorable configuration involving three squared rings as shown in Fig. 3.42.

Topological defects are not only concentrated at the tips but can be present along the tube wall and often appear as pairs of heptagon and pentagon. As shown in Fig. 3.41g, when located on the same side of the tube wall, they induce a small diameter change, whereas when located on opposite sides of the tube wall they form an elbow configuration which is of particular interest since it may transform an armchair configuration into a zigzag one [47]. This latter transformation has been identified by Golberg [41] in a double wall nanotube using HREM imaging of rhombic cells on both sides of the elbow.

Finally, long time exposure to the electron beam is known to induce structural defects and to lead to severe tube deformation and finally to its fracture. Ajayan et al. [51] have studied this destroying process in details and have shown that atoms are removed from graphene by knock-on displacements. Indeed the threshold voltage for carbon atom displacement in graphene is about 120 kV [52]. In practice, rapid image recording is highly recommended for avoiding any structure modification. Contrarywise, this sensitivity to electron irradiation can be used positively. For instance an exposure at high tension of a strongly focused beam mimics high temperature annealing: coalescence of SWNTs has been obtained [53] as well as transformation of MWNTs into onions [54]. For a detailed study of radiation damages and annealing kinetics

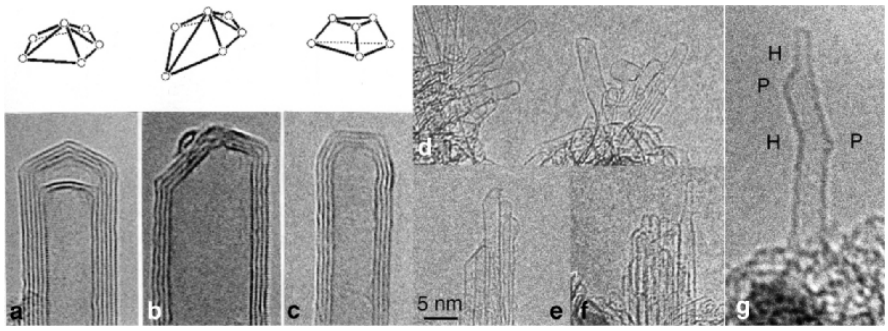


Fig. 3.41. (a, b, c) Images of different carbon MWNT tip morphologies which can be interpreted as being due to different spatial distributions of six pentagons necessary to the tube closure. Corresponding schemes of the topological defects distribution are shown in the upper part. (pentagon locations are indicated by open circles) (adapted from [48]). **(d, e, f)** Examples of SWNT tips hemispherical or conical in shape. **(g)** Image of a single nanotube displaying negative and positive curvature assumed to be due to the presence of pentagons and heptagons marked respectively by P and H

in carbon nanostructures, the reader is referred to the review paper by Banhart [55].

3.3.2 Diffraction by Carbon Nanotubes

The application of the kinematical theory of diffraction (see (3.5) in Sect. 3.1.1) relies on the approximation that the incident radiation may only experience a single scattering event when traveling through the sample. Not only is multiple scattering ignored, which may be valid with X-rays and neutrons due to their small scattering factors, but also any dynamical exchanges between the diffracted beams are neglected. These arise from interferences between the incoming waves and the Bragg scattered beams. In spite of its approximate character, the kinematical theory turns out to yield a good representation of the diffraction pattern of carbon nanotubes, even with electrons. With electrons in the 100-keV energy, the kinematical theory is accurate enough for carbon material composed of a few tens of layers, as mentioned above. Most of the isolated multi-wall nanotubes and ropes of single-walled nanotubes are below this limit.

The intensity of the diffracted beam in the direction of $\boldsymbol{k_0} - \boldsymbol{q}$ is, according to (3.5), proportional to $|S(\boldsymbol{q})|^2$ with

$$S(\boldsymbol{q}) = \sum_j f_j(q) \mathrm{e}^{\mathrm{i}\boldsymbol{q}\cdot\boldsymbol{r}_j} \tag{3.42}$$

the so-called structure factor of the sample, given by a coherent sum of the atomic scattering factors f_j, each multiplied by a phase factor introduced by

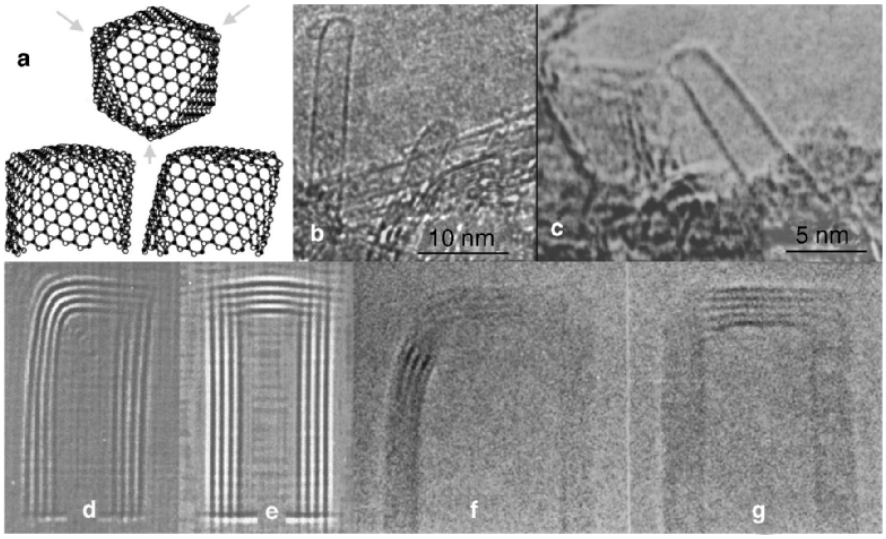


Fig. 3.42. (a) Structural model of the BN tube closure seen in top view and two different edge-views. This closure is the less energetical configuration [49, 50] and involves three squared atomic rings located at the vertices of a triangular facet perpendicular to the tube axis. **(b, c)** Experimental HREM images of BN SWNT tips displaying the characteristic flat cap and tip asymmetrical shape as shown in one of the model edge views. **(d, e)** Simulated images (at Scherzer focus, 400 kV, Cs = 3.2 mm) of a MWNT with 4 layers (30,0)@(39,0)@(48,0)@(57,0) in two edge views. **(f, g)** Experimental HREM images of MWNTs in the same edge views

the atomic position $\boldsymbol{r}_j$. For applications of that formula to nanotubes, detailed in a following section, it is interesting to consider two examples.

The first case is that of a continuous cylinder. In this particular example, the scattering wave vector $\boldsymbol{q}$ is assumed to be much smaller than the reciprocal of the interatomic distances. Then, the atomic structure of the system can be discarded and the sum replaced by an integral. Having in mind a single-walled nanotube, the integral is performed on a cylindrical surface of radius r

$$S_0(\boldsymbol{q}) = f(q)N \int_0^{2\pi} \mathrm{e}^{\mathrm{i}q_\perp r\cos\phi}\, r\, d\phi \int_{-\infty}^{+\infty} \mathrm{e}^{\mathrm{i}q_z z} \tag{3.43}$$

where $q_\perp$ and q_z are the component of $\boldsymbol{q}$ perpendicular and parallel to the cylinder axis (z direction), respectively. In the above equation, N is the number of C atoms per unit area. The calculation of the integrals leads to the following expression

$$S_0(\boldsymbol{q}) = (2\pi)^2 N f(q_\perp) r J_0(q_\perp r)\delta(q_z) \tag{3.44}$$

where J_0 is the Bessel function of the first kind and zero order. The presence of the Dirac delta function in (3.44) is the consequence of the assumed infinite

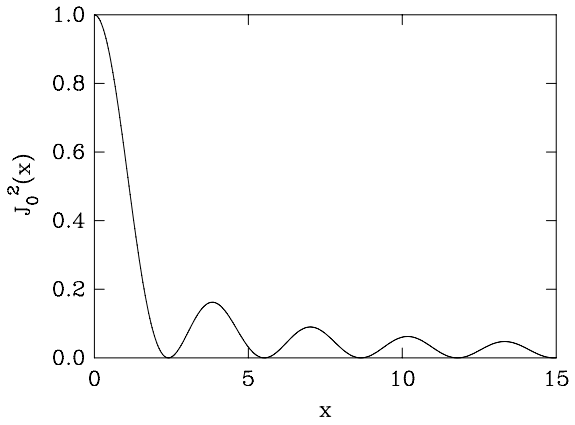


Fig. 3.43. The diffraction intensity along the equatorial line of a continuous cylinder is governed by the J_0^2 Bessel function

length of the cylinder. The delta peak means that all the diffracted beams are concentrated in the plane $q_z = 0$, perpendicular to the axis. The intersection of this plane with an observation screen is a single line, called the equatorial line, along which the intensity is modulated by the expression $|f(q_\perp)J_0(q_\perp r)|^2$. The J_0^2 function has maxima at $q_\perp r = 0$, 3.83, 7.01, 10.17 ... separated by minima of zero intensity (see Fig. 3.43). Since the zeroes of J_0 rapidly become equidistant with separation π, the modulation of intensity along the equatorial line has a period π/r. This intensity oscillation is similar to the Fraunhofer diffraction by a slit of width $2r$.

A second important example is that of an atomic helix, first treated by Cochran, Crick and Vand [56]. The so-called CCV formula obtained by these authors was used to elucidate the structure of the DNA molecule from X-ray diffraction experiments on B-DNA realized by Franklin and Gossling [57]. The CCV theory can also be used for nanotubes [58]. The problem here is to sum the expression (3.42) for discrete atoms located on an infinite cylindrical helix of radius r, pitch P, and atomic repeat distance p_z (the distance between two scattering centers) along the axis, again taken as the z direction. The cylindrical coordinates of the atoms are $\rho_j = r$, $\phi_j = \phi_0 + j2\pi z_j/P$, and $z_j = z_0 + jp_z$. Here ϕ_0 and z_0 are the coordinates of the atom $j = 0$ chosen as conventional origin.

The structure factor of the monoatomic helix derived from (3.42) writes

$$S_1(\boldsymbol{Q}) = f(q) \sum_{j=-\infty}^{+\infty} \mathrm{e}^{\mathrm{i}q_\perp r\cos(\phi_q - \phi_0 - 2\pi j p_z/P)} \mathrm{e}^{\mathrm{i}q_z(z_0 + jp_z)} \qquad (3.45)$$

where ϕ_q is the azimuthal angle of $\boldsymbol{q}$. The Jacobi-Anger formula $\mathrm{e}^{\mathrm{i}x\cos\phi} = \sum_\nu i^\nu J_\nu(x)\mathrm{e}^{\mathrm{i}\nu\phi}$ allows one to expand the first exponential factor in the right-hand side of (3.45) in a series of Bessel functions of integer orders ν

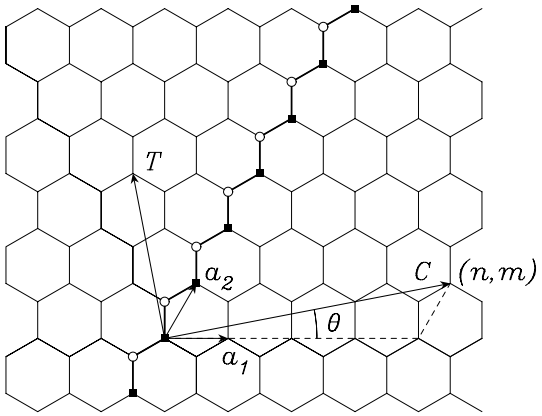


Fig. 3.44. Two-dimensional graphene sheet showing the circumference C and true period T of the (n, m) nanotube, together with the chiral angle θ. The zigzag chain of atoms shown by open circles and black squares becomes a diatomic helix on the rolled up structure

$$S_1(\boldsymbol{q}) = f(q)\mathrm{e}^{\mathrm{i}q_z z_0} \sum_{\nu=-\infty}^{+\infty} \mathrm{i}^{\nu} J_{\nu}(q_{\perp} r)\mathrm{e}^{\mathrm{i}\nu(\phi_q - \phi_0)} \sum_{j=-\infty}^{+\infty} \mathrm{e}^{\mathrm{i}j(q_z - \nu 2\pi/P)p_z} \tag{3.46}$$

In this last equation, the sum over the index j is the Fourier expansion of the periodic distribution of Dirac peaks $(2\pi/p_z)\sum_{\mu}\delta(q_z - \nu 2\pi/P - \mu 2\pi/p_z)$. As a result, (3.46) leads to the CCV formula

$$S_1(\boldsymbol{q}) = \frac{2\pi}{p_z} f(q)\mathrm{e}^{\mathrm{i}q_z z_0} \sum_{\nu,\,\mu} J_{\nu}(q_{\perp} r)\mathrm{e}^{\mathrm{i}\nu(\phi_q - \phi_0 + \pi/2)} \delta\left(q_z - \nu\frac{2\pi}{P} - \mu\frac{2\pi}{p_z}\right) \tag{3.47}$$

where μ is another integer index running from $-\infty$ to $+\infty$. Due to the delta functions, the diffraction pattern of a monoatomic helix is found to be discretized along sharp lines perpendicular to the axis (the so-called layer-line structure) governed by the condition

$$q_z = \nu\frac{2\pi}{P} + \mu\frac{2\pi}{p_z} \tag{3.48}$$

where ν and μ are two arbitrary integers. The intensity along a line is modulated by the Bessel functions.

The relation between the CCV theory just developed and a nanotube can be appreciated in Fig. 3.44 where the chain of atoms shown by the open and black symbols becomes an helix in the rolled up structure. This helix is made from two monoatomic helices, the one with the open circles and the other with the black squares, which can be B and N atoms in a BN nanotube. This particular chain makes an angle $\pi/6+\theta$ with respect to the axis direction, where θ is the chiral angle of the nanotube measured with respect to

the zigzag configuration. With the helical scheme adopted here, the complete nanotube can be generated from n ($m \geq 0$) or $n - |m|$ ($m < 0$) diatomic helices (when m is negative, the chain pointing at 120° is used instead of the one pointing at 60°, see Fig. 3.44). It then suffices to add the contributions of all the monoatomic helices (two per chain), by adding to ϕ_0 and z_0 in (3.47) the appropriate screw operations which transform one helix into the next one. The final result of this calculation is the following expression of the scattering structure factor of the single-walled (n, m) nanotube [59] valid for $-n/2 < m \leq n$

$$S(\boldsymbol{q}) = \frac{4\pi C}{\sqrt{3}a^2} \sum_{l=-\infty}^{+\infty} \mathrm{e}^{\mathrm{i}l2\pi z_0/T} F_l(\boldsymbol{q})\, \delta(q_z - l2\pi/T) \tag{3.49}$$

with

$$F_l(\boldsymbol{q}) = \sum_{s,t=-\infty}^{+\infty} J_{sn'-tm'}(q_\perp r)\mathrm{e}^{\mathrm{i}(sn'-tm')(\sigma\phi_q - \sigma\phi_0 + \pi/2)} \times \left[f_0(q) + f_1(q)\mathrm{e}^{\mathrm{i}2\pi(s+2t)/3}\right] \delta_{s(n'+2m')/d_R + t(2n'+m')/d_R,\, l} \tag{3.50}$$

where

$$n' = n\ ,\ m' = m\ ,\ \sigma = +1 \text{ when } m \geq 0 \tag{3.51}$$

$$n' = n - |m|\ ,\ m' = |m|\ ,\ \sigma = -1 \text{ when } m < 0 \tag{3.52}$$

and

$$T = \frac{\sqrt{3}C}{d_R} \tag{3.53}$$

$$d_R = \text{h.c.d.}(2n' + m', 2m' + n') \tag{3.54}$$

$$C = a\sqrt{n^2 + m^2 + nm}\ . \tag{3.55}$$

In (3.49), T is the Bravais translation of the nanotube along its axis (see Fig. 3.44 and equation (3.53)), C is the length of the circumference (see (3.55)) and a is the lattice parameter of graphene (0.246 nm). Due to the periodicity along the axis, the z component of $\boldsymbol{q}$ is discretized on a lattice with parameter $2\pi/T$. Not all the corresponding layer lines will be present in the diffraction pattern because the Kronecker δ in (3.50) imposes a selection rule on the line index l. In (3.50), s and t are integer numbers, n', m', and σ have the meanings expressed by (3.51–3.52) (σ gives the sign of the handedness of the helices). In (3.50), $q_\perp$ is the component of $\boldsymbol{q}$ perpendicular to the nanotube axis, ϕ_q is the azimuth angle of it, $f_0(q)$ and $f_1(q)$ are the scattering factors of the two atoms that compose a chain (2 C in a carbon nanotube, B and N in a BN nanotube).

From a mathematical point of view, the intensity along a layer line is controlled by the Bessel functions that appear in (3.50). The Bessel function

$J_\nu(q_\perp r)$ is very small when its argument is much smaller than its order, and its first maximum takes place for $q_\perp \sim \nu/r$. Most of the layer lines have no intensity at the center because they are built up by Bessel function of non-zero order. An exception is the equatorial line ($q_z = 0$), which is controlled by $J_0(q_\perp r)$ near the center in agreement with the theory developed above for a continuous cylinder (see (3.44)).

Electron Diffraction by a Single-Walled Nanotube

Recently, nano-diffraction has been successfully applied to identify the helicity parameters of isolated single-walled nanotubes [60]. This identification was made possible by comparison of experimental data with simulated diffraction patterns. Computing the electron diffraction pattern of an isolated SWNT consists merely in representing the square modulus of the structure factor (3.49) *versus* the two components of $\boldsymbol{q}$ perpendicular to the incident electrons. The single-walled $(17, 3)$ tubule is considered as an illustrative example. The atomic structure of this chiral tubule, with radius $r = 0.73$ nm, is shown in the left-hand side of Fig. 3.45. The right-hand side of Fig. 3.45 is a computer simulation of the electron diffraction pattern obtained for a plane wave coming from the direction normal to the drawing. Clearly, the upstream and downstream hemi-cylindrical portions of the tubule project on the drawing plane in the form of two networks that are rotated from each other by twice the chiral angle θ ($= 8°$). As a consequence, the diffraction patterns produced by the front and back halves of the tubule are rotated by the same angle 2θ. The so-called first-order diffraction spots correspond to 10, 11 and equivalent reciprocal vectors of graphene[11] as indicated in Fig. 3.48. These streaked spots are located near the vertices of two hexagons, with parameter $b = 4\pi/\sqrt{3}a = 2.95\,\text{Å}^{-1}$, rotated by 16° from each other in the reciprocal space. The chiral angle of a single-walled nanotube can therefore be obtained by measuring half the angular separation between these two hexagons [61]. Due to the elongated shape of the spots, this angular measurement is not always accurate [62]. However, the chiral angle is also related to the distances of the spots from the equatorial line, and these can be measured accurately [60]. The diffraction spots have a shape elongated in the direction normal to the axis (streaking phenomenon) because of the progressive narrowing of the apparent lattice spacing in this direction as one moves from the center towards the edges of the nanotube. There is no such effect of curvature in the direction parallel to the axis: the spots are sharply defined across layer lines perpendicular to the axis.

The diffraction patterns of the two non-chiral zigzag ($\theta = 0$) and armchair ($\theta = \pi/6$) nanotubes are compared in Fig. 3.46. There is a geometrical correspondence between the positions of the diffraction spots produced by the

[11] The two-index notation refers to the Miller indices of the graphene sheet, related to the primitive rhombic cell defined by two unit vectors $\boldsymbol{a}_1$ and $\boldsymbol{a}_2$ making a 60° angle (see Fig. 3.44).

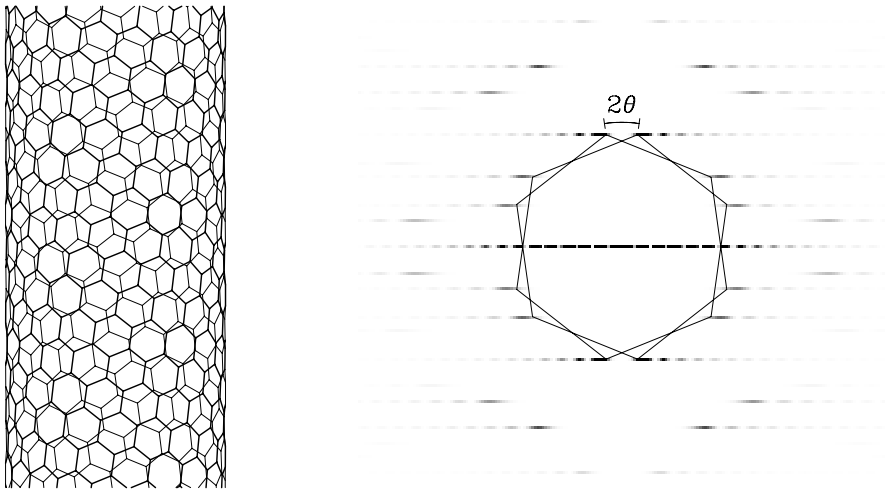


Fig. 3.45. *Left*: Atomic structure of the $(17, 3)$ nanotube projected on the plane normal to the wave vector of the incident electrons. *Right*: Corresponding electron-diffraction pattern represented in reversed intensity, where the brightest features appear in black. In this diffraction pattern, as in all the following illustrations, the vertical direction is parallel to the tubule axis

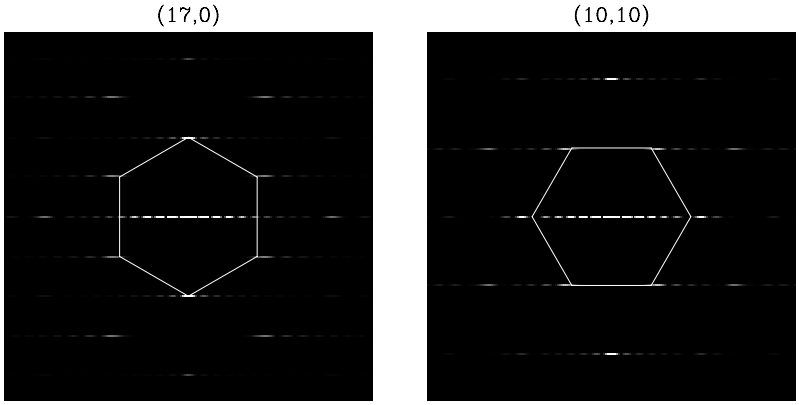


Fig. 3.46. Comparison of the electron diffraction patterns produced by the zigzag $(17, 0)$ nanotube (*left*) and the armchair $(10, 10)$ C nanotube (*right*) in normal incidence

$(n, 0)$ and (n, n) nanotubes, which consists in scaling q_z and $q_\perp$ by $3^{\pm 1/2}$. Here, there is no doubling of the first-order hexagonal array of spots as with the $(17, 3)$ nanotube. As shown in Fig. 3.46, two edges of the hexagon defined by the first-order spots are parallel to the nanotube axis (vertical direction) in the zigzag configuration, whereas two hexagonal edges are perpendicular

to the axis in the armchair geometry. Thus, the first-order hexagon has the same orientation with respect to the nanotube axis as the C honeycomb network in the achiral nanotube. The nanotubes $(17, 0)$ and $(10, 10)$ considered in Fig. 3.46 have nearly identical radii. For that reason, the central parts of their equatorial lines, dominated by $J_0(q_\perp r)$, look the same. For these non-chiral nanotubes, $J_0(q_\perp r)$ also contributes to the central part of every other two layer lines. However, the corresponding modulation of intensity is not as nicely defined as on the equatorial line due to the atomic scattering factor $f(q)$ which decreases with increasing $|\boldsymbol{q}|$.

Electron Diffraction by Multi Walled Nanotubes and Bundles of Single-Walled Nanotubes

The diffraction amplitude of a multi-wall nanotube is obtained by summing the structure factors (3.50) of the individual coaxial layers. In general, there is little structural correlation between the layers so that random values can be given to the coordinates ϕ_0 and z_0 of the origin atom in each layer. The diffraction intensity is the square of the modulus of the complex amplitude so-obtained. An interesting example is shown in Fig. 3.47. The left-hand side of the figure is a selected area diffraction pattern obtained experimentally on a double-wall nanotube (DWNT). A high-resolution TEM micrograph of the very same nanotube is represented at the bottom of Fig. 3.47a[12]. One clearly recognizes two chiralities in the diffraction pattern of Fig. 3.47a. One of the layers has a chiral angle close to 1°. For the other layer, $\theta = 13°$ can be measured. The equatorial line of the DWNT is modulated by a beating between the Bessel functions defining the structure factors of both layers. These interference effects are clearly seen in Fig. 3.47c, which reproduces the equatorial intensity profile computed for the nanotube $(41, 1)@(43, 13)$. The beating figure is very sensitive to the diameters d_1 and d_2 of the two layers. For large values of $q_\perp$, the intensity along the equatorial line oscillates with a short period $4\pi/(d_2 + d_1)$ and the envelope function has a long period $4\pi/(d_2 - d_1)$. From there, the diameters can be adjusted with 10% accuracy. These parameters together with the estimated chiral angles lead to only a few possible sequences of wrapping indices for the two layers. Detailed comparisons of the simulated diffraction patterns of the possible structures with the experimental data make it possible to identify the proper indices in a unique way [63], which is $(41, 1)@(43, 13)$. The theoretical diffraction pattern for this DWNT is shown in Fig. 3.47b.

Electrons traveling across a MWNT view maximum atomic densities on the edges of the cylindrical layers cut by an axial plane normal to the incident beam. These edges form two sets of equidistant lines on both sides of the axis and constitutes the fringes in the HRTEM images, with $c_0 = 0.34\,\text{nm}$ spacing

[12] The analysis of HR image formation from a DWNT is discussed in Sect. 3.3.1, see Fig. 3.33.

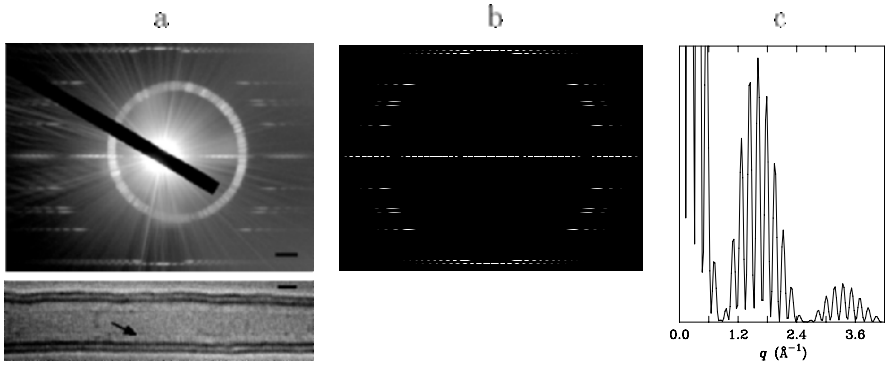


Fig. 3.47. (a) Selected-area electron diffraction pattern (the iris-like ring is an artifact) and HRTEM picture of a double-wall nanotube, the scale bar is approximately 1 nm (adapted from [64] with permission). **(b)** Computed diffraction pattern of the nanotube $(41, 1)@(43, 13)$. **(c)** Intensity profile along the equatorial line of the diffraction pattern shown in (b)

distance. Each set behaves more or less like a grating plate, which leads to a modulation of the equatorial line with constructive interferences taking place at integer multiples of $2\pi/c_0$ in the reciprocal space. These maxima correspond to the $00l$ diffraction spots of graphite [37].[13]

The structure of a bundle of SWNTs can be analyzed by selected area electron diffraction. For a well-ordered and non-twisted rope, the nanotubes crossed over by the electron beam have their axes parallel. The diffraction pattern can then be built up by summing the amplitudes $S(\boldsymbol{q})$ (3.50) of the individual SWNT components multiplied by phase factors $\exp(i\boldsymbol{q}_\perp \cdot \boldsymbol{\rho}_I)$ defined by the positions $\boldsymbol{\rho}_I$ of the tubes axes in the (x, y) plane. As shown in Fig. 3.48a, the diffraction equatorial line of a rope looks spotty because its amplitude is modulated by the rapidly-varying structure factor of the close-packed triangular lattice of the bundle. It often occurs that the electron diffraction pattern of a rope shows diffuse arcs along the first-order and second-order circles, which indicates that the constituent nanotubes have different helicities. For a rope composed of nanotubes with random helicities, calculations indicate that the highest diffraction intensities are concentrated in arcs extending $\sim 40°$ on both sides of the north and south poles on the first-order circle, in agreement with experiments performed on electric-arc synthesized samples [65].

In small bundles of SWNT produced by catalytic CVD, it frequently happens that the constituent nanotubes present very few helicities, by opposition with larger bundles produced at higher temperature by electric arc discharge and laser ablation [66]. An interesting example is provided by Fig. 3.48a, where the experimental diffraction pattern of a bundle is dominated by a single chi-

[13] In ABAB graphite, l must be an even index when referring to a lattice parameter c twice the layer spacing c_0.

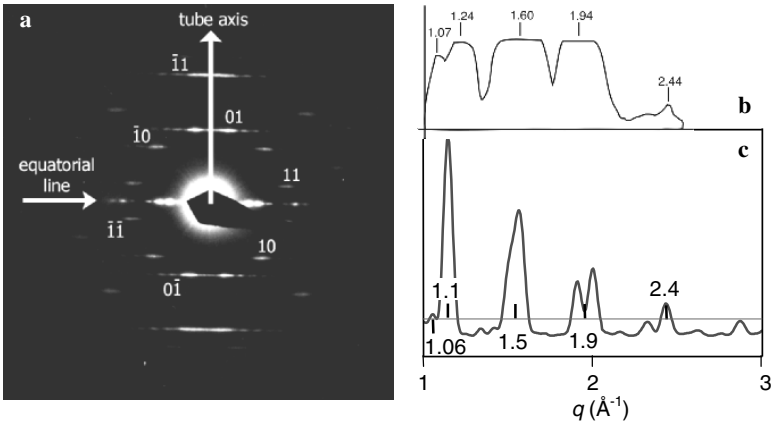


Fig. 3.48. (a) Selected-area electron diffraction pattern of a bundle of SWNTs produced by catalytic CVD. **(b)** Experimental equatorial line intensity profile. **(c)** Intensity profile computed for a bundle made of 31 $(14, 5)$ nanotubes. The horizontal line represents a possible saturation level of the spot intensities in the experimental profile

ral angle $\theta \approx 15°$. The diffraction pattern is well reproduced by assuming a bundle made of (14,5) nanotubes on a lattice with parameter 1.67 nm. The computed equatorial profile is shown in Fig. 3.48c. The peaks are Bragg diffractions generated by the triangular lattice of the bundle, their intensities are modulated by the Bessel function of the SWNTs (see Fig. 3.43). Of course, the intensities are saturated in the experimental equatorial profile (Fig. 3.48b) measured on a photographic plate and, for that reason, they do not compare directly to the calculations. By contrast, the positions of the peaks agree well with the simulation.

X-ray and Neutron Diffraction by Nanotubes

As explained above, both X-ray and neutron diffraction techniques require macroscopic amounts of sample. The nanotubes investigated may not be pure and they certainly are not all identical: they have different diameters and helicities making the interpretation of the diffraction profile less straightforward than with selected area electron diffraction. Neutron and X-ray diffraction experiments are generally performed on powders, with random orientations of the tube axis. In other cases, the nanotubes may be partly oriented within a plane or along an axis. X-ray diffraction may then reveal a useful tool to characterize their degree of ordering by measuring the angular distribution of the scattered intensities around the incident beam direction [67].

The diffraction profile of a powder of MWNTs resembles that of turbostratic polyaromatic carbon (see Sect. 3.2.1). It contains in-plane graphitic $hk0$ Bragg peaks with an abrupt rise at the low-q side and a much longer tail

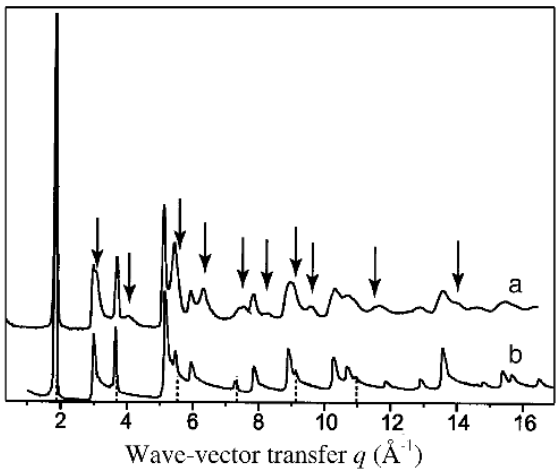


Fig. 3.49. (a) Experimental neutron powder diffraction profile of multi-wall nanotubes produced by arc discharge [69]. **(b)** Theoretical simulation of the diffraction profile (by courtesy of F. Moreau). In the simulation, a polygonized cross section of the largest nanotubes was assumed to best reproduce the weak hkl diffraction peaks indicated by the arrows along curve (a)

on the high-q side [68]. This asymmetrical shape is due to the curvature of the tubular layers, which in electron diffraction is responsible for spots that are sharply defined on their inner side and are fading away along the outer direction. Superposed to these sawtooth profiles, the $00l$ peaks generated by the coaxial layers have symmetrical profiles, because the $00l$ spots are not elongated by curvature. Figure 3.49a is an experimental neutron-diffraction profile of a powder of multi-wall nanotubes synthesized by conventional electric arc discharge [69]. The $00l$ diffractions give sharp, symmetrical peaks at the positions indicated by dotted lines (1.8 Å^{-1}, 3.6 Å^{-1} ...). Most of the other peaks are $hk0$ diffractions set up by the honeycomb array of the individual layers. There are also weak contributions from hkl diffractions at locations indicated by the arrows in Fig. 3.49. Their intensities indicate weak interlayer correlations which theoretical simulations are not able to reproduce with a cylindrical geometry.

When neutron and X-ray scattering techniques are applied to complex structures such as a powder mixing small crystallites or an ensemble of nanoparticles with disordered orientations, it is often advantageous to relate the diffraction intensity to the static pair-correlation function of the sample. The principles of that technique are as follows. Writing the kinematical expression of the structure factor (3.42) as

$$S(\boldsymbol{q}) = f(q) \int \rho(\boldsymbol{r}) \exp(\mathrm{i}\boldsymbol{q}.\boldsymbol{r}) \, \mathrm{d}^3 r \tag{3.56}$$

with $\rho(\boldsymbol{r}) = \sum_j \delta(\boldsymbol{r} - \boldsymbol{r_j})$ being the atomic density, one easily obtains the intensity in the form of a Fourier integral

$$I(\boldsymbol{q}) = |S(\boldsymbol{q})|^2 = |f(q)|^2 \int p(\boldsymbol{r}) \exp(\mathrm{i}\boldsymbol{q}.\boldsymbol{r}) \, \mathrm{d}^3 r \tag{3.57}$$

where $p(\boldsymbol{r}) = \sum_{i,j} \delta(\boldsymbol{r} - \boldsymbol{r}_{ij})$ (sum over all pairs of atoms) is the density autocorrelation function, also known as the Patterson function. If it is admitted the measured diffracted intensity is an average over a statistical ensemble of small systems (e.g. crystallites in a powder or multi-wall nanotubes with random orientations), assuming further that there is no coherent scattering between these systems, one simply has to take an ensemble average of $p(\boldsymbol{r})$ over the sample

$$\langle p(\boldsymbol{r}) \rangle = \langle N \rangle [\delta(\boldsymbol{r}) + g(r)] \tag{3.58}$$

$\langle N \rangle$ being the average number of atoms per small system, and

$$g(r) = \left\langle \sum_{i,j \neq i} \delta(r - r_{ij}) \right\rangle / (4\pi r^2 \langle N \rangle) \tag{3.59}$$

is the average pair correlation function. The intensity follows from (3.57). It only depends on the modulus of $\boldsymbol{q}$ due to the assumed orientational disorder. Away from the incident direction ($q \neq 0$), $I(q)$ is given by [70]

$$I(q) = \langle N \rangle |f(q)|^2 \left\{ 1 + \frac{4\pi}{q} \int_0^\infty r[g(r) - g(\infty)] \sin(qr) \mathrm{d}r \right\}. \tag{3.60}$$

This equation shows that the pair correlation function $g(r)$ of the system can be extracted from a measured diffraction intensity profile by sine Fourier transform. Of course, this mathematical transformation demands that $I(q)$ be measured on the largest possible interval of q. This is where neutron scattering reveals especially useful.

The pair correlation function (3.59) can be obtained by counting the number of CC pairs having their atomic distance between r and $r + dr$ in a given nanotube, and averaging the histogram so obtained over a representative sample. This technique was used to produce the theoretical neutron spectrum shown in Fig. 3.49b. The simulation was performed on a set of multi-wall nanotubes having random numbers of layers, diameters, helicities, and orientations. It was necessary to introduce about 20% of nanotubes with *polygonized* cross section for reproducing the weak intensities observed experimentally for the hkl peaks other than $00l$ and $hk0$. The presence of polyhedral graphitic particles in the sample might explain why such a large proportion of polygonized nanotubes was required to fit the experimental data. In the simulation, only the largest nanotubes were polygonized. The inner diameter of the polygonized nanotubes was taken between 10 and 15 nm, not below, and these nanotubes had between 10 and 15 layers. All polygonized nanotubes had

the zigzag configuration. From one layer to the next, 9 rows of hexagons were added in order to increase the diameter by 0.34 nm. With a 9-edge polygonal cross section, it is then easy to realize a graphite stacking order across each facet.

The crystallinity of SWNT bundles can be controlled with X-ray and neutron diffraction by examining the Bragg peaks produced by the two-dimensional triangular lattice. The most intense peak is due to the 11 node of the reciprocal lattice of the bundle, in the notations of Fig. 3.34, usually located between $0.4\,\text{Å}^{-1}$ and $0.5\,\text{Å}^{-1}$ [44]. For such small scattering wave vectors, the SWNTs can be treated as continuous cylinders. According to (3.44), then, the structure factor of a rope writes

$$S(\boldsymbol{q}) = (2\pi)^2 N f(q) \sum_I r_I J_0(q_\perp r_I) \exp(\mathrm{i}\boldsymbol{q}_\perp.\boldsymbol{\rho}_I)\delta(q_z) \tag{3.61}$$

where the index I runs over all the constituent nanotubes. This formula describes the diffracted amplitude in the equatorial plane $q_z = 0$ of the rope, assumed to be perfectly ordered and non twisted.

The intensity is proportional to the square modulus of $S(\boldsymbol{q})$. With X-ray and neutron powder diffraction, the intensity is an average over all possible orientations of the ropes. Assuming that the nanotubes in a rope have all the same radius, the average intensity becomes [71]

$$I(q) \propto \exp(-2W(q))[f^2(q)/q] \left\langle [rJ_0(qr)]^2 \sum_{I,J} J_0[q|\boldsymbol{\rho}_I - \boldsymbol{\rho}_J|] \right\rangle \tag{3.62}$$

where $< ... >$ denotes the average over all possible structures of the ropes. The intensity is reduced by a Debye-Waller factor $\exp(-2W(q))$ that accounts for the vibrational motions of the atoms. W is proportional to the mean square displacement of the atom about their equilibrium positions [72] through the relation $W(q) = \langle(\boldsymbol{q}.\boldsymbol{u})^2\rangle_\mathrm{t}$. The sum over I, J in this expression describes intertube interferences. For one given rope, the diffracted intensity is sensitive to the nanotube diameter, the intertube separation distance, and the number of tubes in the rope. On the average, the position and width of the 11 Bragg peak depend on the actual distribution of nanotube diameters between different ropes and on and the rope size. Careful examination of the 11 diffraction peak produced by X-rays and neutrons can therefore provide a valuable, statistical characterization of the bundles.

As an illustration, the upper curve in Fig. 3.50 is an experimental X-ray diffraction profile of a C nanotube sample extracted from the collaret in an arc-discharge chamber. The profile presents a clear 11 Bragg peak at $0.43\,\text{Å}^{-1}$ that indicates the presence of SWNT ropes. The peak around $1.85\,\text{Å}^{-1}$ is due to multilayered graphite nanoparticles, probably filled with Ni catalyst whose signature is revealed by two Bragg peaks at 3.1 and $3.5\,\text{Å}^{-1}$. The curve at the bottom of Fig. 3.50 is a theoretical diffraction profile obtained with the help of (3.62). It was computed for a statistical ensemble of bundles,

assuming a Gaussian distribution of nanotube diameters centered at 1.34 nm with root mean square deviation $\sigma = 0.13$ nm. The number of tubes in a bundle was also treated as a Gaussian variable, with average value 25 and deviation $\sigma = 5$. These parameters were adjusted to the experimental diffraction profile. The theoretical diffraction profile presents Bragg peaks associated to the 11, 20, and 31 fringe spacings of Fig. 3.36.

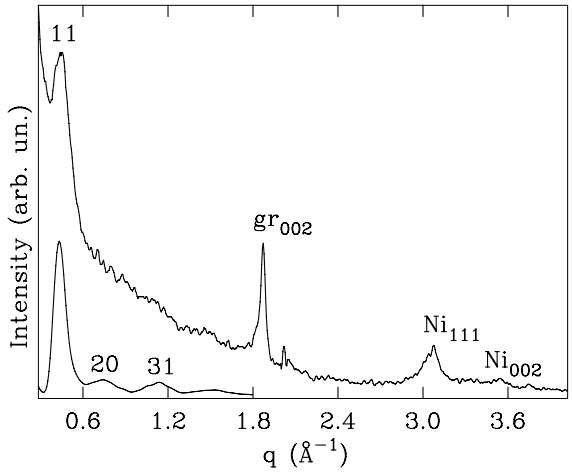


Fig. 3.50. *Top curve*: experimental X-ray powder diffraction profile of a sample of SWNT ropes produced by the arc-discharge technique. *Bottom curve*: theoretical diffraction profile computed for an ensemble of ropes with average nanotube diameter 1.34 nm and average number of tubes 25. The 11, 20, and 31 Bragg indices refer to the bundle rectangular cell of Fig. 3.34 (these indices become 10, 11, and 21 in the hexagonal unit cell)

3.4 Analysis of the Nanotube Structure with STM

The first atomically-resolved STM images and scanning tunneling spectra (STS) of single-walled nanotubes were reported simultaneously and independently by two groups [73, 74]. Figure 3.51 shows atomically-resolved STM images of three single-walled nanotubes with different helicities [75]. Corrugation holes appear at positions corresponding to the centers of the hexagons of the honeycomb structure, defining a triangular lattice with parameter 0.246 nm. These corrugation dips are surrounded by protruding features at the location of the CC bonds. As shown in Fig. 3.51, the CC bonds of a nanotube are not all imaged with the same appearance. This bond anisotropy often destroys the honeycomb symmetry in the STM images [76], such as in Fig. 3.51c.

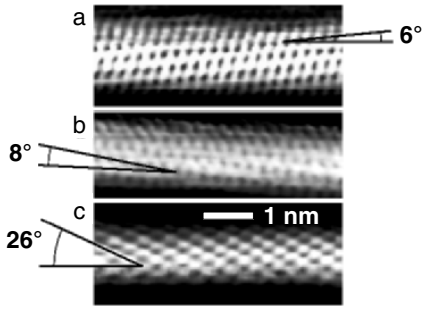


Fig. 3.51. Experimental STM images of three isolated single-walled nanotubes on a Au(111) surface (adapted from ref. [75]). Images (**a**) and (**b**) correspond to nanotubes close to the armchair geometry. Image (**c**) comes from a tube close to the zigzag geometry

Tight-binding [77, 78] and *ab initio* [79] calculations of the STM images have confirmed this observation.

Achieving atomic resolution on a nanotube with an STM demands that the tip presents a nanoscopic protrusion that terminates with a single atom. Otherwise, the curvature radius of the tip can be larger than the radius of the nanotube, which washes out the atomic structure. Furthermore, due to a tip-shape convolution effect, the apparent diameter D of the imaged nanotube (real diameter d_t) depends on the tip curvature radius R through the approximate expression $D \approx 2\sqrt{2R(d_t + h)}$, where h is the nanotube-substrate separation [16, 80]. D can be considerably larger than d_t. In most cases, the apparent height of the nanotube in the STM topographic profile can be used as an estimate of the real diameter. Sometimes, it is possible to determine the nanotube diameter by fitting the STM current measured at various locations above both the nanotube and its support with exponential laws [81].

Even with a point-like tip, a distortion of the STM image can be generated by the curvature of the nanotube. As already pointed out by Ge and Sattler [82], when the tip scans the nanotube, the tunneling current flows along the shortest path, which is normal to the tube. If, accordingly, the current is assumed to flow radially, a C atom at coordinates (x', y', z') on the nanotube will be imaged when the tip has horizontal coordinates $x = x'$ and $y = y'(r + \Delta)/r$, as shown in Fig. 3.52. Here the x-axis is parallel to the tube axis (i.e., perpendicular to the drawing), y is measured normally to the axis, r is the tube radius, and Δ is the tip–nanotube distance. The imaged atomic structure of the nanotube is therefore stretched by the factor $(r + \Delta)/r$ in the y direction [77]. For a nanotube of 1.4 nm diameter, a distortion of 70 % is predicted to occur when $\Delta = 0.5$ nm. Experimentally, distortions of 20–60 % have been observed on single-walled nanotubes with diameter in the range 1.2–1.5 nm [75].

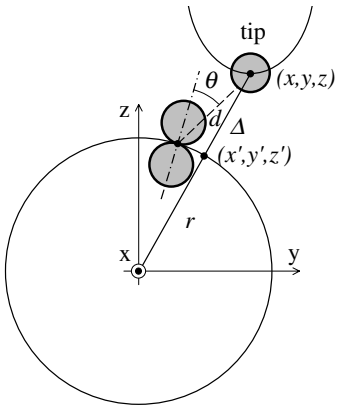


Fig. 3.52. Schematic representation of a STM tip, with an s orbital (*shaded surface*) at the apex, and the nanotube with a π orbital (*shaded surface*) on each carbon atom. Just one atomic orbital is drawn for clarity. The largest tip–nanotube coupling element is taking place along the normal Δ to the nanotube

The tight-binding formalism introduced in Sect. 3.1.4 can readily be applied to the calculation of STM images of carbon nanotubes. In the illustrations that follow, the STM current was calculated with (3.40), by considering a single atom i at the tip apex with an s atomic orbital, very much like in Tersoff-Hamann theory [17]. A Gaussian function of 6 eV full width at half maximum was chosen to represent the density of states $n_{ii}^{t}(E)$ of the tip at the apex. On the nanotube, there is one π orbital per atom. The tip-sample coupling interactions are *sp* Slater-Koster hopping terms having the following expression [77]:

$$v_{ij} = v_0 \; w_{ij} \, \mathrm{e}^{-d_{ij}/\lambda} \cos\theta_{ij} \tag{3.63}$$

$$w_{ij} = \mathrm{e}^{-a d_{ij}^2} \Big/ \sum_{j'} \mathrm{e}^{-a d_{ij'}^2} \tag{3.64}$$

where d_{ij} is the distance between the tip atom i and the sample atom j, θ_{ij} is the angle between the orientation of the π orbital on site j and the ij direction (see Fig. 3.52). The exponential dependence of v_{ij} on d_{ij} is inspired by the expression of the 1D tunneling transmission coefficient (3.34). We use $\lambda = 0.085\,\mathrm{nm}$, which imposes that the current decreases by a factor of 10 each time the distance of the tip increases by 0.1 nm. The Gaussian weight factor w_{ij} was introduced for convergence reasons, and also to confine the tunneling current in a narrow channel ($a = 60\,\mathrm{nm}^{-2}$).

Computed STM images of three metallic single-walled nanotubes with diameter around 1.4 nm are shown in Fig. 3.53a. In each case, the tip apex was positioned 0.5 nm above the central atom. Then the tip was moved along the two horizontal directions x and y, and its vertical position z was adjusted so as to reproduce the current computed at the initial position. Each image is a

three-dimensional representation of the height $z(x, y)$ of the tip at constant current. In agreement with *ab initio* calculations based on Tersoff-Hamann theory [79], the centers of the honeycomb hexagons correspond to sharp corrugation dips in the image of a nanotube, because the tunneling probability is much smaller at the center of an hexagon than above an atom and a CC bond. As a result, the STM tip comes closer to the nanotube there to keep the current constant. The curvature-induced distortion discussed here above is responsible for the elongated shape of the corrugation dips at the center of the hexagons.

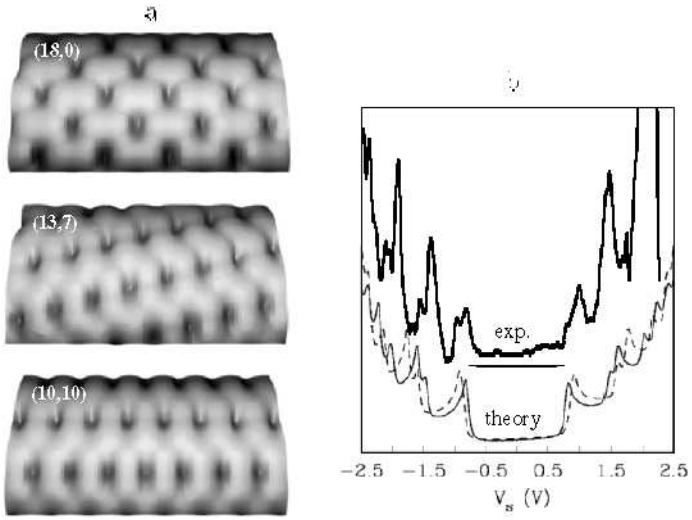


Fig. 3.53. (a) Constant-current STM images ($1.8 \times 1.0\,\mathrm{nm}^2$) of three metallic nanotubes computed with a tip potential of 0.2 V. **(b)** Top curve: experimental STS spectrum of a metallic nanotube [83]; Bottom curves: theoretical $\mathrm{d}I/\mathrm{d}V$ curves [77] *versus* sample potential for two possible candidates, (13,7) (*solid line*) and (12,6) (*dashed line*)

In the $(10, 10)$ armchair nanotube shown in Fig. 3.53a, the largest protrusions are realized on the atoms, all the bonds look the same, and the image has the honeycomb symmetry. In the $(18, 0)$ zigzag nanotube, the largest protrusions are realized on the bonds parallel to the axis. These protruding bonds form a triangular pattern of oblate dots, with 0.246 nm parameter. This resembles the triangular lattice formed by every other two atoms in multilayered graphite. There is a saddle point at the center of the inclined bonds. The image shown in Fig. 3.51c exhibits all the characteristics obtained for the $(18, 0)$ zigzag nanotube. In the chiral $(13, 7)$ nanotube, one third of the bonds protrudes more than the others, like in the zigzag nanotube. The anisotropy of

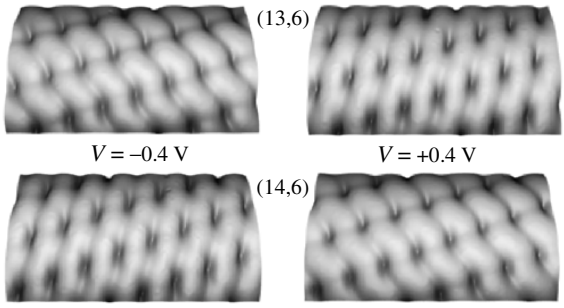


Fig. 3.54. Computed STM images ($1.8 \times 1.0\,\mathrm{nm}^2$) of the semiconductor $(13, 6)$ and $(14, 6)$ nanotubes, for two bias potentials V of the tip, probing the unoccupied (*left*) and occupied electronic states (*right*) of the sample

the imaged bonds is responsible for the appearance of stripes. The resulting stripped pattern is commonly observed in the experimental images [84].

With semiconductors, the valence or conduction states lead to different pictures which the STM gives of the same nanotube. As an illustration, Fig. 3.54 shows STM images of two semiconductor nanotubes computed for bias potentials equal to -0.4 and $+0.4\,\mathrm{V}$, slightly larger than half the band gap. The $(13, 6)$ and $(14, 6)$ nanotubes illustrated in Fig. 3.54 have nearly the same atomic structure. However, their STM images look different. In fact, the image of $(13, 6)$ computed for a positive tip potential resembles closely that of $(14, 6)$ obtained with a negative bias, and vice versa. This is so, because a positive STM tip probes the occupied electronic states of the sample, whereas a negative tip probes the unoccupied states. On going from the $(13, 6)$ nanotube to $(14, 6)$, one chiefly exchanges the wave-function characteristics of the highest occupied states with those of the lowest unoccupied states. In this respect, the semiconducting nanotubes belong to two families, depending on whether the difference $n - m$ between their wrapping indices is a multiple of three *plus* one or *minus* one. In each case, the bonds that appear brighter in the STM image of a chiral nanotube form stripes that spiral around the structure. By switching the tip potential from -0.4 to $+0.4\,\mathrm{V}$, the protruding bonds change from one zigzag chain of atoms to another, which rotates the spiral stripes by $60°$ in the image. This remarkable complementarity of the STM images upon reversing the bias has been observed experimentally [85] and explained theoretically in tight-binding [78]. Figure 3.54 is an example, among others, which demonstrates that STM mixes both structural and electronic properties of the carbon nanotubes.

The two wrapping indices of an isolated single-walled nanotube can in principle be deduced from STM image with atomic resolution by measuring the diameter and the chiral angle. Unfortunately, this *ultimate* structural characterization is not easy to achieve. In principle, the chiral angle of a nanotube can be determined by measuring the angle between the tube axis and

the centers of the closest row of hexagons (see Fig. 3.51). However, the STM image is often distorted by the curvature of the lattice, as explained above, which entails a systematic error in the measurement of the angles. Deriving the diameter from STM information is also challenging, mostly because of the tip-shape convolution effect, also mentioned above. Today, the most reliable and conventional way to evaluate the diameter consists in measuring the positions of the van Hove singularities in the electronic density of states via standard STS measurements, and comparing them with their known relationship with the nanotube radius [75, 83]. Nowadays, STS spectroscopy of nanotubes has progressed to such a stage that this technique can be used for a systematic determination of the tube diameter [86]. In some cases, the combination of both STM imaging and STS spectroscopy allows one to determine the two wrapping indices of a nanotube with a good reliability. As an example, the experimental STS spectrum of a metallic nanotube is shown in Fig. 3.53b. From the STM topographical image of the very same nanotube [83], the diameter and chiral angles were estimated as $d_\mathrm{t} = 1.35 \pm 1\,\mathrm{nm}$ and $\theta = 20 \pm 1\,^\circ$. Two metallic nanotubes have these structural parameters, $(13, 7)$ and $(12, 6)$. $\mathrm{d}I/\mathrm{d}V$ curves computed for these two nanotubes using (3.40), with C-π hopping interaction $\gamma_0 = -2.6\,\mathrm{eV}$, are plotted in Fig. 3.53b. By comparing the positions of the van Hove singularities with those of the spikes in the experimental spectrum, the nanotube can be identified as $(13, 7)$.

Acknowledgments

The writing of this chapter has benefited from input of C. Barreteau, L.P. Biró, J.F. Colomer, F. Ducastelle, L. Henrard, P. Launois, G.I. Márk, V. Meunier, F. Moreau. In particular, parts of the original work presented in Sect. 3.3.1 is the fruit of a very pleasant collaboration with C. Journet, J. Gavillet, R. Lee, and N. Demoncy. We are particularly indebted to F. Willaime for atomistic models extensively used in HREM simulations. Ph. L. acknowledges the financial support of the IUAP Program P5/01 on 'Quantum size effect in nanostructured materials' of the Belgian OSTC offices. The authors acknowledge the financial support of the CNRS.

References

1. J.D. Jackson: *Classical Electrodynamics*, 2nd edn, (John Wiley and Sons, New York 1975) p 679
2. E. Merzbaker: *Quantum Mechanics* (John Wiley and Sons, New York 1970) p 228
3. P.A. Doyle and P.S. Turner: Acta. Cryst. A **24**, 390 (1968)
4. S.W. Lovesey: *Theory of neutron scattering from condensed matter*, vol. 1 (Claredon Press, Oxford 1984) p 11

5. D. Van Dyck and M. Op de Beeck: Ultramicroscopy **64**, 99 (1996)
6. C. Barreteau: PhD Thesis (ONERA, Châtillon, France 1995)
7. J.C. Cowley: *Diffraction Physics* (Elsevier, Amsterdam 1982)
8. P. Busek, J. Cowley, and L. Eyring: *High-Resolution Transmission Electron Microscopy and Associated Techniques* (Oxford University Press, 1988)
9. Xiao-Feng Zhang and Ze Zhang: *Progress in Transmission Electron Microscopy, vol.1, Concepts and Techniques, Series in Surface Sciences* (Springer Verlag, Berlin 2001)
10. S. Amelinkx, D. Van Dyck, J. Van Landuyt, G. Van Tendeloo: *Handbook of Microscopy: Applications: in Materials Science, Solid-State Physics and Chemistry, Methods I* (VCH, Wienheim 1997)
11. J.C.H. Spence: *Experimental High Resolution Electron Microscopy*, 2nd edn (Clarendon Press, Oxford 1988)
12. J. Cowley and A.F. Moodie: Acta Crys. **10**, 609 (1957)
13. P. Stadelmann: Ultramicroscopy **21**, 131 (1987)
14. R.H. Wade and J. Frank: Optik **49**, 81 (1977)
15. A.A. Lucas, H. Morawitz, G.R. Henry, J.P. Vigneron, Ph. Lambin, P.H. Cutler, and T.W. Feuchtwang: J. Vacuum Sci. Technol. **6**, 296 (1988)
16. G.I. Márk, L.P. Biró, and J. Gyulai: Phys. Rev. B **58**, 12645 (1998)
17. J. Tersoff and D.R. Hamann: Phys. Rev. Lett. **50**, 1998 (1983)
18. K. Kobayashi and M. Tsukada: J. Vac. Sci. Technol. A **8**, 170 (1990)
19. A. Oberlin: in *Chemistry and Physics of Carbon* vol. 22, Edit. P.A. Thrower, (Marcel Dekker, New York 1989) p. 1
20. M. Monthioux: in *Carbon Molecules and Materials*, ed by R. Setton, P. Bernier, and S. Lefrant (Taylor and Francis, London 2002) p 127
21. A. Oberlin, J. Goma, and J.N. Rouzaud: J. Chim. Phys. **81**, 701 (1984)
22. H. Allouche and M. Monthioux: Carbon **43**, 1265 (2005)
23. A. Guinier: *X-ray Diffraction in Crystals, Imperfect Crystals and Amorphous Bodies* (Dover Publications, 1994).
24. L. Laffont, M. Monthioux, V. Serin, and B. Lavelle: J. Appl. Phys., submitted
25. A. Oberlin: Carbon **17**, 7 (1979)
26. A. Oberlin: J. Microsc. Spectrosc. Electron. **2**, 729 (1977)
27. M. Monthioux, M. Oberlin, A. Oberlin, X. Bourrat, and R. Boulet: Carbon **20**, 167 (1982)
28. J. Ayache, A. Oberlin, and M. Inagaki: Carbon **28**, 337 (1990)
29. J.B. Donnet, R.C. Bansal and M.J. Wang: *Carbon Black*, (Marcel Dekker, New York 1993)
30. F. Soutric, M. Monthioux E. Musset, and J.F. Després: in *Proceedings of Eurocarbon 98* vol. 2, (ArbeitKreis Kohlenstoff, 1998), p 653
31. J. Goma and M. Oberlin: Thin Solid Films **65**, 221 (1980)
32. J.N. Rouzaud, A. Oberlin, and C. Benny-Bassez: Thin Solid Films **105**, 75 (1983)
33. A. Oberlin, J. Ayache, and M. Oberlin: J. Polym. Sci. **20**, 579 (1982)
34. D. Golberg, Y. Bando, L. Bourgeois, and K. Kurashima: Carbon **39**, 1858 (1999)
35. R. Lee, J. Gavillet, M. Lamy de la Chapelle, A. Loiseau, JL. Cochon, D. Pigache, J. Thibault, F. Willaime: Phys. Rev. B **64**, 121405 (2001)
36. S. Friedrichs, J. Sloan, M.L.H. Green, J.L. Hutchison, R.R. Meyer and A.I. Kirkland: Phys. Rev. B **64**, 045406 (2001)
37. S. Iijima: Nature **354**, 56 (1991)

38. A. Loiseau, F. Willaime, N. Demoncy, G. Hug, and H. Pascard: Phys. Rev. Lett. **76**, 4737 (1996)
39. S. Amelinckx, A. Lucas, and Ph. Lambin: Rep. Prog. Phys. **62**, 1471 (1999)
40. X.F. Zhang, X.B. Zhang, G. Van Tendeloo, S. Amelinckx, M. Op de Beeck, and J. Van Landuyt: J. Cryst. Growth **130**, 368 (1993)
41. D. Golberg, Y. Bando, L. Bourgeois, K. Kurashima, and T. Sato: Appl. Phys. Lett. **77**, 1979 (2000)
42. A.L. Hamon, A. Maraud, and B. Jouffrey: Phil. Mag **81**, 1779 (2001)
43. P. Bernier, W.K. Maser, C. Journet, A. Loiseau, M. Lamy de la Chapelle, S. Lefrant, R. Lee, and J. Fischer: Carbon **36**, 675 (1998)
44. A. Thess, R. Lee, P. Nikolaev, H. Dai, P. Petit, J. Robert, C. Xu, Y. H. Lee, S.G. Kim, A.G. Rinzler, D.T. Colbert, G.E. Scuseria, D. Tománek, J.E. Fischer, and R.E. Smalley: Science **273**, 483 (1996)
45. C. Journet, W.K. Maser, P. Bernier, A. Loiseau, M. Lamy de la Chapelle, S. Lefrant, P. Deniard, R. Lee, and J.E. Fischer: Nature **388**, 756 (1997)
46. L. Henrard, A. Loiseau, C. Journet, and P. Bernier: Eur. Phys. J. B **13**, 661 (2000)
47. Ph. Lambin, A. Fonseca, J.P. Vigneron, J.B. Nagy, and A.A. Lucas: Chem. Phys. Lett. **245**, 85 (1995)
48. J.C. Charlier and S. Iijima: in *Carbon nanotubes: synthesis, structure, properties and applications*, ed by M.S. Dresselhaus, G. Dresselhaus, and Ph. Avouris (Springer Verlag, Berlin 2000) p 55
49. F. Willaime, A. Loiseau, X. Deschanels, N. Demoncy, G. Hug, C. Colliex, and H. Pascard: in *Molecular Nanostructures*, ed by H. Kuzmany, J. Fink, M. Mehring and S. Roth (World Scientific, Singapur 1998) p 399
50. A. Loiseau, F. Willaime, N. Demoncy, N. Shramchenko, G. Hug, C. Colliex, and H. Pascard: Carbon **36**, 743 (1998)
51. P.M. Ajayan, V. Ravikumar, and J.C. Charlier: Phys. Rev. Lett. **81**, 1437 (1998)
52. M. Zaiser and F. Banhart: Phys. Rev. Lett. **79**, 3680 (1997)
53. M. Terrones, H. Terrones, F. Banhart, J.C. Charlier, and P.M. Ajayan: Science **288**, 1226 (2000)
54. F. Banhart and P.M. Ajayan: Nature **382**, 433 (1996)
55. F. Banhart: Rep. Prog. Phys. **62**, 1181 (1999)
56. W. Cochran, F.H.C. Crick, and V. Vand: Acta Cryst. **5**, 581 (1952)
57. R.E. Franklin and R.G. Gosling: Nature **171**, 742 (1953)
58. A.A. Lucas, V. Bruyninckx, and Ph. Lambin: Europhys. Lett. **35**, 355 (1996)
59. Ph. Lambin and A.A. Lucas: Phys. Rev. B **56**, 3571 (1997)
60. M. Gao, J.M. Zuo, R.D. Twesten, I. Petrov, L.A. Nagahara, and R. Zhang: Appl. Phys. Lett. **82**, 2703 (2003)
61. S.I. Iijima and T. Ichihashi: Nature **363**, 603 (1993)
62. L.C. Qin: Chem. Phys. Lett. **297**, 23 (1998)
63. M. Kociak, K. Suenaga, K. Hirahara, T. Nakahira, and S. Iijima: Phys. Rev. Lett. **89**, 155501 (2002)
64. M. Kociak, K. Hirahara, K. Suenaga, and S. Iijima: Eur. Phys. J., in press (2003)
65. L. Henrard, A. Loiseau, C. Journet, and P. Bernier: Synthetic Metals **103**, 2533 (1999)
66. J.F. Colomer, L. Henrard, Ph. Lambin, and G. Van Tendeloo: Eur. Phys. J. B **27**, 111 (2002)
67. P. Launois, A. Marucci, B. Vigolo, P. Bernier, A. Derré, and Ph. Poulin: J. Nanosci. Nanotechnol. **1**, 125 (2001)

68. Y. Saito, T. Yoshikawa, S. Bandow, M. Tomita, and T. Hayashi: Phys. Rev. B **48**, 1907 (1993)
69. A. Burian, J.C. Dore, H.E. Fischer, and J. Sloan: Phys. Rev. B **59**, 1665 (1999)
70. Ch. Kittel: *Introduction to solid state physics*, 7th edn (John Wiley and Sons, New York 1996)
71. S. Rols, R. Almairac, L. Henrard, E. Anglaret, and J.L. Sauvajol: Eur. Phys. J. **10**, 263 (1999)
72. N.W. Ashcroft and N.D. Mermin: *Solid State Physics*, (Harcourt Brace College Publishing, Orlando, Florida 1976) p 792
73. J.W.G. Wildöer, L.C. Venema, A.G. Rinzler, R.E. Smalley, and C. Dekker: Nature **391**, 59 (1998)
74. T.W. Odom, J.L. Huang, Ph. Kim, and Ch.M. Lieber: Nature **391**, 62 (1998)
75. L.C. Venema, V. Meunier, Ph. Lambin, and C. Dekker: Phys. Rev. B **61**, 2991 (2000)
76. L.C. Venema, J.W.G. Wildoër, C. Dekker, A.G. Rinzler, and R.E. Smalley: Appl. Phys. A **66**, S153 (1998)
77. V. Meunier and Ph. Lambin: Phys. Rev. Lett. **81**, 5888 (1998)
78. C.L. Kane and E.J. Mele: Phys. Rev. B **59**, R12759 (1999)
79. A. Rubio, D. Sanchez-Portal, E. Artacho, P. Ordejon, and J.M. Soler: Phys. Rev. Lett. **82**, 3520 (1999)
80. L.P. Biró, S. Lazarescu, Ph. Lambin, P.A. Thiry, A. Fonseca, J.B. Nagy, and A.A. Lucas: Phys. Rev. B **56**, 12490 (1997)
81. T.W. Odom, J.L. Huang, Ph. Kim, M. Ouyang, and Ch.M. Lieber: J. Mater. Res. **13**, 2380 (1998)
82. M. Ge and K. Sattler: Appl. Phys. Lett. **65**, 2284 (1994)
83. Ph. Kim, T. Odom, J.L. Huang, and C.M. Lieber: Phys. Rev. Lett. **82**, 1225 (1999)
84. W. Clauss: Appl. Phys. A **69**, 275 (1999)
85. W. Clauss, D.J. Bergeron, M. Freitag, C.L. Kane, E.J. Mele, and A.T. Johnson: Eur. Phys. Lett. **47**, 601 (1999)
86. I. Wirth, S. Eisebitt, G. Kann, and W. Eberhardt: Phys. Rev. B **61**, 5719 (2000)

4

Electronic Structure

F. Ducastelle, X. Blase, J.-M. Bonard, J.-Ch. Charlier and P. Petit

Abstract. This chapter is devoted to a discussion of the electronic structure of carbon and other nanotubes. It begins with a very general description of *sp* electronic states based on the tight-binding or Hückel approximation. This is sufficient to capture many basic electronic properties of single-walled nanotubes. This is followed by a more detailed analysis of the properties of carbon nanotubes, which is necessary when considering curvature effects, multi-walled nanotubes, bundles, etc. Although much less studied, other non-carbon nanotubes deserve also some attention: because of their ionic character boron nitride nanotubes and other mixed nanotubes offer in particular the opportunity of varying the electronic gap. This is described in a following section. The possibility of monitoring the electronic structure of carbon nanotubes as in the case of graphite, by intercalation and charge transfer are also investigated. Finally an extensive review on field emission is presented.

4.1 Electronic Structure: Generalities

4.1.1 From Atoms to Crystals

In this section, we briefly recall how the electronic energy levels are modified when going from atoms to molecules and crystals. More detailed presentations can be found in many textbooks (see for example [1–9]).

Atoms

The simplest atom is the hydrogen atom. Its ground state of lowest energy is a $1s$ state of energy $E_{1s} = -13.6\,\mathrm{eV}$, and the corresponding wave function $\psi(\boldsymbol{r})$ satisfies the familiar Schrödinger equation

$$\frac{-\hbar^2}{2m}\Delta\psi(\boldsymbol{r}) + V(\boldsymbol{r})\psi(\boldsymbol{r}) = E\,\psi(\boldsymbol{r})\ , \tag{4.1}$$

which can conveniently be written, using Dirac bra and ket notations as

F. Ducastelle et al.: *Electronic Structure*, Lect. Notes Phys. **677**, 199–276 (2006)
www.springerlink.com
© Springer-Verlag Berlin Heidelberg 2006

$$H|\psi\rangle = E|\psi\rangle \quad ; \quad \psi(\boldsymbol{r}) = \langle \boldsymbol{r}|\psi\rangle \ . \tag{4.2}$$

In the case of the hydrogen atom, $V(\boldsymbol{r})$ is just the Coulomb potential of the proton and, in this non-relativistic limit, the Schrödinger equation can be solved exactly. This is no longer the case in general because of the electron-electron interactions. Some approximation have to be made. It is generally assumed that each electron feels a mean effective potential due to the surrounding ions and other electrons. Depending on the treatment of so-called exchange and correlation terms various 'mean field' approximations have been derived, such as the Hartree and the Hartree-Fock approximations, or the local density approximation (LDA). In principle the LDA, which is based on the Density Functional Theory (DFT), fundamentally applies to the calculation of ground state properties, although it can also be used in practice for treating excited states. The advantage of the LDA is that it provides us with a local effective potential for which an effective one-electron Schrödinger equation has exactly the form given by (4.1) [10].

Since the effective potential is spherically symmetric, the wave function takes the usual form $\psi_{nlm}(\boldsymbol{r}) = R_{nl}(r)Y_{lm}(\theta,\phi)$, where n, l, and m are the principal, orbital and magnetic quantum numbers, respectively. $n = 1, 2, 3 \ldots; l = 0, 1, \ldots, n-1$ and $m = 0, \pm 1, \ldots, \pm l$.

Molecules

H_2^+ *Molecule*

Consider first the H_2^+ ion with two protons and one electron. If the protons are far apart it is natural to assume that the ground state wave function can be built from a linear combination of the hydrogenoid wave functions centered on each proton (linear combination of atomic orbitals or LCAO). Let $|A\rangle$ and $|B\rangle$ be the $1s$ states centered on sites $\boldsymbol{r}_A$ and $\boldsymbol{r}_B$, and further assume that

$$|\psi\rangle \simeq a|A\rangle + b|B\rangle \ , \tag{4.3}$$

where a and b are constants. The Hamiltonian H is equal to $T + V_A + V_B$ where T is the kinetic energy operator and V_A and V_B are the ionic potentials. It is then fairly easy to solve the Schrödinger equation in the basis spanned by $|A\rangle$ and $|B\rangle$. We need the matrix elements of H

$$\langle A|H|A\rangle = \langle B|H|B\rangle = E_{1s} + \alpha \ , \tag{4.4}$$

where $\alpha = \langle A|V|A\rangle = \langle B|V|B\rangle = \int \mathrm{d}\boldsymbol{r}\, |\psi_{1s}(\boldsymbol{r} - \boldsymbol{r}_A)|^2\, V(\boldsymbol{r} - \boldsymbol{r}_B)$, and

$$\langle B|H|A\rangle = \langle A|H|B\rangle = E_{1s}S + t \ , \tag{4.5}$$

where $S = \langle A|B\rangle = \int \mathrm{d}\boldsymbol{r}\, \psi_{1s}(\boldsymbol{r} - \boldsymbol{r}_A)\, \psi_{1s}(\boldsymbol{r} - \boldsymbol{r}_B)$, and $t = \langle A|V|B\rangle = \int \mathrm{d}\boldsymbol{r}\, \psi_{1s}\,(\boldsymbol{r} - \boldsymbol{r}_A)\, V(\boldsymbol{r} - \boldsymbol{r}_B)\, \psi_{1s}(\boldsymbol{r} - \boldsymbol{r}_B)$.

The so-called crystalline field integral α and the transfer or hopping integral t are negative because the ionic potentials are negative (attractive). The overlap integral S does not vanish but is frequently neglected by physicists. Actually the LCAO approximation is usually very crude in solids and it is preferable to make it as simple as possible. In chemistry it is usual to keep this overlap integral and further assume that t is proportional to S.

The advantage of neglecting S is that the atomic basis becomes orthonormal. In the following we shall neglect S, so that we just need to diagonalize a 2×2 matrix, to find the eigenvalues $E = E_{1s} + \alpha \pm t$ associated with the eigenstates $|A \pm B\rangle/\sqrt{2}$ respectively. The coupling of the two atomic states lifts the degeneracy of these states and bonding and anti-bonding states, frequently denoted σ and σ^* states, are obtained (Fig. 4.1). The energy gain in the bonding state is due to the fact that the electronic density is reinforced between the two protons. This is an interference effect which is at the root of covalent bonding.

When the inter-ionic repulsive energy is added, the H_2^+ molecule is found to be stable with a bonding energy about 2.8 eV.

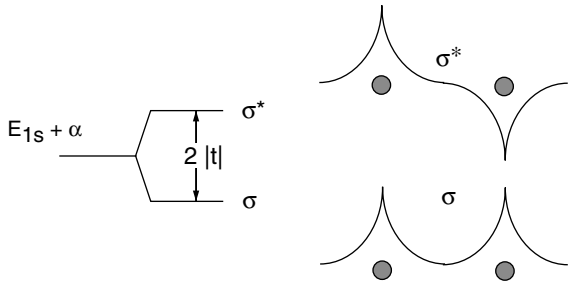


Fig. 4.1. Bonding and anti-bonding states arising from the coupling of the two atomic states

H_2 Molecule

In the case of the hydrogen molecule, the repulsion between the two electrons has to be taken into account. As for multi-electron atoms, V_A and V_B are now defined as effective potentials so that the electronic spectrum is qualitatively identical to that of the H_2^+ molecule. Because of the spin degree of freedom, the bonding level are occupied with two electrons of opposite spin (singlet state), circumstance that maximizes the energy gain (here equal to $2\,|t|$). The final bonding energy is found to be in order of 4.3 eV for an interatomic distance of 0.74 Å.

Electronic Correlations

It has to be noticed that the previous LCAO treatment cannot be accurate in all situations. As a matter of fact, let 1 and 2 denote the two electrons of

the hydrogen molecule. According to Pauli principle, the total wave function should be anti-symmetric with respect to these labels. For the singlet ground state the spin part of the wave function should be anti-symmetric, hence the symmetric spatial part is symmetric and will be given by

$$|\psi_\sigma\rangle_1 |\psi_\sigma\rangle_2 = \frac{1}{2}\left[|A1\rangle + |B1\rangle\right]\left[|A2\rangle + |B2\rangle\right] \ , \tag{4.6}$$

where the σ index denotes the bonding state. Developing this expression, we see that it contains two contributions $|A1\rangle|B2\rangle$ and $|A2\rangle|B1\rangle$ corresponding to neutral H-H configurations and two other ones, $|A1\rangle|A2\rangle$ and $|B1\rangle|B2\rangle$, corresponding to ionic configurations H^+H^-. This is not realistic for large inter-atomic distances. An obvious improvement would be to introduce different weights for these two types of configurations. This amounts to introduce the so-called 'configuration interactions'. Solid state physicists prefer to speak of correlation effects characterized by a 'Hubbard U' which measures the energy cost of ionic configurations. More precisely correlation effects are then characterized by the ratio $U/|t|$, i.e., by the competition between the energy gain due to the electron delocalization (measured by the transfer integral t) and the energy cost of local charge fluctuations (measured by U). If they become significant, the simple abovementioned mean field approximations no longer apply. In the following, correlation effects are mostly neglected; fact that seems somewhat difficult to justify a priori, but the ability of the LCAO approximation to account qualitatively for the electronic structure of carbon phases and nanotubes will provide a good a posteriori justification.

Heteroatomic Molecule

In the case of A–B heteroatomic molecules the diagonal matrix elements $E_A + \alpha_A$ and $E_B + \alpha_B$ are different. We assume that the zero energy is chosen such that these levels take opposite values $\pm\Delta$. Neglecting the crystal field integrals, $\Delta = (E_B - E_A)/2$, which by convention is taken positive ($E_B > E_A$). It is then straightforward to diagonalize the corresponding 2×2 matrix. We obtain again bonding and antibonding states with energies $E = \pm\sqrt{t^2 + \Delta^2}$, but now the weights of the eigenstates on the two atoms are different (see Fig. 4.2). They are respectively proportional to $|t|$ and to $\pm\sqrt{t^2 + \Delta^2} - \Delta$ on the A and B sites. The limit $t \to 0$ corresponds to the atomic limit, or more precisely to an ionic limit since, in general some charge flows from the less to the more electronegative atom. $\Delta = 0$ corresponds to a pure covalent limit, so that $\Delta/|t|$ is a measure of the relative importance of the ionic and covalent character of the molecular chemical bond.

The Crystal

There are basically two opposite and complementary ways to describe the electronic band structure of solids. The historical approach of solid state physicists

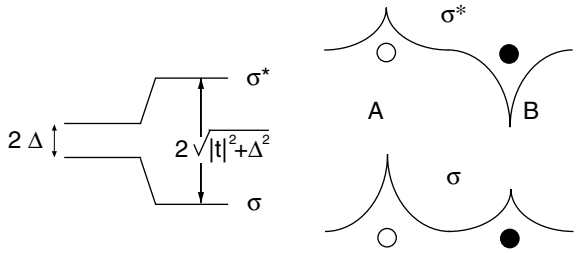


Fig. 4.2. Bonding and anti-bonding states of an heteroatomic molecule

starts from a free electron model in which the electrons are completely delocalized. The influence of the lattice (in the case of crystals) can then be studied by perturbation theory, using Bloch theorem, the main result being the occurrence of gaps separating continuous energy bands. The opposite approach starts from the atomic states and shows how their coupling leads to the formation of energy bands centered on the atomic energy levels for large interatomic distances. This is the approach that is adopted here since it is very well suited to the study of bonding in carbon phases. It has also the advantage to use a language very similar to that used in chemistry where emphasis is put on real space descriptions of chemical bonds.

Linear Chain

For simplicity, we begin with the fictitious example of a linear chain of hydrogen atoms of lattice parameter a. We then use the LCAO approximation which in the context of solids is frequently called the tight-binding approximation, or the Hückel approximation. The latter name is commonly used by chemists whereas the former by physicists. Let now $|n\rangle$ be the $1s$ atomic state centered on site n, we assume that $|\psi\rangle$ is a linear combination of these states, $|\psi\rangle = \sum_n a_n |n\rangle$. We also neglect the overlap integrals $\langle n|m\rangle$ when $n \neq m$ and, quite naturally, we keep only transfer integrals between nearest neighbors. The crystalline field integrals are neglected, whereas E_{1s} is taken as the energy zero, so that

$$\langle n|H|n\rangle = 0 \quad ; \quad \langle n|H|n \pm 1\rangle = t \; . \tag{4.7}$$

Extending the arguments used for the hydrogen molecule, the eigenstates are finally given from the solution of the finite difference equations $\langle n|H|\psi\rangle = Ea_n = t(a_{n+1} + a_{n-1})$. Periodic boundary conditions (Born von Karman conditions) are usually taken for convenience and to allow for the use of Bloch theorem (this topologically corresponds to a ring). If this ring contains N atoms, $N + n \equiv n$ then, using Bloch theorem, it can be shown that, up to a normalization factor a_n is equal to $\exp(\mathrm{i}kna)$, and since $\exp(\mathrm{i}kNa)$ should be equal to unity, the eigenvalues $E(k)$ are readily obtained

$$E(k) = 2t \cos ka \quad \text{with} \quad k = p2\pi/Na, p = 0, \pm 1, \ldots \tag{4.8}$$

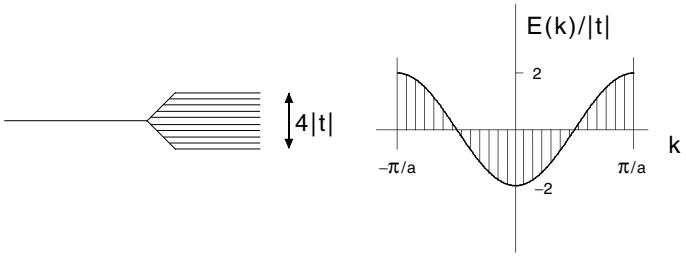


Fig. 4.3. Schematic formation of the energy band of width $4|t|$ (*left*), and dispersion relation $E(k)$ in the first Brillouin zone (*right*). There are exactly N states separated by $2\pi/Na$ on the k axis (notice that the states $k = \pm\pi/a$, which are attained when N is even, are identical)

Accordingly, a quasi-continuum of electronic states of width $4|t|$ is found, together with the dispersion relation $E(k)$ (Fig. 4.3). One also speaks of a band structure, but here we have a single band derived from the $1s$ atomic states. Notice that the k values are restricted to the 'first Brillouin zone' $[-\pi/a, +\pi/a]$.

Density of States

Since the states are separated by $2\pi/L$ on the k axis, where L is the length of the chain, the *density of states* in k-space $n(k)$ is equal to $L/2\pi$, per spin direction. The spacing $\mathrm{d}E$ between neighboring states on the energy axis is given by $\mathrm{d}E = (\mathrm{d}E(k)/\mathrm{d}k)\mathrm{d}k$ from which one easily deduces that the corresponding density of states $n(E)$ is given by $n(k)\mathrm{d}k/\mathrm{d}E$. For our linear chain, this gives (see Fig. 4.4)

$$n(E) = \frac{L}{2\pi}\frac{1}{2|t|a\sin ka} = \frac{N}{2\pi}\frac{1}{\sqrt{E^2 - 4t^2}}\ . \tag{4.9}$$

Van Hove Singularities

From its definition, the density of states is singular when $\mathrm{d}E/\mathrm{d}k = 0$ and displays so-called Van Hove singularities. Consider such a singular point that

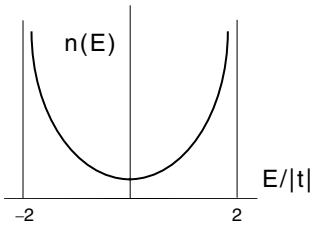


Fig. 4.4. Density of states of a tight-binding linear chain

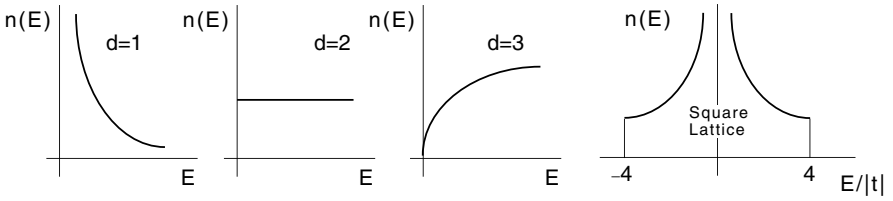


Fig. 4.5. Behavior of the density of states close to minima of $E(\boldsymbol{k})$ in one, two and three dimensions, and density of states of the square lattice with first neighbor interactions

can be assumed to be located at $k = 0$ without loss of generality. Close to this point $E \approx \pm k^2$ and $n(E) \approx 1/\sqrt{|E|}$. This behavior is typical of one dimension Van Hove singularity.

In two or three dimensions, k is replaced by a vector $\boldsymbol{k}$ (see below), and similar singularities occur when $\nabla_{\boldsymbol{k}} E(\boldsymbol{k}) = 0$, i.e., at local minima, maxima or saddle points. Consider for example a minimum. The generic variation of $E(k)$ close to it is again $E \approx k^2$, but now the number of states of energy lower than E is proportional to the volume of a sphere in k-space of radius $\sqrt{E}$, i.e., proportional to $E^{d/2}$ and the density of states is proportional to $E^{d/2-1}$ (see Fig. 4.5). As a simple illustration let us consider a square lattice with first neighbor interactions. The tight-binding analysis is a direct extension of the previous one. We now have quantum numbers k_x and k_y along the two axis which can be considered as the components of a vector $\boldsymbol{k}$ and the dispersion relation is easily found to be

$$E(\boldsymbol{k}) = 2t(\cos k_x a + \cos k_y a) \; . \tag{4.10}$$

Now $\nabla_{\boldsymbol{k}} E(\boldsymbol{k}) = 0$ when k_x and $k_y = 0$ or π, which give three Van Hove singularities at $E/|t| = -4$ (minimum of $E(\boldsymbol{k})$), $+4$ (maximum) or 0 (saddle point with a logarithmic divergence of $n(E)$).

Band Structures of Crystals

In general, the valence electrons of crystals are built from several $s, p, d, \ldots$ atomic states, which results in various energy bands that can overlap, and several dispersion relations. This is in fact a general consequence of Floquet-Bloch theorem which states that in a crystal characterised by translation vectors $\boldsymbol{t}$ the wave function is invariant under such a translation, up to a $\exp(\mathrm{i}\boldsymbol{k}.\boldsymbol{t})$ phase factor, so that $\psi(\boldsymbol{r}) = \exp(\mathrm{i}\boldsymbol{k}.\boldsymbol{r})u(\boldsymbol{r})$, where $u(\boldsymbol{r})$ is periodic, $u(\boldsymbol{r}+\boldsymbol{t}) = u(\boldsymbol{r})$. The Schrödinger equation thus becomes a differential equation within a unit cell for $u(\boldsymbol{r})$, which depends on $\boldsymbol{k}$ and that should satisfy periodic boundary conditions. This again implies a discrete and in principle infinite set of dispersion relations. As an example, the band structure of FCC Cu is shown in Fig. 4.6, where the set of d bands hybridised with nearly free electron bands can clearly be identified. It can be seen in particular that the d states have

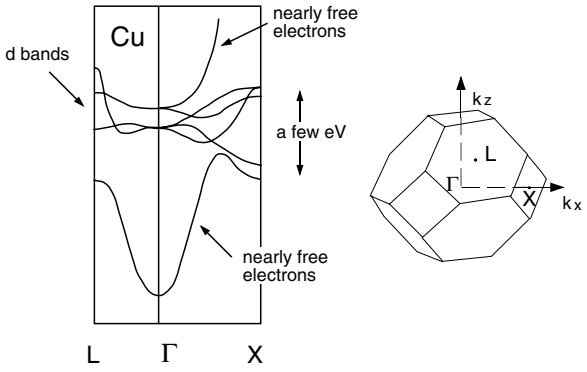


Fig. 4.6. Band structure of copper along some directions of the Brillouin zone, after D. A. Papaconstantopoulos et al. [11]

kept their atomic parentage which is not the case for the other s and p valence electrons. This behavior is common to all transition metals and indicate that the d states can be treated within the tight-binding approximation whereas the other states are better described within the opposite, nearly free electron limit.

4.1.2 Semi-Classical Theory of Electronic Transport

Here also we just recall some elementary results of the semi-classical theory of electronic transport. A very good reference here is the book by Ashcroft and Mermin [2]. We therefore consider a Bloch eigenstate and its time-dependent wave function $\psi_{\boldsymbol{k}}(\boldsymbol{r},t) = \exp(-\mathrm{i}E(\boldsymbol{k})t)\psi_{\boldsymbol{k}}(\boldsymbol{r},0)$. This form suggests at once that the group velocity of an electron in this state is given by

$$v_{\boldsymbol{k}} = \frac{1}{\hbar}\nabla_{\boldsymbol{k}}E(\boldsymbol{k}) \tag{4.11}$$

This result can in fact be proved quite rigorously. Apply now an external force $\boldsymbol{F}$ during a short time δt. The corresponding energy variation is equal to $\delta E = \boldsymbol{F}.\boldsymbol{v}_{\boldsymbol{k}}\delta t$. We then assume that the effect of this force is to modify adiabatically the wave function by just changing the value of $\boldsymbol{k}$ on the same dispersion relation. Thus, $\delta E = \nabla E(\boldsymbol{k})\delta\boldsymbol{k}$, and since $v_{\boldsymbol{k}} = \nabla E(\boldsymbol{k})/\hbar$, we obtain $\mathrm{d}\boldsymbol{k}/\mathrm{d}t = \boldsymbol{F}/\hbar$. Although very fruitful, it is clear that this 'semi-classical' derivation is not rigorous, and it is not very easy to estimate a priori its range of validity.

Electric Conductivity

At zero temperature the electric current is given by

$$\boldsymbol{j} = -\frac{2e}{\Omega} \sum_{\boldsymbol{k}\,\mathrm{occ}} \boldsymbol{v}_{\boldsymbol{k}} \ , \tag{4.12}$$

where $-e$ is the electronic charge and Ω the volume. The sum is over the occupied states and the factor 2 accounts for the spin degeneracy. This reduces to a sum over occupied states below the Fermi level, which can more generally be written $\sum_{\boldsymbol{k}} f_{\mathrm{FD}}(E(\boldsymbol{k}))\boldsymbol{v}_{\boldsymbol{k}}$ where $f_{\mathrm{FD}}(E(\boldsymbol{k}))$ is the Fermi-Dirac function. Without external forces, the states of wave vector $\boldsymbol{k}$ and $-\boldsymbol{k}$ have the same energy and opposite velocities so that the total current $\boldsymbol{j} = 0$. In the presence of a force, the shift in $\boldsymbol{k}$-space implies that some states of wave vector $\boldsymbol{k}$ can be occupied whereas the corresponding states of wave vector $-\boldsymbol{k}$ are not (see Fig. 4.7). The problem is that the shift $\delta\boldsymbol{k} = \boldsymbol{F}\delta t/\hbar$ continuously increases with time, which is not physically sounding. Actually the energy brought by the external force should finally be transferred to other degrees of freedom, to phonons in particular, and the usual assumption is that a stationary state is reached so that $\delta\boldsymbol{k} = \boldsymbol{F}\,\tau/\hbar$ where τ is a so-called relaxation time. Since $\boldsymbol{F} = -e\boldsymbol{E}$ in the presence of an electrical field, the shift $\delta\boldsymbol{k}$ is equal to $-e\tau\boldsymbol{E}/\hbar$. The corresponding energy shift is small compared to the Fermi energy and it is clear that the current will only depend on the velocities at the Fermi surface.

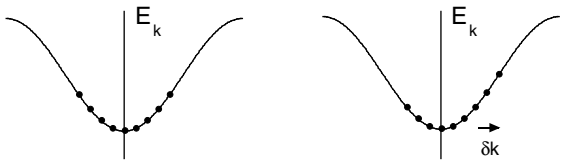


Fig. 4.7. One-dimensional model: in the presence of an electrical field, the occupied states are shifted by δk and the sum of the velocities (proportional to the slopes) no longer vanish

More precisely, the α component of the current is given by

$$j_\alpha = -\frac{2e}{\Omega} \sum_{\boldsymbol{k}} f_{\mathrm{FD}}(E(\boldsymbol{k}-\delta\boldsymbol{k}))\boldsymbol{v}_{\boldsymbol{k},\alpha} = \frac{2e}{\Omega} \sum_{\boldsymbol{k}} \delta(E(\boldsymbol{k}) - E_{\mathrm{F}}) v_{\boldsymbol{k},\alpha} v_{\boldsymbol{k},\beta} \hbar \delta k_\beta \ , \tag{4.13}$$

and finally the conductivity tensor $\sigma_{\alpha\beta}$ defined from $j_\alpha = \sigma_{\alpha\beta} E_\beta$ is given by

$$\sigma_{\alpha\beta} = \frac{2e^2\tau}{\Omega} \sum_{\boldsymbol{k}} \delta(E(\boldsymbol{k}) - E_{\mathrm{F}}) v_{\boldsymbol{k},\alpha} v_{\boldsymbol{k},\beta} = e^2 \tau\, n(E_{\mathrm{F}}) \langle v_x^2 \rangle \delta_{\alpha\beta} \ , \tag{4.14}$$

where a cubic symmetry has been assumed to derive the last equality. $n(E_{\mathrm{F}})$ is the density of states (spin included) at the Fermi level E_{F} per unit volume and $\langle v_x^2 \rangle$ is the average of v_x^2 on the Fermi surface which can also be written v_{F}^2/d where d is the space dimensionality. Another useful formulation is to

introduce the diffusion constant $D = \langle v_x^2 \rangle \tau$ so that the (scalar) conductivity can be written

$$\sigma = e^2 \tau n(E_\mathrm{F}) v_\mathrm{F}^2 / d = e^2 D n(E_\mathrm{F}) \tag{4.15}$$

Drude Model

In the case of free electrons, (4.15) can be rewritten as follows: the velocity v_F is related to the Fermi energy E_F through $m v_\mathrm{F}^2/2 = E_\mathrm{F}$, where m is the electronic mass. Now the density of states is proportional to $E^{d/2-1}$ from which one deduces that $E_\mathrm{F} n(E_\mathrm{F}) = 2n/d$ where n is the electronic density and finally

$$\sigma = n e^2 \tau / m \ , \tag{4.16}$$

which is the familiar Drude formula, generally derived using a *classical* argument. The force acting on an electron is the sum of the electric force $-e\boldsymbol{E}$ and of a friction term $-m\boldsymbol{v}/\tau$. In a stationary regime, the force vanishes and $\boldsymbol{v} = -e\boldsymbol{E}\tau/m$. Assuming that all electrons have the same drift velocity (which is typically a 'classical' approximation), one gets straightforwardly that $\sigma = ne^2\tau/m$. The coincidence of the semi-classical result with the Drude result is somewhat surprising. It can be misleading since it is clear, from (4.15), that the conductivity is determined by the electronic structure at the Fermi level. This formula is itself over-simplified in many cases because of the 'relaxation time' assumption. In practice however Drude result applies if the dispersion relation is quadratic: $E \propto k^2$; if the coefficient of proportionality is defined from $E = \hbar^2 k^2 / 2m^*$ it is then sufficient in the formula to replace the electronic mass by this effective mass m^*. This is quite convenient in the case of semi conductors since only a few electronic states are occupied close to the minimum of the conduction band where the above proportionality holds. Furthermore symmetric arguments can be applied to the holes in the valence band.

4.1.3 sp^n Covalent Structures

s and p Orbitals

When we fill the second shell $n = 2$ (B, C, N, O, ...), $s\,(l = 0)$ and $p\,(l = 1)$ electrons are involved. The s states are isotropic, i.e., the corresponding spherical harmonics is constant, but even if the subspace of p states is invariant as a whole under any space rotation, its bases are not. One generally uses the basis where the angular parts of the wave functions are proportional to x/r, y/r and to z/r and one speaks of p_x, p_y and p_z states. Denoting the $2s$ and $2p$ states at site $\boldsymbol{n}$ as $|\boldsymbol{n}, \alpha\rangle$, $\alpha = s, p_x, p_y, p_z$ the wave function in a LCAO description will be a linear combination of the atomic wave functions $\phi_\alpha(\boldsymbol{r} - \boldsymbol{n}) = \langle \boldsymbol{r} | \boldsymbol{n}, \alpha \rangle$.

Transfer Integrals

The matrix elements of the Hamiltonian become matrices with respect to the degeneracy indices $\alpha, \beta = s, p_x, p_y, p_z$. Neglecting the crystal-field integrals the on-site matrix $\langle \boldsymbol{n}, \alpha | H | \boldsymbol{n}, \beta \rangle$ is diagonal and its diagonal elements are simply the atomic energy levels E_s and E_p. Similarly the transfer integral t between two sites separated by $\boldsymbol{R}$ is replaced by a matrix $t_{\alpha\beta}(\boldsymbol{R})$. Using symmetry arguments, it is then fairly easy to realize that there are only four independent transfer integrals. They can all be defined when $\boldsymbol{R}$ is parallel to the Ox axis; $t_{\alpha\beta}(\boldsymbol{R})$ is then a linear combination of these integrals which depends on the orientation of $\boldsymbol{R}$.

Molecules

Consider a diatomic molecule such as C_2 or O_2. The molecule axis is taken along Ox. It is clear that the two p_y states do not mix with states of other symmetries. They just mix together and are coupled through the $dd\pi$ integral. We are exactly in the situation of the H_2 molecule. The same is true for the p_z states. We have therefore two pairs of bonding and antibonding states separated by $2|pp\pi|$ which are called π states. The remaining four s and p_x states are coupled together but since the molecule has a symmetry center the eigenstates can be classified into odd and even states and their eigenvalues can be found analytically. These are called σ states. In the particular case where $ss\sigma = -pp\sigma = -sp\sigma = t/2$, the energy levels are given by $E = [(E_s + E_p) \pm t \pm \sqrt{t^2 + (E_p - E_s)^2}]/2$. The limit where the transfer integrals are small compared to $E_p - E_s$ is the so-called atomic limit. This is the limit of large interatomic distances (see Fig. 4.8). The limit of short distance is more conveniently studied using hybrid orbitals.

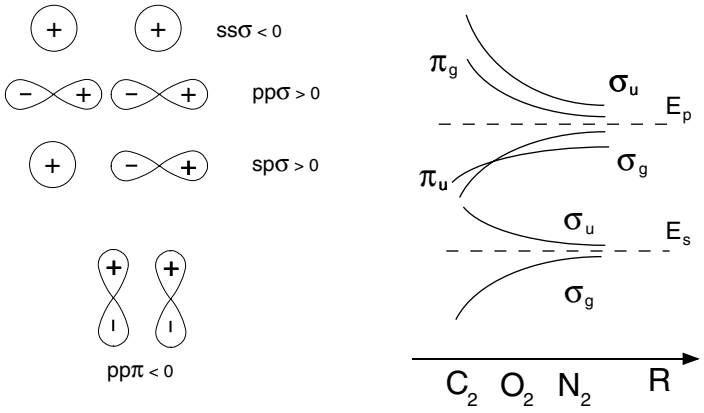


Fig. 4.8. *Left*: the four independent transfer integrals involving s and p states. *Right*: schematic behavior of the energy levels of diatomic sp molecules as a function of the inter-atomic distance R; after Pettifor [5]

Hybrid Orbitals

When $E_p - E_s$ is small compared to the transfer integrals, it is convenient to work directly in the four-dimensional space spanned by the s and p states and to introduce hybrid orbitals pointing along definite directions. For instance, in one dimension we can replace the basis $|s\rangle, |p_x\rangle$ by the basis $|s + p_x\rangle/\sqrt{2}, |s - p_x\rangle/\sqrt{2}$, the corresponding orbitals pointing to the right or to the left, respectively. It is then tempting to define new transfer integrals and to keep only the transfer integral t between the hybrid orbitals pointing towards each other. This precisely amounts to the above approximation $ss\sigma = -pp\sigma = -sp\sigma = t/2$. Assuming $E_s = E_p$, one finds two 'molecular' states corresponding to the coupling of the previous orbitals, $E = \pm t$ and two levels at $E = 0$ corresponding to the two dangling bonds pointing outside the molecule (Fig. 4.9). In the case of a linear geometry it is convenient to use the above hybrid orbitals, called sp hybrids. More generally, sp^n hybrids can be defined $n = 1, 2, 3$ which are appropriate in one, two and three dimensions. Consider for example sp^2 hybrids. By combining the s, p_x, and p_y states one build hybrids pointing towards three equivalent directions in the Oxy plane. The general definition of a sp^n hybrid state pointing along bond J is

$$|J\rangle = \frac{1}{\sqrt{n+1}} |s + \sqrt{n}\, \boldsymbol{p}.\boldsymbol{e}_J\rangle \ , \tag{4.17}$$

where $\boldsymbol{e}_J$ is the unit vector pointing along bond J and $\boldsymbol{p}.\boldsymbol{e}_J$ is the linear combination of p_x, p_y and p_z states given by expanding the scalar product in the usual way.

Linear Chain. Leman-Friedel-Thorpe-Weaire Model

Consider a linear chain along the Ox axis. The p_y and p_z states form independent bands completely equivalent to that obtained for s states, t being replaced by $dd\pi$. These bands are called π bands. Here again the two remaining σ bands derive from the coupling between s and p_x states. In the 'hybrid'

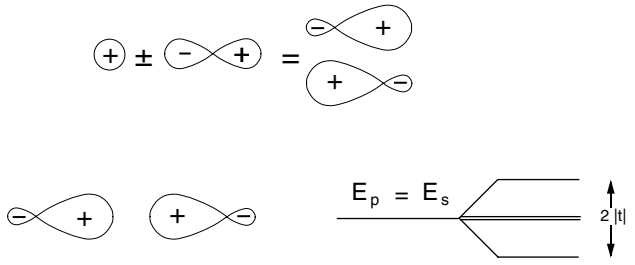


Fig. 4.9. *Top*: sp_x hybrid orbitals. *Bottom*: bonding (σ_g) state (*left*) and energy spectrum of sp molecules when $E_s = E_p$ (*right*)

limit $ss\sigma = -pp\sigma = -sp\sigma = t/2$, the dispersion relation is found to be: $E(\boldsymbol{k}) = \pm\sqrt{\Delta^2 + t^2 + 2\Delta t \cos ka}$, where $\Delta = (E_s - E_p)/2$ with an origin of energy such that $(E_s - E_p)/2 = 0$. An interesting result is that there is always a band gap $2|t - \Delta|$. This is an 'atomic' gap when $t \to 0$ and a 'covalent' gap when $\Delta \to 0$.

There is a very nice generalization of this result in two and three dimensions using sp^2 and sp^3 hybrids, respectively, to describe the σ bands, provided the absence of dangling bonds. This applies to the graphene plane or to the diamond structure, but also to any non-periodic network. This results again in a band gap equal to $|E_p - E_s - 2|t||$ and two opposite, atomic and covalent limits [12]. One should however be careful with the definition of the transfer integral t. Since the definition of the hybrids depends on n, so does t and also its relationship with the four initial transfer integrals. This demonstrates that the hybrids are not so useful when dealing with disordered arrangements of sp, sp^2 and sp^3 local configurations.

In the atomic limit, we have n σ states per atom in the subband starting from E_p and one state in the other one. In the covalent limit, there are two subbands containing $(n+1)/2$ states per atom; it is preferable then to say that there is one state per bond in each bond. This strange behaviour – apparent variation of the number of states in an electronic band – as a function of R is possible, owing to pure p states (corresponding to delta-functions in the density of states) some of which belong to the upper or to the lower subband.

The width of the subbands is equal to $2|t|$ in the atomic limit and to $E_p - E_s$ in the covalent limit, which shows that in some sense the role of the atomic parameters (intra-atomic matrix elements: atomic levels) and of the molecular parameters (inter-atomic matrix elements: transfer integrals) are exchanged when going from one limit to the other. In the extreme covalent limit, where $E_p - E_s$ is negligible compared to $|t|$, one obtains localized bonding and antibonding states on each bond, together with a covalent gap. This is clearly related to the symmetry of the hybrid orbitals, which is itself a consequence of the mixing of orbitals of even ($l = 0$) and of odd ($l = 1$) parity, and also to the topology of the atomic arrangements. Otherwise, one would expect an overlap of the s and p bands (see Fig. 4.10).

4.1.4 From Graphene to Nanotubes

The Graphene Sheet

The crystallographic characterization of the graphene sheet has been given elsewhere. We just recall the definitions of the unit cell and of the Brillouin zone in Fig. 4.11.

Band Structure

Carbon has the configuration $1s^2 2s^2 2p^2$. As a basis for the s and p states of the graphene sheet, one choses sp^2 hybrids in the Oxy plane and p_z states normal

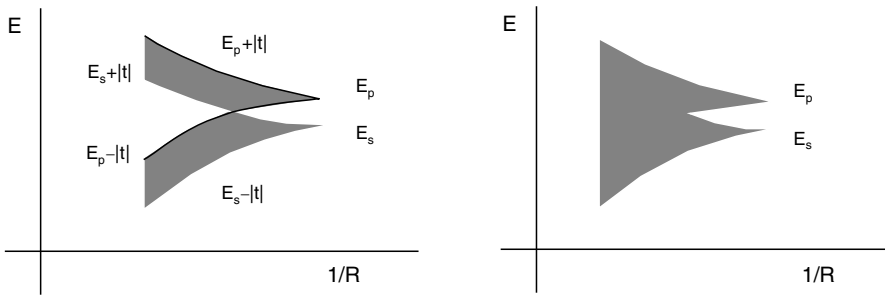


Fig. 4.10. *Left*: typical evolution of the energy spectrum of covalent networks as a function of $1/R$ showing that there is always a gap. In the simple Leman-Friedel-Thorpe-Weaire model there are pure p states indicated by heavy lines. *Right*: expected evolution

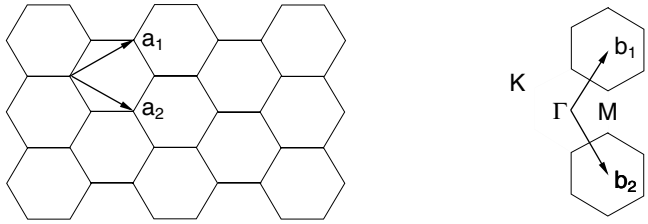


Fig. 4.11. The canonical basis for the graphene sheet and for its reciprocal lattice. The first Brillouin zone is an hexagon; K denotes the vertices and M the middles of the edges. Notice that there are only two distinct K points modulo a vector of the reciprocal space.

to this plane. From the previous discussion, strong σ bonds are expected. Semi-quantitative estimates of the tight-binding parameters can be obtained by fitting tight-binding calculations to first principles ones. Order of magnitudes are $t \approx 8\,\mathrm{eV}$, $dd\pi \approx 2$–$3\,\mathrm{eV}$ and $E_p - E_s \approx 8\,\mathrm{eV}$. It is easily checked that this situation corresponds to the covalent limit with a gap about $8\,\mathrm{eV}$. π electrons on the other hand forms a continuous energy band – with a vanishing gap, see below – so that they govern the electronic spectrum around the Fermi level that is within the gap of σ states (Fig. 4.12).

The cohesive properties (cohesive energy, elastic moduli) are principally governed by the strength of the σ bonds whereas the electronic properties involving excitations up to about $4\,\mathrm{eV}$ (optical properties, ...) are driven by the π states.

π States

We now consider in more detail the π states within a simple tight-binding description. Here again there is no formal difference with s states if the transfer integral between first neighbors is replaced by $dd\pi$. Since there are two atoms

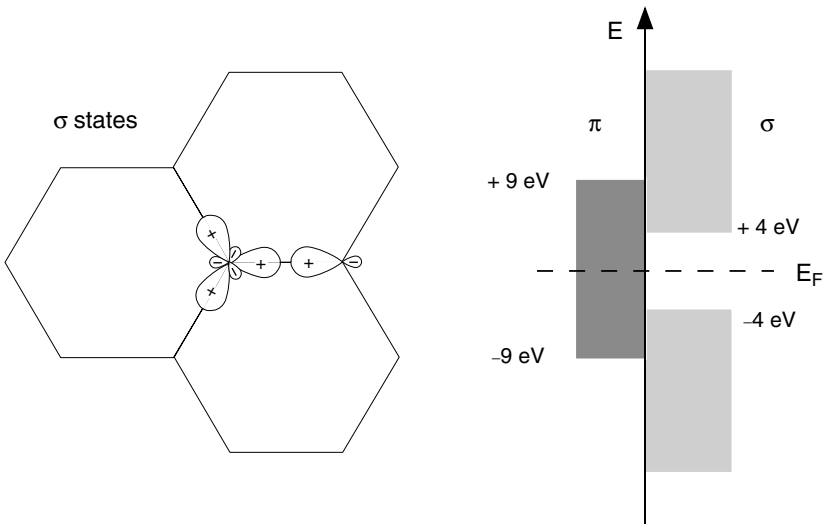


Fig. 4.12. σ bonds on the graphene sheet (*left*) and approximate energy spectrum of π and σ states in graphite (*right*)

per unit cell, two Bloch states $|k1\rangle$ and $|k2\rangle$ are built from atomic states centered on the same sublattice. If the origin of energies is taken at E_p, the Hamiltonian $H(\boldsymbol{k})$ in this basis has only off-diagonal non-vanishing matrix elements: $H(\boldsymbol{k})_{11} = H(\boldsymbol{k})_{22} = 0$ and $H(\boldsymbol{k})_{12} = H^*(\boldsymbol{k})_{21} = f(\boldsymbol{k})$ with $f(\boldsymbol{k}) = pp\pi \sum_\alpha \exp \mathrm{i}\boldsymbol{k}.\boldsymbol{\tau}_\alpha$, where the set of vectors $\boldsymbol{\tau}_\alpha$ is any set joining one atom to its three first neighbors. The eigenvalues are therefore equal $\pm|f(\boldsymbol{k})|$, i.e., to

$$\begin{aligned} E(\boldsymbol{k})/pp\pi &= [3 + 2(\cos \boldsymbol{k}.\boldsymbol{a}_1 + \cos \boldsymbol{k}.\boldsymbol{a}_2 + \cos \boldsymbol{k}.(\boldsymbol{a}_1 - \boldsymbol{a}_2))]^{1/2} \\ &= \left[3 + 4\cos\left(\frac{\sqrt{3}}{2}k_x a\right)\cos\frac{k_y a}{2} + 2\cos k_y a\right]^{1/2} . \end{aligned} \tag{4.18}$$

The dispersion relations and the density of states are shown in Fig. 4.13. The density of states is seen to vanish at zero energy. Additionally, the Fermi energy is precisely located at this energy, since there are two π electrons occupying the lower subband, when spin is taken into account. In k-space, the gap occurs at points K and close to these points where $\boldsymbol{k}$ is written $\boldsymbol{k} = \boldsymbol{K} + \boldsymbol{q}$ the dispersion relation is linear: $E \simeq \hbar v_F q$, where $q = |\boldsymbol{q}|$ and $v_F = 3\,pp\pi\, a_{\mathrm{cc}}/2\hbar$ is the Fermi velocity, a_{cc} being the distance between first neighbors. This velocity is in order of 10^8 cm/s which is quite large and comparable to the Fermi velocities of good metals.

Graphite is in fact a particular stacking of graphene sheets. The small coupling between the planes modifies a little bit the band energies and makes graphite a semi-metal with slightly overlapping bands at Fermi energy and finally a good electric conductor [13].

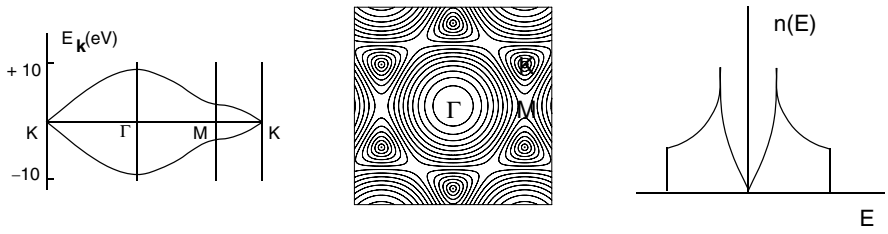


Fig. 4.13. Dispersion of the π bands (*left*) and isointensity curves of the positive branch in k-space (*middle*) and density of states (*right*)

Boron Nitride

It is clear that the above analysis can be easily extended to the case of a boron nitride (BN) sheet since each type of atom occupies a particular sublattice. Let Δ and $-\Delta$ be here the p energy levels of boron and nitrogen, respectively, the diagonal energy elements of the Hamiltonian are precisely equal to these values whereas the off-diagonal one is again given by $f(\boldsymbol{k})$, from which $E(\boldsymbol{k}) = \pm\sqrt{|f(\boldsymbol{k})|^2 + \Delta^2}$ is derived. There is now a gap of width 2Δ which is fairly large in the present case, about 5–6 eV. For a more detailed discussion, see Sect. 4.3.1.

Carbon Nanotubes

Theoretical calculations [14–17] have shown early on that the electronic properties of the carbon nanotubes are very sensitive to their geometric structure. Although graphene is a zero-gap semiconductor, theory has predicted that the carbon nanotubes can be metals or semiconductors with different size energy gaps, depending very sensitively on the diameter and helicity of the tubes, i.e., on the indices (n, m). The physics behind this sensitivity of the electronic properties of carbon nanotubes to their structure can be understood within a band-folding picture. It is due to the unique band structure of a graphene sheet described above, that displays states crossing the Fermi level at only two inequivalent points in k-space, and to the quantization of the electron wavevector along the circumferential direction. This is actually a beautiful and concrete application of the periodic boundary conditions. When forming a tube, owing to the periodic boundary conditions imposed in the circumferential direction, only a certain set of k states of the planar graphite sheet is allowed. More precisely, if $\boldsymbol{C}$ is the wrapping vector of the tube, the allowed values of $\boldsymbol{k}$ should satisfy $\boldsymbol{k}.\boldsymbol{C} = p\,2\pi$, p integer, which defines lines perpendicular to $\boldsymbol{C}$ (Fig. 4.14). Whenever the allowed k's include the point K, the system is a metal with a non vanishing density of states at the Fermi level, resulting in a one-dimensional metal with two linear dispersing bands. When the point K is not included, the system is a semiconductor with different size energy gaps.

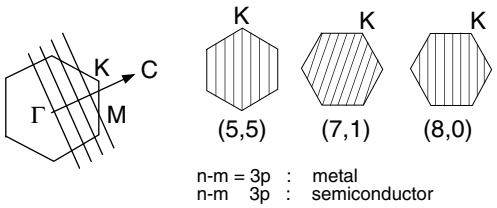


Fig. 4.14. Allowed k-vectors of the (5,5), (7,1) and (8,0) tubes mapped onto the graphene Brillouin zone

The general rules for the metallicity of the single-walled carbon nanotubes are as follows: (n, m) tubes with $n-m = 3p$, where p is an integer are metallic and all others are semiconductors. It is important to note that the states near the Fermi energy in both the metallic and the semiconducting tubes are all from states near the K point, and hence their transport and other electronic properties are related to the properties of the states on the allowed lines. For example, the conduction band and valence bands of a semiconducting tube come from states along the line closest to the K point. In particular this implies that the gap of semiconductors is given by $E_{\mathrm{g}} = |pp\pi|a_{\mathrm{cc}}/R$, where R is the radius of the tube. In the case of metals, the linearity of the dispersion relations also implies that the density of states is constant along a plateau three times larger. This is quite apparent in Fig. 4.15 which shows the density of states for the tubes described in Fig. 4.14. Notice the strong one-dimensional Van Hove singularities as well as the overall shape similar to the density of states of graphene. Actually, because of tube curvature effects, a tiny gap opens when $n-m = 3p$ except when $p = 0$ (armchair tubes). Hence, carbon nanotubes come in three varieties: large-gap, tiny-gap, and zero gap. The armchair tubes are always metallic within the single-electron picture, independent of curvature because of their symmetry. As the tube radius R increases, the band gaps of the large-gap and tiny-gap varieties decrease with a $1/R$ and $1/R^2$ dependence, respectively. Thus, for most experimentally observed carbon nanotube sizes, the gap in the tiny-gap variety which arises from curvature effects would be so small that, for most practical purposes, all the $n - m = 3p$ tubes can be considered as metallic at room temperature.

The previous band-folding picture, based on the tight-binding approach [14–16], is expected to be valid for larger diameter tubes. However, for a small radius tube, because of its curvature, strong rehybridization among the σ and π states can modify the electronic structure. Experimentally, nanotubes with a radius as small as 3.5 Å have been produced. *Ab initio* pseudopotential local density functional (LDA) calculations [18] indeed revealed that sufficiently strong hybridization effects can occur in small radius nanotubes which significantly alter their electronic structure. Strongly modified low-lying conduction band states are introduced into the band gap of insulating tubes because of hybridization of the σ^* and π^* states. As a result, the energy gaps of some

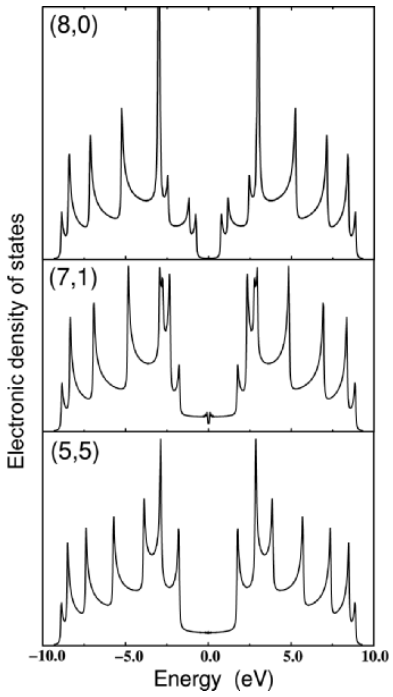


Fig. 4.15. Densities of states for the (5,5), (7,1) and (8,0) tubes. The (5,5) armchair nanotube is metallic for symmetry reasons. The (7,1) chiral tube displays a tiny gap due to curvature effect, but will display a metallic behavior at room temperature. The (8,0) zigzag tube is a large-gap semiconductor

small radius tubes are decreased by more than 50%. For example, the (6,0) tube which is predicted to be semiconducting in the band-folding scheme is shown to be metallic. For nanotubes with diameters greater than 1 nm, these rehybridization σ–π effects are unimportant. Recently, ultra-small radius single-walled carbon nanotubes (diameter about 4 Å) have been produced by confining their synthesis inside inert $AlPO_4$-5 zeolite channels (with inner diameter of about 7.3 Å) [19]. The ultra-small diameter of these tubes gives them many unusual properties such as superconductivity [20]. Such a narrow diameter distribution around 4 Å, reduces the potential candidates to three: (3,3), (4,2), and (5,0). The properties of these ultra-small tubes have already been extensively investigated *ab initio*, as the small unit cell of these tubes allows such accurate calculations [21–23].

There have been many experimental studies [24–28] based on low temperature transport measurement on a single-walled nanotube rope in an attempt to understand their electronic properties. These results have been interpreted in terms of single-electron charging and resonant tunneling through the quantized energy levels of the nanotubes. In addition, there have also been

high-resolution low-temperature scanning tunneling microscopy (STM) studies, which directly probe the relationship between the structural and electronic properties of carbon nanotubes [29, 30]. The resolution of the measurements has allowed for the identification of the diameter and the geometric structure of the tube. Measurement of the normalized conductance in the scanning tunneling spectroscopy (STS) mode was used to obtain the local density of states (LDOS) in very good agreement with theoretical predictions.

4.2 Electronic Properties of Carbon Nanotubes

The present section is devoted to a detailed study of the electronic properties of carbon nanotubes. The relation between geometry and electronic structure is addressed, the influence of structural defects such as pentagons and heptagons is discussed, in conjunction with the possibility of fabricating nanotube-based junctions of different geometries.

4.2.1 Very Small Diameter Nanotubes

The *ab initio* band structure of the (6,0) tube is shown in Fig. 4.16. As mentioned before, in such tube, the curvature is so strong that its electronic properties are strongly modified. The singly degenerate σ^* state, displayed by the arrow in Fig. 4.16, is found to be 0.83 eV (at Γ), below the doubly degenerate state that forms the top of the valence band in tight-binding calculations. This band overlap makes the (6,0) tube a metal within LDA with a density of states at the Fermi level equal to 0.07 state/eV atom.

Most of these calculations [21–23, 31] show that narrow tubes with optimized geometries can be either semiconducting or metallic, but with electronic structures near the Fermi level that often cannot be understood starting from the simple graphene sheet model (Fig. 4.17). These total-energy calculations also indicate that the 4 Å-diameter nanotubes recently observed either as the central shell of a multi-walled tube or encased in a porous zeolite, if isolated, should be stable against complete unzipping along the nanotube axis [31].

4.2.2 Real Ballistic Conductors

All these theoretical works predict that only a special achiral subset of these carbon structures known as armchair nanotubes exhibits a true metallic behavior. These single-walled armchair nanotubes are the only real one-dimensional conductors with only two open conduction channels. Hence, with increasing length, their conduction electrons ultimately become localized owing to residual disorder in the tube which is inevitably produced by interactions between the tube and its environment. However, theoretical calculations [32] have demonstrated that in contrast to normal metallic wires,

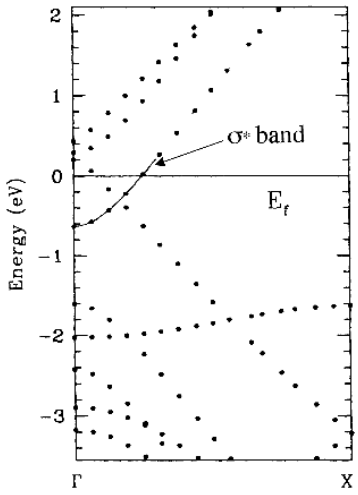


Fig. 4.16. *Ab initio* band structure of a (6,0) nanotube. The energies are in eV and the zero is at the Fermi energy. A new band σ^* appears and crosses the π states around the centre of the Brillouin zone (adapted from Blase et al. [18])

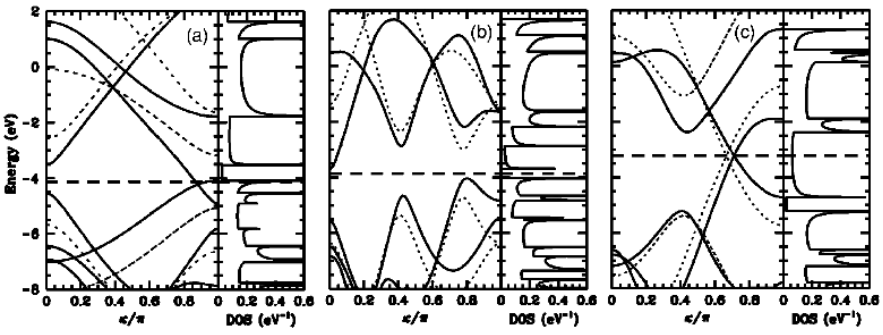


Fig. 4.17. *Ab initio* band structures and density of states for (**a**) (5,0), (**b**) (4,2), and (**c**) (3,3) nanotubes at equilibrium geometries. Also shown as broken lines are the corresponding band structures from a simple tight-binding model obtained by assuming $\gamma_0 = -2.5\,\mathrm{eV}$ and aligning ε_F with the LDA values shown as horizontal dashed lines (from Cabria et al. [31])

conduction electrons in armchair nanotubes experience an effective disorder averaged over the tube circumference, leading to electron mean free paths that increase with nanotube diameter. This increase should result in exceptional ballistic transport properties and localization lengths of 10 μm or more for tubes with the diameters that are typically produced experimentally. These original transport properties of nanotubes are described carefully in Chap. 6.

4.2.3 Nanotubes in Bundles

Although it was expected that the close-packing of individual nanotubes into ropes does not change significantly their electronic properties, first-principles calculations show that a broken symmetry of the (10,10) tube caused by the interactions between tubes in a rope induces a pseudogap of about 0.1 eV at the Fermi level [33]. This pseudogap strongly modifies many of the fundamental electronic properties of the armchair tubes which are suggested to exhibit a semimetal-like temperature dependence of the electrical conductivity and to possess a finite gap in the infrared absorption spectrum.

The electronic properties of an isolated (n, n) armchair nanotubes are dictated by its geometrical structure, which imposes, in particular, that the two linear bands cross at the Fermi energy. These two linear bands give rise to a constant density of states near the Fermi level. One of the band has π-bonding character while the other has a π-antibonding (π^*) character (Fig. 4.18a). An isolated (n, n) nanotube has n mirror planes containing the tube axis. The π-bonding state is even (the wavefunction has no sign change) whereas the π-antibonding state is odd (sign change) under these symmetry operations. The band crossing is allowed and the armchair nanotube is metallic as shown schematically in Fig. 4.18a. It is precisely this symmetry of the isolated (n, n) tube that gives its desired metallic behavior and its extraordinary property of ballistic conductor [32]. Breaking of this symmetry, however, will completely alter the picture. If the tubes in the rope are separated far enough to eliminate any interactions between them, the band structure is identical to that of a single isolated nanotube. However, the actual distances between tubes in the rope are small enough that each nanotube can feel the potential due to all the other tubes [33]. As a result of this perturbation, the Hamiltonian at any point k where the two bands used to cross becomes

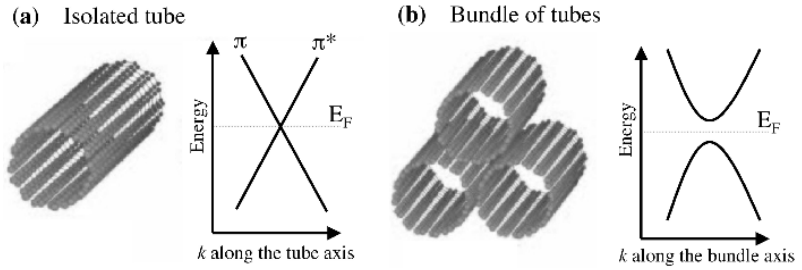


Fig. 4.18. Band crossing and band repulsion. (**a**) Schematic diagram of the crossing of the two linear bands for an isolated (n, n) carbon nanotube. One band has π-bonding character and the other has π-antibonding (π^*) character. E_F is the Fermi energy and k is the wave vector. (**b**) Repulsion of the bands due to breaking of mirror symmetry (adapted from Delaney et al. [33])

$$H_k = \begin{pmatrix} \varepsilon_0 + \delta_{11} & \delta_{12} \\ \delta_{21} & \varepsilon_0 + \delta_{22} \end{pmatrix}$$

where ε_0 is the ground state energy. The diagonal matrix elements δ_{11} and δ_{22} merely act to shift the energy and location in k-space of the band crossing. It is the off-diagonal elements (δ_{12} and δ_{21}) that cause quantum-mechanical level repulsion and therefore open a gap as shown schematically in Fig. 4.18b. If the vertical line through k has high symmetry, the off-diagonal matrix elements may still be zero and a crossing may persist. However, at a general k point, the inter-tube interactions will dramatically change the physics of the ropes. If the symmetry of the nanotube is not broken in the bundle (i.e., for $(6, 6)$ armchair nanotubes), the crossing is also conserved [34]. These inter-tube interactions which break the rotational symmetry of armchair (n, n) tubes due to the local environment has been observed experimentally using low-temperature scanning tunneling spectroscopy [35]. These experimental results also confirm that the magnitude of the pseudogap depends inversely on nanotube radius.

4.2.4 Nanotubes with Polygonized Cross-Section

Consequently, a thorough understanding of the electronic properties of single-walled carbon nanotubes requires the knowledge of their realistic geometrical structure. In most studies, cylindrical tubes with circular cross-sections are assumed with the implicit justification that it is the shape which minimizes the strain energy of the free isolated tube. However, it has been shown that the tubes may deform elastically, without destroying the honeycomb arrangement of the carbon atoms on the tube surface, when they interact either with the substrate in which they are deposited or with other tubes in a bundle which may deform from the ideal circular cross-section of the isolated tubes to a polygonized cross-section [36]. The properties of the deformed tubes may change substantially with respect to the properties of the corresponding circular tubes. Assuming a circular cross-section of the tubes in bundles would then be a poor approximation in some cases and could even lead to wrong predictions.

For instance, the metallic or semiconducting character of the tubes is predicted to change (band gap modifications) after radial deformations giving rise to tubes with polygonized cross-sections [37]. Tubes with different cross-sections exhibit different $\sigma^* - \pi^*$ hybridization and consequently different properties, namely a different metal/insulator character.

The evolution of the electronic properties of a $(10, 0)$ nanotube under polygonization is illustrated in Fig. 4.19. Tight-binding band structures calculations were performed for a $(10, 0)$ cylindrical (Fig. 4.19a), a $(10, 0)^5$ pentagonal (Fig. 4.19c), and a $(10, 0)^{\sim 5}$ intermediate geometry for its cross-section (Fig. 4.19b). In the latter configuration, the sharp edges have been smoothed by structural optimization, and the corresponding curvature radius is 2.366 Å. The energy difference between the $(10, 0)$ and the $(10, 0)^5$ conformations is in

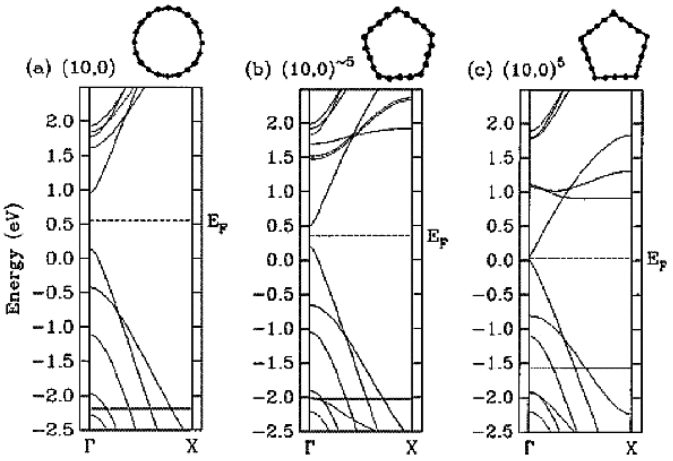


Fig. 4.19. Evolution of the $(10, 0)$ nanotube electronic bands (near the Fermi energy) under polygonization of its cross-section. Pure cylindrical (**a**), and pentagonal (**c**) geometries are illustrated, separated by an intermediate configuration (**b**) where the sharp angles of the pentagon are smoothed using structural optimisation (from Charlier et al. [37])

order of 0.37 eV/atom. In the zigzag orientation, the σ^* and π^* singly degenerate states of a planar graphene sheet mix with each other, and not with states of higher degeneracy [18]. By curving or folding the sheet, the σ^* and π^* states of the same symmetry repel each other, lowering the energy of original π^* state. It is the lowest unoccupied hybridised π^* band which gives rise to a weakly dispersive band about 1 eV above the Fermi energy (E_F) in the band structure of Fig. 4.19c. Simultaneously, a dramatic decrease of the band gap appears at Γ due to a lowering of the symmetry in the pentagonal configuration, where the carbon atoms are no more identical.

4.2.5 Multi-Walled Nanotubes

Another possibility to tailor the electronic properties of nanotube can be found in the 'multi-layering' effect. In fact, the weak interaction between the concentric shells in a multi-walled nanotube may cause dramatic effects on the electronic properties of the constituting isolated nanotubes [38, 39] (see Chap. 6). The inter-wall coupling, which have already been mentioned to open a pseudo-gap in bundle of single-walled nanotubes due to symmetry lowering, may periodically open and close four such pseudo-gaps near the Fermi energy (E_F) in a metallic double-walled nanotube during its rotation normal to the nanotube axis.

Figure 4.20 illustrates the intriguing interplay between geometry and electronic structure during the rotation of the inside $(5, 5)$ armchair nanotube into the outside $(10, 10)$ nanotube, sharing the common axis.

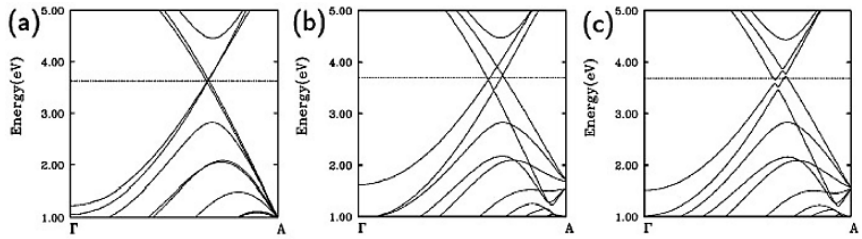


Fig. 4.20. Band structure of aligned nanotube pairs, along the common axis. Near degenerate bands with no gap characterize the $(5,5)@(10,10)$ double-walled nanotube without inter-tube interaction (**a**). In the presence of inter-tube interaction, depending on the mutual tube orientation, the $(5,5)@(10,10)$ system may show zero gap (**b**) in the most symmetric (point group symmetry: D_{5h}), or four pseudogaps (**c**) in a less symmetric and stable configuration (point group symmetry: C_5) (adapted from Kwon et al. [39])

The individual $(5,5)$ and $(10,10)$ tubes are both metallic and show the preferred 'graphitic' inter-wall separation of 3.4 Å when nested. To determine the electronic properties of the double-walled nanotube, a tight-binding technique with parameters determined by *ab initio* calculations for simpler structures has been used [38, 39]. Due to the relatively high symmetry of the coaxial system consisting of a D_{5d} $(5,5)$ nanotube nested inside the D_{10h} $(10,10)$ nanotube, the dependence of the inter-tube interaction on the tube orientation shows a periodicity of 18°. In the absence of inter-tube interaction, the band structure of each tube is characterized by two crossing linear bands near E_{F}, one for the 'left' and one for the 'right' moving electrons.

The band structure of a pair of decoupled $(5,5)$ and $(10,10)$ nanotubes, a mere superposition of the individual band structures, is shown in Fig. 4.20a. Switching on the inter-tube interaction in the $(5,5)@(10,10)$ double-walled tube removes the near degeneracy of the bands near E_{F} as well (see Fig. 4.20b-c). In the most stable orientation, the double-walled system is still characterised by the D_{5d} symmetry of the inner tube. The four bands cross, with a very small change in the slope (Fig. 4.20b). While the same argument also applies to a least stable configuration, a markedly different behavior is obtained at any other tube orientation that lowers the symmetry, giving rise to four band crossings (Fig. 4.20c). This translates into four pseudogaps in the density of states near E_{F}.

At the Fermi level, the density of states of double-walled nanotubes is thus affected by the mutual orientation of the two constituting nanotubes, since the positions of the four pseudogaps depend significantly on it. The opening and closing of pseudogaps during the libration motion of the double-walled tube is a unique property that cannot be observed in single-walled nanotube ropes [39].

At last, self-consistent charge density and potential profiles for double-walled nanotubes, considering various helicities, have been calculated [40]. It

reveals that the atomic structure of the inner tube modifies the charge density associated with states near E_F even outside the outer tube, so that it could even be probed experimentally using a STM. A significant amount of charge, originating mainly from the π electron system of the tubes is transferred mainly into a new inter-wall state, related to the interlayer state in graphite.

4.2.6 Defects in Carbon Nanotubes

In summary, local and global curvature, inter-tube and inter-shell interactions are dramatically modifying the electronic properties of carbon nanotubes from that obtained by simple 'band folding' of the graphene band structure, as proposed in Sect. 4.1 of the present chapter. However, up to now, only the geometrical aspect and the local environment of carbon nanotubes have been investigated. The intrinsic honeycomb network of carbon nanotubes is probably not as perfect as it was initially thought to be. Defects like pentagons, heptagons, vacancies, or dopants are found to modify drastically the electronic properties of these nano-systems. The electronic properties of defected nanotube-based structures are then more complex than infinitely long, perfect nanotubes. The introduction of defects in the carbon network might thus appear as an interesting way to tailor its intrinsic properties, in order to create new potential nano-devices.

4.2.7 Connecting Nanotubes

Since carbon nanotubes are metals or semiconductors depending sensitively on their structures, they can be used to form metal-semiconductor, semiconductor-semiconductor, or metal-metal junctions. These junctions have interesting potential for applications since they are of nanoscale dimensions and made entirely of a single element. In constructing this kind of on-tube junction, the key point is to join two half-tubes of different helicity seamlessly with each other, without too much cost in energy or disruption in structure. It has been shown that the introduction of pentagon-heptagon pair defects into the hexagonal network of a single carbon nanotube can change the helicity of the carbon nanotube and fundamentally alter its electronic structure [41–45]. Both the existence of such atomic-level structures and the measurement of their respective electronic properties have already been resolved experimentally [46, 47].

The defects, however, must induce zero net curvature to prevent the tube from flaring or closing. The smallest topological defect with minimal local curvature (hence less energy cost) and zero net curvature is a pentagon-heptagon pair. When the pentagon is attached to the heptagon as in the aniline structure, it only creates topological changes (but no net disclination) which can be treated as a single local defect. Such a pair will create only a small local deformation in the width of the nanotube, and may also generate a small change in the helicity, depending on its orientation in the hexagonal network.

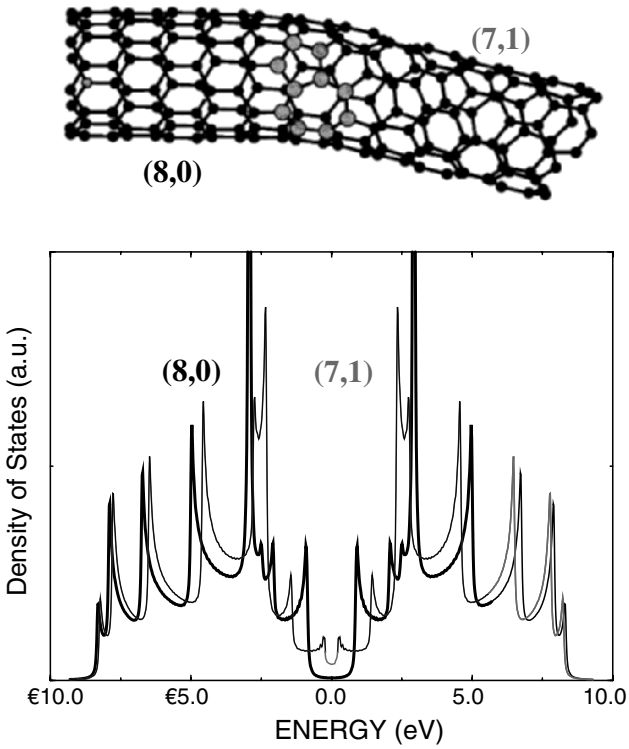


Fig. 4.21. Atomic structure of a (8,0)/(7,1) intramolecular carbon nanotube junction. The large light-gray balls denote the atoms forming the heptagon-pentagon pair. The electron density of states related to the two perfect (8,0) and (7,1) nanotubes are illustrated with thick and thin lines, respectively

Figure 4.21 depicts the connection, using a single 5–7 pair, between two nanotubes exhibiting different electronic properties. As mentioned above, the (8,0) nanotube has a 1.2 eV gap in the tight-binding approximation, and the (7,1) tube is a metal (although a small curvature-induced gap is present close to the Fermi energy).

Joining a semiconducting nanotube to a metallic one, using a pentagon-heptagon 5–7 pair incorporated in the hexagonal network can thus be proposed as the basis of a nano-diode (or molecular diode). The system illustrated in Fig. 4.21 forms a quasi-1D semiconductor/metal junction, since within the band-folding picture the (7,1) half tube is metallic and the (8,0) half tube is semiconducting. This led to the prediction that these defective nanotubes behave as the desired nanoscale metal-semiconductor Schottky barriers, semiconductor heterojunctions, or metal-metal junctions with novel properties, and that they could be the building blocks of nanoscale electronic devices.

4.2.8 Haeckelite Nanotubes

Following the previous idea of introducing 5- and 7-rings into hexagonal networks, a novel class of perfect crystals, consisting of layered sp^2-like carbon and containing periodic arrangements of pentagons, heptagons and hexagons, has been proposed [48]. These sheets are rolled up so as to generate single-walled nanotubes (Fig. 4.22), which resemble locally to the radiolaria drawings of Ernst Haeckel [49].

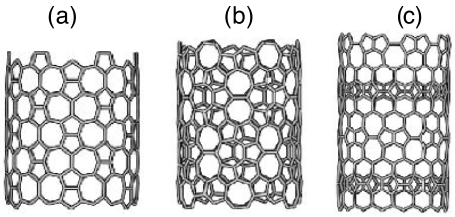


Fig. 4.22. Nonchiral Haeckelite nanotubes of similar diameter (1.4 nm). (**a**) nanotube segment containing only heptagons and pentagons paired symmetrically. (**b**) nanotube segment exhibiting repetitive units of three agglomerated heptagons, surrounded by alternating pentagons and hexagons. (**c**) nanotube segment containing pentalene and heptalene units bound together and surrounded by six-membered rings

These ideally defective tubes exhibit intriguing electronic properties: local density of states (LDOS) calculations of Haeckelite tubes revealed an intrinsic metallic behavior, independent of orientation, tube diameter, and chirality. Particularly, an unusual high intensity LDOS peak at the Fermi level is noticed for the family of tube depicted in Fig. 4.22b, thus suggesting the possible existence of superconductivity as the electron-phonon coupling is expected to be also enhanced by the tube curvature. Considering the metallic properties of Haeckelites, they should offer advantages compared to carbon nanotubes in applications. If they can be manufactured, there is no necessity for diameter or helicity selection to separate metallic structures (i.e., for electronic interconnect applications). Our calculations also reveal that these Haeckelite structures are more stable than C_{60}, and have energies of the order of 0.3–0.4 eV/atom with respect to graphene, allowing the potential synthesis of this new class of nanotubes. The structure of coiled carbon nanotubes, which can be produced by CVD methods, have been recently explained by rolling up Haeckelite-like stripes made of heptagons, pentagons and hexagons, with a predominance for non-hexagonal rings [50].

4.2.9 Molecular Junctions Based on Nanotubes

Connecting nanotubes in a network is a quite interesting issue in order to correlate both the mechanical and electronic properties. Recently, the beam of a

transmission electron microscope has been used to irradiate nano-structures locally. Covalently connected crossed single-walled carbon nanotubes have thus been created using electron beam welding at elevated temperatures [51, 52]. These molecular junctions of various geometries ('X','Y', and 'T') are found to be stable after the irradiation process. To study the relevance of some of these nano-structures, various models of ideal molecular junctions have been generated. The presence of heptagons is found to play a key role in the topology of nanotube-based molecular junctions. Figure 4.23 depicts an ideal 'X' nanotube connection, where a (5,5) armchair nanotube intersects a (11,0) zigzag tube. In order to create a smooth topology of the molecular junctions, six heptagons have been introduced at each crossing point.

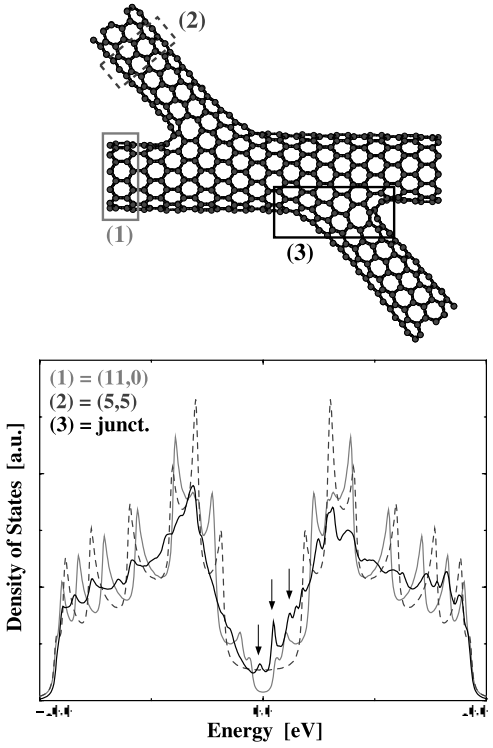


Fig. 4.23. Electronic properties of an ideal X-junction, created by intersecting a (5,5) tube with a (11,0) tube. The one-dimensional electronic densities of states of a semiconducting (11,0) nanotube (*light curve*), a metallic (5,5) nanotube (*dashed curve*) and averaged over the intersecting region of the molecular junction (*black curve*). The Fermi level is positioned at the zero energy. Localized states due to the presence of defects are indicated by arrows

The calculation of the local densities of states (LDOS) has been performed in order to investigate the electronic properties of these molecular junctions. Both the metallic character of the (5,5) nanotube and the semiconducting behavior of the (11,0) nanotube are illustrated in Fig. 4.23. The LDOS of the regions where the two nanotubes cross, reveals an enhancement of the electronic states at the Fermi level, thus suggesting a strong metallic behavior. These metallic sites (tube intersections) may well behave as quantum dots when embedded in a semiconducting tubular system. It is also notable that the presence of localised donor states in the conduction band (as indicated by arrows) is caused by the presence of heptagons. The novel small peak on the valence band (also shown by an arrow), close to the Fermi energy, can probably be attributed to the high curvature of the graphitic system. The Van Hove singularities present in the LDOS of the two achiral nanotubes, are much less spiky in the junction region (Fig. 4.23), thus illustrating a clear loss of the one-dimensional character in this site. Junction models in terms of local density of states, as those created by irradiation, are described to suggest their importance in electronic device applications.

4.3 Non-Carbon Nanotubes

4.3.1 Boron Nitride Nanotubes

We start our review of non-carbon nanotubes by the important case of boron nitride (BN) compounds. Such structures were first theoretically proposed and studied on the basis of tight-binding [53] and *ab initio* [54] calculations motivated by the structural similarities between graphene and the planar form of BN (Fig. 4.24).

Soon after, BN nanotubes were synthesised by a variety of techniques, including arc-discharge experiments [55–57], laser ablation [58–61], CVD techniques [62, 63], or substitution reactions on preformed pure carbon tubes [64, 65]. From the structural point of view, both multi-walled and single-walled BN nanotubes have been synthesised. Further, recent experimental results suggest a selection of helicity towards the zigzag geometry [61]. The cap of BN nanotubes is observed to be rather flat as compared to the carbon ones.

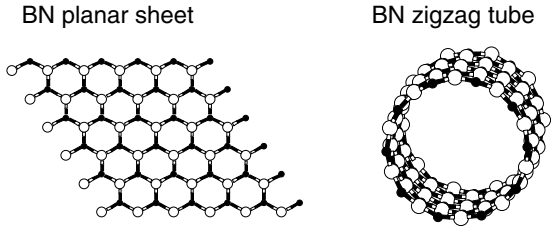


Fig. 4.24. Symbolic representation of BN planar and tubular forms

This has been shown [55–57,66] to be related to the presence of squares in the network, as pentagons are energetically unfavorable due to the cost associated with homopolar B-B or N-N bonds.

The electronic properties of BN nanotubes are very different from those of their carbon analogue. Due to the difference of ionicity between boron and nitrogen, BN systems are strongly ionic and display the largest gap of all III-V compounds (see Sect. 4.1). The band structure of bulk hexagonal BN is represented in Fig. 4.25 within the framework of the DFT-LDA approach and of a more accurate quasiparticule approach within the so-called GW approximation [54]. In the bulk phase, hexagonal BN (h-BN) crystallizes in an AB stacking where all boron atoms are on top of a nitrogen one (and vice-versa). This is another manifestation of the ionic character of BN.

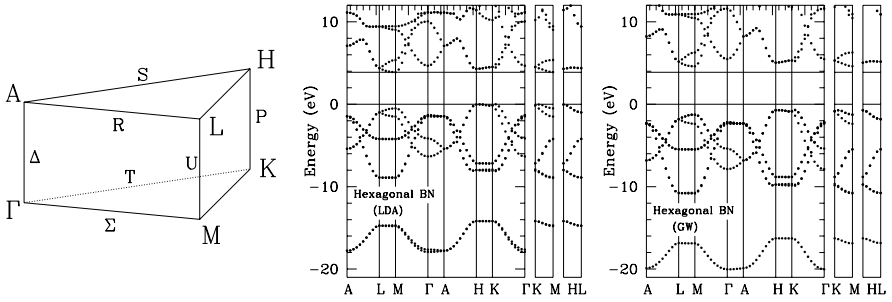


Fig. 4.25. Band structure of bulk h-BN. *Left*: Brillouin zone. Centre: LDA band structure. *Right*: GW band structure (adapted from Blase et al. in [54])

Within the accurate GW approach, the band gap is found to be indirect between the top of the valence bands at point K and the bottom of the conduction bands at point M with a value of 5.4 eV (LDA value: 3.9 eV). This is smaller by about 0.9 eV than the band gap found for cubic BN within the same GW approach but it remains that h-BN is a large gap insulator. We now represent in Fig. 4.26 the charge density associated with the highest occupied (HOMO) and lowest unoccupied (LUMO) states at high-symmetry points of the Brillouin zone. For the states at K and M, the charge density is localized either on the B or N atoms with a strong p_z character (where $\hat{z}$ is the normal to the surfaces).

The most interesting state is certainly the LUMO state at Γ. The charge density is seen to clearly delocalize in between the 'atomic layers' with a maximum of charge midway between two neighboring planes. This feature can be shown to be related to an intrinsic property of the isolated BN layer which we study now. This will also allow us to address the case of single-walled BN nanotubes.

There are difficulties to obtain an accurate band structure of the isolated h-BN sheet. Such difficulties are related to the nature of the LUMO state at

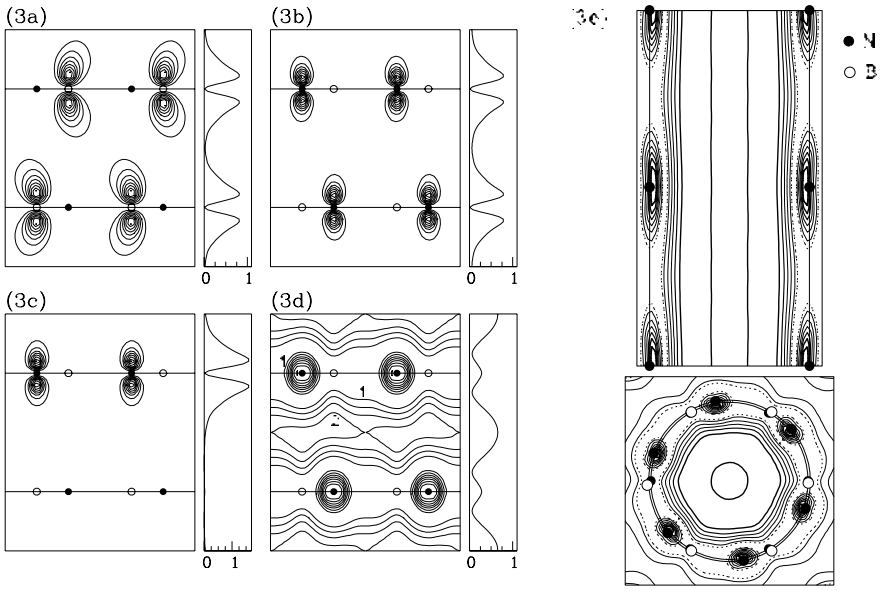


Fig. 4.26. Contour plots, in planes perpendicular to the BN layers, of the charge density of selected states for h-BN. N atoms are in black and B in white. The charge density averaged over planes parallel to the layers is shown. (**a**–**d**) correspond respectively to the LUMO state at M, the HOMO at K, the HOMO at H and the LUMO at Γ. In (**d**) contours labelled 1 and 2 correspond to a charge density of 0.16 $\times$ 10^{-4} and 0.63 $\times$ 10^{-4} electron/(a.u.)^3. The maximum charge density is 1.26 $\times$ 10^{-4} electron/a.u.^{3} on the nitrogen atom. In (**e**), the charge density for the LUMO at Γ in a BN nanotube is represented

Γ and the proximity of the vacuum level. We provide in Fig. 4.27 several band structures of the h-BN sheet, all obtained within the same pseudopotential DFT-LDA approach but with different basis, namely localised atomic-like orbitals (left) and plane waves (center, right). Calculations have been performed with periodic boundary conditions with a distance of 5 Å (left, center) and 10 Å (right) between adjacent layers.

The discrepancies between the three band structures is quite instructive. While with the complete PW basis, the LUMO at Γ is seen to be the lowest unoccupied state, the use of localized orbitals induces an upward shift to higher energy of about 2 eV, with respect to the LUMO-states at M or K. This can be understood as a confinement effect on this state which is not allowed to delocalise away from the atomic layer. Looking now at Fig. 4.27 (center, right), we see that increasing the distance between layers in the calculation induces the occurrence of new states just above the Γ-LUMO state. Such states come from the continuum above the vacuum level. When the distance between layers is too small, confinement again repels these states at higher energy. These results are a clear indication that the bottom of the conduction

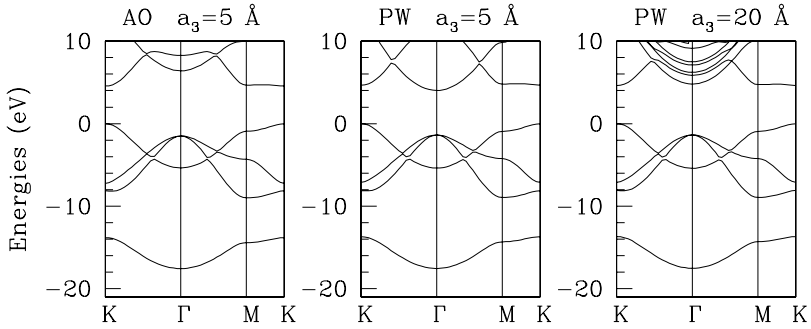


Fig. 4.27. DFT-LDA band structure of an 'isolated' BN sheet. *Left*: calculated with localized orbitals (LO) basis and $a_3 = 5\,\text{Å}$. *Center*: calculated with a plane wave (PW) basis and $a_3 = 5\,\text{Å}$. *Right*: calculated with a plane wave (PW) basis and $a_3 = 20\,\text{Å}$. a_3 is the interplane distance in the periodic boundary conditions imposed in the calculations

bands in h-BN is located just below the vacuum level. This means that the electronic affinity of BN nanotubes is close to zero. In particular, upon doping, one can expect BN nanotubes to be very good field emitters. However, the doping of such large gap systems is difficult to achieve.

We note that, contrary to the case of carbon nanotubes, the band gap of single-walled BN nanotubes will be rather stable with respect to tube radius and helicity. This stems from the relative flatness of the bands along the MK directions and from simple band folding arguments.

Finally, theoretical calculations predicted the existence of a non-zero ground-state polarization in BN (n, m) nanotubes such that $m - n$ is not a multiple of three [67, 68]. This is a non-trivial quantum effect. The existence of non-zero ground-state polarization induces a photo-current in such nanotubes upon arrival of photons with energy larger than the band gap, even if the light is non-polarized. Such polarization effects await experimental confirmation.

4.3.2 $B_xC_yN_z$ Nanotubes

As in the case of pure BN tubes, nanotubes with various $B_xC_yN_z$ stoichiometries have been synthesized using arc-discharge [69–72], pyrolysis of molecules [73, 74], laser ablation [75], CVD [76, 77] or substitution reactions [64, 65, 78]. Following the reports of the synthesis of planar forms of BCN sheets with well defined stoichiometry [79, 80], the two forms of $B_xC_yN_z$ nanotubes first studied were BC_3 and BC_2N structures. Again, the planar graphitic forms were first proposed [81, 82] and it was thus tempting, at the theoretical level, to study their tubular analogs [83–85]. We present in Fig. 4.28 the structures suggested theoretically for both planar compounds.

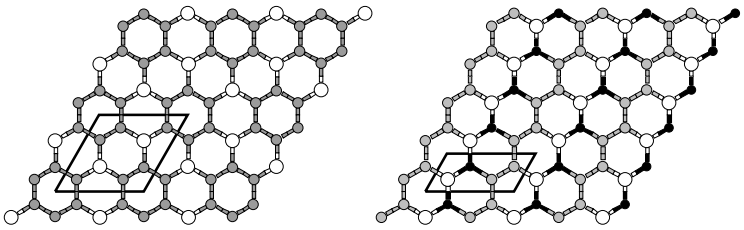


Fig. 4.28. Symbolic representation of the first proposed structures for (*left*) BC_3 and (*right*) BC_2N. Unit cells are indicated. Carbon atoms are in grey

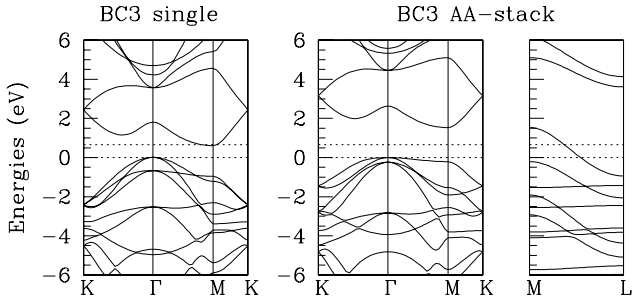


Fig. 4.29. DFT-LDA band structure of BC_3. (*Left*) Isolated sheet. (*Right*) AA stacking. The band gap of the isolated sheet is indicated throughout with dotted lines. The zero of energy has been set to the top of the valence bands at Γ

Ordered Forms of BC_3

The BC_3 structure proposed originally by Tománek et al. [81] exhibits a DFT-LDA band gap of about 0.6–0.7 eV for the isolated sheet but stacking is known to close the gap through dispersion along the $\hat{c}$-axis direction. This is evidenced in Fig. 4.29 in the case of AA stacking but similar conclusions were reached for other types of stacking as well [81, 85]. As in the case of BN systems, charge transfer from B to C induces a significant inter-plane interaction with a band dispersion up to 1.2 eV, leading to valence-conduction bands overlap about 0.5 eV. Another interesting aspect of BC_3 is the complete depletion of the π-bands, an effect which is related to the fact that B atoms in substitution provide one less valence electron to the network than carbon atoms. In the case of the isolated sheet, the band gap is seen (Fig. 4.29) to open between the σ and π bands of the 'modified' graphene sheet.

Ordered Forms of BC_2N

The BC_2N structure shown in Fig. 4.28 has been found to be the lowest energy structure among the class of systems that can be obtained with a hexagonal 8-atom cell (based on the 2×2 graphene unit cell) compatible with the desired stoichiometry [82]. The obtained structure is the one that minimizes

the number of B-C or N-C bonds (or maximizes the number of B-N or C-C bonds). This hierarchy in bond stability is an important criteria which will further be discussed below.

Such a BC_2N structure was found to be semiconducting with a 1.76 eV band gap [82, 83]. As a result, BC_2N tubules are also semiconductors. Small BC_2N (2,2) nanotubes (equivalent in size to the (4,4) nanotubes in the standard notations) were found to have a smaller gap (DFT-LDA value: 1.3 eV) as a result of curvature [86] but nanotubes with larger radius should quickly recover the band gap of the planar structure.

One of the interesting features of this BC_2N compound is its strong anisotropy. As graphite is (semi-)metallic and BN insulating, it can be realized that the electronic conductivity will be larger along the C-C chains than perpendicularly to the B-N chains. As a result, BC_2N nanotubes, with the idealized geometry shown in Fig. 4.28, may exhibit helicoidal C-C chains acting as nano-scale solenoids able to generate magnetic fields upon current flow [84].

It is not clear, however, that synthesized BC_2N structures display such an ideal atomic configuration. Experimentally, there are evidences for segregation of BC_2N structures into pure carbon or BN domains. Both intra- and inter-tube [72, 87] diffusion have been observed as depicted in Fig. 4.30. Intra-tube diffusion leads to quantum dots or metal/insulator C/BN junctions [88] and inter-tube phase separation to coaxial C/BN/C nanotubes.

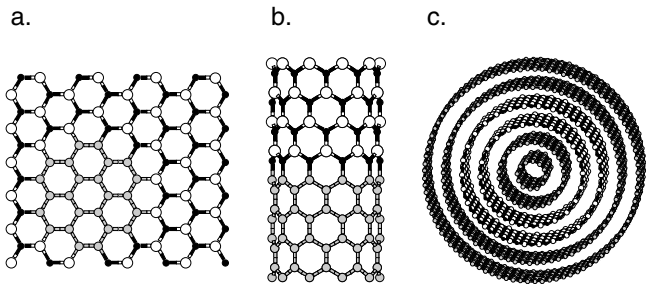


Fig. 4.30. Symbolic representation for (**a**) a carbon quantum dot in a BN matrix and (**b**) a metal/insulator C/BN idealized hetero-junction, and (**c**) a radially segregated C/BN/C multi-walled tube with two BN layers between two carbon layers on each side

As emphasized above, this segregation can be rationalised by the largest stability of B-N and C-C bonds as compared to B-C and N-C ones. Allowing for widest pure carbon or BN strips (see Fig. 4.31 and [89]), that is for more 'intra-tube' C/BN segregation, one obtains more stable structures as shown in Fig. 4.32 (left) on the basis of DFT-LDA calculations.

With increasing width, carbon and BN strips recover the properties of the corresponding infinite pure planar compounds. In particular, the band gap

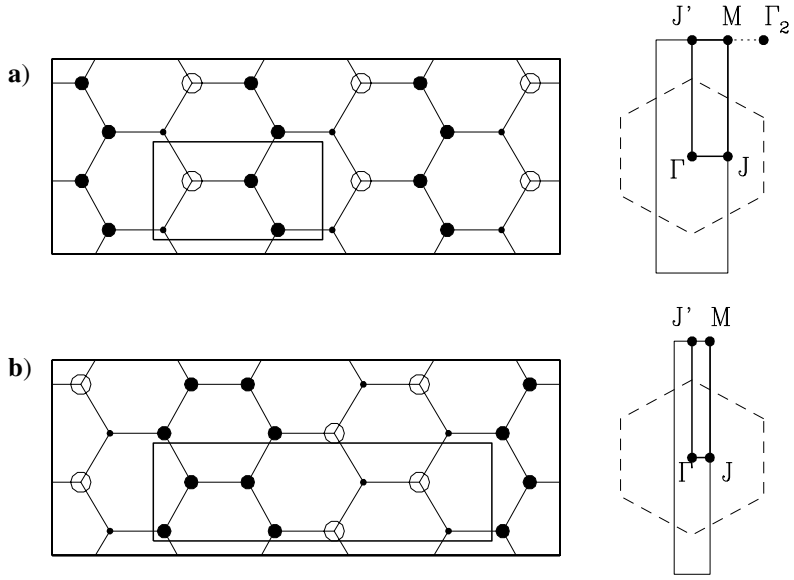


Fig. 4.31. Models for BC_2N materials with segregated strips containing n carbon or BN atomic chains (**a**) $n = 1$ and (**b**) $n = 2$. The corresponding Brillouin zone are also shown

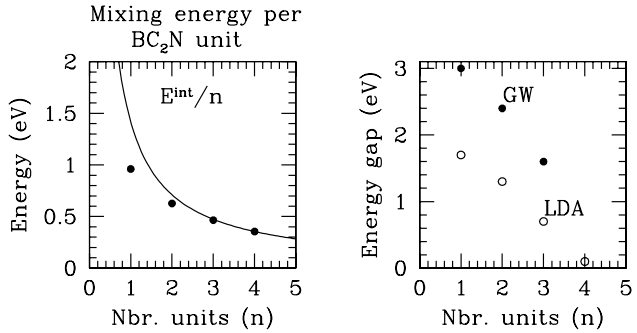


Fig. 4.32. Evolution of (*left*) energy and (*right*) band gap of BC_2N materials as a function of the number n of carbon or BN chains in segregated strips (see Fig. 4.31)

closes along the $\Gamma J'$ direction which includes the K vector of the corresponding graphitic structure. This is emphasized in Fig. 4.32 (right) where both the DFT-LDA and GW band gaps are indicated as a function of segregation [89].

We emphasize however that such systems, with continuous chains or strips, even though more stable than the original structure proposed by Liu et al., remain idealized structures [90]. The size and shape of the domains are expected to depend strongly on the synthesis conditions. While complete radial segregation has been observed (as in Fig. 4.30c), planar BC_2N photoluminescent

compounds with a band gap in the 2–3 eV range have been synthesized [80], suggesting from Fig. 4.32 a rather small segregation. Recently, semiconducting nanotubes and/or nanofibers with blue-violet photoluminescent properties have been reported [76, 91]. Finally, 1 eV band gap BCN nanotubes were also claimed [77] on the basis of two-point conductivity measurements.

Disorder and Doping in BCN Compounds

The arguments proposed above for the formation of well-ordered $B_xC_yN_z$ graphitic or tubular compounds are based on stability considerations. It is important to keep in mind however that the growth of nanotubes is certainly an out-of-equilibrium mechanism driven also by kinetics. Depending on the experimental temperature and other factors, atoms will either tend to form segregated well ordered structures or will be randomly distributed in the network. In this latter case, and in the limit of small (B, N) content, the physics will be the one of B- or N-doped graphitic sheets as emphasized in [92].

The physics of boron-doped tubes has been the subject of several theoretical and experimental studies. This interest stems from several interesting properties. From a structural point of view, B-doped tubes grow longer and seem to be preferentially zigzag [93], with increased crystallinity and are more resistant to oxidation [94]. Further, it is clear that B-doping of carbon nanotubes will lead to p-type tubes which may be used in electronic junctions. In a C (10, 0) insulating tube, the acceptor level was shown to be located 0.16 eV above the top of the valence bands [95] as compared to 0.45 eV in C_{60} and 0.37 eV in diamond. Even in metallic nanotubes where the Drude divergence of the dielectric function would, in 3D materials, rule out the occurrence of localized acceptor states, 'quasi-bound' states overlapping in energy with the states of the metallic pure carbon tube have been predicted theoretically [96] and shown to lead to strong back-scattering effects in the transmittance at energy equal to the one of the B-related states.

The case of nitrogen-doping has also been addressed [95, 96, 98] showing donor character. However the atomic structure of the network around the N atom is still unclear since, beyond the simple substitution of a C atom, nitrogen may induce pyridine-like structures in the carbon tube body following the hexagonal form of C_3N_4 proposed originally by Liu et al. [99–102].

To close this section on doping, we note that on the basis of total energy calculations [103, 104], it has been shown that B atoms prefer to gather in ordered BC_3-like islands rather than remaining isolated. Such a segregation effect was observed experimentally in B-doped nanotubes [105]. Again, competition between thermodynamics and kinetics will drive the formation of more or less ordered structures.

4.3.3 WS_2, MoS_2 and Other Nanotubes: from Synthesis to Predictions

BN and BCN nanotubes were actually not the first non-carbon nanotubes to be synthesized. In 1992, inorganic WS_2 and MoS_2 fullerene and tubular forms were synthesized [106, 107]. Such systems were shown to be useful lubricant materials [108] and to improve STM imaging [109]. The existence of such nanotubes stems from the fact that the most stable forms of WS_2 and MoS_2 are layered materials with weak Van der Waals interaction between the layers (6.15–6.18 Å between layers). Contrary to the case of pure carbon or BCN nanotubes, each nanotube wall is composed of three layers, an inner metallic layer between two sulfur ones as shown in Fig. 4.33.

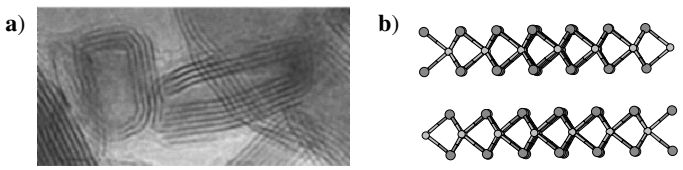


Fig. 4.33. (**a**) WS_2 nanostructures [adapted from: S. Prazad and J. Zabinski, Nature **387**, 761 (1997)] and (**b**) symbolic representation of two adjacent layers of WS_2-2H

The consequence of this multi-layered structure is that bending of the planar form to obtain nanotubes is energetically much more costly as not only bending, but also compression/stretching of bonds must be involved (Fig. 4.34). This is an indication that such nanotubes will certainly tend to have larger diameters than BCN ones.

The electronic band structure of 2H-MoS_2 planar compounds [110] and nanotubes [111] has been studied on the basis of *ab initio* (see Fig. 4.35) or self-consistent tight-binding calculations. The planar layered compound is a semiconductor with a $\Gamma \rightarrow K$ indirect band gap of 1.2 eV (experimental value [112]). The DFT-LDA value is equal to 0.8 eV [110]. Upon formation of nanotubes, the band gap has been shown to decrease strongly with decreasing radius [111] but MoS_2 nanotubes remain semiconducting (Fig. 4.34). Depending on tube helicity, the band gap can be either direct or indirect as the k-point K can be folded (or not) onto Γ.

Following the same idea that layered materials can be rolled onto tubular forms, other nanotubes have been proposed and studied on the basis of theoretical simulations. For instance, GaSe crystallizes into a layered structure, with each wall composed of a double-Ga layer between two Se ones. Again, it was found [114] that rolling such thick layers onto a tubular structure requires more energy than in the case of BCN systems and that these systems are semiconducting with a band gap that decreases with decreasing radius.

More recently, B_2O and BeB_2 nanotubes were proposed [115] following the experimental report that planar structures with corresponding stoichiometry

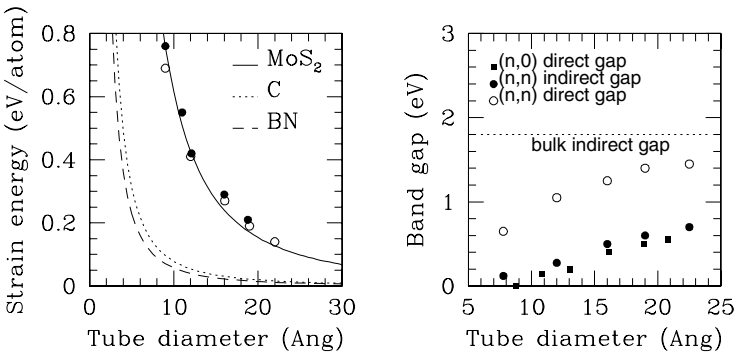


Fig. 4.34. (**a**) Evolution as a function of tube diameter of the energy per atom in carbon (*dotted line*), BN (*short dash*) and MoS_2 tubes. (**b**) Evolution of the band gap for MoS_2 tubes upon curvature (adapted from [111])

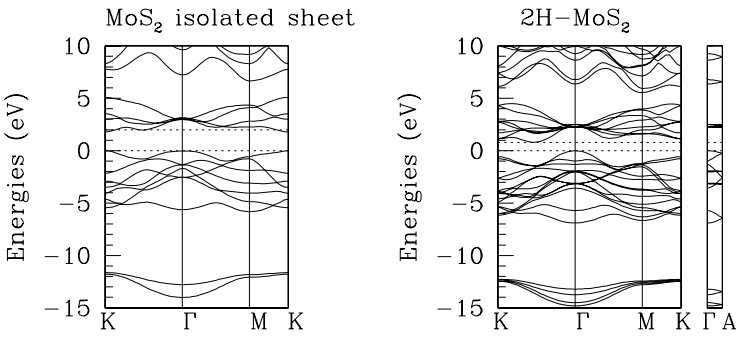


Fig. 4.35. DFT-LDA band structure of MoS_2 using pseudopotentials and a DZP localized basis as generated by the package SIESTA [113]

had been synthesized. Other layered structures have been proposed theoretically for building nanotubes, such as pure boron [116] or even sp^2 silicon tubes [117].

4.4 Monitoring the Electronic Structure of SWNTs by Intercalation and Charge Transfer

4.4.1 Introduction

In this section, we show that the Fermi level of single-walled carbon nanotubes can be tuned by exposure of the material to electron donors or acceptors allowing one to fill or deplete selectively the electronic states of the different kinds of tubes, semiconducting and metallic, that constitute the material and consequently to control their electronic properties. We describe the modifications of the electronic structure of SWNTs associated with the shift of their

Fermi level and the impact of these modifications on both electrical transport and vibrational properties. In Sect. 4.4.2, we show how the electronic structure and vibrational properties of SWNTs can be easily observed by optical absorption and Raman spectroscopy, the electrical transport properties being studied by standard resistivity measurements. Section 4.4.3 reports some experimental proofs of both the intercalation of elements in the material and the charge transfer onto or from SWNTs. However, because there are no preferential intercalation sites between the tubes in the bundles, it is very difficult to estimate the chemical composition of the samples intercalated by alkali metals in vapor phase. In Sect. 4.4.4 we describe a simple way to shift the Fermi level of a known and pre-defined value by redox reactions between SWNTs and organic molecules and reports the corresponding changes in their physical properties.

4.4.2 Optical Absorption and Raman Spectroscopy of SWNTs

As explained in Sect. 4.1, the symmetry of SWNTs leads to energy gaps in the DOS, which displays a set of symmetrical singularities with respect to the Fermi level, the energy between two singularities depending on both the radius and chiral indices of the tubes. The energy scale of the first band gaps in the DOS makes it possible to probe them by optical absorption spectroscopy.

Three sets of optical bands are clearly observable in the optical spectrum of SWNTs, superimposed on a broad absorption band corresponding to π plasmons, i.e., to collective excitations of π electrons, as observed in all conjugated systems (Fig. 4.36) [118, 119].

For pristine samples, or weakly doped samples, the low energy part of the π-plasmons can be linearized within a simple Drude model and subtracted from the overall spectrum allowing one to study accurately the optical transitions of SWNTs (Fig. 4.36, bottom right). The two first features at 0.68 and 1.2 eV originate from band gap transitions in semiconducting tubes, whereas the third at 1.7 eV originates from metallic tubes. In fact, all three absorption bands are the superposition of narrower absorption bands (Fig. 4.36, bottom right) corresponding to the response of individual tubes of different chiral indices and/or of different diameters. These spectra are typical of SWNTs produced by electrical arc discharge [120]. Raman spectroscopy is one of the most efficient tool to investigate the vibrational properties of SWNT in relation to their structure and electronic properties. For SWNTs, it is a resonant process associated with allowed optical transitions in the DOS. Thus, depending on the excitation energy, the response of semiconducting tubes may be enhanced (514.5 nm, green light) with respect to metallic one and vice versa (647.1 nm, red light)(Fig. 4.37) [121]. All these features are detailed in Chap. 5.

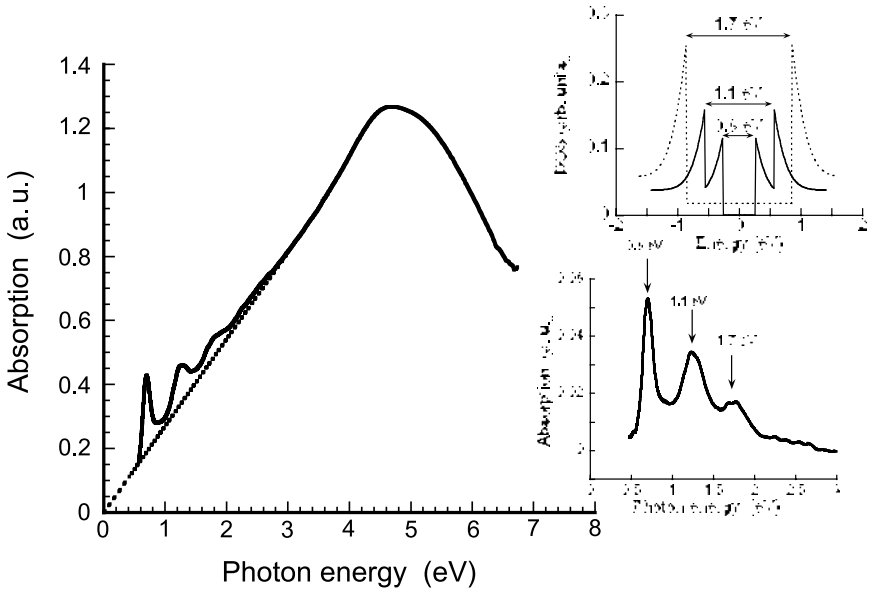


Fig. 4.36. Optical absorption spectrum of SWNTs. The dotted line is the low energy linearization of the π-plasmon spectrum. *Upper right*: schematic representation of the DOS of SWNTs. *Bottom right*: Optical absorption spectrum of SWNTs after the correction of subtracting π-plasmon contribution

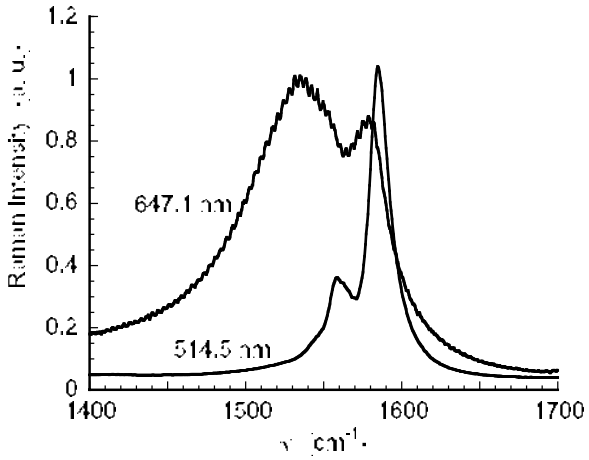


Fig. 4.37. Resonant Raman spectra of TM modes of SWNTs. For the red (647.1 nm) excitation, the response of metallic tubes is enhanced (Breit-Wigner-Fano profile); For the green (514.5 nm) excitation, the response of semiconducting tubes is enhanced (symmetric lorentzian modes)

4.4.3 Experimental Evidences of Intercalation and Charge Transfer in SWNTs

When a new material is synthesized, the first properties which are studied, both theoretically and experimentally, are the electronic structure and electronic transport. This was particularly true for conjugated carbon materials, such as graphite and C_{60} crystals. A non negligible feature of organic compounds is the weak Van der Waals interactions between the constituting units which allow large lattice dilatations as compared to inorganic materials, and thus an ability to be intercalated by elements or molecules. Generally, intercalation affects the electronic properties of these systems because of charge transfer between intercalant and the host material or/and by the change in the interactions between the constituting units. In the search for superconductivity for example, organic systems are extensively studied because two key parameters governing the critical temperature between normal and superconducting states can easily be modified: the density of states at the Fermi level and the lattice parameter, both being associated to the intercalation of electron donor/acceptor species. SWNTs did not escape to this rule and their electronic structures, depending on their radius and chiral indices, have been widely studied (see Sect. 4.1). However, their transport properties are still extensively studied, at least at a theoretical point of view (see Chap. 6).

Evidences of Intercalation in SWNT Material

SWNTs are organised in bundles of tens to hundreds tubes in a two-dimensional triangular lattice characterized by a X-ray diffraction pattern displaying a first order peak (10) around 0.4 $Å^{-1}$ corresponding to the lattice parameter, the width of this peak reflecting both the mean size of the bundles and the disorder within the bundles. The intercalation of an element or a molecule in the lattice of SWNTs should then lead to its expansion, observable by a shift to lower q-values associated to a broadening of the (10) peak. Consistently, intercalation leads to a down shift and a broadening of the (10) peak, all the more when the size of the element is large [122]. The intercalation of potassium in bundles of nanotubes has also been studied by electron diffraction as a function of potassium concentration [123], and the same effect on the (10) peak (Fig. 4.38) is observed: as the concentration of potassium increases, the shift to low q-values and the broadening of the (10) peak increases. Finally, the intercalation of elements in SWNTs can also be evidenced by TEM which shows the loss of coherence in the triangular lattice when SWNT bundles are exposed to cesium vapour (Fig. 4.39) [124].

Evidence of Charge Transfer upon Intercalation of Electron Donors or Acceptors

In graphite and C_{60} crystals, the intercalation of alkali metals leads to drastic changes in their electronic structure, electronic transport and vibrational

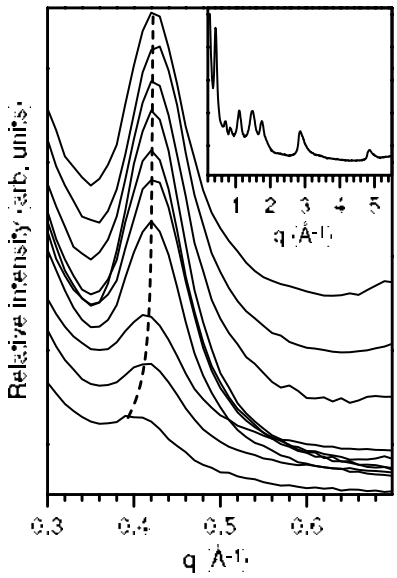


Fig. 4.38. Evolution of the (10) peak in the electron-diffraction pattern as a function of the concentration of intercalated potassium. *Upper curve*: pristine material; *lower curve*: fully intercalated material

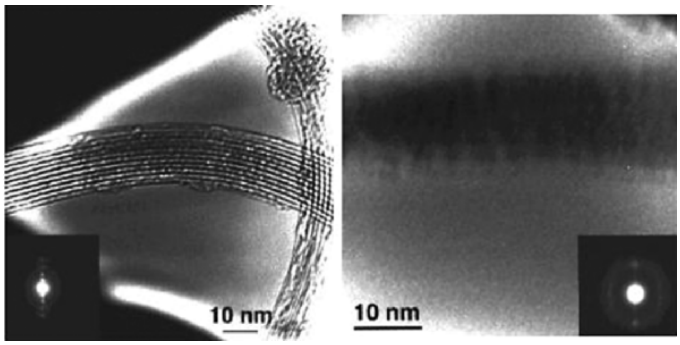


Fig. 4.39. TEM images of pristine (*left*) and Cs-intercalated SWNTs (*right*)

properties because of charge transfer from the intercalated alkali to the host material; the DOS at the Fermi level increases, the electrical resistivity decreases and the tangential modes of vibration soften. The first evidences for charge transfer in intercalated SWNT materials were given in 1998 for saturated doped samples. Exposure of SWNT macroscopic samples to potassium or bromine vapors lead to a drop in the electrical resistivity by more than one order of magnitude [125], the tangential vibrational modes shifting to low (high) frequency for potassium (bromine) intercalated samples [126], consistent with charge transfer to (from) the tubes. Electron energy loss

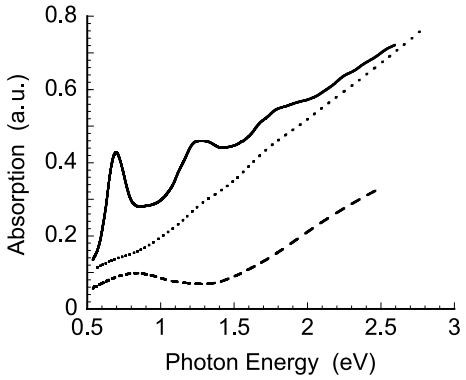


Fig. 4.40. Optical absorption spectra of pristine (*solid line*), bromine-doped (*dotted line*) and naphthalene-lithium-doped (*dashed line*) SWNTs. The new band observed for the naphthalene-lithium-doped sample does not correspond to new transitions in the DOS of SWNTs, but rather to a change in the π plasmons spectrum after charge transfer

spectroscopy has also been one of the first techniques used to show that charge transfer occurs when SWNT samples are exposed to alkali vapors; the charge-carrier plasmon energy increases with potassium concentration, thus with the charge transfer rate [127]. The first direct observation of the modifications in the electronic structure of intercalated SWNT, by optical absorption, were given in 1999 [119]. Both types of doping (n and p) lead to the disappearance of the absorption bands observable for the pristine sample, due to the population (depletion) (see Sect. 4.4.4) of the states in the DOS. More subtle, charge transfer is also observable by scanning tunneling spectroscopy on an individual 'neutral' SWNT. In these latter experiments, which allow one to probe the electronic structure of individual SWNTs, the mid position between Van Hove singularities is shifted with respect to the zero bias voltage (between the tip and the gold substrate), revealing a partial charge transfer from the gold substrate onto the tubes [128]. Many groups have now confirmed these results. Figures 4.40 and 4.41 show the effect of charge transfer on the electronic structure and on the tangential modes of vibration of SWNTs.

4.4.4 Tuning and Monitoring the Electronic Structure of SWNTs

Fermi Level of Two Phases in Contact

Strictly speaking, the Fermi level of a system is its chemical potential at absolute zero temperature and solutions are generally characterized by their redox potentials. However, redox potential and chemical potential correspond to the same physical entity and differ only by their reference level [129]. It is well known from solid state physics that when two phases are brought into contact, their previously different Fermi levels are brought into coincidence

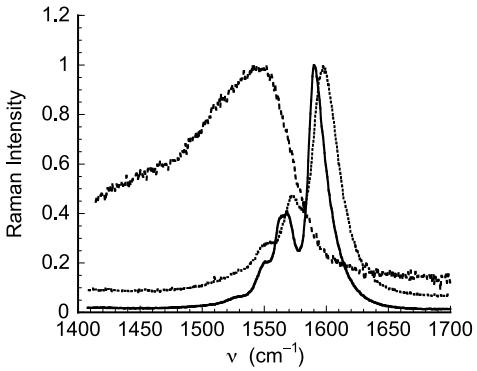


Fig. 4.41. Raman spectra of pristine (*solid line*), iodine-doped (*dotted line*) and rubidium-doped (*dashed line*) SWNTs

when thermodynamic equilibrium is achieved. This is true whatever the physical state of the two phases. For the homogeneity of this paragraph, we will speak about redox potentials for both nanotubes and solutions and convert their value to energy units. As shown in Sect. 4.1 the electronic structure of SWNTs is continuous (electronic bands) whereas isolated molecules display discrete electronic levels, and the crystalline structure does not impose definite intercalation sites (contrary to graphite and C_{60} crystals) as shown below. This can be understood as the honeycomb network of two adjacent tubes does not show any structural coherence. Thus, if a sample of SWNTs is brought into contact with a reservoir containing an excess of atoms or molecules which can intercalate the lattice, the redox potential of the sample will reach that of the atoms or molecules of the reservoir and charge transfer will occur. This is true for metallic tubes whatever the value of the redox potential of the reservoir and holds for semiconducting tubes for absolute values of redox potential larger than half the first optical transition energy.

Chemical Doping Process

The system used for chemical doping consists of a U-shaped glass tube where one branch contains the sample to be doped. The other branch is an ampoule containing neutral molecules in pure THF and in excess compared to the number of carbon atoms of the sample and a piece of alkali metal, lithium for example. The whole apparatus is sealed under high vacuum. THF was chosen because it is a polar solvent which facilitates electron transfer. In detail, the neutral molecules are first solubilized in THF. A first redox reaction occurs between lithium and organic molecules; electron transfer from lithium to organic molecules results in the radical anion form of the molecule with Li^+ as the counter ion. This reaction is easily checked by the change in colour of the solution and the appearance of the characteristic absorption spectrum

Table 4.1. Molecules used for doping SWNTs, redox potentials of the corresponding radical-anion forms, chemical compositions and normalized conductivity of the doped samples

Molecule	naphthalene	benzophenone	fluorenone	anthraquinone	benzoquinone
Redox potential	2.5 eV	1.8 eV	1.3 eV	0.85 eV	0.4 eV
x in Li_xC	0.17	0.14	0.1	0.04	$\simeq 0$
σ/σ_0	14	9.2	6	2.9	$\simeq 1$

of the radical-anion. The solution is then poured onto the sample and the redox reaction between radical-anions and SWNTs occurs, i.e., the electron transfer from radical anions to nanotubes and the intercalation of Li^+ ensures the neutrality of the system. Once doping is achieved, the excess solution is removed and the sample rinsed by internal distillation of the solvent. The sample is then dried by cooling the ampoule and the tube is sealed. This process leads to stable and homogeneously doped samples.

To determine the chemical composition of the sample, a macroscopic amount of known weight of purified SWNT is used and an optical cell is connected to the apparatus in which the solution is poured before and after the redox reaction with the sample and the optical absorption spectra are recorded. The end of the redox reaction is monitored by recording the resistivity of the sample during its exposure to the solution. The difference in optical densities is directly related to the number of molecules which are deactivated by the doping of the sample, i.e., the number of electrons transferred to the sample, leading to a precise chemical composition of the doped sample. Table 1 reports the different molecules used for the doping of SWNTs, the redox potential of their radical anion form, the stoichiometry of the doped samples and their conductivity normalized to that of the pristine sample. It must be pointed out that the highest doping rate obtained by these redox reactions does not correspond to the saturated phase, the latter being obtained by exposure of SWNTs to alkali vapors (redox potentials of alkali elements being close to 3 eV) or by electrochemical intercalation of alkali metals.

For optical-absorption and Raman experiments, the sample consists of a thin film prepared by spraying a homogeneous suspension of SWNTs on a quartz substrate heated with hot air and inserted in an optical cell connected to the ampoule containing the doping solution.

Electronic Structure and Electrical Transport of Doped SWNTs

All the features characteristic of the pristine material are removed after the sample is exposed to a solution of naphthalene-lithium (Fig. 4.42).This provides evidence that, by setting the redox potential of SWNTs to 2.5 eV, the initially empty states of both semiconducting and metallic tubes are filled, suppressing optical transitions between mirror peaks in the DOS. Consequently,

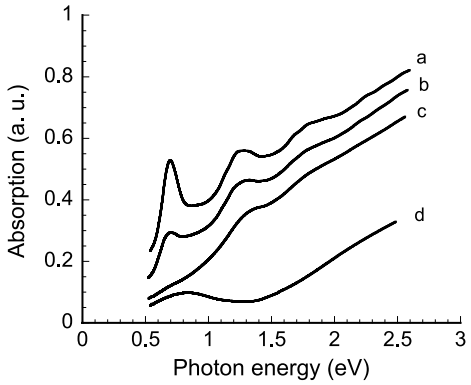


Fig. 4.42. Evolution of the optical absorption spectrum of SWNTs as a function of chemical composition: (**a**) pristine nanotube; (**b**) $Li_{0.04}C$ (redox reaction with anthraquinone-lithium solution); (**c**) $Li_{0.1}C$ (redox reaction with fluorenone-lithium solution); (**d**) $Li_{0.17}C$ (redox reaction with naphthalene-lithium solution)

all tubes constituting the material are metallic. The same observation is made using a solution of benzophenone-lithium.

Exposure of the pristine material to anthraquinone-lithium almost completely removes the first band at 0.68 eV, the other optical transitions being unaffected. Subtracting half the value of the first optical transition to the redox potential of anthraquinone-lithium leads to an estimation of the redox potential of the pristine material of about 0.5 eV, close to the value reported for C_{60} molecules [130]. Doping the sample with a fluorenone-lithium solution completely removes the feature at 0.68 eV and the low-energy shoulder of the second absorption band, while the feature at 1.3 eV and the band corresponding to metallic tubes are unaffected. Thus, the effect of setting the redox potential of SWNTs to 1.3 eV is to fill up the first and second peaks in the DOS of semiconducting tubes characterized by an energy gap lower than $\sim$1.3 eV. This leads to a second estimation of the redox potential of 0.6 eV, close to the value arrived at previously. The original electronic structure of the tubes can be recovered after exposure of the doped sample to molecules of redox potential close to that of SWNT. These reversible redox-reactions allows one to tune the Fermi level of SWNTs. Similar observations have been made by other groups on SWNTs intercalated using the vapor phase process [131] or by electrochemistry [132]. The effect of doping a purified buckypaper of SWNTs obtained by laser ablation [133] with the radical-anion of naphthalene is to reduce its resistivity by more than one order of magnitude (Fig. 4.43) [134]. Repeating this experience with the other doping solutions allows one to draw the energy dependence of the conductivity of the sample versus its energy (inset in Fig. 4.43) which is found to be linear, while the energy dependence of the charge carrier concentration is more complicate, as can be seen in

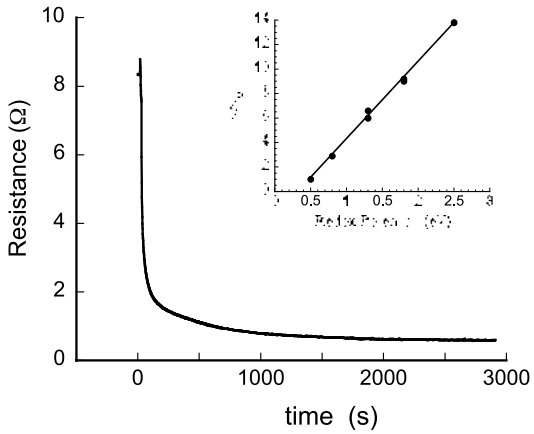


Fig. 4.43. Time evolution of the resistance of SWNTs exposed to a solution of naphthalene-lithium. Inset: variation of the normalized conductivity of SWNTs as a function of their redox potential

Table 4.1. These experiments have been confirmed by Claye et al. on samples of the same batch intercalated by electrochemistry [135].

In order to determine precisely the energy dependence of the charge-carrier concentration, and because the number of molecules of redox potential ranging between 0.5 and 3 eV is limited, a sample was exposed step by step to a solution of naphthalene-lithium and both its resistivity and doping rate were recorded at each step at thermodynamical equilibrium. This allowed to determine the dependence of the conductivity with the charge carrier concentration. Using the linearity of the conductivity versus energy leads to the variation of the charge carrier concentration versus energy (Fig. 4.44), which is found to be monotonically increasing. Two important properties can be derived from this observation: i) there is no stage of intercalation in SWNTs which would have lead to plateaus in the curve, ii) there is no singularities, meaning that Van Hove singularities have disappeared. This last observation could be explained by a crossover between a one-dimensional conducting system to a three-dimensional one because of a change in the inter-tube interactions due to the presence of the cations. However, having in mind that the derivative of the charge-carrier concentration with respect to the energy is the density of state at the Fermi level, Fig. 4.44 should display a $E^{3/2}$ dependence, which is not the case. In fact, the best fit is found to be 0.1 $E^{1/2}$, which would correspond to a one-dimensional band filling. This result is still not understood. The reversibility of the doping by redox reaction is illustrated in Fig. 4.45. In this experiment, a sample was first doped by redox reaction with naphthalene-lithium then progressively de-doped by redox reactions with solutions of neutral benzophenone, fluorenone and benzoquinone.

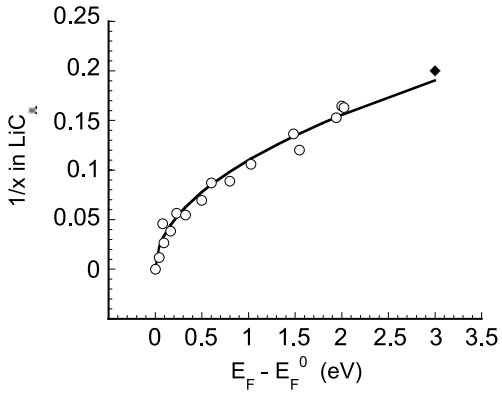


Fig. 4.44. Charge concentration of SWNTs as a function of the Fermi level of SWNTs. Solid line is a $E^{1/2}$ fit of data points ranging from 0 to 2 eV. Data point at 3 eV correspond to the saturated phase obtained by electrochemical intercalation of lithium [135]

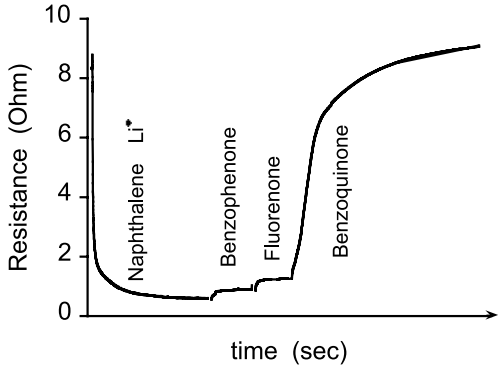


Fig. 4.45. Evolution of the resistance of SWNTs doped with naphthalene-lithium and de-doped progressively with various molecules showing the reversibility of the chemical doping process

Tangential Modes of Vibration of Doped SWNTs

The *n*-doped samples prepared by this chemical process are perfectly stable if kept under vacuum, and the samples used to determine the change of vibrational modes by Raman scattering are the same as those used for optical absorption experiments [121]. The dependence of the Raman response (TM modes) with the stoichiometry in Li_xC films is reported in Fig. 4.46 for two excitation energies (514.5 nm, green and 647.1 nm, red). Significant changes are observed upon doping. For $Li_{0.04}C$, the spectra are close to those measured on pristine samples, specially the resonant character of the Raman response persists in relation with the persistence of Van Hove singularities evidenced in the optical absorption spectrum (Fig. 4.42). In contrast, as expected from their

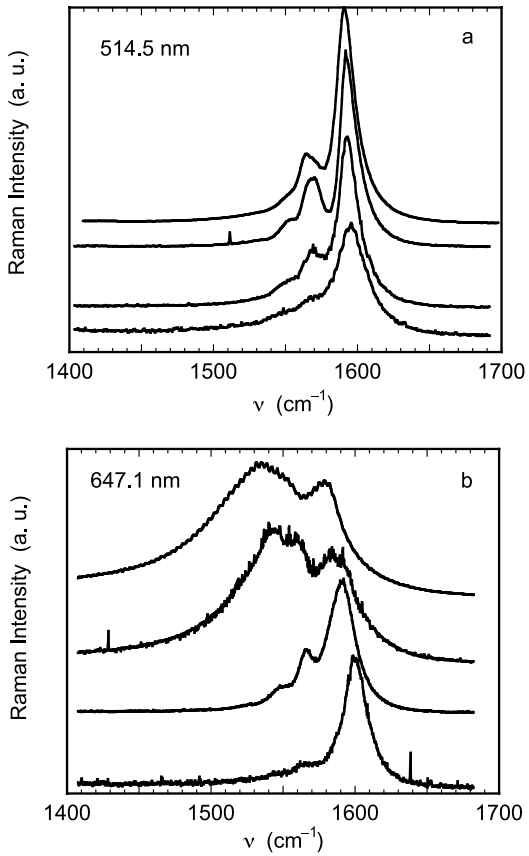


Fig. 4.46. Raman spectra of the TM Modes for doped SWNTs at various Li/C rates excited at 514.5 nm (**a**) and 647 nm (**b**). From *top* to *bottom*: pristine, $Li_{0.04}C$, $Li_{0.14}C$ and $Li_{0.17}C$

optical absorption spectra, the Raman spectra of $Li_{0.14}C$ and $Li_{0.17}C$ films do not show a resonant character as the profile of the spectra is independent of the excitation wavelength. The highest frequency component dominates the spectrum and, unexpectedly, shifts upwards when the stoichiometry increases. The intensity of the component located on the low-frequency side of the main peak (around 1550 and 1567 cm^{-1} in pristine SWNTs) decreases when the stoichiometry decreases, and almost vanishes in $Li_{0.17}C$. These results indicate that there is a hardening of the TM modes preceding the downshift associated to the saturated phase (Fig. 4.37) and are discussed in detail and compared to those obtained in the saturated phase in Chap. 5

4.4.5 Conclusion

We have shown that, by choosing appropriate molecules, it is possible to modify selectively the Fermi level of SWNT and thus to modify the conducting nature of the individual tubes. The investigation of the vibrational properties of SWNT in relation to the change in their structure and electronic properties has revealed a hardening of the TM modes before the expected softening observed in the saturated phase. All the experiments reported here have also been reproduced using potassium as a counter-ion, with identical results, meaning that the change in the electronic structure of SWNTs and the corresponding modifications in their vibrational and transport properties have some universal character.

4.5 Field Emission

4.5.1 Introduction

Field emission was described for the first time at the end of the 19^{th} century. Thorough experiments in the 1920s showed clearly that this emission occurred under high electric field and was not related to thermoelectronic emission. In 1928, Fowler and Nordheim used the concepts of quantum mechanics to estimate the current drawn from a metal surface by elastic tunneling under high electric fields: their model is still widely used today, and its derivation will be considered in detail in Sect. 4.5.2.

Following the development by Müller of field-emission microscopy in 1938 and field-ion microscopy in 1956, field emission was extensively employed as one of the most powerful techniques in surface physics. Field emission was also used by Young in his 'topografiner', the forerunner of the scanning tunneling microscope. Electron sources based on field emission did not find their use in scanning probe microscopes, however, but in conventional electron microscopy. Most high-end electron microscopes take advantage of the low energy dispersion and high brightness of cold or Schottky field emission sources to reach high resolutions.

The interest for field emission from carbon nanotubes does not originate from their potential use as electron sources in high-resolution electron beam instruments – although carbon nanotubes have proven to be a very interesting alternative. It is more in the field of vacuum microelectronics, a term coined by Spindt in 1968, that the great majority of the efforts in carbon nanotube field emission research is concentrated. Spindt developed a field emission array of microtips based on Si microtechnology, which opened the door to the realization of flat panel displays and microwave amplifiers. It appears, after eight years of research and development in carbon nanotube field emission, that nanotubes are under many aspects better suited than microtips for such applications.

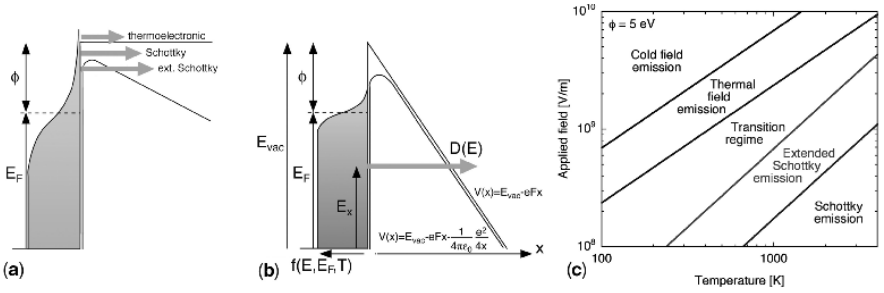


Fig. 4.47. (**a**) Electron emission at high temperature and low applied field; (**b**) Electron emission at low temperature and high applied field (field emission); (**c**) Emission regimes as a function of temperature and field for an emitter with $\phi = 5\,\mathrm{eV}$

We will review here basic theoretical concepts on field emission and field amplification, as well as the most common experimental set-ups and measurements. The mechanism and properties of nanotube field emission will be briefly presented, as a detailed review of their performances and application to devices is outside the scope of this chapter.

4.5.2 Field Emission and the Fowler-Nordheim Model

Electron Emission

The emission of electrons from a solid can be achieved by two means: either by heating to a temperature that is sufficiently high for electrons to overcome the potential barrier (thermoelectronic emission, Fig. 4.47(a)), or by applying an electric field that is sufficiently high for electrons at or near the Fermi level to tunnel through the potential barrier (field emission, Fig. 4.47(b)). Furthermore, several transition regimes appear between these two extremes, depending on field and temperature (Fig. 4.47(c)).

At high temperature and zero applied electric field, the thermoelectronic current density is given by

$$J_{\mathrm{TE}} = \frac{4\pi me}{h^3}(kT)^2 \exp\left[-\frac{\phi}{kT}\right] . \tag{4.19}$$

All symbols have been listed in Table 4.2 for clarity. Typically, the emission probability becomes significant above 2500 K for most metals, but this value can be significantly reduced for metals with a low work function.

An increase of the applied electric field will induce a decrease of the effective work function: this first transition regime is called Schottky emission, and is described by

$$J_{\mathrm{S}} = J_{\mathrm{TE}} \exp\left[\frac{\sqrt{e^3 F/4\pi\epsilon_0}}{kT}\right] . \tag{4.20}$$

As the field is further increased, electron emission by tunneling becomes also significant: this is the extended-Schottky regime, where

$$J_{\mathrm{ES}} = J_{\mathrm{S}} \frac{\pi q}{\sin(\pi q)} \ , \tag{4.21}$$

with

$$q = \frac{\hbar}{\pi\sqrt{m}} \frac{(4\pi\epsilon_0 e F^3)^{(1/4)}}{kT} \ . \tag{4.22}$$

Finally at high field and/or at low temperature, electron emission occurs through tunneling through the potential barrier. Following the thermal field emission model, the current is given by

$$J_{\mathrm{TFE}} = J^{\mathrm{i}}_{\mathrm{F-N}} \frac{\pi\rho}{\sin(\pi\rho)} \ , \tag{4.23}$$

where $\rho = kT/d$, $d = e\hbar F/(2t(y_0)\sqrt{2m\phi})$, and $J^{\mathrm{i}}_{\mathrm{F-N}}$ is the Fowler-Nordheim expression (4.47) that will be derived in the next section. Finally, the last regime is cold field emission, which corresponds to $T = 0$. Setting $T = 0$ induces typically an error of 6 % at 300 K.

The Fowler-Nordheim Model

As outlined above, field emission is the extraction of electrons from a solid by tunneling through the surface potential barrier under a strong electric field. Figure 4.47(a) shows that the potential barrier is square when no electric field is present. Its shape becomes triangular when a negative potential is applied to the solid, with a slope that depends on the amplitude of the local electric field F just above the surface. Although the Fowler-Nordheim (F-N) model has been originally developed to describe field emission from flat metallic surfaces at $T = 0$ [136], it has proven adapted to describe field emission from a wide range of materials, among these carbon-based electron emitters [137].

To derive the current density emitted from a flat unit surface, one starts from the equation

$$J = 2e \int_{\boldsymbol{k}} f(E, E_{\mathrm{F}}, T) D(E) v_{\mathrm{x}} \frac{\mathrm{d}^3\boldsymbol{k}}{(2\pi)^3} \ , \tag{4.24}$$

where $\boldsymbol{k} = \{k_{\mathrm{x}}, k_{\mathrm{y}}, k_{\mathrm{z}}\}$ and where the velocity $v_{\mathrm{x}} = \hbar k_{\mathrm{x}}/m$ within the free electron model, which in first approximation is valid for most solids around the Fermi level. The occupation probability is given by the Fermi-Dirac statistics

$$f(E, E_{\mathrm{F}}, T) = \left[\exp\left(\frac{E - E_{\mathrm{F}}}{kT}\right) + 1\right]^{-1} \ . \tag{4.25}$$

To evaluate the emitted current for the free-electron model, one has therefore to determine the transmission probability $D(E)$ for an electron through a barrier described by (see Fig. 4.47(b))

$$V(x) = E_{\mathrm{vac}} - eFx \ . \tag{4.26}$$

One takes often into consideration the contribution of the image charge, which induces a decrease of the effective work function

$$V^{\mathrm{i}}(x) = E_{\mathrm{vac}} - eFx - \frac{1}{4\pi\epsilon_0}\frac{e^2}{4x} \ . \tag{4.27}$$

Exact Transmission Factor

The transmission factor can be determined analytically in the case of the triangular barrier without the image charge. The Schrödinger equation is solved in two separate domains (the solid, and the barrier and vacuum, respectively) with simple wave matching in between the domains. The solution involves Airy functions Ai, Bi, Ai′ and Bi′ and amounts to

$$D^{\mathrm{e}}_{\mathrm{m}} = \kappa/\pi k_{\mathrm{x}}(x_1^2 + x_2^2)^{-1} \ , \tag{4.28}$$
$$\kappa = (2meF/\hbar^2)^{(1/3)} \ , \tag{4.29}$$
$$x_1 = \mathrm{Bi}(-\eta_0) - (\kappa/k_{\mathrm{x}})\mathrm{Ai}'(-\eta_0) \ , \tag{4.30}$$
$$x_2 = \mathrm{Ai}(-\eta_0) + (\kappa/k_{\mathrm{x}})\mathrm{Bi}'(-\eta_0) \ , \tag{4.31}$$
$$\eta_0 = \kappa(E_{\mathrm{x}} - E_{\mathrm{vac}})/eF \ , \tag{4.32}$$

where $E_{\mathrm{x}} = \hbar^2 k_{\mathrm{x}}^2/2m$ is the kinetic energy perpendicular to the surface. The sub- and superscripts of $D^{\mathrm{e}}_{\mathrm{m}}$ indicate that D has been obtained through matching and is an exact solution.

MWFM Transmission Factor

One can simplify the exact expression for $D^{\mathrm{e}}_{\mathrm{m}}$ by setting $-\eta_0 \gg 1$. In that case, the Airy functions Ai and Ai′ are negligible and the Bi and Bi′ functions can be approximated by exponentials. One obtains that

$$D_{\mathrm{m}} \approx \frac{4(E_{\mathrm{vac}} - E_{\mathrm{x}})^{1/2}E_{\mathrm{x}}^{1/2}}{E_{\mathrm{vac}}} \exp\left[-\frac{4}{3eF}\left(\frac{2m}{\hbar^2}\right)^{1/2}(E_{\mathrm{vac}} - E_{\mathrm{x}})^{3/2}\right] . \tag{4.33}$$

The expression can be further simplified by restricting the energies involved to $E_{\mathrm{x}} \approx E_{\mathrm{F}}$. This allows one to perform a series expansion of the energy-dependent term in the exponential

$$(E_{\mathrm{vac}} - E_{\mathrm{x}})^{3/2} = (E_{\mathrm{vac}} - E_{\mathrm{F}})^{3/2} - \frac{3}{2}(E_{\mathrm{vac}} - E_{\mathrm{F}})^{1/2}(E_{\mathrm{x}} - E_{\mathrm{F}}) \ . \tag{4.34}$$

With $(E_{\mathrm{vac}} - E_{\mathrm{F}}) = \phi$, one obtains the MWFM, or Matching Wave Function Method, approximation

$$D_{\mathrm{m}} \approx \exp\left[-\frac{4\phi^{3/2}}{3eF}\left(\frac{2m}{\hbar^2}\right)^{1/2}\right] \exp\left[\left(\frac{2m}{\hbar^2}\right)^{1/2}\frac{2\phi^{1/2}}{eF}(E_{\mathrm{x}} - E_{\mathrm{F}})\right] . \tag{4.35}$$

The WKB Approximation

The matching wave function approach does not make possible to take into account the decrease of the effective work function due to the image charge. One uses to this end the expression developed by Wentzel, Kramers and Brillouin (WKB) that gives the probability for an electron to tunnel through a potential barrier of arbitrary shape $V(x)$:

$$D_{\mathrm{WKB}} = \exp\left[-2\left(\frac{2m}{\hbar^2}\right)^{1/2} \int_{x_1}^{x_2} \sqrt{V(x) - E_{\mathrm{x}}}\, dx \right], \tag{4.36}$$

where the integration limits are given by $V(x_{1,2}) = E_{\mathrm{x}}$. With the triangular potential barrier $V(x) = E_{\mathrm{vac}} - eFx$, we get

$$D_{\mathrm{WKB}} = \exp\left[-2\left(\frac{2m}{\hbar^2}\right)^{1/2} \int_{0}^{\frac{E_{\mathrm{vac}}-E_{\mathrm{x}}}{eF}} \sqrt{E_{\mathrm{vac}} - eFx - E_{\mathrm{x}}}\, dx \right], \tag{4.37}$$

which, in turn, yields

$$D_{\mathrm{WKB}} = \exp\left[-\left(\frac{2m}{\hbar^2}\right)^{1/2} \frac{4}{3eF} (E_{\mathrm{vac}} - E_{\mathrm{x}})^{3/2} \right]. \tag{4.38}$$

Using again the approximation (4.34), one finally obtains

$$D_{\mathrm{WKB}} \approx \exp\left[-\frac{4\phi^{3/2}}{3eF}\left(\frac{2m}{\hbar^2}\right)^{1/2} \right] \exp\left[\left(\frac{2m}{\hbar^2}\right)^{1/2} \frac{2\phi^{1/2}}{eF} (E_{\mathrm{x}} - E_{\mathrm{F}}) \right]. \tag{4.39}$$

This is in fact the same result as the MWFM approximation.

WKB Approximation with Image Charge Correction

To take the image charge potential (4.27) into account is not easy, and was done by Nordheim in 1928 for the first time. He obtained the following expression:

$$D^{\mathrm{i}}_{\mathrm{WKB}} = \exp\left[-\left(\frac{2m}{\hbar^2}\right)^{1/2} \frac{4}{3eF} (E_{\mathrm{vac}} - E_{\mathrm{x}})^{3/2}\, v(y) \right], \tag{4.40}$$

which, with (4.34), is approximated by

$$D^{\mathrm{i}}_{\mathrm{WKB}} \approx \exp\left[-\frac{4\phi^{3/2}}{3eF}\left(\frac{2m}{\hbar^2}\right)^{1/2} v(y) \right] \exp\left[\left(\frac{2m}{\hbar^2}\right)^{1/2} \frac{2\phi^{1/2}\, t(y)}{eF} (E_{\mathrm{x}} - E_{\mathrm{F}}) \right]. \tag{4.41}$$

The functions $v(y)$ and $t(y)$ are related to elliptical functions, where y corresponds to the relative decrease of the work function due to the image charge potential

$$y = \frac{\Delta\phi(F)}{\phi} = \sqrt{\frac{e^3 F}{4\pi\epsilon_0}} \frac{1}{\phi}. \tag{4.42}$$

The functions are tabulated [136] and can be approximated by $t(y) \approx 1.049$ or $t^2(y) \approx 1.1$ and $v(y) \approx 0.96 - y^2$.

The Fowler-Nordheim Equation

To finally derive the Fowler-Nordheim equation, one inserts the WKB transmission factors (4.39) or (4.41) into (4.24), with $f(E, E_\mathrm{F}, T)$ described by Fermi-Dirac statistics (4.25) at $T = 0$. Without the image charge, the current J [A] per unit area varies with the local field at the emitter surface F [V/m] as

$$J_{\mathrm{F-N}} = 2e \int_{|\boldsymbol{k}|^2 \leq \frac{2mE_\mathrm{F}}{\hbar^2}} D_{\mathrm{WKB}}(E) \frac{\hbar k_\mathrm{x}}{m} \frac{\mathrm{d}^3\boldsymbol{k}}{(2\pi)^3} \,, \tag{4.43}$$

and, once the integration is performed,

$$J_{\mathrm{F-N}} = \frac{e}{4(2\pi)^2 \hbar\phi} F^2 \exp\left[-\frac{4\sqrt{2m}\phi^{3/2}}{3\hbar eF} \right] . \tag{4.44}$$

Inserting numerical values with F in V/m, ϕ in eV, and J in A/m^2 yields

$$J_{\mathrm{F-N}} = \frac{1.56 \cdot 10^{-6}}{\phi} F^2 \exp\left(-\frac{6.83 \cdot 10^9 \phi^{1.5}}{F} \right) \tag{4.45}$$

With image charge, the integration yields

$$J^\mathrm{i}_{\mathrm{F-N}} = \frac{e}{4(2\pi)^2 \hbar\phi \; t^2(y)} F^2 \exp\left[-\frac{4\sqrt{2m} \; v(y) \; \phi^{3/2}}{3\hbar eF} \right] , \tag{4.46}$$

so that one obtains, with numerical values,

$$J^\mathrm{i}_{\mathrm{F-N}} = \frac{1.42 \cdot 10^{-6}}{\phi} F^2 \exp\left(\frac{10.4}{\sqrt{\phi}} \right) \exp\left(-\frac{6.56 \cdot 10^9 \phi^{1.5}}{F} \right) . \tag{4.47}$$

The values of the constants have been known to vary depending on the approximation used for the Nordheim elliptical functions. Also, the physical quantity that is usually measured is a current, whereas the F-N equation gives a current density. One writes therefore that

$$I = AJ \,, \tag{4.48}$$

where A has the dimension of an area and represents *in a first approximation* the emitting area. Equation (4.47) and (4.48) show that for typical values encountered in carbon-based emitters ($A = 10^{-12} - 10^{-14}\,\mathrm{m}^2$, $\phi = 4.9 \pm 0.1\,\mathrm{eV}$ [137]) one obtains a current of $I = 1\,\mathrm{nA}$ at $F = 3.3 \pm 0.4\,\mathrm{V/nm}$. Figure 4.48(a) shows an experimental I–V curve, with the fit to the F-N equation (4.47). The most notable fact is that the current increases sharply with the field: as a rule of thumb, I varies by a factor 10 as F varies by 10 %.

It is useful at this point to recapitulate the assumptions that lead to the model: the tunneling electrons are taken as a free-electron gas described by Fermi-Dirac statistics, with an energy comparable to the Fermi energy. The temperature is taken equal to 0 (inducing an error of 6 % at 300 K). The tunneling is elastic, and occurs from a flat surface, yielding a current density in the F-N equation. Several models based on the Fowler-Nordheim approach have been developed, especially for semi-conductors, but are outside the scope of this contribution.

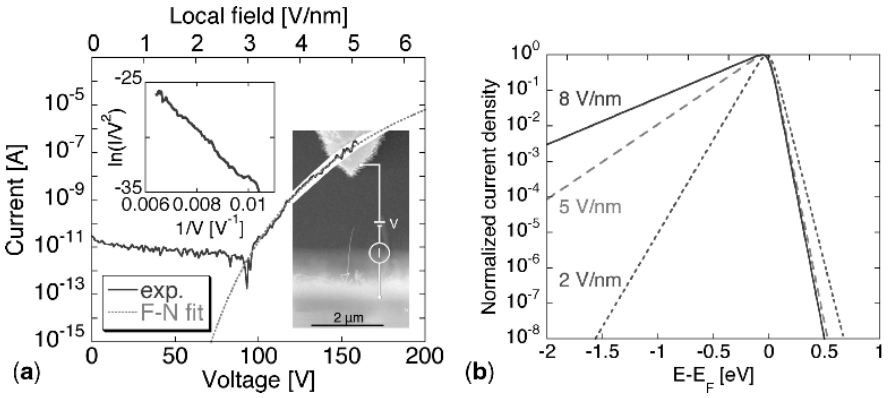


Fig. 4.48. (**a**) I-V curve acquired in a Scanning Electron Microscope on the single MWNT grown by Hot Filament CVD show in the *right* inset, with the fit to the F-N (4.47) yielding $A = 5 \times 10^{-16}\,\mathrm{m}^2$ and $\gamma = 85 \pm 15$ ($\phi = 5\,\mathrm{eV}$, $d = 2.65\,\mu\mathrm{m}$). The upper scale gives the local field $F = \gamma V/d$, and the *left* inset shows the F-N plot. (**b**) Theoretical energy distributions derived from (4.54) for different fields with $\phi = 5\,\mathrm{eV}$

Total Energy Distribution

The Fowler-Nordheim equation (4.47) gives the *total* emitted current density as a function of the applied field. It is also useful to consider the repartition of this current as a function of the energy of the emitted electrons, $P(E)$, with $J = \int P(E)\,\mathrm{d}E$. To determine $P(E)$, the integration in (4.24) has to be performed over $|\,\boldsymbol{k}\,|^2 = 2mE/\hbar^2$

$$P(E) = 2ef(E, E_\mathrm{F}, T) \int_{|\boldsymbol{k}|^2 = \frac{2mE}{\hbar^2}} D_\mathrm{WKB}(E) \frac{\hbar k_\mathrm{x}}{m} \frac{\mathrm{d}^3\boldsymbol{k}}{(2\pi)^3}\,, \tag{4.49}$$

which yields

$$P(E) = B(F, \phi) f(E, E_\mathrm{F}, T) \exp\left[2\frac{\sqrt{2m}}{e\hbar}\frac{\phi^{1/2}}{F}(E - E_\mathrm{F})\right], \tag{4.50}$$

where $B(F, \phi)$ is a term that is independent of the energy and equal to

$$B(F, \phi) = \frac{\sqrt{2m}}{4(2\pi)^2\hbar^2}\frac{eF}{\phi^{1/2}} \exp\left[-\frac{4\sqrt{2m}\phi^{3/2}}{3\hbar eF}\right]. \tag{4.51}$$

Taking again the Fermi-Dirac statistics (4.25) to describe the electron population around the Fermilevel, we obtain

$$P(E) = B(F, \phi) f(E, E_\mathrm{F}, T) \exp\left[2\frac{\sqrt{2m}}{e\hbar}\frac{\phi^{1/2}}{F}(E - E_\mathrm{F})\right]. \tag{4.52}$$

The same development can be also performed for the image charge potential:

$$P^{\mathrm{i}}(E) = B^{\mathrm{i}}(F,\phi) f(E, E_{\mathrm{F}}, T) \exp\left[2\frac{\sqrt{2m}}{e\hbar}\frac{\phi^{1/2}}{F} t(y)(E - E_{\mathrm{F}})\right], \qquad (4.53)$$

where $B^{\mathrm{i}}(F,\phi)$ is a term that is independent of the energy and equal to

$$B^{\mathrm{i}}(F,\phi) = \frac{\sqrt{2m}}{4(2\pi)^2\hbar^2}\frac{eF}{\phi^{1/2}}\frac{1}{t(y)} \exp\left[-\frac{4\sqrt{2m}\phi^{3/2}}{3\hbar eF} v(y)\right]. \qquad (4.54)$$

Figure 4.48(b) shows that the energy distribution peaks at an energy close to E_{F}. Moreover, the tails decrease exponentially, with a rate proportional to $F/\phi^{0.5}$ for the low energy side ($E < E_{\mathrm{F}}$) and that depends on kT, F and ϕ for the high energy side. Energy distribution measurements allow to obtain far more information on the emission mechanism than standard $J - V$ measurements, as will be outlined below.

4.5.3 Field Amplification

The Fowler-Nordheim equation (4.47) predicts that the emitted current becomes significant for fields in excess of a few V/nm. Such fields are quite high: 3 V/nm represent, for two flat surfaces spaced 1 mm apart, an applied voltage of 3 MV. To reach this value, one usually uses sharp objects or protrusions to amplify the electric field. We need to distinguish from the outset two basic cases for field emitters that are schematized in Fig. 4.49, namely the infinitely long emitter and the emitter on a surface.

The infinitely long emitter, Fig. 4.49(a), is the typical case of a single field emission source, as for example a nanotube mounted on a sharpened wire. The emitter on a surface, Fig. 4.49(b), is encountered in most studies of field emission from nanotubes, as the favoured application of nanotubes involve their use in emitter arrays.

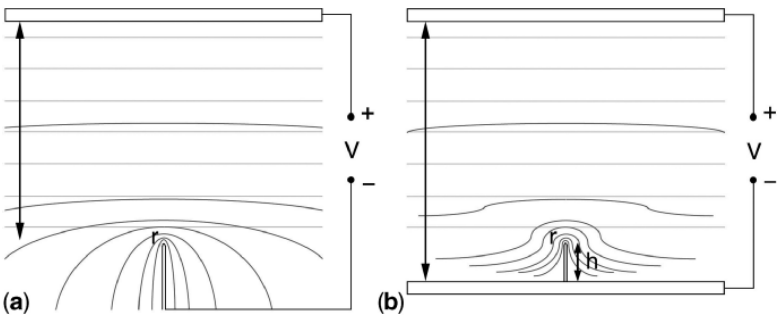


Fig. 4.49. Standard configuration in field emission measurements: (**a**) the infinitely long emitter and (**b**) the emitter on a surface

Historically, the field at the apex of the emitter tip was written as $F = \beta V$. One prefers today to use the definition $F = \gamma E = \gamma V/d$, where E is the macroscopic field obtained with an applied voltage V between two planar and parallel electrodes separated by a distance d. γ is then a proportionality factor that gives the aptitude of the emitter to amplify the applied voltage or field, and is accordingly termed the field enhancement factor. γ is a strictly geometrical parameter, and we consider in this section models that allow to estimate the field enhancement as a function of the dimensions and shape of the emitter and of its surroundings.

Field Enhancement for Infinitely Long Emitters

The most basic approximation for an infinitely long emitter with a radius at the apex r is to approximate it as a sphere of the same radius. As $F = V/r$, $\gamma = d/r$. This approximation is far too drastic to be meaningful, and an empirical correction factor k is introduced so that $F = V/(k{\cdot}r)$, or $\gamma = d/(k{\cdot}r)$. k is taken usually as $k \approx 5$ for a hemisphere on a cylinder [138]. Even with this correction, the obtained values are of little practical use.

One of the only models that takes into account the geometry of both emitter and experimental set-up for infinitely long emitters is the one presented by Dyke and Dolan [138]. The idea is to take a geometry for which Laplace's equation can be resolved analytically, and to approximate the shape of the emitter with a suitable equipotential surface. They found that a charged sphere of radius a placed at the apex of a cone and located at a distance d of a planar electrode gave the most satisfactory results [136,139]. The model of Dyke and Dolan is quite reliable for single emitters, but has proven to be less adapted for emitters deposited on flat substrates [139].

Emitters on Surfaces

The models for field enhancement factors of protrusions on flat surfaces have been recently reviewed [140], and only the most important results will be presented here. Four different configurations have been considered over the years to approximate the experimental situation of Fig. 4.49(b).

The first one is the most simple and corresponds to a hemisphere of radius r on a surface. In that case, $\gamma = 3$ and is independent of r and d, which implies that any protrusion on a surface should produce a field enhancement of at least 3.

The second one is a sphere of radius r floating at a distance L of the planar surface. Its only interest is that it can be resolved semi-analytically, with $\gamma \approx 2.5 + L/r$, but is of limited practical use as the values are very approximate. The third one is the hemi-ellipse on a flat surface, which can be resolved analytically but is less adapted to our case.

The fourth one corresponds most closely to the situation encountered in nanotube field emission, and is the hemisphere-on-cylinder model, which cannot be resolved analytically. Up to recently, the most popular formula was $\gamma \approx 3 + h/r \approx h/r$ for $h \gg r$, but its origin (and scientific justification) has proven difficult to assess.

Recent studies based on numerical simulations have challenged this 'historical' expression [140]. The most accurate expression to date is the one proposed by Edgcombe and Valdré [141]

$$\gamma \approx 1.2 \cdot (2.15 + h/r)^{0.9} \,, \tag{4.55}$$

and is valid for $4 \leq h/r \leq 3000$. Equation (4.55) shows that $\gamma \approx 0.7 \cdot h/r$, and that the usually used expression significantly overestimates the field enhancement factor. Equation (4.55) does not make any predictions as to the influence of the counter-electrode, and especially of the inter-electrode distance, although experimental results show that γ varies with d [142].

Other Effects Influencing the Field Enhancement

The above models assume that the counter electrode is flat. This is not the case in most experimental set-ups, and the measured γ is therefore not only due to the nanotube, but also to the anode where the field will be greater than V/d. Simulations show that there is a decrease of only 10% in the field at the tip of the nanotube for an anode of 45° opening angle as compared to a flat one. The shape of the anode does therefore not have a significant influence on the obtained value of γ, which comes probably from the fact that the radius of curvature of the nanotube is much smaller than that of the anode.

The tip of nanotube emitters (especially for multi-walled nanotubes) is seldomly hemispherical but tapered, and may furthermore be opened and/or present nanometer-sized protrusions. Numerical simulations reveal that a deviation from the hemispherical shape produces an increase of the field enhancement factor up to over a factor of two. This underlines the difficulty of predicting γ for a given emitter, and may also account for the fact that the agreement between the field enhancement factors measured from single nanotubes and estimated from their dimensions do agree within experimental error in 30% of the cases only [142].

Finally, the geometrical shape of the emitter may not be the only factor that influences the field enhancement factor. Experimental [143,144] and theoretical [145] studies have pointed out that localized states at the end of the tubes are involved in the emission process. Such localized states could enhance the field amplification. Theoretical investigations also suggest that, in the case of MWNTs, the field enhancement is not determined by the outermost but by the *innermost* shell. The γ factor of a MWNT is lower than for the isolated innermost shell, due to screening of the applied field by the outer shells, but remains higher than for the isolated outermost shell [145].

Shielding and Screening Effects

Up to now, we have only considered one emitter on a surface. As soon as several emitters are assembled to form an array, influences between the emitters have to be taken into account as electrostatic screening becomes significant even for large distances between the emitters l. Several studies, both theoretical and experimental, reveal that the electric field at the apex of the emitters will decrease with decreasing spacing. In fact, the effective field amplification drops rapidly for spacings $l \leq 2\,h$. This effect influences critically the field emission properties of individual nanotubes and of nanotube films [146, 147]. Other effects have to be taken into account, such as the fact that not all emitters will show the same γ because of varying lengths and diameters: indeed, this distribution of γ can be estimated by measuring the field emission locally with a sharp tip and has been shown to be exponential for typical MWNT films [148].

4.5.4 Measuring Field Emission

Experimental Techniques

I–V Measurements

The most basic (and most often used) experimental set-up for field emission measurements is to place an anode (be it planar, spherical or a sharp needle) at a given distance d and to use the nanotube (or nanotube film) as the cathode to perform I–V characterization. The measurement has to be performed in a vacuum chamber evacuated to a pressure below 10^{-6} mbar. The three anode shapes mentioned above are roughly equivalent when a single emitter is measured. In the case of an array, each one has advantages.

The plane-to-plane configuration is easy to set up, as d is given by the thickness of the spacers and the emission area can be well defined. However, the spacers and/or edges of the electrodes can give raise to border effects and the parallelism of the electrodes is not always warranted. Furthermore, d cannot be easily varied. The disadvantages of the plane-to-plane set-up can be circumvented with the plane-to-sphere (and to a lesser degree with the plane-to-needle): there is no problem of parallelism and border effects, but the anode has to be brought into contact with the sample to determine d (alternatively, the capacity of the electrode assembly can be measured [149]). Furthermore, the emission area is not well defined and has to be estimated (the diameter of the emission area is roughly 1/10 of the anode diameter). Finally, a sharp needle allows to measure the local field emission properties (see also below).

One important variant of the plane-to-plane configuration is the use of a phosphor screen as the anode, which allows to collect the current and to image its spatial distribution. This is known as field emission microscopy (see next

section) with a single emitter, and allows to assess the homogeneity of the emitting sites (and to determine the emission site density, ESD) of an emitter array.

Field Emission Microscopy

The goal of field emission microscopy (FEM) is to image the spatial distribution of the emitted current of single emitters, by using a phosphor screen as the anode. The emitter is usually mounted on a heating loop for cleaning the tip apex by desorbing absorbed molecules, and a third electrode is often placed near the cathode to extract the electrons at voltages lower than the final anode voltage. The emission of a metallic tip should be homogeneous (at least over the tip apex if ϕ is constant), while emission from localized states or from adsorbates produces well-defined patterns [150]. FEM has allowed to draw important conclusions on the emission mechanism of nanotubes (see also below) [151, 152].

Field ionization microscopy (FIM), its sister technique, was used in 1956 resolve the structure of a sharp tip with atomic resolution. In FIM, the sample is used as the anode and a partial pressure of imaging gas is introduced in the chamber. The gas atoms or molecules are ionized by the field, especially at terrace edges where the field is highest. Only a handful of FIM studies have been published on nanotubes and the suitability of the technique has not been demonstrated yet.

Field Emission Electron Energy Distribution

The measurement of the energy distribution of the emitted field electrons (FEED) is performed with an analyser similar to the ones used for photoelectron spectroscopy. An extraction electrode is also often used. The energy distribution can be directly compared to the theoretical expression (4.54), allowing to extract informations on the emission mechanism, and is the only reliable mean to determine the work function [137].

Scanning and Transmission Electron Microscopy

Large-area I–V measurements do not allow to measure the emission properties locally, nor to observe the emitting nanotubes. This difficulty can be circumvented by performing I–V measurements in a scanning or transmission electron microscope (SEM, TEM), using a sharp needle as the anode [153].

Using SEM it is possible to image the nanotubes before, during and after field emission (and therefore to determine the emitter dimensions and control the inter-electrode distance) and to measure the current extracted from one emitter only in a well controlled geometry [142]. The TEM offers far higher resolution, is able to image the graphitic sidewalls and to assess the crystallographic structure by electron diffraction [154], and makes possible to image the electric field around the nanotube by electron holography [155]. However,

a dedicated probe holder with electrical contacts and a piezoelectric stage is needed to position the emitters with respect to the anode and to apply the extraction voltage. The high voltage electrons of the TEM can also irreversibly damage the observed nanotubes.

Local Probe Microscopy

A variation of scanning tunneling microscopy, scanning anode field emission microscopy (SAFEM), has been developed to map the emission properties of emitter arrays with μm resolution [156]. A sharpened tip mounted on a x-y-z piezoelectric drive scans the surface of the film at a constant tip-to-substrate distance (typically 10 μm). This allows to map the emission current $I(x, y)$ when a constant voltage V is applied, as well as to map the extraction voltage $V(x, y)$ needed to extract a given current I. A constant extracted current implies that the field at the emitter apex has to be constant, and as $F = \gamma V/d$, $\gamma(x, y) = Fd/V(x, y)$ [148]. The latter mode is hence of particular interest as it makes possible to map the field enhancement factor $\gamma(x, y)$ and to determine its distribution.

What Can we Learn from Field Emission Results?

Field Enhancement Factors

The field enhancement factor can be estimated from I–V characteristics, provided that the emitter follows the F-N model (4.47). This can be assessed with a so-called Fowler-Nordheim plot, $\ln(I/V^2)$ versus $1/V$. The measurement should appear as a linear function with a slope p that depends only on d, ϕ and γ (e.g., $p = -6.56 \times 10^9 \phi^{1.5} d/\gamma$ with the image charge correction). Since d is known from the experimental configuration, such a plot can be used to determine either γ or ϕ if the other parameter is known. γ can hence be calculated by taking a reasonable value for ϕ (e.g., 5 eV for carbon-based emitters [137]). In addition, A can be estimated from the intercept of the F-N plot with the y-axis [136]. Typical experimental errors are on the order of ±15 % on the intercept and slope, leading to an error of ±15 % on γ and ±10 × (a factor of ten) on A.

Emission Fields

To compare the performances of different emitter arrays, one usually uses the turn-on and threshold fields, which are the macroscopic fields needed to extract current densities of $10\,\mu\mathrm{A\,cm^{-2}}$ and $10\,\mathrm{mA\,cm^{-2}}$, respectively. These values correspond to the current densities needed to light and saturate a pixel in a display. One can also add the onset field E_i, corresponding to $10\,\mathrm{nA\,cm^{-2}}$, to characterize the onset of the emission.

The fact that the macroscopic fields E, rather than the voltages, are used for comparison originates from the assumption that E does not depend on

the experimental set-up (and especially on d). This, however, has not proven to be true for nanotube films as both emission fields and field-enhancement factors vary with d. Different film field emitters can therefore be compared only if they have been tested in identical experimental configurations.

Work Function

The work function ϕ should never be determined from I–V measurements only. It is extremely difficult to estimate γ accurately from the shape of the emitter, especially on emitter assemblies such as those encountered on carbon nanotube films. Equation (4.54) shows instead that the energy distribution decreases exponentially with a rate that is proportional to $F/\phi^{0.5}$ for the low energy side ($E < E_\mathrm{F}$). This makes hence possible to determine A, γ and ϕ unequivocally [137].

Is the Fowler-Nordheim Model Valid for Nanotubes?

As examplified by Fig. 4.48(a), most I–V measurements follow the F-N model (4.47), at least at low emitted currents. In the above example, the F-N plot yields $A = 5 \times 10^{-16}\,\mathrm{m}^2$ and $\gamma = 85$. Deviations are often observed and will be discussed in Sect. 4.5.5.

However, the fact that an emitter shows a linear behavior in the F-N plot does not imply that the emission occurs from a metallic continuum of states. Indeed, emission from a single, narrow state or from a band of states will also produce a constant F-N slope. To distinguish between these cases, energy distribution measurements are again needed. The energy distribution is well described by the standard model (4.54) on nanotube films, where several nanotubes contribute to the emitted currents [137]. Deviations from the F-N model are, however, frequently observed on single emitters [157].

Do's and Don'ts in I–V Measurements

Field emission I–V measurements are simple to carry out, and the use of carbon nanotube films as emitter arrays is at present one of the most serious possibilities for the large-scale application of nanotubes. A few guidelines should be considered if the results of such studies are to be of practical use. First, the experimental parameters have to be completely listed. Strictly, field emission results such as emission fields and field-enhancement factor should be compared only when acquired in comparable conditions, and the geometry, inter-electrode distance, and resulting emission area should always be mentioned.

Second, the field emission properties of an array are often not reproducible as the voltage is ramped up for the first time: one observes a 'training' process which results in a shift of the I–V characteristics to higher fields as the maximal extracted current is increased [147]. Ideally, the emission properties (fields, γ) should be determined once this training is stabilized, e.g., after prolonged

emission at a current above the target value for the application one has in mind (e.g., $30\,\mathrm{mA/cm^2}$ if one wants to reach $10\,\mathrm{mA/cm^2}$). The values are otherwise of little use, as the onset field can increase by a factor of 3 (or more) following the training phase [147].

Third, one should perform measurements over a sufficiently large emission area. Extracting a current over a small area does not allow to draw any conclusion on the behavior of the whole array: a *single* nanotube emitting 10 nA in an area of $10\times10\,\mu\mathrm{m}^2$ results in a current density of $10\,\mathrm{mA/cm^2}$. The emission area needs to be sufficiently large to be representative of the behavior of the array as a whole, and should therefore incorporate at least 100 emitters. With the emitter density commonly observed on nanotube films, this corresponds to an emission area of at least $1\,\mathrm{mm}^2$. Ideally, the measurements should be performed with a phosphor screen over several cm^2, which will also allow to estimate the emission site density, ESD.

Fourth, the ESD is a crucial parameter for applications, and one that is most often neglected. Indeed, the fields needed for field emission are in most cases well below the target specifications for a device, and one should therefore aim more at maximizing the ESD than at minimizing E.

Fifth, measurements should be performed in a comparative mode, i.e., comparing an improved solution (e.g., metal-covered nanotubes) with a reference sample (e.g., the same nanotube film, but uncovered) measured in the same set-up and conditions. One should also remember that the emission current increases by an order of magnitude when the field (and hence γ) varies by 10%: small geometrical variations can hence induce huge changes in the emission properties. Field emission is highly selective, and two films that appear identical in SEM micrographs can show huge differences in emission properties - simply because the maximal length of a few nanotubes changes. Extreme caution should therefore be used in the interpretation of the results.

4.5.5 Selective Overview of Experimental Results

The goal of the section is not to present an exhaustive review of the literature, but rather to illustrate the introduced concepts with a few selected experimental examples.

Effect of the Applied Field

A lot of efforts have been devoted to the growth of nanotubes that are aligned perpendicularly to the substrate to maximize the field amplification effect. However, it appears that as soon as a potential difference is applied, the nanotubes begin to align themselves parallel to the electric field under the action of the electrostatic force [154]. A 'perfect' alignment is reached at typically a quarter of the onset voltage of field emission [158]. The effect underlines that the emitters are mechanically under tensile stress during field emission.

Field Enhancement Factor

The fact that nanotubes follow the F-N model, at least at low emission current, can be used to extract γ from the measurements (see Fig. 4.48(a)). However, a study of 40 emitters in an SEM revealed that it is extremely difficult to predict γ values accurately, even when nanotube radius and length are known. For 30 % of the emitters, the experimental and estimated values matched within experimental error. The presence of neighboring nanotubes could account for some cases where the estimated value was too high, as screening and shielding effects can significantly influence γ (and the ESD) [146, 147]. Finally, short anode-to-nanotube distances could account for some cases where the estimated value was too low. No satisfactory explanation for the discrepancy was found in 15 % of the cases.

Nevertheless, γ depends critically on r and h: Figure 4.50 shows I–V curves of a MWNT and a SWNT rope of comparable length acquired at similar d. The onset voltage is lower by a factor 6 for the SWNTs, with $\gamma = 515$ as compared to 100 for the MWNT. This difference in γ is in fact due to the difference in emitter radius and suggests that $r = 1.6\,\mathrm{nm}$ for the SWNT rope, which is entirely in the expected range. Interestingly, one can also estimate the local field from V/d and γ: it amounts to $3.2\,\mathrm{V/nm}$ to extract 1 nA in the case of Fig. 4.48(a), which is exactly in the range predicted by the F-N model.

In Fig. 4.50, the macroscopic field $E = V/d$ is very high, and γ is quite low. On the same carbon nanotube film, onset fields about $2\,V/\mu\mathrm{m}$ and field enhancement factors of γ about 1800 are obtained from large area

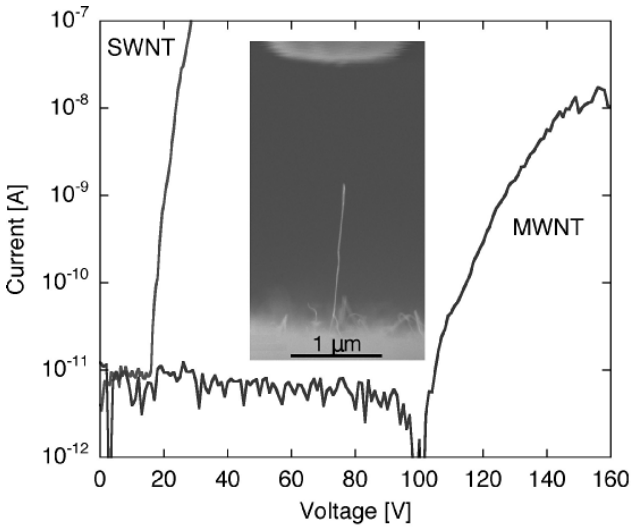


Fig. 4.50. I–V curves acquired on a SWNT rope ($h = 1.6\,\mu\mathrm{m}$, $d = 2.13\,\mu\mathrm{m}$) and on a MWNT ($h = 1.7\,\mu\mathrm{m}$, $d = 2.35\,\mu\mathrm{m}$, $r = 8$ nm, shown in the inset)

measurements [142]: the values of γ measured on single emitters in the SEM (even for SWNTs) remain far lower than those obtained from large area measurements. This suggests strongly that the γ of the emitters in large area measurements are even higher than for the SWNTs of Fig. 4.50. Field emission is a very selective process with a highly non-linear behavior. Nanotubes with the highest γ dominate the emission, even when present in very low densities [148]. The enhancement factor measured in large area measurements is representative of a very small population of nanotubes only.

In the ideal case, γ should be identical for all nanotubes to obtain a homogeneous emission and high ESD, while being sufficiently high to obtain a significant emission at low applied fields. The dispersion on γ (and hence on the combination of h, r and l) should be less than 4 %, which is difficult to achieve even when the growth is well controlled [159]. One possibility to circumvent this problem is to include a suitably scaled ballast resistor in series with the emitter to produce a voltage drop above a given current. This limitation of the emitted current also protects the emitters against degradation, significantly improves the homogeneity of the emission, and increases the ESD to acceptable values. It is probable that nanotube films used as emitter arrays in devices will sooner or later incorporate a ballast resistor.

Emitter Degradation

Single Emitters

Few facts are currently available on the lifetime of individual nanotube emitters. Stable emission was measured for arc-discharge grown multi-wall nanotubes during more than 2 months at 0.4 µA emitted current without any observable degradation [157].

The phenomena leading to the degradation of the emitters are not completely understood at present, and it seems that several factors play an important role. First, electrostatic deflection or mechanical stresses can cause alterations in the shape and/or surroundings of the emitter, which may lead to a decrease of the local field amplification.

Second, high currents can rapidly damage a nanotube. A gradual decrease of field enhancement due to field evaporation was also found on single-wall nanotubes when the emitted current was increased beyond a given limit (300 nA to 1 µA) [160]. On multi-walled nanotubes, a shortening of the emitter over time [153] or damage to the outer walls of the nanotube due to high currents (∼0.2 mA) [161] were also reported. Tube layers or caps are removed, peeled back, or the end of the tube is amorphized [154, 161]. In all cases a strong decrease in the emission current occurs and the voltage has to be substantially increased to obtain comparable currents.

Third, it seems that residual gases have a significant influence. Irreversible damage can occur through bombardment from gas molecules ionized by the emitted electrons [162]. As an example, no degradation was measured on a

single nanotube over more than 350 h with an emitted current of 3 µA at 10^{-9} mbar. Conversely, irreversible continuous decreases in the current were provoked by exposure to oxygen and water and were attributed to reactive sputter etching. In contrast, exposure to Ar and H_2 did not lead to permanent damage [162].

The above mechanisms involve a gradual degradation of the emitters, but the failure can also be abrupt. On multi-walled carbon nanotubes grown by CVD, the failure occurred at or near the contact during field emission in the SEM [158]. This suggests a degradation mechanism that is due either to mechanical failure due to the tensile loading of the emitter under the applied electric field or to resistive heating at the contact that is enhanced by the mechanical stress. The former cause could be assigned to failures occurring at applied fields and currents below 4 V/nm and 1 µA, and the latter cause to failures occurring at higher fields and currents.

Another catastrophic mechanism is arcing, i.e., an arc between cathode and anode that is initiated by field emission. Such arcing is commonly observed on diamond and DLC films and seems needed to initiate the emission [163]. These events are caused usually by a high field-emission current, anode outgassing or local evaporation of cathode material that create a conduction channel between the electrodes, leading to a discharge which destroys or damages the emitter.

Nanotube Films

The degradation of a film emitter is seldom abrupt, but gradual and occurs during initial I–V testing [147] as well as during measurements at constant applied voltage over long periods [164]. Several studies on nanotube arrays have shown that the field emission properties are degraded when the field is ramped up to progressively higher values, which shows itself as a shift of the I–V curve towards higher fields. The decrease in γ associated with the degradation, as well as the observed decrease in emitter density [148, 165] leads one to conclude that this gradual degradation is in fact due to the failure of individual emitters, which can occur already for currents of 300 nA per emitter.

In spite of all these effects, it seems that carbon nanotubes can withstand long operation once they have been broken in. The longest test up-to-date has been performed by Saito et al. who report an increase of 11% only of the applied field to maintain an emission current of 10 mA/cm^2 during 8000 h [164].

Work Function

Typical values of $\phi = 4.9 \pm 0.1$ eV and $A = 10^{-14\pm2}$ m^2 have been obtained for arrays of multi-walled (arc discharge and CVD-grown) and single-walled nanotubes. Measurements on single-walled nanotubes remain rare: Fransen

et al. measured $\phi = 7.3\,\text{eV}$ (but on one emitter only), which suggests that ϕ may vary significantly from one emitter to the next [157]. Typically for nanotubes, a very narrow FWHM of $\leq 0.25\,\text{eV}$ was found. Finally, Gao et al. studied the mechanical properties under electrical excitation in the TEM to estimate the work function of multi-walled nanotubes [166]. They found two populations, with work functions of 4.6–4.8 eV and ∼5.6 eV, respectively. This was attributed to a metallic versus semiconducting character of the studied nanotubes.

Emission Mechanisms

The fact that I–V characteristics follow the Fowler-Nordheim law (at least over a certain current range) could lead one to the conclusion that carbon nanotubes behave as metallic emitters (Fig. 4.51(a)). The very low turn-on fields measured for nearly all emitters originate certainly from the small diameter and elongated shape of the tubes that lead to a high geometrical field enhancement. In fact, the local electric field just above the emitter surface needed for field emission is around 2–3 V/nm as for metallic emitters, as can

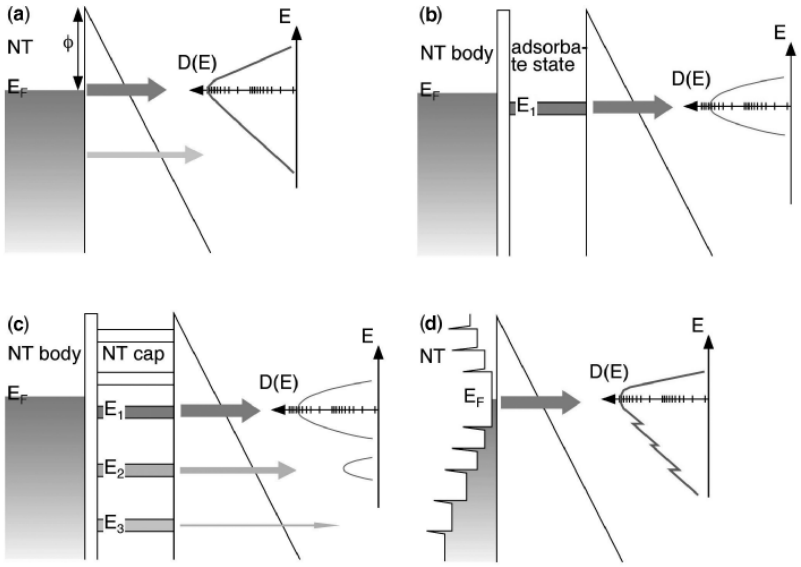


Fig. 4.51. (**a**) Standard field emission model from a metallic emitter; (**b–d**) models for the field emission from nanotubes: (**b**) adsorbate resonant tunneling, (**c**) emission through energy bands corresponding to electronic states localized at the nanotube cap, (**d**) emission from a typical metallic SWNT DOS. The potential barrier and the corresponding FEED (energy on the vertical axis, current on the horizontal logarithmic axis) are given for each model

be estimated from the applied field and the field amplification factor, e.g., on Fig. 4.48(a) [147, 167].

On the other hand, several FEM studies have shown clearly that the emission behavior of nanotubes is more complex than the one expected from a very sharp metallic tip with a work function of ∼5 eV [168], and several mechanisms seem to be involved. A first regime corresponding to resonant tunneling through an adsorbate (Fig. 4.51(b)) was found under 'usual' experimental conditions at low temperatures and applied fields. The involved molecule has been identified as water and it appears that this adsorbate-assisted tunneling is the stable field emission mode at room temperature [168]. Figure 4.52(b) shows FEM images of a SWNT: a pattern typical of adsorbed molecules is observed at low emitted currents (bottom row).

One point noted by nearly all researchers is that the I–V characteristics of nanotubes does not follow a Fowler-Nordheim behavior over the whole current range, as shown in Fig. 4.52(a). Interestingly, this behavior is directly linked to the presence of adsorbates. In Fig. 4.52(a), the onset of saturation occurs for currents of 0.1–0.3 µA and is accompanied by increased current fluctuations [168]. These fluctuations disappear nearly completely at higher currents,

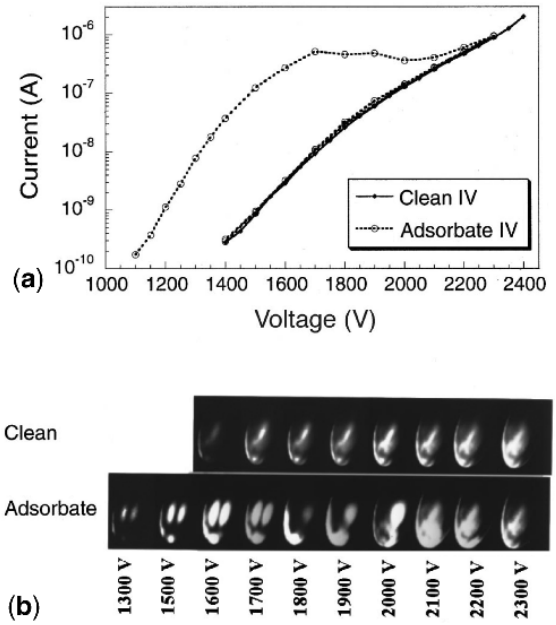


Fig. 4.52. (**a**) I–V characteristics and (**b**) corresponding FEM patterns of a single SWNT with and without adsorbates. The FEM pattern with an adsorbate (**b**, bottom row) changes during the I–V sweep concurrent with the onset of current saturation, while the FEM pattern of the clean SWNT is stable over the voltage sweep. Adapted from [168]

while the FEM pattern changes completely beyond the saturation and shows a complex, adsorbate-free structure. Interestingly, this structured pattern persists when the current is ramped down (upper row of Fig. 4.52(b)), but the emitted current is markedly lower than with the adsorbate. The emission is therefore enhanced in the presence of adsorbed molecules, which desorb either at high fields and emitted currents or at temperatures higher than 400°C.

Note, however, that the saturation behavior is not always due to adsorbates. In some cases, it is due to a large resistance of the emitter [169] or in series with the emitter (e.g., at the contact [158]). In that case, the voltage drop across the resistance leads to a decrease of the effective applied voltage, and therefore to a flattening of the characteristics. Including the effect of a series resistance in the F-N equation is not trivial, but the I–V curves can be numerically fitted. Large resistances can also lead to stable Joule heating of the nanotube to up to 2000 K and to field-emission induced light emission [169].

The intrinsic emission from the cleaned tube shows a far lower emitted current for comparable voltages with strongly reduced current fluctuations [168]. The non-homogeneous current density of the clean nanotube (upper row of Fig. 4.52(b)) suggests also that the electrons are emitted from localized states at the cap and not from delocalized conduction-band states as in metals.

In FEED measurements, any deviation from the shape predicted by the F-N model (4.54) is due either to adsorbates [136] or to a non-metallic DOS. FEED can therefore be used to gain information on the DOS of the emitting electrons as well as to determine the work function. Measurements on nanotubes consistently show that the FEED is significantly narrower than for a metal and additional features suggest that the emission is more complicated than for a metallic emitter. High-temperature measurements on single SWNTs revealed the presence of additional peaks in the spectrum above the Fermi level due to emission from states above the Fermi level (Fig. 4.51(c)) [144]. Unusual features in the low-energy tail of FEED spectra from one SWNT were also detected at room temperature and were attributed to singularities in the DOS (Fig. 4.51(d)) [170].

In short, the present understanding is that the emission involves adsorbate-resonant tunneling at low emitted currents, and a non-metallic DOS once the adsorbates are removed at high emitted currents and/or high temperatures. Supplementary informations on the electronic structure of the nanotube cap and on the influence of adsorbates or bonded groups are clearly required for a better comprehension of the emission.

Field Emission as a Characterization Method

Field emission is usually studied with the goal of realizing a device. Advances in the preparation or growth of nanotubes have also originated from the need of a better control of the film morphology to enhance the field emission properties. More rarely, the electronic properties of the nanotubes, and especially of their tips, have been investigated with field emission. Several studies have

shown, however, that field emission has a huge potential as a characterization method with unique possibilities.

First, field emission makes possible to follow the CVD growth of carbon nanotubes [171]. To this end, a field emission microscope (FEM) is combined with a CVD reactor, in order to detect the field emitted current from one or from an assembly of tubes *during the growth*. A thin wire covered with catalyst is used as a substrate and heated to typically 700°C, while a C_2H_2 partial pressure below 10^{-2} mbar is introduced and a potential difference of a few kV is applied. The growth can be followed by FEM (watching the spots corresponding to emitting nanotubes) and by measuring the field emitted current. It appeared that the growth of the emitters is neither simultaneous nor homogeneous and that most emitters appear over a very short time scale ($\leq$10 s). The method allows also to estimate the growth rate: very little information is available up to now on this crucial parameter for the control of the length of the nanotubes. Typical activation times below 10 s were found, with growth rates between 0.65 and 3.6 µm/s [172].

Second, field emission allows to observe directly the mechanical vibration resonances of nanotubes [173]. In fact, the tensile loading created by the applied field permits the tuning of these resonances, which are observable by the changes they create in the field emission pattern or current. The mechanical properties of individual MWNTs can hence be studied within an assembly of emitters, and the Young's modulus could be determined if the dimensions of the emitter are known. As field emission also permits under some circumstances to provoke a controlled Joule heating of individual emitters and to estimate the nanotube resistance [169], one could in principle measure the temperature dependence of the electrical and thermal conductivities.

Finally, field emission offers the possibility of measuring the electronic DOS by FEED and the exact structure of the tube cap by FIM [170]. This simultaneous determination of the electronic and structural properties of individual nanotubes will without doubt yield valuable insights on the emission mechanism.

Applications

The use of carbon nanotube electron emitters is under active consideration for a variety of devices. A first possibility is to replace a thermoelectronic source with a field emitter, which offers several advantages. The emitter does not have to be heated, which eliminates the need of a heat source or of a heating loop. The energy spread of the emitted electrons is also far smaller, and the emitted current can be controlled with the applied voltage. Nanotubes could hence be used in electron beam instruments, as they have high coherence [174] and brightness [175]. They could also provide better reliability and lower energy consumption, e.g., in microwave amplifiers or X-Ray tubes. The latter type of devices is very promising: X-Ray sources based on a carbon nanotube cold

Table 4.2. Main symbols used throughout this section

A	Prefactor in the Fowler-Nordheim equation [m^2]
d	Interelectrode (or cathode-anode) distance [m or μm]
$D(E)$	Transmission probability
E	Energy [J or eV]
E_F	Fermi energy [J or eV]
E	Macroscopic electric field ($E = V/d$) [V/m or V/μm]
E_i	Onset field (emitted current density of $10\,nA\,cm^{-2}$) [V/μm]
E_{thr}	Threshold field (emitted current density of $10\,mA\,cm^{-2}$) [V/μm]
E_{to}	Turn-on field (emitted current density of $10\,\mu A\,cm^{-2}$) [V/μm]
F	Local electric field ($F = \gamma E$) [V/m or V/nm]
$f(E, E_F, T)$	Occupation probability of the level with energy E at temperature T
h	Emitter length [m or μm]
I	Emitted current [A]
J	Emitted current density [A cm^{-2}]
l	Spacing between the emitters in an array [m or μm]
$P(E)$	Emitted current density as a function of electron energy E
p	Fowler-Nordheim slope
r	Emitter radius of curvature [m or nm]
$t(y)$, $v(y)$	Nordheim elliptic functions
V	Applied voltage [V]
y	Relative decrease $\Delta\phi/\phi$ of the work function due to the image charge potential
γ	Field enhancement factor
ϕ	Work function [eV]

cathode are commercially available, such as Oxford Instruments' Horizon600 portable X-Ray spectrometer.

Nanotube devices provide also better technical solutions for several consumer applications, where the market is potentially huge but where the competition with well-established technologies is fierce. The two main devices under consideration are lighting sources and flat-panel displays. In both cases, field emitters are used to produce light by bombarding a phosphor-coated surface with electrons.

Cathode-ray tubes (also called 'jumbotron lamps'), which have the shape of the old vacuum tubes and where the top surface is illuminated, have been under investigation since 1998 and are commercially available [164]. These tubes form the pixel elements in giant screen displays and have a brightness typically higher by a factor of 2 as compared to conventional thermoionic lighting elements, with demonstrated lifetimes of 8000 h [164]. There have been also some attempts to realize lighting elements with field emitters to offer an alternative to incandescent or fluorescent lamps. Fully sealed luminescent tubes, where electrons are emitted from nanotubes deposited on a wire, have been demonstrated, with luminances that are comparable to the one of commercial fluorescent tubes [176].

Nanotube flat-panel displays were proposed in 1995 already as an enticing alternative to other film emitters. Several manufacturers (e.g., Candescent, Motorola, PixTech, Samsung) have produced displays with field emitters (most of them Spindt-type arrays) with an impressive picture quality. Although numerous technological hurdles related to the deposition of nanotubes in gated structures, and problems such as display sealing, phosphor lifetime, and charging of spacers, need to be considered, there is no doubt that nanotube displays are feasible and will offer advantages over existing solutions. However, the major concern is not the feasibility, but the yield of the fabrication and the final cost of the display. Field emission displays compete against LCDs at the small dimensions and plasma displays at the large dimensions: the gap which is at present 'free' of established competitors is shrinking. The viability of nanotube displays will ultimately be a decision of the market, and not a scientific or technical one.

4.5.6 Conclusion

As was apparent from the very beginning, nanotubes are excellent electron sources operating at low emission fields, providing a stable current and capable of operating in moderate vacuum. The Fowler-Nordheim model of field emission describes well the behavior of carbon nanotubes for simple I–V characterization, although nanotubes do not behave as metallic emitters. The electron emission involves adsorbate-resonant tunneling at low emitted currents, and a non-metallic DOS once the adsorbates are removed at high emitted currents and/or high temperatures. Field emission is also a highly non-linear process, where the current increases typically by a factor 10 when the field F varies by 10 % (be it through a variation of the applied voltage or of the field enhancement factor). The field enhancement factor depends on many parameters, such as the length and radius of the nanotube, but also its surroundings, the shape of the tip and the presence of small protrusions.

References

1. C. Kittel: *Introduction to Solid State Physics* (Wiley, 7th edition 1995); *Physique de l'Etat Solide* (Dunod, Paris 1998)
2. N.W. Ashcroft and N.D. Mermin: *Solid State Physics* (International Thompson Publishing 1976); *Physique des Solides* (EDP, Les Ulis 2003)
3. J.K. Burdett: *Chemical Bonding in Solids* (Oxford University Press 1995)
4. A.P. Sutton: *Electronic Structure of Materials* (Oxford University Press 1993)
5. D.G. Pettifor: *Bonding and Structure of Molecule and Solids* (Oxford University Press 1995)
6. W.A. Harrison: *Electronic Structure and the Properties of Solids* (Dover 1989)
7. S. Elliott: *The Physics and Chemistry of Solids* (Wiley 1998)
8. J.-L. Rivail: *Eléments de Chimie Quantique* (EDP, Les Ulis 1999)
9. M. Gerl and J.-P. Issi: *Physique des Matériaux* (PUPR, Lausanne 1997)

10. There are of course many textbooks and review articles where the modern first principles methods are described, see e.g. M.C. Payne, M.P. Teter, D.C. Allan, T.A. Arias, and J.D. Joannopoulos: Rev. Mod. Phys. **64**, 1045 (1992), W. Kohn: Rev. Mod. Phys. **71**, 1253 (1999), J.M. Thijssen: *Computational Physics* (Cambridge University Press 1999), C. Delerue and M. Lannoo: *Nanostructures, Theory and Modelling* (Springer 2004), R. M. Martin: *Electronic Structure* (Cambridge University Press 2004), and the site www.abinit.org
11. D.A. Papaconstantopoulos et al., Electronic Structure Data base, www@cst-www.nrl.navy.mil
12. D. Weaire and M.F. Thorpe: Phys. Rev. B **4**, 2508 (1971); M.F. Thorpe and D. Weaire: Phys. Rev. B **4** 3518 (1971); J. Friedel and M. Lannoo: J. Physique **34** 115 and 481 (1973); G. Allan, in: *Electronic Structure of Crystal Defects and of Disordered Systems* (Les Editions de Physique, Orsay 1981) p 3
13. J.-C. Charlier, X. Gonze, J.-P. Michenaud: Phys. Rev. B **43**, 4579 (1991)
14. N. Hamada, S. Sawada, A. Oshiyama: Phys. Rev. Lett. **68**, 1579 (1992)
15. R. Saito, M. Fujita, G. Dresselhaus, M.S. Dresselhaus: Appl. Phys. Lett. **60**, 2204 (1992)
16. J.W. Mintmire, B.I. Dunlap, C.T. White: Phys. Rev. Lett. **68**, 631 (1992)
17. For general reviews, see e.g. R. Saito, G. Dresselhaus, and M.S. Dresselhaus: *Physical Properties of Carbon Nanotubes* (Imperial College Press, 1998); S.G. Louie, in: *Carbon Nanotubes Synthesis, Structure, Properties and Applications* ed by M.S. Dresselhaus, G. Dresselhaus, and P. Avouris (Springer 2001); P.J.F. Harris: *Carbon Nanotubes and Related Structures* (Cambridge University Press 1999); P. Lambin: C. R. Physique **4** 1009 (2003)
18. X. Blase, L.X. Benedict, E.L. Shirley, S.G. Louie: Phys. Rev. Lett. **72**, 1878 (1994)
19. N. Wang, Z.K. Tang, G.D. Li, and J.S. Chen: Nature **408**, 51 (2000)
20. Z.K. Tang, L. Zhang, N. Wang et al: Science **292**, 2467 (2001)
21. O. Dubay, G. Kresse, and H. Kuzmany: Phys. Rev. Lett. **88**, 235506 (2002)
22. H.J. Liu and C.T. Chan: Phys. Rev. B **66**, 115416 (2002)
23. M. Machon, S. Reith, C. Thomsen et al: Phys. Rev. B **66**, 155410 (2002)
24. S.J. Tans, M.H. Devoret, H. Dai et al: Nature (London) **386**, 474 (1997)
25. M. Bockrath, D.H. Cobden, P.L. McEuen et al: Science **275**, 1922 (1997)
26. L. Langer, V. Bayot, E. Grivei et al: Phys. Rev. Lett. **76**, 479 (1996)
27. T.W. Ebbesen, H.J. Lezec, H. Hiura et al: Nature **382**, 54 (1996)
28. H. Dai, E.W. Wong, and C.M. Lieber: Science **272**, 523 (1994)
29. J.W.G. Wildöer, L.C. Venema, A.G. Rinzler et al: Nature **391**, 59 (1998)
30. T.W. Odom, J.L. Huang, P. Kim, C.M. Lieber: Nature **391**, 62 (1998)
31. I. Cabria, J.W. Mintmire, and C.T. White: Phys. Rev. B **67**, 121406R (2003)
32. C.T. White and T.N. Todorov: Nature **393**, 240 (1998)
33. P. Delaney, H.J. Choi, J. Ihm et al: Nature **391**, 466 (1998)
34. J.-C. Charlier, X. Gonze, J.-P. Michenaud: Europhys. Lett. **29**, 43 (1995)
35. M. Ouyang, J.L. Huang, C.L. Cheung, C.M. Lieber: Science **292**, 702 (2001)
36. M.J. Lopez, A. Rubio, J.A. Alonso et al: Phys. Rev. Lett. **86**, 3056 (2001)
37. J.-C. Charlier, Ph. Lambin, T.W. Ebbesen: Phys. Rev. B **54**, R8377 (1996)
38. Ph. Lambin, L. Philippe, J.-C. Charlier, J.-P. Michenaud: Comput. Mater. Science **2**, 350 (1994)
39. Y.K. Kwon and D. Tomanek: Phys. Rev. B **58**, R16001 (1998)
40. Y. Miyamoto, S. Saito, and D. Tomanek: Phys. Rev. B **65**, R041402 (2001)

41. B.I. Dunlap: Phys. Rev. B **49**, 5643 (1994)
42. P. Lambin, A. Fonseca, J.P. Vigneron et al: Chem. Phys. Lett. **245**, 85 (1995)
43. R. Saito, G. Dresselhaus, and M.S. Dresselhaus: Phys. Rev. B **53**, 2044 (1996)
44. J.-C. Charlier, T.W. Ebbesen, and P. Lambin: Phys. Rev. B **53**, 11108 (1996)
45. L. Chico, V.H. Crespi, L.X. Benedict et al: Phys. Rev. Lett. **76**, 971 (1996)
46. Z. Yao, H.W.Ch. Postma, L. Balents, and C. Dekker: Nature **402**, 273 (1999)
47. M. Ouyang, J.-L. Huang, C.L. Cheung, and C.M. Lieber: Science **291**, 97 (2001)
48. H. Terrones, M. Terrones, E. Hernandez et al: Phys. Rev. Lett. **84**, 1716 (2000)
49. E. Haeckel: *Die Radiolarien*, 1852
50. L.P. Biro, G.I. Mark, A.A. Koos et al: Phys. Rev. B. **66**, 165405 (2002)
51. M. Terrones, H. Terrones, F. Banhart et al: Science **288**, 1226 (2000)
52. M. Terrones, F. Banhart, N. Grobert et al: Phys. Rev. Lett. **89**, 075505 (2002)
53. A. Rubio, J. Corkill, M.L. Cohen: Phys. Rev. B **49**, 5081 (1994)
54. X. Blase et al: Europhys. Lett. **28**, 335 (1994); ibid, Phys. Rev. B **51**, 6868 (1995)
55. N.G. Chopra et al: Science **269**, 966 (1995)
56. A. Loiseau et al: Phys. Rev. Lett. **76**, 4737 (1996)
57. M. Terrones et al.: Chem. Phys. Lett. **259**, 568 (1996)
58. D. Golberg et al: Appl. Phys. Lett. **69**, 2045 (1996)
59. D.P. Yu et al: Appl. Phys. Lett. **72**, 1966 (1998)
60. G.W. Zhou et al: Solid State Comm. **109**, 555 (1999)
61. R.S. Lee et al: Phys. Rev. B **64**, 121405 (2001)
62. R. Ma et al: Chem. Phys. Lett. **337**, 61 (2001)
63. E. Bengu et al: Phys. Rev. Lett. **86**, 2385 (2001)
64. W. Han et al: Appl.Phys.Lett. **73**, 3085 (1998)
65. D. Golberg, Y. Bando, W. Han, K. Kurashima, T. Sato: Chem. Phys. Lett. **308**, 337 (1999); D. Golberg et al: J. of Appl. Phys. **86**, 2364 (1999)
66. X. Blase, A. De Vita, J.-C. Charlier, R. Car: Phys. Rev. Lett. **80**, 1666 (1998)
67. P. Král et al: Phys. Rev. Lett. **85**, 1512 (2000)
68. E.J. Mele and P. Král: Phys. Rev. Lett. **88**, 056803 (2002)
69. O. Stephan et al: Science **266**, 1683 (1994)
70. Z. Weng-Sieh et al: Phys. Rev. B **51**, 11229 (1995)
71. Ph. Redlich et al: Chem. Phys. Lett. **260**, 465 (1996)
72. K. Suenaga et al: Science **278**, 653 (1997)
73. M. Terrones et al: Chem. Phys. Lett. **257**, 576 (1996)
74. R. Sen et al: Chem. Phys. Lett. **287**, 671 (1998)
75. Y. Zhang et al: Chem. Phys. Lett. **279**, 264 (1997)
76. J. Yu et al: Appl. Phys. Lett. **77**, 1949 (2000)
77. D. Golberg et al: Chem. Phys. Lett. **359**, 220 (2002)
78. D. Golberg et al: Appl. Phys. Lett. **82**, 1275 (2003)
79. R.B. Kaner et al: Mater. Res. Bull. **22**, 399 (1987); J. Kouvetakis et al: Synth. Met. **34**, 1 (1989); T. Sasaki et al: Chem. Mater. **5**, 695 (1993)
80. M.O. Watanabe, S, Itoh, T. Sasaki, K. Mizushima: Phys. Rev. Lett. **77**, 187 (1996); erratum: Phys. Rev. Lett. **77**, 2846 (1996); Y. Chen, J.C. Barnard, R.E. Palmer et al: Phys. Rev. Lett. **83**, 2406 (1999)
81. D. Tomanek et al: Phys. Rev. B **37**, 3134 (1988); Q. Wang et al: Phys. Rev. B **54**, R2271 (1996)
82. A.Y. Liu, R.M. Wentzcovitch, M.L. Cohen: Phys. Rev. B **39**, 1760 (1989)

83. Y. Miyamoto, A. Rubio, M.L. Cohen, S.G. Louie: Phys. Rev. B **50**, 4976 (1994)
84. Y. Miyamoto, S.G. Louie, M.L. Cohen: Phys. Rev. Lett. **76**, 2121 (1996)
85. Y. Miyamoto et al: Phys. Rev. B **50**, 18360 (1994)
86. X. Blase, L.X. Benedict, E.L. Shirley, S.G. Louie: Phys. Rev. Lett. **72**, 1878 (1994)
87. R. Ma, Y. Bando, T. Sato: Chem. Phys. Lett. **350**, 1-5 (2001)
88. X. Blase, J.-C. Charlier, A. De Vita: Appl. Phys. Lett. **70**, 197 (1997); ibid, Appl. Phys. A **68**, 293 (1999)
89. X. Blase: Comp. Mat. Sci. **17**, 107-114 (2000)
90. H. Nozaki and S. Itoh: J. Phys. Chem. Solids **57**, 41 (1996)
91. X.D. Bai, E.G. Wang, J. Yu, H. Yang, Appl. Phys. Lett. **77**, 67 (2000).
92. P.E. Lammert, V.H. Crespi, A. Rubio: Phys. Rev. Lett. **87**, 136402 (2001)
93. X. Blase et al: Phys. Rev. Lett. **83**, 5078-5081 (1999)
94. L.E. Jones, P.A. Thrower: J. Chem. Phys. **84**, 1431 (1987); ibid, Carbon **29**, 251 (1991)
95. J.-Y. Yi and J. Bernholc: Phys. Rev. B **47**, 1708 (1993)
96. H.J. Choi et al: Phys. Rev. Lett. **84**, 2917 (2000)
97. B. Wei et al: Appl. Phys. Lett. **74**, 3149 (1999)
98. C.-C. Kaun et al: Phys. Rev. B **65**, 205416 (2002)
99. A. Liu and M.L. Cohen: Science **245**, 841 (1989)
100. A. Liu and R.M. Wentzcovitch: Phys. Rev. B **50**, 10362 (1994)
101. D. Teter and R.J. Hemley: Science **273**, 53 (1996)
102. R. Czerw et al: NanoLetters **1**, 457 (2001)
103. X. Blase et al: Appl. Phys. A **68**, 293-300 (1999); ibid: Comp. Mat. Sci. **17**, 107-114 (2000)
104. R. Magri: Phys. Rev. B **49**, 2805 (1994)
105. D.L. Carroll et al: Phys. Rev. Lett. **81**, 2332-2335 (1998)
106. R. Tenne et al: Nature **360**, 444 (1992); L. Margulis et al: Nature **365**, 113 (1993)
107. R. Tenne et al: Chem. Mater **10**, 3225 (1998)
108. L. Rapoport et al: Nature, **387**, 791 (1997)
109. A. Rothschild, S.R. Cohen, R. Tenne: Appl. Phys. Lett. **75**, 4025 (1999)
110. K. Kobayashi, J. Yamauchi: Phys. Rev. B **51**, 17085-17095 (1995)
111. G. Seifert, H. Terrones, M. Terrones et al: Phys. Rev. Lett. **85**, 146 (2000)
112. K.K. Kam and B.A. Parkinson: J. Phys. Chem. **86**, 463 (1982)
113. J.M. Soler, E. Artacho, J.D. Gale et al: J. Phys. Condens. Matter **14**, 2745 (2002)
114. M. Côté, M.L. Cohen, D.J. Chadi: Phys. Rev. B **58**, R4277 (1998)
115. P. Zhang and V.H. Crespi: Phys. Rev. Lett. **89**, 056403 (2002)
116. I. Boustani and A. Quandt: Europhys. Lett. **39**, 527 (1997)
117. S.B. Fagan et al: Phys. Rev. B **61**, 9994 (2000)
118. H. Kataura, Y. Kunazawa, Y. Maniwa et al: Synth. Met. **103**, 2555, (1999)
119. P. Petit, C. Mathis, C. Journet, P. Bernier: Chem. Phys. Lett. **305**, 370 (1999)
120. C. Journet, W.K. Maser, P. Bernier et al: Nature **388**, 756 (1997)
121. N. Bendiab, E. Anglaret, J.-L. Bantignies et al: Phys. Rev. B **64**, 245424 (2001)
122. L. Duclaux: Carbon **40**, 1751 (2002)
123. X. Liu, T. Pichler, M. Knupfer, J. Fink: Phys. Rev. B **67**, 125403 (2003)
124. C. Bower, S. Suzuki, K. Tanigaki, O. Zhou: Appl. Phys. A **67**, 47 (1998)
125. R.S. Lee, H.J. Kim, J.E. Fischer et al: Nature **388**, 255 (1997)

126. A.M. Rao, P.C. Ecklund, S. Bandow et al: Nature **388**, 257 (1997)
127. T. Pichler, M. Knupfer, M.S. Golden et al: Phys. Rev. Lett. **80**, 4729 (1998)
128. J.W.G. Wildoer, L.C. Venema, A.G. Rinzler, R.E. Smalley: Nature **391**, 59 (1998)
129. H. Reiss: J. Phys. Chem. **89**, 3783 (1985)
130. D. Dubois, G. Moninot, W. Kutner et al: J. Phys. Chem. **96**, 7137 (1992)
131. S. Kazaoui, N. Minami, R. Jacquemin et al: Phys. Rev. B **60**, 13339 (1999)
132. L. Kavan, P. Rapta, L. Dunsch: Chem. Phys. Lett. **328**, 363 (2000)
133. A. Thess, R. Lee, P. Nikolaev et al: Science **273**, 483 (1996)
134. E. Jouguelet, C. Mathis, P. Petit: Chem. Phys. Lett. **318**, 561 (2000)
135. A. Claye and J.E. Fischer: Mol. Cryst. Liq. Cryst. **340**, 743 (2000)
136. J.W. Gadzuk and E.W. Plummer: Rev. Mod. Phys. **45**, 487 (1973)
137. O. Groening, O.M. Kuettel, C. Emmenegger et al: J. Vac. Sci. Technol. B **18** 665 (2000)
138. W.P. Dyke and W.W. Dolan: Adv. Electron. Electron Phys. **8**, 89 (1956)
139. J.-M. Bonard, M. Croci, I. Arfaoui et al: Diamond Rel. Mater **1**, 763 (2002)
140. R.G. Forbes, C.E.J. Edgcombe, U. Valdré: Ultramicroscopy **95**, 57 (2003)
141. C. Edgcombe and U. Valdré: J. Microscopy **203**, 188 (2001)
142. J.-M. Bonard, K.A. Dean, B.F. Coll, C. Klinke: Phys. Rev. Lett. **69**, 197602 (2002)
143. J.-M. Bonard, T. Stöckli, F. Maier et al: Phys. Rev. Lett. **81**, 1441 (1998)
144. K.A. Dean, O. Groening, O.M. Kuttel, L. Schlapbach: Appl. Phys. Lett. **75**, 2773 (1999)
145. C. Adessi and M. Devel: Phys Rev B **65**, 075418 (2001)
146. L. Nilsson, O. Gröning, C. Emmenegger et al: Appl. Phys. Lett. **76**, 2071 (2000)
147. J.-M. Bonard, N. Weiss, H. Kind et al: Adv. Mater **13**, 184 (2001)
148. L. Nilsson, O. Groening, P. Groening et al: J. Appl. Phys. **90**, 768 (2001)
149. W. Zhu, C. Bower, O. Zhou et al: Appl. Phys. Lett. **75**, 873 (1999)
150. R. Gomer: *Field Emission and Field Ionization* (Harvard University Press, Cambridge MA 1961)
151. K. Hata, A. Takakura, Y. Saito: Surf. Sci. **490**, 296 (2001)
152. K.A. Dean and B.R. Chalamala: J. Appl. Phys **85**, 3832 (1999)
153. Y.Y. Wei, K.A. Dean, B.F. Coll, and J.E. Jaskie: Appl. Phys. Lett. **79**, 4527 (2001)
154. Z.L. Wang, P. Poncharal, W.A. De Heer: Microscopy and Microanalysis **6**, 224 (2000)
155. J. Cumings, A. Zettl, M. McCartney, J.C.H. Spence: Phys. Rev. Lett. **88**, 056804 (2002)
156. L. Nilsson, O. Groening, P. Groening, L. Schlapbach: J. Appl. Phys. **20**, 326 (2002)
157. M.J. Fransen, T.L. van Rooy, P. Kruit: Appl. Surf. Sci. **146**, 312 (1999)
158. J.-M. Bonard, C. Klinke, K.A. Dean et al: Phys. Rev. B **67**, 115406 (2003)
159. V. Semet, Vu Thien Binh, P. Vincent et al: Appl. Phys. Lett. **81**, 343 (2002)
160. K.A. Dean, T.P. Burgin, B.R. Chalamala: Appl. Phys. Lett **79**, 1873 (2001)
161. Z.L. Wang, P. Poncharal, W.A. de Heer: Appl. Phys. Lett. **80**, 856 (2002)
162. K.A. Dean and B.R. Chalamala: Appl. Phys. Lett. **75**, 3017 (1999)
163. O. Gröning, O.M. Küttel, E. Schaller et al: Appl. Phys. Lett. **69**, 476 (1996)
164. Y. Saito and S. Uemura: Carbon **38**, 169 (2000)
165. L. Nilsson, O. Gröning, P. Gröning, L. Schlapbach: Appl. Phys. Lett. **79**, 1036 (2001)

166. R. Gao, Z. Pan, Z.L. Wang: Appl. Phys. Lett. **78**, 1757 (2001)
167. J.-M. Bonard, F. Maier, T. Stöckli et al: Ultramicroscopy **73**, 9 (1998)
168. K.A. Dean and B.R. Chalamala: Appl. Phys. Lett. **76**, 375 (2000)
169. S.T. Purcell, P. Vicent, C. Journet, V.T. Binh: Phys. Rev. Lett. **88**, 105502 (2002)
170. D. Lovall, M. Buss, E. Graugnard et al: Phys. Rev. B **61**, 5683 (2000)
171. J.-M. Bonard, M. Croci, F. Conus et al: Appl. Phys. Lett. **81**, 2836 (2002)
172. J.-M. Bonard, M. Croci, C. Klinke et al: Phys. Rev. B **67**, 085412 (2003)
173. S.T. Purcell, P. Vicent, C. Journet, and V.T. Binh: Phys. Rev. Lett. **89**, 276103 (2002)
174. H. Schmid and H.-W. Fink: Appl. Phys. Lett. **70**, 2679 (1997)
175. N. de Jonge, Y. Lamy, K. Schoots, T.H. Oosterkamp: Nature **420**, 393 (2002)
176. J.-M. Bonard, T. Stöckli, O. Noury, A. Chatelain: Appl. Phys. Lett. **78**, 2775 (2001)

5

Spectroscopies on Carbon Nanotubes

J.-L. Sauvajol, E. Anglaret, S. Rols and O. Stephan

Abstract. In a spectroscopy experiment, radiation is used as a probe of the properties of a system. A typical experiment of spectroscopy is schematized in Fig. 5.1. The source (probe) can be X-rays, laser light (visible and infrared radiations), neutrons, electrons, ... A monochromatic radiation is obtained by using a relevant monochromator device. As long as the response of the material to the radiation is linear, the function which describes the interaction is called the response function and it can be calculated using the linear response model. This response function $\chi(\boldsymbol{Q},\omega)$ relates the field associated with the source, $E(\boldsymbol{Q},\omega)$ to the response of the system, $R(\boldsymbol{Q},\omega)$

$$R(\boldsymbol{Q},\omega) = \chi(\boldsymbol{Q},\omega)E(\boldsymbol{Q},\omega) \tag{5.1}$$

The response of the system is analyzed by a spectrometer and sent in appropriate detector and acquisition systems. The different elements of the experimental set-up – monochromator, spectrometer, detector – are specific of each radiation and spectroscopy technique.

In this chapter, we briefly review the concepts of the main spectroscopy techniques used in the study of carbon nanotubes. We especially focus on the spectroscopies which provide informations (i) on the vibrational modes (phonons) in carbon nanotubes, namely resonance Raman scattering, (ii) on the electronic states of carbon nanotubes, namely electron energy loss spectroscopy (EELS). We then review and discuss recent results on carbon nanotubes obtained from these techniques.

5.1 Vibrational Spectroscopies

Infrared absorption and Raman scattering are, with inelastic neutron scattering, the most popular spectroscopic techniques which provide informations on phonons in condensed matter. As far as nanotubes are concerned, only a few infrared investigations have been carried out. The main reason is the very weak infrared signal due to the weak difference of charge state between carbon atoms leading to very small induced electric dipole. By contrast, Raman

J.-L. Sauvajol et al.: *Spectroscopies on Carbon Nanotubes*, Lect. Notes Phys. **677**, 277–334 (2006)
www.springerlink.com
© Springer-Verlag Berlin Heidelberg 2006

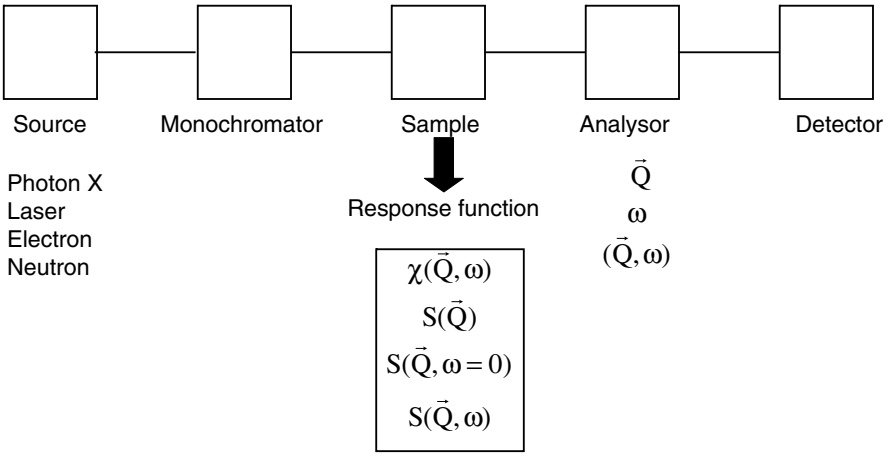


Fig. 5.1. Sketch of a spectroscopy experiment

scattering is known as an efficient tool to investigate phonons in carbon nanotubes. Furthermore, the peculiar resonance properties of the Raman signal for carbon nanotubes allow us to distinguish between metallic and semiconducting tubes. In this section, we will first review general concepts on the phonon dynamics, and its application to carbon nanotubes. In the following, we will present basic concepts on Raman scattering, and will especially focus on the resonance effects.

5.1.1 Phonons

An extensive review on phonon dynamics is beyond the scope of this contribution. We will only summarize the most general (and simple) approach and provide a list of relevant references for details and special cases. We restrict the presentation to vibrations within the harmonic approximation. In this case, the expression of the Hamiltonian is

$$H = \frac{1}{2}\sum_{i,\alpha} M_i \dot{u}_\alpha(i)^2 + \phi \tag{5.2}$$

where ϕ is the potential energy of particles in interaction, while $\boldsymbol{u}(i)$ is the displacement of atom i. ϕ is given by

$$\phi = \phi_0 + \frac{1}{2}\sum_{ij,\alpha\beta} \phi_{\alpha\beta}(i,j) u_\alpha(i) u_\beta(j) \tag{5.3}$$

where ϕ_0 is the static potential energy of the system (molecule or crystal). The starting point is the calculation of the dynamical matrix $\tilde{D}$ [1–3]

$$\tilde{D}_{\alpha\beta}(i,j) = \frac{1}{\sqrt{M_i M_j}}\phi_{\alpha\beta}(i,j) \tag{5.4}$$

where $\phi_{\alpha\beta}(i,j)$ are the force constants between i and j atoms, $M_i(M_j)$ the mass of the $i(j)$th atom. The symmetry of the system permits to reduce the number of independent coefficients $\phi_{\alpha\beta}(i,j)$. The equations of motion follow immediately

$$M_i \ddot{u}_\alpha(i) = -\sum_{j,\beta} \phi_{\alpha\beta}(i,j) u_\beta(j) \tag{5.5}$$

A solution for this set of coupled equations is

$$u_\alpha(i) = \frac{1}{\sqrt{M_i}} e_\alpha(i) e^{-i\omega t} \tag{5.6}$$

where $\boldsymbol{e}(i)$ is the polarization vector of the displacement. The set of equations (5.5) has a solution only if the determinant of the coefficients vanish

$$\mid \tilde{D}_{\alpha\beta}(i,j) - \omega^2 \delta_{\alpha\beta}\delta_{ij} \mid = 0 \tag{5.7}$$

When the system contains a large number N of atoms, which is the case for long finite nanotubes, the size of the dynamical matrix $\tilde{D}$ $(3N \times 3N)$ is very large. Therefore, the resolution of equations (5.7), which involves the diagonalization of the dynamical matrix, is not straightforward. For large systems (polymers, amorphous, nanostructures of finite size), specific methods, like the spectral moments method, can be used [4,5]. Alternatively, molecular dynamics simulations can be developed [6].

In the case of crystals, the periodic conditions allow one to simplify the equations of motion

$$u_\alpha(l\kappa) = \frac{1}{\sqrt{M_\kappa}} e_\alpha(\kappa) e^{(i\boldsymbol{q}\boldsymbol{R}(l) - i\omega t)} \tag{5.8}$$

The $i(j)$ atom index is now replaced by the couple $l\kappa$ $(l'\kappa')$, where l (l') refers to a unit cell and κ (κ') to a particular atom in the unit cell, $\boldsymbol{q}$ is a wave vector of the first Brillouin zone. The equilibrium position of the κth atom in the lth unit cell is given by the vector $\boldsymbol{R}(l\kappa) = \boldsymbol{R}(l) + \boldsymbol{R}(\kappa)$, $\boldsymbol{u}(l\kappa)$ is the displacement of an atom when a single mode of wave vector $\boldsymbol{q}$ is excited. $\boldsymbol{e}(\kappa)$ is the polarization vector of the displacement. $\boldsymbol{e}(\kappa)$ is independent of the cell index l and the components of this vector satisfy the equation

$$\omega^2 e_\alpha(\kappa) = \sum_{\kappa'\beta} D_{\alpha\beta}(\boldsymbol{q} \mid \kappa\kappa') e_\beta(\kappa'), \tag{5.9}$$

with the so-called Fourier dynamical matrix given by

$$\tilde{D}_{\alpha\beta}(\boldsymbol{q} \mid \kappa\kappa') = \frac{1}{\sqrt{M_\kappa M_{\kappa'}}} \sum_l \phi_{\alpha\beta}(0l \mid \kappa\kappa') e^{-i\boldsymbol{q}\boldsymbol{R}(l)} \tag{5.10}$$

Here, the size of the dynamical matrix decreases to $3s \times 3s$, where s is the number of atoms in the unit cell. Therefore, the matrix can be easily diagonalized. There are $3s$ solutions for ω^2 for each value of $\boldsymbol{q}$ and these will be denoted by ω_j^2 where $j = 1, 2, \ldots, 3s$. For each of the $3s$ values of ω_j^2, one can define a $3s$-component vector $e_\alpha(\kappa)$. To make explicit the dependence of this vector on the value of $\boldsymbol{q}$, as well as its assignment to a particular branch j, it will referred as $e_\alpha(\boldsymbol{q}j \mid \kappa)$. Because the dynamical matrix is hermitian, we can assume that the eigenvectors $e_\alpha(\boldsymbol{q}j \mid \kappa)$ satisfy the orthonormality and closure conditions. The displacement pattern obtained by substituting into (5.8) a particular eigenvector $e_\alpha(\boldsymbol{q}j \mid \kappa)$ and the corresponding frequency $\omega_j(\boldsymbol{q})$,

$$u_\alpha(l\kappa) = \frac{1}{\sqrt{M_\kappa}} e_\alpha(\boldsymbol{q}j \mid \kappa) e^{i(\boldsymbol{qR(l)} - \omega_j(\boldsymbol{q})t)} \tag{5.11}$$

is called a normal mode $(\boldsymbol{q}, j)$ of the crystal described by the wave vector $\boldsymbol{q}$ and the branch index j. $\omega_j(\boldsymbol{q})$ is called the dispersion curve of mode j. As an illustration, the dispersion curves for isolated and infinite bundles of $(9, 9)$ carbon nanotube calculated using this method [7] are displayed in Fig. 5.2 and Fig. 5.3.

Since the Hamiltonian is the sum of two quadratic forms, one in the components of the momenta and the other in the components of the displacements of the atoms, it is possible to find a transformation which simultaneously diagonalizes the kinetic and potential energies in the Hamiltonian. Such a principal axis transformation is generated by the following expansion of $u_\alpha(l\kappa)$ in terms of plane waves

$$u_\alpha(l\kappa) = \frac{1}{\sqrt{NM_\kappa}} \sum_{\boldsymbol{q},j} e_\alpha(\boldsymbol{q}j \mid \kappa) Q_j(\boldsymbol{q}) e^{i\boldsymbol{qR(l)}} \tag{5.12}$$

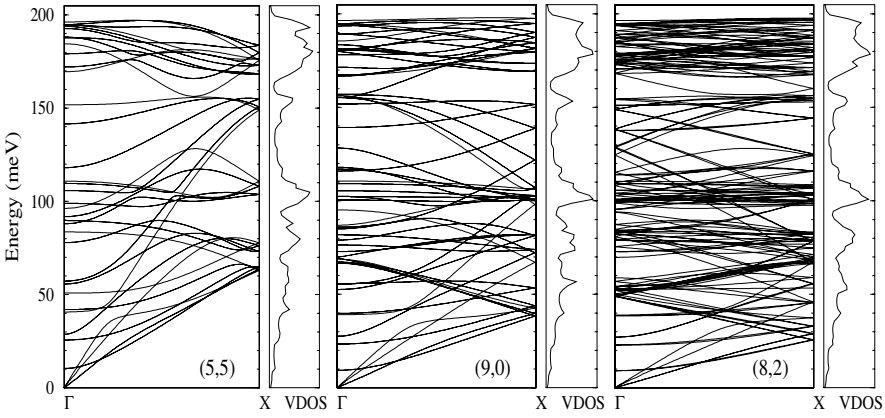


Fig. 5.2. Phonon dispersion curves and Vibrational Density of States (VDOS) for three tubes of similar diameter (about 0.7 nm) and different chiral angles: armchair, zigzag, chiral (from [7])

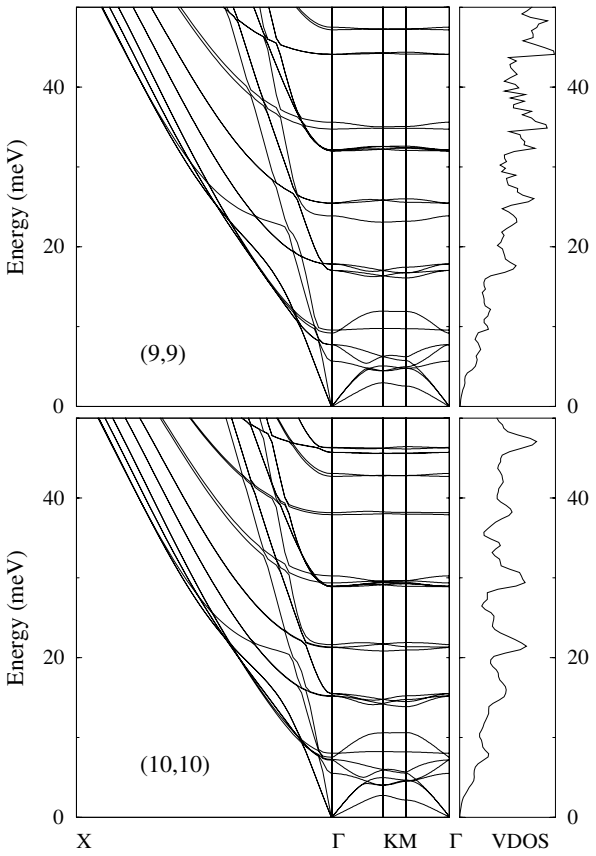


Fig. 5.3. Phonon dispersion curves and Vibrational Density of States (VDOS) for crystalline infinite bundles of (9,9) tubes (top) and (10,10) tubes (bottom) (from [7])

where the normal coordinate $Q_j(\boldsymbol{q})$ is defined by inverting the previous expression

$$Q_j(\boldsymbol{q}) = \frac{1}{\sqrt{N}} \sum_{l\kappa\alpha} e^*_\alpha(\boldsymbol{q}j \mid \kappa)\sqrt{M_\kappa} u_\alpha(l\kappa) e^{-i\boldsymbol{q}\boldsymbol{R}(l)} \tag{5.13}$$

The Hamiltonian for the lattice can be rewritten using the normal coordinates, as a sum of independent harmonic oscillators

$$H = \phi_0 + \frac{1}{2} \sum_{\boldsymbol{q},j} [\dot{Q}^*_j(\boldsymbol{q})\dot{Q}_j(\boldsymbol{q}) + \omega^2_j(\boldsymbol{q}) Q^*_j(\boldsymbol{q}) Q_j(\boldsymbol{q})] \tag{5.14}$$

The results above are obtained in the framework of classical dynamics. However, the transition to quantum mechanics is easy. Let's apply to each harmonic oscillator the quantum mechanical results expressed in the framework of second quantization. Defining $P_j(\boldsymbol{q}) = \dot{Q}_j(\boldsymbol{q})$, one can express $Q_j(\boldsymbol{q})$

and $P_j(\boldsymbol{q})$ in terms of creation ($\hat{a}_j^+(\boldsymbol{q})$) and annihilation operators ($\hat{a}_j(\boldsymbol{q})$) as [8]

$$\hat{Q}_j(\boldsymbol{q}) = \sqrt{\frac{\hbar}{2\omega_j(\boldsymbol{q})}}[a_j^+(-\boldsymbol{q}) + a_j(\boldsymbol{q})] \tag{5.15}$$

and

$$\hat{P}_j(\boldsymbol{q}) = i\sqrt{\frac{\hbar\omega_j(\boldsymbol{q})}{2}}[\hat{a}_j^+(-\boldsymbol{q}) - \hat{a}_j(\boldsymbol{q})] \tag{5.16}$$

The Hamiltonian can be expressed as a function of these operators in the simple form

$$\hat{H} = \sum_{\boldsymbol{q},j} \hbar\omega_j(\boldsymbol{q}) \left[\hat{a}_j^+(\boldsymbol{q})\hat{a}_j(\boldsymbol{q}) + \frac{1}{2}\right] \tag{5.17}$$

The energy of an eigenstate of the Hamiltonian is thus given by

$$E_n = \sum_{\boldsymbol{q},j} \hbar\omega_j(\boldsymbol{q}) \left[n_j(\boldsymbol{q}) + \frac{1}{2}\right] \tag{5.18}$$

where $n_j(\boldsymbol{q})$ is the number of phonons of energy $\hbar\omega_j(\boldsymbol{q})$ in the vibrational mode $(\boldsymbol{q}, j)$. At temperature T, the average number of phonons in the vibrational mode $(\boldsymbol{q}, j)$, $\bar{n}_j(\boldsymbol{q})$, is given by the Bose-Einstein distribution.

$$\bar{n}_j(\boldsymbol{q}) = \frac{1}{e^{\frac{\hbar\omega_j(\boldsymbol{q})}{kT}} - 1} \tag{5.19}$$

The transformations given by (5.15) and (5.16) are used to describe the inelastic processes in radiation-matter interactions in which phonons are involved. They are also used in the perturbation theory of anharmonic crystals. In the following, we present the Raman technique which is known as en efficient tool to study phonons in carbon nanotubes.

5.1.2 Raman Scattering

The theory of Raman scattering from molecules was recently reviewed by D.A. Long [9]. The theory of Raman scattering from crystals was treated by many authors, among them Fabelinski [10], Loudon [11], Turell [12], Poulet and Mathieu [13], Hayes and Loudon [14]. (For an introduction on the solid-state spectroscopy, including Raman spectroscopy, see [15]). Resonance Raman scattering (RRS) was addressed in detail in the paper of Martin and Falicov [16]. Many useful informations can also be found in the series 'Topics in Applied Physics' devoted to Light Scattering in Solids [17]. For example, reviews of Raman scattering in graphite, conducting polymers, superconductors, can be found in this series. Specific Raman techniques like SERS (surface enhanced raman spectroscopy) are presented as well. In this section, our aim is limited to an introduction to Raman scattering as an efficient technique to study carbon nanotubes.

In both, the classical and quantum mechanical treatments of the Raman effect, the main origin of the scattered radiation is considered to be an electric oscillating dipole, $\boldsymbol{P}$, induced in the medium (molecules, amorphous materials, glasses, crystals), by the electromagnetic incident field $\boldsymbol{E}_1$. At first order, the induced dipole moment is given by

$$\boldsymbol{P} = \tilde{\alpha}\boldsymbol{E}_1 \tag{5.20}$$

where $\tilde{\alpha}$ is the electronic polarizability tensor. Indeed, due to the high frequency of the probe (laser light in the visible or near infrared range), only the electrons of the system can follow the field, leading to an instantaneous electronic polarization of the medium. The electronic polarizability of a molecule or, equivalently, the electronic susceptibility of a crystal, is modulated by vibrations in molecules, and phonons in crystals. These fluctuations in the polarizability tensor of the system are responsible for Raman scattering.

Polarizability Theory for Molecules

In a Raman experiment (Fig. 5.4), a visible, or near infrared light, of circular frequency ω_1, wave vector $\boldsymbol{k}_1$, polarization unit vector $\boldsymbol{e}_1$, and incident laser irradiance I_1 ($=\epsilon_0 c\eta_1 E_1^2$), is incident in an isotropic medium, (ϵ_0 is the dielectric constant of vacuum, c is the speed of light in vacuum, and η_1 is the index of refraction of the medium at the laser frequency).

The radiant intensity of the oscillating electric dipole (point source) induced in a molecule by the incident electric field, $\boldsymbol{P} = \tilde{\alpha}\boldsymbol{E}_1$, vibrating within a frequency range $\mathrm{d}\omega_2$ of the frequency of the scattered light ω_2, and within a solid angle $\mathrm{d}\Omega$ of the scattered wave vector $\boldsymbol{k}_2$, is given by [18]

$$\frac{\mathrm{d}^2 W_2}{\mathrm{d}\Omega \mathrm{d}\omega_2} = \frac{\eta_2 \omega_2^4}{16\pi^2 \epsilon_0 c^2} \mid \boldsymbol{e}_2 \tilde{\alpha} \boldsymbol{e}_1 \mid^2 \mid E_1 \mid^2 \tag{5.21}$$

c is the speed of light in the medium, η_2 is the indice of refraction of the medium at the scattered frequency.

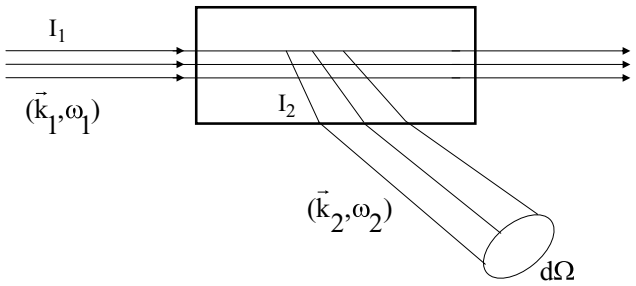


Fig. 5.4. Sketch of a Raman scattering experiment

The differential scattering cross section, $\frac{\mathrm{d}\sigma}{\mathrm{d}\Omega \mathrm{d}\omega_2}$, is obtained by dividing the previous expression by I_1.

$$\frac{\mathrm{d}^2\sigma}{\mathrm{d}\Omega \mathrm{d}\omega_2} = \frac{\eta_2}{\eta_1} \frac{\omega_2^4}{16\pi^2\epsilon_0^2 c^4} \mid \boldsymbol{e}_2 \tilde{\alpha} \boldsymbol{e}_1 \mid^2 \tag{5.22}$$

The differential cross section given above is a *power* cross section. It is defined as the ratio of scattered to incident power. In photon counting systems, the quantum cross section is usually measured. The differential cross section is converted into quantum ones by multiplication by ω_1/ω_2, leading to the usual expression of the quantum differential cross section

$$\frac{\mathrm{d}^2\sigma}{\mathrm{d}\Omega \mathrm{d}\omega_2} = \frac{\eta_2}{\eta_1} \frac{\omega_1\omega_2^3}{16\pi^2\epsilon_0^2 c^4} \mid \boldsymbol{e}_2 \tilde{\alpha} \boldsymbol{e}_1 \mid^2 \tag{5.23}$$

For first order Raman scattering, we expand the $\alpha\beta$ component of the electronic polarizability tensor, $\tilde{\alpha}$, to first order in $u_\gamma(\kappa)$ (the displacement along the γ^{th} cartesian direction of atom κ)

$$\tilde{\alpha}_{\alpha\beta}^{(1)} = \sum_{\kappa,\gamma} \left(\frac{\partial \alpha_{\alpha\beta}}{\partial u_\gamma(\kappa)} \right)_0 u_\gamma(\kappa) \tag{5.24}$$

Using the normal coordinate Q_j previously defined (5.13), we then express the expansion of $\alpha_{\alpha\beta}$ as

$$\tilde{\alpha}_{\alpha\beta}^{(1)} = \sum_j \frac{\partial \alpha_{\alpha\beta}}{\partial Q_j} Q_j \tag{5.25}$$

where

$$\frac{\partial \alpha_{\alpha\beta}}{\partial Q_j} = \sum_{\kappa,\gamma} \left(\frac{\partial \alpha_{\alpha\beta}}{\partial u_\gamma(\kappa)} \right)_0 \frac{1}{\sqrt{M_\kappa}} e_\gamma(j \mid \kappa) \tag{5.26}$$

In Raman scattering for a molecule, the normal coordinate and polarization vector do not depend on $\boldsymbol{q}$. This is why $\boldsymbol{q}$ doesn't appear in the previous expressions. In the harmonic approximation, each normal mode contributes separately to the scattered intensity.

By taking into account the properties of Q_j in a quantum mechanics approach (5.15), one calculates $\langle \mid Q_j \mid^2 \rangle$

$$\langle \mid Q_j \mid^2 \rangle = \bar{n}_j + 1 \tag{5.27}$$

in a creation process of a vibrational quantum and

$$\langle \mid Q_j \mid^2 \rangle = \bar{n}_j \tag{5.28}$$

in an annihilation process of a vibrational quantum. In consequence, the quantum differential cross section can be expressed in the following form

$$\frac{\mathrm{d}^2\sigma}{\mathrm{d}\Omega \mathrm{d}\omega_2} = \frac{\eta_2}{\eta_1} \frac{\omega_1\omega_2^3}{16\pi^2\epsilon_0^2 c^4} \sum_{\alpha\beta\gamma\lambda} e_{2\alpha} e_{2\beta} H_{\alpha\gamma\beta\lambda}(\omega) e_{1\gamma} e_{1\lambda} \tag{5.29}$$

where

$$H_{\alpha\gamma\beta\lambda}(\omega) = \sum_j a^{\star}_{\alpha\gamma}(j) a_{\beta\lambda}(j) \frac{\hbar}{2\omega_j} [(\bar{n}(\omega_j) + 1)\delta(\omega - \omega_j) + \bar{n}(\omega_j)\delta(\omega + \omega_j)] \tag{5.30}$$

with the Raman shift ω is given by

$$\omega = \omega_1 - \omega_2 \tag{5.31}$$

and

$$a_{\alpha\beta}(j) = \frac{\partial \alpha_{\alpha\beta}}{\partial Q_j} \tag{5.32}$$

$a_{\alpha\beta}(j)$ is the $\alpha\beta$ component of the so-called Raman polarizability tensor of the j^{th} mode, and ω_j is the frequency of the j^{th} vibration mode. The first term of (5.30), associated to the creation of a vibrational quantum, describes the Stokes scattering with a downshift in frequency ($\omega\rangle 0$), the second term, related to an annihilation of a vibrational quantum, describes the anti-Stokes scattering, with an upshift frequency ($\omega < 0$). The j^{th} mode is Raman active if one component of the Raman polarizability tensor, $a_{\alpha\beta}(j)$, is different of zero. From group theory, the symmetry of the Raman tensor for each j^{th} Raman-active mode can be determined from the symmetry point group which describes the molecular symmetry. These tensors are tabulated in many books (see [13] for instance).

The previous cross section, defined for one molecule, is a property of this molecule. When the scattering volume contains N_{S} molecules, the expression of the scattered intensity (5.21) is multiplied by N_{S}.

In the *bond polarizability model*, the $a_{\alpha\gamma}(j)$ component is expressed as

$$a_{\alpha\gamma}(j) = \sum_{\kappa\delta} \frac{\pi^{\kappa}_{\alpha\gamma,\delta}}{\sqrt{M_\kappa}} e_\delta(j \mid \kappa) \tag{5.33}$$

where the coefficients $\pi^{\kappa}_{\alpha\gamma,\delta}$ relate the polarization fluctuations to the atomic motions [19]. They are obtained by expanding the atomic polarizability tensor $\widetilde{\pi}^{\kappa}$ in terms of atom displacements u^{κ}_{δ}, with

$$\pi^{\kappa}_{\alpha\gamma,\delta} = \sum_{\kappa'} \left(\frac{\partial \pi^{\kappa'}_{\alpha\gamma}}{\partial u_\delta(\kappa)} \right)_0 \tag{5.34}$$

An usual method to calculate the Raman spectrum is to inject in the expressions above the values of ω_j and $e_\delta(j \mid \kappa)$ obtained by solving the equation of motion (5.5). The Raman intensity is calculated within the non-resonant bond-polarization theory in which bond-polarization parameters are used [20]. In this approach, the $\pi^{\kappa}_{\alpha\beta,\gamma}$ coefficients are given by

$$\pi^{\kappa}_{\alpha\beta,\gamma} = \sum_{\kappa'} \frac{1}{3}(2\alpha'_p + \alpha'_l)\delta_{\alpha\beta}\hat{r}_\gamma + (\alpha'_l - \alpha'_p)\left(\hat{r}_\alpha\hat{r}_\beta - \frac{1}{3}\delta_{\alpha\beta}\right)\hat{r}_\gamma \qquad (5.35)$$

$$+ \frac{(\alpha_l - \alpha_p)}{r}(\delta_{\alpha\gamma}\hat{r}_\beta + \delta_{\beta\gamma}\hat{r}_\alpha - 2\hat{r}_\alpha\hat{r}_\beta\hat{r}_\gamma) \,,$$

where $\hat{r}$ is a unit vector in direction r of the bond between κ and κ' atoms. α_l and α_p correspond to the longitudinal and perpendicular bond polarizability, respectively, $\alpha'_l = (\partial\alpha_l/\partial r)_0$ and $\alpha'_p = (\partial\alpha_p/\partial r)_0$.

The Differential Cross Section in Crystals

In crystals, the vibrational excitations, namely the phonons, involved in the Raman scattering process extend coherently over distances much greater than the molecules and cell sizes. Therefore, the differential cross section is a collective property. For the description of Raman scattering in crystals, one should consider the susceptibility tensor $\tilde{\chi}$ (polarizability per unit volume), and the polarization of the medium is now given by

$$\boldsymbol{P} = \epsilon_0\tilde{\chi}\boldsymbol{E}_1 \qquad (5.36)$$

At first order

$$\chi_{\alpha\beta} = (\chi_{\alpha\beta})_0 + \sum_j \left(\frac{\partial\chi_{\alpha\beta}}{\partial Q_j}\right) Q_j \qquad (5.37)$$

where $\chi''_{\alpha\beta}(j) = \frac{\partial\chi_{\alpha\beta}}{\partial Q_j}$ is a component of the derived susceptibility tensor known as the Raman tensor of the j^{th} mode.

Light scattering experiments are most often performed with visible incident light, where the typical frequency is 5×10^{14} Hz. The wave vector magnitude k_1 corresponding to the typical incident frequency is

$$k_1 \approx 1.5 \times 10^7 \text{m}^{-1} \qquad (5.38)$$

On the other hand, the vibrational excitations studies by Raman scattering cause a shift in the scattered frequency lying in the approximate range

$$3 \times 10^{11}\,\text{Hz}(\approx 10\,\text{cm}^{-1}) < \frac{\omega}{2\pi} < 10^{14}\,\text{Hz}(\approx 3400\,\text{cm}^{-1}) \qquad (5.39)$$

and the range of vibrational excitation wave vectors accessible to light-scattering experiments is:

$$0 < q < 3 \times 10^7\,\text{m}^{-1} \qquad (5.40)$$

The upper limit of q is three orders of magnitude smaller than the magnitude of the typical Brillouin zone in crystal. In a first approximation one can consider that the phonons involved in the first-order Raman scattering

process are only those of the center of the Brillouin zone ($q = 0$). Consequently, the primitive cell of a crystal can be viewed as a *supermolecule*, and the majority of the expressions derived for a molecule can be generalized to this *supermolecule*. Especially, the spectral differential cross section can be calculated from (5.23), (5.29), (5.30) with the Raman (susceptibility) tensor instead of the Raman (polarizability) tensor. The quantum differential cross section is

$$\frac{\mathrm{d}^2\sigma}{\mathrm{d}\Omega\mathrm{d}\omega_2} = \frac{\eta_2}{\eta_1}\frac{\omega_1\omega_2^3 V_\mathrm{c}}{16\pi^2 c^4} \mid \boldsymbol{e}_2\tilde{\chi}\boldsymbol{e}_1 \mid^2 \tag{5.41}$$

where V_c is the volume of the primitive cell. Thus one obtains for Stokes Raman scattering

$$\frac{\mathrm{d}^2\sigma}{\mathrm{d}\Omega\mathrm{d}\omega_2} = \frac{\eta_2}{\eta_1}\frac{\omega_1\omega_2^3 V_\mathrm{c}}{16\pi^2 c^4 2\omega_j(\mathbf{0})} \mid \boldsymbol{e}_2\tilde{\chi}\prime\prime(j)\boldsymbol{e}_1 \mid^2 [n_j(\mathbf{0}) + 1] \tag{5.42}$$

When the scattering volume V contains N primitive cells ($N = \frac{V}{V_\mathrm{c}}$), the scattered intensity is obtained by multiplying the previous expression by N. The scattered intensity is found to be proportional to the scattering volume.

From group theory, the symmetry of the Raman tensor for each j^{th} mode can be determined from the symmetry point group which is isomorphic to the factor group $F(\boldsymbol{q} = 0)$ of the crystal [13]. As an illustration, we calculated the Raman spectra for 1-D carbon nanotube crystals in the framework of the bond-polarization theory [21]. Calculations are performed for carbon nanotubes of similar diameters, but various chiral angles, and for different polarizations of the beam with respect to the tube axis (Fig. 5.5).

Resonant Raman Scattering

In order to discuss the resonance effects in Raman scattering, it is necessary to develop a microscopic theory of light scattering, based on a complete quantum mechanical treatment of the light scattering processes. In the quantum mechanical approach, the radiation field is described by the Hamiltonian $\hat{H}_\mathrm{R}$, and the material system (molecule, crystal) is described by the Hamiltonian $\hat{H}_\mathrm{M}$. Radiation and matter interact via the interaction Hamiltonian $\hat{H}_\mathrm{MR}$. In such an approach, it is found that the differential cross section is directly related to the transition polarizability (susceptibility) matrix elements tensor, $K_{2f,1g}$, defined by [16]

$$K_{2f,1g} = \sum_a [\frac{\langle \omega_2 f \mid \hat{H}_\mathrm{MR} \mid 0a\rangle\langle 0a \mid \hat{H}_\mathrm{MR} \mid \omega_1 g\rangle}{(\hbar\omega_1 - \tilde{E}_a)} \tag{5.43}$$

$$+ \frac{\langle \omega_2 f \mid \hat{H}_\mathrm{MR} \mid \omega_1\omega_2 a\rangle\langle \omega_1\omega_2 a \mid \hat{H}_\mathrm{MR} \mid \omega_1 g\rangle}{(-\hbar\omega_2 - \tilde{E}_a)}]$$

g, a and f denote the ground, intermediate and final states of the system, respectively. The ket $\mid \omega_s l\rangle$ indicates the presence of a photon of frequency

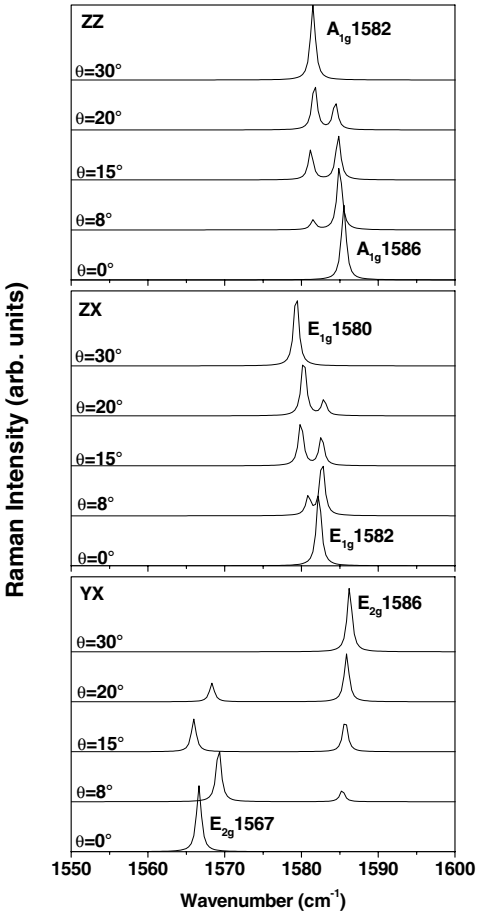


Fig. 5.5. Dependence of polarized Raman spectra of infinite crystals of SWNT in the tangential modes range as a function of the chiral angle (from [21])

ω_s ($s = 1$ or 2) in the l^{th} state, while $\mid 0l\rangle$ means that this photon has been destroyed. Because Raman scattering involves two photons (one absorbed, ω_1, and one emitted, ω_2), it is a second order process in $\hat{H}_{\mathrm{MR}}$. $\tilde{E}_a$ contains lifetime effects in the form of a small imaginary term

$$\tilde{E}_a = E_a + i\hbar\gamma_a \tag{5.44}$$

where $\gamma_a = \frac{2\pi}{\tau_a}$, τ_a being the lifetime of an excited state a. In a resonant Raman scattering process, the incident frequency ω_1 is such that $\hbar\omega_1 \cong E_a$. It is a good approximation to consider in the expression of the transition polarizability (susceptibility) matrix elements (5.43) only the first term, with a small denominator

$$K_{2f,1g} \cong \sum_{E_a \cong \hbar\omega_1} \frac{\langle \omega_2 f \mid H_{\mathrm{MR}} \mid 0a\rangle\langle 0a \mid H_{\mathrm{MR}} \mid \omega_1 g\rangle}{(\hbar\omega_1 - E_a - i\hbar\gamma_a)} \tag{5.45}$$

In order to take into account the nature of the intermediate states, it is convenient to describe the Hamiltonian of the system, $\hat{H}_{\mathrm{M}}$, as

$$\hat{H}_{\mathrm{M}} = \hat{H}_0 + \hat{H}_{\mathrm{I}} \tag{5.46}$$

$\hat{H}_0$ is the Hamiltonian of the various kinds of elementary excitations present in the medium, $\hat{H}_{\mathrm{I}}$ is the Hamiltonian which represents the interaction between these excitations. In the calculations, the Hamiltonian $\hat{H}_{\mathrm{I}}$ is considered as as a perturbation. For the radiations normally used in Raman scattering experiments, $\hat{H}_{\mathrm{MR}}$ couple the electrons of the medium to the radiation. It is the so-called electron-radiation (photon) coupling: $\hat{H}_{\mathrm{MR}} \equiv \hat{H}_{\mathrm{er}}$. In Raman scattering, $\hat{H}_{\mathrm{I}}$ is the electron-vibration (phonon) interaction: $\hat{H}_{\mathrm{I}} \equiv \hat{H}_{\mathrm{ep}}$.

In this assumption, the expansion of eigenfunctions and eigenvalues of $\hat{H}_{\mathrm{M}}$ in a perturbation series in $\hat{H}_{\mathrm{ep}}$ leads to, at first order

$$K_{2f,1g} = \sum_{ab} \left[\frac{M_{fb} M'_{ba} M_{ag}}{\hbar^2(\omega_1 - \omega_a - i\gamma_a)(\omega_1 - \omega_b - i\gamma_b)} \right] \tag{5.47}$$

state $\mid a\rangle$ is coupled to $\mid g\rangle$ by $\hat{H}_{\mathrm{er}}$:

$$M_{ag} \equiv \langle a \mid \hat{H}_{\mathrm{er}} \mid g\rangle \tag{5.48}$$

state $\mid b\rangle$ is coupled to $\mid f\rangle$ by $\hat{H}_{\mathrm{er}}$:

$$M_{fb} \equiv \langle f \mid \hat{H}_{\mathrm{er}} \mid b\rangle \tag{5.49}$$

state $\mid a\rangle$ is coupled to state $\mid b\rangle$ by $\hat{H}_{\mathrm{ep}}$:

$$M'_{ba} \equiv \langle b \mid \hat{H}_{\mathrm{ep}} \mid a\rangle \tag{5.50}$$

At the second order

$$K_{2f,1g} = \sum_{abc} \left[\frac{M_{fb} M'_{bc} M'_{ca} M_{ag}}{\hbar^3(\omega_1 - \omega_a - i\gamma_a)(\omega_1 - \omega_c - i\gamma_c)(\omega_1 - \omega_b - i\gamma_b)} \right] \tag{5.51}$$

state $\mid a\rangle$ ($\mid b\rangle$) is coupled to state $\mid c\rangle$ by $\hat{H}_{\mathrm{ep}}$. In the expressions above, $\hat{H}_{\mathrm{er}}$ involves the creation or destruction of electronic states. Consequently, state $\mid a\rangle$ is a pure electronic state and the state $\mid b\rangle$ is the state of the quasi-particle found in $\mid f\rangle$. When this quasi-particle is a phonon, one can write the following usual expression, which can be used to describe the Raman spectrum in carbon nanotubes in the so-called *single resonance process* [22]

$$K_{2f,1g} = \sum_{ab} \left[\frac{M_{fb} M'_{ba} M_{ag}}{\hbar^2(\omega_1 - \omega_a^e - i\gamma_a)(\omega_2 - \omega_b^e - i\gamma_b)} \right] \tag{5.52}$$

with $\omega_2 - \omega_1 = \pm\omega_j(0)$.

At second order and for a Stokes process, one obtains the so-called *double resonance process*

$$K_{2f,1g} = \sum_{abc} \left[\frac{M_{fb} M'_{bc} M'_{ca} M_{ag}}{\hbar^3 (\omega_1 - \omega_a^e - i\gamma_a)(\omega_1 - \omega_{j_1}(\boldsymbol{q}_1) - \omega_c^e - i\gamma_c)} \right. \tag{5.53}$$

$$\left. \frac{1}{(\omega_1 - \omega_{j_2}(\boldsymbol{q}_2) - \omega_b^e - i\gamma_b)} \right]$$

where $\omega_{j_1}(\boldsymbol{q}_1)$ and $\omega_{j_2}(\boldsymbol{q}_2)$ are the two phonons involved in the process. The conservation of quasi momentum requires: $\boldsymbol{q}_1 = -\boldsymbol{q}_2$, and that of energy: $\omega_1 - \omega_2 = \omega_{j_1}(\boldsymbol{q}_1) + \omega_{j_2}(-\boldsymbol{q}_1)$. The double resonance process has been successfully used to explain the excitation energy dependence of combination bands (the G' band) in carbon nanotubes [23, 24].

In the double-resonance approach, one can also consider the Stokes process in which: (i) state $\mid c\rangle$ is filled by the phonon, $(\boldsymbol{q}, j)$, found in $\mid f\rangle$, and (ii) the phonon $(\boldsymbol{q}, j)$ is scattered by a defect in state $\mid b\rangle$. In this case the susceptibility matrix can be written as

$$K_{2f,1g} = \sum_{abc} \left[\frac{M_{fb} M'_{bc} M'_{ca} M_{ag}}{\hbar^3 (\omega_1 - \omega_a^e - i\gamma_a)(\omega_1 - \omega_j(\boldsymbol{q}) - \omega_c^e - i\gamma_c)} \right. \tag{5.54}$$

$$\left. \frac{1}{(\omega_1 - \omega_j(\boldsymbol{q}) - \omega_b^e - i\gamma_b)} \right]$$

The M'_{ca} (M'_{bc}) transition matrix elements represent the phonon (defect) which scatters the electron from state a to c (from state c to b). This latter double resonance process has been successfully used to explain the excitation energy dependence of the D-band in carbon nanotubes [25, 26]. Recently, Thomsen and co-workers have also considered this process to describe the excitation energy dependence of the first-order Raman modes (tangential and radial breathing modes) in single-walled carbon nanotubes [27].

5.2 Electron Energy-Loss Spectroscopy

5.2.1 Principles of Electron Energy-Loss Spectroscopy in a Transmission Scattering Geometry

Scattering Geometry

Generally speaking, when one wants to perform an electron energy-loss spectroscopy (EELS) experiment, one needs an electron source, a spectrometer made of magnetic or electrostatic sectors and a detector. Then one has to choose the scattering geometry. When slow electrons are used (of primary kinetic energy less than 10 eV), it is necessary to use a reflection geometry. The illuminated area on the sample is then of the order of 1 cm^2. Energy and

momentum transfer resolution are then optimal (1 meV and 0.01 Å^{-1} respectively). This kind of experiment, called HREELS (high resolution EELS) [28], is used to study phonons and low-energy plasmons (in the infrared domain) and more specifically to generate accurate dispersion curves in the centre of the Brillouin zone (typically for momentum transfer $\langle 0.5\,\text{Å}^{-1}$). Since very few HREELS experiments have been carried out on nanotubes, this mode will not be detailed here. In the experiment by Fink and co-workers [29] the illuminated area is a few mm^2 and one detects instead the signal transmitted by the sample. Energy and momentum transfer resolutions are lower than in HREELS (100 meV and 0.03 Å^{-1} respectively) but are much better than those accessible with a standard transmission electron microscope (TEM) experiment. This technique allows the study of dispersion behavior of interband transitions and plasmon modes (from 0.01 eV to a few tens of eV: infrared and ultraviolet) as well as core-losses. Finally, performing an EELS experiment in a TEM has the advantage of combining a spectroscopic analysis with the usual imaging and diffraction capabilities of a microscope. In this way, it is possible to see the sample and probe its electronic structure at a nanometer scale and even at the atomic scale. The measured range of energy scans 2-3 eV to thousands of eV (soft X-rays). Typical energy and momentum transfer resolutions are between 0.15 and 1 eV and 0.1 Å^{-1} and 1 Å^{-1} respectively depending on the microscope and the operating mode.

In the context of a transmission electron microscope, a primary beam of high-energy electrons (typically between 100 and 300 keV), interacts with a thin specimen. A suitable aperture defines at the level of the specimen a solid angle of collection (of acceptance half angle β of a few mrad) – see Fig. 5.6 – and the velocity of the electrons contained within this aperture is analyzed with a spectrometer (usually a magnetic sector spectrometer). At the exit of this prism the distribution in energy of these electrons can be recorded and the result displayed as an electron energy loss spectrum, similar to that shown in Fig. 5.7. This double selection (in angle and energy) allows an analysis of the scattering events in terms of momentum transfer $\boldsymbol{q}$ and of energy transfer ΔE (see Fig. 5.6).

A typical EELS spectrum exhibits the following features: the major contribution to the detected intensity is a very intense and narrow peak (zero-loss peak) corresponding to the electrons which intersect the specimen without measurable inelastic scattering. Inelastically scattered electrons are responsible for a complex spectrum which contains two major types of excitations: the low energy-loss range associated with electronic excitations of the valence electrons in the 5 to 40 eV range, and the core-loss range above 40 eV, where characteristic edges are superposed on a monotonously decaying background.

The low-energy class of excitations involves the valence (and conduction) electrons, which can be excited either collectively in plasmon modes, or individually as interband transitions (see Fig. 5.8). The theoretical description of these modes is not straightforward as it encompasses a complex mixture of

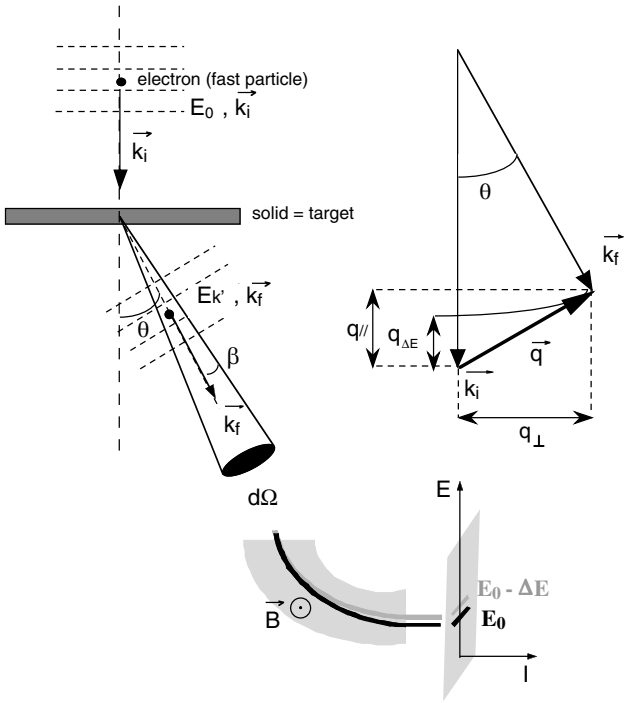


Fig. 5.6. Schematic representation of the parameters involved in an EELS measurement and relation with the geometry of the scattering event: incident electron of wave vector $\boldsymbol{k}_i$, scattered electron wave vector $\boldsymbol{k}_f$, transferred wave vector $\boldsymbol{q}$. The momentum transfer $\boldsymbol{q}$ can be decomposed into parallel and perpendicular components, which depend respectively on the energy loss ΔE and the scattering angle θ

transitions involving a population of particles in strong Coulomb interaction. As a first approximation, it is common to use a phenomenological macroscopic approach based on classical electrodynamics, since we are dealing with charged particles. This involves free charges in a metallic case and oscillators with eigenmodes in a dielectric medium. The main physical quantity which accounts for the response of a material to an impinging point charge, the incident electron, is the dielectric response $\epsilon(\omega, \boldsymbol{q})$, where ω is related to the energy loss by $\Delta E = \hbar\omega$ and $\boldsymbol{q}$ is the wave vector transfer defined above. The differential inelastic cross section per incident electron for such a scattering event $(\omega, \boldsymbol{q})$ is in fact related to the dielectric response by

$$\frac{\mathrm{d}^2\sigma}{\mathrm{d}\Omega \mathrm{d}E} \propto \frac{1}{q^2} Im\left(\frac{1}{\epsilon(\omega, \boldsymbol{q})}\right) \tag{5.55}$$

where ϵ is a complex function that can be written as the sum of a real part and an imaginary part. The real part ϵ_1 describes a dispersion process while the imaginary part ϵ_2 is related to electromagnetic absorption in the $\boldsymbol{q} = \boldsymbol{0}$

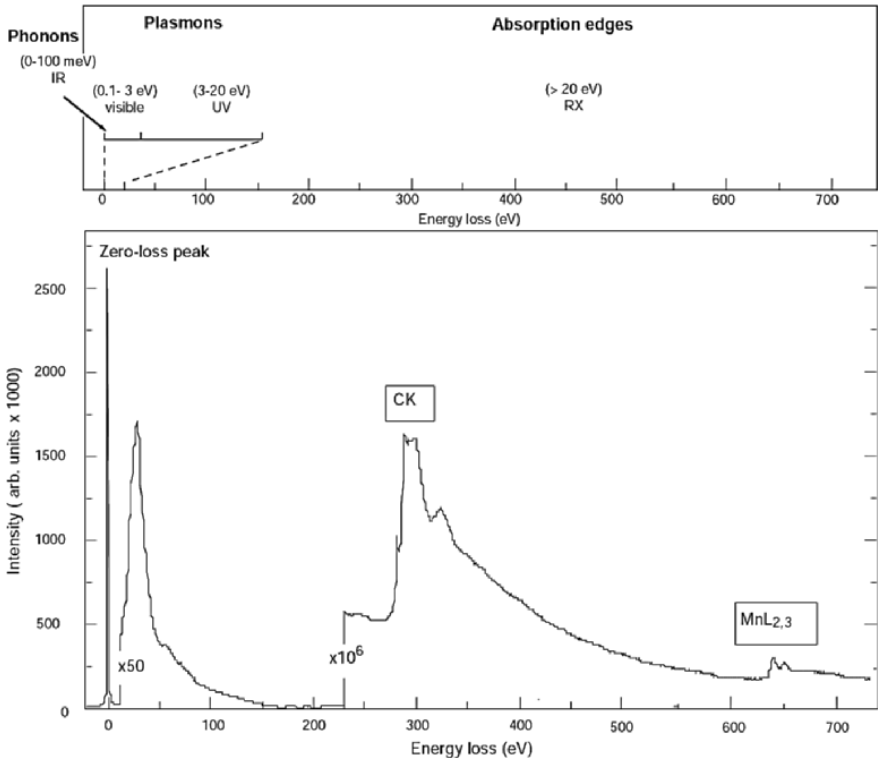


Fig. 5.7. *Bottom*: a typical EELS spectrum acquired on a carbon nanotube filled with manganese. The whole spectrum extending over 1000 eV covers four orders of magnitude in intensity when comparing the non-saturated zero-loss peak and the details of Mn edge around 600 eV loss. *Top*: associated types of excitations and spectral domains

limit. $\mathrm{d}\Omega$ and $\mathrm{d}E$ are the differential elements associated with the solid angle of collection Ω, and the energy loss E. Equation (5.55) is the basic formula for the interpretation of electron energy-loss spectra in the low-loss region in bulk materials.

Volume plasmon modes (polarization excitations) are defined as longitudinal solutions of the Maxwell equation $\boldsymbol{\nabla}\epsilon\boldsymbol{E} = 0$, which is equivalent to the condition: $\epsilon(\omega, \boldsymbol{q}) = 0$ for isotropic materials. Such a condition is reached when $\epsilon_1 = 0$ and ϵ_2 is small. This situation is associated with the occurrence of a peak in the EELS spectrum. EELS is thus a powerful technique for studying longitudinal excitations as they appear directly as intense peaks in the energy-loss spectrum. When the collection angle is small enough and centered on the optical axis, the limit $\boldsymbol{q} \to 0$ is reached. A Kramers-Kronig analysis can be performed to extract the $\epsilon_1(\omega, 0)$ and $\epsilon_2(\omega, 0)$ optical constants from the energy-loss function. Such a transformation relies on the causality of the

dielectric response (see [30] for a review). Another piece of valuable information that can be extracted in the vicinity of the zero-loss peak is the joint density of states at the band gap in insulating materials. For practical reasons this only has been tried with materials of relatively large band gap [36–38]. In these bulk materials, the nature, direct or indirect, and the energy E_g of a band gap can be deduced from the study of the first eV of the imaginary part ϵ_2 of the dielectric function $\epsilon(\omega)$, which is deduced from the energy loss function $\mathrm{Im}(-\frac{1}{\epsilon(\omega,0)})$ through Kramers-Kronig transformation. It is likely that this technique will be used in a near future to map the band gap variations in luminescent heterostructures (preferentially in the blue). However, such use of plasmon losses remains rather limited when one deals with structures and objects of nanometer size. It has been demonstrated that its value may shift and its width rapidly increases when the size of the investigated structure becomes smaller than a few nms and bulk plasmon modes indeed completely vanish for smaller objects [31]. For these dimensions, the contribution of the surface modes to the total spectrum becomes dominant. These modes are generated when certain boundary conditions are satisfied. In particular, they are generated when an incident electron travels along a non-intersecting trajectory at a small distance from the outer surface of a nano-object, in a mode called 'aloof' or 'near-field' geometry [32, 33]. It has been shown that the response then depends on the nature and the shape of the surface, and in the case of hollow objects (such as nanotubes) on the coupling between the outer and inner surfaces for small wall thickness [34, 35].

Absorption edges (or core-edges) occurring at higher energy losses arise from individual electron transitions from atomic-type core levels to unoccupied states lying above the Fermi level (see Fig. 5.8). They are identified and labeled following the notation generally used in atomic physics. Their position in energy is defined by the nature of the atom and the type of level from which the excitation occurs (K for 1s electrons, L_{23} for 2p electrons, M_{45} for 3d electrons, etc). In Fig. 5.7, one notices the carbon K edge with threshold at 284 eV and the manganese L_{23} edge with threshold at 642 eV. Such signals appear superimposed on the non-specific decaying background and are useful for three reasons. First, when identified, they demonstrate the presence of the related atoms along the trajectory of the incident electrons through the specimen; this is the basis of a qualitative elemental analysis. Second, their total intensity after subtraction of the underlying non-characteristic background and integration over an extended energy window, can be related to the number of such atoms encountered by the impinging electrons, providing therefore access to a quantitative elemental analysis. Third, as shown in Fig. 5.7, their shape varies from edge to edge and from compound to compound for the same edge. These variations of the edge fine structures are very useful for extending the analysis of the solid from elemental quantification to determination of bonds. These last two issues will be further discussed below.

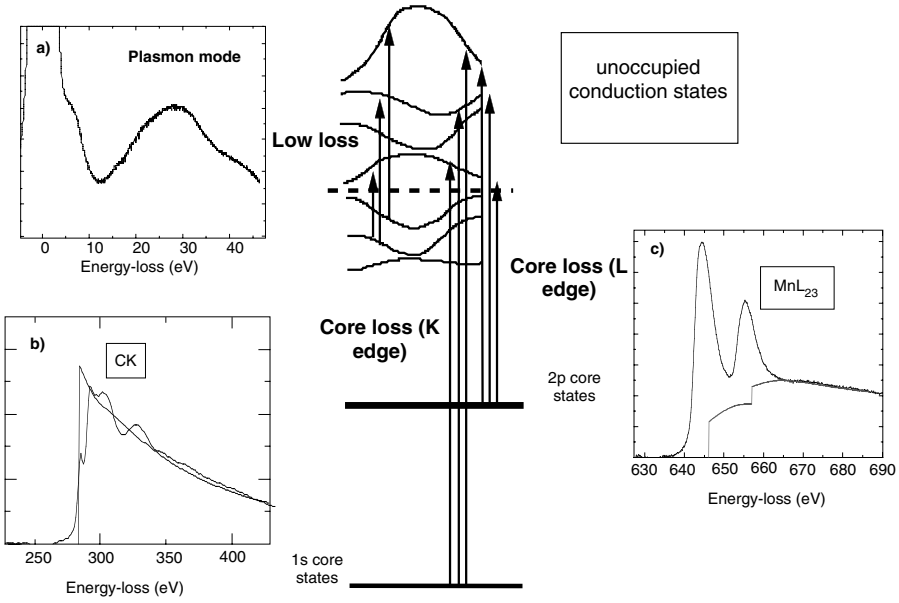


Fig. 5.8. Schematics of the different populations of electrons involved in the different excitation processes (low energy-loss and core-loss domains) investigated in an EELS experiment and examples of measured spectroscopic signals: plasmon modes and detailed shapes of core-edges (C K and Mn L_{23}) extracted from the whole spectrum shown in Fig. 5.7. The edges are displayed after background subtraction and fitted to calculated atomic cross sections. Discrepancies involve solid state effects (near edge structures) as well as transitions towards bound states (white line features)

5.2.2 Basic Tools Developed for Interpreting and Using Core-Loss Signals

Expression of the Inelastic Cross Section

The expression for the energy-loss function as given in (5.55) is very general and needs to be detailed depending on the type of excitation involved in the scattering process. When dealing with core-losses, it is more convenient to re-write (5.55) as a derivation from the Fermi Golden rule

$$\frac{\mathrm{d}^2\sigma}{\mathrm{d}E\mathrm{d}\Omega} = \left(\frac{2me^2}{(\hbar q)^2}\right)^2 \frac{k_f}{k_i} \sum_f \sum_{j=1}^{N} |\langle \Psi_f | e^{i\boldsymbol{q}\cdot\ \boldsymbol{r}_j} | \Psi_i \rangle|^2 \delta(E_i - E_f + \hbar\omega) \qquad (5.56)$$

where the energy loss $\Delta E = \hbar\omega = E_f - E_i$ has been introduced; k_i and k_f are the modulus of the wave vectors associated with the incident and the scattered wave respectively (approximated as plane waves); Ψ_f and Ψ_i are the final and initial wave functions of the target and the sum on j is a sum on all the j atoms of the target concerned by the scattering event.

This expression of the differential cross section actually consists of two factors of different nature. The factor $(2me^2/q^2)^2 \cdot k_f/k_i$ is evaluated from the observable quantities k_i, k_f, concerning the fast electron only. The squared matrix element concerns the target only, representing the conditional probability that the atom of the solid undergoes the transition to a particular excited state upon receiving a momentum transfer $\boldsymbol{q}$. Therefore, this quantity reflects the dynamics of the involved atom. It is known as the inelastic form factor or the generalized oscillator strength. This factor together with the δ-function expressing the conservation of energy, constitutes one key quantity to be extracted from an EELS experiment. In order to compute this cross section, some useful approximations can be made. The first one consists in considering the atoms of a solid as non-interacting. Then, the many-body wave electronic function Ψ_f can be written as ϕ_f, a one electron atomic wave function (one writes also $\Psi_i = \phi_i$). The second approximation is the dipole approximation. It is valid for the small scattering angles generally met in the experimental conditions depicted in Fig. 5.6 with collection angles in the range 1–30 mrad and primary electrons of 100–300 keV energy. Under these conditions, $|\boldsymbol{q}.\boldsymbol{r}| \ll 1$ and $|\phi_f\rangle$ and $|\phi_i\rangle$ are orthogonal, so that the matrix element is reduced to a dipolar term obtained in the zero limit value of $\boldsymbol{q}$. Consequently, the most intense atomic transitions to be probed are those corresponding primarily to $l \rightarrow l+1$ (i.e. $s \rightarrow p$, $p \rightarrow d$ or $d \rightarrow f$), which are more intense than the other allowed transitions $l \rightarrow l-1$. Then, it is relatively simple to calculate atomic cross sections for isolated atoms, resulting in tables of $\frac{\mathrm{d}^2\sigma}{\mathrm{d}E\mathrm{d}\Omega}$. Such cross section computations based on the hydrogenic model [39] or on the more sophisticated Hartree-Slater method using a self-consistent atomic potential [40], provide profiles of the energy dependence of the cross sections and of their absolute intensities. Their major use is for quantitative analysis. If we compare such calculations with experimental profiles of edges such as shown in Fig. 5.8, one sees obvious discrepancies concerning the shapes. These are the fine structures (called ELNES for energy-loss near edge structures), the interpretation of which is of highest importance in identifying the coupling of the excited atom to its neighboring atoms and therefore its coordination and bonding character. For the carbon K edge, modulations of the atomic profile account for the solid state environment of the carbon atoms within this structure, which is of graphite type. For the Mn L_{23} edge, one notes the presence of two extra lines at the edge onset, which correspond to transitions of the 2p electrons towards 3d states of bound character which are not accounted for by the simple atomic calculations. The atomic calculation normally provides a satisfactory description of the general shape of the edge, as a saw-tooth (hydrogenic) profile or as a delayed maximum induced by a centrifugal barrier within the intra-atomic potential of the excited atom. For a more complete description of the experimental process, one has to take into account many-body effects that occur in a solid. One common way is to describe the electronic wave functions as Bloch functions (one-electron wave functions). The associated energy-level distribution follows that of a band

structure. Due to the dispersive character of the electronic states, the sum over the delta functions written in (5.56) has to be replaced by a density-of-states term. It is possible to show that the transition probability calculated by the matrix elements introduced in (5.56) is modulated by the respective densities of unoccupied states $D_l(E)$ with the right angular symmetry at the site of the excited atom

$$\frac{\mathrm{d}^2\sigma}{\mathrm{d}\Omega \mathrm{d}E} = |M_{l-1}(E)|^2 D_{l-1}(E) + |M_{l+1}(E)|^2 D_{l+1}(E) \tag{5.57}$$

where $M_{l\pm1}(E)$ are matrix elements of proper angular symmetry and E is the energy loss.

Elemental Quantification

The measurement of the intensity of a characteristic signal in an EELS spectrum provides access to quantitative elemental analysis. Using the definition of the inelastic scattering cross section (see [39,41]), one extracts the absolute number of atoms N of the relevant species within a cylinder with section equal to the probe area A_{probe}, from

$$S(\beta, \Delta E) = I_0(\beta, \Delta E) \cdot (N/A_{\mathrm{probe}}) \cdot \sigma(\beta, \Delta E) \tag{5.58}$$

where $S(\beta, \Delta E)$, $I_0(\beta, \Delta E)$ and $\sigma(\beta, \Delta E)$ are, respectively, the measured characteristic signal, the low energy-loss including the zero-loss peak and the calculated cross section for the relevant signal, all quantities being integrated over all scattering angles encompassed within the collection aperture of semi-angle of acceptance β, and over the energy window ΔE above threshold. From this formulation, it appears clearly that such quantitative analysis relies on a good extraction of the characteristic signal S (i.e. a good subtraction of the non-characteristic background) and a good estimation of the ionization cross section. The extraction of the characteristic edge implies background modeling over a fitting window before threshold and extrapolation of this model curve in the edge energy region. The most generally used model is an empirical $A.E^{-R}$ power-law where A and R are parameters to be determined [42]. The cross section is satisfactorily estimated using a hydrogenic model for the K and L shells [43]. For outer shells of M, N and O types, reliable values are obtained using a self-consistent calculation based on a Hartree-Slater description [40]. As noted above, such calculations are supposed to reproduce the general shape of the edge without modeling the fine structures occurring from solid state effects. Therefore, special care must be taken when choosing the integration energy window, so that these fine structures are properly averaged over this energy window. When one is only interested in measuring relative concentrations (of different elements A and B) in order to work out the stoichiometry of the sample, formula 5.58 can be simplified to

$$\frac{N_A}{N_B} = \frac{S_A(\beta, \Delta E)}{S_B(\beta, \Delta E)} \times \frac{\sigma_B(\beta, \Delta E)}{\sigma_A(\beta, \Delta E)} \tag{5.59}$$

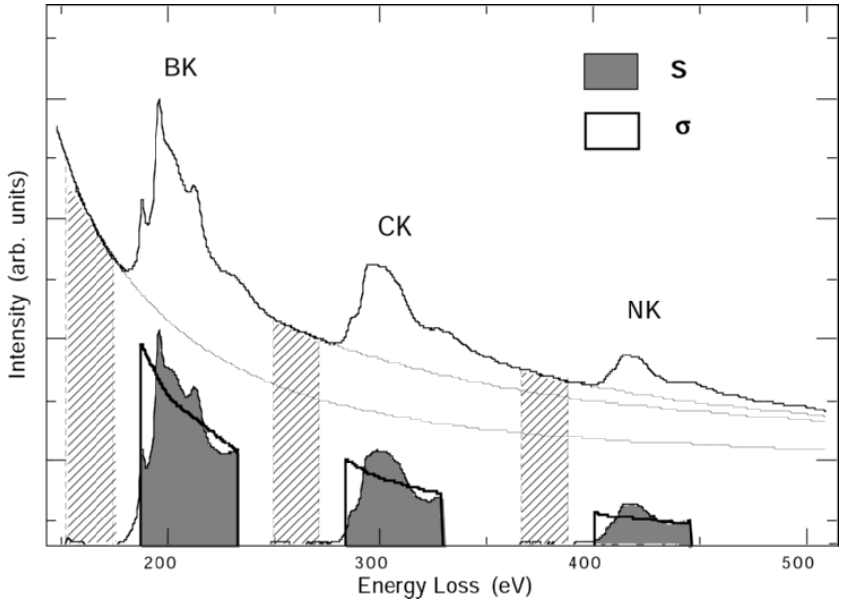


Fig. 5.9. Illustration of the conventional quantification process on an EELS spectrum including 3 absorption edges: B K, C K and N K at 188 eV, 284 eV and 401 eV respectively. All three edges are shown after background subtraction (the background is modeled and extrapolated under the edges using a power law AE^{-R}) with the calculated ionization cross sections in a hydrogenic model

An example of the quantification procedure is given in Fig. 5.9 for a turbostratic BC_2N sample.

5.2.3 Spatially Resolved EELS

The 3D Data Cube

The power of EELS in a TEM or a STEM (scanning transmission electron microscope) lies in the possibility of combining spectroscopic measurements (acquisition of an EELS spectrum $J(E)$) with the usual possibilities of imaging and diffraction delivered by a microscope. A majority of such experiments consists in acquiring data where the space coordinates (x, y) or alternatively the scattering angle coordinates (θ_x, θ_y) are correlated to the energy loss E. Such set of data has been sketched in the literature as a cube (see Fig. 5.10) where each pixel of the cube corresponds to a unique triplet (x, y, E) or alternatively (θ_x, θ_y, E). To acquire $J(x, y, E)$ or $J(\theta_x, \theta_y, E)$, two approaches have been developed corresponding to two different set-ups: the filtered image mode in a conventional TEM [44–46] and the spectrum image mode [47, 48]

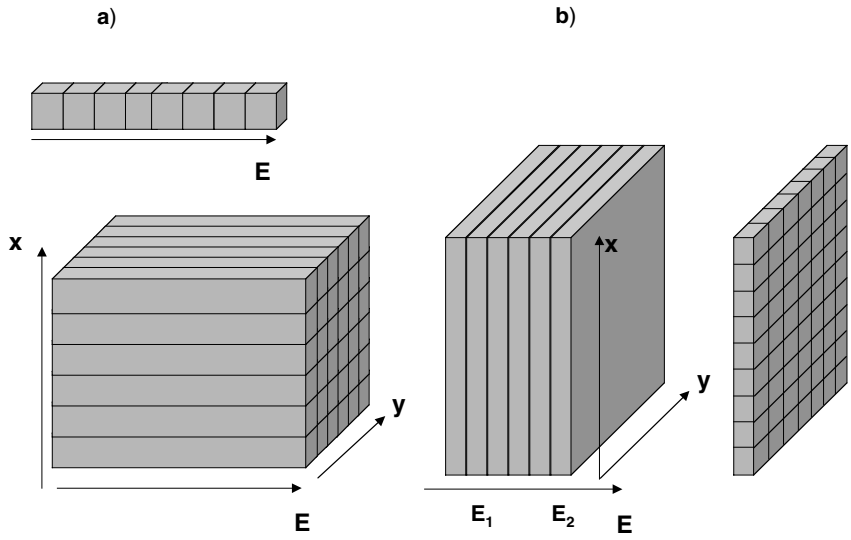


Fig. 5.10. The mixed space-energy resolved 3D data cube recorded in a TEM equipped with an EELS spectrometer or filter: (**a**) STEM mode and parallel acquisition EELS for the 'spectrum-image' mode; on top: one individual EELS spectrum acquired for one position of the probe. (**b**) TEM mode and energy filtered images through an energy selection slit, for the 'image-spectrum' mode; right: one individual filtered image

in a STEM. In the energy filtering approach, the parallel beam of a conventional TEM (CTEM) is used, the analyzed electrons are filtered using an energy-slit and recombined to form an energy-filtered image (energy filtered TEM–EFTEM). All pixels (x, y) of the filtered image (schematized as a horizontal "slice" of the cube $J(x, y, E)$ in Fig. 5.10) are recorded at once over a limited acquisition time to obtain $J(x, y)$. In this mode, spatial resolution is limited by the chromatic aberrations [49]. The EELS data are recorded over a very limited energy-loss range ΔE defined by the width of the energy-slit, and therefore the spectroscopic information is lost. However, a series of filtered images can be acquired by shifting the energy-slit for multi-element analysis. Similarly to filtered images $J(x, y)$, filtered diffraction patterns $J(\theta_x, \theta_y)$ can be acquired. In the STEM approach, the beam is focused onto a small probe on the sample and an EELS spectrum from the corresponding analysis nanovolume is recorded over a large energy range. The cube $J(x, y, E)$ is constructed by scanning the probe along the x and y axes over a given specimen area and by acquiring an EELS spectrum for every probe position. The function $J(x, y, E)$ is called a *spectrum image*. Energy-filtered images can be then calculated *a posteriori* by integrating over an energy-window ΔE the EELS spectrum intensity associated with every position (x, y). In the STEM mode, the spatial resolution is limited by the probe size. In practice, it is also

possible to record a *spectrum diffraction* $J(\theta_x, \theta_y, E)$. Whatever the approach, all (S)TEM-EELS measurements use the same principle. An analyzer is used to disperse and focus in the achromatic plane the inelastically scattered electrons as a function of their velocity. Electrons can be filtered and recombined to form an energy-filtered image (CTEM approach). If not, the image of this plane constitutes the EELS spectrum (STEM approach or spectroscopy mode in a CTEM). The differences between the different modes are contained in:

- The type of illumination (parallel or convergent)
- The analyzer and/or filtering system (in or post-column filters for acquisition of energy-filtered images and post column parallel or serial spectrometers for spectroscopic studies)
- The type of source and detector
- The total time T required for recording the whole set of 3D data cube (i.e. $N \cdot N \cdot n$ measurements, where $N \cdot N$ is the number of pixels in an image and n the number of energy-loss channels) is in the first case: $N \cdot N \cdot \Delta t_1$ and in the second one $n \cdot \Delta t_2$, but the total dose D received by the elementary area $dx.dy$ is proportional to $J_1.\Delta t_1$ for the STEM and to $J_2.n.\Delta t_2$ for the EFTEM. This leads to

$$T1/T2 = (N^2/n).(\Delta t_1/\Delta t_2) \tag{5.60}$$

and

$$D1/D2 = 1/n \tag{5.61}$$

Consequently the pros and cons of both approaches can be summarized as follows:

(i) The spectrum-imaging mode in a STEM is always more performant in terms of dose required, because of the intrinsic superiority of the technique for recording all energy-loss channels in parallel, while the EFTEM technique requires as many images (and irradiations) as the number of required energy-loss channels. Generally speaking, the spectrum-image mode is the best approach when mapping fine structures of EELS spectra is the goal. It is also an obvious solution for recording time-dependent variations of EELS spectra, as one records sequences of spectra in fixed probe mode and as a function of time, dose and eventually of a variable external parameter;

(ii) The comparison is not as obvious when considering the total time required for the acquisition. For small numbers of pixels and high numbers of n loss channels, the STEM is better, while for large values of N and small n the EFTEM is to be preferred. Of course, for a single filtered image such as the elastic one, EFTEM is the solution.

5.2.4 Elemental Mapping Using Core-Loss Signals

Background Extrapolation and Subtraction

The most common application of analytical microscopy is chemical mapping. It consists in obtaining images where the contrast is related to the spatial distribution of a given chemical species in the imaged area of the sample. In the spectrum imaging mode, the method consists in acquiring a collection of spectra in the energy range including the characteristic signals of interest by scanning the probe over a 2D (spectrum-image) or a 1D (spectrum-line) area. Since for each probe position the whole spectrum is recorded, as many chemical maps as desired can be *a posteriori* calculated by applying to each spectrum of the spectrum image the background extrapolation and subtraction method [42] described in Fig. 5.8. In the filtered image approach, all the $N \cdot N$ pixels of an image are acquired in parallel for a chosen energy loss. Therefore, an image acquired for an energy-loss value in the range of a given characteristic signal already contains some chemical contrast. However, the total intensity contained in each pixel of such an unprocessed image includes a strong contribution from the intense and non-chemically characteristic background. In order to obtain a purely chemical contrast, this contribution has to be removed. To do so, a series of images is acquired for different energy-loss values inferior to that of the onset of the characteristic edge (pre-edge images) and one image on the characteristic edge (edge image). The series of pre-edge images is used to model the background intensity before the edge in order to evaluate in the edge image the background intensity contribution and to subtract it out. This procedure is illustrated on Fig. 5.11.

Multiple Least Square Fitting

For cases where the above routine fails (for instance deviation from the power law model, overlap of different characteristic edges, detection of small concentrations), another straightforward method has been introduced: the use of multiple least square fitting techniques. One searches for the combination of reference signals which best reproduces an experimental curve, encompassing both background and characteristic edges [50, 51]. This procedure only applies to the image spectrum approach as it needs the acquisition of a whole spectrum. It uses reference spectra generally recorded from adjacent areas or calculated when none is directly available. It is quite versatile and may be used for different purposes. It has also been implemented for processing sequences of spectra [52]. The major limitation is due to the fact that the detailed shape exhibits variable fine structures depending on the local environment. However, this effect can also be used as a new possibility for mapping fine structures depending on bonding states or on orientation [53]. An example of such a procedure is given in Sect. 5.4.2.

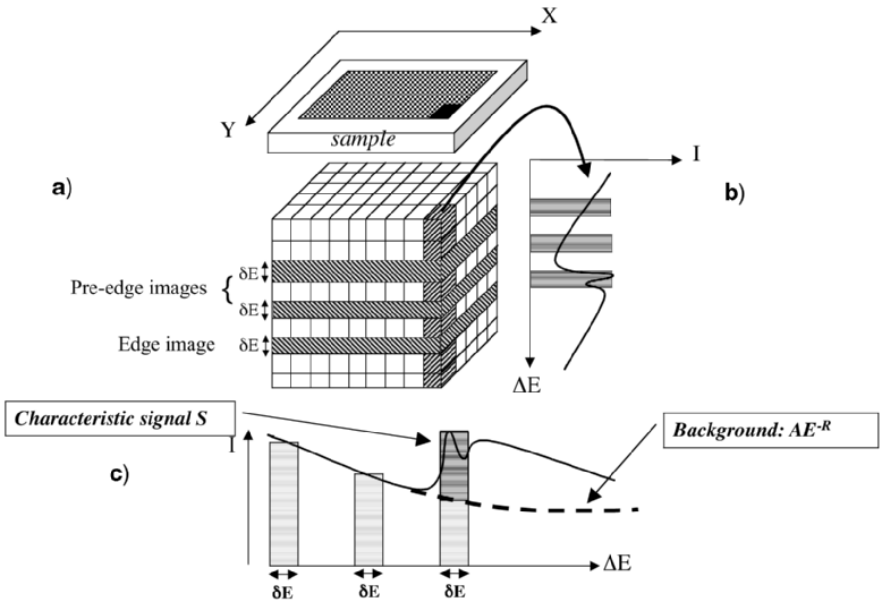


Fig. 5.11. Principle of chemical mapping using EFTEM. (**a**) The datacube, with on top of it, the imaged area of the sample. Three horizontal slices are displayed, corresponding to three filtered images. The vertical column corresponds to the EELS spectrum associated with one pixel of the image. (**b**) The same EELS spectrum displayed in superposition with the energy windows ΔE chosen for the 3 filtered images. (**c**) Illustration of the background extrapolation and subtraction with the 3 energy windows (Illustration after drawing from P. Bayla-Gullarnaud, CEA Grenoble)

5.3 Raman Spectroscopy of Carbon Nanotubes

5.3.1 Introduction

Since the pioneering work by Rao et al. [54], Raman spectroscopy has been widely used as a powerful tool for the study of single-walled carbon nanotubes (SWNT). It is estimated than in one paper over eight dealing with nanotubes science, Raman is used as an investigation or characterisation tool [55]. Several reviews were published on the theoretical and experimental aspects of Raman scattering by SWNT [56–59]. Our goal here is not to duplicate these references. In this introduction, we will only recall the major results and will try to explain why Raman spectroscopy became so essential in nanotube sciences. In the second part, we will consider different nanotube-based systems and will discuss how Raman can help in the investigation of the structure and electronic properties of these systems. We will first address the case of charge transfer compounds (doped nanotubes). We will also consider anisotropic bulk samples, especially fibers. We will then focus on functionalization and separation

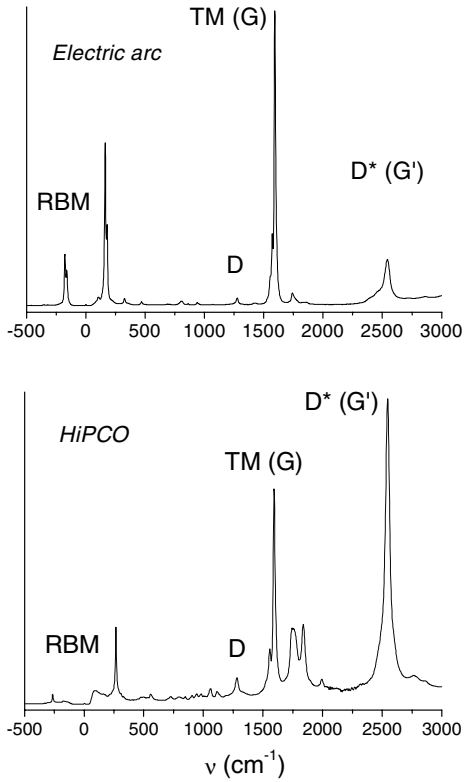


Fig. 5.12. Typical Raman spectra for electric arc (*top*) and HiPco (*bottom*) samples, with laser energy 1.16 eV. At this scale, one observes essentially, from low to high Raman shifts: both Anti-Stokes and Stokes RBM bunches, D band, TM bunch and D* band

of metallic and semiconducting nanotubes. We will finally discuss the recent features of the Raman spectra measured for isolated nanotubes.

The Raman signature of SWNT is unique and easily recognizable (Fig. 5.12). It is generally dominated by four bunches of peaks (Fig. 5.12). The first is in the range 1500-1600 cm^{-1} and corresponds essentially to some elongations of the carbon-carbon bonds usually referred to as tangential modes (TM) because the atomic motions remain in the plane of the graphene sheet, or as G-band since similar modes are observed in graphite (Fig. 5.14). Note that most of the carbonaceous species made of sp^2 hybridized atoms present a Raman signature in this spectral range. However, we will see below that it is rather easy to identify SWNT with respect to graphite, nanoparticles, fullerenes or multiwall carbon nanotubes. The second characteristic bunch is really specific to SWNT. It is usually observed in the range 100–300 cm^{-1}. It corresponds to in-phase radial motions of the carbon atoms and it is therefore usually referred to as radial breathing modes (RBM) (Fig. 5.13). Two other

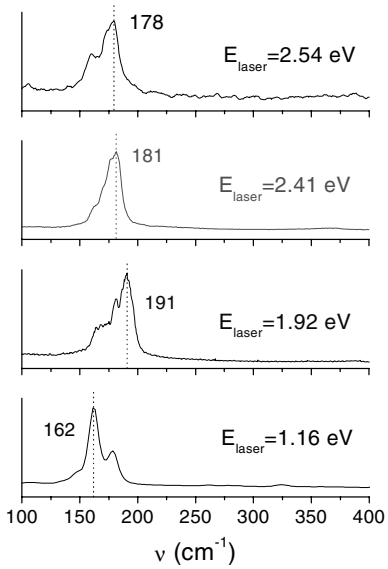


Fig. 5.13. RBM range for an electric arc sample and various laser energies. The diameter of the resonant tubes is predicted by the Kataura plot (Fig. 5.15) and explains why the RBM peaks apparently shift from a laser energy to another: the smaller diameters (larger RBM frequencies) are resonant at 1.92 eV, while the larger diameters (smaller RBM frequencies) are resonant at 1.16 eV

intense and broad features are generally observed: the so-called D-band in the range 1250–1350 cm^{-1} and its second harmonic, called D* or G' band in the range 2500–2700 cm^{-1}. These bands are not specific to SWNT, they are expected for most of carbonaceous materials. They are both observed because of a double-resonant process involving two resonant electronic states of the SWNT [57, 58]. Furthermore, in the double resonant mechanism responsible for the D-band, the electron is scattered elastically by a structural defect (vacancy, impurity, sp^3 carbon). This explains why the band is called D-band (D for defects) and why its intensity is often used as a probe of the structural or chemical purity of SWNT samples (see also Sect. 5.3.4). By contrast, the double-resonance mechanism responsible for the D* band doesn't involve any elastic scattering phenomenon, and the band can be observed on defect-free materials [57].

Let's focus on the two intrinsic features of SWNT, the TM and RBM bunches. These specific signatures are particularly intense and therefore easy to detect because Raman scattering by SWNT is a strongly resonant phenomenon [7, 54, 56, 57]. The resonance phenomenon makes even possible to detect the Raman signal from a single isolated nanotube because of the very large density of electronic states in the vicinity of the van Hove singularities, which

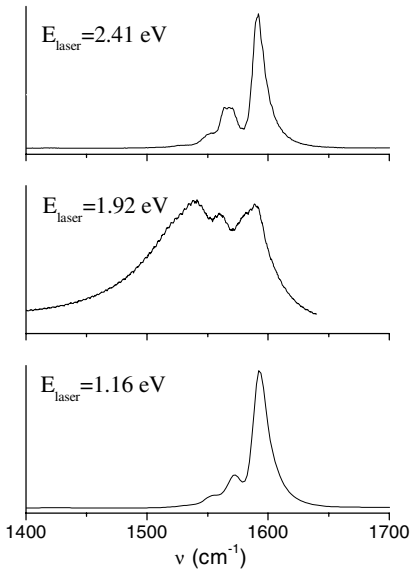


Fig. 5.14. TM range for an electric arc sample. The diameter distribution for this sample is between 1.2 and 1.5 nm

are characteristic singularities in the density of states of these unidimensional systems [56, 57, 60, 61].

In the single-resonance process scheme, which was shown to be relevant for the interpretation of the main features of the spectra, the Raman intensity goes through a maximum for spectra excited with an energy corresponding to an optical absorption threshold of the material [7, 56, 57, 60]. In SWNT, the allowed optical absorption (AOT) spectrum is strongly dependent on the structure of the nanotube. The AOT can be measured directly by optical spectroscopy [62]. The allowed optical transitions (AOT) were first assigned to electronic transitions between van Hove singularities [56]. Calculations of the energy of the van Hove singularities were achieved with a simple zone-folding scheme on the basis of nearest-neighbor tight binding calculations of the electronic properties of graphite. The plot of the AOT as a function of tube diameter was widely used to interpret the Raman data, and commonly referred as a 'Kataura plot' [60]. Although it does not describe the underlying physics completely, this first form of the Kataura plot was found to be very useful and relevant to interpret the Raman spectra for tube diameters between 1.2 and 1.5 nm and for laser energies between 1.9 and 2.5 eV.

For each pair of singularities, the AOT energy follows in first approximation the simple law [63]

$$\Delta E = \frac{2k\gamma_0 a_{CC}}{d} \tag{5.62}$$

where k is an integer, γ_0 is the nearest neighbor carbon-carbon overlap energy which is in the range 2.7–3.0 eV [56, 60, 64], a_{CC} is the nearest neighbor distance between carbon atoms (about 0.14 nm) and d is the nanotube diameter. Rigorously, the AOT energy depends not only on tube diameter but also on chiral angle because of the so-called 'trigonal warping effect' [57]. Another important result is that, at least for the four (two) first transitions, the ranges of AOT are well separated for semi-conducting (metallic) tubes. In (5.62), they correspond to $k = \{1,2,4,8\}$ ($k = \{3,6\}$), respectively. This is probably a unique case in solid state physics and this makes resonant Raman a very powerful tool for studying selectively semiconducting or metallic SWNT. Figure 5.15 presents the diameter-dependence of the AOT, as calculated in references [59]. It is amazing to observe on this diagram that the low-energy domains of AOT corresponding to semiconducting and metallic SWNT don't superimpose on each other. Moreover, it was reported by several groups that the TM profile of semiconducting and metallic SWNT is clearly different (see Fig. 5.14): the former is composed of a series of narrow and symmetric lines which can be well fitted by a set of Lorentzians, while the latter displays a broad and assymetric component which was assigned to Breit-Wigner-Fano (BWF) interferences between the phonon and an electronic continuum [64,65]. Since macroscopic samples are usually characterized by broad diameter distributions, the Kataura plot was successfully used to understand: (i) the changes of the TM profile of various macroscopic samples for various laser excitation lines as illustrated in Fig. 5.15 [60,65,66], (ii) the changes between Stokes and anti-Stokes spectra for the same sample [64], and (iii) the diameter-dependence of the relative intensities of RBM and TM bunches [67]. It is extensively used currently to probe the effectiveness of selecting or separating metallic from semiconducting tubes, as discussed in Sect. 5.3.4.

In order to extend the validity of the Kataura plot, corrections to the simple nearest-neighbor tight-binding scheme, including many-body interactions and chirality-dependent factors were recently proposed [68]. This so-called 'extended tight-binding' model was used to get a 'revised Kataura plot' (Fig. 5.16) which was shown to be a relevant tool to interpret the Raman data for small tubes and/or small laser energies [68–70]. Recently the role of excitons in the optical properties of carbon nanotubes was definitely demonstrated from two-photon absorption experiments [71, 72].

A third, and very popular, property of the Raman spectra of SWNT is that (because of its specific motion) the frequency of the RBM is, to first approximation, proportional to the inverse of the tube diameter ([7,56,57] and references therein). Therefore, a low-frequency Raman measurement is a very easy way to estimate SWNT diameters. Note that because of the resonance phenomenon, it is not straightforward to get an accurate determination of the diameter distribution. However, by scanning the Raman spectra over a broad range of laser excitation lines, one can get a signature of all the tubes in a sample and get a semi-quantitative picture of the diameter distribution (Fig. 5.13). Several calculations, in the valence force field (VFF) or tight-

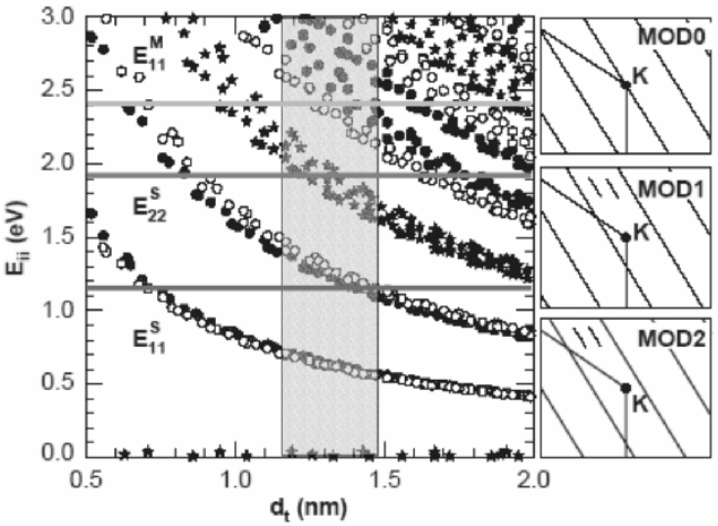


Fig. 5.15. Diameter-dependence of the allowed optical transitions (AOT), the so-called Kataura plot, as calculated by the first-neighbor tight-binding model. Stars, open and filled circles stand for metallic (MOD0), semiconducting I (MOD1) and semiconducting II (MOD2). The right panels show schematic figures defining the SWNTS classes: MOD0-metallic, where one cutting line crosses the K point, MOD1 and MOD2-semiconducting, with an opposite chirality dependence for the energy transitions (from [59]). The horizontal lines correspond to the laser energies used to measure the spectra in Fig. 5.14. The dashed vertical frame corresponds to the range of diameters for electric arc samples studied in Fig. 5.12

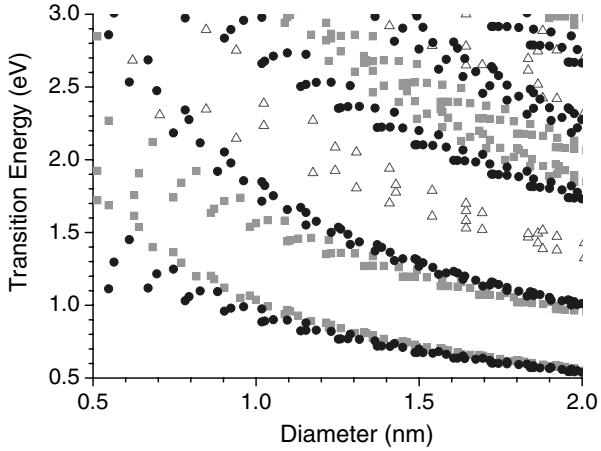


Fig. 5.16. Diameter-dependence of the allowed optical transitions (AOT), the so-called Kataura plot, as calculated in extended tight-binding model. *Open triangles*, *filled circles* and *squares* stand for metallic, semiconducting I and semiconducting II respectively (by courtesy of A. Jorio).

binding models, were carried out to determinate the relation between RBM frequency and SWNT diameter [7, 54, 56, 73]. For single tubes, the frequency is inversely proportional to the diameter, with a proportionality constant that depends on the model and the parameters used in the calculations

$$\nu_{\mathrm{RBM}}(\mathrm{cm}^{-1}) = \mathrm{A}/\mathrm{d(nm)} \tag{5.63}$$

Equation (5.63) was derived by several groups ([56] and references therein). However, the value of the prefactor A, is model-dependent (from 220 to $250\,\mathrm{cm}^{-1}\,\mathrm{nm}$). Moreover, in most materials, SWNT self-assemble in bundles of a few tens to a few hundreds tubes and the frequency of the RBM increases because of van der Waals tube-tube interactions. This was accounted for in some works, for example by considering a Lennard-Jones potential in the VVF model to describe intertube interactions [74, 75]. The most relevant way to discuss the validity of calculations is to compare with experimental data. A coupled diffraction and Raman study on different samples with various mean diameters was performed by Rols et al. [73]. The mean diameter of the tubes in each sample was determined by the analysis of the X-ray or neutron powder diffraction pattern. The Raman study of the same samples was carried out using several excitation energies and the mean RBM frequency was calculated as the average of the frequencies of all RBM peaks. An experimental master curve relating tube diameter and RBM frequency was derived from this study. This master curve was in good agreement with calculations [73]. Both data and calculations were well fitted by the following phenomenologic power law

$$\nu_{\mathrm{RBM}}(\mathrm{cm}^{-1}) = 238/\mathrm{d(nm)}^{0.93} \tag{5.64}$$

In the range 1–2 nm, equation (5.64) is equivalent to the relation:

$$\nu(\mathrm{cm}^{-1}) = 224/\mathrm{d(nm)} + 14 \tag{5.65}$$

where the first term corresponds to what is expected for isolated tubes while the second accounts for intertube interaction in the bundles. Equation (5.65) can be used to estimate the diameter distribution of SWNT *in bundles*. On the other hand, extended works were performed on aqueous suspensions of individual SWNT [69, 70], or on isolated tubes deposited on a substrate [57, 61, 76]. Different $\nu_{\mathrm{RBM}} = f(d)$ laws were derived from these works, illustrating the effect of the environment on the RBM frequency. We will come back on the main results of these studies in Sect. 5.3.5. In summary, Raman spectroscopy on SWNT provides a specific signature for each nanotube, with an indication on its diameter, possibly its chiral angle, and its semi-conducting or metallic character. One must also remember that Raman is a non-destructive technique [78] which can be used directly on any kind of sample (powder, suspension, mat, film, fiber, isolated tubes, ...). This explains why Raman scattering became such an essential technique in the science of nanotubes. In the next sections, we will illustrate the effectiveness of the technique to study various nanotube-based systems of current interest: doped SWNT, anisotropic fibers of SWNT, functionalized and chemically selected nanotubes, isolated tubes.

5.3.2 Charge-Transfer Compounds (Doping) of SWNT

The possibility of preparing synthetic metals from organic systems was early demonstrated with conjugated polymers and extensively studied for graphite and fullerenes [79,80]. The general idea is to prepare intercalation compounds where the intercalated species oxidize or reduce (p-or n-doping) the organic compound. Note that here doping means *intercalation* with *charge transfer*, rather than substitution of an atom by another one. Amphoteric doping, i.e. doping from both donors (alkali atoms) and acceptors (iodine, bromine) of SWNT was demonstrated by concductivity [81], Raman spectroscopy [82], and optical absorption studies [62]. Like for graphite and fullerenes, charge transfer can be probed in Raman scattering through the frequency of modes involving CC stretchs. Rao et al. reported significant down(up) shifts of the TM for SWNT doped with donors (acceptors) [82]. Alkali-doping was studied in details [83–88].

Typical spectra for saturation-doped samples are presented in Fig. 5.17 [89]. The TM component is much broader and more asymmetric than that of pristine samples, its maxima is downshifted with respect to pristine samples. For K doping in an electrochemical cell and a stoechiometry K/C above 0.02, Claye et al. measured a monotonically shift of $-370\,\mathrm{cm}^{-1}/\mathrm{e}^{-}/\mathrm{C\,atom}$ [85]. This shift is close to that measured for alkali-doped fullerenes ($-340\,\mathrm{cm}^{-}/\mathrm{e}^{-}/\mathrm{C\,atom}$ [79]) but larger than that measured for K-doped graphite ($-280\,\mathrm{cm}^{-1}/\mathrm{e}^{-}/\mathrm{C\,atom}$ [80]). The spectra measured at various laser energies are close to each other [83,88]. This indicates a loss of the resonance character of the Raman signal, due to a filling of electronic states and a shift of the Fermi level. Another consequence of the loss of resonance is the very weak intensity of the RBM signal (not shown) [83, 86]. By contrast, the downshift of the TM is not continuous and proportional to the charge transfer in the first steps of doping [85–88]. Claye et al. first reported an upshift of the TM peak in the first steps of Li and K-doping using an electrochemical method [85]. This phenomenon was addressed in detail in an in situ Raman and conductivity combined study on SWNT mats [86,87]. The changes of resistivity with doping and the corresponding Raman signatures are presented in Fig. 5.18. In the first steps of doping, the TM bunch broadens and shifts to high frequencies (Fig. 5.18) while the intensity of the RBM bunch decreases continuously (not shown [86]). When a first plateau of conductivity is reached (point d on Fig. 5.18), the spectrum is featured by a single broad line, upshift of about $4\,\mathrm{cm}^{-1}$. Here, the downshift expected for charge transfer is dominated by an upshift, likely associated with structural changes. Spectra d must be associated to a peculiar organisation of the alkali atoms, named 'phase I', possibly at the surface of the bundles. Note that at this step of doping, the resonance is already lost [86, 88]. Therefore, the (weak) RBM signal is not anymore selective over some particular diameters. The RBM bunch can be well fitted by a Gaussian function which is directly related to the distribution of diameters [90]. Phase I was further observed in Li or Na-doped samples prepared by

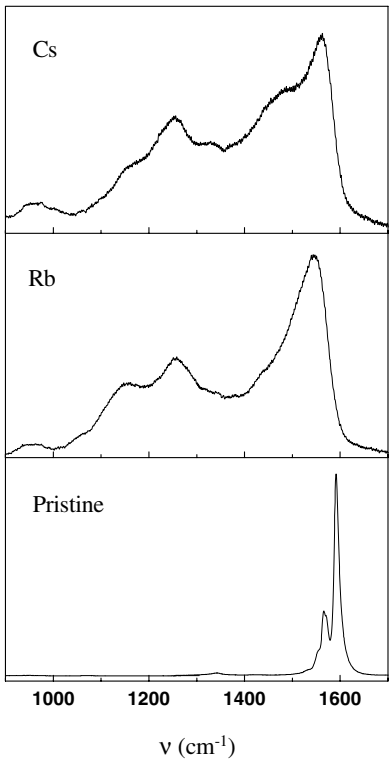


Fig. 5.17. Comparison of Raman TM spectra for an electric arc sample, with laser energy 2.41 eV, before doping and after saturation-doping with Rb and Cs (adapted from [83])

a controlled chemical method, where alkali ions are associated to counter-ions of various redox potentials in THF solutions [87, 91–93]. Very similar Raman features were observed from chemical doping and vapor phase doping. For further doping from phase I, one observes a drop of the resistivity down to a minimum and a second plateau (e in Fig. 5.18). The TM spectrum at e is close to that of saturation-doped samples, and the RBM signal is almost unmeasurable. The stoichiometry of saturation-doped samples was estimated to be about AC_8 [94]. The structure of saturation-doped samples was studied by X-ray and neutron diffraction [90]. It was evidenced that the dilatation of the bidimensional hexagonal array of nanotubes is weak. Comparison of diffraction experiments and calculations suggests that the alkali atoms are preferentially at the surface of the bundles and within the nanotubes [90]. Further studies are in progress to precise the structure and especially the presence of alkali atoms in the hollow channels between the tubes [95]. One also observed that Raman profiles are independent of the nature of the

alkali atoms for saturation doped samples [83, 87], which strongly suggests the universal character of the structure of alkali-doped samples.

As far as p-doping is concerned, various systems were studied. The main effect on the Raman spectrum is an upshift of the TM for saturation-doped samples, of about $8\,\mathrm{cm}^{-1}$ for iodine (the intercalated species are in this case (I_5^- and I_3^- linear chain complexes) [90, 96] and more than 20 cm^{-1} for bromine [82]. On the other hand, SWNT were shown to be oxidized in solutions of sulfuric acid [97, 98]. The BWF profile typical of metallic tubes is not observed when acid molecules are intercalated in the bundles. After a degassing treatment above 400°C which eliminates the intercalated species, the BWF profile is recovered. For H_2SO_4 doping, in situ studies reported an upshift of about 320 cm^{-1}/hole/carbon atom [98] of the main TM component when the laser energy matches resonance for semiconducting tubes. Recently, Izard et al. reported charge transfer involving likely SO_4^{2-} ions from SWNT suspended in sodium dodecyl sulfate (SDS) [99]. As a matter of fact, SWNT may be good candidates for doping with various species. The redox potential of the couple SWNT/reduced SWNT ($SWNT^-$) was estimated to be about $-0.5\,\mathrm{V}$ for tube diameters in the range 1.2–1.5 nm [91] and that of the couple oxidized SWNT ($SWNT^+$)/SWNT is likely only slightly larger. The

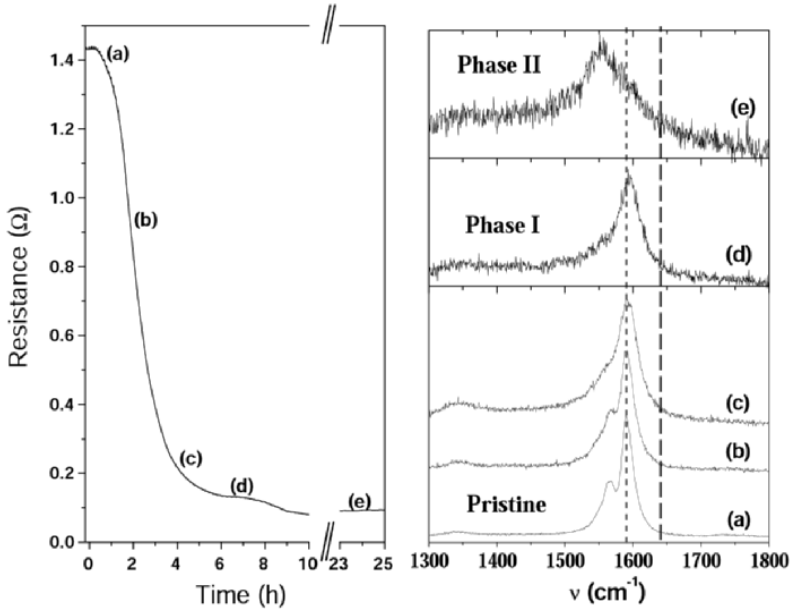


Fig. 5.18. Electrical resistance and a selection of TM Raman spectra for a buckypaper of electric arc SWNT, studied with laser energy 2.41 eV in an in situ Rb-doping experiment in the vapor phase. Phases I and II correspond to the two plateaus of conductivity ([86])

study of the diameter-dependence of the redox potential of SWNT was addressed in [100]. SWNT are therefore expected to be reduced not only by alkali metals (potential redox between -3 and $-2.7\,\mathrm{V}$), but also by other metals like chromium. On the other hand, SWNT can be oxidized by iodine, bromine (redox potential 0.5 and 1.0 V, respectively), by several acid compounds and metal salts. Alternatively, doping can be achieved by varying the potential at the contact between nanotube interface with an electrolytic solution [101,102]. A fine tuning of the added charge can be accomplished this way [102]. In the first steps of doping, coupled Raman and surface-area measurements suggest that SWNT bundles participate in charge transfer only with their external surface [102].

5.3.3 Anisotropic Fibers of Nanotubes

Several groups have carried out Raman experiments on anisotropic bulk samples of nanotubes. Rao et al. showed that the angle dependence of the Raman intensity of the TM mode calculated in a non-resonant model fitted well the experimental data for aligned multiwall carbon nanotubes, and especially went through a minimum for an angle of about 55° between the nanotube axis and the laser polarisation [103]. By contrast, the polarisation dependence of the Raman intensity for SWNT could generally not be interpreted with non-resonant calculations [104–106]. Gommans et al. showed that the VV (vertical/vertical, i.e. polarisations of the incident and scattered beam parallel one to each other) intensity of all Raman modes for metallic tubes assembled in a fiber decrease monotically when the angle ψ between the axis of the fiber and the incident light polarisation increases from 0° to 90° [104]. They proposed a simple model where the only non zero absorption cross section, and therefore the only non-zero component of the Raman polarisability tensor, is for light polarized parallel to the tube axis (the so-called antenna effect [57]). Duesberg et al. measured a similar ψ dependence on isolated or thin bundles of metallic SWNT [105]. The same result was obtained for SWNT aligned in fibers prepared by a spinning process, for resonance on both semiconducting and metallic tubes [106]. Typical spectra are displayed in Fig. 5.19 and Fig. 5.20. The VV intensity decreases continuously when ψ increases (Figs. 5.19 and 5.21). As far as the VH intensity is concerned (vertical/horizontal, i.e. crossed polarisations of incident and scattered beam), the signal first increases with ψ, goes to a maximum for $\psi = 45°$ and then decreases symmetrically down to $\psi = 90°$ (Figs. 5.20 and 5.21).

These results were fully interpreted by considering a single non-zero value of the Raman tensor and a Lorentzian distribution of the orientation of the nanotubes in the fiber with a cylindrical symmetry with respect to the fiber axis. A good agreement with the data was obtained with only two fitting parameters: the width of the distribution and an optical parameter taking account the anisotropy of the optical absorption. A typical fit of a whole series of data is presented in Fig. 5.21. One observes that the ψ dependence of

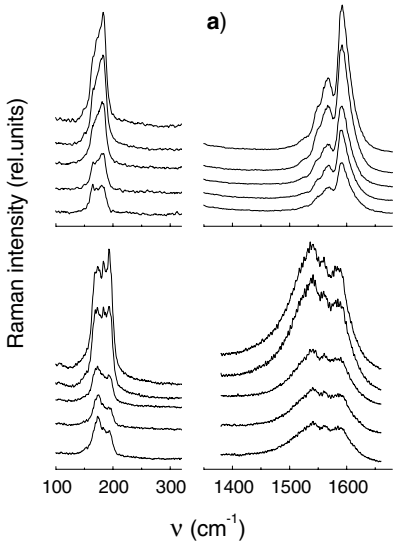


Fig. 5.19. Typical Raman spectra in VV polarisations for a fiber of SWNT prepared by the electric arc method in the RBM (*left*) and TM (*right*) ranges for laser energy 2.41 eV (*top*) and 1.92 eV (*bottom*). For each figure, from top to bottom: $\psi = 0°$, 11°, 45°, 68°, 90° (from [106])

the Raman signal is very close for RBM and TM, and for semiconducting and metallic tubes. The best fit of the data gives a full width at half maximum (FWHM) of the distribution of about 35° [106]. Raman spectroscopy appears as a useful tool to probe the orientational order in anisotropic bulk samples of nanotubes. However, systematic discrepancies were obtained with FWHM determined by X-ray diffraction on similar samples [107]. The differences may be related to different orientations of isolated tubes and bundles, or different organisations at the surface and in the bulk of the fibers. Further experiments are still in progress to understand these differences.

Alternatively, Zhou et al. considered a two-phase model of aligned and non-aligned nanotubes to describe the orientational order in fibers. They combined XRD and Raman to estimate the FWHM for the oriented part and the fraction of oriented nanotubes, respectively [108].

5.3.4 Functionalization and Separation

In the science of nanotubes, actual exciting challenges are 1) to modify chemically the nanotubes in order to prepare various nanotube-based systems and composites with tailored properties, 2) to separate tubes as a function of their diameter and chiral angle and/or to separate semiconducting and metallic tubes. Many contributions to these topics appear presently in the literature.

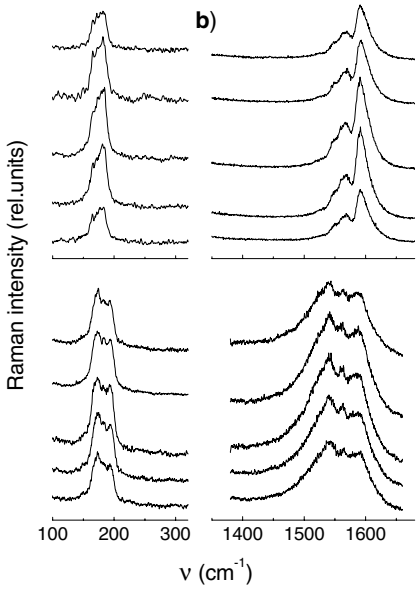


Fig. 5.20. Typical Raman spectra in VH polarisations for a fiber of SWNT prepared by the electric arc method in the RBM (*left*) and TM (*right*) ranges for laser energy 2.41 eV (*top*) and 1.92 eV (*bottom*). For each figure, from top to bottom: $\psi = 0°$, 11°, 45°, 68°, 90° (from [106])

Raman spectroscopy is systematically used as one of the techniques relevant to probe the chemical, structural or electronic changes in the nanotubes. Our goal here is neither to comment on the effectiveness of the functionalization or separation techniques, nor to give an exhaustive review of these works. We will simply choose a few examples in the literature and discuss the informations which can be obtained from the Raman spectra as well as the limits of the technique.

Raman spectroscopy was widely used as a sensitive probe of functionalization. One usually focus on the intensity of the D-band, whose frequency is laser energy dependent in the range 1250–1350 cm^{-1} [57]. We recalled in the introduction that this band does not correspond to a vibrational mode at the center of the Brillouin zone (Γ point) and should therefore be non-Raman active. Its observation is due to a double resonant process which involves scattering of an electron on a structural 'defect' that breaks the symmetry of the graphene sheet. Therefore, it is known as the 'defect band' and its intensity, often measured with respect to that of the G-band, is expected to increase with the density of structural defects, including sp^3 hybridized carbon atoms. However, the relation between the intensity of the D-band and the density of defects is not straightforward for several reasons: i) other carbonaceous species present in the samples, like graphite (except HOPG), carbon nanoparticles or

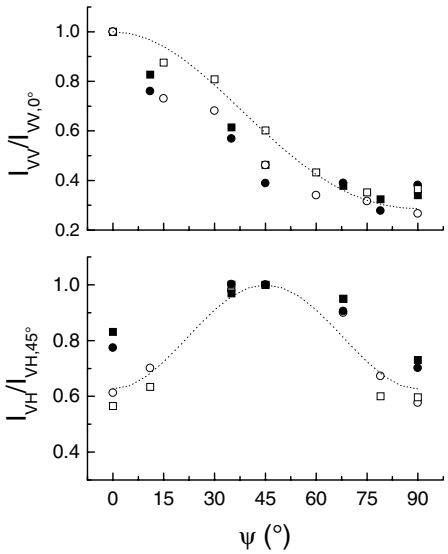


Fig. 5.21. Raman intensity as a function of angle ψ between fiber axis and incident light polarisation. Open (*solid*) symbols are for laser energy 2.41 eV (1.92 eV). Squares (*circles*) are for RBM (TM). The *dotted line* is the best fit of the whole data (from [106])

nanoshells, may also contribute to the intensity of the D-band, ii) the G-band is strongly polarized and therefore its intensity is very sensitive to the orientation of the nanotubes with respect to laser polarisation. Therefore, one cannot estimate reliably the relative intensity of the D-band on anisotropic samples, like buckypaper or fibers, or even on powders which easily orientate under uniaxial pressures, iii) the Raman signal for both the D and G-bands is a resonant signal which is by definition, sensitive to the electronic properties of the nanotubes. If the electronic properties change with functionalization, the Raman intensities for the pristine and functionalized material can not be directly compared, iv) there is a debate in the literature on the relation between chiral angle and observation of D-band. From the analysis of the dispersion curves, Maultzsch et al. proposed that the D-band can only be observed for metallic SWNT [26]. This was not checked in experiments where the D-band was observed both for semiconducting and metallic tubes [57]. However, the intensity of the D-band is likely chiral angle dependent. In summary, it is worth pointing out that a change in the intensity of the D-band may have various origins. It can only be considered as a signature of functionalization if it is associated with other characteristic spectral or physico-chemical signatures. Several examples of multi-spectroscopic studies are found in the literature. Bahr et al. studied the functionalization of SWNT by electrochemical redution of aryl diazonium salts [109]. Not only they measured a huge increase of the relative intensity of the D-band after functionalization, but they also reported

a general loss of intensity of the Raman signal, as well as significant changes in the optical spectra. Clear signatures of the functionalized moieties in infrared spectroscopy and electron microprobe chemical analysis were observed. A strong mass loss was measured in thermogravimetric analysis, and the same Raman signal as for the pristine sample was recovered at the end of the thermic treatment. All these results together give convincing indications that the SWNT were functionalized [109]. Holzinger et al. achieved covalent binding of various organic groups on SWNT via the addition of (R-)oxycarbonyl nitrenes [110]. Changes in the intensity of the D-band were moderated (increases from 50 to 200%) but they were associated to upshifts of the RBM bunch, attributed to additional covalent bonds on the carbon atoms and to a drastic change of the TM profile for resonance on metallic tubes, associated to charge transfer. Associated with X-ray photoelectron spectroscopy (XPS) and ^{1}H nuclear magnetic resonance (NMR), this allows the authors to evidence that functionalization succeeded [110].

On the other hand, several routes for bulk separation of semiconducting and metallic tubes were tested. Linear alkylamines were reported to physisorb on acid-treated SWNT [111]. It was suggested that the amine groups come in contact with the nanotube walls and that adsorption is more stable on semiconducting tubes than on metallic tubes. Therefore, it is expected that sedimentation, or solvent evaporation will favor separation of semiconducting and metallic tubes in the supernatant and the precipitate, respectively [111]. Raman measurements were used to support such hypothesis. It is shown that the TM of the supernatant displays a narrow and symmetric profile while that of the precipitate displays a BWF profile. In addition, the spectra are significantly different in the RBM range, and the attribution of the RBM peaks is in agreement with expected resonances for semiconducting and metallic tubes [111]. Strano et al. developed a functionalization technique using diazonium reagents which was shown to be highly selective for metallic tubes versus semiconducting ones [112]. The increase of the D-band intensity was associated to a drop of the BWF component in the TM bunch and of the RBM peaks associated to metallic tubes in the RBM bunch (Fig. 5.22). Selective functionalization was confirmed by expected changes in the UV-visible optical spectrum [112].

Finally, let us mention the recent study by Krupke et al. who developed a method of separation based on alternative current dielectrophoresis [113], taking advantage of the difference of the relative dielectric constants of semiconducting and metallic tubes with respect to the solvent. The spectra measured on a microelectrode, expected to be enriched in metallic tubes, were measured with a laser energy of 2.41 eV. They are featured by an increase (decrease) of the RBM intensity for RBM frequencies between 220 and 300 cm^{-1} (180 and 200 cm^{-1}), which correspond to resonance on metallic (semiconducting) tubes (Fig. 5.15). The authors also observe a concomitant increase of the intensity of the BWF component in the TM spectra, as expected in the case of selection of metallic bundles [113].

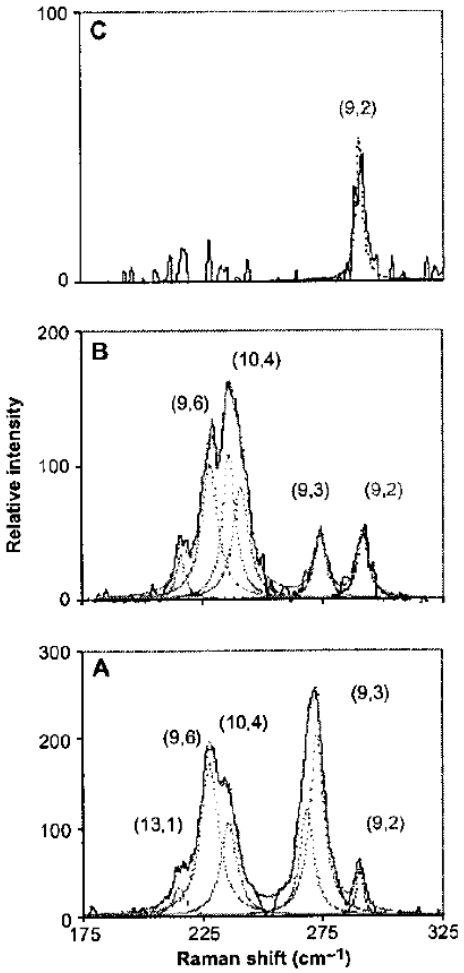


Fig. 5.22. RBM Raman spectra of HiPco samples (diameter distribution from 0.7 to 1.3 nm) for laser energy 2.33 eV. From the Kataura plot, essentially five tubes are expected to be in resonance, among which four metallic and one semiconducting (9,2). Selective reaction of diazonium reagents on metallic tubes is illustrated by the loss of RBM intensity for metallic tubes (from A to C, the functionalization rate increases) [112]

5.3.5 Isolated Tubes

Many theoretical studies of the vibrational properties of isolated tubes have been carried out so far, while Raman experiments on isolated tubes have been performed only recently. A detailed review of both theoretical predictions and experimental results was published recently [114]. First, Rao et al. [115] studied solutions of functionalized tubes, expected to be exfoliated from the

bundles, prepared with the method developed by Chen et al. [116]. Contrarily to what is expected from (5.63) and (5.64), an upshift of the RBM for the isolated tubes is observed with respect to the bundled tubes. This surprising result was interpreted as due to changes in the resonance conditions for the isolated tubes. Calculations showed that the AOT energy in bundled tubes is upshifted of a few tenths of eV with respect to isolated tubes. Therefore, the same laser line is exciting different tube diameters in isolated and bundled tubes, which can explain the shift of the RBM peak. However, part of the upshift reported in [115] must be attributed to molecular pressure from the solvent in the solutions, as stated by recent studies on suspensions [99].

A large number of experiments on isolated dry tubes prepared by a chemical vapor deposition technique on Si-SiO_2 substrates were carried out by Jorio et al. [61]. Single tubes or small bundles were first studied with a laser line at 1.58 eV. Only specific tubes can be in resonance at this energy. The plot of the Raman intensity as a function of RBM frequency measured for a large number of tubes goes through two maxima which correspond to an optimal resonance on the second (first) AOT for semi-conducting (metallic) tubes, respectively (Fig. 5.23). On the basis of the Kataura plot (Figs. 5.15 and 5.23) and considering that because of the trigonal wrapping effect (see introduction), armchair or chiral nanotubes with a large chiral angle have a higher probability for giving a strong signal, it was possible to assign a RBM frequency to a specific (n,m) tube, namely the (13,10) SWNT [61]. From the assignment of this single tube, the constant A in (5.63) can be estimated, which makes therefore possible the assignment of other RBM peaks. From the results of [61], the authors found $A = 248\,\mathrm{cm}^{-1}\,\mathrm{nm}$.

The same authors extended the study on isolated tubes to several laser lines [76]. This allowed them to study the frequency and intensity of the components of the TM bunch (G-band). They found that two peaks dominate the bunch: one is located around $1591\,\mathrm{cm}^{-1}$ (ω_{G^+}) independently of the diameter of the tube as predicted by calculations in the zone folding scheme. By contrast, the low frequency component (ω_{G^-}) follows a diameter dependence which is different for semi-conducting and metallic tubes (Fig. 5.24).

In these experiments an asymmetric BWF profile of the TM was measured for isolated metallic tubes [76,97]. By contrast, in several other studies on powders, doped films or suspensions, it was reported that the exfoliation of the tubes was associated to a drop of the BWF component (see for instance [117]). A strong enhancement of the BWF line was reported for thick bundles, both experimentally [117] and theoretically [118]. Recently, using a complete procedure including the preparation of the substrate, the sample preparation, atomic-force-microscopy imaging and Raman spectroscopy, it was unambiguously shown that the BWF component can be totally absent in the Raman response of an individual metallic tube [119]. In other words, a symmetric semiconducting-like profile of TM can also originate from a metallic tube (see also [120]).

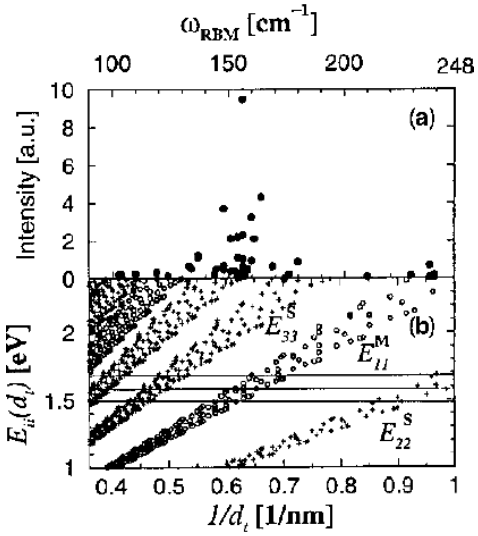


Fig. 5.23. Intensity of RBM peaks as a function of Raman shift for a series of 42 isolated dry tubes deposited on Si/SiO_2 substrates. The two maxima correspond to the two optimal resonance conditions, as illustrated in the Kataura plot presented in the bottom part of the figure ($\gamma_0 = 2.9\,\text{eV}$). For scaling the top and bottom X-axis, the authors used equation (5.63) with $A = 248\,\text{cm}^{-1}\,\text{nm}$. From [61]

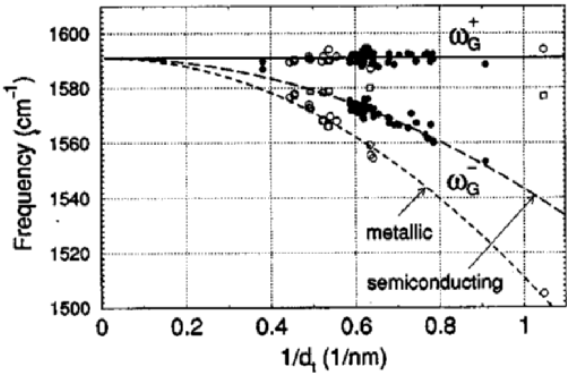


Fig. 5.24. Diameter-dependence of the Raman shift of the two main components of the TM bunch, as measured on isolated dry tubes deposited on Si/SiO_2 substrates. The frequency of the high frequency component (ω_{G^+}) is independent of the tube diameter. *Dotted lines* are best fits of the frequency of the low frequency component (ω_{G^-}): $\omega_{G^-} = 1591 - C/d^2$ with $C = 47.7\,(79.5)\,\text{cm}^{-1}\,\text{nm}^2$ for semiconducting (metallic) tubes (from [76])

On the other hand, the preparation of aqueous suspensions of SWNT (usually the tubes are wrapped with a surfactant which prevent them from rebundling) has allowed Raman [69, 70] and photoluminescence experiments to be performed on individual nanotubes [121, 122]. The excitation profile of each RBM was measured, leading to the determination of the experimental transition energies E_{ii}^{exp} for each tube characterized by its RBM frequency (ω_{RBM}). The comparison between the experimental (E_{ii}^{exp}, $1/\omega_{RBM}$) patterns and the (E_{ii}^{the}, d) Kataura plot obtained in the framework of a third neighbor tight-binding calculations leads to the assignment of each RBM to a specific (n,m) tube (Fig. 5.25).

Within each band in the Kataura plot of Fig. 5.25, the E_{ii} energies follow family patterns. The dashed line in the theoretical plot of Fig. 5.25 indicates branches that are formed by tubes with $2n+m$ constant. The indices of neighboring tubes in a given branch are related through $(n+1, m-2)$ or $(n-1, m+2)$ where $n \geq m$. In a same branch the tubes belong to the $(n-m) \bmod 3 = q$ family, with $q = -1$ for semiconducting type I SWNT, $q = 1$ for semiconducting

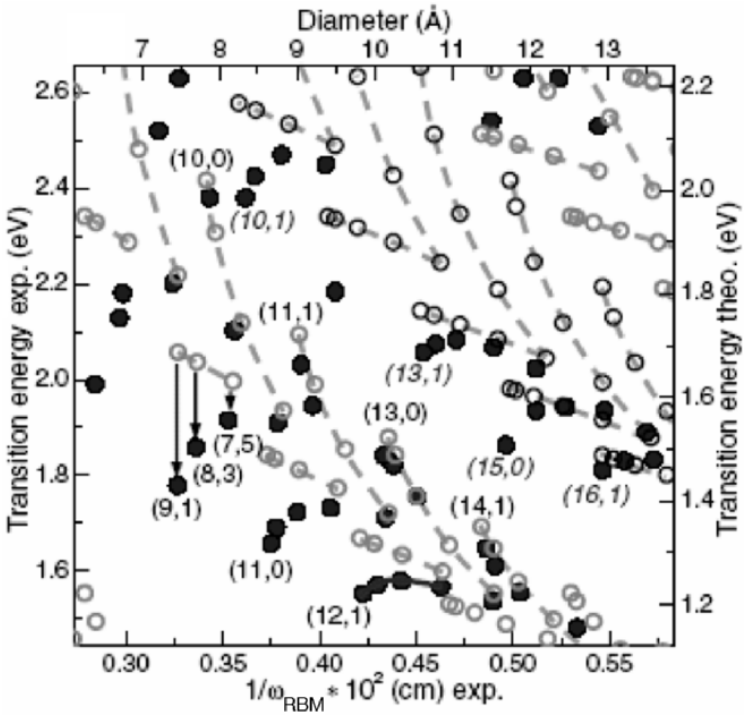


Fig. 5.25. Kataura plot from third neighbor tight-binding calculations (*open circles, right-top axes*). Gray and black indicate semiconducting (2nd and 3rd transitions)and metallic tubes respectively. Experimental results (*filled circles, left-bottom axes*) (from [69])

type II SWNT. The best overlap between the experimental (E_{ii}^{exp},$1/\omega_{RBM}$) pattern and the calculated (E_{ii}^{the}, d) pattern allows to assign the (n,m) indices of the tubes [69, 70]. An example of such an assignment is shown on Fig. 5.25. From this assignment the diameter dependence of the RBM is fitted by the following relation: $\omega_{RBM} = A/d + B$ with $A = 214.4\,cm^{-1}\,nm$ and $B = 18.7\,cm^{-1}$ [69] ($A = 218\,cm^{-1}\,nm$ and $B = 10\,cm^{-1}$ were found in [70]). The origin of the constant B term is assigned to environmental effects (the interaction between the tubes and the surfactant/solvent). These (n,m) assignments can be compared with previously proposed (n,m) assignments for semiconducting SWNTs, based on photoluminescence (PL) measurements [122]. Initially, the PL results were expected to be fully interpreted from the Kataura plot calculated in the simplest tight-binding approach. However, even if these calculations provide a good qualitative understanding of the PL phenomenon, there are significant deviations in the values of the emission energies. It was recently demonstrated that these discrepancies are due to the excitonic character of the optical transitions [71,72], which are not accounted for in the simple tight-binding model. Figure 5.26 plots the ratio of excitation and emission energies as a function of excitation wavelength [122]. The experimental data form typical patterns. From a comparison of these patterns with tight binding calculations (Fig. 5.26.b), each solid line in Fig. 5.26.a was assigned to a series of SWNT that shares the same n-m value. The fluctuations of the ratio V_{22}/V_{11} as a function of chiral angle are expected from the trigonal warping effect [57]. However, the mean-value for the ratio expected from calculations is 2 (k = 1,2 in (5.62)) while it is close to 1.75 for the experimental results (Fig. 5.26.a). These discrepancies were assigned to excitonic interactions [123]. In order to assign each spectral feature of Fig. 5.26 to a given tube diameter, measurements of the Raman RBM frequencies were achieved. The best fit of the data gave a diameter dependence of the RBM frequency close to $\omega_{RBM}(cm^{-1}) = 223.5\,(cm^{-1}\,nm)/d\,(nm) + 12.5\,cm^{-1}$.

Finally, very recently, by combining Raman spectroscopy and electron diffraction on the same free-standing SWNTs, the (n,m) indices and the RBM frequencies of several SWNTs were accurately and independently measured [77]. The RBM frequency versus the inverse of the diameter has been derived in a broad diameter range (from 1.4 to 3 nm). The best fit of the data gives: $\omega_{RBM}(cm^{-1}) = 204\,(cm^{-1}\,nm)/d\,(nm) + 27\,cm^{-1}$. Since most of the environmental influences are absent for free-standing SWNTs, the assignment of the constant term to the effect of the environment is questionable here, and these results rather suggest that the dependence of the RBM frequency with the inverse of the diameter might be slightly non-linear. It was shown by first principles calculations that the relation between ω_{RBM} and $(1/d)$ is non-linear for tubes with very small diameters [124]. To elucidate this point definitely, investigation on well-characterized (n,m) free-standing SWNTs of small diameters are in progress.

In summary, it was demonstrated that Raman spectroscopy is a complete tool to study the structure and electronic properties of isolated SWNT. The

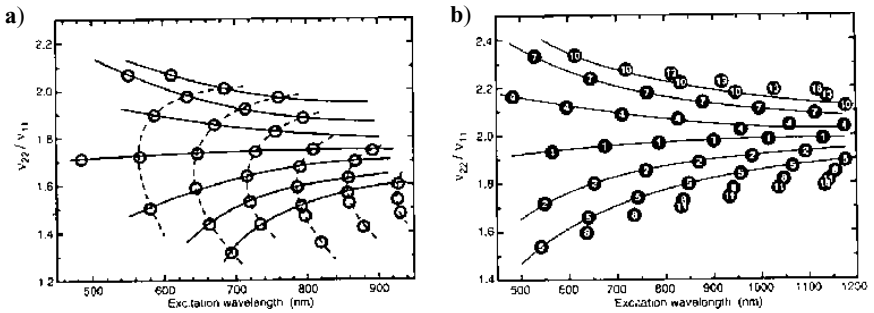


Fig. 5.26. Ratio of excitation to emission energies as a function of optical excitation wavelength (**a**) for individual SWNT dispersed in an aqueous suspension, (**b**) as calculated from an extended tight binding model. *Solid lines* correspond to series of nanotubes which share the same (*n*-*m*) values. *Dashed lines* show other perceived patterns (from [122])

coupled study of RBM frequency and resonance conditions potentially allows to identify the structure of a particular isolated nanotube, i.e. its diameter and chiral angle. One must, however, underline that the attribution is in part model-dependent. It was suggested that the relation between RBM frequency and (*n*,*m*) indices could be dependent on the environment of the tubes, including tube-tube interactions in bundles and interactions with substrates of adsorbed molecules. Recently, the combination of Raman spectroscopy and electron diffraction on the same free-standing SWNTs provided the first accurate and independent determination of the (*n*,*m*) indices and the RBM frequencies [77].

5.4 Applications of EELS to Nanotubes

5.4.1 A Few Examples of Elemental Mapping with EELS Core Edges

Filtered Images from Catalytic Particles in SWNT Samples

The first example deals with the investigation of the chemical composition of catalyst particles in relation to the morphology of as-produced single-walled carbon nanotubes by arc-discharge. Two co-catalysts were used: a transition metal, Ni and a rare earth, Ce. Figure 5.27 shows the computation of the chemical maps for Ni (top) and Ce (bottom) from a series of filtered images. In order to optimise the signal to noise ratio in the chemical maps, Ni $M_{2,3}$ and Ce $N_{4,5}$ edges were used due to their high ionisation cross section. For both elements, two pre-edge images and one edge image are shown. The pre-edge image contains a thickness information (the intensity of the non-characteristic

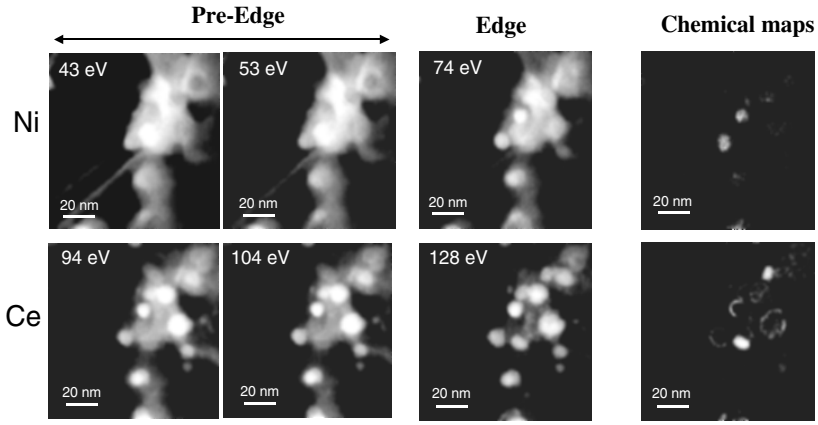


Fig. 5.27. Example of chemical mapping using the image-spectrum mode on Ni-Ce catalyst particles in a SWNTs sample. The chemical maps for Ni (*top*) and Ce (*bottom*) were calculated from a series of filtered images acquired before and on the Ni $M_{2,3}$ and Ce $N_{4,5}$ edges respectively. Filtered images courtesy of Julie Gavillet et al. [125]

background is proportional to the local total thickness of the sample). One sees that the edge image already contains chemical information (the particles are visible). This chemical contrast is much enhanced after background subtraction. One interesting feature is the non-homogeneous distribution of Ce within the different particles. In particular, it is possible to observe the formation of cerium-based surface compounds. This example illustrates one important implication amongst numerous ones of the characterization work. Here, chemical mapping provides precious experimental inputs for the elaboration of growth mechanism models [125]. This coupled interplay between precise structural and chemical characterisation studies and the conception of growth models is described in detail in Chap. 2.

Sensitivity, Limits of Detection in EELS Elemental Mapping

From its first introduction as a powerful microanalytical tool, EELS was recognized as a potential technique to tackle the identification of isolated atoms [46, 126, 127]. These studies were performed on random distributions of heavy atoms on ultra-thin objects and the criterion for identification was that the signal-to-noise ratio for the characteristic signal be above a threshold value. It did not require the spatial resolution for separating different atoms. The first real demonstration of these ultimate capabilities has been realized on gadolinium doped peapods [128]. In this case, the spectrum-image technique has been used and quantitative maps for Gd and C atoms contained in the self supported fullerene molecules and nanotube envelopes have been obtained (see Fig. 5.28). The signal-to-noise ratio for identifying one Gd atom with its

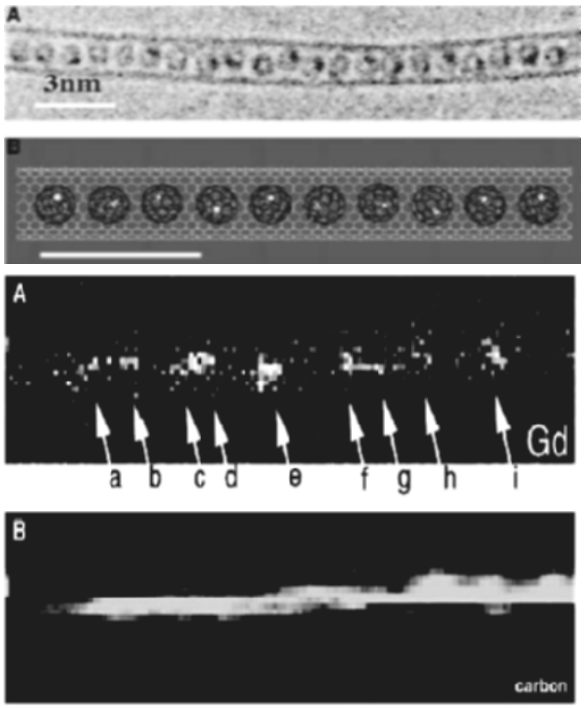


Fig. 5.28. EELS mapping of individual Gd atoms encapsulated in C_{82} fullerene molecules inserted along the empty core of an individual SWNT. Top of the figure: structure of the nano-object. (**A**) HREM image, (**B**) schematic representation of an analyzed nanostructure; Bottom of the figure: chemical maps extracted from a 32×128 pixes spectrum-image, 35 ms per pixel, bar length is 3 nm. (A) Gd N_{45} map. Intense pixels have been shown to correspond to aggregated Gd clusters made of a few atoms, grown under the incident electron beam irradiation. (B) C K map (courtesy of Suenaga et al. [128])

M_{45} edge signal is of the order of ten. The resolution to separate two of them is reached, in spite of a probe diameter of the order of 0.7 nm, because the Gd atoms are generally maintained apart from one another by more than one nanometer as they are trapped in separate adjacent C_{82} molecules.

5.4.2 Mapping Bonding States and Electronic Structures with ELNES Features

An example of multiple least square fitting is given in a complex situation found in some BN nanotube samples synthesized according to the procedure described in [129]. The unexpected large number of species found in these samples such as B, C, Ca, N, O, made the analysis complicated and the information gained by comparing the different chemical maps appeared insufficient for an accurate characterization of the different boron chemical states.

In Fig. 5.29a are shown the 3 different BK near-edge fine structures (ELNES), which were chosen as the reference spectra to model the experimental spectrum. They are characteristic of the three following chemical states for boron: boron in hexagonal boron nitride, boron oxide and pure boron. These three materials were expected to be coexisting in the sample. Figures 5.29b–d show an example of different NNLS maps computed from a 64×64 spectrum image and associated with the different boron states mentioned earlier: B in pure boron (Fig. 5.29b), B in hexagonal boron nitride (h-BN) (Fig. 5.29c) and B in B_2O_3 boron oxide (Fig. 5.29d). The maps provide a clear understanding of the morphology of the investigated area: pure boron particles of two distinct sizes and oxidized at their surface are sitting on a network of BN nanotubes and polyhedral h-BN particles.

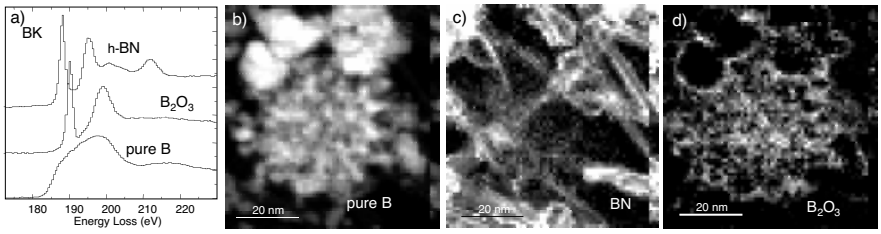


Fig. 5.29. Multiple least square fitting maps deduced from a 64×64 spectrum image acquired on a BN nanotubes sample. **a**) BK ELNES references from h-BN, B_2O_3 and pure born **b**) Pure B. **c**) B in hexagonal boron nitride (h-BN) **d**) Boron in B_2O_3 boron oxide

5.4.3 Curvature Induced Effects on the Chemical Bonding in Single Shell Carbon Nanotubes

It is now clear that core-edge signals contain more than just a chemical information. Indeed they constitute a powerful signature of the solid state effects on the excited site. Valuable information is retrieved when the ELNES are used as fingerprints in a first approach (see previous section). But in many cases, when the experimentalist is confronted with a new situation, the understanding of the measured ELNES needs the support of simulations. This is the case for single shell nanotubes which unoccupied density of states differs from that of graphite. Let us compare now EELS data from graphite with those from a single shell carbon nanotube. The respective CK ELNES are shown in Fig. 5.30 left (from [130]). A large change is observed in the σ^* band of the single shell nanotube while no significant modification of the π^* peak is observed. Ab initio calculations are needed in order to reproduce the

experimental spectrum and to interpret the physical origin of the changes in the fine structures. The results of such calculations are shown in Fig. 5.30 right (from [131]) for graphene, a (10,0) nanotube (R = 0.4 nm) and a (5,0) nanotube (R = 0.24 nm). The dashed line in each figure represents planar graphite. It shows that the loss of interplanar interaction between graphene and graphite does not affect significantly the EELS spectrum. By contrast, the effect of curvature is responsible for a loss in the structuration of the σ^* band, while no significant change is observed in the π^* peak for low curvature. The fact that, experimentally, the π^* peak remains unchanged is at first glance surprising, since the local coordination is changed in single-shell nanotubes compared to planar graphene and graphite. However, a rough estimation of the change in interaction with change of the local coordination following a simple tight binding approach, confirms that a broadening of only 0.3 eV of the π^* peak is to be expected for 1 nm diameter nanotubes, which is beyond the resolution of the spectrometer used in this experiment. As shown on Fig. 5.30 right, ab initio calculations predict a splitting in the π^* peak for single shell nanotubes with diameters smaller than 0.5 nm. Therefore no significant modification of the π^* band is expected in experimentally available nanotubes (nanotubes with a diameter larger than around 1 nm). This is a valuable information since it is indicative of the preservation of the covalent nature of the chemical bonds is such tiny nanotubes. Further measurements performed with higher energy resolution are now required to probe finer effects such as the potential presence of van Hove singularities in the measured signal.

5.4.4 Study of the Valence Electron Excitations in Nanotubes

Although less investigated than the core-loss energy region in the nanotube research field, the low-loss energy-region (from 1–2 eV to 50 eV) provides useful complementary information on the electronic properties of solids. As a matter of fact, studies on the dielectric or optical properties of solids (metals, semiconductors, quasicrystals, ...) by EELS are numerous. However nanoparticles such as nanotubes present extra difficulties. Indeed, due to the small sizes considered, standard concepts like the dielectric response have to be refined as well as the usual physical related quantities (dielectric constant, reflectivity, ...). Let us be more precise and start from a bulk material. Studying the dielectric properties consists in probing the response to an electromagnetic field, for example by measuring the reflectivity or the absorption of the material (optical measurements) or the loss function (in an EELS experiment). These quantities are in a straightforward way related to the dielectric constant. The boundary conditions are then playing no role. In the case of an anisotropic material, this basic idea remains valid, except that the dielectric constant has to be replaced by a dielectric tensor. Then, care has to be taken to orient the optical anisotropic axis with respect to the polarization of the electromagnetic field (optical measurement) or to the $\boldsymbol{q}$-vector (EELS measurement).

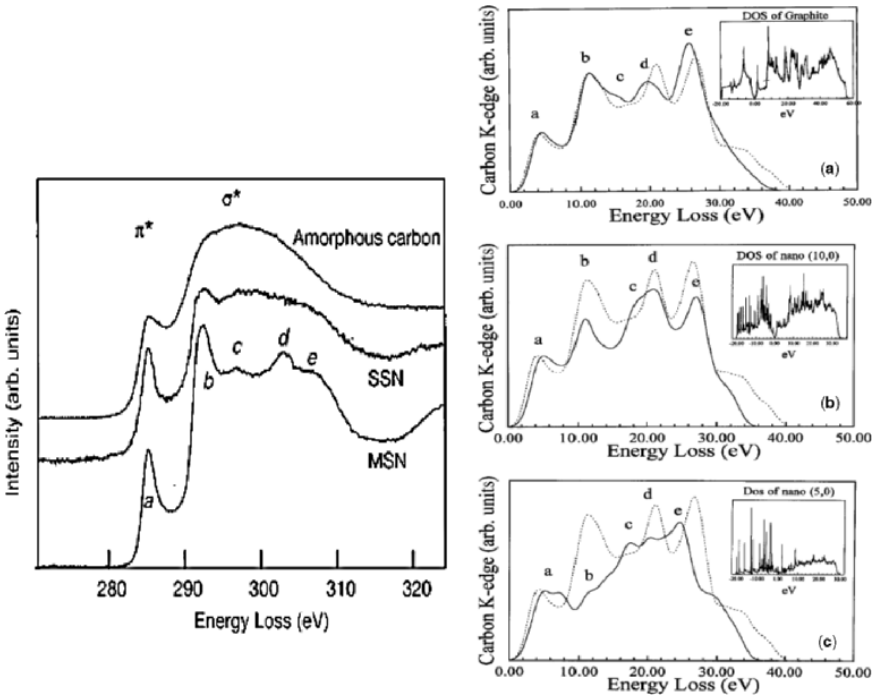


Fig. 5.30. Curvature induced effects on the chemical bonding in single shell carbon nanotubes. *Left*: experimental Carbon K-edge ELNES on a 30-nm-diameter MWNT (MSN) compared with that on a 1-nm-diameter SWNT (SSN). For reference, ELNES from amorphous carbon is given and exhibits a wider π^* peak (from [130]). *Right*: calculated EELS spectra for graphene ($R = \infty$), a (10, 0) SWNT (R = 0.4 nm) and a (5, 0) SWNT (R = 0.2 nm). The dashed line in each figure represents the simulated ELNES for planar graphite. Inset is the calculated total density of states for each (from [131])

Now, let us reduce the size of the material being considered. We then face a new situation, which covers three topics. First of all, the surface effects are becoming predominant (or, from a theoretical point of view, the boundary conditions are beginning to play a role). In the case of hollow nano-objects like nanotubes, these surface effects are all the more important as electromagnetic surface modes from both surfaces (inner and outer) can couple and affect greatly the response of the nanotube. Secondly, the option of studying one individual nanoparticle becomes impossible in an optical experiment, as soon as the size of the particle is less than $\lambda/2$ (let us say 200 nm), which is much larger than the diameter of a nanotube. One needs then to use an EELS experiment, combined with the imaging abilities of a TEM. Thirdly, in the case of anisotropic particles such as nanotubes, the use of a parallel beam averages the response of the nanotube over all the relative orientations

of the anisotropic axis with respect to the momentum transfer $\boldsymbol{q}$ of the incoming electron wave. To avoid this averaging effect, a first solution is to use a very small electronic probe (compared to the typical size of the nanotube) which can be driven from outside of the particle to the inside of it. For a non penetrating beam, one probes the evanescent field induced by the coulombic field of the incident electron. By analogy with optical methods, such measurements are referred to as near-field EELS measurements. This solution is interesting because, not only does it discriminate between surface and bulk polarization effects, it also provides access to the relevant measurable quantities: the multipolar polarizabilities, which take into account the geometry of the particle. In particular, polarizability (which is defined as the proportionality coefficient linking an external potential to the induced one) can be accurately experimentally probed. The use of a dielectric model to relate the polarizability to the bulk dielectric constant allows then to define and describe the dielectric response of a nanotube. An alternative solution is to use a $\boldsymbol{q}$-resolved experiment [29] (see Sect. 5.4.5), at the cost of the loss of spatial resolution. In that case, complementary information on the nature of the involved valence excitations in a thin film of nanotubes can be extracted from the dispersive character of the identified energy modes.

Near Field EEL Spectroscopy Experimental Evidence of Surface Plasmon Coupling in Nanotubes

To investigate the dielectric response of isolated SWNTs, spatially resolved EELS measurements have been carried out using a scanning transmission electron microscope in a near-field geometry. Spectra have been compared with those acquired on multiwalled carbon nanotubes made of different numbers of layers, and with simulations performed within the framework of the continuum dielectric theory, taking into account the local anisotropic character of these nanostructures and adapted to the cylindrical geometry. As shown in Fig. 5.31, for thin MWNTs, two polarization modes have been identified at 15 and 19 eV. It has been demonstrated that this response can be understood by accounting for the strong-coupling limit of surface plasmons in thin MWNTs. Indeed, each mode can be indexed as a tangential or radial plasmon mode respectively, resulting from the coupling of the two surface modes on the internal and external surfaces of the nanotubes. These modes named after the symmetry of their field lines (see Fig. 5.31) are the counter part of the symmetric and asymmetric modes in a thin slab. Moreover, it can be shown that the tangential mode can be exclusively associated with the in-plane excitation of the electron gas while the radial mode noticeably implies out-of-plane excitations [34]. Finally, it was shown that the dielectric response of a SWNT, displaying a single energy mode at 15 eV, can be understood in the dielectric model as the thin layer limit of surface plasmon coupling in MWNTs: the single mode of SWNTs, centered at 15 eV, can then be described as the limiting case when the radial mode vanishes and the only tangential mode

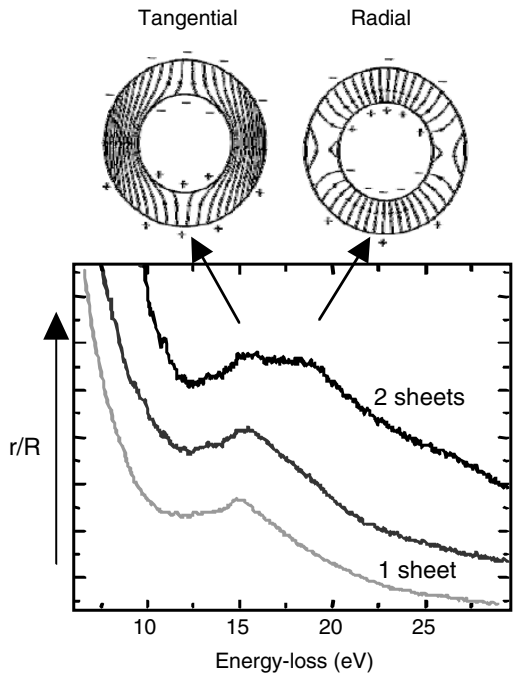


Fig. 5.31. Near-field EELS spectra for a double layer tube and two SWNTs. The modes at 15 eV and 19 eV are associated with tangential and radial modes respectively, which result from surface plasmon coupling on both surfaces of the tube

remains [53]. Importantly, these results show that the notion of dielectric continuum remains relevant for the description of such a monoatomic layer object.

5.4.5 Plasmon Dispersion Relations in Ropes of SWNTs

A complementary way of studying the valence electron excitations in nanotubes is to perform EELS momentum resolved experiments. This allows, in principle, the study of momentum dependence of the different excitations found in an EELS spectrum in order to gain an insight into the nature of the excitations. In particular, the dimensionality of the 'electron gas' in the nanotubes could be probed. To date, only one experimental work [132] and a few theoretical works have been published on that subject [133]. Here, we describe briefly the experimental work. EELS was carried out in a high-resolution spectrometer, extensively described in [132]. This spectrometer provides a resolution of 115 meV and 0.05 $Å^{-1}$ in the momentum space. Such high $\boldsymbol{q}$ resolution, unreachable in a microscope, is achieved at the cost of the spatial resolution, which is then non-existent. The sample is a thin film, about 1000 Å-thick, containing approximately 60% of purified SWNT (mean radius

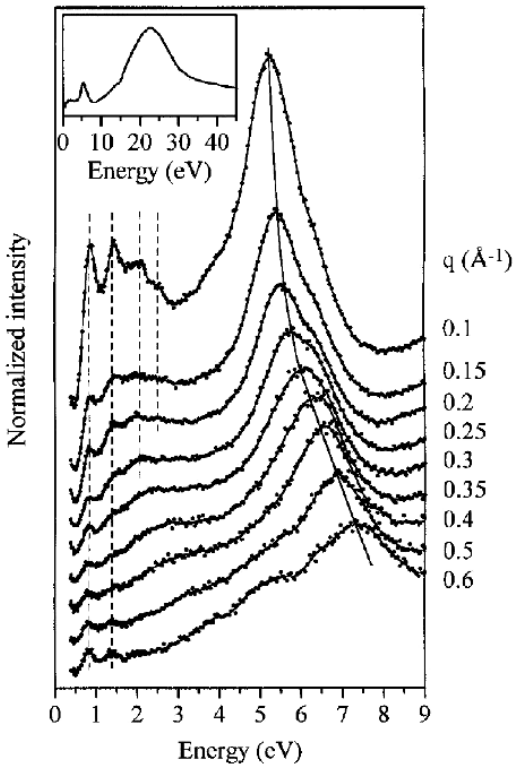


Fig. 5.32. The loss function of purified SWNTs from EELS in transmission for the different q values shown. The inset contains the loss function over an extended energy range for q = 0.15 Å^{-1}, showing the π plasmon and the $\pi + \sigma$ plasmon at around 5 and 22 eV, respectively (courtesy of Pichler et al. [132])

1.4 nm) with no preferable orientation within the film. The measured loss function $Im(-\frac{1}{\epsilon(\omega,\boldsymbol{q})})$ is shown in Fig. 5.32. Because no spatial resolution is accessible, one obtains in that case the loss function of the whole film including graphite, fullerenes and amorphous carbon from the 40% non-purified part of the sample. Moreover, due to the disorientation of the nanotubes within the film, the measure is averaged on the direction of the $\boldsymbol{q}$ vector within the film. From the different loss functions, the two dispersion behaviors of the π excitations can be identified out ($\pi + \sigma$ excitations are not considered here). At low energy (see Fig. 5.32) a collection of modes shows no dispersion. They are identified as localized excitations around the circumference of the tubes, or to put it another way, as the remnants of the Van Hove singularities in the density of states that is interband transitions at one dimension. These excitations are absent in graphite. At higher energy (5–7 eV), a dispersive excitation is found, which is identified as the π plasmon, when polarization occurs along the tube.

References

1. M. Born and K. Huang: *Dynamical theory of crystal lattices* (Clarendon Press, Oxford 1954)
2. A.A. Maradudin, E.W. Montroll, and H.H. Weiss (eds.): *Theory of lattice dynamics in the harmonic approximation*, Solid State Physics, Supplement 3 (Academic Press, 1963)
3. G.K. Horton and A.A. Maradudin (eds.): *Dynamical properties of solids*, vol. 1 (North-Holland Publishing Company, 1974)
4. P. Lambin and J.P. Gaspard: Phys. Rev. B **26**, 4365 (1982) and references therein
5. C. Benoit, E. Royer and J.P. Poussigue: J. Phys.: Condens. Matter **4**, 3125 (1992)
6. M.P. Allen, D.J. Tildesley, *Computer Simulation of Liquids* (Clarendon Press, Oxford 1987)
7. J.-L. Sauvajol, S. Rols, E. Anglaret and L. Alvarez: Carbon **40**, 1697 (2002)
8. C. Cohen-Tanoudji, B. Diu, F. Laloe: *Mécanique Quantique* (Hermann Editeurs, Paris 1973)
9. D.A. Long: *The Raman effect* (John Wiley and Sons Ltd, Baffins Lane, Chichester 2002)
10. I.L. Fabelinskii: Usp. Fiz. Nauk. **63**, 355 (1957)
11. R. Loudon: *Quantum theory of light* (Clarendon Press, Oxford 1973)
12. G. Turell: *Infrared and Raman spectra of crystals* (Academic Press, New York 1972)
13. H. Poulet and J.-P. Mathieu: *Vibrational spectra and symmetry of crystals* (Gordon and Breach, New York 1976)
14. W. Hayes and R. Loudon: *Scattering of light by crystals* (John Wiley and Sons, New York 1978)
15. H. Kuzmany: *Solid State Spectroscopy* (Springer-Verlag, Berlin, Heidelberg 1998)
16. R.M. Martin and L.M. Falicov: in *Light Scattering in Solids I*, Topics in Applied Physics vol 8, ed by M. Cardona (Springer-Verlag, Berlin, Heidelberg 1983)
17. M. Cardona (Ed.): *Light Scattering in Solids II-IV*, Topics in Applied Physics, (Springer-Verlag, Berlin, Heidelberg 1982, 1983, 1984, 1989)
18. L.D. Landau and E.M. Lifschitz: *Classical Field Theory* (Addison-Weslay, Reading, Mass. 1962)
19. G. Viliani, R. DellÁnna, O. Pilla and M. Montagna: Phys. Rev. B **37**, 6500 (1998)
20. S. Guha, J. Menéndez, J.B. Page, G.B. Adams: Phys. Rev. B **53**, 13106 (1996)
21. A. Rahmani, J.-L. Sauvajol, S. Rols and C. Benoit: Phys. Rev. B **66**, 125404 (2002)
22. M.S. Dresselhaus, P.C. Eklund: Adv. Phys. **49**,705 (2000) and references therein
23. C. Thomsen, S. Reich: Phys. Rev. Lett. **85**, 5214 (2000)
24. A.G. Souza Filho, A. Jorio, A.K. Swan et al: Phys. Rev. B **65**, 85417 (2002)
25. R. Saito, A. Jorio, A.G. Souza Filho et al: Phys. Rev. Lett. **88**, 27401 (2002)
26. J. Maultzsch, S. Reich, C. Thomsen: Phys. Rev. B **64**, 121407(R) (2001)
27. J. Maultzsch, S. Reich, C. Thomsen: Phys. Rev. B **65**, 233402 (2002)
28. H. Ibach, M. Balden, and S. Lehwald: J. Chem. Soc.-Far. Trans. **92**, 4771 (1996)

29. J. Fink: Recent developments in energy-loss spectroscopy. In: *Advances in Electronics and Electron Physics*, vol 75 (Academic Press, Boston 1989)
30. J. Daniels, C.V. Festenberg, H. Raether, and K. Zeppenfeld: Optical constants of solids by electron spectroscopy. In: *Springer Tracts in Modern Physics*, vol 54 (Springer-Verlag, Berlin, Heidelberg, New York 1970) pp 78–135
31. M. Acheche, C. Colliex, H. Kohl, A. Nourtier, and P. Trebbia: Ultramicroscopy **20**, 99 (1986)
32. A. Howie: *Topics in Electron Diffraction and Microscopy of Materials* (Inst. of Physics Publications, Bristol UK, 1999)
33. M. Kociak, L. Henrard, O. Stephan, K. Suenaga, C. Colliex: Phys. Rev. B **61**, 13936 (2000)
34. M. Kociak, O. Stephan, L. Henrard, V. Charbois, A. Rothschild, R. Tenne, C. Colliex: Phys. Rev. Lett. **87**, 075501 (2001)
35. O. Stephan, D. Taverna, M. Kociak, K. Suenaga, L. Henrard, and C. Colliex: Phys. Rev. B **66**, 155422 (2002)
36. B. Rafferty and L.M. Brown: Phys. Rev. B **58**,10326 (1998)
37. S. Lazar, G.A. Botton, M.Y. Wu, F.D. Tichelaar, H.W. Zandbergen: Ultramicroscopy **96**, 535 (2003)
38. S. Schamm and G. Zanchi: Ultramicroscopy **96**, 559 (2003)
39. R.F. Egerton: Quantitative analysis of the energy-loss spectrum. In: *Electron Energy-Loss Spectroscopy in the Electron Microscope*, 2nd edn (Plenum Press, New York 1986) pp 245–297
40. R.D. Leapman, P. Rez, and D.F. Mayers: J. Chem. Phys. **72**, 1232 (1980)
41. R.F. Egerton: Ultramicroscopy **3**, 243 (1978)
42. R.F. Egerton: Electron scattering theory. In: *Electron Energy-Loss Spectroscopy in the Electron Microscope*, 2nd edn (Plenum Press, New York 1986) pp 131–238
43. R.F. Egerton: Ultramicroscopy, **4**, 169 (1979)
44. H. Castaing and L. Henry: C. R. Acad. Sci. Ser. B **255**, 76 (1962)
45. H. Rose and W. Pejas: Optik **54**, 235 (1979)
46. O.L. Krivanek, C. Mory, M. Tencé, and C. Colliex: Microscopy Microanalysis Microstructures **2**, 257 (1991)
47. C. Jeanguillaume and C. Colliex: Ultramicroscopy, **28**, 252 (1989)
48. C. Colliex, M. Tence, E. Lefevre et al: Mikrochimica Acta **114**, 71 (1994)
49. O.L. Krivanek, A.J. Gubbens, N. Dellby, C.E. Meyer: Microscopy Microanalysis Microstructures **3**, 187 (1992)
50. R.D. Leapman and C.R. Swyt: Ultramicroscopy **26**, 393 (1988)
51. T. Manoubi, M. Tence, M.G. Walls, C. Colliex: Microscopy Microanalysis Microstructures **1**, 23 (1990)
52. M. Tence, M. Quartuccio, C. Colliex: Ultramicroscopy **26**, 42 (1995)
53. O. Stephan, A. Vlandas, R. Arenal de la Concha, A. Loiseau, and S. Trasobares: *Electron Microscopy and Analysis 2003*, ed by S. McVitie and D. McComb, Conference Series Number 179 (Institute of Physics Publishing, Bristol and Philadelphia 2003) pp 437–442
54. A.M. Rao, E. Richter, S. Bandow et al: Science **275**, 187 (1997)
55. Results from a research in the Web of Science data base
56. M.S. Dresselhaus, P.C. Eklund: Adv. Phys. **49** 705 (2000)
57. M.S. Dresselhaus, G. Dresselhaus, A. Jorio et al: Carbon **40**, 2043 (2002)
58. S. Reich, C. Thomsen, and J. Maultzsch: *Carbon nanotubes. Basic Concepts and Physical Properties* (Wiley-VCH, Weinheim 2004)

59. M.S. Dresselhaus, G. Dresselhaus, R. Saito, A. Jorio: Phys. Rep. **409**, 47 (2005)
60. H. Kataura, Y. Kumazawa, Y. Maniwa et al: Synth. Metals **103**, 2555 (1999)
61. A. Jorio, R. Saito, J.H. Hafner et al: Phys. Rev. Lett. **86**, 1118 (2001)
62. S. Kazaoui, N. Minami, R. Jacquemin et al: Phys. Rev. B **60**, 13339 (1999)
63. J.C. Charlier, P. Lambin: Phys Rev. B **57**, R15037 (1998)
64. S.D.M. Brown, P. Corrio, A. Marucci et al: Phys. Rev. B **61**, 5137 (2000)
65. S.D.M. Brown, A. Jorio, P. Corrio et al: Phys. Rev. B **63**, 5414 (2001)
66. L. Alvarez, A. Righi, G. Guillard et al: Chem. Phys. Lett. **316**, 186 (2000)
67. L. Alvarez, A. Righi, S. Rols et al: Phys. Rev. B **63**, 53401 (2001)
68. A. Jorio, C. Fantini, M. A. Pimenta et al: Phys. Rev. B **71**, 75401 (2005)
69. H. Telg, J. Maultzsch, S. Reich, F. Hennrich, and C. Thomsen: Phys. Rev. Lett. **93**, 177401 (2004)
70. C. Fantini, A. Jorio, M. Souza et al: Phys. Rev. Lett. **93**, 147406 (2004)
71. F. Wang, G. Dukovic, L.E. Brus, T.F. Heinz: Science **308**, 838 (2005)
72. J. Maultzsch, R. Pomraenke, S. Reich, E. Chang et al: arXiv:cond-mat/0505150 (2005)
73. S. Rols, A. Righi, A.L. Alvarez et al: Eur. Phys. J. B **18**, 201 (2000)
74. D. Kahn, J. Ping Lu: Phys. Rev. B **60**, 6535 (1999)
75. L. Henrard, E. Hernandez, P. Bernier, A. Rubio: Phys. Rev. B **60**, 8521 (1999)
76. A. Jorio, A.G. Souza Filho, G. Dresselhaus et al: Phys. Rev. B **65**, 155412 (2002)
77. J.C. Meyer, M. Paillet, T.M. Michel, A. Moreac, A. Neumann, S. Roth, and J.L. Sauvajol: Phys. Rev. Lett. **95**, 217401 (2005)
78. This is true as far as the laser power density is low. Heating of pristine samples in air at room temperatures can be observed above some tens $\mu W\,\mu m^{-2}$ (some $kW\,cm^{-2}$). Irreversible damages, including combustion, are observed above some hundreds of $\mu W\,\mu m^{-2}$ (some tens of $kW\,cm^{-2}$), which corresponds to heating above 400°C
79. H. Kuzmany, M. Matus, B. Burger, J. Winter: Adv. Mater. **6**, 731 (1994)
80. M.S. Dresselhaus, G. Dresselhaus: Adv. in Phys. **30**, 139 (1981)
81. R.S. Lee, H.J. Kim, J.E. Fischer et al: Nature **388**, 255 (1997)
82. A.M. Rao, P.C. Eklund, S. Bandow et al: Nature **388**, 257 (1997)
83. N. Bendiab, A. Righi, E. Anglaret et al: Chem. Phys. Lett. **339**, 205 (2001)
84. A. Claye, N. Nemes, A. Janossy, J.E. Fischer: Phys. Rev. B **62**, R4845 (2000)
85. A. Claye, S. Rahman, J.E. Fischer et al: Chem. Phys. Lett. **333**, 16 (2001)
86. N. Bendiab, L. Spina, A. Zahab et al: Phys. Rev. B **63**, 153407 (2001)
87. N. Bendiab, E. Anglaret, J.L. Bantignies et al: Phys. Rev. B **64**, 245424 (2001)
88. J.L. Sauvajol, N. Bendiab, E. Anglaret, P. Petit: C.R. Physique **4**, 1035 (2003)
89. N. Bendiab, J.L. Sauvajol, M. Paillet, R. Almairac: Chem. Phys. Lett. **372**, 210 (2003)
90. N. Bendiab: PhD thesis, Université Montpellier II, 2003
91. P. Petit, C. Mathis, C. Journet, P. Bernier: Chem. Phys. Lett. **305**, 370 (1999); E. Jouguelet, C. Mathis, P. Petit: Chem. Phys. Lett. **318**, 561 (2000)
92. A. Pénicaud, P. Poulin, A. Derré, E. Anglaret et al: J. Am. Chem. Soc. **127**, 8 (2005)
93. J. Cambedouzou, S. Rols, N. Bendiab et al: Phys. Rev. B **7**, 41404 (2005)
94. C. Bower, S. Suzuki, K. Tanigaki, O. Zhou: Appl. Phys. A **67**, 47 (1998)
95. L. Duclaux, K. Metenier, J.P. Salvetat et al: Mol. Cryst. Liq. Cryst. **34**, 769 (2000)

96. L. Grigorian, K.A. Williams, S. Fang et al: Phys. Rev. Lett. **80**, 5560 (1998)
97. Z. Yu and L.E. Brus: J. Phys. Chem. A **104**, 10995 (2000)
98. G.U. Sumanasekera, J.L. Allen, S.L. Fang et al: J. Phys. Chem. B **103**, 4292 (1999)
99. N. Izard, D. Riehl, E. Anglaret: Phys. Rev. B **71**, 195417 (2005); N. Izard, PhD thesis, Université Montpellier II (2004)
100. M.J. O'Connell, E.E. Eibergen, S.K. Doorn: Nature Mat. **4**, 415 (2005)
101. L. Kavan, P. Rapta, L. Dunsch: Chem. Phys. Lett. **328**, 33 (2000)
102. M. Stoll; P.M. Rafailov, W. Frenzel, C. Thomsen: Chem. Phys. Lett. **375**, 625 (2003)
103. A.M. Rao, A. Jorio, M.A. Pimenta et al: Phys. Rev. Lett. **84**, 1820 (2000)
104. H.H. Gommans, J.W. Alldredge, H. Tashiro et al: J. Appl. Phys. **88**, 2509 (2000)
105. G.S. Duesberg, I. Loa, M. Bughard et al: Phys. Rev. Lett. **85**, 5436 (2000)
106. E. Anglaret, A. Righi, J.L. Sauvajol et al: Phys. Rev. B **65**, 165426 (2002)
107. P. Launois, A. Marucci, B. Vigolo et al: J. Nanoscience Nanotech. **1**, 125 (2001)
108. W. Zhou, J. Vavro, C. Guthy et al: J. of Appl. Phys. **95**, 649 (2004)
109. J.L. Bahr, J. Yang, D.V. Kosynkin et al: J. Am. Chem. Soc. **123**, 6536 (2001)
110. M. Holzinger, J. Abraham, P. Whelan et al: J. Am. Chem. Soc. **125**, 8566 (2003)
111. D. Chattopadhyay, I. Galeska, F. Papadimitrakopoulos: J. Am. Chem. Soc. **125**, 3370 (2003)
112. M.S. Strano, C.A. Dyke, M.L. Usrey et al: Science **301**, 1519 (2003)
113. R. Krupke, F. Hennrich, H.V. Lohneysen, M.M. Knappes: Science **301**, 344 (2003)
114. M.S. Dresselhaus, G. Dresselhaus, R. Saito, and A. Jorio: Physics Report **409**, 47 (2005)
115. A.M. Rao, J. Chen, E. Richter et al: Phys. Rev. Lett. **86**, 3895 (2001)
116. J. Chen et al: Science **282**, 95 (1998); J. Chen et al: J. Phys. Chem. B **105**, 2525 (2001)
117. C. Jiang, K. Kempa, J. Zhao et al: Phys. Rev. B **66**, 161404 (2002)
118. K. Kempa: Phys. Rev. B **66**, 1945406 (2002)
119. M. Paillet, Ph. Poncharal, A. Zahab et al: Phys. Rev. Lett. **94**, 237401 (2005)
120. J. Maultzsch, S. Reich, U. Schlecht, and C. Thomsen: Phys. Rev. Lett. **91**, 087402 (2003)
121. M.J. O'Connell, S.M. Bachilo, C.B. Huffman et al: Science **297**, 593 (2002)
122. S.M. Bachilo, M.S. Strano, C. Kittrell et al: Science **298**, 2361 (2002)
123. C.L. Kane and E.J. Mele: Phys. Rev. Lett. **90**, 207401 (2003)
124. J. Kürti, V. Zólyomi, M. Kertesz, and G. Sun: New J. Phys. **5**, 125 (2003)
125. J. Gavillet, J. Thibault, O. Stephan et al: J. Nanosc. and Nanotech., **4**, 346 (2004)
126. M. Isaacson and D. Johnson: Ultramicroscopy **1**, 32 (1975)
127. C. Mory and C. Colliex: Ultramicroscopy **28**, 339 (1989)
128. K. Suenaga, T. Tence, C. Mory et al: Science **290**, 2280 (2000)
129. R. Lee, J. Gavillet, M. Lamy de la Chapelle et al: Phys. Rev. B **64**, 121405 (2001)
130. O. Stephan, P.M. Ajayan, C. Colliex et al: Phys. Rev. B **53**, 13824 (1996)
131. K. Suenaga, E. Sandre, C. Colliex et al: Phys. Rev. B **63**, 165408 (2001)
132. T. Pichler, M. Knupfer, M.S. Golden et al: Phys. Rev. Lett. **80**, 4279 (1998)
133. F.L. Shyu and M.F. Lin: Phys. Rev. B **62**, 8508 (2000)

6

Transport Properties

S. Roche, E. Akkermans, O. Chauvet, F. Hekking, J.-P. Issi, R. Martel, G. Montambaux and Ph. Poncharal

Abstract. In this chapter, we first review the fundamental theoretical concepts of mesoscopic transport for low-dimensional systems and disordered materials. Emphasis is put on the Landauer formulation of electronic transmission, weak localization and Aharonov-Bohm phenomena, as well as Coulomb interactions through screening effects and Luttinger liquid model. A pedagogical effort is made to present the currently established physics of quantum conduction in some analytical detail, enabling the reader to further deepen the understanding of more specialized literature. In a subsequent part, the main theoretical features of quantum transport in carbon nanotubes are elaborated, mostly within the non-interacting electron regime, that is to date less controversial. The experimental part starts with a discussion of the commonly employed measurement techniques. Several transport experiments are then analyzed, with a particular focus on device-oriented aspects (field effect, Schottky barriers, etc). Finally, the main physical properties of nanotube-based composites are outlined, followed by a presentation of our current understanding of thermal properties of carbon tubules.

6.1 Quantum Transport in Low-dimensional Materials

6.1.1 Ballistic Conduction and Quantized Conductance

Drude-Sommerfeld Theory of Metals

Conductivity and Conductance

In ordinary metals, transport is conveniently described using Drude-Sommerfeld theory [1]. In this theory, the conduction electrons (mass m, charge $-e$) form a degenerate Fermi gas (Fermi energy E_{F}). Momentum relaxation occurs with a rate $1/\tau$, where τ is the *mean time* between successive scattering events. The mean free path ℓ_{e} is the average distance over which electrons propagate *ballistically*, i.e., without being scattered. It is given by $\ell_{\mathrm{e}} = v_{\mathrm{F}}\tau$, where $v_{\mathrm{F}} = \sqrt{2E_{\mathrm{F}}/m}$ is the Fermi velocity.

S. Roche et al.: *Transport Properties*, Lect. Notes Phys. **677**, 335–437 (2006)
www.springerlink.com
© Springer-Verlag Berlin Heidelberg 2006

In metals, the mean free path is usually long compared to the Fermi wavelength $\lambda_{\mathrm{F}} = 2\pi\hbar/(mv_{\mathrm{F}})$. Hence the electron motion is quasi-classical on the scale ℓ_{e} and can be described by Newton's laws. In particular, an applied electric field $\boldsymbol{E}$ will accelerate the electrons up to a time τ. Beyond this time, scattering events completely randomize the electron momentum and destroy all (quantum-mechanical) correlations. This is the central assumption of the Drude-Sommerfeld theory. As a result the acquired momentum is on average $\boldsymbol{p} = m\boldsymbol{v} = -e\boldsymbol{E}\tau$. Introducing the current density $\boldsymbol{j} = -n_0 e\boldsymbol{v}$, where n_0 is the electron density, we immediately obtain Ohm's law $\boldsymbol{j} = \sigma_{\mathrm{D}}\boldsymbol{E}$ where

$$\sigma_{\mathrm{D}} = \frac{n_0 e^2 \tau}{m} \tag{6.1}$$

is the Drude conductivity. Equation (6.1) constitutes a local relation between $\boldsymbol{j}$ and $\boldsymbol{E}$: the current density at position $\boldsymbol{r}$ is determined by the value of $\boldsymbol{E}$ at the same position $\boldsymbol{r}$.

The Drude conductivity is a material parameter: it does not depend on the geometry of the sample. Often we write Ohm's law as $I = \mathcal{G}V$, where I is the total current, V the applied voltage, and $\mathcal{G}$ the conductance. This is a non-local relation: the total current I through the sample is determined by the voltage difference applied to the sample boundaries. For a wire of length L and cross-section S, we have $\mathcal{G} = \sigma_{\mathrm{D}} S/L$. This implies that the resistance $R = 1/\mathcal{G}$ scales linearly with L, and is inversely proportional to S, in agreement with the usual rules for series and parallel addition of resistances, respectively.

Momentum Relaxation; Residual Conductivity

Momentum relaxation occurs due to the fact that the electrons undergo scattering events [2]. The most important mechanisms contributing to momentum relaxation are electron-phonon scattering, electron-electron scattering and scattering off static impurities. The first two mechanisms are inelastic: they involve a change in both energy and momentum. Scattering off static impurities is purely elastic: only the direction of the momentum changes.

At room temperature, inelastic phonon scattering dominates. The energy acquired by the electron during the acceleration in an electric field is dissipated during collisions to the phonons, leading to heating of the sample. As the temperature T is lowered, phonons become less effective; the mean free time and hence the conductivity rapidly grow, $\sigma_{\mathrm{D}} \sim 1/T^5$. The temperature dependence changes at low temperatures, where in principle inelastic electron-electron collisions dominate (although this is often masked by impurity scattering). According to Fermi liquid theory (see Sect. 6.1.2 below), $\tau \sim 1/T^2$ such that the conductivity increases more slowly with decreasing temperature, $\sigma_{\mathrm{D}} \sim 1/T^2$.

The inelastic scattering time τ diverges as $T \to 0$. Nevertheless, at the lowest temperatures, the conductivity approaches a constant value $\sigma_{\mathrm{D}} = \sigma_0 = n_0 e^2 \tau_{\mathrm{e}}/m$. This is the so-called residual conductivity of the metal, and it is

due to elastic scattering off static impurities. The elastic mean free time $\tau_{\rm e}$ defines the elastic mean free path $\ell_{\rm e} = v_{\rm F}\tau_e$. On length scales larger than $\ell_{\rm e}$, the electron motion is *diffusive*, with a diffusion coefficient $D = v_{\rm F}\ell_{\rm e}/d$, where d is the dimension of the sample. Inelastic scattering still occurs, but on longer time scales $\tau \gg \tau_e$. The associated inelastic length is then defined by the diffusive result $L_{in} = \sqrt{D\tau} \gg \ell_{\rm e}$. As we have seen above, at the lowest temperatures, this length is determined by electron-electron scattering events.

Mesoscopic Phenomena in Metals

In a mesoscopic sample [3,4], i.e. a sample whose characteristic size L is large compared to the elastic mean free path ℓ_e, but small compared to the inelastic length $L_{\rm in}$, electrons undergo elastic scattering only. The central assumption of the Drude-Sommerfeld theory, stating that quantum correlations are lost as a a result of scattering, becomes clearly questionable in this limit. In fact, as long as the scattering is elastic, the electron phase memory is conserved and the electron motion should be described quasi-classically on length scales up to $L_{\rm in}$. For a mesoscopic sample this means in particular that the electron follows classical trajectories through the entire sample, supplemented with a quantum mechanical phase. As a result, quantum-interference phenomena can occur involving two or more trajectories with different phases. These interference phenomena lead to corrections to transport properties; examples are the weak-localization correction to the conductivity, the occurrence of Aharonov-Bohm oscillations in small metallic rings and the universal sample-to-sample fluctuations of the conductance.

In what follows, we will discuss a general approach, based on ideas due to Landauer, that enables one to formulate the problem of phase-coherent transport. We will express the conductance of a phase-coherent sample in terms of its quantum-mechanical transmission properties [3, 4]. This approach can then be used to obtain the conductance in specific cases of interest. We will see that conductance in the quantum limit obeys rules that are very different from those known from Drude-Sommerfeld theory. The Landauer approach also provides answers to important additional questions. For instance, if there is elastic scattering only in the sample, one may ask where the dissipation arises. We will also see what happens in clean phase-coherent samples with $L < \ell_{\rm e}, L_{in}$. It turns out that even these ballistic conductors are still characterized by a finite resistance. In Sect. 6.2, quantum-interference phenomena will be analyzed in more details by means of an analytical description.

The Scattering Approach to Quantum Transport

Multi-Mode Quantum Wire

In order to set the stage, we start our discussion by considering a two-dimensional quantum wire of width W (Fig. 6.1) in the ballistic conduction

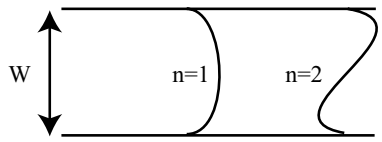


Fig. 6.1. Clean quantum wire of width W with two propagating modes

regime. Electrons in such a wire obey the two-dimensional Schrödinger equation

$$\left[-\frac{\hbar^2}{2m}\left(\frac{\partial^2}{\partial x^2}+\frac{\partial^2}{\partial y^2}\right)+U(x,y)\right]\Psi(x,y)=E\Psi(x,y) \tag{6.2}$$

Here $U(x,y)$ is the potential confining the electrons to the wire. Supposing free propagation in x-direction and an infinite square well confining potential in y-direction, we can write the solution

$$\Psi(x,y)=\Psi_{nk}(x,y)=\mathrm{e}^{\mathrm{i}kx}\chi_n(y) \tag{6.3}$$

where $\chi_n(y)=\sqrt{2/W}\sin[n\pi(y+W/2)/W]$ with $n=1,2,3,\ldots$ These wave functions vanish at the edges of the wire, i.e. for $y=\pm W/2$. The dispersion of these electrons is $E=E_n(k)=\hbar^2k^2/2m+\epsilon_n$, where $\epsilon_n=\hbar^2n^2\pi^2/(2mW^2)$ is the discrete spectrum due to confinement in the y-direction. From this we see: for a given energy $E<\epsilon_1$, k is purely imaginary and no propagating modes are available in the wire. For $\epsilon_1<E<\epsilon_2$, we find one propagating mode, corresponding to $n=1$; generally speaking, for $\epsilon_N<E<\epsilon_{N+1}$, N propagating modes are found.

The group velocity of an electron in a given mode is obtained from the energy dispersion in the usual way,

$$v_{n,\pm}(E)=\pm v_n(E)\equiv\pm\frac{1}{\hbar}\left.\frac{\mathrm{d}E_n(k)}{\mathrm{d}k}\right|_E=\pm\sqrt{2(E-\epsilon_n)/m} \tag{6.4}$$

Here $+$ $(-)$ refers to a right-moving (left-moving) electron, respectively. The *density of states* per unit length (for one spin direction) for a given mode and a given direction of propagation is

$$\rho_n(E)=\frac{1}{2\pi}\left.\frac{1}{\mathrm{d}E_{nk}/\mathrm{d}k}\right|_E=\frac{1}{2\pi\hbar v_n(E)} \tag{6.5}$$

This means in particular that the product $\rho_n(E)v_n(E)=1/(2\pi\hbar)$ is a constant. The electric current (per unit energy), carried by a given mode n in a given direction at energy E is then given by

$$I_{n,\pm}(E)=-e\rho_n(E)v_{n,\pm}(E)=\mp e/(2\pi\hbar) \tag{6.6}$$

independent of energy E and mode index n. This equipartition rule is due to the cancellation of the one-dimensional density of states and group velocity.

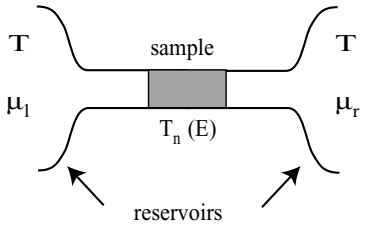


Fig. 6.2. Generic two-terminal set-up

Landauer Formula

We now formulate the quantum transport problem using the generic set-up depicted in Fig. 6.2 for a typical two-terminal transport measurement.

We distinguish three parts:

1. *Reservoirs.* The two terminals or reservoirs are the electron source and drain. They are massive electrodes at thermodynamic equilibrium, kept at temperature T and electro-chemical potential μ_i ($i = l, r$ refers to the left and right reservoir, respectively). The electrons that are injected into the sample from a reservoir i are distributed over energy E according to the Fermi-function
$$f_i(E) = \frac{1}{\mathrm{e}^{\beta(E-\mu_i)}+1} \tag{6.7}$$
where $\beta = 1/k_\mathrm{B}T$ is the inverse temperature. The reservoirs absorb all incoming electrons, regardless of their energy. For a given reservoir, there is no correlation between absorbed and subsequently re-injected electrons.
2. *Perfect leads.* Between the reservoirs and the sample, electrons propagate along perfect leads, which are multi-mode quantum wires.
3. *Sample.* The sample contains only elastic scattering. It transmits an incoming electron with energy E in mode n of one of the perfect leads with quantum-mechanical transmission amplitude $t_{n,n'}(E)$ into mode n' of the other perfect lead (at the same energy E). The corresponding transmission probability is $T_{n,n'}(E) = |t_{n,n'}(E)|^2$. As a result, the total probability that an incoming mode n is transmitted is given by $T_n(E) = \sum_{n'} T_{n,n'}(E)$.

In view of the above, the total current from left to right can be written as

$$I_{\ell\mathrm{r}} = 2\int \mathrm{d}E \sum_n f_\ell(E) I_{n,+}(E) T_n(E) \tag{6.8}$$

and similarly for $I_{\mathrm{r}\ell}$. Here, a factor 2 is included to account for the electron spin. As a result, the total current can be written as $I = I_{\ell\mathrm{r}} - I_{\mathrm{r}\ell}$,

$$I = -\frac{e}{\pi\hbar}\int \mathrm{d}E \sum_n [f_\ell(E) - f_\mathrm{r}(E)] T_n(E) \tag{6.9}$$

We write $\mu_\ell = E_\mathrm{F} + eV/2$ and $\mu_\mathrm{r} = E_\mathrm{F} - eV/2$, where eV is the bias voltage applied between the two terminals. Assuming eV is small, we can expand the Fermi functions and obtain, in the low-temperature limit,

$$I = \frac{e^2}{\pi\hbar} V \sum_n T_n(E_\mathrm{F}) = \mathcal{G}V \tag{6.10}$$

where the conductance $\mathcal{G}$ is given by

$$\mathcal{G} = \frac{e^2}{\pi\hbar} \sum_n T_n(E_\mathrm{F}) \tag{6.11}$$

This is the well-known Landauer formula that relates the conductance of a sample to its elastic quantum mechanical transmission probability. Some implications of this important result in various examples will be presented in the next section.

Quantum Resistance Properties

Conductance of a Multi-Mode Quantum Wire

We start our discussion of quantum resistance properties by considering a multi-mode quantum wire of width W, connected to two reservoirs with $\mu_\ell = E_\mathrm{F} + eV/2$ and $\mu_\mathrm{r} = E_\mathrm{F} - eV/2$. Let $E_N < E_\mathrm{F} < E_{N+1}$ such that there are N propagating modes at the Fermi energy E_F. Since there is no obstacle in the channel, $T_n(E_\mathrm{F}) = 1$ for $n \leq N$. For $n > N$, there are no propagating modes, $T_n(E_\mathrm{F}) = 0$. Therefore, at small bias,

$$I = \frac{e^2}{\pi\hbar} V \sum_n T_n(E_\mathrm{F}) = \frac{Ne^2}{\pi\hbar} V \tag{6.12}$$

and $\mathcal{G} = Ne^2/\pi\hbar$. A few remarks are in order here:

1. Each mode contributes an amount $e^2V/(\pi\hbar)$ to the current: this is a direct consequence of the aforementioned equipartition rule.
2. The total conductance is $Ne^2/(\pi\hbar)$, i.e. $e^2/(2\pi\hbar)$ per mode and per spin direction. This so-called unitary conductance is usually referred to as the *conductance quantum* $\mathcal{G}_\mathrm{K} = e^2/(2\pi\hbar) = e^2/h$. We see that even a perfectly transmitted mode is characterized by a finite conductance.
3. The total conductance of the quantum wire is independent of the length L of the wire. Thus the classical result $\mathcal{G} \propto 1/L$, implying the usual rules for series addition of resistances, is violated for a quantum conductor.

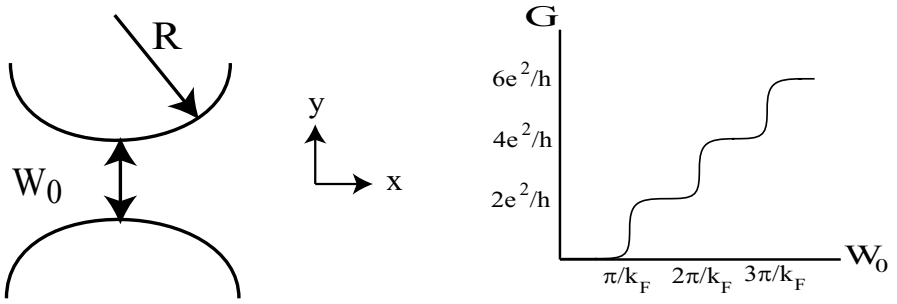


Fig. 6.3. *Left*: Quantum point contact. *Right*: Conductance quantization as a function of W_0

Conductance of an Adiabatic Quantum Point Contact

We next turn our attention to the set-up shown in Fig. 6.3. A narrow, two-dimensional constriction or quantum point contact of width W_0 at the narrowest point is defined in a two-dimensional electron gas (2DEG). We are interested in the behavior of the conductance of the constriction as a function of W_0.

We assume that the width $W(x)$ of the constriction varies slowly with x, on a scale $R \gg W_0$. Furthermore the constriction is narrow: at most a few propagating modes are present, meaning that $W_0 \sim \lambda_\mathrm{F}$. This implies that the electron motion along the x-direction can be treated quasi-classically and scattering between modes can be neglected. We are thus faced with a number of independent modes, each obeying the one-dimensional, effective Schrödinger equation

$$\left(-\frac{\hbar^2}{2m}\frac{\mathrm{d}^2}{\mathrm{d}x^2} + U_n(x)\right)\psi_n(x) = E\psi_n(x) \tag{6.13}$$

where $U_n(x) = \epsilon_n(x)$ is a slowly varying potential: the discrete spectrum due to confinement in the y-direction $\epsilon_n(x) = \hbar^2 n^2\pi^2/(2mW(x)^2)$ is x-dependent due to the slow variation of the width $W(x)$ along the channel. Whether or not a given mode n is transmitted depends on the position of the Fermi energy with respect to the maximum of $U_n(x)$, reached at $x = 0$ where $W(x = 0) = W_0$. For $W_0 = 0$, this maximum exceeds E_F for any n: all modes are reflected. Increasing W_0 from zero, we gradually lower the energy $U_n(0)$. When W_0 approaches the value $n\pi/k_\mathrm{F}$, the maximum $U_n(0)$ of the mode n approaches E_F; tunneling can occur through the effective barrier $U_n(x)$. At these values, the corresponding transmission probability $T_n(E_\mathrm{F})$ increases rapidly from zero to unity: tunneling occurs only within the narrow interval $\sqrt{W_0/k_\mathrm{F}^2 R}$ around $n\pi/k_\mathrm{F}$. The fact that the increase is rapid means that a given mode is either completely transmitted or completely reflected. This is in accordance with the physics of the quasi-classical limit $R \gg \lambda_\mathrm{F}$: classically,

there is no tunneling and an electron either passes the constriction or is reflected. Increasing W_0, we thus increase the number of propagating modes one by one, at $W_0 = \pi/k_\mathrm{F}$, $2\pi/k_\mathrm{F}$, $3\pi/k_\mathrm{F}\ldots$. Therefore, the total transmission $\sum_n T_n(E_\mathrm{F})$ is expected to increase stepwise with W_0. The conductance also increases stepwise, in units $2e^2/h$, see Fig. 6.3. This *conductance quantization* has indeed been experimentally observed, see [5]. It corresponds to another violation of Ohm's law: changing the cross-section of a small conductor leads to a stepwise, rather than a linear, increase of the conductance.

Conductance of an Aharonov-Bohm Loop

As it is well-known, for an electron in a magnetic field $\boldsymbol{B}$, the canonical momentum is given by the replacement $\boldsymbol{p} \to (\boldsymbol{p} + e\boldsymbol{A}/c)$, where $\boldsymbol{A}$ is the vector potential with $\boldsymbol{B} = \mathrm{rot}\ \boldsymbol{A}$. An electron propagating in a magnetic field thus acquires an additional phase-factor: $\psi_k(\boldsymbol{r}) = \exp(\mathrm{i}(\boldsymbol{k}\cdot\boldsymbol{r} + \int^{\boldsymbol{r}} e\boldsymbol{A}.\mathrm{d}\boldsymbol{r}'/\hbar c))$. Let us consider a clean one-mode quantum wire, forming a loop of area S, threaded by a flux $\phi = BS$ (see Fig. 6.4).

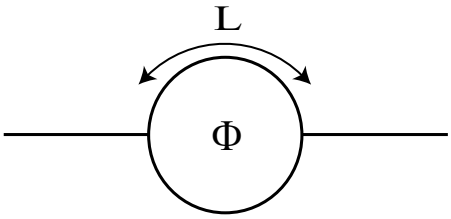


Fig. 6.4. Aharonov-Bohm loop

For an electron propagating around the loop, the additional phase factor is

$$\frac{e}{\hbar c}\oint\limits_{loop} \boldsymbol{A}\cdot\mathrm{d}\boldsymbol{r} = \frac{e}{\hbar c}\int \mathrm{rot}\ \boldsymbol{A}\cdot\mathrm{d}\boldsymbol{S} = \frac{e}{\hbar c}\int \boldsymbol{B}\cdot\mathrm{d}\boldsymbol{S} = 2\pi\phi/\phi_0 \tag{6.14}$$

where $\phi_0 = hc/e$ is the *flux quantum*. Hence, the total phase for an electron propagating from left to right along the upper arm (length L) is given by $kL - \pi\phi/\phi_0$, whereas an electron propagating along the lower arm (same length L) acquires a phase $kL + \pi\phi/\phi_0$. The transmission amplitude for propagation from left to right is thus given by

$$t_{\ell r}(E_\mathrm{F}) = (\mathrm{e}^{\mathrm{i}(k_\mathrm{F}L + \pi\phi/\phi_0)} + \mathrm{e}^{\mathrm{i}(k_\mathrm{F}L - \pi\phi/\phi_0)})/2 \tag{6.15}$$

where $k_\mathrm{F} = mv_\mathrm{F}/\hbar$ is the Fermi wave vector. As a result, $T(E_\mathrm{F}) = |t_{\ell r}(E_\mathrm{F})|^2 = |\mathrm{e}^{\mathrm{i}(k_\mathrm{F}L+\pi\phi/\phi_0)} + \mathrm{e}^{\mathrm{i}(k_\mathrm{F}L-\pi\phi/\phi_0)}|^2/4 = (1+\cos 2\pi\phi/\phi_0)/2$. This is a *periodic function* of the applied flux ϕ, with period ϕ_0. Therefore, the conductance of the loop, $\mathcal{G} = (2e^2/h)T(E_\mathrm{F})$, will be characterized by periodic oscillations as a function of flux: these are the so-called Aharonov-Bohm oscillations.

Diffusive Quantum Wire

So far we have considered quantum ballistic conductors, with a total length L smaller than the elastic mean free path l_e. Consider now a two-dimensional diffusive quantum wire longer than the elastic mean free path ℓ_e, but still smaller than the inelastic length L_{in}, and connected to two reservoirs. We assume that there are many modes, $N = k_F W/\pi \gg 1$, which guarantees that the electron states are not localized [3]. As we have seen in the previous section, we expect such a wire to be characterized by its residual conductivity. In terms of the conductance this means that we should find $\mathcal{G} = \sigma_0 W/L$ in this case. In order to verify this, we need to know the transmission coefficients $T_n(E_F)$ for a diffusive wire. Let us present the expected residual conductance $\mathcal{G}$ as

$$\mathcal{G} = \frac{n_0 e^2 \tau_e}{m} \frac{W}{L} \tag{6.16}$$

Using the fact that the two-dimensional electron density $n_0 = k_F^2/(2\pi^2)$, we obtain

$$\mathcal{G} = N \frac{e^2}{\pi\hbar} \frac{\ell_e}{2L} \tag{6.17}$$

Naively, one thus expects that $T_n(E_F) = \ell_e/(2L)$: each mode is transmitted with a small probability $\propto \ell_e/L$. In fact this is incorrect; a more detailed analysis shows that the transmission probabilities of a disordered wire are random numbers, distributed according to a bimodal distribution [6]

$$p(T) = \frac{\ell_e}{\pi L} \frac{1}{\sqrt{T(1-T)}} \tag{6.18}$$

The distribution is maximal for $T = 0$ or $T = 1$, other values of T are in fact very improbable. In other words, a given mode has either transmission 1 or 0. This is, once more, a quasi-classical result: a particle is either transmitted or reflected. The average transmission per channel, however, $\langle T \rangle = \int \mathrm{d}T T p(T) = \ell_e/(2L)$ is small. Unfortunately, no information concerning the bimodal character of the distribution $p(T)$ is contained in the conductance as the latter depends on the average value of T_n only. In order to obtain more information on $p(T)$, one could measure the fluctuations of the current around its average value, i.e. the current noise [7].

We have seen that quantum transport in a phase-coherent conductor (typical size L smaller than the inelastic length L_{in}) can be formulated in terms of a scattering problem. The formulation is essentially non-local: the total current I across the sample is found as a function of the bias applied to the terminals. As a result we find the nonlocal conductance rather than the local conductivity. This reflects the fact that quantum-mechanical correlations are maintained throughout a phase-coherent sample.

The conductance is determined by the elastic transmission coefficient. As long as scattering within the sample is elastic, it is clear that the dissipation associated with electric transport cannot occur in the sample itself. Indeed, the excess energy due to a finite applied bias voltage is dissipated in the reservoirs. The elastic transmission probability is phase-sensitive, which opens up the possibility of quantum-interference phenomena. As an example we discussed the single-mode, ballistic Aharonov-Bohm loop; for the diffusive multi-mode case, see Sect. 6.2. The various examples showed that simple, classical rules concerning parallel or series addition of resistances do not apply in the quantum limit. We also saw that ballistic samples, i.e. samples without any elastic impurity scattering ($L < \ell_{\mathrm{e}}$) are still resistive.

So far we have treated electrons as if they were non-interacting particles. In reality electrons interact through Coulomb repulsion. According to the Landau Fermi-liquid theory, the non-interacting picture remains correct under certain conditions, even in the presence of interactions. We will review these ideas briefly below, and then discuss that the conditions for Landau Fermi-liquid theory to hold are sometimes violated in low-dimensional systems.

6.1.2 Coulomb Interactions

Fermi Liquid

Non-Interacting Electrons

As it is well-known, the ground state of a non-interacting Fermi gas is a filled Fermi sea: all states are occupied up to the Fermi energy E_{F}, which is a function of the electron density n_0. Adding or removing particles therefore simply leads to a shift of E_{F}. Excitations are induced by creating particle-hole pairs: an electron of wave vector $\boldsymbol{k}$ is taken from the Fermi sea and put to an empty state $\boldsymbol{k'}$ outside. We have created two quasi-particles: a particle with wave vector $\boldsymbol{k'}$ and a hole with wave vector $\boldsymbol{k}$. These particle-hole pairs form a continuum of states that carry a momentum $\boldsymbol{p} = \hbar(\boldsymbol{k'} - \boldsymbol{k})$ and an energy $E = \frac{\hbar^2}{2m}(k'^2 - k^2)$.

At finite temperature T, these excitations are created thermally, which leads to the characteristic smearing of the Fermi distribution over a width proportional to T. However, the smearing is in typical metals always small compared to the Fermi energy: this is why even at finite temperature the physics of non-interacting electrons is determined by *Fermi surface properties* only. An example is the specific heat of the three-dimensional non-interacting electron gas, given by $c_V = \pi^2 k_{\mathrm{B}}^2 T \rho(E_{\mathrm{F}})/3$, which is determined by the density of states at the Fermi level, $\rho(E_{\mathrm{F}}) = m k_{\mathrm{F}}/(\hbar^2 \pi^2)$. Another example is the Landauer conductance $\mathcal{G} = 2(e^2/h)\sum_n T_n(E_{\mathrm{F}})$, which is determined by the transmission probabilities $T_n(E_{\mathrm{F}})$ at the Fermi level.

Landau Theory of Fermi Liquids; Screening in Metals

According to Landau, in the presence of repulsive interactions, the above description remains largely intact as long as the interactions are weak and short-ranged [1, 2]. More precisely: *there exists a one-to-one correspondence between the eigenstates of the non-interacting and the interacting Fermi gas.*

This hypothesis means that:

(1) The filled Fermi sea as a ground state persists in the interacting case;
(2) The concept of quasi-particles (particles and holes) persists in the interacting case.

How do interactions manifest themselves? Consider a filled Fermi sea with zero total momentum and one additional quasi-particle of momentum $\hbar\boldsymbol{k}$ close to the Fermi surface, $k \sim k_{\mathrm{F}}$. Now, let us switch on the interactions between electrons. Since interactions conserve the total momentum, the quantity $\hbar\boldsymbol{k}$ cannot change. Moreover, by continuity, the minimum momentum $\hbar k_{\mathrm{F}}$ needed to create a quasi-particle cannot change either. Consequently, the energy has to change following

$$E(\boldsymbol{k}) - E_{\mathrm{F}} \simeq \frac{\hbar^2}{2m} k_{\mathrm{F}}(k - k_{\mathrm{F}}) \rightarrow \frac{\hbar^2}{2m^*} k_{\mathrm{F}}(k - k_{\mathrm{F}}) \tag{6.19}$$

We see that interactions renormalize the electron mass $m \rightarrow m^*$. More generally speaking, interactions lead to parameter renormalization, but the structure of the theory, and hence the behavior of various physical quantities remains unchanged. An example is the electronic specific heat of the interacting electron gas $c_V = \pi^2 k_{\mathrm{B}}^2 T \rho^*(E_{\mathrm{F}})/3$: its temperature dependence is unchanged but it is determined by the renormalized density of states $\rho^* = m^* k_{\mathrm{F}}/(\hbar^2\pi^2)$ at the Fermi level.

As already stated above, in order for Fermi-liquid theory to hold, electron-electron interactions must be weak and short-ranged. Coulomb interactions are, generally speaking, strong and long ranged. In free space, a positive test charge q induces a potential $\varphi(r) = q/r$. In metals it is the *screening* of this potential by conduction electrons that makes the potential effectively short-ranged. In fact, in a metal, a positive test charge q will attract a screening cloud of negatively charged electrons around it, such that the potential drops rapidly over a short distance. According to the quasiclassical Thomas-Fermi theory [1,2], the resulting potential follows $\varphi(r) = q\mathrm{e}^{-r/r_0}/r$, where $r_0 \sim \lambda_{\mathrm{F}}$ is the *screening length*. Screening is very effective in an ordinary bulk metal: the electrons are relatively free and fast and will screen any charge inhomogeneity from all sides on a short scale $\sim\lambda_{\mathrm{F}}$. This is why Fermi liquid theory works quite well for ordinary (clean) metals.

For weak, short-ranged interactions, a simple perturbative calculation enables us to show that quasi-particles close to the Fermi surface are indeed long-lived objects [1, 2]. Consider the interaction between an electron outside the

Fermi sphere (wave vector $\boldsymbol{k}_1$) with an electron within the Fermi sea (wave vector $\boldsymbol{k}_2$); these particles scatter into two states outside the Fermi sphere (wave vectors $\boldsymbol{k}_3$ and $\boldsymbol{k}_4$). Momentum conservation implies that $\boldsymbol{k}_1 + \boldsymbol{k}_2 = \boldsymbol{k}_3 + \boldsymbol{k}_4$. With the help of Fermi golden rule, the inverse scattering time $1/\tau$ of this process is derived

$$\frac{1}{\tau} = \frac{2\pi}{\hbar} \sum_{\boldsymbol{k}_2, \boldsymbol{k}_3} |U(|\boldsymbol{k}_3 - \boldsymbol{k}_1|)|^2 \delta(E_{k_1} + E_{k_2} - E_{k_3} - E_{k_1+k_2-k_3}) \tag{6.20}$$

Here $\boldsymbol{k}_3 - \boldsymbol{k}_1 \equiv \boldsymbol{q}$ is the wave vector transferred between the particles by the interaction; the corresponding matrix element is the Fourier transform of the screened Coulomb interaction, $U(q) = e^2/[q^2 + (2\pi/r_0)^2]$. Note that, due to screening on distances beyond r_0, this matrix element remains finite for small values of $q < 1/r_0$, such that $U(q = 0) \sim e^2 r_0^2 \sim e^2 \lambda_\mathrm{F}^2 \sim e^2/k_\mathrm{F}^2$. Further calculations use energy conservation and the fact that the first electron is close to the Fermi surface, $k_1 \sim k_\mathrm{F}$. As a result we have $k_{2,3} \sim k_\mathrm{F}$ and $q \approx 0$, so that

$$\frac{1}{\tau} \sim |U(0)|^2 (E_{k_1} - E_\mathrm{F})^2 \sim \left(\frac{k_\mathrm{B} T}{E_\mathrm{F}} \right)^2 \tag{6.21}$$

Here we used the fact that at finite temperatures, $E_{k_1} - E_\mathrm{F} \sim k_\mathrm{B} T$. We finally obtain the temperature-dependent lifetime for Fermi liquid quasi-particles, $\tau \sim 1/T^2$, as anticipated in Sect. 6.1.1. Interaction effects can be described by Fermi-liquid theory at sufficiently low temperatures, where this lifetime (and the corresponding inelastic length) is long enough.

Weakened Screening in Low-Dimensional Systems

There are various situations in which the screening phenomenon is less effective and interactions become strong:

1. *Metals of low dimensionality.* In a two-dimensional electron system for instance, electrons are confined to a plane. The screening cloud forms only within this plane: there are no electrons perpendicular to the plane. As a result, electric field lines can escape in this direction and give rise, within the plane, to a residual long-range component of the interaction.
2. *Low density systems.* In order to understand when Coulomb interactions between electrons are weak, the average Coulomb energy U has to be compared with the average kinetic energy E_F. The average separation between electrons being λ_F, $U \sim e^2/\lambda_\mathrm{F}$, and the ratio U/E_F is thus given by $U/E_\mathrm{F} \sim e^2/(\hbar v_\mathrm{F})$. The Fermi velocity decreases with decreasing electron density n_0, hence the ratio U/E_F increases as n_0 is reduced. If the density is so low that $U \sim E_\mathrm{F}$, interactions can no longer be considered as weak and Fermi-liquid theory usually breaks down.
3. *Presence of impurities.* As we have seen, impurities cause diffusive electron motion on scales beyond the elastic mean free path. Diffusion is slower than ballistic propagation, hence the formation of the screening cloud around

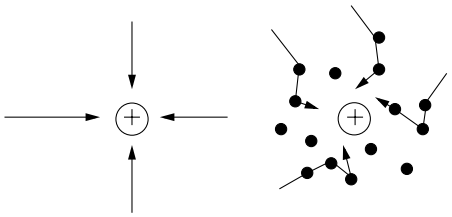


Fig. 6.5. Formation of the screening cloud in ballistic and diffusive systems

a charged inhomogeneity will take place on longer time scales in diffusive systems than in ballistic systems (see Fig. 6.5). This reduces the efficiency of screening in diffusive systems [8].

In these situations, the simple perturbative analysis presented in the previous paragraph is not correct and the Fermi-liquid description may cease to be valid. Generally, this implies that interaction effects do not lead to simple parameter renormalization; the entire structure of the theory changes and new phenomena can occur. Below, two important examples are analyzed, namely charging effects in tunnel junction systems and interaction effects in clean, single-mode quantum wires.

Tunnel Junctions and Coulomb Blockade

Coulomb Effects in Tunnel Junctions

Let us consider a *tunnel junction*, as depicted in Fig. 6.6. It consists of two diffusive multi-mode quantum wires (electrodes), separated by a tunnel barrier. The transport through such a junction is achieved through the phenomenon of quantum tunneling: in order for a charge to pass from one wire to the other, it must tunnel through the barrier separating them. If the conductance of the wires is large, the total conductance $\mathcal{G}_T$ of the system will be determined entirely by properties of the tunnel barrier:

$$\mathcal{G}_T = \frac{2e^2}{h} N T_B(E_\mathrm{F}) \tag{6.22}$$

where N is the number of modes in the diffusive wires and T_B is the transmission coefficient of the barrier at the Fermi energy. Since tunneling is a rare

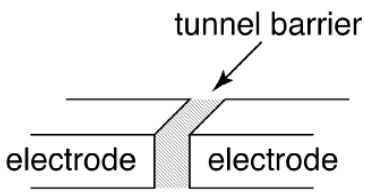


Fig. 6.6. Tunnel junction

event, $T_B(E_F) \ll 1$. In principle, apart from the conductance, we can also assign a capacitance, C, to the tunnel junction. As long as the dimensions of the tunnel junction are large, this capacitance will also be large, and its effects on the transport can be neglected. However, as the size of the junction is decreased, C decreases as well, and interesting new phenomena may arise [9].

Consider a single tunnel junction, biased by a voltage V. In view of the above discussion, the junction will be polarized by a charge $Q = CV$. Transport is achieved by tunneling of individual electrons with charge $-e$. Consider such a tunneling phenomenon, which leads to a change of the polarization charge by an amount $-e$. As a result, the difference ΔE in energy before and after the tunneling event is given by

$$\Delta E = \frac{Q^2}{2C} - \frac{(Q-e)^2}{2C} = \frac{e(Q-e/2)}{C} \tag{6.23}$$

We see that ΔE is positive if $Q > e/2$, i.e. if $eV > E_c \equiv e^2/2C$, where E_c is the *charging energy*. In other words, at low temperatures $k_B T \ll E_c$, we expect transport to be blocked if the bias voltage is smaller than E_c. This is the so-called *Coulomb blockade of tunneling*.

In order to observe this phenomenon in practice, a few conditions should be satisfied. Obviously, any energy scale entering the problem (voltage, temperature, ...) should be small compared to E_c. This implies working at low temperatures, or, alternatively, with small junctions such that the capacitance is small and the charging energy is large. Moreover, in order to observe the charging effect, the charge imbalance $Q - e$ with respect to Q must survive for sufficiently long a time. This implies a sufficiently opaque barrier, i.e. $\mathcal{G}_T \ll e^2/h$, such that a second tunneling event will not restore the charge Q. In addition, if the electrodes are good metals, screening is effective and a fast redistribution of the charge will inhibit the Coulomb blockade. Thus, not only the barrier but also its direct environment must be sufficiently resistive in order to observe the effect. Below we will study the effect of a resistive environment in some detail.

Single Junction in a Resistive Environment

Consider a single junction, embedded in a circuit, as depicted in Fig. 6.7. The tunnel junction 'sees' its capacitance C in parallel. Furthermore, the circuit contains a resistor R, representing the metallic electrodes or any other additional external resistance close to the junction. The junction is voltage biased by an ideal voltage source, kept at a voltage V_x. We can readily understand the effect of R on Coulomb blockade using a simple argument based on the uncertainty principle. Placing a resistor close to a junction with capacitance C introduces a charge redistribution time of the order of the time constant RC. According to the uncertainty principle, in order to observe Coulomb blockade, charges should not redistribute on scales shorter than $\hbar/E_c$. Thus, in order to observe the Coulomb blockade, $RC > \hbar/E_c$, which yields $R > h/e^2$ as the condition on R.

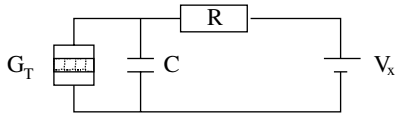


Fig. 6.7. Single junction embedded in a circuit

This simple estimate can be put on firmer ground, using a theoretical description of the environment, see [9]. The central idea in this theory is that, in the presence of a resistor, the voltage V across the junction does not equal V_x but fluctuates, $V(t) = V_x + \delta V(t)$, the fluctuating part being due to the Johnson-Nyquist noise induced by the resistor. In other words, the spectrum of the fluctuations is given by the fluctuation-dissipation theorem [10]

$$\langle \delta V(t) \delta V(t') \rangle_\omega = \hbar\omega \Re\mathrm{e}\,[Z_t(\omega)] \coth\left(\frac{\hbar\omega}{2k_\mathrm{B}T}\right) \tag{6.24}$$

where $Z_t(\omega)$ is the total impedance seen by the junction,

$$Z_t(\omega) = \frac{R}{1 + \mathrm{i}\omega RC}$$

The electrons which tunnel through the barrier interact *inelastically* with these fluctuations. The inelastic transmission through the barrier is characterized by the function $P(E)$: the probability to pass the barrier, thereby transferring an amount of energy E to the environment. In general, the current through the junction will be given by

$$I(V) = \frac{\mathcal{G}_T}{e}\left(1 - \mathrm{e}^{-\beta eV}\right) \int \mathrm{d}E \frac{E}{1 - \mathrm{e}^{-\beta E}} P(eV - E) \tag{6.25}$$

where $\beta = 1/k_\mathrm{B}T$. The probability $P(E)$ is determined essentially by the above spectrum (6.24). A detailed discussion of this function can be found in [9]. Here we will discuss the limiting case $T = 0$ only. In this case, $P(E) \sim E^{(2R/R_K - 1)}$ at low energies. Here $R_K = 1/\mathcal{G}_K = h/e^2$ is the *quantum resistance*. As a result, according to (6.25), we expect a non-linear $I - V$ characteristic, $I \sim V^{2R/R_K + 1}$. In the absence of any resistance ($R = 0$) the usual result $I = \mathcal{G}_T V$ is recovered with no hint of Coulomb blockade. As R is increased, a gap develops in the $I - V$ curve. In the limiting case $R \gg R_K$, one finds $P(E) \sim \delta(E - E_\mathrm{c})$, leading to a complete blockade of transport, $I = 0$, at voltages below E_c/e.

It is not so easy to experimentally verify the presence of Coulomb blockade in a single junction connected to a resistive environment. Diffusive quantum wires are in general not resistive enough: their resistance is typically small, $R = 1/\mathcal{G} = h/(2Ne^2) \ll R_K$. The corresponding gap in the $I - V$ curve is difficult to measure. It is not so easy to insert an additional big resistance close to the junction. An elegant way to circumvent this problem consists of using a second tunnel junction, as we discuss in the next section.

SET Transistor

In order to prevent fast charge redistribution close to the tunnel junction, one usually simply inserts a second tunnel junction. The so-called double junction device obtained this way, and depicted in Fig. 6.8, is known as the *single electron tunneling transistor* (SET transistor), a device pioneered by Fulton and Dolan [9].

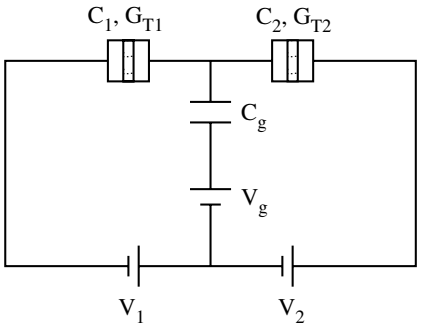


Fig. 6.8. The SET transistor

If the conductance of both junctions is sufficiently weak, $\mathcal{G}_{T,i} \ll e^2/h$ for $i = 1, 2$, the discrete number M of electrons inside the island between the junctions is well-defined. This number can be controlled by an additional gate-voltage V_g, capacitively coupled to the central island. Indeed, the electrostatic energy of the central island containing M electrons is given by

$$U(M) = \frac{(C_g V_g - Me)^2}{2C_\sigma} \tag{6.26}$$

where $C_\sigma = C_1 + C_2 + C_g$, see Fig. 6.9a. At low temperatures and for small enough bias voltages, the number of electrons inside the island remains fixed (Coulomb blockade) unless V_g is tuned to one of a set of special values such that $U(M) = U(M + 1)$. This happens for $C_g V_g/e = M + 1/2$. At these values of V_g, the charge of the island can be changed from M to $M + 1$, leading to a finite value of the linear conductance $\mathcal{G}$. This leads to the so-called Coulomb oscillations, see Fig. 6.9b. Note in particular the periodicity of these oscillations: if plotted as a function of $eN_g = C_g V_g$, they are separated by the electron charge e.

The SET transistor is an extremely useful device, which is not only used in fundamental research, but has also found applications in various fields of interest such as metrology (accurate electron pumps used as current or capacitance standards) and applied physics (the SET as an electrometer or as a thermometer).

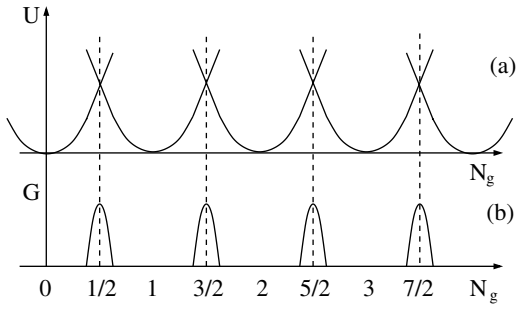


Fig. 6.9. (**a**) Charging energy of the central island as a function of $N_g = C_g V_g/e$. (**b**) Coulomb oscillations

Interactions in One-dimensional Systems

Peculiarities in One Dimension

The ground state of the non-interacting one-dimensional (1D) electron gas has quite remarkable properties. The Fermi surface is peculiar: it consists of two points only, at $-k_\mathrm{F}$ and k_F. This implies that the particle-hole spectrum is very different from its higher dimensional counterpart. Rather than a continuum of particle-hole states, the low energy excitations occur in sectors, located around wave vectors 0 and $\pm 2k_\mathrm{F}$, see Fig. 6.10. No low-energy excitations exist around $\pm k_\mathrm{F}$, as this implies particles far from the Fermi surface, which costs an energy of the order of at least E_F.

Here we are interested in *long-wavelength excitations*, involving particle-hole pairs with small total momentum $p \equiv \hbar q = \hbar(k' - k)$. We then find a linear dependence of the energy on momentum:

$$E = \frac{\hbar^2}{2m}(k'^2 - k^2) = \hbar|k' - k|\hbar k_\mathrm{F}/m = \hbar v_\mathrm{F}|q| \tag{6.27}$$

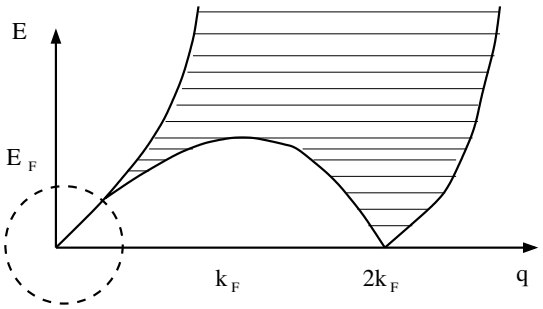


Fig. 6.10. Particle-hole spectrum of a one-dimensional Fermi gas. The *dotted circle* is the low-energy region of interest, where the dispersion is linear

The nature of a particle-hole pair, which consists of two fermions, is bosonic. It is therefore natural to write down the following effective bosonic Hamiltonian describing the low-energy, long-wavelength excitations of the 1D electron gas [11]:

$$\hat{H} = \sum_q \hbar v_{\mathrm{F}} |q| \hat{b}_q^\dagger \hat{b}_q \tag{6.28}$$

Here the operators $\hat{b}_q^\dagger$ and $\hat{b}_q$ satisfy standard bosonic commutation rules like $[\hat{b}_q, \hat{b}_{q'}^\dagger] = \delta_{q,q'}$. This Hamiltonian describes the low-lying excitations of the 1D electron gas in terms of an ensemble of harmonic oscillators, each with a frequency $\omega_q = v_{\mathrm{F}}|q|$. Below, rather than formally analyzing this bosonized Hamiltonian, we will proceed in a more transparent way. We will understand what the oscillating modes correspond to physically and see how interactions affect them.

Form of the Interaction

We consider a single-mode clean quantum wire of length L, located at a distance D_0 from a metallic substrate (see Fig. 6.11). We ignore the reservoirs for the moment and consider spinless electrons for simplicity. As discussed above, screening is ineffective in one dimension, hence the Coulomb repulsion between electrons is, in principle, long-ranged. The presence of the substrate provides screening of the interactions at distances larger than D_0. We assume that $\lambda_{\mathrm{F}} \ll D_0 \ll L$: the interaction potential $U(x)$ is short-ranged on the scale L, but long-ranged on the scale λ_{F}. The latter condition means that we can ignore exchange effects, and restrict ourselves to a density-density interaction energy of the form $U_{int} = (1/2) \int \mathrm{d}x\mathrm{d}x' n(x) U(x-x') n(x')$, where $n(x)$ is the electron density in the wire at the point x. On the scale L, $U(x)$ is short-ranged, and we approximate $U(x) = U_0 \delta(x)$. As a result $U_{int} = (U_0/2) \int \mathrm{d}x n^2(x)$.

Charge Density Waves

We next consider fluctuations of the electron density in the wire. To this end, the total density is written as $n(x,t) = n_0 + \delta n(x,t)$, where $n_0 = k_{\mathrm{F}}/\pi$ is the 1D homogeneous equilibrium spinless electron density and δn the fluctuating part. It is a common practice to introduce the associated displacement field

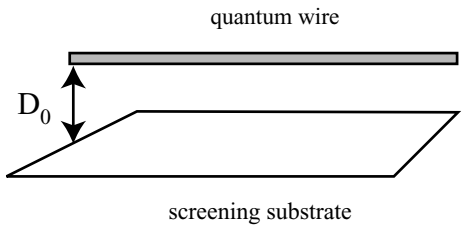


Fig. 6.11. Interacting quantum wire with a screening substrate

$u(x,t)$ such that $\delta n(x,t) = -n_0 \partial u/\partial x$. We also introduce the velocity $v = \partial u/\partial t$, such that the 1D electric current density can be written as $j = -n_0 e v$. We seek the (classical) equation of motion of the field u.

If the density of the 1D electron gas is locally increased by an amount δn with respect to n_0, a force will try to restore the equilibrium value n_0. As long as δn is small, the force will be harmonic, i.e. $\propto \delta n$. The origin of the restoring force is two-fold: the pressure in the gas and the Coulomb repulsion. For fermions, the pressure is given by $P = \hbar^2 \pi n^3/3m$; the associated restoring force is

$$-\partial P/\partial x = -\frac{\hbar^2 \pi^2 n_0^2}{m} \frac{\partial \delta n}{\partial x} = \frac{\hbar^2 \pi^2 n_0^3}{m} \frac{\partial^2 u}{\partial x^2} \tag{6.29}$$

The Coulomb repulsion leads to the restoring force

$$-U_0 \frac{\partial \delta n}{\partial x} = n_0 \frac{\partial^2 u}{\partial x^2} \tag{6.30}$$

Therefore, the equation of motion reads

$$m n_0 \frac{\partial^2 u}{\partial t^2} = \left[U_0 + \frac{\hbar^2 \pi^2 n_0}{m} \right] n_0^2 \frac{\partial^2 u}{\partial x^2} \tag{6.31}$$

We seek wave-like solutions of the form $u \sim \mathrm{e}^{\mathrm{i}(qx-\omega t)}$, that correspond to *charge density waves* of the form $\delta n \sim \mathrm{e}^{\mathrm{i}(qx-\omega t)}$. The dispersion relation of these waves is obtained immediately from (6.31),

$$\omega^2 = \left[\frac{n_0 U_0}{m} + \left(\frac{\hbar \pi n_0}{m} \right)^2 \right] q^2 \tag{6.32}$$

We see that the dispersion is *linear*, $\omega_q = s|q|$, characterized by a *velocity*

$$s = v_\mathrm{F} \sqrt{1 + \frac{U_0}{\pi \hbar v_\mathrm{F}}} \equiv v_\mathrm{F}/g \tag{6.33}$$

Here we used $n_0 = k_\mathrm{F}/\pi$ and introduced the *interaction parameter* $g = 1/\sqrt{1 + U_0/(\pi \hbar v_\mathrm{F})}$. For non-interacting electrons, $U_0 = 0$, we have $g = 1$; repulsive interactions decrease g such that $g < 1$. In the absence of interactions, $g = 1$, we find $s = v_\mathrm{F}$. This corresponds to the results obtained at the beginning of this section for the non-interacting 1D electron gas. A comparison with those results shows that the particle-hole excitations of momentum $p = \hbar q$ and energy $\hbar v_\mathrm{F}|q|$ in fact correspond to charge density waves with a linear dispersion $\omega_q = v_\mathrm{F}|q|$. They propagate along the wire at the Fermi velocity v_F. We thus identified the physical origin of the bosonized oscillator modes. In the presence of interactions, the charge-density wave picture remains largely intact. Interactions mainly will renormalize the velocity $v_\mathrm{F} \to s = v_\mathrm{F}/g$. As a result, charge density waves propagate faster in a repulsively interacting electron gas.

Electrical Transport without Reservoirs

In order to study the effect of interactions on the transport properties of a one-mode quantum wire, we first consider the response of the 1D interacting Fermi gas (Luttinger liquid) without reservoirs to an external electric field $\mathcal{E}(x,t) = \mathcal{E}_{k,\omega}\mathrm{e}^{\mathrm{i}(kx-\omega t)}$. This leads to an additional force $-e\mathcal{E}(x,t)$, that should be added to the right hand side of the equation of motion (6.31). The solution can be written as $u_{k,\omega}e^{\mathrm{i}(kx-\omega t)}$, with

$$u_{k,\omega} = -\frac{e\mathcal{E}_{k,\omega}}{m}\frac{1}{s^2k^2-(\omega+\mathrm{i}\eta)^2} \tag{6.34}$$

where the small imaginary part $\mathrm{i}\eta$ has been added to ensure convergence. We conclude that the current density obeys the relation $j_{k,\omega} = \mathrm{i}\omega e n_0 u_{k,\omega} = \sigma_{k,\omega}\mathcal{E}_{k,\omega}$ with the conductivity [12]

$$\sigma_{k,\omega} = -\frac{e^2n_0}{m}\frac{\mathrm{i}\omega}{s^2k^2-(\omega+\mathrm{i}\eta)^2} \tag{6.35}$$

The conductivity is a non-local quantity: it depends not only on frequency but also on the wave vector. The non-local nature of transport is clearly seen upon Fourier transformation to real space: we find $j(x) = \int \mathrm{d}x'\sigma(x-x',\omega)E(x')$ meaning that the current at x generally depends on the values of the electric field at different points x'. The scale for non-locality is determined by the conductivity; as can be seen from (6.35), typical contributions come from $k \sim \omega/s$, hence the scale is given by $L_\omega \sim 1/k \sim s/\omega$. In the zero-frequency limit, $L_\omega \to \infty$, and non-locality persists over the entire length L of the wire. We are interested in the real part of the conductivity, in the zero-frequency limit,

$$\Re\mathrm{e}\,[\sigma_{k,\omega}]_{\omega\to 0} = \frac{\pi\mathrm{e}^2n_0}{ms}\delta(k) \tag{6.36}$$

Then, upon Fourier transformation,

$$\mathcal{G} = \int\frac{\mathrm{d}k}{2\pi}\mathrm{e}^{-\mathrm{i}kx}\Re\mathrm{e}\,[\sigma_{k,\omega}]_{\omega\to 0} = ge^2/h \tag{6.37}$$

For $g = 1$ we recover the familiar Landauer result $\mathcal{G} = e^2/h$ for a non-interacting, single-mode quantum wire with spinless electrons. However, according to the result (6.37), the conductance of an interacting quantum wire is suppressed in the presence of repulsive interactions.

Role of the Reservoirs

It is important to realize that the above result has been obtained in the absence of electron reservoirs. In the presence of reservoirs, a different result is found.

According to the Landauer formulation, for a conductor coupled to reservoirs, the conductance is proportional to the electron transmission coefficient of the wire. As long as the transmission is perfect, i.e. in the absence of any backscattering, we expect that $T(E_\mathrm{F}) = 1$, and $\mathcal{G} = e^2/h$ for a spinless single-mode quantum wire. In the presence of Coulomb interactions this result should not change: Coulomb interactions conserve momentum, and thus cannot induce any backscattering. Therefore, we expect that $T(E_\mathrm{F}) = 1$ even in the interacting case; hence $\mathcal{G}$ should be *unaffected by interactions*, $\mathcal{G} = e^2/h$. These statements can be substantiated by more detailed calculations, see [12–14].

We conclude that a DC transport measurement on a clean interacting quantum wire, well-connected to reservoirs such that the transmission coefficient is unity, will not reveal any interaction effects. Below we will discuss two possible ways to make interactions in the wire visible in a transport measurement.

Transport at Finite Frequency

If a time-dependent bias voltage is applied at a finite frequency ω, the electrons perform an oscillatory motion within the quantum wire over a distance $L_\omega = s/\omega$. If ω is large enough, such that L_ω is smaller than the length L of the wire, the oscillating electrons are confined to the wire and do not 'feel' the reservoirs anymore. At these frequencies, the presence of reservoirs can be ignored and the conductivity is given by the result (6.35), which depends on the interaction strength through the renormalized velocity $s = v_\mathrm{F}/g$.

There is a practical problem, though. The frequencies needed to achieve the conditions $L_\omega < L$ are rather high; for $L \sim 1$ μm and a Fermi velocity $\sim 10^5$ m/s, we have $\omega > 10^{11}$ radian/s. It is difficult to perform transport experiments at such high frequencies.

Alternatively, if the wire is capacitively connected to a side-gate, frequency-dependent three-terminal measurements can be performed [15]. It turns out that even at low frequencies, such that $L < L_\omega$, the frequency-dependent side-gate conductance is modified by interactions. It has been shown that a measurement of the frequency-dependent, out-of-phase part of the side-gate conductance at low frequencies can be used to determine the interaction constant g directly.

Tunneling in an Interacting Quantum Wire

As we have seen in Sect. 6.1.2 in the case of Coulomb blockade, tunnel junctions can be used to make interactions visible in transport phenomena at zero frequency. As we will see, this is also true for interacting quantum wires. Indeed, in the presence of a tunnel barrier, momentum is no longer conserved, and the transmission coefficient will be suppressed, $T(E_\mathrm{F}) < 1$, even in the absence of interactions. It turns out that in the presence of interactions, $T(E_\mathrm{F})$ becomes strongly energy-dependent and is further suppressed [16]. The

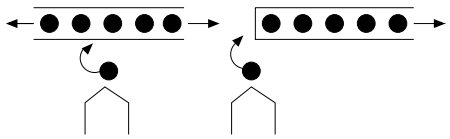


Fig. 6.12. Tunneling into a one-dimensional quantum wire

physical origin of this effect is that the tunneling electron has to overcome a Coulomb barrier in order to enter the interacting wire but the other electrons in the wire have to be displaced first.

The theoretical analysis of this phenomenon is quite complicated, and will not be discussed here. The main idea is similar to the one discussed in Sect. 6.1.2. We introduce the transmission probability $T(\epsilon)$ for an electron to tunnel into the quantum wire at energy $E = E_{\rm F} + \epsilon$ close to the Fermi energy, thereby interacting with the charge-density excitations. It turns out that this probability also shows a power-law behavior at low energies, $T(\epsilon) \sim \epsilon^{\alpha}$, where the power exponent α depends on the interaction constant g and on the precise set-up. This generally leads to a non-linear $I-V$ characteristic such as $I \sim V^{\alpha+1}$. We will illustrate this below with some relevant examples.

We first consider tunneling from a Fermi liquid metallic reservoir to an interacting quantum wire [17], see Fig. 6.12. In the left panel, tunneling occurs in the middle of the wire and electrons can be displaced both to the left and to the right to accommodate the incoming electron. Detailed calculations show that $T(\epsilon) \sim \epsilon^{\alpha_m}$ where $\alpha_m = (1/g + g - 2)/8$. In the absence of interactions, $g = 1$ and the power α_m vanishes. The transmission coefficient is a constant and the current is given by $I = \mathcal{G}_T V$. Increasing the interaction strength such that $g < 1$, the exponent α_m grows, and tunneling is strongly suppressed at low energies. This leads to a non-linear $I-V$ characteristic with $I \sim V^{\alpha_m+1}$. In the right panel, tunneling occurs at the end of the wire, so electrons can be displaced only in one direction in order to accommodate the incoming particle. Indeed, the tunneling is more strongly suppressed in this case, $T(\epsilon) \sim \epsilon^{\alpha_{\rm e}}$ where $\alpha_{\rm e} = (1/g - 1)/4$. We see that $\alpha_{\rm e} > \alpha_m$ in the interacting case $g < 1$.

We finally consider the case where the tunneling occurs within the quantum wire itself, due to the presence of an impurity. In this case $T(\epsilon) = \epsilon^{1/g-1}$, and $\alpha = 1/g - 1$. In particular, this means that the wire becomes insulating at the Fermi energy, i.e. for $\epsilon = 0$, which is a direct consequence of the repulsive interactions. This effect is a possible explanation for the suppression of conductance at low temperatures, experimentally found in disordered quantum wires [13].

6.2 Quantum Transport in Disordered Conductors

6.2.1 Introduction: Phase Coherence, Mesoscopic Regime, Physical Length Scales

This tutorial part describes in more detail some consequences of phase coherence in disordered conductors in the diffusive regime, i.e. when the length of the system is much larger than the elastic mean free path ℓ_e. It will be shown how physical properties of phase-coherent conductors can be simply related to the classical return probability for a diffusive particle. We shall mainly focus on weak-localization corrections, universal conductance fluctuations and the density-of-states anomaly. We consider weakly disordered conductors, for which the mean free path ℓ_e is much larger than the distance between electrons: $k_F \ell_e \gg 1$, where k_F is the Fermi wave vector. More details about this topic will be available at [18].

Length Scales

A disordered conductor is described by four length scales: the sample[1] size L, the mean free path ℓ_e which describes the elastic collisions, the Fermi wave length λ_F which depends on the density of electrons and the coherence length L_ϕ. This latter scale is very important because the effects we aim to describe result from the phase coherent interferences of the wave functions and thus disappear beyond L_ϕ. Smaller distances define *the mesoscopic regime*. Here, we shall mostly consider an electron gas in the following limits

$$\lambda_F \ll \ell_e \ll L \ll L_\phi \tag{6.38}$$

which correspond to a *weakly disordered* ($\lambda_F \ll \ell_e$), *mesoscopic* ($L \ll L_\phi$) metal in the *diffusive regime* ($\ell_e \ll L$). When the disorder strength becomes such that $\ell_e \sim \lambda_F$, the wave functions become localized on a typical scale ξ called the localization length [19]. Here, we shall restrict the discussion to the diffusive regime where $\xi \to \infty$. In this regime, an electron propagates diffusively because it experiences many elastic collisions while moving through the sample. The typical distance covered by the diffusive particle in a time t varies as $r^2(t) \simeq Dt$. The diffusion coefficient D is given by

$$D = \frac{v_F^2 \tau_e}{d} = \frac{v_F \ell_e}{d}. \tag{6.39}$$

$\tau_e = \ell_e / v_F$ is the elastic collision time and v_F is the Fermi velocity. The diffusive motion is thus characterized by a new time scale τ_D, called the *Thouless time*, which is the typical time for an electron to travel through the sample. It is defined as $\tau_D = L^2/D$. This time scale corresponds to a new energy scale E_c named the *Thouless energy*:

[1] If the shape is anisotropic, we define L_x, L_y and L_z.

$$E_{\mathrm{c}} = \frac{\hbar}{\tau_D} = \frac{\hbar D}{L^2}. \tag{6.40}$$

This energy plays a very important role in the description of transport and spectral properties (see for example [20]). Finally, in the diffusive regime, the phase coherence length L_ϕ is related to the phase coherence time τ_ϕ, which accounts for the breaking of the phase coherence $L_\phi^2 = D\tau_\phi$.

Classical Transport

Although electrons behave like waves, physical properties like conductivity can be calculated, in a first approximation, assuming that interferences between electronic waves can be neglected. For the conductance, this leads to the classical expression $\sigma_0 = se^2 D\rho_0$, which is known as the Einstein relation [1]. ρ_0 is the average density of states per spin direction and $s = 2$ is the spin degeneracy. For free electrons where $\epsilon = \hbar^2 k^2/2m$, the density of states ρ_0 at the Fermi level can be written in any dimension d as a function of the electronic density n

$$\rho_0 = \frac{nd}{2s\epsilon_{\mathrm{F}}} \tag{6.41}$$

so that, from Einstein relation and (6.41), one recovers the usual expression of the Drude conductivity [1][2]:

$$\sigma_0 = \frac{ne^2\tau_{\mathrm{e}}}{m} \tag{6.42}$$

For a sample of length L and section S, Ohm's law relates the conductance $\mathcal{G}$ to the conductivity through: $\mathcal{G} = \sigma_0 S/L$. More generally, for an isotropic system in dimension d: $\mathcal{G} = \sigma_0 L^{d-2}$. The conductance has the dimension of e^2/h, and it is convenient to define a dimensionless conductance $g = \mathcal{G}/(e^2/h)$. Using Ohm's law and the Einstein relation, the dimensionless conductance can be rewritten as

[2]Remember that the density of states ρ_0 at the Fermi level can be written as

$$\rho_0 = \frac{dA_d}{(2\pi)^d}\frac{mk_{\mathrm{F}}^{d-2}}{\hbar^2} \propto \frac{1}{\hbar\lambda_{\mathrm{F}}^{d-1}v_{\mathrm{F}}}$$

where $k_{\mathrm{F}} = \sqrt{2m\epsilon_{\mathrm{F}}}/\hbar$ and where A_d is the volume of the unit sphere in dimension d:

$$A_d = \frac{\pi^{d/2}}{\Gamma(1+d/2)} \qquad A_3 = \frac{4\pi}{3} \qquad A_2 = \pi \qquad A_1 = 2$$

Thus from Einstein relation, the conductivity and the conductance can be rewritten as

$$\sigma_0 = sA_d\frac{e^2}{h}\left(\frac{k_{\mathrm{F}}}{2\pi}\right)^{d-1}\ell_{\mathrm{e}} \qquad\qquad \mathcal{G}_0 = s\frac{A_d}{(2\pi)^{d-1}}\frac{e^2}{h}(k_{\mathrm{F}}L)^{d-2}k_{\mathrm{F}}\ell_{\mathrm{e}}$$

$$g = \frac{\mathcal{G}}{e^2/h} = \frac{\sigma_0 L^{d-2}}{e^2/h} = 2\pi s \frac{E_c}{\Delta} \tag{6.43}$$

We have introduced the average spacing between energy levels, which is simply related to the inverse of the density of states: $\Delta = 1/(\rho_0 L^d)$. Thus, the dimensionless conductance measures the ratio between the Thouless energy and the interlevel spacing. Finally, one notes that the dimensionless conductance can also be written as the ratio of two volumes

$$g = sdA_d \frac{\Omega}{\lambda_F^{d-1} v_F \tau_D} \tag{6.44}$$

Ω is the volume of the system and the significance of the volume $\lambda_F^{d-1} v_F \tau_D$ will become clear in Sect. 6.2.3.

Quantum Transport: Outline

Deviations from the classical Drude transport arise because of phase coherence. In the following sections, we explain why phase-coherent effects are small in the limit $k_F \ell_e \gg 1$. Their influence is most important when the system size is smaller than the phase coherence length L_ϕ, which corresponds to the mesoscopic regime. In the next section, the conductance is demonstrated to be related to the probability for an electron to diffuse through the sample. By looking at the structure of this probability, which is the product of two quantum amplitudes, we study the conditions under which deviations from classical transport may appear, using an intuitive trajectory approach. We introduce the notion of quantum crossing which is the source of the quantum behavior. In Sect. 6.2.4, the weak-localization correction is related to the trajectories with one quantum-crossing and a loop. In Sect. 6.2.5, some relevant solutions of the diffusion equation are presented, and used to calculate the weak-localization correction in a few specific geometries. In Sect. 6.2.7, the origin of the universal conductance fluctuations in the mesoscopic regime is explained as being related to trajectories with two quantum crossings. Finally, Sect. 6.3 concludes by a brief discussion on the role of the electron-electron interactions for understanding the anomaly of the density of states appearing at the Fermi level in a diffusive system.

6.2.2 Diffusive Electronic Transport, Transmission Coefficient and Conductance

Classical Probability

One aims at describing the propagation of a particle of energy ϵ from a point $\boldsymbol{r}$ to a point $\boldsymbol{r}'$. In quantum mechanics, this propagation is inferred from a probability amplitude, which is commonly expressed through a Green's function $G_\epsilon(\boldsymbol{r}, \boldsymbol{r}')$. We do not aim to develop the theory of Green's functions. For our

purpose here, it is sufficient to note that there are many possible scattering trajectories from $\boldsymbol{r}$ to $\boldsymbol{r}'$. Thus a Green function has the following structure: it is the sum of the probability amplitudes corresponding to various multiple scattering trajectories from $\boldsymbol{r}$ to $\boldsymbol{r}'$, each trajectory being characterized by an amplitude and a phase proportional to its action [21]

$$G(\boldsymbol{r},\boldsymbol{r}') = \sum_j A_j(\boldsymbol{r},\boldsymbol{r}') \tag{6.45}$$

Now, one asks about the probability to find a particle at point $\boldsymbol{r}'$ if it was initially injected at point $\boldsymbol{r}$. Such probability to go from $\boldsymbol{r}$ to $\boldsymbol{r}'$ is given by the squared modulus of the amplitude. From (6.45), this probability appears as the sum of amplitude squared terms, plus interference terms which pair different trajectories j and j'

$$|G(\boldsymbol{r},\boldsymbol{r}')|^2 = \sum_{j,j'} A_j(\boldsymbol{r},\boldsymbol{r}')A_{j'}(\boldsymbol{r},\boldsymbol{r}') = \sum_j |A_j(\boldsymbol{r},\boldsymbol{r}')|^2 + \sum_{j'\neq j} A_j(\boldsymbol{r},\boldsymbol{r}')A^*_{j'}(\boldsymbol{r},\boldsymbol{r}') \tag{6.46}$$

Since it is well known that in quantum mechanics, one must add amplitudes instead of intensities, the interference term (the second term in (6.46)) cannot be a priori neglected. However this second term describes interferences between different trajectories j and j'. Each of the contributions in this sum has a random phase which depends on the detail of the impurity configuration. After disorder averaging, the second term cancels and the probability is essentially given by the sum of intensities

$$\overline{|G(\boldsymbol{r},\boldsymbol{r}')|^2} = \sum_j \overline{|A_j(\boldsymbol{r},\boldsymbol{r}')|^2} \tag{6.47}$$

Since all phase factors have disappeared, the remaining term is completely classical. Indeed, let us assume that some event changes the phase of the amplitude A_j. The complex amplitude A^*_j gets the opposite phase, leaving the probability unchanged. The quantity $\overline{|G(\boldsymbol{r},\boldsymbol{r}')|^2} = \sum_j \overline{|A_j(\boldsymbol{r},\boldsymbol{r}')|^2}$ ressembles the classical probability and is the solution of a diffusion equation. We call it a 'diffuson'. To be more precise, but without any proof, we define the probability $P(\boldsymbol{r},\boldsymbol{r}',\omega)$ as

$$P(\mathbf{r},\mathbf{r}',\omega) = \frac{1}{2\pi\rho_0}\overline{G_\epsilon(\mathbf{r},\mathbf{r}')G^*_{\epsilon-\omega}(\mathbf{r}',\mathbf{r})}. \tag{6.48}$$

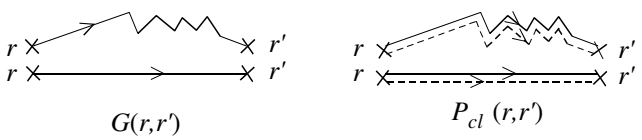


Fig. 6.13. Schematic representations of a Green's function $G(\boldsymbol{r},\boldsymbol{r}')$ and of the classical probability $P_{\rm cl}(\boldsymbol{r},\boldsymbol{r}') \propto \sum_j \overline{|A_j(\boldsymbol{r},\boldsymbol{r}')|^2}$. The upper diagrams exhibit a few collision events. They are not represented on the lower diagrams

The Green's function and its complex conjugate are taken at different frequencies. One can check that this probability is correctly normalized, that is $\int_0^\infty P(\boldsymbol{r},\boldsymbol{r}',t)\mathrm{d}\boldsymbol{r}'=1$, where $P(\boldsymbol{r},\boldsymbol{r}',t)$ is the Fourier transform of $P(\boldsymbol{r},\boldsymbol{r}',\omega)$. Starting from the Schrödinger equation in a random potential and after disorder averaging, it is possible to demonstrate that in the limit $k_\mathrm{F}\ell_\mathrm{e}\gg 1$ and for slow variations, the probability $P(\boldsymbol{r},\boldsymbol{r}',\omega)$ defined by (6.48) is the solution of a classical diffusion equation

$$(-\mathrm{i}\omega - D\Delta)\, P_\mathrm{cl}(\boldsymbol{r},\boldsymbol{r}',\omega) = \delta(\boldsymbol{r}-\boldsymbol{r}') \tag{6.49}$$

where D stands for the diffusion coefficient defined by (6.39). Doing this, we have only considered classical contributions to the average. We will study later the corrections to this classical probability.

Conductance

Our starting point to describe electric transport is the Landauer formalism. We stay at a very qualitative level but this formalism is quite natural since it expresses the *conductance as a transmission coefficient* through the disordered sample. Consider a disordered conductor of length L and section $S=W^{d-1}$. It is connected to perfect conductors (Fig. 6.14) which can be considered as wave guides where free electronic waves propagate. In this geometry, the transverse wave vectors of the eigenmodes (also called channels) are quantized by transverse boundary conditions. One can define a transmission coefficient T_{ab} from an incoming channel a (ingoing wave vector $\boldsymbol{k}_a$) to an outgoing channel b (wave vector $\boldsymbol{k}_b$). The Landauer formula is written as

$$\mathcal{G} = s\frac{e^2}{h}\sum_{a,b} T_{ab}\ . \tag{6.50}$$

To calculate the number of transverse channels, one considers that electrons are injected at the Fermi energy, i.e. such that $|\boldsymbol{k}_a|=|\boldsymbol{k}_b|=k_\mathrm{F}$. The transverse component is quantized in units of $2\pi/W$, which imposes the number of channels. In $d=2$ and $d=3$, their number is given by

$$N_\perp^{(d=2)} = \frac{2\pi k_\mathrm{F}}{2\pi/W} = k_\mathrm{F}W \qquad\qquad N_\perp^{(d=3)} = \frac{\pi k_\mathrm{F}^2}{4\pi^2/W^2} = \frac{k_\mathrm{F}^2 S}{4\pi} \tag{6.51}$$

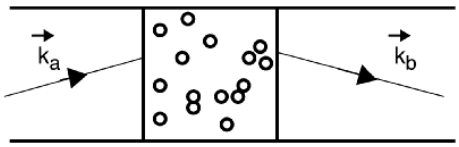


Fig. 6.14. In the Landauer formalism, the conductance is related to the transmission coefficient between different incoming and outgoing channels

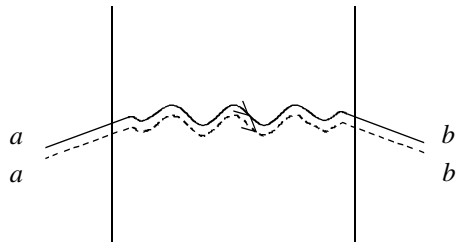


Fig. 6.15. The conductance is proportional to the classical probability to transmit a channel a to a channel b (summed over channels). The object (called diffuson) which represents this probability is the sum of contributions of paired trajectories

Now let us consider the structure of the transmission coefficient T_{ab}. It is the square of an amplitude and it has, with minor differences, the same structure as the probability $P(\boldsymbol{r}, \boldsymbol{r}', \omega)$. The main difference is the following: instead of injecting a particle at a point $\boldsymbol{r}$ inside the sample, a plane wave $\boldsymbol{k}_a$ is injected from outside the sample. In particular, the boundary conditions have to be properly treated. But, without entering into the details, it may be easily understood that, after disorder averaging, the average transmission coefficient and consequently the conductance can be related to the probability to cross the sample. More precisely for a $3d$ sample, one can show that the dimensionless conductance reads

$$g = \frac{4}{9} N_\perp v_\mathrm{F} P(0, L) \tag{6.52}$$

where $P(0, L)$ is the solution of the diffusion equation (6.49) with appropriate boundary conditions. It is given by $P(0, L) = \ell_\mathrm{e}^2 / DL$ so that

$$g = \frac{4}{3} N_\perp \frac{\ell_\mathrm{e}}{L} \tag{6.53}$$

which is equivalent to the Drude result (6.42–6.44). To obtain these results quantitatively, there are some technicalities that are not described here [18]. What should be remembered is the message of Fig. 6.15: the conductance is proportional to the classical probability to cross the sample. This is enough to understand how coherence effects appear and develop.

6.2.3 Deviations From Classical Transport: Quantum Interferences

The diffuson is a classical object. It does not depend on the phases of the complex amplitudes, and in the diffusive regime, it is the solution of a diffusion equation. However, we may have to check whether no additional effects have been left aside, when throwing out all the interference terms in relation (6.46). It turns out that some of these terms have quite interesting consequences.

Indeed, quantum effets can appear when two diffusons cross, or when a diffuson crosses with itself. The notion of quantum crossing is extremely important because it is the source of quantum effects. The diffuson being a

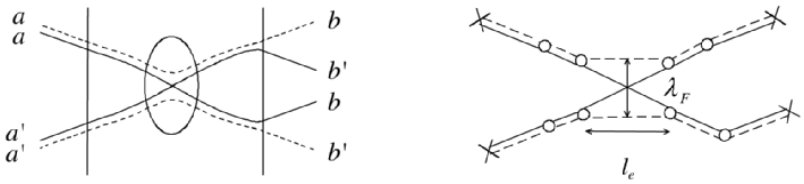


Fig. 6.16. *Left*: Crossing of two diffusons. *Right*: Detail showing that the volume of the intersection region is proportional to $\lambda_{\rm F}^{d-1} l_{\rm e}$

classical object, coherence effects can only appear because of these quantum crossings. They are at the origin of the weak-localization correction and of universal conductance fluctuations. Let us try to get some intuition about these crossing events.

Figure 6.16-Left illustrates that a crossing mixes four complex amplitudes which belong to two incoming diffusons and pair them differently. The two emerging diffusons are built with amplitudes A_j and $A_{j'}$ coming respectively from each of the incoming diffusons. They have the same phase since they follow the same path. The quantum crossing[3] is thus an object whose role is to permute the quantum amplitudes. It is necessarily short range, because trajectories have to be as close as possible to each other to avoid dephasing (Fig. 6.16-Right). Since it appears between two successive collisions on impurities, and since the phase mismatch between trajectories has to be smaller than 2π, one sees that the volume of this object is of order $\lambda_{\rm F}^{d-1}\ell_{\rm e}$.

It is important to evaluate the probability of occurrence of such quantum crossings. This probability will be a measure of the contribution of quantum effects. Since the volume of a quantum crossing is of order $\lambda_{\rm F}^{d-1}\ell_{\rm e}$, a diffuson propagating during a time t can be seen as an effective object of length $\mathcal{L} = v_{\rm F}t$ and of 'cross-section' $\lambda_{\rm F}^{d-1}$. Thus, it has a finite volume $v_{\rm F}\lambda_{\rm F}^{d-1}t$. The probability of crossing of two diffusons after a time dt in a volume $\Omega = L^d$ is thus proportional to the ratio between the volume of a diffuson and the volume of the system. As a result, the probability $\mathrm{d}p_\times(t)$ of the occurrence of a quantum crossing for two diffusons after a time $\mathrm{d}t$ writes

$$\mathrm{d}p_\times(t) = \frac{\lambda_{\rm F}^{d-1} v_{\rm F} \mathrm{d}t}{\Omega} \propto \frac{1}{g}\frac{\mathrm{d}t}{\tau_D} \tag{6.54}$$

where (6.44) has been used to introduce the dimensionless conductance g. Consider now an open system coupled to reservoirs. The time needed to travel throughout the sample is the Thouless time $\tau_D = L^2/D$. The probability of crossing during this time is given by

$$p_\times(\tau_D) = \int_0^{\tau_D} \mathrm{d}p_\times(t) = \frac{\lambda_{\rm F}^{d-1} v_{\rm F} \tau_D}{\Omega} \simeq \frac{1}{g}\,. \tag{6.55}$$

[3]Such a quantum crossing is often called a Hikami box.

This probability is the ratio of two volumes and it is proportional to the inverse dimensionless conductance (6.44). Thus the probability of crossing scales like $1/g$. Since, in the weak-disorder limit $k_{\mathrm{F}} l_{\mathrm{e}} \gg 1$, g is large, phase-coherent effects are small. The ratio $1/g$ being a small number in a metal, this explains why phase-coherent effects are weak.

There is also a very important feature to notice: when amplitudes are interchanged at a quantum crossing, the paired amplitudes belong to *different* channels. It is not at all obvious that they will stay in phase: assume that some event changes the phase of the amplitude A_j. As seen above, the complex conjugate A_j^* gets the opposite phase so that nothing happens. The same for the $A_{j'}$ and $A_{j'}^*$. However, after the crossing, since A_j and $A_{j'}^*$ follow the same path, they have the same action, except if some perturbation has changed the phase of one of them. So the new object formed after the quantum crossing looks like a diffuson but it is more *fragile*: it is sensitive to dephasing and its lifetime τ_ϕ is finite.

6.2.4 Weak Localization

We have seen that the classical probability $P(\boldsymbol{r}, \boldsymbol{r}', \omega)$ and the conductance can be expressed as a sum of contributions of pairs of complex conjugated trajectories. Since trajectories can have quantum crossings, they can form closed loops (Fig. 6.17). It turns out that in such a loop (whose contribution is not included in (6.47)), the trajectories are *time reversed*. One trajectory j and its time reversed j^T go in opposite directions. However, if there is time-reversal symmetry, they have the same action and thus they have exactly the same phase. This phase can be quite complicated because it depends on the disorder configuration but it is the same for both trajectories. The contribution of these loops do not cancel on average. If the end points are far away like in Fig. 6.17, the contribution of these new trajectories is small, of order $1/g$, but it leads to an experimentally observable effect: the weak-localization correction to the conductance. This is a phase-coherent effect because only trajectories of a size smaller than the phase coherence length L_ϕ will contribute to this additional term. Using the same type of argument as in the previous section, let us evaluate the probability to have a loop for a trajectory which travels through the sample. Since there is a quantum crossing, the probability is small, of order $1/g$. Moreover, it depends on the distribution of loops in the disordered system. Let us call it $P_{\mathrm{int}}(t)$. The probability of traversing the sample with a loop then reads

$$p_0(\tau_D) = \int_0^{\tau_D} P_{\mathrm{int}}(t)\ \mathrm{d}p_\times(t) = \frac{1}{g}\int_0^{\tau_D} P_{\mathrm{int}}(t)\frac{\mathrm{d}t}{\tau_D}\ . \tag{6.56}$$

We also have to remember that because of decoherence in the loop, only those with time t smaller that τ_ϕ contribute. The resulting probability of having trajectories with loops of time smaller than τ_ϕ is

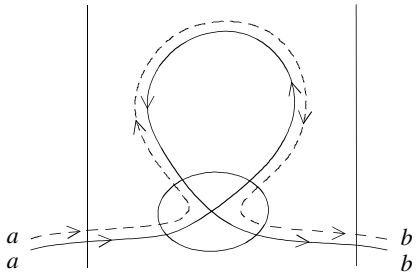


Fig. 6.17. Trajectory with a quantum crossing and a loop. In the loop, the two propagations are time reversed

$$p_0(\tau_\phi) = \int_0^{\min(\tau_D,\tau_\phi)} P_{\rm int}(t) \mathrm{d}p_\times(t) = \frac{1}{g} \int_0^{\min(\tau_D,\tau_\phi)} P_{\rm int}(t) \frac{\mathrm{d}t}{\tau_D} \qquad (6.57)$$

where $P_{\rm int}(t)$ is the probability to have loops of time t. This leads to a relative correction to the conductivity (or to the conductance) given by

$$\frac{\Delta\sigma}{\sigma_0} = \frac{\Delta\mathcal{G}}{\mathcal{G}_0} = -p_0(\tau_\phi) \; . \qquad (6.58)$$

The sign of the correction is negative because the trajectories j and j^T have opposite momenta. This quantum correction to the classical Drude conductivity is called the *weak-localization* correction [22,23]. The phase coherence is broken by inelastic events due to the coupling of the electrons to other degrees of freedom or due to electron-electron interactions. Such coherence breakdown is temperature dependent and can be phenomenologically described by a temperature dependent phase coherence length $L_\phi(T) = \sqrt{D\tau_\phi(T)}$: trajectories larger than L_ϕ do not contribute to the weak-localization corrections.

As we have seen above, the amplitude of the correction is proportional to $P_{\rm int}(t)$, the distribution of loops. The number of loops of time t is precisely given by the return probability, solution of the diffusion equation. We calculate this quantity in the next section. Moreover (6.57) and (6.58) have a meaning only in the diffusive regime for which $t > \tau_{\rm e}$ (otherwise a loop cannot be formed). The contribution of the return probability has thus to be integrated between $\tau_{\rm e}$, the smallest time for diffusion, and the phase coherence time τ_ϕ. Replacing the bounds by exponential cut-offs, the weak-localization correction can be cast in the form

$$\Delta\mathcal{G} = -2s\frac{e^2}{h} \int_0^\infty P_{\rm int}(t) \; (\mathrm{e}^{-t/\tau_\phi} - \mathrm{e}^{-t/\tau_{\rm e}}) \frac{\mathrm{d}t}{\tau_D} \qquad (6.59)$$

In order to evaluate $\Delta\mathcal{G}$ in various situations, we now study the diffusion equation and its solutions.

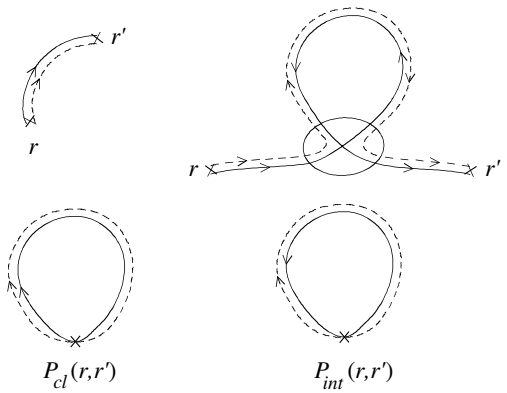


Fig. 6.18. Classical probability $P_{\rm cl}(\boldsymbol{r},\boldsymbol{r}',t)$ and the quantum correction $P_{\rm int}(\boldsymbol{r},\boldsymbol{r}',t)$. When $\boldsymbol{r}\neq\boldsymbol{r}'$, the correction is small because the probability of quantum crossing is small. When $\boldsymbol{r}=\boldsymbol{r}'$, the two contributions are equal so that the return probability is twice its classical value. The pair of time reversed trajectories is called a cooperon

6.2.5 Diffusion Equation

Explicit calculation of the probability $P_{\rm int}(t)$ requires the solution of the diffusion equation. We now open a parenthesis devoted to the derivation of some relevant solutions of this equation. As seen on Fig. 6.18, the probability $P(\boldsymbol{r},\boldsymbol{r}',t)$ has two contributions, a classical one, $P_{\rm cl}(\boldsymbol{r},\boldsymbol{r}',t)$, and a additional contribution, $P_{\rm int}(\boldsymbol{r},\boldsymbol{r}',t)$, which contains a loop. The total number of loops in (6.59) is precisely the integrated return probability

$$P_{\rm int}(t)=\int P_{\rm int}(\boldsymbol{r},\boldsymbol{r},t){\rm d}\boldsymbol{r} \tag{6.60}$$

Classical Diffusion and Quantum Correction

In Sect. 6.2.2, we have seen that the classical probability has been derived as the solution of a classical diffusion equation (written here for the Fourier transform):

$$\left(\frac{\partial}{\partial t}-D\Delta\right)P_{\rm cl}(\boldsymbol{r},\boldsymbol{r}',t)=\delta(\boldsymbol{r}-\boldsymbol{r}')\delta(t)\;. \tag{6.61}$$

However, we have seen that the probability has another component which results from trajectories with loops $P_{\rm int}(\boldsymbol{r},\boldsymbol{r}',t)$. When $\boldsymbol{r}\neq\boldsymbol{r}'$ this second contribution is very small, in the order $1/g$. When $\boldsymbol{r}=\boldsymbol{r}'$, Fig. 6.18 shows that it has exactly the same structure as the classical term. Thus the return probability is *doubled*. The interference term is *not* a solution of a diffusion equation (it is negligible when $\boldsymbol{r}'\neq\boldsymbol{r}$), but can be easily calculated when $\boldsymbol{r}'=\boldsymbol{r}$. In this case, and if there is time-reversal symmetry, we have $P_{\rm int}(\boldsymbol{r},\boldsymbol{r},t)=$

$P_{\rm cl}(\boldsymbol{r},\boldsymbol{r},t)$. However $P_{\rm int}(\boldsymbol{r},\boldsymbol{r},t)$ is phase sensitive. For example, it is modified by a magnetic field. It can be shown that it obeys the following 'diffusion-like' equation [22, 23]:

$$\left[\frac{1}{\tau_\phi}+\frac{\partial}{\partial t}-D\left(\nabla+\frac{2\mathrm{i}e\boldsymbol{A}}{\hbar c}\right)^2\right]P_{\rm int}(\boldsymbol{r},\boldsymbol{r}',t)=\delta(\boldsymbol{r}-\boldsymbol{r}')\delta(t) \tag{6.62}$$

whose solution has to be taken at $\boldsymbol{r}'=\boldsymbol{r}$. The effect of the magnetic field is described by a covariant derivative where the charge coupled to the vector potential $\boldsymbol{A}$ is $-2e$. The doubling of the charge reflects the fact that the time reversed amplitudes entering $P_{\rm int}$ accumulate *opposite* phases. The scattering rate $1/\tau_\phi$ describes the breaking of phase coherence. We now consider a few solutions of (6.61) and (6.62).

Solutions of the Diffusion Equation

The discussion of physical quantities like weak-localization correction requires the solution of the diffusion equation in some simple cases. Thus a useful quantity is the space integrated (dimensionless) return probability:

$$P(t)=\int P(\boldsymbol{r},\boldsymbol{r},t)\mathrm{d}\boldsymbol{r}\ . \tag{6.63}$$

Free Diffusion

The solution of equation (6.61) in the free space of dimension d is a gaussian function. To obtain it, one starts from the Fourier transform $P(\boldsymbol{q},t)$ of (6.61) which obeys the equation

$$\left(\frac{\partial}{\partial t}+Dq^2\right)P(\boldsymbol{q},t)=\delta(t) \tag{6.64}$$

whose solution is

$$P(\boldsymbol{q},t)=\theta(t)\mathrm{e}^{-Dq^2t} \tag{6.65}$$

so that the inverse Fourier transform $P(\boldsymbol{r},\boldsymbol{r}',t)=\int\frac{\mathrm{d}\boldsymbol{q}}{(2\pi)^d}P(\boldsymbol{q},t)\mathrm{e}^{\mathrm{i}\boldsymbol{q}.(\boldsymbol{r}-\boldsymbol{r}')}$ is

$$P(\boldsymbol{r},\boldsymbol{r}',t)=\frac{1}{(4\pi Dt)^{d/2}}\mathrm{e}^{-|\boldsymbol{r}-\boldsymbol{r}'|^2/4Dt} \tag{6.66}$$

As a result, the typical distance reached by diffusion after a time t is given by $\left\langle R^2(t)\right\rangle=2dDt$, and the return probability to the origin after a time t is obtained from (6.66) by taking $\boldsymbol{r}=\boldsymbol{r}'$. Precisely one gets $P(\boldsymbol{r},\boldsymbol{r},t)=1/(4\pi Dt)^{d/2}$, so that the integrated return probability $P(t)$ in a volume Ω, as defined by (6.63), is

$$P_{\rm cl}(t)=P_{\rm int}(t)=\frac{\Omega}{(4\pi Dt)^{d/2}} \tag{6.67}$$

2d Diffusion in a Magnetic Field

Consider the diffusion of an electron in a infinite plane placed in a perpendicular magnetic field B. The classical probability $P_{\rm cl}(\boldsymbol{r},\boldsymbol{r}',t)$ is not affected by the field. To obtain its effect on the interference part $P_{\rm int}(\boldsymbol{r},\boldsymbol{r},t)$, one has to solve the covariant diffusion equation (6.62). To that purpose, we first remark that $P_{\rm int}(\boldsymbol{r},\boldsymbol{r}',t)$ does not need to be calculated, but instead $P_{\rm int}(t)$. To evaluate directly this quantity, one notes that the general solution of the diffusion equation (6.62) has the form

$$P(\boldsymbol{r},\boldsymbol{r}',t)=\theta(t)\sum_n \psi_n^*(\boldsymbol{r})\psi_n(\boldsymbol{r}')\mathrm{e}^{-E_n t} \tag{6.68}$$

where $\theta(t)$ is the step function and $\{E_n,\psi_n\}$ are the eigenvalues and eigenfunctions of the eigenvalue equation associated to (6.62)

$$-D\left(\nabla_{\boldsymbol{r}}+\frac{2\mathrm{i}e\boldsymbol{A}}{\hbar c}\right)^2\psi_n(\boldsymbol{r})=E_n\psi_n(\boldsymbol{r}) \tag{6.69}$$

From (6.68), we find that the integrated probability $P(t)$ has the simple form

$$P(t)=\theta(t)\sum_n \mathrm{e}^{-E_n t} \tag{6.70}$$

This relation is quite useful to calculate $P_{\rm int}(t)$ in a magnetic field. The eigenvalues E_n are solutions of an effective Schrödinger equation for a free particle of mass $m=\hbar/2D$ and charge $-2e$ in a uniform field B. They are precisely the Landau levels, namely

$$E_n=\left(n+\frac{1}{2}\right)\frac{4eDB}{\hbar} \tag{6.71}$$

where n is an integer. The degeneracy of these levels for an area S is $g_n=\frac{2eB}{h}S$, while the integrated return probability $P_{\rm int}(t)$ is simply related to $\sum_n g_n\mathrm{e}^{-E_n t}$, that is

$$P_{\rm int}(t,B)=\frac{BS/\phi_0}{\sinh(4\pi BDt/\phi_0)} \tag{6.72}$$

where $\phi_0=h/e$ is the flux quantum. In the limit $B\to 0$, one recovers the solution of free diffusion: $S/(4\pi Dt)$. For large times, $P_{\rm int}(t,B)$ decreases exponentially with a characteristic time $\tau_B=\phi_0/4\pi BD$, which describes the dephasing of time reversed trajectories, and can be associated to a characteristic length $L_B=\sqrt{\hbar/2eB}$ (magnetic length).

Diffusion on a Ring or on a Cylinder

Consider now a ring of perimeter L pierced by an Aharonov-Bohm flux ϕ. The solution of (6.62) on such a ring is quite easy to guess. Starting from (6.66),

one sees that the return probability on a ring is the probability to return to the original point without making a loop around the ring plus the probability of return after one loop, two loops, etc. Then one should take (6.66) with $|\boldsymbol{r}-\boldsymbol{r}'| = mL$, and sum over all possible values of m. Moreover each turn around the loop accumulates a phase $2 \times 2\pi\phi/\phi_0$. We obtain

$$P_{\rm int}(t,\phi) = \frac{L}{\sqrt{4\pi Dt}} \sum_{m=-\infty}^{+\infty} {\rm e}^{-m^2L^2/4Dt} \cos 4\pi m\phi/\phi_0 \tag{6.73}$$

Each harmonic of this expansion represents the return probability after m loops around the ring. For a cylinder of height L_z, the diffusion is free along the z direction of the cylinder axis. The same argument as for the ring gives immediately

$$P_{\rm int}(t,\phi) = \frac{LL_z}{4\pi Dt} \sum_{m=-\infty}^{+\infty} {\rm e}^{-m^2L^2/4Dt} \cos 4\pi m\phi/\phi_0 \tag{6.74}$$

6.2.6 Back to Weak-Localization

The weak-localization correction is now computed in various situations.

Dependence on the Dimensionality

The weak-localization correction is proportional to the integrated return probability $P_{\rm int}(t)$. As a result it depends on space dimensionality d. Consider a sample whose typical size $L = \Omega^{1/d}$ is larger than L_ϕ. For time scales smaller than τ_ϕ, diffusion is like in an infinite medium and the return probability is given by (6.67), that is $P_{\rm int}(t) = \Omega/(4\pi Dt)^{d/2}$. Using the integral (6.94), one obtains the conductivity correction expressed in units of the quantum of conductance e^2/h, in the limit $L_\phi \gg \ell_{\rm e}$, namely for quasi-1D systems: $\Delta\mathcal{G} = -s\dfrac{e^2}{h}L_\phi$, whereas for $d = 2$ (or $d = 3$), $\Delta\mathcal{G} = -s\dfrac{e^2}{\pi h}\ln\dfrac{L_\phi}{\ell_{\rm e}}$ (or $\Delta\mathcal{G} = -s\dfrac{e^2}{2\pi h}\dfrac{L}{\ell_{\rm e}}$) [18,24]. The strictly $1D$ case is not considered here because the diffusion approximation does not apply in this case. Instead, we consider the case of a *quasi one-dimensional* wire of finite section S, in which the diffusive motion is $1D$ but which is $3d$ in the sense that its section is larger than the Fermi wavelength, so that many transverse channels are opened to conduction. Then one uses the relation (6.59) with $\Omega = LS$ and $P_{\rm int}(t) = L/\sqrt{4\pi Dt}$. The $2d$ result corresponds to a strictly $2d$ gas. For a quasi-2D system with a finite width a, the conductivity has to be divided by a.

Magnetoresistance

A very convenient way to measure the weak-localization correction is to study its magnetic field dependence. Indeed, the magnetic field breaks time-reversal

symmetry and suppresses the weak-localization correction. Since this correction is negative, its suppression leads to a increase of conductance or a negative magnetoresistance, which is amongst the most spectacular signature of weak-localization[4]. In a magnetic field, the weak-localization correction is still given by (6.59) where $P_{\rm int}(t,B)$ is the return probability in a magnetic field given by (6.72). The weak-localization correction is then

$$\Delta\mathcal{G}(B) = -2s\frac{e^2D}{h}\int_0^\infty \frac{B/\phi_0}{\sinh 4\pi BDt/\phi_0}\left(\mathrm{e}^{-t/\tau_\phi}-\mathrm{e}^{-t/\tau_{\rm e}}\right)\mathrm{d}t \tag{6.75}$$

Using (6.95), the integral gives

$$\Delta\mathcal{G}(B) = -s\frac{e^2}{2\pi h}\left[\Psi\left(\frac{1}{2}+\frac{\hbar}{4eDB\tau_{\rm e}}\right)-\Psi\left(\frac{1}{2}+\frac{\hbar}{4eDB\tau_\phi}\right)\right] \tag{6.76}$$

where $\Psi(x)$ is the digamma function. This expression involves a characteristic field B_ϕ defined by $B_\phi = \phi_0/8\pi L_\phi^2$, corresponding to one flux quantum through an area L_ϕ^2. The weak-localization correction disappears beyond this field (i.e. when the time τ_B is smaller than τ_ϕ) which is in order of 10^{-3} Tesla for $L_\phi \simeq 1\,\mu$m. The magnetoconductance $\mathcal{G}(B)-\mathcal{G}(0)$ is the difference between the weak-localization corrections $\Delta\mathcal{G}(B)-\Delta\mathcal{G}(0)$ and it is given by

$$-s\frac{e^2}{2\pi h}\left[\ln\left(\frac{\hbar}{4eDB\tau_\phi}\right)-\Psi\left(\frac{1}{2}+\frac{\hbar}{4eDB\tau_\phi}\right)\right] \tag{6.77}$$

The magnetoresistance $\Delta R(B) \propto -\Delta\mathcal{G}(B)/\mathcal{G}_0^2$ is thus *negative*. In the limit $B \ll B_\phi$, the expansion (6.96) gives

$$\Delta\mathcal{G}(B)-\Delta\mathcal{G}(0) \simeq \frac{s}{96\pi^2}\frac{e^2}{\hbar}\left(\frac{B}{B_\phi}\right)^2. \tag{6.78}$$

The field dependence of the weak-localization correction has been studied very carefully, in particular in metallic films as shown on Fig. 6.19 on a famous example [25]. It is a way commonly used to obtain a precise determination of the dependence $\tau_\phi(T)$.

Altshuler-Aronov-Spivak Oscillations on a Cylinder

One of the most famous experiments showing phase-coherence effect on transport is the one performed by Sharvin and Sharvin [26] who measured the magnetoresistance of a cylinder threaded by a magnetic flux ϕ. In this case the return probability $P_{\rm int}(t,\phi)$ is modulated by the flux through the cylinder and is given by (6.73). Using the integral (6.98), one obtains the flux dependence of the conductance $\Delta\mathcal{G}$ of the cylinder of length L_z:

[4]There is an additional contribution to the conductivity which results from electron-electron interaction. It does not depend on the magnetic field.

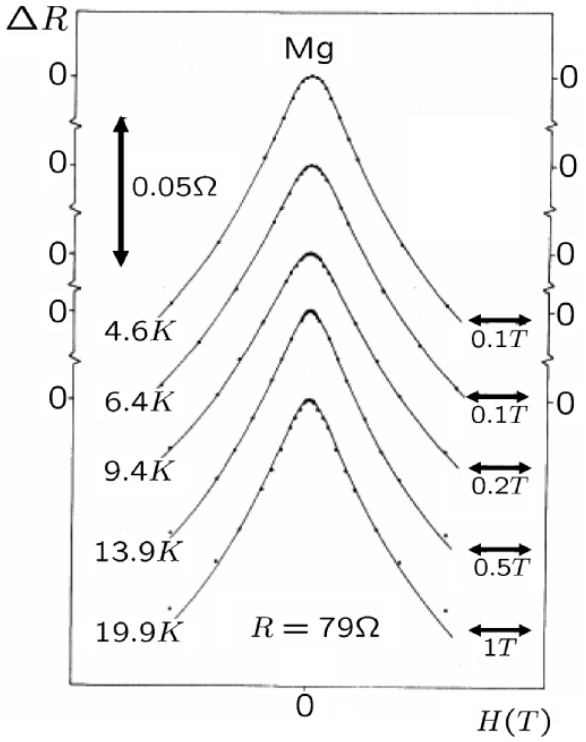


Fig. 6.19. Magnetoresistance of a Mg film, as a function of the applied field, for several temperatures. The dots are experimental data, while the curves correspond to (6.77). The time τ_ϕ is an adjustable parameter [25]

$$\Delta\mathcal{G}(\phi) = -s\frac{e^2}{\pi h}\frac{L}{L_z}\left[\ln\frac{L_\phi}{\ell_{\rm e}} + 2\sum_{m=1}^{+\infty} \mathrm{K}_0(mL/L_\phi)\,\cos 4\pi m\phi/\phi_0\right] \qquad (6.79)$$

where K_0 is the modified Bessel function. The amplitude of the oscillations of period $\phi_0/2$ decreases exponentially with the perimeter L of the cylinder and becomes negligible when $L \gg L_\phi$.

These oscillations have been predicted by Altshuler, Aronov and Spivak [27]. As shown on Fig. 6.20, the agreement between theory and experiment is excellent (note the presence of negative magnetoresistance). Similar oscillations have been observed in multiwalled nanotubes (MWNT) in a parallel magnetic field [28]. This strongly suggests that the MWNT are diffusive.

6.2.7 Universal Conductance Fluctuations

Another important signature of the coherent nature of quantum transport is the phenomenon of *Universal Conductance Fluctuations* [29, 30]. When a physical parameter is varied, such as the Fermi energy, the magnetic field (Fig. 6.21) or the disorder configuration, the conductance fluctuates around its

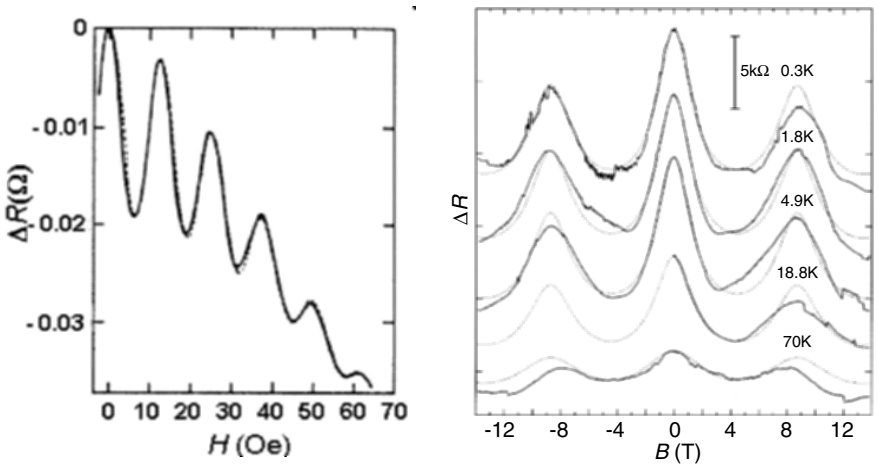


Fig. 6.20. *Left*: Magnetoresistance $\Delta R(B)$ of a lithium film on a cylinder quartz compared with (6.79) (*dashed line*) [26]. *Right*: Magnetoresistance of a MWNT in a parallel field [28]

average value. In the mesoscopic regime, these fluctuations are reproducible and provide the signature of the interference pattern associated to a given impurity configuration. The width of the distribution is universal and of the order of e^2/h [29, 30]

$$\delta\mathcal{G}^2 = \langle\mathcal{G}^2\rangle - \langle\mathcal{G}\rangle^2 \sim \left(\frac{e^2}{h}\right)^2 \tag{6.80}$$

Here we aim to understand qualitatively why the fluctuations are universal, using our picture of quantum crossings. The quantity $\delta\mathcal{G}^2$ implies the correlation between pairs of diffusive trajectories, with quantum crossings (otherwise $\delta\mathcal{G} = 0$). As each crossing has a weight $1/g$, terms with one crossing would give a correlation $\delta\mathcal{G}^2 = \mathcal{G}^2/g \propto \mathcal{G}e^2/h$. However, when summing the Landauer formula over all outgoing channels, it can be shown that the contribution with one crossing turns out to be negligible. The main contribution has *two crossings*, as shown in Fig. 6.22. The variance $\delta\mathcal{G}^2$ is thus proportional to $\mathcal{G}^2/g^2 = (e^2/h)^2$ and is therefore universal.

Let us be more precise and try to estimate the variance of the fluctuations. It is related to the probability to have two diffusons crossing the sample, with two quantum crossings. The probability $\mathrm{d}p_{\times\times}$ to have two quantum crossings in the time interval $[t, t + \mathrm{d}t]$ resembles the probability $\mathrm{d}p_0(t)$ to have a loop, because the two crossings indeed form a loop. But the relative position of the two crossings which has still to be chosen, gives an additional factor t (Fig. 6.22):

$$dp_{\times\times}(t) = \left(\frac{\lambda_{\mathrm{F}}^{d-1} v_{\mathrm{F}}}{\Omega}\right)^2 \; t \; P(t)\mathrm{d}t \simeq \frac{1}{g^2} P(t) \frac{t \; \mathrm{d}t}{\tau_D^2} \tag{6.81}$$

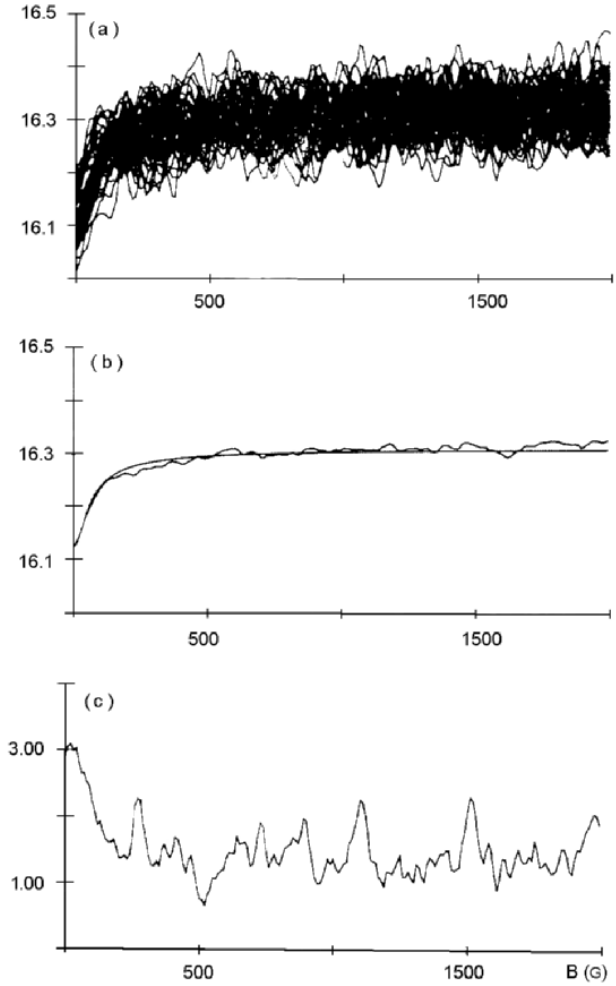


Fig. 6.21. Reproducible fluctuations of the magnetoconductance in units of e^2/h, at T = 45 mK for Si doped GaAs. Top panel shows 46 plots as function of the magnetic field, for the same sample after successive annealing. Each plot corresponds to a disorder configuration and is called a *magnetofingerprint*. Middle panel presents the average conductance versus field. The weak-localization correction disappears beyond a characteristic field. Above the same field, the variance of the fluctuations is divided by a factor 2 (*bottom panel*), corresponding to the destruction of the cooperon [31]

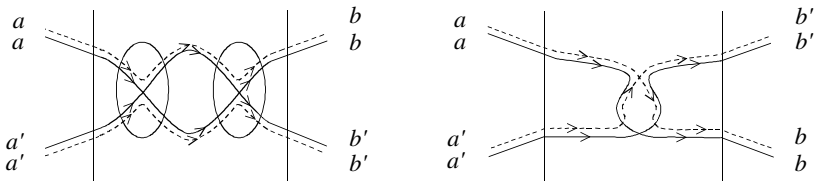


Fig. 6.22. The correlation function of the conductance implies the correlation of two diffusons, with two quantum crossings. *Left*: A contribution where the loop forms two diffusons. *Right*: A contribution where the loop forms two cooperons. The latter contribution is suppressed by a magnetic field

and the relative fluctuation is proportional to the probability of having two quantum crossings during the time τ_ϕ:

$$\frac{\delta\mathcal{G}^2}{\mathcal{G}^2} \simeq p_{\times\times}(\tau_\phi) = \frac{1}{g^2}\int_0^{\min(\tau_D,\tau_\phi)} P(t)\frac{t\mathrm{d}t}{\tau_D^2} \tag{6.82}$$

There are several ways to arrange quantum crossings (see Fig. 6.22). A careful calculation gives:

$$\delta\mathcal{G}^2 = 6s^2\left(\frac{e^2}{h}\right)^2\int_0^\infty t\,[P_{\mathrm{cl}}(t)+P_{\mathrm{int}}(t)]\mathrm{e}^{-t/\tau_\phi}\frac{\mathrm{d}t}{\tau_D^2} \tag{6.83}$$

There is an equal contribution of loops with diffusons or cooperons. In a magnetic field, the cooperon contribution is suppressed so that the variance is reduced by a factor 2, as seen on Fig. 6.21c.

Universal Conductance Fluctuations in a Quasi-1D Wire

As an example, consider a quasi-1D wire of length L connected to leads. First let us assume that the system is mesoscopic, i.e. $L \ll L_\phi$. The return probability in this case is $P_{\mathrm{int}}(t) = P_{\mathrm{cl}}(t) = \sum_q \mathrm{e}^{-Dq^2t}$ where the modes are quantized as $q = n\pi/L$, with $n > 0$. Equation (6.83) gives

$$\delta\mathcal{G}^2 = \frac{12s^2}{\pi^4}\left(\frac{e^2}{h}\right)^2\sum_{n>0}\frac{1}{n^4} \tag{6.84}$$

so that the fluctuation of the conductance is given by a universal quantity, namely independent of disorder [30]:

$$\delta\mathcal{G}^2 = \frac{2s^2}{15}\left(\frac{e^2}{h}\right)^2.$$

In the opposite limit of a macroscopic system, i.e. for $L \gg L_\phi$, $P(t)$ can be replaced by its expression (6.67) for an infinite system and one gets

$$\langle \delta \mathcal{G}^2 \rangle = 3s^2 \left(\frac{e^2}{h}\right)^2 \left(\frac{L_\phi}{L}\right)^3 .$$

In d dimensions, this result is easily generalized to obtain: $\langle \delta \mathcal{G}^2 \rangle \propto (L_\phi/L)^{4-d}$.

6.3 An Interaction Effect: the Density-of-States Anomaly

Up to now, we have neglected the interactions between electrons. In a metal the Coulomb interaction leads to modifications in some physical properties and the diffusive nature of the electronic motion plays an important role, increasing the interaction effect. This can be understood qualitatively in the following manner. The probability that two electrons interact is increased because electrons have a diffusive and not ballistic motion. The effective interaction between electrons is thus enhanced, since the probability to stay in the interaction region is increased. The change in the related physical quantities $X(E)$ at energy scale E is proportional to the time spent in the interaction region. Namely, it is proportional to the return probability in the interaction region during the time $\hbar/E$:

$$\frac{\delta X(E)}{X} \propto \frac{\lambda_{\mathrm{F}}^{d-1} v_{\mathrm{F}}}{\Omega} \int_0^{\hbar/E} P(t) \mathrm{d}t \, . \tag{6.85}$$

For instance, there is a correction to the conductance, of the same order as the weak-localization correction, but independent of the magnetic field, at low fields. There is also an anomaly in the density of states which can be measured by tunneling measurements. Here we briefly discuss the origin of this anomaly. To that purpose, we use the Hartree-Fock approximation (for details, see [1]). In this approximation the Schrödinger equation writes

$$\epsilon_i \phi_i(\boldsymbol{r}) = -\frac{1}{2m} \Delta \phi_i(\boldsymbol{r}) + V(\boldsymbol{r}) \phi_i(\boldsymbol{r}) - \sum_j^{\mathrm{occ}} \int U(\boldsymbol{r} - \boldsymbol{r}') \phi_j^*(\boldsymbol{r}') \phi_j(\boldsymbol{r}) \phi_i(\boldsymbol{r}') \mathrm{d}\boldsymbol{r}' \tag{6.86}$$

Here, only the exchange term are considered. $U(\boldsymbol{r}-\boldsymbol{r}')$ is the screened Coulomb potential. This non-linear equation should be solved self-consistently, but we treat it as a perturbation. First of all, we evaluate the correction to the density of states by calculating the shift of energy levels $\Delta\epsilon_i$. The average shift of a level i at energy ϵ is given by

$$\Delta\epsilon = -\sum_j^{\mathrm{occ}} \int U(\boldsymbol{r} - \boldsymbol{r}') \overline{\phi_j^*(\boldsymbol{r}') \phi_j(\boldsymbol{r}) \phi_i^*(\boldsymbol{r}) \phi_i(\boldsymbol{r}')} \mathrm{d}\boldsymbol{r} \mathrm{d}\boldsymbol{r}' \tag{6.87}$$

where $U(\boldsymbol{r})$ is the screened Coulomb interactions $U(\boldsymbol{r}) = \frac{e^2}{R} \mathrm{e}^{-\kappa R}$ with the inverse screening length κ given by $\kappa^2 = 8\pi e^2 \rho_0$. The ϕ_i are the eigenfunctions of the non-interacting Hamiltonian. One can show that the average of the

product of four wave functions can be related to the classical probability [18, 32]:

$$\overline{\phi_j^*(\boldsymbol{r}')\phi_j(\boldsymbol{r})\phi_i^*(\boldsymbol{r})\phi_i(\boldsymbol{r}')} = \frac{1}{\pi\rho_0\Omega^2}P_{\rm cl}(\boldsymbol{r},\boldsymbol{r}',\epsilon-\epsilon') \tag{6.88}$$

for two levels i and j at respective energies ϵ and ϵ'. The demonstration is beyond the scope of this chapter. Replacing the sum over occupied states by an integral over energy ($\sum_j^{\rm occ} = \rho_0 \int_{-\infty}^{0} {\rm d}\epsilon'$), one finds (the origin of energies is taken at the Fermi level):

$$\Delta_\epsilon = -\frac{1}{\pi\Omega^2}\int_{-\infty}^{0}{\rm d}\epsilon' \int U(\boldsymbol{r}-\boldsymbol{r}'){\rm Re}P_{\rm cl}(\epsilon-\epsilon'){\rm d}\boldsymbol{r}{\rm d}\boldsymbol{r}' \tag{6.89}$$

The interaction term varies on a length κ^{-1} much shorter than $\ell_{\rm e}$, so that in (6.89), the spatial integration can be factorized to obtain $\int U(\boldsymbol{r}){\rm d}\boldsymbol{r} = 1/2\rho_0$, so that the average energy shift is

$$\Delta_\epsilon = -\frac{1}{2\pi\rho_0}\int_{-\infty}^{0}{\rm d}\epsilon'{\rm Re}P_{\rm cl}(\boldsymbol{r},\boldsymbol{r},\epsilon-\epsilon') \tag{6.90}$$

Since, on the average, each energy ϵ is changed into $\epsilon + \Delta_\epsilon$, the distance between two levels ϵ_1 and ϵ_2 becomes $(\epsilon_2 - \epsilon_1)\,[1 + \partial\Delta_\epsilon/\partial\epsilon]$. This shift leads to a change in the density of states given by $\frac{\delta\rho}{\rho_0} = -\frac{\partial\Delta_\epsilon}{\partial\epsilon}$ so that the correction to the density of states due to interactions is related to the return probability

$$\delta\rho(\epsilon) = -\frac{1}{2\pi}{\rm Re}P_{\rm cl}(\boldsymbol{r},\boldsymbol{r},\epsilon) = -\frac{1}{2\pi\Omega}\int_0^\infty P_{\rm cl}(t)\cos\epsilon t\ {\rm d}t \tag{6.91}$$

This correction depends on the diffusive nature of the electronic motion and therefore on the dimensionality, through the dependence $P_{\rm cl}(t)$ given by (6.67). From (6.97), one obtains

$$\delta\rho(\epsilon) \propto (d-2)\frac{\epsilon^{d/2-1}}{D^{d/2}} \qquad \text{for} \qquad d = 1, 3 \tag{6.92}$$

$$\delta\rho(\epsilon) \propto \frac{1}{D}\ln\epsilon\tau_{\rm e} \qquad \text{for} \quad d = 2 \tag{6.93}$$

6.3.1 Some Useful Formulas

$$\int_0^\infty \frac{1}{t^{d/2}}({\rm e}^{-\gamma t} - {\rm e}^{-\delta t}){\rm d}t = \Gamma\left(1-\frac{d}{2}\right)[\gamma^{\frac{d}{2}-1} - \delta^{\frac{d}{2}-1}] \quad \text{for } d < 4 \tag{6.94}$$

$$\frac{1}{2}\int_0^\infty \frac{{\rm e}^{-yt} - {\rm e}^{-zt}}{\sinh(t/2)}{\rm d}t = \Psi\left(z+\frac{1}{2}\right) - \Psi\left(y+\frac{1}{2}\right) \tag{6.95}$$

$$\Psi\left(\frac{1}{2}+x\right) \simeq \ln x + \frac{1}{24x^2} + \cdots \qquad \text{for} \quad x \to \infty \tag{6.96}$$

$$\int_0^\infty \frac{1}{t^{d/2}} \mathrm{e}^{-\mathrm{i}\omega t} \mathrm{d}t = \Gamma\left(1 - \frac{d}{2}\right) (\mathrm{i}\omega)^{\frac{d}{2}-1} \quad \text{for } d < 4 \tag{6.97}$$

$$\int_0^\infty \mathrm{e}^{-\frac{\beta}{x} - \frac{\gamma x}{x}} \mathrm{d}x = 2\mathrm{K}_0(2\sqrt{\beta\gamma}) \tag{6.98}$$

6.4 Theory of Quantum Transport in Nanotubes

Electronic transport in carbon nanotubes has many different manifestations, from the 1D ballistic behavior for metallic or even doped semiconducting SWNTs, to quasi-2D fingerprints in weakly disordered MWNTs. Most of the universal properties presented in Sect. 6.1 and Sect. 6.2 have been found in experiments, demonstrating the richness of the field. However, in addition to such quantum properties, common to other mesoscopic systems or nanowires, carbon nanotubes also manifest unique transport features, such as upscaling of the mean free path with nanotube diameter or anomalous conductance scaling in defect-free incommensurate MWNTs. This section is aimed at reviewing both aspects, on the basis of recent analytical or numerical results.

6.4.1 Ballistic Conduction in Single-walled and Multiwalled Carbon Nanotubes

Bandstructure and Conducting Channels

The conduction regime in nanotubes is said to be ballistic whenever the measured conductance does not scale with the system length, but rather depend on the number of available quantum channels at a given energy (Sect. 6.1.1). This occurs in case of perfect or ohmic contacts between and a metallic nanotube and metallic electrodes with similar work functions. In this regime, the electronic conductance writes

$$\mathcal{G}(E) = \frac{2e^2}{h} \times N_\perp(E)$$

with $N_\perp(E)$ is the number of channels at energy E. Band structure calculations allows to extrapolate on the expected energy-dependent conductance spectrum. For all metallic nanotubes (especially armchairs), two quantum channels are available in the vicinity of Fermi energy $E_\mathrm{F} = 0$ (for undoped tubes), resulting in $\mathcal{G}(E_\mathrm{F}) = 2\mathcal{G}_0$ (with $\mathcal{G}_0 = \frac{2e^2}{h}$ the quantum conductance) [33]. At higher energies, the conductance increases as more channels become available to conduction, but it still remains quantized. As an illustration the electronic bands and conductance of the (5,5) metallic tube are displayed on Fig. 6.23.

These values are the highest that can be expected in an experiment for such a nanotube. Usually lower values are found since transmission at the interface

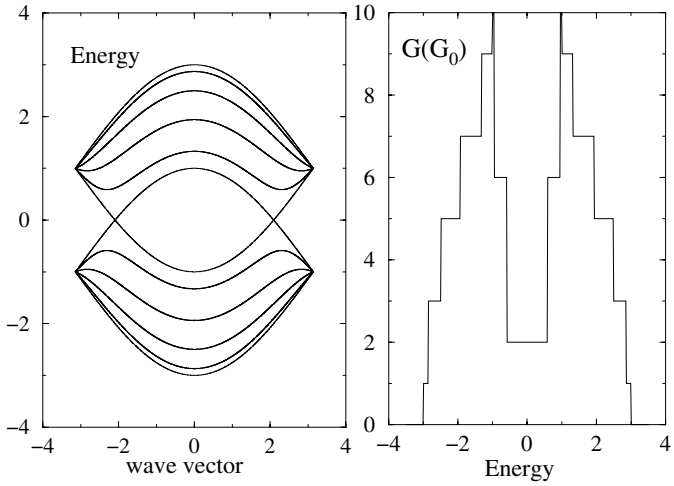


Fig. 6.23. Energy dispersion of bands (*left*) and quantum conductance as a function of energy (*right*) for the (5,5) metallic nanotube

between the voltage probes and the nanotubes are not perfectly reflectionless and partial backscattering along the tube axis (due to some topological or chemical disorder) also reduces the conductance. Generally, one introduces $T_n(E)$, the transmission amplitude for a given channel, at energy E (Landauer formula, see Sect. 6.1.1):

$$\mathcal{G}(E) = \frac{2e^2}{h} \sum_{n=1,N_\perp} T_n(E)$$

Quantized conductance is associated with a ballistic conduction of electronic wavepackets in between voltage probe. To follow simultaneously the intrinsic conduction mechanism, together with the corresponding conductance scaling, the Kubo formulation of the problem is appropriate. The Kubo conductance of a nanotube of length $L_{\rm tube}$ can be written as [34]

$$\mathcal{G}(E, L_{\rm tube}) = \frac{2e^2}{L_{\rm tube}} \lim_{t\to\tau} {\rm Tr}[\delta(E-\mathcal{H})\hat{\mathcal{D}}(t)]$$

where $\delta(E-\mathcal{H})$ is the spectral operator (whose trace gives the density of states) and $\hat{\mathcal{D}}(t) = (\hat{\mathcal{X}}(t) - \hat{\mathcal{X}}(0))^2/t$ is the diffusion operator ($\hat{\mathcal{X}}$ is the position operator along the tube axis). The voltage-probe separation is in this case given by $L_{\rm tube}$, and τ is the associated relevant time scale that fixes the value of the conductance. In such an approach, spurious effects of the contacts are fully discarded. The ballistic regime denotes that the electronic displacement scales linearly with time. The slope of the diffusion coefficient evaluated at Fermi level $\langle\hat{\mathcal{D}}(t)\rangle_{E_{\rm F}} = (\hat{\mathcal{X}}(t) - \hat{\mathcal{X}}(0))^2/t$ gives the square of the Fermi velocity

$v_{\mathrm{F}} = 3a_{\mathrm{cc}}\gamma_0/2\hbar$ ($a_{\mathrm{cc}} = 1.44\mathring{A}$ and $\gamma_0 = 2.7 - 2.9\,\mathrm{eV}$). In the previous formula, with $L_{\mathrm{tube}} = v_{\mathrm{F}}\tau$, a linear time scaling of the diffusion coefficient is found, i.e. $\mathcal{D}(t) \simeq v_{\mathrm{F}}^2 t$, and owing to the value of the density of states is $N_\perp/2\pi\hbar v_{\mathrm{F}}$, the conductance is then recovered to be length independent

$$\mathcal{G} = 2N_\perp e^2/h$$

The Kubo formula thus enables to demonstrate directly that the ballistic regime yields quantization of electronic conductance whenever metal-nanotube contacts are reflectionless.

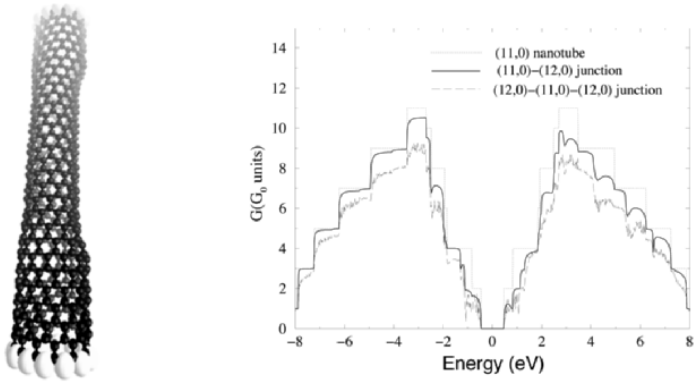


Fig. 6.24. *Left*: Illustration of a nanotube-based metal (12,0)-semiconductor (11,0)-metal (12,0) heterojunction. *Right*: Corresponding conductance spectra for the single nanotube (11,0) showing the exact number of conduction channels, together with the conductance of the double-junction (12,0)-(11,0)-(12,0)

One should note that in most cases, the contact effects yield lowering of the transmission coefficient across the interface. Indeed, even in the most favorable case, as shown in Fig. 6.24 for a nanotube based heterojunction, the symmetry mismatch between electronic states of nanotubes with different helicities reduces the transmission probability [35]. This is general to all realistic nanoscale junction between a nanotube and a metallic electrode.

6.4.2 Effects of Disorder and Doping

Conduction Regimes

To account for the effect of disorder on electronic transport of carbon nanotubes one must first notice that there is a subtle change of conduction dimensionality as the diameter of individual shells or the number of inner shells is increased. A typical instance is to consider a single vacancy (removing one carbon atom within the unit cell) and study its effect on the conductance pattern. For a (4,4) tube, a tight-binding simulation (or an effective

mass description) finds a broad dip around the charge neutrality point, which corresponds to a transition from two to one quantum channels [36]. As the diameter of the tube is increased the dip is narrowed until the modification of conductance with energy becomes single valued. This corresponds to a change of dimensionality. Whenever disorder within the tube (topological, dopants, ...) is encountered, the conduction regime departs from the ballistic regime. In the coherent regime, the presence of disorder produces elastic scattering which eventually yield a *diffusive regime*. Expressed in our language, the diffusive regime is related to a saturation of the diffusion coefficient of electronic wavepackets

$$\mathcal{D}(t \geq \tau_{\rm e}) = \ell_{\rm e} v_{\rm F}$$

where the mean free path $\ell_{\rm e}$ is introduced, while $\tau_{\rm e}$ is the corresponding elastic mean free time ($\tau_{\rm e} = \ell_{\rm e}/v_{\rm F}$). The conductance in the diffusive regime thus writes $\mathcal{G} \simeq N_\perp e^2/h(\ell_{\rm e}/L_{\rm tube})$(see Sect. 6.2.2). Such a formula, however, completely neglects quantum interferences that produce localization, and yield an exponential decrease of the conductance $\mathcal{G}(L_{\rm tube}) = (h/2N_\perp e^2)\exp(\xi/L_{\rm tube})$, as soon as $L_{\rm tube} \geq \xi \sim N_\perp \ell_{\rm e}$ (ξ: localization length).

In this section we address separately, the demonstration of suppression of backscattering in the energy window close to Fermi level, inferred from the particular symmetries of eigenstates. An analytical expression of the elastic mean free path is then derived within the Fermi golden rule and for diagonal Anderson-type disorder, an expression that is further extrapolated for a chemical disorder given by a concentration of impurities (such as boron or nitrogen). The effect of quantum interferences is finally addressed through the study of Aharonov-Bohm oscillations of the magnetoresistance.

6.4.3 Absence of Backscattering in Undoped Nanotubes

The symmetry of eigenstates of graphite or metallic nanotubes close to the Fermi level is very peculiar in the sense that under certain circumstances complete suppression of elastic backscattering is found. The original demonstration of this property for carbon nanotubes is due to Ando and coworkers [37]. First, one remembers that the eigenvalues at a $\boldsymbol{k}$ point in graphite or in carbon nanotubes, are written in a general way as $E(\boldsymbol{k}) = \pm\gamma_0\sqrt{3 + 2\cos(\boldsymbol{k}.\boldsymbol{a}_1) + 2\cos(\boldsymbol{k}.\boldsymbol{a}_2) + 2\cos(\boldsymbol{k}.(\boldsymbol{a}_1 - \boldsymbol{a}_2))}$. At the corners of the Brillouin zones, i.e. at the $\boldsymbol{K}$-points, one gets $E(\boldsymbol{K}) = 0$ with two degenerate eigenvectors (graphite or metallic tubes)

$$\Psi_{\boldsymbol{K},s}(\boldsymbol{r}) = \sum_{\boldsymbol{\ell}\ \text{all cells}} \frac{{\rm e}^{{\rm i}\boldsymbol{K}.\boldsymbol{\ell}}}{\sqrt{2}}(p_z(\boldsymbol{r} - \boldsymbol{r}_A) + p_z(\boldsymbol{r} - \boldsymbol{r}_B)) \quad \text{bonding state} \quad |\,\boldsymbol{K}_+\rangle$$

$$\Psi_{\boldsymbol{K},a}(\boldsymbol{r}) = \sum_{\boldsymbol{\ell}} \frac{{\rm e}^{{\rm i}\boldsymbol{K}.\boldsymbol{\ell}}}{\sqrt{2}}(p_z(\boldsymbol{r} - \boldsymbol{r}_A) - p_z(\boldsymbol{r} - \boldsymbol{r}_B)) \text{ antibonding state} \quad |\,\boldsymbol{K}_-\rangle$$

Exactly at these $\boldsymbol{K}$-points, one can estimate the amplitude of a scattering event from a state $|\,\boldsymbol{K}_+\rangle$ to a state $|\,\boldsymbol{K}_-\rangle$ as

$$\begin{aligned}\langle \boldsymbol{K}_+ \mid \hat{\mathcal{U}} \mid \boldsymbol{K}_- \rangle &= \int \mathrm{d}\boldsymbol{r}\mathrm{d}\boldsymbol{r'}\langle \boldsymbol{K}_+ \mid \boldsymbol{r}\rangle \mathcal{U}(\boldsymbol{r},\boldsymbol{r'})\langle \boldsymbol{r'} \mid \boldsymbol{K}_-\rangle \\ &= \int \mathrm{d}\boldsymbol{r}\mathrm{d}\boldsymbol{r'}\langle \boldsymbol{K}_+ \mid \boldsymbol{r}\rangle (u_A\delta(\boldsymbol{r}-\boldsymbol{r}_A)+u_B\delta(\boldsymbol{r}-\boldsymbol{r}_B))\langle \boldsymbol{r'} \mid \boldsymbol{K}_-\rangle \\ &= \frac{1}{2}\Big(u_A\{(p_z^{A^*}+p_z^{B^*})p_z^B\}+u_B\{(p_z^{A^*}+p_z^{B^*})(-p_z^B)\}\Big) \\ &= \frac{1}{2}(u_A-u_B)\ .\end{aligned}$$

From this calculation one sees that if the disorder potential is long-ranged with respect to the unit cell, i.e $u_A \simeq u_B$ (conservation of pseudospin symmetry), the term $\langle \boldsymbol{K}_+ \mid \mathcal{U} \mid \boldsymbol{K}_-\rangle = 0$, which means a disappearance of backscattering. One can extend this special property to the low-energy range by considering the eigenstates in the vicinity of $\boldsymbol{K}$-points. Around some $\boldsymbol{k}$ point, the wavefunction can be written as $\Psi(\boldsymbol{k},\boldsymbol{r}) = c_A(\boldsymbol{k})\tilde{p}_z^A(\boldsymbol{k},\boldsymbol{r}) + c_B(\boldsymbol{k})\tilde{p}_z^B(\boldsymbol{k},\boldsymbol{r})$ with

$$\begin{aligned}\tilde{p}_z^A(\boldsymbol{k},\boldsymbol{r}) &= \frac{1}{\sqrt{N_{\text{cells}}}}\sum_{\boldsymbol{\ell}} \mathrm{e}^{\mathrm{i}\boldsymbol{k}.\boldsymbol{\ell}} p_z(\boldsymbol{r}-\boldsymbol{r}_A-\boldsymbol{\ell}) \\ \tilde{p}_z^B(\boldsymbol{k},\boldsymbol{r}) &= \frac{1}{\sqrt{N_{\text{cells}}}}\sum_{\boldsymbol{\ell}} \mathrm{e}^{\mathrm{i}\boldsymbol{k}.\boldsymbol{\ell}} p_z(\boldsymbol{r}-\boldsymbol{r}_B-\boldsymbol{\ell})\end{aligned}$$

One then has to compute in particular the factors

$$\begin{aligned}\mathcal{H}_{AA}(\boldsymbol{k}) &= \frac{1}{N_{\text{cells}}}\sum_{\boldsymbol{\ell},\boldsymbol{\ell'}} \mathrm{e}^{\mathrm{i}\boldsymbol{k}.(\boldsymbol{\ell}-\boldsymbol{\ell'})}\langle p_z^{A,\boldsymbol{\ell}} \mid \mathcal{H} \mid p_z^{A,\boldsymbol{\ell'}}\rangle \\ \mathcal{H}_{AB}(\boldsymbol{k}) &= \frac{1}{N_{\text{cells}}}\sum_{\boldsymbol{\ell},\boldsymbol{\ell'}} \mathrm{e}^{\mathrm{i}\boldsymbol{k}.(\boldsymbol{\ell}-\boldsymbol{\ell'})}\langle p_z^{A,\boldsymbol{\ell}} \mid \mathcal{H} \mid p_z^{B,\boldsymbol{\ell'}}\rangle\end{aligned}$$

It is readily shown that for instance (following the definitions of Fig. 6.25)

$$\begin{aligned}\mathcal{H}_{AB}(\boldsymbol{k}) &= \langle p_z^{A,0}|\mathcal{H}|p_z^{B,0}\rangle + \mathrm{e}^{-\mathrm{i}\boldsymbol{k}.\boldsymbol{a}_1}\langle p_z^{A,0}|\mathcal{H}|p_z^{B,-\boldsymbol{a}_1}\rangle + \mathrm{e}^{-\mathrm{i}\boldsymbol{k}.\boldsymbol{a}_2}\langle p_z^{A,0}|\mathcal{H}|p_z^{B,-\boldsymbol{a}_2}\rangle \\ &= -\gamma_0\alpha(\boldsymbol{k})\end{aligned}$$

in other terms

$$\begin{pmatrix} E(\boldsymbol{k}) & -\gamma_0\alpha(\boldsymbol{k}) \\ -\gamma_0\alpha(\boldsymbol{k}) & E(\boldsymbol{k})\end{pmatrix}\begin{pmatrix} b_1 \\ b_2\end{pmatrix} = 0$$

with $\alpha(\boldsymbol{k}) = 1 + \mathrm{e}^{-\mathrm{i}\boldsymbol{k}.\boldsymbol{a}_1} + \mathrm{e}^{-\mathrm{i}\boldsymbol{k}.\boldsymbol{a}_2}$ and $\boldsymbol{k} = \boldsymbol{K} + \delta\boldsymbol{k}$ ($\boldsymbol{K} = (4\pi/(3\sqrt{3}a_{cc}), 0)$). One obtains $\alpha(\boldsymbol{k}) = 1 + \mathrm{e}^{-2\mathrm{i}\pi/3}\mathrm{e}^{-\mathrm{i}\delta k_x a/2} + \mathrm{e}^{2\mathrm{i}\pi/3}\mathrm{e}^{-\mathrm{i}\delta k_y a/2}$ and the problem is recast to

$$\begin{pmatrix} E(\delta\boldsymbol{k}) & \frac{3\gamma_0 a_{cc}}{2}(\delta k_x + \mathrm{i}\delta k_y) \\ \frac{3\gamma_0 a_{cc}}{2}(\delta k_x - \mathrm{i}\delta k_y) & E(\delta\boldsymbol{k})\end{pmatrix}\begin{pmatrix} b_1 \\ b_2\end{pmatrix} = 0$$

Thus the expansion around the $\boldsymbol{K}$-points yields some particular linear dispersion relation given by $E(\delta k) = \pm\hbar v_{\mathrm{F}}|\delta\boldsymbol{k}|$, and since $b_1^2(\delta k_x - \mathrm{i}\delta k_y) = b_2^2(\delta k_x + \mathrm{i}\delta k_y)$, the corresponding eigenstates can be rewritten as

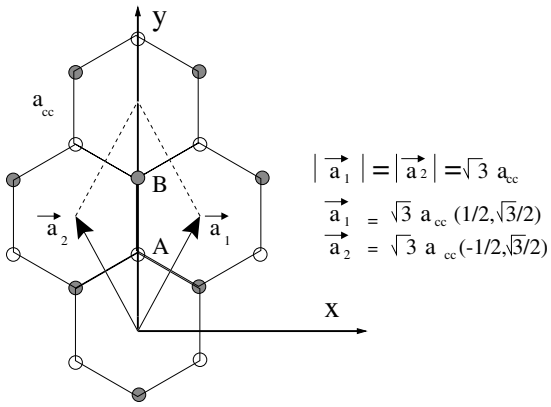


Fig. 6.25. Representation of graphite lattice vector basis

$$\Psi_{nsk}(\boldsymbol{r}) = \langle \boldsymbol{r}|n,s,\boldsymbol{k}\rangle = \frac{1}{\sqrt{2L_{\rm tube}|\boldsymbol{C}_h|}} \begin{pmatrix} \mathrm{e}^{-\mathrm{i}\theta_k} \\ s \end{pmatrix} \mathrm{e}^{\mathrm{i}(\kappa(n)x+ky)} \tag{6.99}$$

taking $\delta k_x + \mathrm{i}\delta k_y = \kappa(n) + \mathrm{i}k = |\delta k|\mathrm{e}^{\mathrm{i}\theta_k}$ ($\theta_k = \arctan(\delta k_y/\delta k_x)$, $\kappa(n) = 2n\pi/|\boldsymbol{C}_h|$) and by setting the proper normalization factors (e.g. for a nanotube with length $L_{\rm tube}$ and helical vector $\boldsymbol{C}_h$). To finally estimate the intensity of backscattering in the vicinity of Fermi level, one needs to compute the scattering matrix $\langle n=0,s,-k \mid \hat{\mathcal{T}} \mid n=0,s,+k\rangle$ with $\hat{\mathcal{T}} = \hat{\mathcal{U}} + \hat{\mathcal{U}}\mathcal{G}_0\hat{\mathcal{U}} + \hat{\mathcal{U}}\mathcal{G}_0\hat{\mathcal{U}}\mathcal{G}_0\hat{\mathcal{U}} + \ldots$

$$= \hat{\mathcal{U}} + \hat{\mathcal{U}}\frac{1}{E-\mathcal{H}_0}\hat{\mathcal{U}} + \hat{\mathcal{U}}\frac{1}{E-\mathcal{H}_0}\hat{\mathcal{U}}\frac{1}{E-\mathcal{H}_0}\hat{\mathcal{U}} + \ldots .$$

By virtue of

$$\begin{aligned}\frac{1}{E-\mathcal{H}_0-\hat{\mathcal{U}}} &= \frac{1}{E-\mathcal{H}_0}\left(1-\frac{\hat{\mathcal{U}}}{E-\mathcal{H}_0}\right)^{-1} \\ &= \mathcal{G}_0\left(1+\frac{\hat{\mathcal{U}}}{E-\mathcal{H}_0}+\left(\frac{\hat{\mathcal{U}}}{E-\mathcal{H}_0}\right)^2+\ldots\right)\end{aligned}$$

and by developing $\langle n,s,-k \mid \hat{\mathcal{T}} \mid n,s,+k\rangle$ on the basis of eigenstates one is left with

$$\begin{aligned}\langle n',s',k' \mid \hat{\mathcal{U}} \mid n,s,k\rangle &= \frac{1}{\sqrt{2L_{\rm tube}|\boldsymbol{C}_h|}}\ \mathcal{U}_{n-n'}(k-k')\left(\mathrm{e}^{\mathrm{i}\theta_k},s\right)\begin{pmatrix}\mathrm{e}^{-\mathrm{i}\theta_{k'}}\\ s'\end{pmatrix} \\ &= \frac{1}{\sqrt{2L_{\rm tube}|\boldsymbol{C}_h|}}\ \mathcal{U}_{n-n'}(k-k')(\mathrm{e}^{\mathrm{i}(\theta_k-\theta_{k'})}+ss')\ .\end{aligned} \tag{6.100}$$

If one considers the backscattering event for states on the same band close to Fermi energy ($E = E(\boldsymbol{k}=\boldsymbol{K}) = 0$), and further assuming that the disorder

potential is a sufficiently smooth function of space (long range potential that prohibits interband scattering), one thus gets

$$\langle 0, s, k \mid \hat{\mathcal{U}} \mid 0, s, -k\rangle = \mathcal{U}_0(2k)(\mathrm{e}^{\mathrm{i}(\theta_k - \theta_{-k})} + 1) = \mathcal{U}_0(2k)(\mathrm{e}^{\mathrm{i}\pi} + 1) = 0$$

This is also readily generalized to higher order terms, i.e. $\langle 0, s, -k \mid \hat{\mathcal{T}}(E)^p \mid 0, s, +k\rangle =$

$$\frac{1}{(\sqrt{2L_{\mathrm{tube}}C_h})^p}\sum_{s_1k_1}\sum_{s_2k_2}\cdots\sum_{s_pk_p}\frac{\mathcal{U}_0(-k-k_p)\mathcal{U}_0(k_p-k_{p-1})\ldots\mathcal{U}_0(k_p-k)}{(E-\varepsilon_{s_p}(k_p))(E-\varepsilon_{s_{p-1}}(k_{p-1}))\ldots(E-\varepsilon_{s_1}(k_1))}$$

$$\times\langle s|\mathcal{R}[\theta_{-k}]\mathcal{R}^{-1}[\theta_{k_p}]|s_p\rangle\langle s_{p-1}|\mathcal{R}[\theta_{k_p}][\mathcal{R}^{-1}[\theta_{k_{p-1}}]|s_{p-1}\rangle\ldots\langle s_1|\mathcal{R}[\theta_{k_1}]\mathcal{R}^{-1}[\theta_k]|s\rangle$$

where the rotation matrix $\mathcal{R}[\theta_{k_p}]$ is defined as

$$\mathcal{R}[\theta_{k_p}] = \begin{pmatrix} \mathrm{e}^{\mathrm{i}\theta_{k_p}/2} & 0 \\ 0 & \mathrm{e}^{-\mathrm{i}\theta_{k_p}/2} \end{pmatrix}. \tag{6.101}$$

According to the symmetries of eigenstates, the product reduces to: $\langle s|\mathcal{R}[\theta_k]\mathcal{R}^{-1}[\theta_{-k}]|s\rangle = \cos(\frac{\theta_k-\theta_{-k}}{2}) = 0$. Thus to all orders the backscattering is suppressed in the low-energy range around the charge neutrality point for metallic nanotubes. The applicability of such result is, however, restricted to long-range disorder and for energy windows that shrink to zero around the charge neutrality point as the diameter of metallic tubes increases. For a more general and realistic description of disorder, a study of the mean free path within the Fermi golden rule, as described hereafter, is necessary.

6.4.4 Nature of Disorder and Defects

Disorder in carbon nanotubes can be classified into two main categories. First, topological defects that change the coordination number of a finite number of carbon atoms yield undoped disordered tubes. Vacancies have been widely studied [36,38,39], as well as heptagon-pentagon pair (or Stone-Wales) defects [40] that might additionally bridge nanotubes with different helicities [41]. If n_c is the density of such defects randomly distributed within the tube, it is expected that at small concentration, the mean free path would roughly scale as $\ell_{\mathrm{e}} \sim 1/n_c$. Accounting for such defects in a tight-binding description requires a careful geometrical parametrization of the Hamiltonian energetics. Ab-initio calculations predict that the effect of a single vacancy, in a short metallic tube connected to reflectionless contacts, is likely to produce a dip in the conductance spectra roughly at $-0.4\,\mathrm{eV}$ away from the Fermi level (charge neutrality point). The second kind of defects are *substitutional impurities*. In particular, chemical substitutions of carbon atom by boron (B) or nitrogen (N) atoms have been demonstrated. These impurities introduce random scattering inside the nanotube but also produce charge transfer to

or from the tube, resulting in a shift of the position of Fermi level. Semiconducting tubes may thus become either p-doped (B) or n-doped (N), if their diameters are sufficiently large to allow small enough bandgaps.

To mimick a substitution of C by N, one can consider the defect strength as the energy difference between respective $p_\perp$-orbital. For instance $\Delta\varepsilon_{\rm CN} = \varepsilon_{p_\perp}({\rm Carbon}) - \varepsilon_{p_\perp}({\rm Nitrogen}) = -2.5\,{\rm eV}$ whereas $\Delta\varepsilon_{\rm CB} = 2.33\,{\rm eV}$.

Within a tight-binding implementation, one can establish a mapping between the parameters for the Anderson-type disorder and a more realistic description of substitutional impurities (characterized by their disorder strength and probability $\mathcal{P}$). Both disorder descriptions can be related through their distribution function defined through a common variance $\sigma_\varepsilon \sim \sqrt{\mathcal{P}(1-\mathcal{P})}|\Delta\varepsilon_{\rm CN}| = W/2\sqrt{3}$. This gives us a mapping between a random site-energy modulation of strength W and a disorder defined by a certain scattering strength ($\Delta\varepsilon_{\rm CN}$ or $\Delta\varepsilon_{\rm CB}$) and by a given density of chemical substitutions ($n_c \sim \mathcal{P}$).

6.4.5 Elastic Mean Free Path

Derivation Within the Fermi Golden Rule

Under the approximation of weak disorder, one can treat disorder effects perturbatively and write down the Fermi golden rule (FGR) for a qualitative estimation of the mean free path $\ell_{\rm e} = v_{\rm F}\tau$. First, one must derive the total density of states (TDOS) in the vicinity of Fermi level. Generally the TDOS writes $\rho(E) = {\rm Tr}[\delta(E-\mathcal{H})]$ where the trace has to be developed over a complete basis set. Assuming that the spectrum is structured by eigenstates $|\Psi_n(k)\rangle$ corresponding to eigenvalues $\varepsilon_n(k)$, one thus rewrites (note that the k_n are defined by $E - E(k_n) = 0$)

$$\rho(E) = \frac{2}{\Omega}\sum_n \int {\rm d}k\delta(E-\varepsilon_n(k)) = \frac{2}{\Omega}\sum_n \int {\rm d}k\delta(k-k_n) \times \left|\frac{\partial\varepsilon_n(k)}{\partial k}\right|^{-1}$$

with $\Omega = (8\pi^2/a^2\sqrt{3})/(2\pi|\boldsymbol{\mathcal{C}}_h|^{-1}) = 4\pi|\boldsymbol{\mathcal{C}}_h|/\sqrt{3}a^2$ is the volume of k-space per allowed value divided by the spacing between lines. The TDOS per carbon atom is finally expressed as [42]:

$$\rho(E_{\rm F}) = \frac{2\sqrt{3}a_{\rm cc}}{\pi\gamma_0|\boldsymbol{\mathcal{C}}_h|}$$

Therefore, the application of the FGR yields

$$\frac{1}{2\tau_{\rm e}(E_{\rm F})} = \frac{2\pi}{\hbar}\left|\langle\Psi_{n1}(k_{\rm F})|\ \hat{\mathcal{U}}\ |\Psi_{n2}(-k_{\rm F})\rangle\right|^2 \rho(E_{\rm F}) \times N_{\rm c}N_{\rm Ring}$$

with $N_{\rm c}$ and $N_{\rm Ring}$, the respective number of pair atoms along the circumference and the total number of rings taken in the unit cell used for diagonalization. On the other hand, the eigenstates at the Fermi level can be written as

$$\mid \Psi_{n1,n2}(k_{\mathrm{F}})\rangle = \frac{1}{\sqrt{N_{\mathrm{Ring}}}} \sum_{m=1,N_{\mathrm{Ring}}} \mathrm{e}^{\mathrm{i}mk_{\mathrm{F}}} \mid \alpha_{n1,n2}(m)\rangle$$

and with

$$\begin{aligned}
\mid \alpha_{n1}(m)\rangle &= \frac{1}{\sqrt{2N_{\mathrm{c}}}} \sum_{n=1}^{N_{\mathrm{c}}} \mathrm{e}^{\frac{2\mathrm{i}\pi n}{N_{\mathrm{c}}}} \Big(\mid p_{\perp}^{A}(mn)\rangle + \mid p_{\perp}^{B}(mn)\rangle \Big) \\
\mid \alpha_{n2}(m)\rangle &= \frac{1}{\sqrt{2N_{\mathrm{c}}}} \sum_{n=1}^{N_{\mathrm{c}}} \mathrm{e}^{\frac{2\mathrm{i}\pi n}{N_{\mathrm{c}}}} \Big(\mid p_{\perp}^{A}(mn)\rangle - \mid p_{\perp}^{B}(mn)\rangle \Big)
\end{aligned} \tag{6.102}$$

while the disorder considered here is an uncorrelated white noise distribution given by

$$\begin{aligned}
\langle p_{\perp}^{A}(mn) \mid \hat{\mathcal{U}} \mid p_{\perp}^{A}(m'n')\rangle &= \varepsilon_A(\mathrm{random}, m, n)\delta_{mm'}\delta_{nn'} \\
\langle p_{\perp}^{B}(mn) \mid \hat{\mathcal{U}} \mid p_{\perp}^{b}(m'n')\rangle &= \varepsilon_B(\mathrm{random}, m, n)\delta_{mm'}\delta_{nn'} \\
\langle p_{\perp}^{A}(mn) \mid \hat{\mathcal{U}} \mid p_{\perp}^{A}(m'n')\rangle &= 0
\end{aligned} \tag{6.103}$$

where $\varepsilon_B(\mathrm{random}, m, n)$ and $\varepsilon_A(\mathrm{random}, m, n)$ are the site energies of electron at atoms A and B in position (m, n), randomly distributed within the interval $[-W/2, W/2]$ following uniform distribution with probability $\mathcal{P} = 1/W$. By replacing such expressions of eigenstates in the previous form for elastic scattering time, one finds

$$\frac{1}{2\tau_{\mathrm{e}}(E_{\mathrm{F}})} = \frac{2\pi}{\hbar}\frac{1}{4}\Bigg(\frac{1}{\sqrt{N_{\mathrm{c}}N_{\mathrm{Ring}}}} \sum_{N_{\mathrm{c}}N_{\mathrm{Ring}}} \varepsilon_A^2 + \frac{1}{\sqrt{N_{\mathrm{c}}N_{\mathrm{Ring}}}} \sum_{N_{\mathrm{c}}N_{\mathrm{Ring}}} \varepsilon_B^2 \Bigg) \rho(E_{\mathrm{F}})$$

Thus if the disorder is described by random fluctuations of site energies with uniform probability $1/W$, with W the disorder bandwidth, the mean free path can be finally analytically derived as [43, 44]

$$\ell_{\mathrm{e}} = \frac{18 a_{\mathrm{cc}} \gamma_0^2}{W^2} \sqrt{n^2 + m^2 + nm} \tag{6.104}$$

For a metallic nanotube ($N_T = 5, N_T = 5$), with $W = 0.2\gamma_0$ one finds $\ell_{\mathrm{e}} \sim 560\,\mathrm{nm}$ which is much more larger than the circumference length. As shown in Fig. 6.26, numerical studies confirm the scaling law of the mean free path with the nanotube diameter close to the charge neutrality point. For semiconducting bands, the $1/W^2$ is still satisfied, but mean free paths are seen to be much smaller and do not scale with diameter [45].

In the work of Liu et al. [46], the electronic transport of boron-doped nanotubes has been investigated experimentally. The concentration of boron atoms with respect to carbon atoms was evaluated to be $\simeq 1\%$ whereas the diameters of tubes were estimated in the range $[17\,\mathrm{nm}, 27\,\mathrm{nm}]$ and mean free paths in the order of $\ell_{\mathrm{e}} = 220 - 250\,\mathrm{nm}$ were inferred from weak-localization theory. Applying (6.104) with the corresponding parameters, one finds a theoretical estimate of $\ell_{\mathrm{e}} \simeq 274\,\mathrm{nm}$ for the tube with diameter 17 nm, in agreement

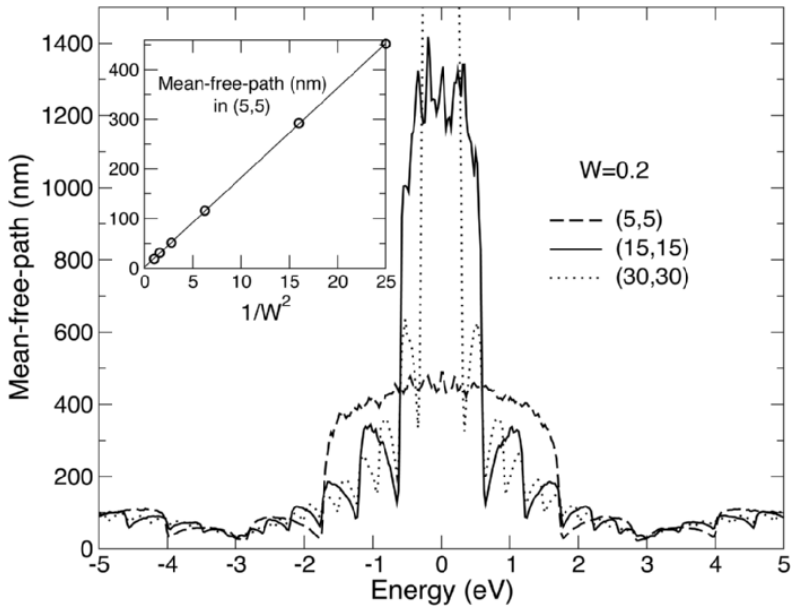


Fig. 6.26. Main frame: Energy dependent mean free path as a function of diameter. Inset: $1/W^2$-scaling in agreement with the Fermi golden rule. Adapted from [45]

with experimental estimates. Ab-initio calculations can be also very useful to address the quantitative effect of chemical impurities on both charge transfer and elastic scattering in long nanotubes. In Fig. 6.27, the mean free path for long metallic nanotubes doped with boron is reported as a function of doping level and diameters, at Fermi energy. The FGR and mean free path increase with tube diameter are correctly reproduced [39].

In low-dimensional systems, the relation between the mean free path and the localization length is an interesting problem. Thouless [56] was the first to derive a simple relation $\xi = 2\ell_e$ between both quantities in strictly 1D systems, further noticing that in quantum wires with higher number of conducting channels $N_\perp$, $\xi \sim N_\perp \ell_e$ [57]. In metallic carbon nanotubes at E_F, one thus expects to have a localization length given by $\xi = \frac{36 a_{cc} \gamma_0^2}{W^2} \sqrt{n^2 + m^2 + nm}$ that also scales linearly with the tube diameter for low disorder.

6.4.6 Quantum Interference Effects and Magnetotransport

Applying a magnetic field is a powerful tool to unveil quantum interferences effects as detailed in Sect. 6.2.4. In the presence of elastic disorder, the weak-localization scheme can be illustrated for metallic nanotube. The magnetoresistance depends on the probability $\mathcal{P}$ for an electronic wavepacket to go from one site $|P\rangle$ to another $|Q\rangle$, which can be written as

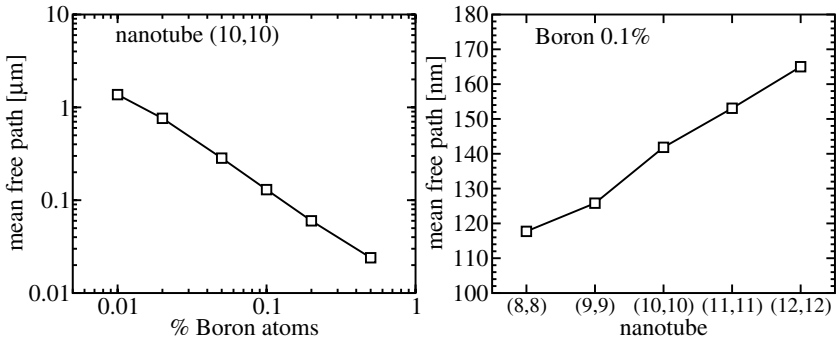


Fig. 6.27. Scaling of the mean free path at Fermi level, for a B-doped (n, n) nanotube. *Left*: in the case of a (10,10) nanotube with various boron concentrations, $\ell_{\rm e}$ behaves like the inverse of the doping rate. *Right*: for a fixed concentration of B atoms, $\ell_{\rm e}$ is a linear function of the nanotube's diameter

$$\mathcal{P}_{|P\rangle\to|Q\rangle} = \sum_i \mid \mathcal{A}_i \mid^2 + \sum_{i\neq j} \mathcal{A}_i \mathcal{A}_j {\rm e}^{{\rm i}(\alpha_i - \alpha_j)}$$

with $\mathcal{A}_i {\rm e}^{{\rm i}\alpha_i}$ the probability amplitude to go from $|P\rangle$ to $|Q\rangle$ via the i-path. Most of those terms, when averaged over disorder, vanish. In the special case of a cylinder or nanotube, two paths returning back to the origin yield a constructive contribution of quantum interferences, reducing the conductance (weak-localization correction). Switching on a magnetic field removes time-reversal symmetry of these paths, resulting in an increase of the conductance or decrease of resistance (negative magnetoresistance). The second effect of the magnetic field is to modulate the field-dependent resistance that becomes $\phi_0/2$-periodic. Indeed, since the phase factors can then be written as ($\boldsymbol{A}$ the vector potential)

$$\alpha_\pm = \pm \frac{e}{\hbar c} \oint \boldsymbol{A}.{\rm d}\boldsymbol{r} = \pm \frac{2\pi}{\phi_0} \oint \boldsymbol{A}.{\rm d}\boldsymbol{r}$$

the amplitude is then written $|\mathcal{A}|^2 \; |1 + {\rm e}^{{\rm i}(\alpha_+ - \alpha_-)}|^2$ resulting in a $\cos(2\pi\phi/\phi_0)$ modulation factor. Below, the behaviors of field-dependent diffusion coefficients are shown for a (9,0) metallic nanotube, as a function of the mean free path evaluated following the analytical formula [104]. By using the Anderson-type disorder, the value of the mean free path can be tuned by the disorder strength W, so that several situations of interest can be explored. First the weak-localization regime [27] is analyzed under the condition $\ell_{\rm e} < |\boldsymbol{C}_h| < L(\tau_\phi)$.

Figure 6.28 shows that the diffusivity increases at a low fields (negative magnetoresistance) and that the periodic Aharonov-Bohm oscillations are dominated by a $\phi_0/2$ period, that is

$$\mathcal{D}(\tau_\phi, \phi + \phi_0/2) = \mathcal{D}(\tau_\phi, \phi)$$

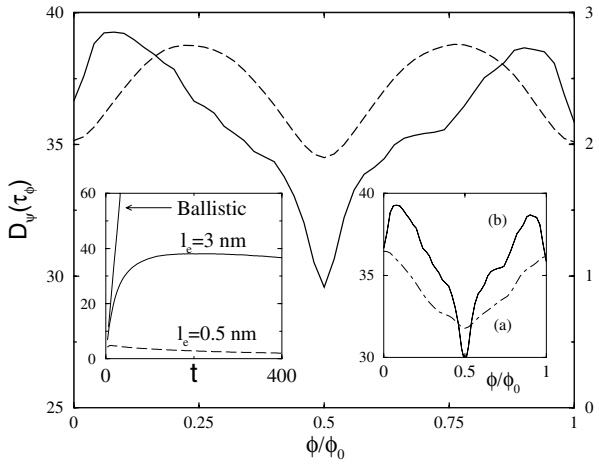


Fig. 6.28. *Main frame*: $\mathcal{D}(\tau_\phi, \phi/\phi_0)$ (in units $\text{Å}^2\gamma_0/\hbar$) for a metallic SWNT $(9,0)$ evaluated at time $\tau_\phi \gg \tau_\mathrm{e}$, for two disorder strengths, $W/\gamma_0 = 3$ and 1, such that the mean free path ($\ell e \sim 0.5$ and 3 nm, respectively) is either shorter (*dashed line*) or larger (*solid line*) than the nanotube circumference ($|\boldsymbol{C}_h| \sim 2.3$ nm). The right-hand y-axis is associated with the dashed line and the left-hand y-axis with the solid line. *Left inset*: Time dependent diffusion coefficients for the corresponding disorder values (ballistic motion is also shown for comparison with diffusive regimes). *Right inset*: $\mathcal{D}(\tau_\phi, \phi/\phi_0)$ for $\ell_\mathrm{e} = 3$ nm and $L(\tau_\phi) < 2\ell_\mathrm{e}$ (*dot-dashed*) or $L(\tau_\phi) > 2\ell_\mathrm{e}$ (*solid line*). Adapted from [55]

in agreement with weak-localization predictions. In contrast, when $\ell_\mathrm{e} > |\boldsymbol{C}_h|, L(\tau_\phi) < 2\ell_\mathrm{e}$, the system is found to exhibit a *positive magnetoresistance* associated with

$$\mathcal{D}(\tau_\phi, \phi + \phi_0) = \mathcal{D}(\tau_\phi, \phi)$$

(ϕ_0 Aharonov-Bohm period). For the case $\ell_\mathrm{e} > |\boldsymbol{C}_h|, L(\tau_\phi) > 2\ell_\mathrm{e}$, a negative magnetoresistance and an Aharonov-Bohm period Φ_0 are obtained. To compare with the experiment of Bachtold et al. [28], we use the analytical formula for the mean free path (6.104) and with a reasonable value of the disorder parameter, we get $\ell_\mathrm{e} \simeq 10^4 \times |\boldsymbol{C}_h|$ ($|\boldsymbol{C}_h|$ the circumference of the outer nanotube in the experiment). The apparent inconsistency between the value of the mean free path and the observation of $\phi_0/2$ Aharonov-Bohm oscillations point out that the interpretation of the experiments has to be elaborated with care, also because the precise position of the Fermi level and contribution of inner shells remain elusive.

6.4.7 Contribution of Intershell Coupling

Multiwalled nanotubes or bundles of single-walled nanotubes present additional geometrical complexity. Indeed, they are made from a few to tens of

shells with random helicities weakly coupled mainly through Van der Waals intershell interaction. The intershell coupling has also been expressed within a tight-binding scheme, which is believed to provide a good description of the electronic structure of multiwalled nanotubes. In the standard model, still one $p_\perp$-orbital per carbon atom is kept, with zero onsite energies, whereas constant nearest-neighbor hopping on each layer n, and hopping between neighboring layers are defined as [58–60]:

$$\mathcal{H} = \gamma_0 \left[\sum_{i,j} |p_\perp^j\rangle\langle p_\perp^i| \right] - \beta \left[\sum_{i,j} \cos(\theta_{ij}) \mathrm{e}^{-\frac{d_{ij}-a}{\delta}} |p_\perp^j\rangle\langle p_\perp^i| \right]$$

where θ_{ij} is the angle between the $p_\perp^i$ and $p_\perp^j$ orbitals, and d_{ij} denotes their relative distance. The parameters used here are: $\gamma_0 = 2.9\,\mathrm{eV}$, $a = 3.34$ Å, $\delta = 0.45$ Å [59]. The difference between SWNTs and MWNTs stems from the parameter β, and the limit $\beta = 0$ corresponds to uncoupled shells. An ab-initio estimate gives $\beta \simeq \gamma_0/8$ [60]. Besides, two kinds of multiwalled nanotubes can be distinguished. The first class corresponds to periodic objects as exemplified by the $(6,4)@(12,8)@(18,12)$ case (Fig. 6.29-Left). Consisting of two semiconducting shells enclosed by a metallic one, there exists a common unit cell for all shells, which is defined by a unique translational vector $|\boldsymbol{T}| \simeq 18.79$Å. In contrast, for the $(6,4)@(10,10)@(17,13)$ tube (Fig. 6.29-Right), the translational vectors along each shell are respectively $|\boldsymbol{T}_{(6,4)}| = 3\sqrt{19}a_{\mathrm{cc}}$, $|\boldsymbol{T}_{(10,10)}| = \sqrt{3}a_{\mathrm{cc}}$, $|\boldsymbol{T}_{(17,13)}| = 3\sqrt{1679}a_{\mathrm{cc}}$, which indicates that there is no unit cell, because of incommensurability (ratio of lengths of individual shell translational vectors are irrational numbers). These two cases illustrate the possibility of obtaining either translationally invariant intertube coupling or aperiodic coupling along the MWNT axis. The natural concern is to search for the related fundamental electronic (transport)-properties intrinsic to MWNTs.

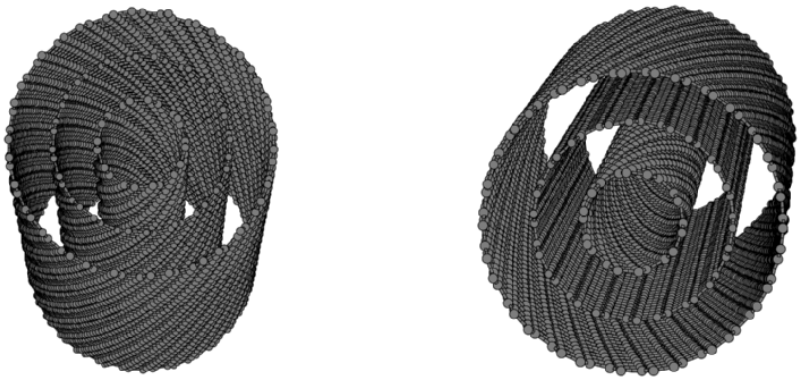


Fig. 6.29. *Left*: Commensurate $(6,4)@(12,8)@(18,12)$ MWNT. *Right*: Incommensurate $(6,4)@(10,10)@(17,13)$ triple-wall nanotube

Commensurate Multiwalled Nanotubes

Commensurate MWNTs are periodic objects with a well-defined unit cell. Bloch theorem applies and the bandstructure can be easily computed. Given that shells only weakly interact, the conductance spectrum of the MWNT in the ballistic conduction regime should be given as the sum of all conducting channels at a given energy (as exemplified on Fig. 6.30). Consequently, one excepts a very small intrinsic resistance at E_{F} for a metallic MWNT. As discussed below, at certain energies, the intershell interaction might be at the origin of a stepwise reduction of conduction channels.

Let us consider the generic MWNT made of coaxial metallic shells with perfect commensurability, namely the armchair double-walled $(5,5)@(10,10)$ and triple-walled $(5,5)@(10,10)@(15,15)$ nanotubes. Such MWNTs have a fivefold common symmetry. Their respective orientation might also possess additional symmetry planes perpendicular to the tube axis. In that case, interwall interaction does not modify the overall spectrum, which is a superposition of independent spectra. For instance, at the charge neutrality point the conductance for the triple-walled will be $\mathcal{G} = 6\mathcal{G}_0$ (see Fig. 6.30). If, however, the symmetry is lowered by misorienting (rotationally and translationally) one nanotube with respect to another, then splitting of the degeneracy occurs, and pseudogaps are formed [60, 61]. The presence of pseudogaps in the density of states has direct consequences on the total number of conduction channels available at a given energy. As shown by Tomanék and coworkers [62], the conductance in the ballistic regime might then be reduced in the vicinity of Fermi level. Such modifications of the conductance in the ballistic regime

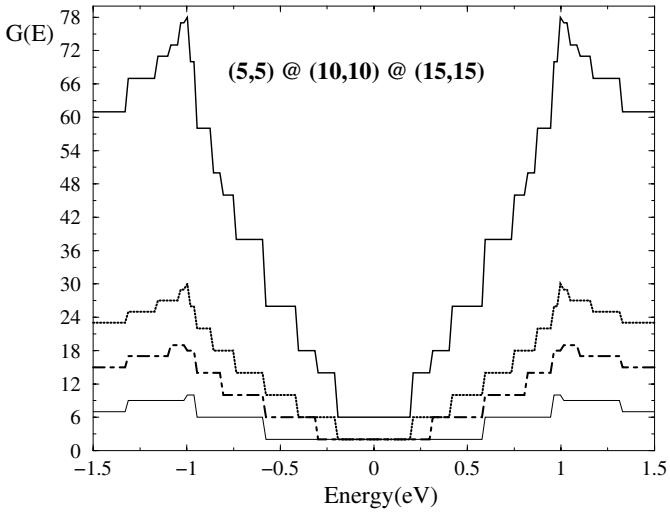


Fig. 6.30. Conductance patterns of the $(5,5)@(10,10)@(15,15)$ MWNT and its constitutive shells

are singular to shell-conformation of multiwalled tubes. Associated with the pseudogaps, charge redistribution can also be investigated [61]. One notes, however, that such a strong effect of intershell interaction is specific to unsymmetrical orientations of neighboring shells, but that is absent for other commensurate walls such as $(6,6)@(11,11)$ with no C_{5h} symmetry.

Incommensurate Multiwalled Nanotubes

The case of incommensurate shells is even more complicated to consider, since no Bloch theorem applies in the strict sense. It is thus more difficult to anticipate the consequences of intershell coupling, e.g. in terms of pseudogaps, on the conductance of such aperiodic MWNT objects. It turns out that the conduction mechanism in MWNTs is quite sensitive to the value of β and to the position of the Fermi energy. To illustrate specific patterns of electronic motion in incommensurate tubes, it is instructive to follow the time dependent evolution of an electronic wavepacket initially localized in the outer shell.

In a commensurate system, assuming a wavepacket initially localized on the outer shell of the MWNT, a rapid redistribution of the weight of the wavefunction on each shell is found to be given by a time scale $\tau_{ll} \sim \hbar\gamma_0/\beta^2$, following the corresponding Fermi golden rule. By increasing the amplitude of β in the range $[\gamma_0/8, \gamma_0]$, the expected scaling form of τ_{ll} is checked numerically [55]. For two electrodes separated by 1μm and assuming ballistic transport with a Fermi velocity of 10^6 ms^{-1}, the corresponding time flight between electrodes is $\sim$4500 $\hbar/\gamma_0$. This is two orders of magnitude larger than τ_{ll} (for $\beta = \gamma_0/8$), and points towards an important contribution of interwall coupling in experiments [63]. In contrast to commensurate MWNTs, the redistribution phenomenon in incommensurate tubes is found much slower with a higher redistributed weight from the outer to inner shells [55]. Such efficient wave redistribution to inner shells seems consistent with the fact that incommensurate systems are intermediate between periodic and disordered systems. The behavior of the diffusion coefficient further allows to unveil that the carrier motion might strongly depart from ballistic motion because of multiple-scattering effects that develop along the conduction pathway. The conduction is found to be *non-ballistic*, with $\sqrt{\mathcal{D}(t) \times t} \sim \mathcal{A}t^{\eta}$ [45, 55].

The coefficient η is found to decrease from 1 to $\sim 1/2$ by increasing either β or the number of coupled incommensurate shells [55]. On Fig. 6.31, the conduction mechanism is followed at specific Fermi energies, through the time dependence of the diffusion coefficients, for the incommensurate $(6,4)@(17,0)@(15,15)$ and commensurate $(5,5)@(10,10)@(15,15)$ MWNTs [45]. Whatever the Fermi energy of wavepackets, the conduction mode remains ballistic in the defect-free commensurate MWNT. In contrast for incommensurate systems, depending on the considered energy of charge carriers, the resulting strength of hybridization between states lying on separate layers may strongly fluctuate, with the occurrence of power-law behavior of $\mathcal{D}(t)$.

This anomalous diffusion has subsequent effects on the length scaling of conductance as shown on Fig. 6.31 (right frame). At the charge neutrality point, wavepackets essentially remain confined onto the outer shell as they spread in time, carrier motion is ballistic and a quantized conductance $\mathcal{G} = 4e^2/h$ follows. In contrast, at the energy $E = 1.5\,\mathrm{eV}$, $\mathcal{G}(L) \sim (2e^2/h)(L/L_0)^{\frac{\eta-1}{\eta}}$, with L_0 (or η) an energy dependent length (or exponent). Recent experiments on boron-doped MWNTs have reported on anomalous scaling of the conductance [64]. They found $\eta \sim 1/2$, which points towards a diffusive regime. Similarly, an intershell resistance of $\sim$10 k$\Omega\mu$m has been experimentally estimated in [65].

6.4.8 Role of Electrode-Nanotube Contacts

Two different kinds of metal/nanotube junctions can be defined, namely a *metal-metallic nanotube-metal* or a *metal-semiconducting nanotube-metal* junctions. The latter ones are often subjected to Schottky barriers that forbid electronic transmission at zero or low bias voltage, whereas the former present several atomic-scale properties. Indeed, let us take $|k_m\rangle = \sum_p \mathrm{e}^{\mathrm{i}k_m p}|\varphi_m\rangle$ (or $|k_\mathrm{F}\rangle = \sum_p \mathrm{e}^{\mathrm{i}k_\mathrm{F} p}|\varphi_\mathrm{NT}\rangle$) as the propagating states with k_m (k_F) the wavector in the metal (or nanotube). We take $|\varphi_\mathrm{NT}\rangle$ the localized basis vectors, that will have nonzero overlap with $|\varphi_m\rangle$ only for a few unit cells (p) defining the contact area. The scattering rate between the metal and the nanotube can be

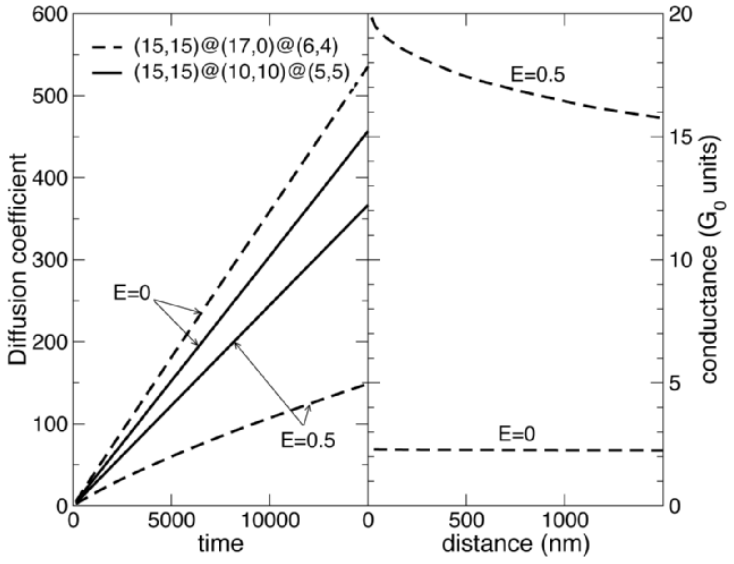


Fig. 6.31. *Left*: time dependent diffusion coefficient for incommensurate/commensurate disorder-free MWNTs (with $\beta = \gamma_0/8$). *Right*: length dependence of conductance for two Fermi energies for $(6,4)@(17,0)@(15,15)$. Adapted from [45]

written following the Fermi golden rule and will be related to

$$\langle k_m|\mathcal{H}_{\text{contact}}|k_{\text{F}}\rangle \sim \gamma'\langle\varphi_{\text{NT}} \mid \varphi_m\rangle \sum_p \mathrm{e}^{\mathrm{i}(k_m-k_{\text{F}})p}$$

with $\mathcal{H}_{\text{contact}}$ the coupling operator between the tube and electrodes. From such an estimate various physical aspects can be outlined: first the factor γ' is related to the chemical nature of interface bonding (covalent, ionic,...). In the most favorable case of a covalent coupling, one expects an ohmic contact resistance given by $R_c = h/2e^2$, whereas ionic bonding would mostly favor a tunneling contact with resistance $R_c \sim h/(e^2|\gamma'|^2)$. The factor $\langle\varphi_{\text{NT}}|\varphi_m\rangle$ is related with the geometry and contact configuration between the nanotube and electrodes: end or side contacts, length of the contact area (see Fig. 6.32). The last term is obviously maximized whenever wavevector conservation is best satisfied, i.e. $\sim \delta(k_m - k_{\text{F}})$. For instance, in the case of metallic armchair tubes, larger coupling will be achieved for $k_m \simeq 2\pi/3\sqrt{3}a_{cc}$. Much smaller metallic wavevector will yield small coupling rate. The tunneling rate from the metal to the nanotube is given by

$$\frac{1}{\tau} \sim \frac{2\pi}{\hbar}|\langle k_m|\mathcal{H}_{\text{contact}}|k_{\text{F}}\rangle|^2 \rho_{\text{NT}}(E_{\text{F}})\rho_m(E_{\text{F}})$$

with $\rho_{\text{NT}}(E_{\text{F}})$ ($\rho_m(E_{\text{F}})$) the density of states of the nanotube (metal) at Fermi level. Note that these considerations are derived for a low-bias regime. For higher bias voltage between voltage probes, the modifications of bands along the tube axis might produce additional backscattering due to the perturbed profile of available states [66]. Detailed ab-initio studies have recently revealed that titanium contacts would achieve better transmission to metallic tubes than silver or gold contacts [67].

6.4.9 Inelastic Mean Free Path

Electronic transport is also sensitive to inelastic effects either stemming from electron-phonon scattering or weak electron-electron collisions. Again, the special electronic structure of carbon nanotubes leads to unconventional behavior

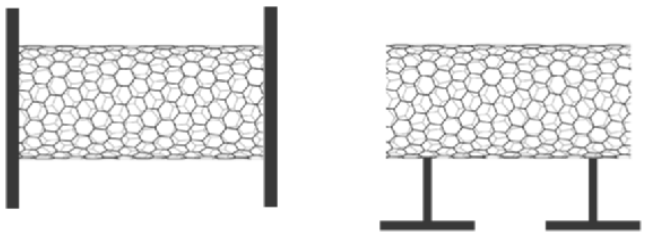


Fig. 6.32. Different contact configuration – end contacts (*left*), side contacts (*right*) – between nanotube and electrodes

as for instance observed in the temperature dependence of resistivity. Balents and Fisher [47] demonstrate for instance that Umklapp scattering due to electron-electron interactions yield a resistivity linear in temperature. Concerning electron-phonon scattering, three important phonon modes yield contributions to inelastic backscattering. As depicted in Fig. 6.33, a first process is driven by acoustic phonons with low energy and small momentum. Within the FGR, the scattering rate (with phonon emission) $\tau_{el-ph}^{-1}(\boldsymbol{q})$ writes

$$\frac{2\pi}{\Omega\hbar}\sum_{k}|\langle \boldsymbol{k}+\boldsymbol{q},n_q+1|\hat{\mathcal{U}}_{el-ph}|\boldsymbol{k},n_q\rangle|^2\delta(\varepsilon_{k-q}-\varepsilon_k-\hbar\omega_q)(1+n_q)(1-f(\varepsilon_{k-q}))f(\varepsilon_k)$$

with Ω the surface of the tube, $\hat{\mathcal{U}}_{el-ph}$ the electron-phonon scattering operator, while n_q and $f(\varepsilon_k)$ give the phonon and electron distributions respectively. In metallic tubes, the acoustic torsional mode (twisting mode or twiston) is made of pure circumference-directional deformation, while its velocity is equal to that of the TA mode of the graphene sheet ($\omega(\boldsymbol{q}) = v_{twist}|\boldsymbol{q}|$). A crude estimation due to such inelastic scattering gives $\tau_{el-ph}^{-1} \sim 4\pi/\hbar \times \Xi^2(k_{\rm B}T/2\rho_M v_{twist}^2)/hv_{\rm F}$ with ρ_M the mass density, and Ξ the deformation potential. It has to be noted that different from ordinary metals, the linear temperature dependence of the electronic resistivity persists to well below the Debye temperature, essentially because these phonon modes are heavily thermally populated [48]. Now, with reasonable parameters, an inelastic acoustic scattering time is found to be $\simeq 3.10^{-12}$s, with a subsequent inelastic mean free path $\ell_{el-ph} = v_{\rm F}\tau_{el-ph} \simeq 2.4\mu$m for a 1.8 nm nanotube [49, 50]. A theoretical derivation has also predicted some helical-dependent contribution of

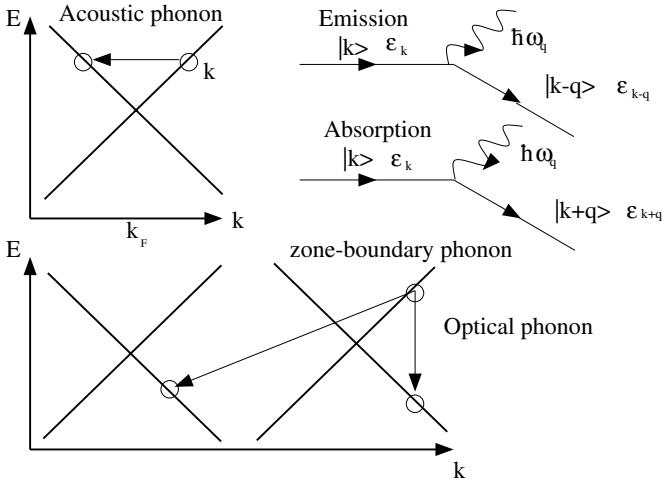


Fig. 6.33. Schematic representation of main phonon contributions to backscattering (acoustic, optical and zone-boundary modes)

electron-phonon backscattering and resistance value in the high-temperature regime [51].

Optical as well as zone-boundary phonon modes also bring some important contributions to backscattering, especially for nanotubes studied in the high-bias regime. For single-walled tubes, recent experiments [50] have inferred typical values of the electron-phonon mean free path in the order of 180 nm for optical phonons, whereas zone-boundary modes yield $\ell_{el-ph} \sim 30$–40 nm. Note that all these inelastic scattering length scales are expected to increase with the nanotube diameter [44].

Perebeinos, Tersoff and Avouris [52] recently proposed to investigate the effect of inelastic scattering on conductance by following the semiclassical Bloch-Boltzmann treatment of transport theory. The authors derive a phenomenological law for the zero-field charge-carrier mobility $\mu(T, d_{\text{tube}}) = \tilde{\mu}(300\text{K}/T).(d_{\text{tube}}/1\text{nm})^{\alpha}$, exhibiting some specific temperature and diameter dependences (here $\tilde{\mu} = 12000\,\text{cm}^2/\text{Vs}$, and $\alpha \sim 2.25$).

In contrast, other theoretical works have investigated the influence of structural lattice fluctuations on the elastic electron transport [53, 54]. The superimposed contribution of phonon vibrations has been shown to yield quantum dephasing [53]. For the case of optical phonon modes, the resulting conductance scaling spectrum shows pronounced modifications, making the use of the semi-classical Fermi Golden Rule inapplicable for a rigorous description of charge transport. Clearly, additional work is required to understand how electron-phonon coupling and electrostatic effects jointly contribute to modulate the properties of nanotubes-based field effect transistors.

6.4.10 Electron-Electron Interactions

Carbon nanotubes have provided new possibilities to search for deviations from the Fermi-liquid theory in low-dimensional systems. As discussed in Sect. 6.1.2, strongly repulsive Coulomb interactions likely restrict the range of applicability of the Fermi liquid approximation in describing transport properties. The theoretical possibility for Luttinger-liquid in metallic SWNTs has been proposed when electronic transport through the nanotube-based device is dominated by tunneling through a contact of low transparency. Additionally, the energy of charge carriers should be close to the charge neutrality point, where electronic bands are linearly dispersed. In this case, the interaction parameter g uniquely determines the power-law temperature-dependent (for $eV \ll k_{\text{B}}T$) and voltage-dependent (for $eV \gg k_{\text{B}}T$) tunneling conductances. The generic form $(1 + \frac{2U_0}{\Delta})^{-1/2}$ (U_0 the charging energy, Δ the single particle level spacing) of g is, in this framework, directly related to the power-law exponents (α_m or α_{e} depending on measurement configuration), see Sect. 6.1.2. Notwithstanding, while the single-particle level spacing is unequivocally given by $\hbar v_{\text{F}}/2L_{\text{tube}}$, the charging energy follows from the capacitive properties of metal-nanotube junction as well as from the electronic structure. In some

approximation [68], it can be derived from simple electrostatics, and the interaction parameter will follow

$$g = \left(1 + \frac{8e^2}{\pi\kappa\hbar v_{\mathrm{F}}} \ln \frac{L_{\mathrm{tube}}}{R_{\mathrm{tube}}}\right)^{-\frac{1}{2}} \tag{6.105}$$

with κ the dielectric constant, and R_{tube} the tube radius. Taking $L_{\mathrm{tube}}/R_{\mathrm{tube}}$ $\sim 10^3$, one finds that the theoretical interaction parameter for a metallic armchair nanotube is $g \simeq 0.28$. Subsequently the bulk-tunneling and end-tunneling exponents are respectively given by $\alpha_m \simeq 0.24$ and $\alpha_{\mathrm{e}} \simeq 0.65$ [68]. Some experiments have reported on similar behaviors and exponent values [69]. Interestingly, one notes that in the case of MWNTs composed of N metallic armchair shells, a certain screening of interactions occur since the exponents are renormalized by a factor $1/N$ (α_m/N and α_{e}/N) which is equivalent to an increase of g that tends to 1 in the limit $N \to \infty$ (Fermi-liquid regime) [70]. This also underscores the consequences on the transport properties with the change of dimensionality from the SWNT to the MWNT case.

Following theoretical predictions by Eggert [71], recent STM experiments have provided strong evidence for non-Fermi-liquid properties of metallic nanotubes [72]. In this work, the tunneling properties of electrons from a metallic tip to a metallic tube deposited on a gold substrate have evidenced that the Coulomb interactions are strong enough to induce charge-spin separation, although screening by the metallic substrate also results in some reduction of the predicted interaction strength.

This is illustrated in Fig. 6.34, where a tight-binding calculation shows the two standing waves with different wavelengths caused by separate spin and charge bosonic excitations. The slopes calculated near the **K**-points ± 8.8 cm^{-1} and ± 11.9 cm^{-1} correspond to larger charge mode group velocity of $\sim v_{\mathrm{F}}/0.55$, whereas the spin-mode velocity remains similar to the Fermi velocity v_{F} obtained for non-interacting electrons.

The deduced values for the g-parameter is thus ~ 0.55, much smaller than the predicted value given by the unscreened coulomb potential ($g \sim 3$). This clearly evidences the screening phenomenon caused by the underlying metallic substrate, and that can be substantiated by replacing in (6.105) L_{tube} by a screened length (found to be $\sim 1.4 R_{\mathrm{tube}}$ in experiments [72]).

6.5 Measurement Techniques

A measurement of the electrical properties of an object, as diverse as it seems (with temperature, magnetic field, gate voltage, etc), always reduces to our ability to measure simultaneously the injected electron flow (current) and the resulting potential drop (voltage) in the sample. The simplest measurement that can be done is that of the classical electric resistivity of a material. This

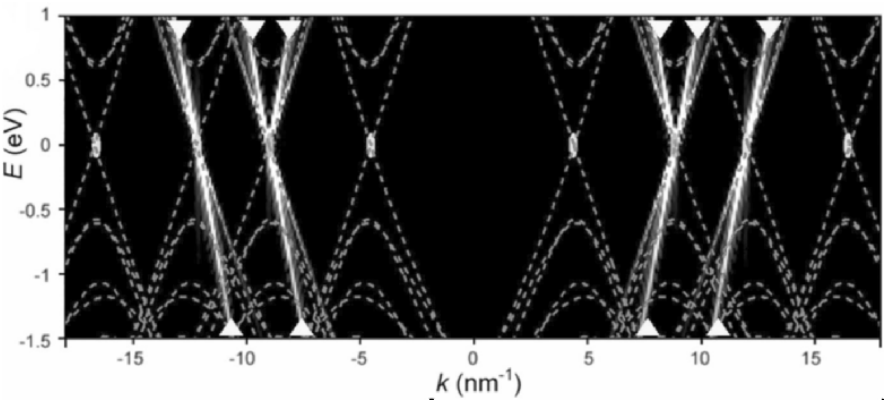


Fig. 6.34. Fourier transformed mas of $\mathrm{d}I/\mathrm{d}V$ (density of states) as a function of electron momentum k, and sample bias V. Ovals near the Fermi levels indicate the corners of the brillouin zone nearest (*green*) or second nearest (*orange*) to the Γ-point. Red curves give the energy dispersions of the (19,7) tube by tight-binding, whereas superimposed color lines indicate the Luttinger-liquid result. Adapted from [72] by courtesy of S. Eggert

requires to measure the resistance $R = U/I$ and to know the exact geometry of the sample used. As we will see later, the second point is not as trivial as it seems.

6.5.1 Classical (Macroscopic) Approach

Two-Probe Measurement

On a macroscopic sample, the so-called 2-probe resistance measurement is still often performed. The injected current and the voltage drop are measured using the same lead on a versatile apparatus (ohm-meter) (Fig. 6.35a). Knowledge of the sample size allows straightforward calculation of the resistivity with the hypothesis of a uniform voltage drop across the sample. However, the main draw-back of this set-up is that the voltage drop in the lead is included in the total voltage drop, so the sample resistance is over-estimated. Of course, low-resistance leads can bring these effects to extremely small values. However, another effect can appear: a poor contact between the lead and the sample. Poor (or bad) contact can simply result from surface oxidation. In the two-probe configuration the voltage drop at the contact is also included in the whole measurement.

Four-Probe Measurement

To avoid this problem, physicists use the 4-probe measurement technique. Two independent circuits are considered: one to inject the current, the second

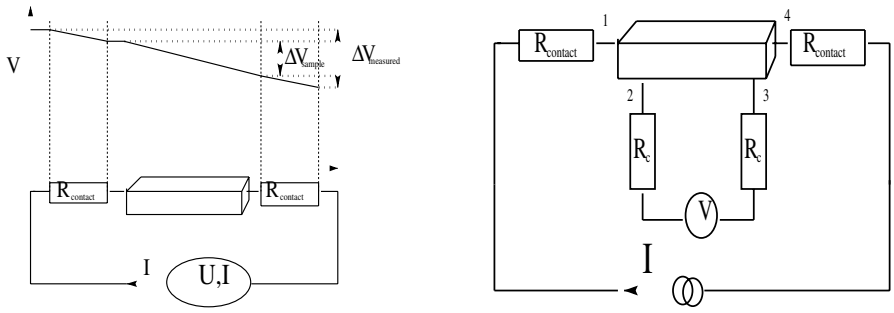


Fig. 6.35. *Left*: Two-probe measurement overestimating of the resistance drop in the sample. *Right*: Four-probe measurement configuration (current through voltmeter is negligible)

to measure the voltage drop (usually between the current-injection leads) Fig. 6.35-Right. The only practical condition is to have a high impedance voltmeter (high compared to the sample resistance). In this set-up, as no (or very little) current is passing through the voltmeter circuit, the injected current is, to a great accuracy, the current that flows through the sample, regardless of the lead and contact resistance. The measured voltage drop is the genuine voltage drop across the points 2 and 3 of the sample (contact and lead resistance effects are negligible because the current through the voltmeter is minute). Calculation of the sample resistivity is now also simple, provided that the distance between lead 2 and 3 is accurately known.

Importance of the Contact Size

The contact size of the lead that is injecting the current is irrelevant provided the contacts have a sufficient distance from one another, i.e. the electron flow is uniform in all the sample by the time it reaches the inner contacts (Fig. 6.36-Left). However, in the case of a strongly anisotropic material (as graphite or MWNT), this condition might not be automatically reached (Fig. 6.36-Right).

In contrast, the size of the voltage probe contact must be as small as possible: large contact area can induce errors in the resistivity calculation if the metal used for the contact pad has a lower conductivity than the sample. Figure 6.37 depicts, in an exaggerated fashion, such an effect. Getting a contact area negligible compared to the distance between probes is easy to achieve on a macroscopic sample (20 µm gold wire for the probe, 5 to 10 mm, between the two probes), however, as we will see, mesoscopic samples are much prone to such problems.

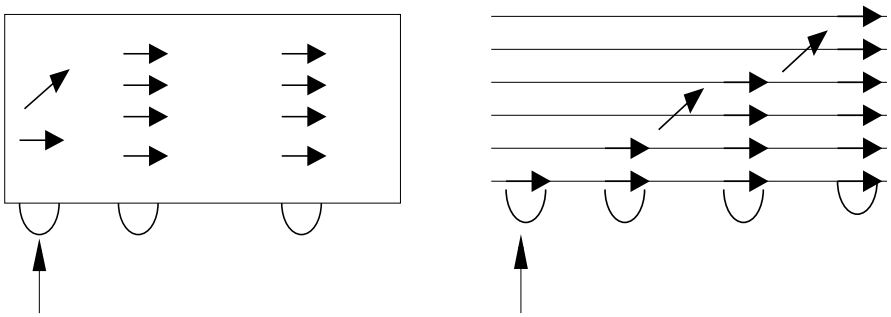


Fig. 6.36. *Left*: Isotropic material, current flow is homogenous on the sample even if injected from a single entry. *Right*: For anisotropic material, non-homogeneity in current flow can extented far from the injection point

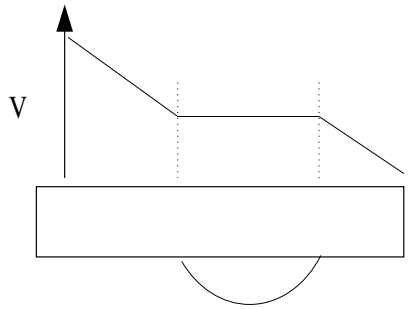


Fig. 6.37. Voltage probe with low resistivity on highly resistive sample. The potential drop is no longer uniform along the sample

6.5.2 Experimental Problems on Mesoscopic Samples

Choice of the Contact Type and Realization

The sample we are now looking at is of micrometer dimensions. First, we have to compare the size of the available electrode to the sample size: if our sample is smaller than the electrode width technically available in the laboratory, there are only two-probe measurements to consider. We will first have a short tour of the actual techniques, from the most crude (and cheap) to the most refined (and expensive). The objective is not to explain technical details but to give an overview of what can be made, how difficult it is and what the advantages are.

Direct Evaporation

The simplest way to realize a metallic contact is to evaporate a metal film (usually gold, but other choices are possible [67]) over the sample after part of it has been shielded from the evaporator. This technique has been successfully

used by de Pablo et al. [73] on MWNT. They used 4 µm tungsten wires for a mask. As a result, both end of the MWNT were buried in metal and a two-probe transport measurement was achieved (Fig. 6.38).

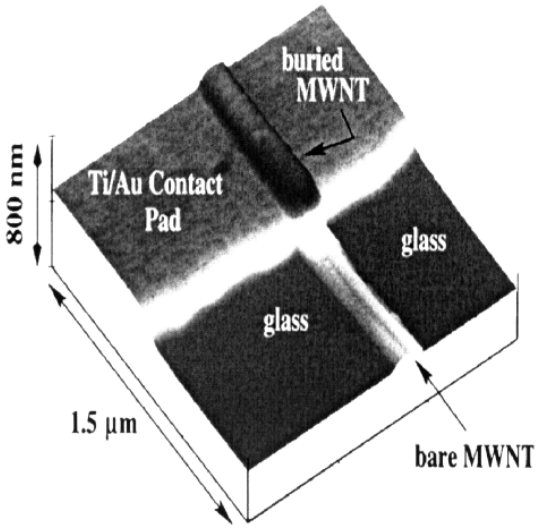


Fig. 6.38. Result of a direct evaporation on a MWNT deposited on a glass substrate. The central part of the MWNT has been protected by a 4 µm tungsten wire

This technique is inexpensive (tungsten wire of 4 µm diameter costs about 2 Euros/10 cm, while an evaporator can be home made). The problem is that only large samples can be processed in that way as 4 µm is the limit of what can be manipulated with tweezers on a table top.

Lithographic Processes

In a lab equipped with lithographic facilities, sub-micron electrodes can be processed. The width is limited by optical diffraction. Depending on the facilities, a width of 300 nm can be obtained with the desired pattern. If a specific mask has to be made, the cost can increase substantially. Electron beam lithography allows even lower widths to be processed [74], see Fig. 6.39. The cost for the mask can easily reach a thousand Euros depending on complexity. In the case of the electrode on top approach (see next section), the experimenter must make sure that the lithographic process (resin, exposure, dissolution, etc) does not alter the sample.

Focus Ion Beam (FIB)

In this set-up, a metallic ion beam is extracted from a metallic source, focused and deposited in a controlled way on the substrate. Widths are in the 10 nm

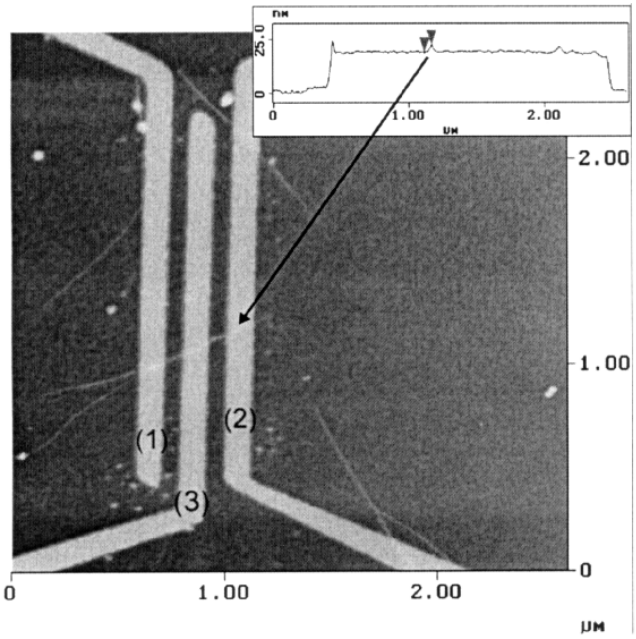


Fig. 6.39. Three 100 nm wide electrodes on top of a SWNT bundle (electron beam lithography). Note the relative width between the probes and the sample

range (16 nm with gallium in the FEI Dual Beam System 620). This setup can be implemented on an existing scanning electron microscope. The cost is heavy: about 400 000 Euros for a complete FIB installation (example on Fig. 6.40).

Sample on Top Versus Electrode on Top

As sub-micrometer patterns are always made on top of an insulating flat surface, two routes are possible: the sample can be deposited first, located and the electrode further deposited on top, or the electrode pattern can be made (or bought) before and the sample deposited afterwards. In the case of a rigid sample, the two methods should be essentially equivalent. However, in the case of soft and deformable samples, the electrode pattern can induce distortions that alter the sample transport properties (see Bezryadin [76]).

The sample-on-top configuration has the strong advantage that one can buy ready-to-use patterned substrate with the required electrode spacing. The problem is usually to obtain intimate contact between the sample and the electrodes as only Van der Waals forces are playing a role. Spot-welding techniques have been used to increase the contact quality in some cases [77]. The electrode-on-top configuration seems better in several aspects. First, there is no or little distortions of the sample when the contacts are deposited. Second,

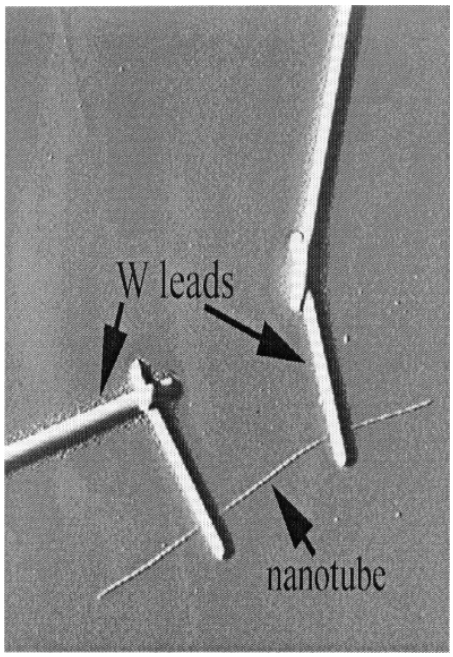


Fig. 6.40. Nanotube contacted with tungsten lead made by FIB lithography [75]

the contact is essentially of better quality (that of course depends on the sample preparation). In both techniques, the ability to position and/or locate the sample with required accuracy is a compulsory step. This stage is crucial in several aspects: one of them is the inherent risk of sample damaging during the process. First, risk occurs when the samples are produced in large quantity and must be dispersed over the surface. Dispersions are often achieved through combined chemical (surfactant) and mechanical (sonication) action. For carbon nanotubes, which are chemically and mechanically extremely stable samples, it has been demonstrated that surfactants can substantially affect the transport properties [63] and that sonication is a convenient tool to cut them into pieces [78]. In that respect, however strong the sample seems, tests must be carried out to check that theses processes are reversible (surfactant can be washed away) and non-destructive for the sample. Second, risk appears when the sample is manipulated to be positioned onto a specific place after deposition [79]. Once again, potential damaging of the sample must be considered.

Measurement of the Voltage and Current

Now that our sample is contacted, some amount of current can be injected and a measurement of the voltage drop can be achieved. We will discuss the

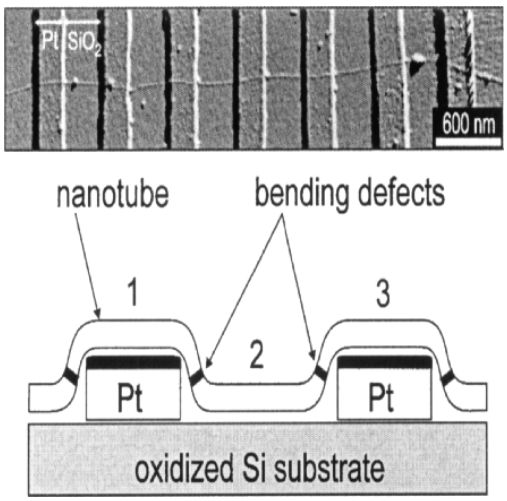


Fig. 6.41. Long SWNT deposited on top of Pt electrodes (*top*). Occurrence of bending defect near the electrodes (*bottom*). Adapted from [82]

(almost ideal) case where the sample is long enough to be used in a four-probe configuration, with the electrodes on top of the sample and assuming that the contacts are fairly good. It seems now that the resistance of our object is simply the ratio of the measured voltage drop to the measured current. Unfortunately, several problems can occur. First, as was said at the beginning, the width of the electrodes that pick-up the voltages must be small compared to their distance. This might be difficult, if not impossible (see Fig. 6.40). Solutions to this problem consist of assuming that the measured voltage drop occurs between the end of the first electrode and the beginning of the second. Secondly, it has been known since 1898 [80] that when two metals of different work functions are put into contact, a contact potential appears between them. This effect is well known in semi conductors (p-n junction). The same effect holds for metal/semi conductor junction (better known as Mott or Schottky Barrier). Between metals, the depletion width is negligible, so this barrier is usually considered to be completely transparent to the electrons. i.e. a metal electrode will eventually inject electrons in a metallic sample, even if their work functions did not match. But what happens to the conduction electron of the mesoscopic sample if a large metal electrode disturbs its band structure as in Fig. 6.39.

Krstic et al. [74] have observed the effect of an electrode laid on top of a nanotube bundle on its transport properties and concluded that the mere presence of this electrode disturbs the transport. A proposed solution is to use for the electrode a metal with a work function that matches the studied sample [81]. Despite its advantages, it seems that the four-probe method is not well suited for mesoscopic samples. The coupling between the sample and the

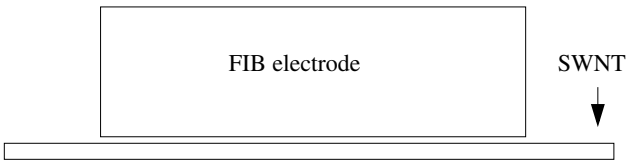


Fig. 6.42. Drawn at the same scale, the narrowest metal electrode that can actually be made with FIB (about 10 nm width) on top of a SWNT (1.4 nm diameter). Work function difference can disturb the band structure over non-negligible distance and alter transport properties

electrode is not as simple as it seems, since differences in work function will locally alter the band structure with important consequences for extremely sensitive systems (such as one dimensional transport). For a more detailed discussion, see Datta [4]. Then how to process it? Two alternative approaches have been envisioned, both based on the two-probe configuration.

The first alternative is to use local probe-techniques such as electrostatic force microscope (EFM). While current is driven through the sample, a tip probes the potential drop along the sample [82]. Influence on the transport properties seems minute and can be controlled by approaching the probe while monitoring the effects on the two point transport. The measured potential drop can be linked to the resistance. The second approach consists of using several samples of identical cross-sections and different lengths with the same contact method or to vary the distance between electrodes on the same sample (one side is usually fixed) [63, 83, 84]. If the contact contribution is the same, the only change can be attributed to the intrinsic sample resistance. The major challenge resides in the difficulty to realize reproducible (and comparable) contacts.

Reproducibility of the Measurements

The point of this section is not to look for a resistance variation on a single sample (which we expect to be stable, except for variation of temperature, humidity, magnetic field, etc), but from the sample to sample reproducibility.

As discussed previously, measuring several samples of different length in a two-probe configuration might be an alternative to the four-probe method. From a theoretical point of view, identical nanoscopic objects, contacted in an identical manner, should have identical behavior. Identical is not experimental, objects are produced with defects and some dispersion in size. To illustrate this point, we will study the very simple case of the gold break-junction experiment: Two clean pieces of gold in contact are pulled apart. A thin short-lived gold wire is created. The width is so small that transport quantification is obtained. This experiment is well documented [85] and transport quantization is known to occur in this mesocopic system. However, if we observe a single event (Fig. 6.43 right), nothing special is usually observed. In

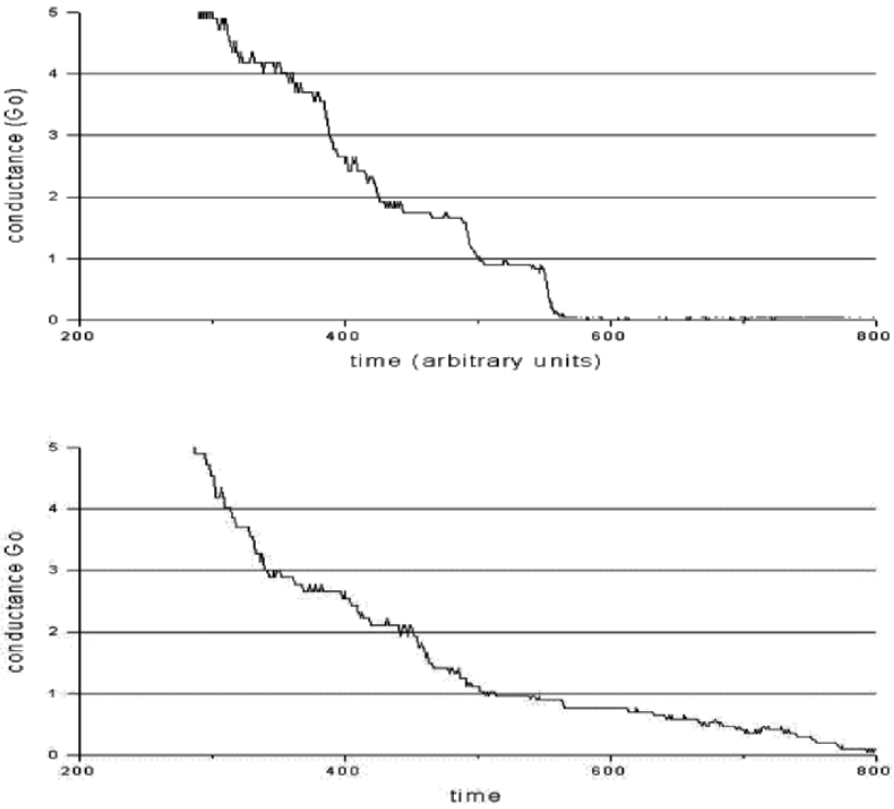


Fig. 6.43. Two traces of gold break junction, plotted on the same time scale. The first one (*upper part*) exhibits two clear plateaus while no clear quantification is visible in the second one

other cases, clear plateaus, that coincide with quantized transport, are roughly observed (Fig. 6.43 left). So in one experiment quantization is observed, but not in the other. What to conclude? Simply that observations based on a single event might not be representative. Only statistical approaches (repeated experiments on several samples) have a physical meaning.

In the above case, the object was clearly defined: a pure, well contacted, gold wire. Fluctuations were mainly due to the geometry of the sample and some random scattering (contact, crystallographic defects in the wire, etc). Now imagine what could happen if the object itself is not well defined (defect densities, shapes, size), prepared through different processing (surfactant, sonication, AFM-manipulation, spot welding on contact, etc) and measured with various methods. Of course one can expect the results to be different (see [86] as an example of how the result vary).

Calculation of the Resistivity

If eventually we succeed in pulling some numbers out of these tricky experiments, can we compute the resistivity? What was simple for a macroscopic object is no longer easy. First let us take a large semiconducting mesoscopic sample: a regular line 80 nm wide, and 5 nm thick, distance between electrode 2 μm. Assuming that we have extracted the value of 10 kΩ for its 'resistance', what about its resistivity? If the above numbers are correct, then ρ is 2 μΩm. Unfortunately the above mentioned numbers are only known to a limited accuracy. Even in the best case: height measured with AFM ($\Delta h = 0.1$ Å), width and length by high resolution Scanning Electron Microscope ($\Delta x = 1$ nm), lead to a 3% error (2.03 μmΩ.m to 1.97 μmΩ.m). Things get worse for smaller objects like nanotubes given that their cross-section is not well defined. The diameter of a SWNT is typically 1.4 nm, but its wall thickness can be estimated from 3.4 Å (from interlayer distance in HOPG) down to 0.66 Å (carbon atomic radius). Here differences can reach a factor 5 (for resistivity, but also for current density).

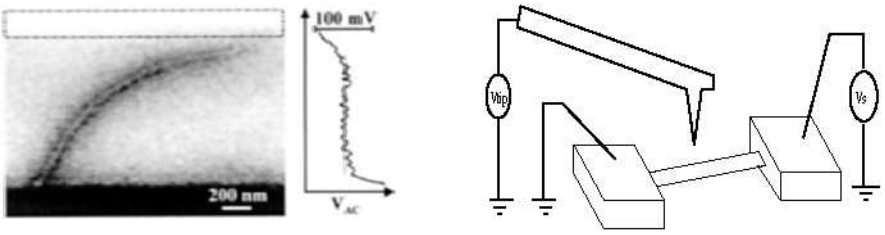


Fig. 6.44. *Left*: EFM record of the potential drop along a SWNt bundle. *Right*: Experimental setup. Adapted from [87]

6.6 The Case of Carbon Nanotube

6.6.1 Study of Some Experimental Measurements

As we have seen, four-probe experiments are maybe not always the best suited approach for mesoscopic objects. In the case of carbon nanotubes, it is noteworthy to remark that four-probe experiments have usually failed to point out the extremely long electronic mean free path that occurs in these systems.

Measuring the Voltage Drop Using EFM Techniques

In the experiment by Bachtold et al. [87], the electrostatic potential is measured along a SWNT bundle connected on its two extremities while a voltage

drop is applied. The recorded voltage drop leads to a bundle resistance per unit length ρ_l below 1.5 kΩ/μm. This gives a mean free path longer than 1 μm at room temperature providing there is only two conducting nanotubes (in this 2.5 nm high, 2 μm long bundle). Note also that, using the same experimental setup, the authors found individual MWNT to be a dissipative conductor (voltage drop is linear along the nanotube).

Extracting the Intrinsic Resistivity by Reducing the Inter-Electrode Gap

Individual MWNT were used in these setups [63]. One side of the nanotube is connected to a conductive fiber, while the other side is dipped into liquid metal. The resistance is monitored while the distance between contact is continuously reduced.

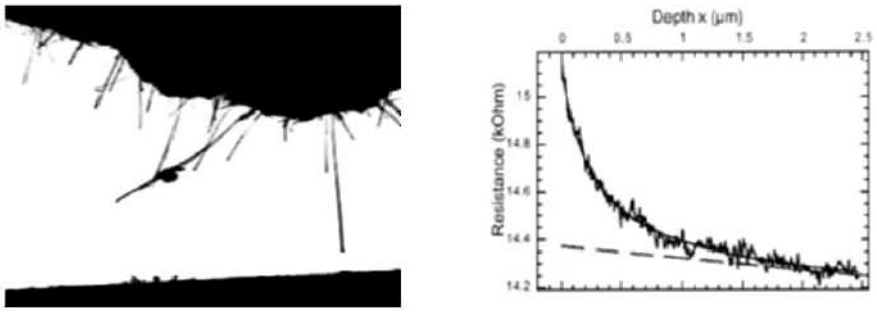


Fig. 6.45. *Left*: TEM picture of a measured individual MWNT. *Right*: Measured two-probe resistance versus depth. From a simple model, one can the extract contact resistance (14 kΩ) and the intrinsic nanotube resistance ($\rho_l = 14\ ,\Omega/\mu\text{m}$)

An analysis of one simple trace led to the conclusion of a mean free path longer than the system ($\rho_l \gg 14\,\Omega/\mu\text{m}$, see [63] for detailed calculation). However, on a single measurement, one cannot distinguish between an highly conductive nanotube and a classical contact resistance (about 14 kΩ at the fiber side) or a small contact resistance and a reduced transmission in the nanotube due to conductance quantification (transport quantification within the nanotube). To discriminate, the experiment has been repeated over 40 to 50 different nanotubes (i.e. different diameter and fiber-connected length). The contact resistance always turns out to be in a 13–15 kΩ range, unexpectedly stable in regard to the studied variety of MWNT (only from diameter, the contact resistance should have changed from a factor 2 to 3). This statistical result let the author consider that this 'contact resistance' is intrinsic to the nanotube and is actually a signature of the transport quantification within the nanotube.

6.7 Experimental Studies of Transport in Nanotubes and Electronic Devices

6.7.1 Introduction

Nanotubes and other nanostructures form new classes of materials with remarkable and unique properties for electronics and optoelectronics applications. Their electrical properties are often distinct from those of their bulk counterparts, due to the confinement of the electronic states and the surface contributions. The nanostructures are often made by self-assembly, which is compatible with large-scale production, and they present dimensions covering a length scale that is not easily achievable by the conventional top-down approaches. The first comprehensive electrical studies on carbon nanotubes were performed in 1997 [88, 89].

This section presents a selection of experimental studies and aims to review some of the important electrical properties of metallic and semiconducting carbon nanotubes. First, we will discuss the scattering mechanisms in metallic carbon nanotubes. Second, we present the recent results on the field-effect transistor based on individual SWNT. Last, we review the general properties of the 1D Schottky barrier at the metal-nanotube junctions and describe the operation of a nanotube Schottky-barrier transistor (SB-CNFET).

6.7.2 Electrical Transport in Metallic Carbon Nanotubes

The unperturbed transport in metallic carbon nanotubes takes place through a limited number of sub-bands close to the charge neutrality point. In this region, the 1D dispersion relation for the nanotube can be approximated by $E(k) = E_{\mathrm{F}} \pm \hbar \cdot \nu_{\mathrm{F}} (k - k_{\mathrm{F}})$, where $k_{\mathrm{F}} = \pm(2/3) \cdot \pi / a$ is the Fermi wavevector for armchair nanotubes and the lattice constant $a = 2.46$Å. The situation around E_{F} is schematically illustrated in Fig. 6.46.

In total, four sub-bands contribute to the conductance of the nanotube with both positive and negative slopes at $-k_{\mathrm{F}}$ and $+k_{\mathrm{F}}$. This 1D nanotube band structure limits the various scattering events at finite temperature. That is, the 1D confinement allows electron motion in only two specific directions along the length of the nanotube. This constraint along with the requirements for energy and momentum conservation severely reduces the phase space for scattering.

As illustrated in Fig. 6.46, only few processes are possible. These are essentially mediated by impurity, electron-phonon scattering or electron-electron (e-e) collisions. The impurity scattering is an elastic event while electron-phonon and electron-electron scattering are inelastic by their nature. Moreover, inter-band scattering involving higher-energy sub-bands can also take place, but the probability of this process is very weak since the energy separation with the other sub-bands is large (of the order of the electron volt).

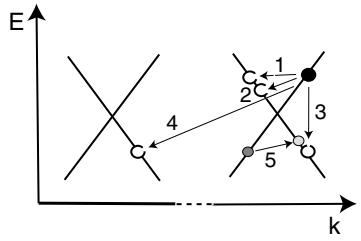


Fig. 6.46. Band-structure diagram showing elastic (**1**) and inelastic (**2**–**4**) backscattering in a carbon nanotube satisfying energy and momentum conservation. Process (**1**) is for impurity scattering and (**2**) involves the emission of an acoustic phonon with small energy and momentum transfer. Processes (**3**) and (**4**) show the emission of an optical phonon for low and high momentum transfer, respectively. Process (**5**) is an e-e scattering process as described in the text

The number of scattering events in a carbon nanotube segment of length L is therefore limited. They can be probed by two-terminal resistance measurements as a function of temperature according to:

$$R_{2t} = R_0 + \frac{dR}{dT} \cdot T = \frac{h}{4e^2} L \left(\frac{1}{L_0} + \frac{1}{L_{e-ph}} + \frac{1}{L_{e-e}} \right) \tag{6.106}$$

L_0, L_{e-ph} and L_{e-e} are the mean free paths for impurity, electron-phonon and electron-electron scattering respectively. In absence of collisions, i.e. in the ballistic regime, we expect conductance quantization and no temperature dependance. In that case, (6.106) is reduced to : $R_{2t} = h/4e^2$.

The intrinsic properties of a single carbon nanotube are difficult to measure because of the 1D nature of the nanotube and the strong perturbation introduced by the contact leads. This point is discussed below. In principle, it is possible to discriminate between the different scattering mechanisms using a careful analysis of R vs. T curves.

Impurity Scattering

The scattering of an electron by an impurity involves another state that is at the same energy but of opposite momentum direction (see process **1** in Fig. 6.46). This is backscattering and it leads to a residual resistance that is higher than the resistance of a pristine nanotube.

Phonon Scattering

Scattering with phonons, such as in processes **2**–**4** in Fig. 6.46, is an inelastic event where backscattering occurs with the emission (or the excitation) of a phonon of energy $E_{ph} = \hbar c_{ph} k_{ph}$, where c_{ph} is the phonon velocity. Here, E_{ph} depends on the available phonon modes in the nanotube. For example, acoustic phonons have a broad energy spectrum for scattering at low energy

while optical phonon scattering can be neglected for energy transfer of less than 100 meV [90, 91].

Electron-Electron Scattering

This scattering has typically little impact on the resistance of a conductor, but it is expected to be more pronounced for 1D conductors. The case of carbon nanotubes is special because of the linear dispersion around E_{F}. The modes are crossing at E_{F} and backscattering as in process **2** in Fig. 6.46 can also be promoted by e-e scattering, although its probability remains weak. Electron-electron collision can also take place with its counterpart being scattered in the reverse position as in the process **5** (Fig. 6.46). In this case, the total momentum and energy is conserved.

Temperature Effects

While impurity scattering has no (or very little) temperature dependence, the total initial and final states for e-e collisions increase with temperature (or with electric excess energy, i.e. bias). As a result, the electron-electron scattering time increases linearly with temperature (i.e. $\tau_{ee} \propto T^{-1}$) [92]. The temperature dependence of the electron-phonon scattering rate follows the same trend, i.e. $\tau_{e-ph} \propto T^{-1}$ [93]. As a result, the R vs. T curves for a SWNT is expected to be linear for both electron-electron and electron-phonon backscattering according to $L_{e-x} = v_{\mathrm{F}}\tau_{e-x}$ and (6.106). Therefore, the basic scattering mechanisms can hardly be discriminated on the basis of the trend seen in the R vs. T plots. However, it is reasonable to assume that electron-phonon scattering dominates at room temperature. The arguments are discussed in [48, 92–96]. Complementary investigations of the resistivity using bias voltage dependence provide further details on the relative contributions. As it is today, there are still unanswered questions about the backscattering mechanisms observed in carbon nanotubes. To illustrate the current status in this area, three important examples are given below.

Experimental Evidences of Electron-phonon Scattering

There is strong evidence that the elastic mean free path in SWNT reaches several microns in length at room temperature [98–101]. This conclusion comes from cumulated evidence acquired on rope and on individual SWNTs from both laser-ablation and CVD growth techniques. In fact, the measurement of the scattering length is difficult because the contact electrodes introduce significant barriers along the current path (invasive probes). In general, R vs. T curves show a resistance that increases with decreasing temperature, a behavior that is not expected for scattering with either impurity, electron or phonon. It is therefore important that we understand the impact of the contacts and find ways to optimize the contact configuration. An example

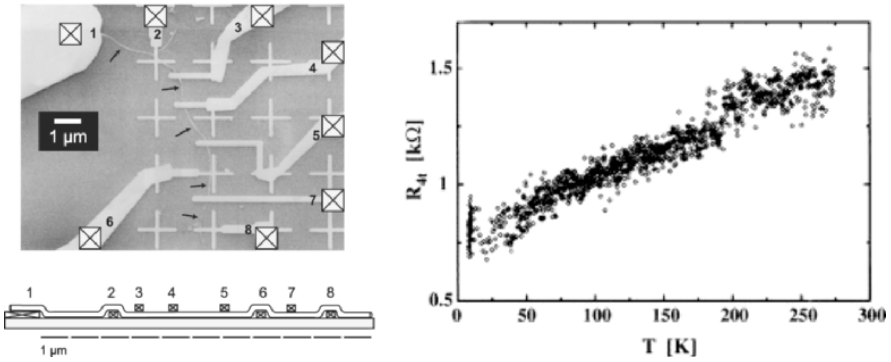


Fig. 6.47. *Left*: SEM image of a single-wall carbon nanotube rope attached with a combination of top and bottom gold contacts. *Right*: Four-terminal resistance with temperature obtained with bottom contacts for current drive and top contacts for voltage probe. Adapted from [101]

of unperturbed R vs. T curve with the expected linear response is shown in Fig. 6.47.

It was obtained using a special four-terminal measurement [101]. Here, the contact electrodes are connected to a nanotube rope. The current probes are directly in contact with the bottom of the rope while the voltage probes make contact to the top-most nanotubes of the rope. Thus, the current bias is applied to the bottom nanotubes and the weak tube-tube interaction forces the current to pass only at the bottom of the rope [101]. In this configuration, the voltage probes do not perturb the bottom nanotubes and allow to measure the voltage drop across the current carrying nanotubes without introducing backscattering. The measurement gives a weak linear dependence of the resistance with temperature and a positive slope $d\rho/dT$ of 2.4 $\times$ 10^6 Ωm/K. This result presents a clear signature of weak electron-phonon scattering in the nanotubes [101]. The characteristic length for electron-phonon scattering from this experiment is $L_{\mathrm{e-ph}} \times N = 11\,\mu\mathrm{m}$, where N is the number of metallic nanotubes directly contacted by the bottom electrodes. N is estimated to be between 1 and 3 nanotubes, which gives an elastic mean free path between 3 and 11 µm at room temperature.

Yao et al. have shown that the scattering length in SWNTs depends on the electron excess energy, eV, which is given by the applied voltage across the carbon nanotube [96]. At high bias (up to 5 V), they observed that the current saturates at about 20 mA (Fig. 6.48) and the whole IV curve can be fit by a simple function: $R = R_0 + V/I_0$, where R_0 is the low-bias resistance of the device and I_0 is the extrapolated saturation current.

Two possible candidates can be invoked to explain this behavior: electron-electron and electron-phonon collisions. However, scattering with optical or zone-boundary phonons is theoretically more likely to lead to the current saturation at I_0 [96]. The key point here is that the electron is first accelerated

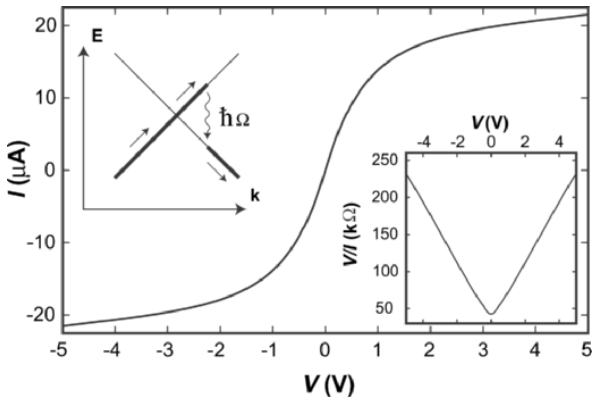


Fig. 6.48. High-bias $I - V$ characteristics of a metallic single-walled carbon nanotube. The right inset re-plots the data as V/I versus V, while the left inset shows the schematic of the phonon emission model. Adapted from [96]

under the applied field inside the nanotube because of the weak scattering with acoustic phonons. Then, it backscatters as soon as it reaches enough energy to emit an optical or zone-boundary phonon. This situation is illustrated in the inset of Fig. 6.48. In the steady state, the forward moving electrons travels across the nanotube with an excess energy $E_{\rm opt}$ above that of backward moving ones. With this, the saturation current I_0 is given by

$$I_0 = \frac{4e^2}{h}\left(\frac{e}{E_{\rm opt}}\right) \tag{6.107}$$

Under these conditions, the mean free path L_{e-ph} for backscattered phonons is the distance an electron must travel in the electric field to gain an excess energy that is equal to the phonon energy:

$$L_{\rm opt} = \frac{e}{E_{\rm opt}}\frac{L}{V} \tag{6.108}$$

where L/V is the electric field along the SWNT. The dominant scattering mechanism at high bias has therefore a mean free path that scales inversely with applied voltage. A substitution of (6.108) into (6.106) leads to a relation that grasps the physics of scattering at large bias

$$R_{2t} = \frac{h}{4e^2 L_0}L + \frac{h}{4eE_{\rm opt}}V \tag{6.109}$$

Here the acoustic phonon scattering is neglected for the obvious reasons explained below. In this model, an optical phonon of $E_{\rm opt} = 0.16\,\text{eV}$ leads to the saturation of current at 25 mA. This value is consistent with the onset estimated for the optical phonons in SWNTs [96]. Other experiments [97] performed on nanotubes-based field effect transistors, and showing ballistic

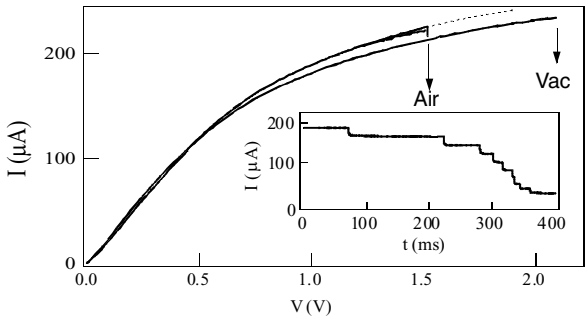


Fig. 6.49. Four-probe $I - V$ and time resolved I curves for two segments of a MWNT. Segment A is electrically broken in high vacuum, while segment B is broken in air. Before failure, both segments have nearly identical $I - V$ characteristics in vacuum (segment B in vacuum shown as dashed line). Vacuum breakdown occurs in segment A at 2.2 V and 235 mA. At this high power, the breakdown proceeds to completion in less than 1 ms. In air, segment B exhibits a much slower breakdown initiated at a lower power. Adapted from [102]

conductance at low bias, have reported values of the inelastic mean free path in the range of 10 nm for high voltage situations.

Current Saturation and Breakdown

Carbon nanotubes can withstand remarkable current densities, exceeding 10^9 $A/\mathrm{c\,m}^2$, in part due to their strong carbon-carbon bonding and the relatively weak electron-phonon scattering. However, at high enough currents nanotubes ultimately fail. The breakdown of the nanotube can occur because significant dissipation takes place at high field through the optical phonon and inter-band scattering. Figure 6.49 presents such a dramatic event observed with two segments of the same MWNT (14 nm diameter) in air and in vacuum [102]. In both cases, the IV curves saturate at a current I_0 that is much larger that the saturation values for SWNTs. In fact, I_0 for MWNTs is sample dependent and the breakdown is never below the point of inflection in the IVs. This observation suggests that the onset of saturation and the eventual breakdown process are linked to a common dissipative process, most likely involving the excitation of high energy optical or zone boundary phonons [102]. Moreover, the threshold power for breakdown in air is lower, probably due to the rapid oxidation of the outermost carbon shell. AFM images indicate that MWNT breakdown usually occurs midway between two electrodes, which is precisely where dissipative self-heating will produce a peak temperature.

More detail of the failure process is shown in the inset of Fig. 6.49. The current vs. time plot shows abrupt drops of current indicating that the MWNT thinning occurs with the loss of individual carbon shells. This also suggests that the steps in $I(t)$ are due to shell-by-shell failure of the MWNT. Similar

thinning has been seen by in-situ transmission electron microscopy [103]. The value of each step is somehow close to the current saturation (25 mA) observed in individual SWNTs and does not change much as the process goes on. The origin of the steps is therefore linked to the saturation current observed with individual SWNTs. Therefore, the current saturation seen before breakdown in MWNTs involves several shells carrying a maximum of current I_0. In addition, as discussed by Yao and coworkers [96], the scattering with the optical phonons seems to be the origin of the overall behavior presented in Fig. 6.49.

6.7.3 Nanotube-Based Transistors

Prototype field-effect transistor devices with carbon nanotubes (CNTFET) have recently shown performance exceeding that of the best silicon-based metal-oxide-semiconductor FET (MOSFET) [104, 105]. This surprising result has also been confirmed by other groups [106, 107]. Then, why a CNFET is able to outperform the best silicon MOSFET? Early experiments [108] on SWNT FETs demonstrated that they behave much like conventional MOSFETs. However, there are some important differences: (i) the carbon nanotube is 1D and the scattering probability is weak. As a result, CNFETs of less than a micron in length are likely to operate in the ballistic regime, which is not the case for silicon MOSFETs even for 10 nm devices. (ii) The nanotubes are made of chemically satisfied carbon atoms and no dangling bond is present at the surface. Therefore, there is no need for careful passivation of the interface between the nanotube channel and the gate dielectric, i.e. there is no equivalent of the silicon/silicon dioxide interface. These properties make the one-dimensional transistor action in nanotubes unique and interesting. Last, doping, as used in microelectronics, is not yet an option for the optimization of CNFETs. As a result, a Schottky barrier is often present at the nanotube-metal contacts. Therefore, most of the CNFETs are Schottky barrier transistors [109].

Top-Gate Nanotube-Based Transistors

Early nanotube FETs used a non-local back-gate with the nanotube being contacted by noble metal electrodes. This arrangement gave large contact resistances and poor characteristics [108, 110, 111] . Since then, significant improvements in the performance of CNFETs have been achieved [105, 106]. New structures are now built with top-gate geometry and they resemble, in many respects, to conventional silicon MOSFETs. An example of the characteristics of a top-gated CNFET is shown in Fig. 6.50. This CNFET is contacted with titanium electrodes and the gate is made of Al separated by 15 nm of gate oxide (SiO_2) [105]. First, a very large improvement was observed compared to the early nanotube devices. This is mainly due to the scaling of the dimensions (mostly the gate oxide thickness) and the adoption of a better device geometry. A comparison of key parameters has been made and suggests that the performance of CNFETs exceed the best conventional Si MOSFET [104–106].

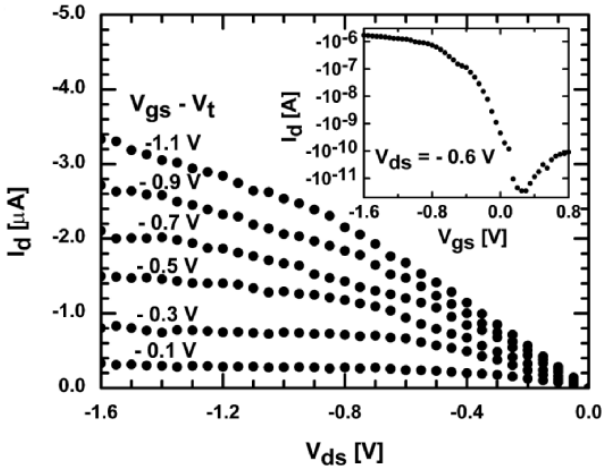


Fig. 6.50. Output characteristics of a high performance carbon nanotube field-effect transistor. The gate is placed on top of the nanotube and separated by 15 nm oxide thickness. The inset shows the sub-threshold characteristics of the transistor highlighting the 6 orders of magnitude ON-OFF ratio. Adapted from [105]

Nanotube-Metal Schottky Barrier

The CNFETs measured in air, as in Fig. 6.50, are usually p-type, i.e. the tubes conduct holes upon applying a negative gate voltage and they show no evidence of electron conduction even at very large positive gate voltage. In addition, the ON state of CNFETs in air show ohmic IVs at small source-drain voltage. This is a clear indication that the metal-nanotube contact has no (or only little) effect on the injection. This situation changes when the devices are annealed in vacuum. This step removes the adsorbed oxygen and yields to a reversible transformation of the CNFETs from p- to n-type. An example of such a transformation is presented in Fig. 6.51.

Initially, a p-type CNFET (**1**) is annealed in vacuum and transformed into a n-type device (**2**). Then, oxygen is slowly introduced into the chamber and IVs are acquired at intermediate stages of the transformation [112]. The intermediate stages (e.g. curve **3** in Fig. 6.51) are ambipolar, i.e. the tube can conduct both electrons and holes. This transformation can be easily rationalized by considering the presence of barriers at the contacts. Each situation is presented in Fig. 6.51. In air, the Fermi level at the metal-nanotube junction is closer to the valence band of the nanotube. This leads to hole conduction and p-type behavior. The annealing step changes the line-up of the bands at the junction and lowers of the barrier for electron injection. This modification at the contacts also introduces an increase of the barrier height for hole injection, leading to an n-type CNFET. The intermediate stage, however, simply occurs when the contact Fermi level is around mid-gap. This special situation

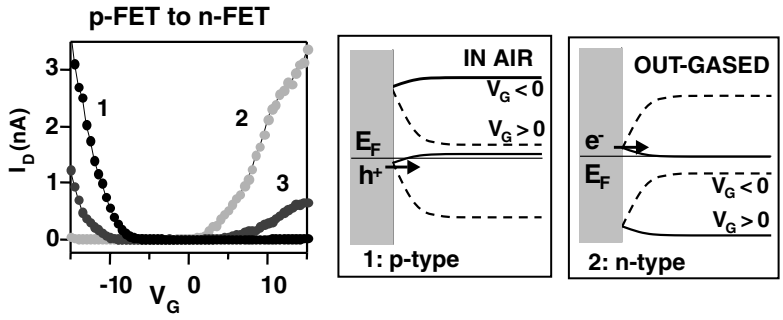


Fig. 6.51. Inter-conversion between p- and n-type CNTFETs using vacuum annealing and oxygen exposure and the related band diagrams. n-type CNTFET are obtained by annealing a p-type CNTFET in vacuum at 700 K for 10 minutes. The gradual convertion of a n-FET (**2**) back into a p-FET (**1**) is done by oxygen exposure. Adapted from [112]

gives similar barrier height (i.e. half of the bandgap, E_g) for electron and hole injection and the device is ambipolar.

6.7.4 Ambipolar Carbon Nanotube Transistors

The ambipolar CNFET is particularly interesting in that it allows us to explore in depth the properties of one-dimensional (1D) metal-nanotube junctions. The contact situation for the ambipolar device is perhaps the worst since it involves a mid-gap alignment of the Fermi level and therefore the barriers for electron and hole injection are the highest ($E_g/2 \sim 300\,\text{meV}$). Surprisingly, the IVs at room temperature are ohmic (see Fig. 6.52) as if there was no (or little) barrier at the metal-nanotube junction [113].

This behavior is unique and not seen in Schottky barriers at 3D metal-semiconductor junctions. The temperature dependence of the IV curves for the ambipolar device in the hole accumulation region are presented on the right panel of Fig. 6.52. The results are essentially the same for the electron accumulation region. The data for both electron and hole injection gives very small barrier heights using a conventional thermal activation plot (Arrhenius plot) [114]. The number is at least 20 times lower than expected ($\sim$15 meV instead of $\sim$300 meV) barrier height, which is obviously wrong. Therefore, the injection process across the Schottky barrier involves another mechanism which is more likely to be due to tunneling across the barrier. In fact, the barrier in 1D is so thin that the junction is quasi-transparent for carrier tunneling, i.e. there is a very efficient injection through the barrier. The shape of the barrier is triangular with some non-uniformity at the bottom. Moreover, it strongly depends on the gate field (see an example of calculation in Fig. 6.53) [115]. As a result, the injection of carriers may become very asymmetrical depending on the conditions at the contact.

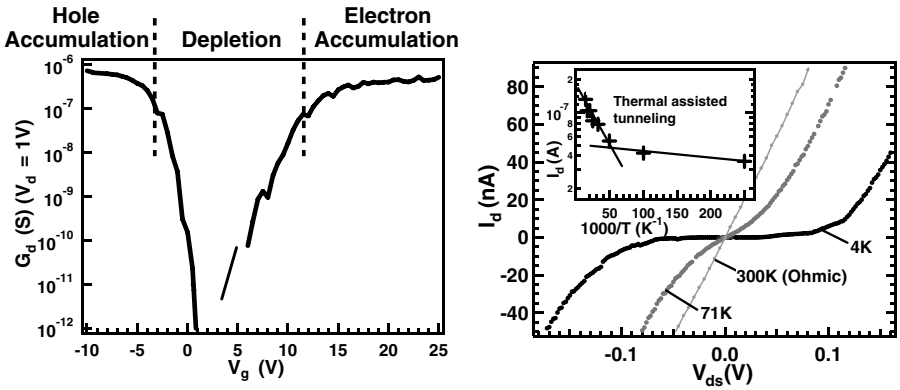


Fig. 6.52. *Left*: Sub-threshold characteristics of an ambipolar nanotube field-effect transistor. *Right*: Characterization of the Schottky barrier for the ambipolar transistor ($L = 800$ nm) as a function of temperature. The IV curves in the hole accumulation are ohmic at room temperature, which is consistent with only small barrier. This is surprising since the barrier is estimated to be around 300 meV, i.e. much higher than $k_{\mathrm{B}}T$. Adapted from [113]

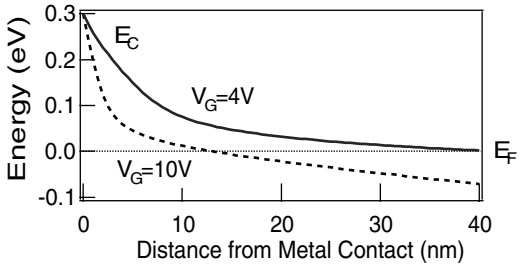


Fig. 6.53. Calculation of the Schottky barrier near the metal-nanotube contacts. Conduction-band energy plot near the contact shows a thin triangular shape barrier for gate voltage of 4 and 10 V. Tunneling current is modulated by the change of the barrier shape under the gate field. Adapted from [115]

The properties of the metal-nanotube Schottky barrier are useful and interesting. In particular, they allow the simultaneous injection of electrons and holes when large drain bias are applied to an ambipolar CNFET (the current is balanced at $2V_d = V_g$). This effect results in polarized infrared emission peaking at the bandgap of the carbon nanotube [116]. The ambipolar CNFETs are currently the smallest electrically driven optical source ever made.

Schottky Nanotube Transistor: Operating Mode

The nanotube transistor characteristics resemble those of the conventional MOSFET, but the underlying physics of operation is very different. The

Schottky barrier at the contact is hard to eliminate and there is no good scheme to dope locally the nanotube in the contact region. Moreover, the presence of a contact barrier is hard to identify from the IV curves. In fact, the transistor action for CNFETs is usually limited by the injection process at nanotube-metal contact. They have been shown to be Schottky barrier transistors (SB-CNFETs) [109].

The main question is why the characteristics of the SB-CNFET resemble those of a regular MOSFET? To answer this, we need to consider in detail the band evolution under the influence of the gate and the drain fields. The output characteristics of a SB-CNFET is schematically illustrated in Fig. 6.54.

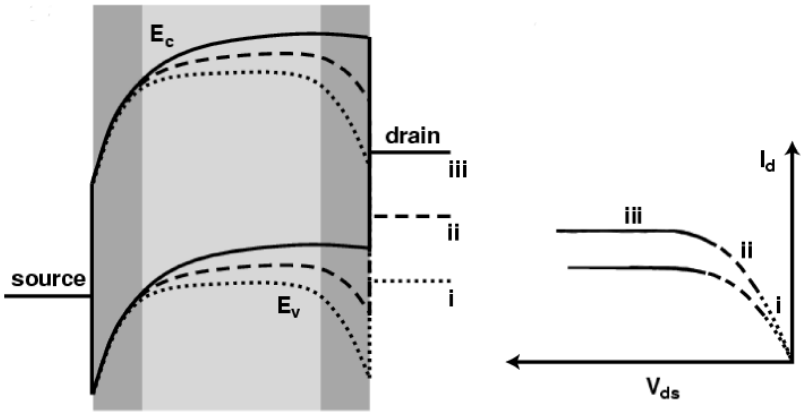


Fig. 6.54. *Left*: qualitative band diagram describing the operation a Schottky barrier nanotube field-effect transistor in the ON state. *Right*: the corresponding output characteristics for two arbitrary gate voltage. Adapted from [117]

The dark gray regions highlight the band close to the metal contact. The Fermi level at the contact is somewhere inside the bandgap of the nanotube. Here we assume that no scattering takes place in the nanotube. The ON state operation of a p-type SB-CNFET goes as following: *region i*: I_d (current at the drain) changes linearly with V_d (drain bias) since the tunneling barrier is thin on the source side. That is, the gate field is strong on the source side (the device is ON) and determines the shape of the barrier. *Region ii*: I_d becomes non-linear because the situation on the drain side approaches the flat band condition. This is because the drain voltage is getting close to the gate voltage and the drain to gate field is gradually vanishing. *Region iii*: I_d saturates when the barrier in the drain region vanishes. This saturation is NOT the pinch off of the channel as usually observed in conventional MOSFET [118]. A change of the gate bias will have the effect of shifting the current up or down because it has a direct effect on the thickness of the source contact barrier. As a result, the current in all three regions is affected by the gate. Last, in this

band scheme, the bulk of the nanotube channel has no effect on the IVs. Thus, the nanotube channel is not limiting the current of the SB-CNFET. This implies that the intrinsic properties of the nanotube are NOT probed by the SB-CNFETs unless the contact barrier is eliminated.

6.8 Transport in Nanotube Based Composites

6.8.1 Introduction

As shown in previous sections, their electronic properties lead at a nanoscopic level to fascinating phenomena such as quantum box effects, Coulomb blockade, ballistic transport, and so on. On the other hand, it is also possible to take advantage of these properties at the macroscopic scale, by embedding the nanotubes into a matrix, i.e. by building a composite. Here we focus on the transport properties of composites where the matrix is a polymer and the nanotubes act as loading particles or fillers. These composites are sometimes referred to as extrinsic conducting polymers. The fillers which are commonly used are carbon blacks, metallic nanoparticles, organic needles. Indeed the mechanical properties of CNT make them even more interesting than the conventional fillers. Potential applications of these heterogeneous materials are transport layers in organic devices such as LED or solar cells, electrostatic shields, electromagnetic shields.

We first introduce some basic concepts relevant for the transport properties of heterogeneous systems, followed by a short survey of the published works regarding CNT based composites. Section 6.8.2 is devoted to the transport mechanisms. The last two sections are concerned with non-linear transport and magnetotransport. Since very few works on CNT based composites is published, their properties applied to CNT mats (buckypaper, pressed pellets, etc.) are briefly discussed.

6.8.2 Transport in a Heterogeneous Medium

Basic Percolation Theory and Effective Medium Approach

We consider the situation in which a volume fraction p of conducting particles with conductivity σ_0 are embedded into an insulating matrix. Indeed, when $p = 0$ the composite is an insulator while it is conducting if $p = 1$ with conductivity σ_0. In between, a finite conductivity ($0 < \sigma(p) < \sigma_0$) is obtained when a continuous conduction path connects both sides of the sample. Assuming that the particle-to-particle contact is electrically transparent and that the fillers are randomly dispersed into the matrix, the transition between the insulating to the conducting state occurs above a threshold fraction p_c. This topologically driven transition is referred to as the percolation transition. Percolation theory has a broad range of applications. A comprehensive introduction is

given in [119, 120]. This phase transition is second order and as such, critical behavior is expected close to the percolation threshold p_c. Within this theory, above and close to p_c, the conductivity of the composite obeys the power law:

$$\sigma = \sigma_0[(p - p_c)/(1 - p_c)]^{\beta} \tag{6.110}$$

The conductivity exponent β depends only on the dimensionality of the system ($\beta \sim 2.0$ in 3D) while p_c also depends on the network coordination. In 3D and for randomly dispersed conducting spheres, $p_c \sim 0.16\%$. Smaller thresholds are obtained when the fillers are non-spherical. In this case, it was suggested that the excluded volume has to be considered instead of the actual volume of the fillers [121]. This results in a percolation threshold following $\Phi \times p$ a constante, and $\Phi = L/r$ being the aspect ratio of the filler. Alternative models can be used to describe the electrical properties of composites [120]. Far from p_c and close to 1, it has been shown that the effective medium theory which gives $\sigma \propto p$ nicely describes the evolution of the conductivity [122].

Application to Nanotube-Based Composites

Several groups have reported on CNT-polymer composites (SWNT [123, 124] or MWNT [125]). Quite generally, a percolation-like transition is observed with reported thresholds that vary from 0.02% to 10%. This broad range of p_c values originates from the sample preparation but p_c also depends on the experimental setup used for conductivity measurements. Because of the very high aspect ratio of CNT, transverse or sandwich geometry leads to finite size effects that lower p_c.

In PMMA/SWNT composite films, typical values give $p_c \sim 0.3\%$ and $\beta \sim 2.1$, whereas $\sigma_0 \sim 83$ S/cm [124]. Using the excluded volume concept, this small p_c may be explained by an aspect ratio of $\Phi \sim 100$ while the exponent β is in agreement with transport in 3D. When p tends to 10%, effective medium theory applies, and gives a room temperature conductivity of the SWNT mat of the order of σ_0. Measurements on a pressed pellet (i.e. a $p = 1$ composite) gives the same order of magnitude.

6.8.3 Transport Mechanism

Very few reports have been published regarding the transport mechanism in CNT based composites. Here, we summarize what is usually discussed in extrinsic conducting polymers.

6.8.4 Localization and Hopping

In most cases, the charge carriers are localized on the fillers with a localization length ξ. For SWNT fillers, the carriers originate from metallic tubes, and transport occurs via tunneling or hopping (phonon assisted tunneling) from

one filler to another. At the microscopic scale and low temperatures, hopping is described by a transition rate Γ between two sites given by:

$$\Gamma = \nu_0 \exp\left(-\frac{2r}{\xi} - \frac{\Delta}{k_\mathrm{B}T}\right) \tag{6.111}$$

r is the distance between the two sites, and Δ is related to their energy difference. Pure tunneling obeys (6.111) without the $\Delta/k_\mathrm{B}T$ contribution. The macroscopic conductivity is obtained by optimizing all Γ that defines a temperature dependent conduction path. Without interactions between the carriers and assuming a constant density of states $\rho(E_\mathrm{F})$ at the Fermi level, optimization leads to Mott's variable range hopping (VRH) [126]. The VRH conductivity follows:

$$\sigma \propto \exp\left[-\left(\frac{T_0}{T}\right)^{1/(d+1)}\right] \tag{6.112}$$

where d is the dimensionality and $T_0 \propto 1/\rho(E_\mathrm{F})\xi^d$. This temperature dependence is widely observed in buckypapers or SWNT mats (with $d = 3$) [124, 127]. The VRH model gives ξ in the order of a few tens of nanometers, if one considers the metallic SWNT $\rho(E_\mathrm{F})$.

6.8.5 Coulomb Interactions and Coulomb Gap

Charging a metallic particle requires one to overcome the Coulomb charging energy E_c which scales with $1/s$ where s is the typical particle size. The charging effect is important when the fillers are nanoscopic such as in cermets [128]. It is quite similar to the case of VRH in presence of Coulomb interactions where a soft Coulomb gap Δ_CG digs at the Fermi level during the transport process [129]($\Delta_\mathrm{CG} = e^3\sqrt{(\rho(E_\mathrm{F})/(\varepsilon_\mathrm{PMMA} + 4\pi\rho(E_\mathrm{F})\xi^2)^3}$, $\varepsilon_\mathrm{PMMA}$ the PMMA dielectric constant). This process leads to $\sigma \propto \exp[-(T_0/T)^{1/2}]$ where T_0 is related to Δ_CG (respectively to E_c) and to ξ (or s). Such a temperature dependence in PMMA/SWNT composites has been observed below 50 K [124], and was attributed to the digging of a Coulomb gap of magnitude $\Delta_\mathrm{CG} \sim 10\,\mathrm{meV}$. Loading the composite more and more leads to a partial (mutual) screening of the charging energy, and thus to a disappearance of the charging effects in $p = 1$ sample. Mott's VRH is thus recovered at high p fraction.

When E_c is small, as for example in carbon blacks (CB) or carbon fibers loaded composites, Sheng et al. [130] have proposed that transport occurs via direct tunneling between adjacent fillers. However, the tunneling probability is modified by the thermal noise which induces fluctuations of the tunneling barrier. This fluctuation induced tunneling model gives $\sigma \propto \mathrm{e}^{-T_0/(T+T_1)}$ which has also been used to describe the conductivity of SWNT mats [131].

6.8.6 Percolation Network

The percolation pathway depends on temperature as does the hopping/tunneling process. A special case has been invoked in CB loaded composites

where it is believed that localization occurs at the scale of the incipient infinite cluster of the percolation theory. This kind of localization is referred as superlocalization and leads to VRH with a non fractional exponent of the conductivity [132].

6.8.7 High-Electric-Field Effects

High electric field E also influences the transition rates which results in non-ohmic behavior. Here we just discuss the mechanisms involving tunneling or hopping which are invoked in CNT based materials.

A high electric field may cause emission across a tunnel barrier. This Fowler-Nordheim emission process is at the origin of the field-emission properties of CNT (see Chap. 4). At high field, it is found that the current density J increases as $J \propto E^2 \mathrm{e}^{-a/E}$. When fluctuation induced tunneling is relevant, $J \propto \mathrm{e}^{-a(E/E_0-1)^2}$ [130]. Such a field dependence was invoked in SWNT buckypaper [131].

Several processes have been proposed when VRH occurs. They depend on the field magnitude and on the details of the material. In a weak field and with a small DOS at the Fermi level, 'heating' of the electron gas due to the potential energy gain may occur (not to be confused with Joule effect). The energy distribution of the carriers is disturbed and an 'electric temperature' T_{el} can be introduced at $T = 0$ K:

$$k_{\mathrm{B}} T_{\mathrm{el}} = \gamma e E \xi \tag{6.113}$$

where γ is a numerical factor close to 1. This model was used by Fuhrer and coworkers in SWNT buckypaper [129]. When the thermal temperature is finite, VRH transport occurs in the same way as it does at zero field but at the price of replacing the real temperature by an effective one $T_{\mathrm{eff}} = T + T_{\mathrm{el}}$ [133].

The field dependence observed in PMMA/SWNT composite seems in agreement with this picture [124]. Using the effective temperature concept allows one to build master curves which unify the ohmic temperature dependence and the electric field dependencies for all investigated p fractions. It suggests that localization is intrinsic in this system.

Increasing the field also changes the transport pathway. In very high fields, VRH is lost and simple tunneling occurs [126].

6.8.8 Magnetoresistance

Two kinds of magnetoresistance effects may be considered. The spin dependent contribution is weak in CNTs as long as magnetic particles are absent. Still, the presence of catalysts may contribute to a negative magnetoresistance (MR) in weak field. In CNT based materials, the main contribution is orbital in nature.

In a weak field, application of a magnetic field H partly destroys the quantum interferences which appear along the transport path [134]. A negative magnetoresistance is found quadratic (or linear) in field. This effect is the strong localization counterpart of the weak localization negative MR discussed in Sect. 6.8.2. Indeed MR saturates as soon as the magnetic flux through the hopping area scales with the flux quantum Φ_0.

$$H(R_{\rm hop}^3.\xi)^{1/2} = \Phi_0 \tag{6.114}$$

where $R_{\rm hop} \propto \xi(T_0/T)^{\alpha}$ is the hopping length. In the left panel of Fig. 6.55, we show such a behavior in $p = 8$ % PMMA/SWNT composite. Below 20 K, the MR is linear and the saturation field corresponds to $\xi \sim 7\,$nm. Above 20 K, a quadratic MR is observed without saturation effects in the field range. The same behavior was also observed in SWNT mat [129].

In high fields ($\Phi > \Phi_0$), shrinkage of the wavefunctions occurs which reduces the transfer between adjacent sites. A positive magnetoresistance is found:

$$\ln(R(H)/R(0)) \propto H^2\xi^4(T_0/T)^{3/2} \tag{6.115}$$

here in the presence of Coulomb interactions [129]. This positive MR has been observed at low temperatures ($T < 8\,$K) as shown in Fig. 6.55. Once again, a localization length $\xi \sim 7\,$nm is deduced.

6.9 Thermal Transport in Carbon Nanotubes

6.9.1 Introduction

Some forms of carbons are the best known heat conductors at room temperature (Table 6.1) and it was easy to figure out soon after the discovery of carbon nanotubes (NT) that they should exhibit a very large thermal conductivity.

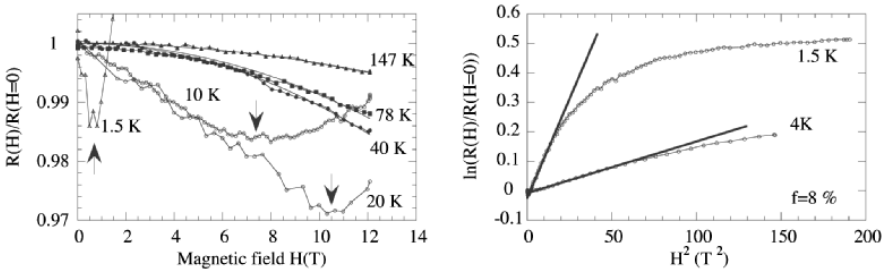


Fig. 6.55. *Left*: Negative MR due to quantum interferences in a SWNT/PMMA composite with $p = 8\%$. The arrows show the saturation field of (6.114). At $T =$ 1.5K, the saturation comes from scattering with catalytic particles. *Right*: Positive MR due to orbit shrinkage (see (6.115)) in the same sample at low temperature. In both cases, $\xi \sim 7\,$nm is found

This should lead, as for the case of some carbon fibers heat treated at high temperatures, to interesting applications as 'hyperconductors' of heat in the form of composites [135]. However, due to the difficulty of measurements (cf. below 6.9.4), preliminary experimental results were only available recently to confirm this view. Indeed, in order to interpret correctly the experimental results by comparing them to theoretical predictions, measurements need to be performed on individual nanotubes. This is a very delicate experiment to perform which was only realized recently on a MWNT by Kim et al. [136] using sophisticated nanolithographic techniques. The first thermal conductivity measurements on NT, which were performed on bundles [137], did not lead to a straightforward interpretation, since measurements pertained to an average taken over a group of different nanotubes. Moreover, for the case of bundles, to the thermal resistance of the individual nanotubes should be added that of the contacts between them, and contact resistances are always difficult to evaluate. This is not the case for the specific heat where contact resistances do not play a direct role. On Table 6.1, we have listed the orders of magnitude of the thermal conductivity of carbons and graphites at room temperature. We have also shown for comparison the room-temperature value for copper and the range of conductivities for most polymeric materials.

Table 6.1. Thermal conductivity of carbons and graphites at room temperature

Material	Conductivity ($Wm^{-1}K^{-1}$)	Heat Treatment
Nanotubes	$>10^3$	
Diamond	10^3	
HOPG	10^3	$>3000°C$
Vapor deposited Fibers	10^3	$<3000°C$
Pitch Fibers	10^2–10^3	2000–3000°C
Pure Copper	5×10^2	
PAN Fibers	10	
Polymeric Materials	10^{-1}	

The phonon spectrum of graphite is highly anisotropic and may be considered as quasi-2D for frequencies above a few THz. This anisotropy is naturally reflected in the lattice thermal conductivity which is the dominant heat transport mechanism, except at very low temperatures. In-plane we find the highest room-temperature thermal conductivities, comparable to that of diamond, which is the best known heat conductor (Table 6.1). Normal to the graphene layers, the thermal conductivity is two orders of magnitude lower at 300 K (Fig. 6.56). This anisotropy is reduced as the temperature is lowered. Owing to their reduced dimensions, the phonon spectrum of NT may be quantized at low temperatures, as is the case for the charge carriers. This quantization should be reflected in the specific heat and thermal conductivity.

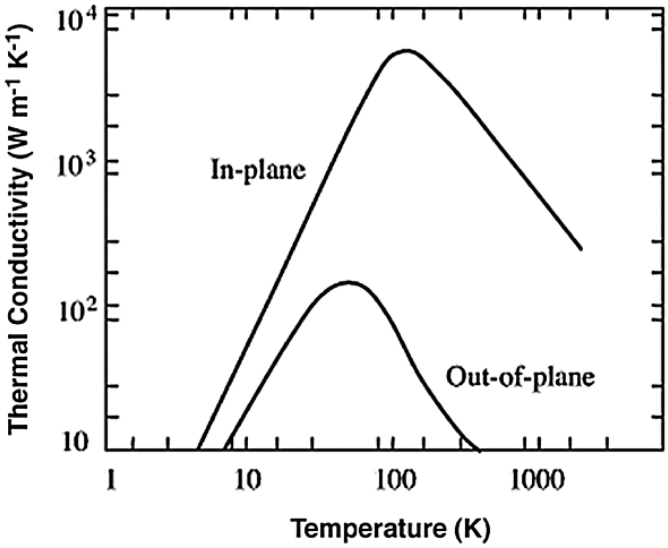


Fig. 6.56. Schematic representation of the temperature variation of the thermal conductivity of HOPG in-plane and out-of-plane showing the strong anistropy in the higher temperature range. This anisotropy is reduced as the temperature is lowered

We will now discuss the thermal conductivity (Sect. 6.9.2) and the thermoelectric power (Sect. 6.9.3) data available on carbon nanotubes (NT) and then briefly comment on the problems encountered when performing their measurement (Sect. 6.9.4). Emphasis will be placed on the recent results obtained on an individual MWNT [136], since they may be compared to theoretical estimations. We will lean heavily on the knowledge accumulated through the study of other forms of carbons [138].

6.9.2 Thermal Conductivity

In Chap. 1 of this volume [138], we introduced some basic principles concerning the thermal conductivity of solids in general, and gave an overview over the main features of this property for carbons and graphites. We refer to this chapter and to other recent review papers [135, 139, 140] for an introduction of this property in carbonaceous materials. We have seen that the lattice thermal conductivity results of graphites may be discussed using the Debye relation:

$$\kappa_g = \frac{1}{3} C v \ell_e \tag{6.116}$$

in the dominant phonon-approximation. This means that instead of considering the entire phonon spectrum, we introduce an average phonon frequency

which is proportional to the absolute temperature, and to which is associated an appropriate mean free path ℓ_e. C is the lattice specific heat per unit volume and v is an average phonon velocity, the velocity of sound. Despite its simplicity, relation [135] is useful for the discussion of most thermal conductivity results. For different samples of a given crystalline solid, since the specific heats and the phonon velocities are the same, the thermal conductivity is directly proportional to the phonon mean free path. This phonon mean free path depends essentially on the lattice perfection of the sample at low temperatures [135, 138].

Specific-heat measurements are now available for CNs. Hone et al. [141] reported on the results of measurements performed on SWNT ropes in the temperature range $2 < T < 300\,\mathrm{K}$. Later on, Lasjaunias et al. [142] presented experimental data pertaining to the low-temperature specific heat of SWNT bundles. These results extended for the first time the specific heat data to ultra-low temperatures (down to about 100 mK) showing clearly a T^3 dependence in the lowest temperature range. This temperature dependence, characteristic of a three-dimensional system, which was ascribed to inter-tube interaction, does not reflect the behavior expected from an individual one-dimensional SWNT.

At the lowest temperatures, when phonon-phonon umklapp processes are frozen out due to the decrease in phonon density and phonon wave number, crystallite or the sample boundaries are the main phonon scatterers and the phonon mean free path should then be temperature insensitive. So is the velocity of sound which is almost temperature insensitive at all temperatures. At low temperatures, the temperature dependence of the thermal conductivity should then follow that of the specific heat. Thus, the larger the crystallites or the sample-size the higher the thermal conductivity. Above the thermal conductivity maximum (Fig. 6.56 and Fig. 6.57), phonon scattering is mainly due to an intrinsic mechanism, phonon-phonon umklapp processes, and the thermal conductivity should thus be the same for different well-ordered samples of the same material. At intermediate temperatures, i.e. around the thermal conductivity maximum, scattering of phonons by point defects (small scale defects) is the dominant scattering process. The position and the magnitude of the thermal-conductivity maximum will thus depend on the competition between the various scattering processes (boundary, point defect, phonon, etc). So, for different samples of the same material, the position and magnitude of the maximum will depend on the point defects and the in-plane coherence length, L_a, since phonon-phonon interactions are assumed to be the same [135]. This will have an important bearing on the discussion of the experimental results, as discussed below.

Since the main mechanism responsible for heat flow in carbons, including MWNTs, is via the lattice waves, we should expect the same general trends in these materials. Indeed, while for different carbons the electronic structure might be quite different leading to various types of electronic conductions, metallic, semimetallic or semiconducting, this is not the case for

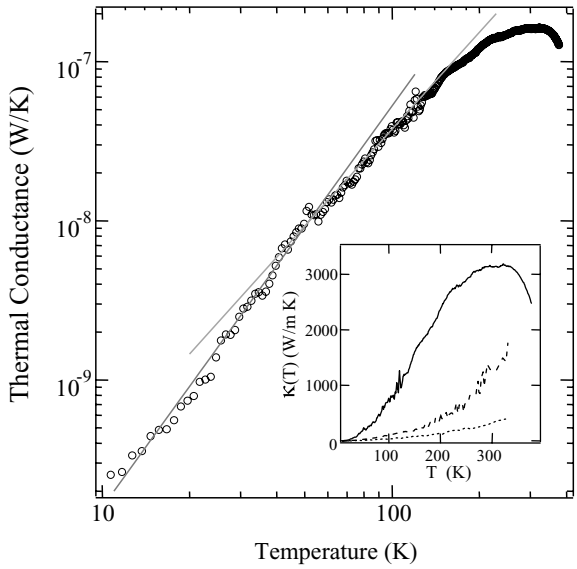


Fig. 6.57. Log-log representation of the temperature variation of the thermal conductance of an individual MWNT of diameter 14 nm. The *solid lines* represent the linear fits with slopes 2.5 and 2.0 respectively for different temperature range. Inset: Temperature variation of the thermal conductivity of an individual MWNT (*solid curve*), and a bundle of diameters 80 nm (*broken curve*) and 200 nm (*dotted curve*) respectively. Adapted from [136] (by courtesy of P. Kim)

phonon transport. If we exclude phonon quantization in nanosystems, the phonon spectrum should not differ widely from one carbon sample to another provided that they remain in the crystalline state. It is only the phonon mean free path which will differ since it is very sensitive to lattice defects [135, 138].

The first thermal-conductivity data reported for nanotubes were performed by Hone et al. [137] on as-grown NT bundles. They estimated a room temperature thermal conductivity around $35\,\mathrm{W\,m^{-1}K^{-1}}$. This low value is not unexpected for their samples since it includes contact resistances between nanotubes of undefined crystal perfection. Indeed, subsequent calculations by Berber et al. [143] predicted much higher values for an ideal individual SWNT, of the order of a few $10^4\,\mathrm{W\,m^{-1}K^{-1}}$ around 100 K with a room temperature value close to $7000\,\mathrm{W\,m^{-1}K^{-1}}$. These values, which are superior to those of diamond and in-plane graphite (see Table 6.1) are more realistic, since they are close to that which might be expected from a perfect graphene sheet. As will be shown below, further experimental data have confirmed these views.

Since they were realized on an individual MWNT, the measurements performed by Kim et al. [136], though still subject to certain experimental uncertainties, lend themselves to the first reliable analysis allowing comparison with theoretical predictions. Using nanolithographic techniques, Kim et al.

designed a submicronic sample holder enabling the measurement of the thermal conductivity and thermoelectric power (cf. Sect. 6.9.3) of an individual MWNT of 14 nm diameter and a few micrometers in length. The temperature range $8\,\mathrm{K} < T < 370\,\mathrm{K}$ was investigated. The results are shown in Fig. 6.57. One may see from Fig. 6.57 that the estimated room temperature thermal conductivity lies around $3000\,\mathrm{W\,m^{-1}K^{-1}}$, with a peak around 320 K. Moreover, Kim et al. estimated from their data a phonon mean free path of the order of 500 nm, at low temperatures.

Although the high thermal-conductivity values obtained by Kim et al. [136] are not surprising, they are not consistent with the position of the maximum observed if we compare their data to those relative to other graphitic systems. In these systems, a low-temperature mean free path around 500 nm, due to boundary scattering, would indeed lead to a thermal conductivity maximum around room temperature, but with a value 3 to 4 times lower than that observed for the MWNT investigated [135]. This discrepancy could be attributed to a different thermal behavior of NTs with respect to bulk graphitic systems. While this is probably true for SWNTs, it is not likely that MWNTs would exhibit a different qualitative behavior from bulk graphitic systems. If this is indeed the case, one should then ascribe the discrepancy to some experimental uncertainties discussed by Kim et al. or, possibly, to the presence of heat losses which are not explicitly addressed in their paper [136]. Also, for the same boundary scattering length, a sample free of point defects might exhibit higher values around the maximum. Finally, the quasi-ballistic motion of phonons invoked by the authors and ascribed to the short length of the sample might lead to a qualitatively different behavior when compared to a sample of infinite length. Further experimental work will be needed to determine the reason for this apparent discrepancy.

6.9.3 Thermoelectric Power

Contrary to the case of the thermal conductivity, the interpretation of the thermoelectric power (TEP) results for most known solids is a rather delicate task. Indeed, except for the case of typical semiconductors such as germanium or silicon, the interpretation of this property for most solids is hardly convincing. This is particularly true for the case of carbons and graphites [135].

The TEP or Seebeck coefficient, S, is the potential difference generated by an applied unit temperature difference across an electrical conductor. The diffusion thermoelectric power is due to the diffusion of charge carriers from hot to cold caused by the redistribution of their energies caused by the temperature gradient. The charge carriers accumulating at the cold end of the sample give rise to the thermoelectric voltage. This potential difference tends to counterbalance the flow of diffusing carriers until a steady state is reached. Another mechanism, known as the phonon-drag thermoelectric power, consists in a transfer of momentum from the out-of-balance phonon system to the electron system under certain conditions (cf. below). This results in a

drag on the charge carriers which causes an additional electronic drift. An electric field is generated to counterbalance this extra electronic motion. For a given group of charge carriers, the general expression for the diffusion TEP is given by the Mott formula

$$S_d = \frac{\pi^2 k_{\mathrm{B}}^2}{3q} T \left[\frac{\partial \ln \sigma}{\partial \varepsilon} \right]_{E_{\mathrm{F}}}$$

where E_{F} is the Fermi energy and σ the electrical conductivity. The derivatives is taken at the Fermi level. When, as is the case for HOPG, there is more than one type of carrier, the total thermoelectric power is obtained by considering the different groups of carriers with partial thermoelectric powers that contribute to the total thermoelectric power as electromotive forces in parallel [135, 138].

Hone et al. [144] have reported on the temperature variation of the TEP of SWNTs bundles in the temperature range $4.2\ \mathrm{K} < T < 300\ \mathrm{K}$. They have also measured the electrical resistivity of these bundles in the same temperature range. The three samples investigated, two pristine and one sintered, exhibited the same qualitative behavior and almost the same values (Fig. 6.58). The thermoelectric power was found to be positive in the whole temperature range investigated. As may be seen from Fig. 6.58, it increases first linearly at low temperature then tends to saturate around 100 K to increase slowly again with temperature around 200 K. The room-temperature values, around $50\,\mu\mathrm{V/K}$, are considerably higher than those observed for metallic samples (a few $\mu\mathrm{V/K}$), but are comparable to those observed in semimetals. Oddly

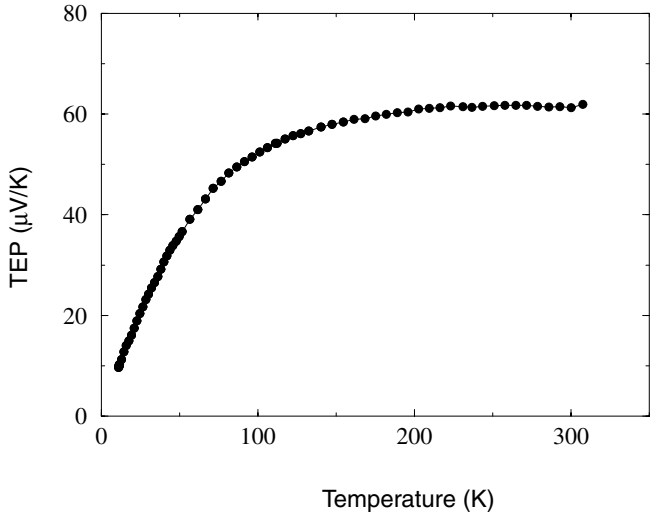


Fig. 6.58. Temperature variation of the TEP of a SWNT bundle. Adapted from [144] (by courtesy of J. Hone)

enough, the temperature variation looks more like that observed in graphite intercalation compounds (see for example [145]) than in the pristine material, though the room temperature value measured in SWNTs is about twice that reported for GICs.

In the case of SWNTs the earlier results of Hone et al. [144] have shown that the data are not consistent with those calculated from the known band structure which predicts much smaller values than those actually observed. Hone et al. suggest from their data that the predicted electron-hole symmetry of metallic nanotubes is broken when they are assembled into the form of ropes. Kim et al. [136] have also measured the temperature dependence of the TEP of the individual MWNT, whose thermal conductivity is reported in Fig. 6.57, from liquid helium temperatures up to room temperature (Fig. 6.59). At first sight, since the TEP is positive in the entire temperature range, one may deduce that it is generated by a majority of holes. The temperature variation is roughly linear and the high room temperature value observed ($80\,\mu V/K$) indicates that the Fermi energies are small, akin to what is observed for semimetallic systems. However, for a sound interpretation of the results, one needs to know at least the electronic band structure of the investigated sample. To illustrate the complexity of TEP analysis one should note that, if we exclude magnetic systems, there are two types of mechanisms for TEP generation: diffusion and phonon-drag. Besides, although the TEP is essentially sensitive to the Fermi energies, it is also dependent on the dominant scattering mechanism, but not on the magnitude of the scattering time. For the diffusion case, this means that it depends on the way the relaxation time depends on energy, i.e. the scattering parameter. It is worth noting too that

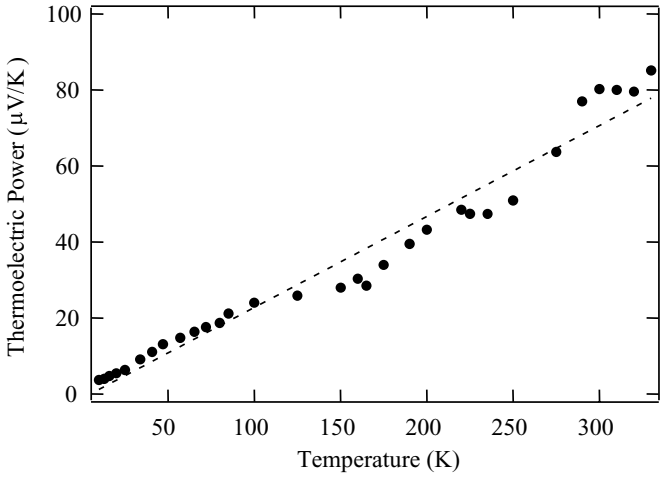


Fig. 6.59. Temperature variation of the thermoelectric power of the single MWNT which thermal conductivity is presented in Fig. 6.57. Adapted from [136] (by courtesy of P. Kim)

normal and umklapp electron-phonon scattering leads to TEPs of opposite signs. However, in most cases, electron-phonon umklapp scattering is unlikely to dominate the scene.

One important point to note is that, contrary to 3D systems, where the phonon-drag contribution generally shows up at low temperatures, in low-dimensional systems, whether 2D or 1D, this contribution might be dominant at all temperatures. Cantrell and Butcher [146, 147] have shown that this is the case for a 2D electron gas coupled to 3D phonons. Piraux et al. [148] have suggested independently that for first stages graphite acceptor intercalation compounds, which are typical 2D hole gases, the thermoelectric power is most probably dominated by a phonon-drag contribution up to room temperature with a negligible diffusion contribution [145]. More recently, Vavro et al. [149] have adapted the Cantrell-Butcher 2D model to a 1D electron gas interacting with 1D phonons to the case of p-doped SWNT and attributed the unusual behavior of the thermoelectric power they observed to 1D phonon-drag.

More generally, the phonon-drag contributions invoked from time to time can be justified using a naive physical picture. Phonon-drag shows up when the phonons which are allowed to interact with electrons, the drag phonons as opposed to the thermal phonons [145], have larger relaxation times for all other interactions, i.e. phonon-phonon, phonon-defects, etc. Note that the drag phonons are not necessarily those which dominate the scene at a given temperature and which carry most of the heat, i.e. those we call here the thermal phonons. The drag phonons are, in the case of semimetals and semiconductors, restricted to lower energies determined by energy and momentum conservation requirements [145]. For semimetallic systems with tiny Fermi surfaces like HOPG, we have pointed out [150] that the phonon-phonon interactions are very weak, even around room temperature, leading to unusually large phonon-phonon relaxation times. Moreover, because of the low energies of the drag phonons they are hardly scattered effectively by point defects (Raleigh scattering). This means that the probability for phonons to interact with electrons is larger than that of interacting with other phonons or point defects. Thus, in the absence of large-scale defects, we are in an ideal situation to observe large phonon-drag effects at all temperatures in semimetallic systems such as HOPG and MWNTs.

All this shows clearly that, contrary to the thermal conductivity, the interpretation of thermoelectric effects involves the knowledge of many physical parameters that are not always at hand. Also, since it is dependent on the details of the electronic structure and on the phonon spectrum, one expects that the TEP of SWNTs and MWNTs should differ since their electronic structures are quite different.

6.9.4 Measurement Techniques

There are specific problems associated with the measurement of the transport properties of macroscopic samples of large ratios of length to cross-section,

such as carbon fibers with diameters of the order of 10 µm, which are not encountered in bulk materials. It is obvious that these problems should be even more pronounced for the measurements on individual nanotubes where samples are of submicron size and are quite difficult to handle. The case of electrical resistivity has been discussed in previous sections, and we shall briefly consider here the additional difficulties encountered when heat flow has to be controlled such as in thermal transport measurements. Since heat flows are more difficult to control than electrical currents, thermal conductivity measurements are time consuming and very delicate to perform. This was found to be particularly true for the case of carbon fibers [151] because of their small diameters ($\sim 10^{-5}$ m). The main reason is that it is difficult to make sure that the heat losses in the measuring system do not far exceed the thermal conductance of the samples measured; the thermal conductance being defined as the heat flow through the sample per unit temperature difference. Moreover, in order to be able to get an insight into the mechanisms of the thermal conductivity of the sample investigated, it is necessary to measure the temperature variation of this property over a wide temperature range on a single well-characterized material, as was done for a vapor deposited fiber [152]. These problems are exacerbated for the case of single CNs [136].

Also, the determination of the sample cross-section may introduce large uncertainties in the estimation of the absolute values of the conductivities. The data obtained are thus more accurate with regard to temperature variation than with regard to absolute magnitudes. Fortunately, for the physical interpretation of the experimental results it is more important to know the temperature variation than the absolute values. These problems are not met in thermoelectric power measurements, since the knowledge of the samples cross-sections is not needed to calculate this transport coefficient. The measurement of samples of submicronic sizes requires a miniaturization of the experimental system, which may in some instances attain a high degree of sophistication. This is particularly true for the case of single CNs, where one has to deal with samples of a few nanometer diameter and about a micrometer length [153]. One has first to detect the sample, then apply to it contacts, which means, in a four-probe measurement, four metallic conductors, two for the injected heat current and two for measuring the resulting temperature difference. This requires the use of nanolithographic techniques [136,153]. Besides, one has to characterize the CN sample which is measured in order to determine its diameter and helicity if its electronic properties are to be known. This is particularly important for the case of the TEP, as mentioned above.

References

1. N. Ashcroft and D. Mermin: *Solid State Physics* (Saunders College, Philadelphia 1976)
2. A.A. Abrikosov: *Fundamentals of the theory of metals* (North-Holland, Amsterdam 1988)

3. Y. Imry: *Introduction to mesoscopic physics* (Oxford University Press, Oxford 2002)
4. S. Datta: *Electronic transport in mesoscopic systems* (Cambridge University Press, Cambridge 1997)
5. C.W.J. Beenakker and H. van Houten: *Solid State Physics* **44**, 1 (1991)
6. C.W.J. Beenakker: Rev. Mod. Phys. **69**, 731 (1997)
7. Ya.M. Blanter and M. Büttiker: Phys. Rep. **336**, 1 (2000)
8. B.L Altshuler and A.G. Aronov: In *Electron-electron interactions in disordered systems*, ed by A.L. Efros and M. Pollak (North-Holland, Amsterdam 1985)
9. H. Grabert and M.H. Devoret: *Single Charge Tunneling* (Plenum Press, New York 1992)
10. L.D. Landau and E.M. Lifshitz: *Statistical Physics, Part 2* (Pergamon Press, Oxford 1980)
11. V.J. Emery: *Highly conducting one-dimensional solids*, ed by J.T. Devreese, R.P. Evrard, V.E. van Doren (Plenum, New York 1979)
12. H.J. Schulz, G. Cuniberti, P. Pieri: In *Field theories for low-dimensional condensed matter systems*, ed by G. Morandi, P. Sodano, A. Tagliacozzo, and V. Tognetti (Springer, Berlin 2000)
13. T. Martin, G. Montambaux, J. Trân Thanh Vân (eds): *Correlated fermions and transport in mesoscopic systems* (Editions Frontières, Gif-sur-Yvette 1996)
14. I. Safi: Ann. Phys. Fr. **22**, 463 (1997)
15. M. Büttiker: J. Low Temp. Phys. **118**, 519 (2000)
16. C.L. Kane, and M.P.A. Fisher: Phys. Rev. B **46**, 15233 (1992)
17. C. Glattli, M. Sanquer, J. Trân Thanh Vân (eds): *Quantum physics at mesoscopic scale* (EDP Sciences, Les Ulis 2000)
18. E. Akkermans and G. Montambaux: *Physique Mésoscopique des électrons et des photons* (EDP Sciences/CNRS-Interéditions, Les Ulis 2004)
19. E. Abrahams, P.W. Anderson, D.C. Licciardello, T.V. Ramakrishnan: Phys. Rev. Lett. **42**, 673 (1979)
20. G. Montambaux: *Quantum Fluctuations, Proceedings of the Les Houches Summer School, Session LXIII*, ed by E. Giacobino et al. (Elsevier, Amsterdam 1996)
21. R.P. Feynman and A.R. Hibbs: *Quantum mechanics and path integrals* (McGraw-Hill, New-York 1965)
22. D.E. Khmelnitskii: Physica **126B**, 235 (1984)
23. S. Chakravarty and A. Schmid: Phys. Rep. **140**, 193 (1986)
24. P.A. Lee and T.V. Ramakrishnan: Rev. Mod. Phys. **57**, 287 (1985)
25. G. Bergmann: Phys. Rep. **107**, 1 (1984)
26. D.Y. Sharvin and Y.V. Sharvin: JETP Lett. **34**, 272 (1981)
27. A.G. Aronov and Y.V. Sharvin: Rev. Mod. Phys. **59**, 755 (1987)
28. A. Bachtold et al.: Nature **397**, 673 (1999). C. Schönenberger, A. Bachtold, C. Strunk, J.P. Salvetat: Appl. Phys. A **69**, 283 (1999)
29. P.A. Lee, D. Stone, H. Fukuyama: Phys. Rev. B **35**, 1039 (1987)
30. B. Altshuler and B. Shklovskiĭ: Sov. Phys. JETP **64**, 127 (1986)
31. D. Mailly and M. Sanquer: Journal de physique I France **2**, 357 (1992)
32. Ya.M. Blanter and A.D. Mirlin: Phys. Rev. E **55**, 6514 (1997)
33. R. Saito, G. Dresselhaus, M.S. Dresselhaus: *Physical Properties of Carbon Nanotubes* (Imperial College Press, London 1998)
34. S. Roche and R. Saito: Phys. Rev. Lett. **87**, 246803 (2001)

35. F. Triozon, Ph. Lambin, S. Roche: Nanotechnology **16**, 230 (2005)
36. L. Chico, L.X. Benedict, S.G. Louie, M.L. Cohen: Phys. Rev. B **54**, 2600 (1996)
37. T. Ando, T. Nakanishi: J. Phys. Soc. of Japan **67**, 1704 (1998). T. Ando, T. Nakanishi, R. Saito: J. Phys. Soc. of Japan **67**, 2857 (1998)
38. H.J. Choi, J. Ihm, S.G. Louie, M.L. Cohen: Phys. Rev. Lett. **84**, 2917 (2000)
39. S. Latil, S. Roche, D. Mayou, J.C. Charlier: Phys. Rev. Lett. **92**, 256805 (2004)
40. J.C. Charlier, T.W. Ebbesen, Ph. Lambin: Phys. Rev. B. **53** 11108 (1996). V.H. Crespi, M.L. Cohen, A. Rubio: Phys. Rev. Lett. **79**, 2093 (1997)
41. L. Chico, V.H. Crespi, L.X. Benedict et al: Phys. Rev. Lett. **76**, 971 (1996). Ph. Lambin and V. Meunier: Appl. Phys. A **68**, 263 (1999)
42. J.W. Mintmire and C.T. White: Phys. Rev. Lett. **81**, 2506 (1998)
43. C.T. White and T.N. Todorov: Nature **393**, 240 (1998)
44. S. Roche, G. Dresselhaus, M.S. Dresselhaus, R. Saito: Phys. Rev. B. **62**, 16092 (2000)
45. F. Triozon, S. Roche, A. Rubio, D. Mayou: Phys. Rev. B **69**, 121410 (2004)
46. K. Liu, Ph. Avouris, R. Martel, W.K. Su: Phys. Rev. B **63**, 161404 (2002)
47. L. Balents and M.P.A. Fisher: Phys. Rev. B **55**, 11973 (1997)
48. C.L. Kane, E.J. Mele, R.S. Lee et al: Europhys. Lett. **41**, 683 (1998)
49. L. Yang and J. Han: Phys. Rev. Lett. **85**, 154 (2000)
50. Ji-Yong Park, S. Rosenblatt, Y. Yaish et al: Nano Letters **4**, 517 (2004)
51. H. Suzuura and T. Ando: Phys. Rev. B **65**, 235412 (2002)
52. V. Perebeinos, J. Tersoff and Ph. Avouris: Phys. Rev. Lett. **94**, 086802 (2005)
53. S. Roche, J. Jiang, F. Triozon, R. Saito: Phys. Rev. Lett. **95**, 076803 (2005)
54. M. Georghe, R. Gutierrez, A. Pecchia, A. di Carlo, G. Cuniberti: Europhys. Lett. **71**, 438 (2005). S. Roche, J. Jiang, F. Triozon, R. Saito: Phys. Rev. B **72**, 113410 (2005)
55. S. Roche, F. Triozon, A. Rubio, D. Mayou: Phys. Rev. B **64**, 121401 (2001); Phys. Lett. A. **285**, 94 (2001)
56. D.J. Thouless: J. Phys. C **6**, 249 (1973)
57. D.J. Thouless: Phys. Rev. Lett. **39**, 1167 (1977)
58. J.C. Charlier and J.P. Michenaud: Phys. Rev. Lett. **70** 1858 (1993). Ph. Lambin, J.C. Charlier, J.P. Michenaud: *Progress in fullerene research*, ed by H. Kuzmany, J. Fink, M. Mehring, S. Roth (World Scientific, Singapore 1994), pp 130
59. R. Saito, G. Dresselhaus, M.S. Dresselhaus: J. Appl. Phys. **73**, 494 (1993)
60. Ph. Lambin, V. Meunier, A. Rubio: Phys. Rev. B **62**, 5129 (2000)
61. Y-K. Kwon and D. Tománek: Phys. Rev. B **58**, 16001 (1998). Y. Miyamoto, S. Saito, D. Tománek: Phys. Rev. B **65**, 041402 (2001)
62. S. Sanvito, Y.K. Kwon, D. Tománek, C.J. Lambert: Phys. Rev. Lett. **84** 1974 (2000)
63. S. Frank, P. Poncharal, Z.L. Wang, W.A. de Heer: Science **280**, 1744 (1998). P. Poncharal, C. Berger, Z.L. Wang, W.A. de Heer: J. Phys. Chem. **106**, 12104 (2002). A. Urbina, I. Echeverría, A. Perez-Garrido et al: Phys. Rev. Lett. **90**, 106603 (2003)
64. V. Krstic, S. Blumentritt, J. Muster et al: Phys. Rev. B **67**, 041401 (2003)
65. B. Bourlon et al: Phys. Rev. Lett. **93**, 176806 (2004)
66. M.P. Anantram: Phys. Rev. B **62**, 4837 (2000)
67. J.J. Palacios, J. Pérez-Jiménez, E. Louis et al: Phys. Rev. Lett. **90**, 106801 (2003)

68. C.L. Kane, L. Balents, M.P.A. Fisher: Phys. Rev. Lett. **79**, 5086 (1997). R. Egger, A.O. Gogolin: Phys. Rev. Lett. **79**, 5082 (1997); Eur.Phys. J. B **3**, 281 (1998)
69. M. Bockrath, D.H. Cobden, J. Lu et al: Nature **397**, 598 (1999)
70. R. Egger: Phys. Rev. Lett. **83**, 5547 (1999)
71. S. Eggert: Phys. Rev. Lett. **84**, 4413 (2000).
72. J. Lee et al: Phys. Rev. Lett. **83**, 166403 (2004)
73. P.J. de Pablo et al: Appl. Phys. Lett. **74**, 323 (1999)
74. V. Krstic, S. Roth, M. Burghard: Phys. Rev. B **62**, 16353 (2000)
75. B.Q. Wei, R. Vajtai, P.M. Ajayan: Appl. Phys. Lett. **79**, 1172 (2001)
76. A. Bezryadin, A.R. Verschueren, S.J. Tans, C. Dekker: Phys. Rev. Lett. **80**, 4036 (1998)
77. H. Hirayama, Y. Kawamoto, Y. Ohshima, K. Takayanagi: Appl. Phys. Lett. **79**, 1169 (2001)
78. K.B. Shelimov et al: Chem. Phys. Lett. **282**, 429 (1998)
79. L. Roschier et al: Appl. Phys. Lett. **75**, 728 (1999)
80. L. Kelvin: Phil. Mag. **46**, 82 (1898)
81. J. Tersoff: Appl. Phys. Lett. **74**, 2122 (1999)
82. S.B. Arnason, A. Rinzler, A.F. Hudspeth, A.F. Hebard: Appl. Phys. Lett. **75**, 2842 (1999)
83. M. Freitag, M. Radasavljevic, W. Clauss, A.T Johnson: Phys. Rev. B **62**, R2307 (2000)
84. P.J. de Pablo et al: Appl. Phys. Lett. **80**, 1462 (2002)
85. M. Brandbyge, J. Schiotz, M.R. Sorensen et al: Phys. Rev. B **52**, 8499 (1995)
86. T.W. Ebbesen et al: Nature **382**, 54 (1996)
87. A. Bachtold, M.S. Fuhrer, S. Plyasunovet et al: Phys. Rev. Lett. **84**, 6082 (2000)
88. M. Bockrath, D.H. Cobden, P. McEuen et al: Science **275**, 1922 (1997)
89. S.J. Tans, M.H. Devoret, H. Dai et al: Nature **386**, 474 (1997)
90. R.A. Jishi, M.S. Dresselhaus, G. Dresselhaus: Phys. Rev. B **48**, 11385 (1993)
91. M.S. Dresselhaus, G. Dresselhaus, P.C. Eklund: *Science of Fullerenes and Carbon Nanotubes* (Academic, San Diego 1996)
92. L. Balent and M.P.A. Fisher: Phys. Rev. B **55**, R11973 (1997)
93. This is the case in 1D systems at temperature below the Debye temperature as discussed by J. Appenzeller, E. Joselevich, W. Honlein: *Nanoelectronics and Information Technology – Advanced Electronic Materials and Novel Devices*, vol 19, ed by R. Waser (Wiley-VCH, 2003)
94. E. Fischer, H. Dai, A. Thess et al: Phys. Rev. B **55**, R4921 (1997)
95. R.S. Lee, H.J. Kim, J.E. Fischer et al: Phys. Rev. B **61**, 4526 (2000)
96. Z. Yao, C.L. Kane, C. Dekker: Phys. Rev. Lett. **84**, 2941 (2000)
97. A. Javey, J. Guo, M. Paulsson et al: Phys. Rev. Lett. **92**, 106804 (2004)
98. P.L. McEuen, M. Bockrath, D.H. Cobden et al: Phys. Rev. Lett. **83**, 5098 (1999)
99. L. Wenjie, M. Bockrath, D. Bozovic et al: Nature **411**, 665 (2001)
100. J. Kong, E. Yenilmez, T.W. Tombler et al: Phys. Rev. Lett. **87**, 106 801 (2001)
101. J. Appenzeller, R. Martel, Ph. Avouris et al: Appl. Phys. Lett. **78**, 3313 (2001)
102. P.G. Collins, M. Hersam, M. Arnold et al: Phys. Rev. Lett. **86** 3128 (2001)
103. J. Cumings, P.G. Collins, A. Zettl: Nature **406**, 586 (2000)
104. R. Martel, H.-S. Wong, K. Chan, Ph. Avouris: IEDM Tech. Dig., 320 (2001)

105. S. Wind, J. Appenzeller, R. Martel, et al: Appl. Phys. Lett. **80**, 3817 (2002)
106. A. Javey, H. Kim, M. Brink et al: Nature Materials **1**, 241 (2002)
107. A. Javey, J. Guo, Q. Wang et al: Nature **424**, 654 (2003)
108. R. Martel, T. Schmidt, H.R. Shea et al: Appl. Phys. Lett. **73**, 2447 (1998)
109. J. Appenzeller, J. Knoch, V. Derycke et al: Phys. Rev. Lett. **89**, 126801 (2002)
110. S.J. Tans, A. Verschueren, C. Dekker: Nature (London) **393**, 49 (1998)
111. H.T. Soh et al: Appl. Phys. Lett. **75**, 627 (1999)
112. V. Derycke, R. Martel, J. Appenzeller, Ph. Avouris: Appl. Phys. Lett. **80**, 2773 (2002)
113. R. Martel, V. Derycke, C. Lavoie et al: Phys. Rev. Lett. **87**, 256805 (2001)
114. In 1D, the thermal emission over the barrier is reduced to a simple Arrhenius expression with temperature. This is in contrast with the typical expression of thermionic emission over 3D barriers discussed in [118]
115. S. Heinze, J. Tersoff, R. Martel et al: Phys. Rev. Lett. **89**, 106801 (2002)
116. J. Misewich, R. Martel, J. Tsang, Ph. Avouris: Science **300**, 783 (2003)
117. J. Appenzeller, J. Knoch, R. Martel et al: IEEE Transactions on nanotechnology **1**, 184 (2002)
118. S.M. Sze: *Physics of Semiconductor Devices* (Wiley, New York 1981)
119. D. Stauffer and A. Aharony: *Introduction to percolation theory*, 2nd edn (Taylor and Francis, London 1994)
120. J.P. Clerc et al: Annales de Physique **8**, 1 (1983)
121. I. Balberg, N. Binebaum, N. Wagner: Phys. Rev. Lett. **52**, 1465 (1984)
122. S. Kirkpatrick: Rev. Mod. Phys. **45**, 574 (1973)
123. C.A. Grimes et al: Chem. Phys. Lett. **319**, 460 (2000). E. Kymakis et al: Synth Met **127**, 59 (2002). B.E. Kilbride et al: J. Appl. Phys. **92**, 4024 (2002)
124. J.M. Benoit et al: Synth. Met. **121**, 1215 (2001). J.M. Benoit, B. Corraze and O. Chauvet: Phys. Rev. B **65**, 241405(R) (2002)
125. J.N. Coleman et al: Phys Rev B **58**, R7492 (1998). J. Sandler et al: Polymer **40**, 5967 (1999); C. Stephan et al: J. Mater. Res **17**, 396 (2002)
126. N.F. Mott and E.A. Davis: *Electronic processes in non crystalline materials* (Clarendon Press, Oxford, 1979)
127. Y. Yosida and I. Oguro: J. Appl. Phys. **86**, 999 (1999). M.S. Fuhrer et al: Synth. Met. **103**, 2529 (1999). R. Gaal et al: Phys. Rev. B **61**, 7320 (2000)
128. P. Sheng, B. Abeles, Y. Arie: Phys. Rev. Lett. **31**, 44 (1973)
129. B. Shklovskiĭ and A.L. Efros: *Electronic properties of doped semiconductors* (Springer Verlag, Berlin 1984)
130. P. Sheng, E.K. Sichel, J.L. Gittleman: Phys. Rev. Lett **40**, 1197 (1978)
131. A.B. Kaiser et al: Synth Met **103**, 2547 (1999). G.T. Kim et al: Synth Met **117**, 123 (2001)
132. D. Van der Putten et al: Phys. Rev. Lett. **69**, 494 (1992) and references therein
133. S. Marianer and B. Shklovskiĭ: Phys. Rev. B **46**, 13100 (1992) and references therein
134. V.L. Nguyen, B.Z. Spivak, B. Shklovskiĭ: Sov. Phys. JETP **62**, 1021 (1985). U. Sivan, O. Entin Wohlman, Y. Imry: Phys. Rev. Lett. **60**, 1566 (1988)
135. J-P. Issi and B. Nysten: *Electrical and thermal transport properties in carbon fibers in Carbon Fibers*, ed by J-B. Donnet, S. Rebouillat, T. K. Wang, J. C. M. Peng (Marcel Dekker Inc., New-York 1998)
136. P. Kim, L. Shi, A. Majumdar, P.L. McEuen: Phys. Rev. Lett. **87**, 215502 (2001)
137. J. Hone, M. Whitney, C. Piskotti, A. Zettl: Phys. Rev. B **59**, R2514 (1999)

138. P. Delhaes, J-P. Issi, S. Bonnamy, P. Launois: Chapter 1, *Polymorphism and Structures of Carbons*, this volume
139. B.T. Kelly: *Physics of Graphite* (Applied Science Publishers, London 1981)
140. M.S. Dresselhaus, G. Dresselhaus, K. Sugihara et al: *Graphite Fibers and Filaments*, Springer Series in Materials Science 5 (Springer-Verlag, Berlin 1988)
141. J. Hone, B. Batlogg, Z. Benes et al: Science **289**, 1730 (2000)
142. J.C. Lasjaunias, K. Biljakovic, Z. Benes et al: Phys. Rev. B **65**, 113409 (2002)
143. S. Berber, Y-K. Kwon, D. Tomànek: Phys. Rev. Lett. **84**, 4613 (2000)
144. J. Hone, I. Ellwood, M. Muno et al: Phys. Rev. Lett. **80**, 1042 (1998)
145. J-P. Issi, Transport properies of metal chloride acceptor graphite intercalation compounds, *Graphite Intercalation Compounds II*, vol. 18, ed by H. Zabel and S.A. Solin (Springer Series in Materials Science, Springer Verlag, Berlin 1992)
146. D.G. Cantrell and P.N. Butcher: J. Phys. C **20**, 1985 (1987)
147. D.G. Cantrell and P.N. Butcher: J. Phys. C **20**, 1993 (1987)
148. L. Piraux, M. Kinany-Alaoui, J-P. Issi et al: Phys. Rev. B **38**, 4329 (1988)
149. J. Vavro, M.C. Llaguno, J.E. Fischer: Phys. Rev. Lett. **91**, 065503 (2003)
150. J-P. Issi: In *World of Carbon*, ed by P. Delhaes (Gordon and Breach, London 2001)
151. L. Piraux, J-P. Issi, P. Coopmans: Measurement **5**, 2 (1987)
152. L. Piraux, B. Nysten, A. Haquenne et al: Solid State Commun. **50**, 69 (1984)
153. J-P. Issi and J-C. Charlier: in *Science and technology of carbon nanotubes*, ed by K. Tanaka (Elsevier, London 1998)

7

Mechanical Properties of Individual Nanotubes and Composites

J.-P. Salvetat, G. Désarmot, C. Gauthier and P. Poulin

Abstract. After introducing some basic notions on mechanical properties of solids, focusing particularly on polymers, properties of a single nanotube will be treated, before those of nanotube-containing composites. This chapter aims to show why nanotube-based composites are promising materials, how their properties could be improved, and what the main problems are currently encountered by the community. The use of nanotubes in composites, first delayed by the lack of cheap products available in large quantities, is now expanding and we can reasonably believe that new important applications will soon appear. In particular, significant progress have been made in making macroscopic fibers of aligned nanotubes.

7.1 Mechanical Properties of Materials, Basic Notions

From a very general point of view, mechanical behavior is the response of a solid to mechanical strain. The atoms of a solid under load are displaced from their equilibrium position, which induces restoring forces that are opposed to the deformation and tend to restore the initial shape as the load is removed. In the elastic regime, usually for small deformations, the behavior remains wholly reversible. Increasing load leads to formation and propagation of defects that allows mechanical stress to be relaxed. We introduce in this section basic notions on mechanical properties of materials, with a special care to polymers since they are used in most nanotube-based composites. Additional information can be found in a number of reference books that have been published on testing and mechanical properties of materials [1–3].

7.1.1 Elasticity of Solids

The classical (macroscopic) analysis of elasticity is based on Hooke's law, stating that stress is proportional to strain. The elastic modulus is defined as the ratio of stress to strain, and the inverse quantity is known as the compliance. Simple deformation experiments are performed in order to determine the corresponding moduli: Young's modulus E is measured from a tensile test, the

J.-P. Salvetat et al.: *Mechanical Properties of Individual Nanotubes and Composites*, Lect. Notes Phys. **677**, 439–493 (2006)
www.springerlink.com
© Springer-Verlag Berlin Heidelberg 2006

shear modulus G from a shear test, and the bulk modulus K from hydrostatic compression.

Uniaxial Tensile Measurement

The length of a parallelepipedic sample submitted to a uniaxial tensile load (Fig. 7.1a) increases proportionally to its initial value L_0. The ratio between the length increase and the initial length defines the strain in the longitudinal direction:

$$\epsilon_x = \frac{\delta L}{L_0} \tag{7.1}$$

This length increase occurs in response to a given mechanical stress σ_x, defined as the applied force or load (F) divided by the cross-sectional area of the original undeformed sample S_0:

$$\sigma_x = \frac{F}{S_0} \tag{7.2}$$

Hooke's law is then written

$$\sigma_x = E\epsilon_x \tag{7.3}$$

where E is the modulus of elasticity or Young's modulus, which characterizes the solid resistance to uniaxial stretching. At the same time, the stretching in the longitudinal direction leads to a lateral contraction: $\epsilon_y = \delta y/y_0$ and $\epsilon_z = \delta z/z_0$. For a material with uniaxial symmetry, $\epsilon_y = \epsilon_z$. The lateral contraction is generally quantified through the Poisson's ratio ν, defined for very small elongation as the ratio of transversal to longitudinal strain:

$$\nu = -\epsilon_y/\epsilon_x = -\epsilon_z/\epsilon_x \tag{7.4}$$

This coefficient can be used to quantify the volume variation due to longitudinal stretching $\delta V/V_0 \approx \epsilon_x(1-2\nu)$. When Poisson's ratio is 0.5 (its maximum value), the volume of the specimen remains constant under stretching. This condition of constant volume holds for liquids and ideal rubbers.

Simple Shearing

In a simple shear test (Fig. 7.1b), the specimen is fixed by one of its sides (surface S_0) while the opposite side is loaded transversally with a shear stress $\sigma_s = F/S_0$. Shear strain is calculated by the shear angle $\gamma = \delta y/z_0$ where δy is the shear displacement and z_0 the distance between shearing surfaces. The shear modulus G can be defined by $\sigma_s{=}G\tan\gamma \approx G\gamma$. Volume is conserved in the case of simple shearing.

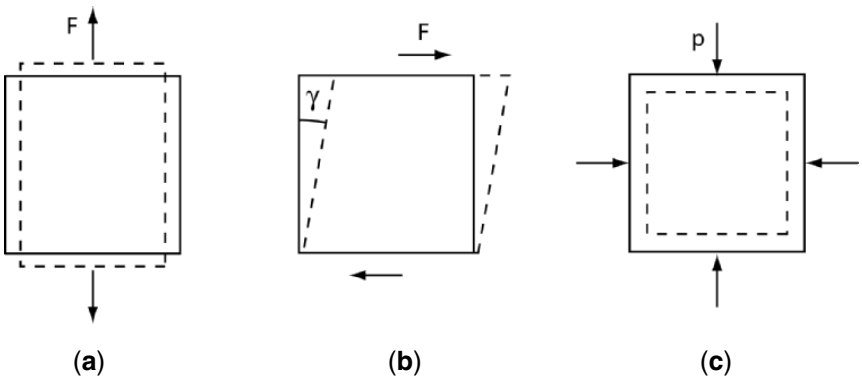


Fig. 7.1. (**a**) tensile test, (**b**) shear test, (**c**) hydrostatic compression

Hydrostatic Compression

The third type of simple deformation is hydrostatic (or uniform) compression. The bulk modulus K links the applied hydrostatic pressure (p) to the volume variation by $p = -K(\delta V/V_0)$. Hydrostatic compression is generally (but not necessarily) a shape preserving test but is not easy to realize from a practical point of view. In case of a homogeneous isotropic solid, the three moduli and Poisson's ratio are linked by:

$$E = \frac{9KG}{G + 3K} = 3K(1 - 2\nu) = 2G(1 + \nu) \tag{7.5}$$

Thus, elasticity of isotropic solids is characterized by only two constants. For anisotropic solids, 21 independent constants are necessary to characterize elastic behavior. The generalized Hooke's law can be written as [4]:

$$\sigma_{ij} = C_{ijkl} \cdot \epsilon_{kl} \tag{7.6}$$

with σ_{ij} the stress tensor, ϵ_{kl} the strain tensor, and C_{ijkl} the elasticity tensor which is symmetric and composed of 21 elastic moduli (or elastic constants). Young's modulus E, shear modulus G, and bulk modulus K may be expressed as functions of the elastic constants.

Microscopic Origin of Elasticity

The mechanical engineering approach is mostly based on the previous formalism, which is robust, normalized and well-documented. It does not, however, take into account microscopic details that govern the mechanical response of a solid and determine the elastic constants. Elastic behavior reflects the way atoms of a solid are bound together, and so depends on the interatomic potentials. Young's modulus is linked to microscopic parameters by modeling

the interatomic interaction with an harmonic potential, hence introducing the force constant, or stiffness, associated with a chemical bond

$$S = \left(\frac{\mathrm{d}^2U}{\mathrm{d}x^2}\right)_{x=x_0}$$

U being the interatomic potential and x_0 the equilibrium interatomic distance. The restoring force between two atoms is then $F = S(x - x_0)$, and the strain is $\sigma_x = NS(x - x_0)$, $N \approx 1/x_0^2$ being the bond density per unit aera. It follows that $\sigma_x = (S/x_0)\epsilon_x$ and so $E = S/x_0$. The interatomic distance is very near 0.25 nm in most solids, so that E depends essentially on the bond stiffness. S = 20–200 N/m for covalent solids, 15–100 N/m for metals and ionic solids, and 0.5–1 N/m for polymers, so that E is higher than 1 GPa for non porous crystalline solids at low temperature, reaching 1 TPa in diamond and graphite.

The elasticity may also depend on entropic configuration at non-zero temperature, especially when $T > T_\mathrm{g}$, the glass transition temperature. In perfect crystalline solids, the entropy contribution is negligible at low temperature (Nernst principle) so that elasticity is determined by the variation of the enthalpy. In that case, the restoring force results from a very small displacement of the atoms. The cohesion energy of these solids is high, which leads to high values of modulus. In soft non-crystalline solids, like rubber, the variation of the configurational entropy under stress can be important. This occurs when long and soft molecules can adopt different equilibrium configurations at temperature higher than T_g. Molecules of such materials tend to align in the stress direction. Rubber, for instance, is constituted by long polymer chains linked to each other by crosslinking nodes. The network elasticity is entropic by nature and deduced from a statistical description of its possible conformations. The simplest theoretical description, valid only for small strain, leads to $E = 3nk_\mathrm{B}T$, where n is the number of chemical crosslinks [5]. This means that for entropic elasticity the modulus increases with temperature. In that case, restoring forces are small but displacements involve segments of polymer chains. The Young's modulus is very low (a few MPa) but the limit of application of Hooke's law is much higher (ϵ = 10 to 50%). Incorporating fillers and fibers in such matrices may result in a strong modification of the entropic term in the mechanical response.

Perfect elastic behavior implies that strain is a single-valued function of stress alone and is totally recovered when the stress is released. This is only valid, for most of the materials, for small strains. At higher strains, the mechanical response deviates from the elastic behavior by exhibiting either time-dependent (viscoelastic) or permanent (plastic) deformation.

7.1.2 Viscoelasticity

Viscoelasticity implies a behavior between that of a purely elastic solid (in which the deformation is proportional to the applied force) and a viscous

liquid (which is elastic only in a uniform compression ($E = G = 0$)). For viscous liquids, the deformation rate is proportional to the applied force, which introduces a time dependent response [6, 7]. Viscoelastic behavior can be investigated by static tests such as creep or stress relaxation tests.

Stress Relaxation Test

In stress relaxation tests, the specimen is quickly loaded at a given amount, and the stress required to hold the strain constant is measured as a function of time. Stress relaxation tests are illustrated for an elastic solid, a viscous liquid and a viscoelastic solid in Fig. 7.2. In the latter case, a modulus that decreases over time is obtained.

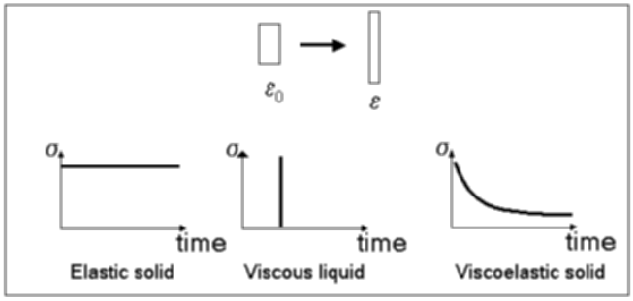


Fig. 7.2. Stress relaxation test for a elastic solid, a viscous liquid and a viscoelastic solid

Creep Test

In creep tests, the deformation brought about by a constant load is measured over a period of time. The strain $\epsilon(t)$ increases as a function of time and the compliance, $J(t) = \epsilon(t)/\sigma$ sometimes called creep function, can be calculated. For linear viscoelastic solids, the creep function is independent of the stress level. If the load is removed after some time, the specimen tends to return to its initial length or shape. An immediate recovery, related to the elastic part of the deformation, is followed by a progressive *anelastic* response (delayed elasticity). The recovery can be total (viscoelastic behavior), partial (viscoelastoplastic behavior) or zero (elastoplastic behavior). Thus, three different components can be identified in the mechanical response of a viscoelastic solid (Fig. 7.3): an elastic component (ϵ_{el}), which is instantaneously recovered, an anelastic (or viscoelastic) component, which can give rise to a time-dependent recovery (ϵ_{an}), and a viscoplastic component (ϵ_{vp}), non-recoverable.

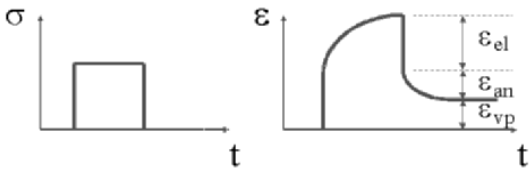


Fig. 7.3. Creep test for a viscoelastoplastic solid

Dynamic Test

Viscoelastic behavior can be also investigated by dynamic tests that measure the response of the material to a sinusoidal stimulus. Since stress and strain are generally not in phase, two quantities can be determined: a modulus and a phase angle or damping parameter. Using the complex notation, the periodic stress can be written $\sigma^* = \sigma_0 \exp(i\omega t)$ leading, if the mechanical behavior is linear, to the response $\epsilon^* = \epsilon_0 \exp(i\omega t - \phi)$. A complex modulus can be introduced $M^* = \sigma^*/\epsilon^* = M' + iM'$, where M' is the storage modulus and M' the loss modulus. The damping parameter, or loss factor, is given by $\tan\phi = M'/M'$. Static (creep, stress relaxation) and dynamic tests provide equivalent information since the complex compliance is the Fourier transform of the time-dependent compliance.

Generally, for crystalline materials (metals, crystalline ceramics) the viscoelastic strain is negligible compared to the viscoplastic strain [8,9]. Actually, viscoelastic effects can be observed in crystalline solids stressed at a temperature near their melting point (T_m) but they are generally neglected at ambient temperature ($T/T_\mathrm{m} < 0.5$–0.7). For non-crystalline materials, the viscoelastic contribution is a major part of the response. Non-crystalline solids are characterized from a structural point of view by the lack of order at long distance in the atomic arrangement, and from a thermodynamic point of view by a nonequilibrium state. To characterize their behavior, use is made of the glass transition temperature that corresponds to the transition from liquid (super cooled state) to glass (frozen state) (Fig. 7.4). Amorphous materials exhibit several relaxation processes, each being associated with a more or less pronounced decrease of M' for increasing temperature or decreasing frequency. This leads to a strong dependence of the mechanical behavior versus temperature and time.

Figure 7.5 displays the typical viscoelastic behavior of several polymers studied in dynamic torsion as a function of temperature, at constant frequency [10–12]. Let us first consider the case of an amorphous thermoplastic polymer (TP). At low temperature, the material is in the glassy state, so out of equilibrium, and can display secondary relaxations such as the β relaxation, generally associated with local molecular motions of a few segments of the main chain. In this temperature range, the stiffness is mainly due to the intermolecular Van der Waals bonds. The resulting shear modulus G'' is close to 1 GPa. The imaginary part of the modulus G'' is low (1 MPa).

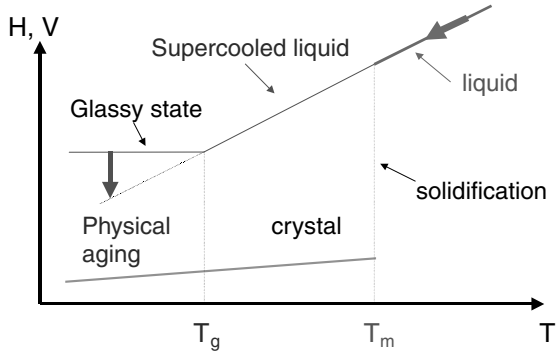


Fig. 7.4. Variation of volume and enthalpy when cooling from the liquid. Glassy state forms below T_g

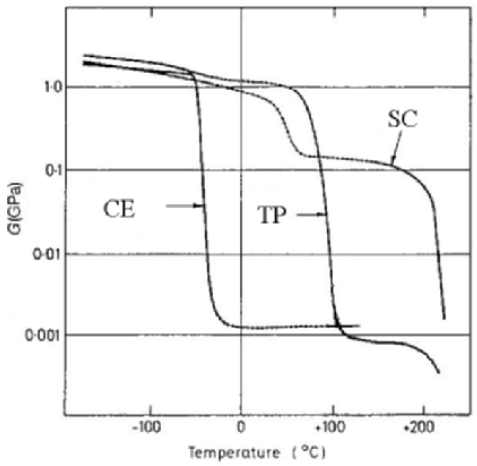


Fig. 7.5. Typical G versus temperature curves for an amorphous thermoplastic polymer (TP), a cross-linked elastomer (CE) and a semi-crystalline polymer (SC)

The behavior is mainly elastic. At higher temperature, for $T \approx T_\alpha \approx T_g$, a strong decay of G' is observed during the so-called main or α relaxation. At the same time, G'' and the loss factor $\tan\phi$ display a maximum. Alpha relaxation is the dominant and slowest process involved in the glass transition. The time and temperature dependence of the α relaxation corresponds to a non-Arrhenius behavior. It can be analyzed as the result of hierarchically correlated motions of segments of polymer chains. The most noteworthy feature is the wide distribution (over more than 10 orders of magnitude) of characteristic times (see review [13] for details). Above T_α, the thermal agitation makes the Van der Waals bonds negligible. The entropic forces become predominant. If the polymer chains are short, the material flows. However, if the length of

macromolecules is larger than a critical length (above which chain entanglements can occur), a *rubbery plateau* is observed. The modulus at the rubbery plateau is proportional to the entanglement density. Its length depends on the molecular weight, which controls the time necessary for disentanglement [14]. For chemically cross-linked polymers (elastomers for example), the behavior in the glassy state is close to that observed for linear polymers (Fig. 7.5). The only significant difference lies in the rubbery plateau where no flow can occur. The main differences between elastomers and thermosets (epoxy, unsaturated polyesters...) are (*i*) the temperature of the main relaxation, which is well below room temperature for elastomers and above for thermosets, (*ii*) the modulus in the rubbery plateau, generally higher for thermosets than for elastomers, in agreement with their respective crosslink densities.

The typical viscoelastic behavior of a semi-crystalline polymer is also presented in Fig. 7.5. The semi-crystalline polymer structure consists of sequences of crystalline and amorphous lamellae. In most cases, the lamella thickness varies between 2 and 30 nm depending on the crystallization conditions (the other dimensions are of the order of a few microns). These lamellae are often organized in larger structures evidenced by the observation of spherulites. Their size depends on the crystallization conditions (cooling kinetic) but is often in the range 1–10 μm. On average the elastic modulus of the crystallites is only slightly higher than the modulus of the amorphous part below T_α. Consequently, in this temperature range, the elastic modulus of a semi-crystalline polymer is close to that of an amorphous polymer. Two successive decreases of the modulus are observed with increasing temperature, the first being associated to the main relaxation of the amorphous phase (T_α), the second to the melting of the crystallites (T_m). Between T_α and T_m, the modulus of a semi-crystalline polymer is strongly dependent on the amount, dimension, and texture of the crystalline phases.

7.1.3 Non-Linear Behavior and Rupture

Like human beings, solids do not like to be under stress. When strain exceeds 0.1% most materials exhibit non-linear and irreversible behavior. Non-linear elasticity (reversible) is often observed for molecular solids above T_g and is related to entropy effect. The linear to non-linear transition in the mechanical response of a polymer is clearly evidenced by creep measurements performed at increasing levels of stress as illustrated on Fig. 7.6 in the case of an epoxy resin. The plot of the compliance at a given time versus applied stress is also reported on the same figure: horizontal part of the curve corresponds to the linear domain [15]. In the non-linear regime, the superposition principle of Boltzmann, which states that the effect of applying several stresses is equal to the sum of the effects of separately applied stresses, is no longer valid.

The most commonly used test to investigate non-linear mechanical behavior is the stress-strain test, which measures the force applied to a specimen being loaded at a constant rate. Among the solids with an enthalpic elasticity,

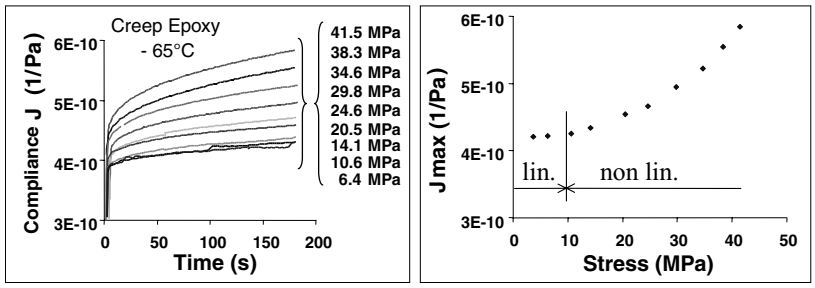


Fig. 7.6. Linear to non-linear transition from creep experiments for an epoxy resin

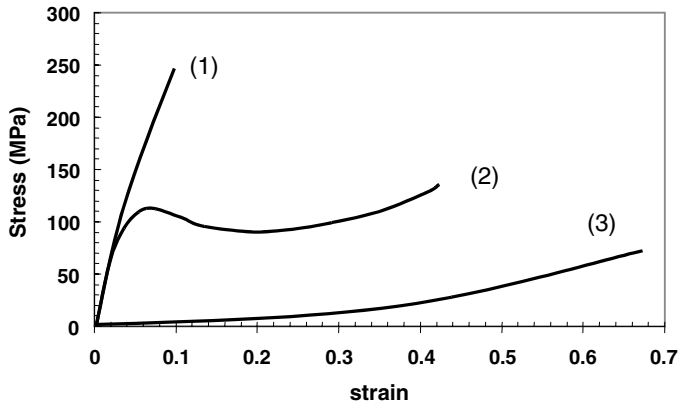


Fig. 7.7. Typical stress-strain behaviors of a polymer as measured at a constant strain rate and increasing temperature from (1) to (3)

one can distinguish brittle solids (like ceramics), which break before plastic deformation, and ductile solids, which can deform plastically before breaking (like metals). In the case of polymers, a great variation in stress-strain behaviors can be observed [1,10,11]. The typical behaviors that can be measured at a constant strain rate and increasing temperature are illustrated in Fig. 7.7.

The top curve (1) is typical of hard brittle polymers, at low temperature and high deformation rate. Generally speaking, brittle material response is ruled by the presence of microcracks at the surface. A crack will propagate in a catastrophic mode when the increase of its length decreases the total energy of the system. Two important factors are the applied stress and the dimension of the microcrack, that are combined in one parameter, the factor of stress intensity. Fracture occurs when this factor reaches a critical value. The resistance of brittle materials to crack propagation is often characterized by the fracture toughness, reported as the critical energy release rate G_c or the stress concentration factor K_c. In the case of polymers, toughness is sensitive to rate and temperature. G_c ranges from $5000\,\mathrm{J/m^2}$ for a tough nylon or PC down to $50\,\mathrm{J/m^2}$ for some brittle thermosets.

The second curve (2) is typical of hard ductile polymers, when the mechanical test is performed in the temperature range above T_β and below T_α, and within the classical strain rate range (10^{-1}–$10^{-4}\mathrm{s}^{-1}$). The curve first consists of a nearly straight section corresponding to the viscoelastic response of the polymer. The initial slope is close to the Young's modulus but already corresponds to a partly relaxed response. Then, a yield point is observed: the stress reaches a maximum often called yield stress (σ_y) and then decreases towards a minimum value called plastic flow stress (σ_p). A steady state regime is observed where the stress is minimum and almost independent of strain. Strain hardening appears at increasing strain due to the chain orientation and stretching in the strain direction, and increases gradually up to the break point. During this test, polymers store a great amount of elastic and anelastic energy that can be restored when the stress is removed. The anelastic deformation induces a small change in the intermolecular bonds, leading to both a slight increase of density and a very strong increase of the molecular mobility [16]. In contrast, the microstructural modifications induced by the plastic component of the strain do not change deeply the density and the molecular mobility. The physical modeling of such a behavior has been studied for wholly amorphous polymers by several authors [17–25]. In the case of chemically cross-linked polymers tested below T_α, the only significant difference lies in the hardening observed for stresses higher than σ_p. For instance, the chain length between cross-links in thermosets is much smaller than the distance between entanglements in linear or branched polymers. Therefore, hardening occurs more rapidly and more strongly. In the case of semi-crystalline polymers used below the main relaxation temperature (T_α), it is observed that (σ_y) and (σ_p) increase, and that hardening occurs for lower deformation as the crystallinity increases, because crystallites act as crosslinks. Large deformations lead to the destruction of crystallites and their transformation into a fibrilar structure [26]. Despite the numerous studies reported in the literature [26–28], the mechanisms involved in plastic deformation of semi-crystalline polymers between T_α and T_m are still under discussion.

The third curve (3) is typical of unfilled elastomers tested at room temperature (i.e. above T_α). In the deformation range below 0.5, a quasi-linear behavior is observed. In this range, the deformation remains well below the maximum extensibility of the chains (large deformation is possible because the chain length between nodes is large). At higher level of strain, the behavior becomes non-linear and strain-hardening is observed (prior to break) [5]. It appears that crosslinking allows an increase in the elastic modulus but induces a decrease of the strain at break. This can be largely improved by filler incorporation.

7.2 Mechanical Properties of a Single Nanotube

In treating the problem of single-nanotube mechanics, the question rapidly arises whether macroscopic equations used for describing mechanics of beams can be applied to a giant elongated molecule. Both theory and experiments have an answer to this question, as will be shown in this section. The important quantity to be determined in mechanical engineering is the Young's modulus, E, which is constant for a given material. The unusual fact with nanotubes is that E is expected to vary slightly with the diameter, since curvature modifies C–C bond hybridization hence stiffness. Some difficulties and confusion arise due to the practical interest in treating a nanotube like a continuous medium, which implies determining the shell thickness. We try here to reconcile various experimental and theoretical results that could look contradictory. An important result is that continuous shell approximation is a good approximation and that Young's modulus and thickness of a single-walled nanotube are not very different from that of a single graphene sheet. This values are found when both axial stiffness and bending rigidity are considered. Young's modulus of multiwalled nanotubes are instead very similar to bulk graphite or carbon fibers. Specific nanotube behavior appears in fact at high strain. In particular, fracture modes, which can be either brittle or plastic, are found to depend on helicity.

7.2.1 Theory and Simulations

Elasticity of Carbon Nanotubes

Since 1991 were performed a number of calculations on nanotube elasticity and some confusion may arise from the different results reported by various authors. Yackobson and some others reported $E \approx 5\,\mathrm{TPa}$ and a thickness t of $\approx 0.07\,\mathrm{nm}$ [29–31], while many authors reported $E \approx 1\,\mathrm{TPa}$ with $t = 0.34\,\mathrm{nm}$ [32–35]. Unlike that of a macroscopic tube, the 'thickness' of a graphene wall seems to be a rather arbitrary notion because it has a meaning only in the framework of a continuum model. It is however an important quantity since it determines the moment of inertia of the nanotube, speaking in terms of continuous elasticity, and so the flexural behavior. The first fundamental question is thus whether classical elasticity is applicable or not to nanostructures. A number of papers have addressed this problem using different approaches [36–40]. Harik [37] discussed specifically the applicability of Euler beam model to carbon nanotubes, an important point since most experiments are interpreted using this concept. We recall that deformation of a homogeneous elastic beam is described by the Bernouilli-Euler equation [41]

$$\frac{\mathrm{d}^2 z}{\mathrm{d}x^2} = -\frac{M(x)}{EI} \tag{7.7}$$

with $M(x)$ the bending moment at x and I the areal moment of inertia, which depends on the beam shape. For a tube

$$I = (\pi/64)((D_\mathrm{o})^4 - (D_\mathrm{i})^4)$$

with D_o and D_i the outer and inner diameters.

Equation (7.7) can be used to calculate the deflection of a *long* beam of length L clamped at one end and submitted to the force F at the other end

$$\delta = \frac{FL^3}{3EI} \tag{7.8}$$

The higher I, the lower δ. Thus it appears, whereas elongation (or contraction) of a beam depends only on its cross-section area (A), that the flexural behavior is strongly influenced by the cross-section shape, as is well-known to mechanical engineers. Axial and lateral deformations can all be described using only the Young's modulus, provided the beam aspect ratio (width/length) is larger than 10. For short beams, shearing adds another component to the deflection

$$\delta_\mathrm{s} = \frac{f_\mathrm{s} FL}{GA}$$

where G is the shear modulus, and f_s the shear coefficient which varies with the beam shape [42].

Concerning a single-walled nanotube, the main question is whether it can be described as a homogeneous tube made from an *isotropic* shell of finite thickness t (to be determined), whose deformations can be calculated using classical equations and two independent elastic parameters (e.g. E and ν), without requiring atomistic calculations at least in the linear regime. Answering this question is not straightforward but a positive consensus is found to emerge after a careful examination of various calculations and experiments performed all over the world. Thus, as a first order approximation, we treat the nanotube as a *homogeneous isotropic continuous shell* of thickness t, so that all its elastic deformations can be calculated knowing the Young's modulus, E, and the Poisson ratio, ν [41]. The important point to remember here is that E and t are *uniquely* determined by two non-equivalent equations describing axial and bending deformations. Neglecting curvature, i.e., supposing the tube to be equivalent to a sheet of width $2\pi R$, E and t can be deduced from the bending rigidity (D) and in-plane stiffness (C) of a graphene plate [41]

$$D = \frac{Et^3}{12(1-\nu^2)} \tag{7.9}$$

$$C = Et \tag{7.10}$$

D, C and ν are intrinsic parameters of graphene essentially determined by C–C bond rigidity, that can be calculated without any assumption on t.

The bending rigidity of a graphene sheet D has been approximated using classical elasticity and the out-of-plane vibration frequency of graphite as measured by neutron scattering [43]. It has also been estimated via calculation of the strain energy using a force-field framework i.e. a molecular mechanics

approach [36], molecular dynamics, and first principle calculations [34,44]. The important point is that bending rigidity of a graphene sheet is determined by inversion configuration of the C–C bonds [36]. Without this term, the bending rigidity of the graphene sheet would be zero. D is found to vary between 0.85 eV and 1.5 eV depending on the method used. In-plane (or axial) stiffness is usually derived from the second derivative of the strain energy with respect to the axial strain, $\mathrm{d}^2E_\mathrm{s}/\mathrm{d}\epsilon^2$ [34, 44–46]. It depends on bond stretching and angle variation force constants in a molecular force field framework. C is found to be close to 60 eV/atom and seems less dependent on the calculation method than D. The Poisson's ratio ν has been also calculated in a number of papers [31, 34, 45, 46], with a significant dispersion of values, between 0.16 and 0.34. Note that the effect of ν on E and t is small.

Combining (7.9) and (7.10), one finds $E \approx 5$ TPa and $t \approx$0.07 nm. There is thus no doubt that the effective thickness of a single shell nanotube, *in an isotropic continuous shell approximation*, is less than 0.1 nm, similar to that of a single graphene layer. Many authors use, however, $t = 0.34$ nm and $E = 1$ TPa, since it compares directly with bulk graphite values. Although it is equivalent to the couple (5 TPa, 0.07 nm) for describing axial stiffness, it should not be correct in bending. What error does this lead to when considering flexural behavior? In fact, a nanotube has an effective flexural rigidity, EI, with I the moment of inertia, much higher than that of a graphene sheet. More precisely, we can write

$$EI = E\frac{\pi D_o^4}{64}\left(1 - \left(\frac{D_i}{D_o}\right)^4\right) = E\frac{\pi D_o^4}{64}\left(1 - \left(1 - \left(\frac{2t}{D_o}\right)\right)^4\right)$$

and if $2t \ll D_o$, $(1 - (2t/D_o))^4 \approx 1 - 4(2t/D_o)$, so that

$$EI = \frac{\pi}{8}D_o^3 Et = \frac{\pi}{8}D_o^3 C \tag{7.11}$$

which means that the bending rigidity of large diameter SWNTs is governed by the in-plane stiffness of graphene. Thus a SWNT can be approximated by a shell of thickness $t = t_\mathrm{G} = 0.34$ nm with $E = E_\mathrm{G} = 1$ TPa. This remains an approximation that should be used with care. For example, with a (10,10) SWNT, an error of 30% is made on EI using (1 TPa, 0.34 nm) instead of (5 TPa, 0.07 nm).

It has to be well understood here that this continuum approach remains approximative, since defining a thickness for one-atom-thick layers does not have a rigorous physical meaning, even when using the notion of an electronic density cloud. It should not, however, be concluded that a continuum elastic model cannot be applied rigorously. Arroyo and Belytschko [38] proposed recently a method to describe one-atom-thick layer deformations extending hyper-elastic models used for bulk materials. They also show the limitations of continuum models, especially in the non-linear elastic regime.

Multishell Nanotube Elasticity

We first consider a two-layer graphene slab as an *anisotropic* shell of thickness $t_{\mathrm{D}} = t + d_{\mathrm{i}}$, d_{i} being the interlayer distance (about 0.34 nm). Supposing that no sliding can occur between the two layers thanks to Van der Waal forces, the neutral plane is located between the layers and the bending stiffness is determined now by the in-plane stiffness of C–C bonds [47], unlike the bending stiffness of a single graphene sheet that depends essentially on the out-of-plane stiffness. The two-layer slab (or tube) is well-described by a shell of Young's modulus ≈1 TPa and thickness about 0.34 nm.

More precisely, it was found that the Young's modulus shows a discontinuous behavior as a function of the number of shells N [31]:

$$E_N = \frac{N}{N - 1 + (t/d_{\mathrm{i}})} \frac{t}{d_{\mathrm{i}}} E$$

with $E = 4.7\,\mathrm{TPa}$, $t = 0.074\,\mathrm{nm}$.

Crystal of SWNTs

Bulk SWNT materials are usually made of ropes and bundles, not individual nanotubes. While covalent C–C bonds ensure strong intratube stiffness, transverse properties are governed by van der Waals forces very similar to those at work in graphite interplane cohesion. The SWNT crystal is thus highly anisotropic, with low torsion and shear moduli. Elastic constants can be approximated with classical elasticity theory using those of graphite, in good agreement with more rigorous calculations [48, 49, 146]. Supposing in-plane stiffness is the same for graphite and for SWNT, it is straightforward that $E_{bundle}/E_{graphite} = \pi D d_{\mathrm{i}}/S$, where D is the SWNT diameter, d_{i} the interplane spacing in graphite and S the area of the unit cell in bundles, i.e. $S = (D + d_{\mathrm{i}})^2 \cos(\pi/6)$. So we get a Young's modulus close to 650 GPa for a 1.4 nm diameter SWNT bundle. We can estimate as well a shear modulus of 20 GPa.

It is thus found that the various forms of carbon nanotubular structures exhibit different Young's modulus according to their structure. This should be taken into account when determining the elastic properties of any nanotube-based nanocomposite.

Dependence on Diameter and Helicity

The hexagonal symmetry of a graphene sheet ensures a perfect isotropy of its in-plane elastic behavior. As the sheet is rolled seamlessly into a tube, the bending strain induces a slight out-of-plane distortion of the C–C bonds, resulting in a hybridization of the σ bonds, which increases as the diameter decreases. The hexagonal symmetry is thus broken so that its elastic behavior may vary slightly with the shell helicity. The dependence of the elastic strain energy to the diameter and helicity is an important issue especially for growth

models. Suppose that the energy difference between armchair and zigzag nanotube is much higher than $k_{\mathrm{B}}T$, one may hope to find out a synthesis method producing only one helicity.

It seems clear that calculating the diameter and helicity dependence of the Young's modulus goes beyond the isotropic elastic shell approximation. Only with models taking explicitly into account the bound deformation due to curvature one may expect to find anisotropic effects in elastic properties. Different approaches are reported in the literature, which often bring different results (sometimes contradictory), and discerning the origin of these differences is often a case for the specialists.

The simplest approach to this problem is to consider that curving a C–C bond results in decreasing its stiffness (rotating a bond is much easier than stretching it). This implies a lowering of the nanotube axial stiffness as the diameter decreases. An armchair nanotube is thus expected to have a lower stiffness than a zigzag tube since all its C–C bonds are curved. Our assumption implicitly assumes that the in plane isotropy is lost in the cylindrical geometry.

Do these basic (simplistic) arguments find a serious justification with sophisticated models? First-principles calculation [34] shows that bonds are inequivalent in length depending on their orientation to the tube axis, and that the bond length increases with decreasing tube radius, the greatest increase being for perpendicular bonds. This is a rigorous statement of our qualitative approach since bond stiffness and bond length are correlated. Indeed most calculations agree that Young's modulus slightly decreases with tube diameter [35, 45, 46, 50] (see Fig. 7.8).

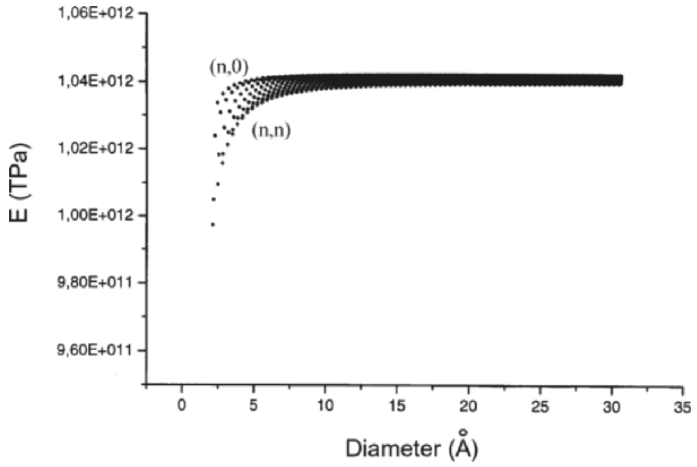


Fig. 7.8. Young's modulus as a function of the diameter for zigzag and armchair SWNTs. Tersoff-Brenner potential, fully-optimized cell, $t = 0.34\,\mathrm{nm}$. By courtesy of Philippe Lambin (unpublished results)

Strain energy has been determined as a function of helicity by Zhang et al. [51]. They found that zigzag nanotubes have the lowest energy, in agreement with the previous arguments (less bonds have to be curved to form a zigzag nanotube from a graphene ribbon). The energy difference is however too small for producing selectively zigzag nanotubes, at least with current synthesis methods, which involve high temperature processes.

All the results reported so far agree that corrections due to curvature and helicity are small in the elastic regime, of the order of few % so that it can be neglected in most cases.

Non-Linear Elastic Regime

Carbon nanotubes are unique in their capability to sustain high strain without breaking, which allows non-linear regime to be studied both theoretically [29, 52–54] and experimentally [55–57]. The interesting point is that at high strain the hexagonal lattice symmetry is broken with the result that differences appear as a function of chirality. For example, Poisson's ratio was found to depend on chirality at high strain [54].

Deformation and Rupture of Carbon Nanotubes

A good estimation of ideal strength of carbon nanotubes is given by the Orowan-Polanyi equation which states that ultimate limit to elasticity is reached when strain energy equal the energy needed to separate two crystallographic planes in 3d or lines in 2d:

$$\sigma_{th} = \sqrt{\frac{E\gamma}{a}} \tag{7.12}$$

where γ is the surface energy and a the interplane separation. Using typical values for graphite (7.12) leads to $\sigma_{th} \approx 300\,\mathrm{GPa}$ taking $E \approx 5\,\mathrm{TPa}$ or $\approx 150\,\mathrm{GPa}$ with $E \approx 1\,\mathrm{TPa}$, in agreement with more sophisticated calculations [58, 59].

This represents an upper limit to the experimental strength, which is usually lowered by the presence of defects. Strength of carbon nanotubes depends on their ability to prevent initiation and propagation of defects. Therefore studying deformation modes and rupture implies studying defects. Once defects are identified, the important quantities to be determined are their formation energy and activation barriers. Temperature playing an important role in mechanical relaxation, different fracture behavior may occur at low and high temperature. The main imperfections in solids are grain boundaries, cracks, and dislocations. While grain boundary has hardly an equivalent in a nanotube, cracks may be present in the form of non-bonding trapped states [60] and elongated vacancy clusters [58].

Dislocations and Stone-Wales Transformation

Although extended defects like dislocation lines or loops are obviously absent in nanotubes due to their 2d structure, it has been shown that a (5–7) pentagon-heptagon pair is equivalent to a dislocation core [61].

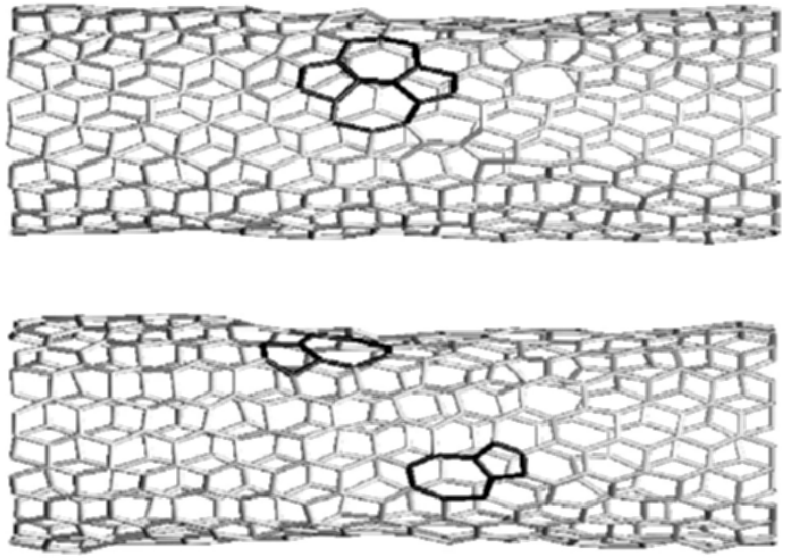


Fig. 7.9. Mechanical relaxation at high temperature (2000 K) by formation and propagation of Stone-Wales defects for a (10,10) carbon nanotube under 10% uniaxial strain. The defect (*highlighted in black*) splits and starts diffusing. From [63]

A possible mechanical relaxation path involves the formation of (5-7-7-5) defect pairs by a 90° bond rotation, known as the Stone-Wales (SW) transformation (Fig. 7.9). Subsequent SW rotations can produce brittle or plastic flow depending on the nanotube helicity and external conditions [63, 64]. The high energetic cost of a SW transformation requires high temperature, irradiation or long time under normal strain conditions (less than a few %). When strain increases, molecular dynamics simulations showed that S-W defect formation energy and activation barrier decrease [63, 65]. A catalytic effect of carbon adatoms (like those produced during irradiation) on SW transformation, lowering formation barrier, has been demonstrated by ab initio methods [65, 66].

Crack Nucleation and Propagation

Crack propagation is the most probable failure mechanism for brittle solids in tension. Strain being concentrated at the crack tip, the minimum strain to initiate propagation of a crack of length l and tip radius ρ_t is:

$$\sigma = \frac{1}{2}\left(\frac{\gamma E \rho_{\mathrm{t}}}{al}\right)^{1/2} \tag{7.13}$$

This is known as the Griffith criterion.

The low temperature mode of rupture in carbon nanotube is supposed a priori to be fragile due to the covalent C–C bonds that ensure high Peierls barriers. In particular in case of shock or rapid excitation at room temperature no plastic deformation is expected.

It has been shown recently that cracks may spontaneously form in a nanotube under tension via formation of bond-breaking bifurcation states [60]. This occurs when strain energy per bond approaches the cohesive energy so that a C–C bond starts to switch between a bonding and a non-bonding state. Once a nucleation state is formed, a crack can propagate and leads to rupture. Classically treated with the help of Griffith criteria, it has to be considered in nanotubes within an atomistic framework due to the discreteness of the crack length. When lattice discreteness is taken into account, a trapping lattice effect [67] appears that delays crack propagation because of potential barriers, in a similar way dislocation propagation is hampered by the Peierls barrier. In contrast to SW transformation, activation energy for trapped states is small (about 10 meV) so that the process more likely occurs at low temperature. Formation of these states, however, requires high strain (>10%).

Besides, a single vacancy, known as a stable defect of graphite, can be considered as the smallest pre-existing crack of a nanotube. It effectively reduces the nanotube strength [58].

Brittle or Ductile?

Plastic deformation via SW transformation, as an activated process, needs time or energy [68]. It is supposed to dominate at high temperature and long times. Brittle failure is expected at room temperature for practical strain rates [60], although plastic deformation of SWNTs has once been reported at room temperature [69]. It is indeed a peculiar characteristic of nanotubes to show plasticity, because of their capacity to sustain high strain, which reduces both formation energy and activation barrier of SW transformation. Admittedly, additional experiments are needed to address this problem, since numerical results depend on the choice of potentials and methods, thus provide clues but no definitive answers.

7.2.2 Experiments

Experimental methods and principles used to investigate mechanical properties of carbon nanotubes are not conceptually different from those applied to macroscopic materials. Technically, however, they differ from usual testing tools since they measure nanometer size displacement and nanonewton forces. At such a small scale experimental uncertainties are important drawbacks that will have to be overcome in the future.

Vibration Analysis

Ultrasonic tests and sonic resonances of a bar are routine methods for measuring elastic constants of solids. Longitudinal wave velocity in a bar is [41]:

$$v_{\mathrm{l}} = \sqrt{E/\rho} \tag{7.14}$$

where ρ is the material density. Pulsed ultrasonic methods allowed determination of the elastic constants of single-crystals of various metals by a direct measurement of wave propagation velocities at liquid helium temperature [70]. Such a technique is, unfortunately, not easily transposable to the nanometer scale.

The vibrational modes of a bar depend on the elastic constants of the material, and vibration frequencies and amplitudes can be calculated with classical elasticity [41, 42]. The general equations are known as Timoshenko's beam equations, which extend Bernouilli-Euler formula by incorporating shear and torsion effects. Shear deformation and rotatory inertia have a small effect on the first mode of vibration but must be incorporated in higher modes [71]. As a first order approximation, Bernouilli-Euler formula can be used to calculate the Young's modulus. For a nanotube clamped at one end:

$$E = \frac{16\pi L^2 f_n}{\beta_n^2} . \frac{\rho}{D_{\mathrm{i}}^2 + D_{\mathrm{o}}^2} \tag{7.15}$$

where f_n is frequency of vibration of transversal mode n and β_n is solution to $\cos\beta_n \cosh\beta_n = -1$, and so $\beta_1 = 1.88$, $\beta_2 = 4.69$, $\beta_3 = 7.85$, $\beta_4 = 11$, $\beta_n = (n - 1/2)\pi$ for $n \geq 5$.

Both thermal and stimulated transversal vibrations of a nanotube were measured using a TEM. When limited to small vibration amplitudes, analysis of results using continuous elasticity model gave a good approximation to the Young's modulus. The first work reported in the literature used a TEM equipped with a variable temperature sample holder to follow variation of amplitude versus temperature [72]. According to the law of equipartition, mean-square vibration amplitude equal $(k_{\mathrm{B}}T/c_n)$, c_n being the effective stiffness of mode n, given by

$$c_n = \frac{\pi\beta_n^4 E(D_{\mathrm{o}}^4 - D_{\mathrm{i}}^4)}{256L^3} \tag{7.16}$$

The total amplitude is obtained by summing over n. A complete treatment should take into account shear and inertia by solving Timoshenko's beam equations. The resulting correction affects mostly the higher modes, so it remains small and is usually neglected when the beam length and the vibration wavelength are much larger than the diameter, which is usually the case with carbon nanotubes.

Frank et al. [73] applied an oscillating voltage in a TEM and measured the resonant frequency of the first and second harmonic thus deducing the Young's

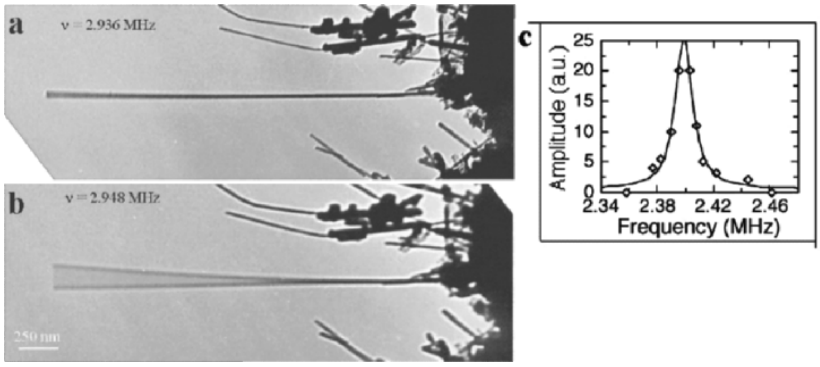


Fig. 7.10. A carbon nanotube at (**a**) off-resonance and (**b**) on-resonance. (**c**) The resonance peak. Reproduced from Wang et al. [73]

modulus in what seems to be the most accurate way so far (Fig. 7.10). Note that at high excitation amplitude, non-linear behavior (rippling effects) occurs that decreases the bending modulus as the diameter increases. Recently, it has been shown that vibration resonances can also be measured by field emission. The tension applied by an electric field was used to tune resonances by up to a factor of 10 [74].

Nanomechanics with an AFM

The atomic force microscope (AFM) in its initial conception was designed to image flat insulating surfaces with atomic resolution. Its use has now been extended far beyond this initial goal especially in the field of nanomechanics. Indeed, its special ability is to simultaneously measure a displacement (by the vertical piezoelectric tube) and a force (by the cantilever deflection). Its weakness comes from the intrinsic non-linearity and hysteresis of the scanner, and the cantilever which needs a proper individual calibration if one wants to perform quantitative measurements, such as determining Young's modulus. Cantilever stiffness is an important parameter that can be determined by various methods. Analysis of cantilever thermal vibrations seems so far the most accurate and reliable method, since the stiffness is measured directly [75, 76]. This method is similar to that used by [72] for measuring MWNT stiffness, except that vibration amplitude is measured optically, which ensures a much better accuracy.

Stiffness and strength, in bending and in tension, have been measured using an AFM [78–82] for MWNT and SWNT ropes, confirming the high Young's modulus and exceptional strength predicted by theory. Combining TEM and AFM, it has been shown that the bending modulus of SWNT bundles can be increased by cross linking SWNTs by means of electron irradiation [83].

7.3 Reinforcing Composite Materials with Nanotubes

7.3.1 Composite Materials and Nanocomposites

Composite materials may be defined as materials made up of two or more components and consisting of two or more phases [1, 84, 85]. Their particular properties rely on the load transfer efficiency between strained phases. Such materials are heterogeneous at least on a microscopic scale. Composites may be divided into two general classes: (1) filled materials consisting of a continuous matrix phase and a discontinuous filler phase made up of discrete particles, (2) fiber-filled composites. The role of the continuous matrix is to bind the filler, give the shape and ensure stress transfer whereas the fibers are mainly used for their mechanical performances. Most of the materials traditionally considered as composites have used fibers as the filler phase. These composites are normally strongly anisotropic (properties are different in different directions) and they have at least five or six independent elastic moduli. The so-called high-performance composites include boron, carbon, glass and aramid fibers in thermoset resins. The importance of fiber-filled composites arises largely from the fact that such materials can have unusually high strength and stiffness for a given weight of material. The specific strength (tensile strength/density) and specific modulus (modulus/density) can surpass the values of the best metals. Consequently, fiber-filled composites are extensively used in structural applications.

On the other hand, the use of particulate materials (fillers) for enhancement of polymer properties dates back to the earliest years of the polymer industry. Initially used as extending agents to reduce the cost of polymer-based products, fillers were soon recognized to be an integral component in many applications involving polymers, particularly in reinforcement. Depending on the shape factor and the filler orientation in the matrix, the composites can be either isotropic or anisotropic. Associated with high performance fillers such as nanotubes, their development might be interesting especially for multifunctional applications. The aim of this section is to recall the main aspects of filled polymers and nanocomposites to be able to clearly identify the specific interest of nanotubes as fillers in a composite material.

Mechanical Behavior of Filled Polymers. Case of Micron Sized Rigid Fillers

Generally, fillers are added when the polymer is in a viscous state (melted or in solvent). This incorporation leads to an increase of viscosity directly related to the amount of fillers ϕ as described by Einstein's law (for spherical particles) [86] $\eta/\eta_s = 1 + 2.5\phi + \ldots$ where η_s is the solvent viscosity. The resultant filled polymers display an increase of the elastic modulus compared to the unfilled matrix, as measured by the initial slope of the stress-strain

curve. The important factors in determining the modulus are the filler concentration, the particle shape, the moduli of the components, and the way particles pack (often called morphology). Particle size is reported to have little if any effect on the modulus of a composite except with very fine particles [1]. Fillers also introduce a broadening in the α relaxation peak accompanied by a slight shift to higher temperature. This broadening is often interpreted as a change in the relaxation mechanism but this is still under discussion. Fillers usually decrease the damping but the opposite is often observed due to additional damping mechanisms including particle-particle friction in agglomerates, particle-polymer friction in case of poor adhesion at the interface, and excess damping in the polymer near the interface because of induced thermal stresses or changes in polymer conformation or morphology.

As a drawback, fillers often cause a dramatic decrease in elongation at break. They sometimes decrease the tensile strength of a material, but there are numerous exceptions, especially with such fillers as carbon blacks in rubber. In this case, the elongation at break can increase. Fillers modify the shape and often induce yield points in the stress-strain curves of ductile polymers and rubbers. The yielding phenomenon is interpreted in terms of crazing effect (generation of fine cracks in the matrix) or dewetting effect in which the adhesion between the filler and the matrix is lost. At the same time, voids are created and the specimen undergoes dilatation. Tensile strength increases when particle size decreases [87]. Several possible mechanisms can be suggested: while the stress fields near a particle are independent of the particle size, the volume of polymer under stress increases with the particle size, so the probability of finding a large flaw within this volume also increases. If a large flaw exists within the area of stress concentration, the tensile strength will be reduced according to Griffith's theory. Moreover, in case of dewetting, large particles induce large voids, which lower the strength.

The stress-strain behavior of many filled polymers can be changed by adhesion promoters and silane coupling agents. All types of surface treatments may change the state of agglomeration of the fillers in addition to acting as coupling agents. The nature of the interface and the degree of adhesion do not affect the elastic modulus, but determine the strength and the stress-strain behavior of a composite [88]. The breaking stress is often raised, whereas the breaking strain is almost always lowered, usually dramatically.

Mechanical Coupling Models

The analysis of the mechanical response of heterogeneous materials requires comparing experimental data to theoretical predictions. Various models are proposed in the literature to display a prediction of the elastic modulus of polymer composites. All attempt to model the mechanical coupling i.e. how the energy of deformation is distributed between the distinct phases. They can be useful to understand the complex interplay between the parameters that are known to affect the mechanical behavior (elastic properties of the constituting

phases, aspect ratio, dispersion). Different authors propose a more or less exhaustive review of these models [4,89,90]. It is generally accepted that these elastic calculations can be extended to the description of the viscoelasticity of filled polymers through the correspondence principle of Hashin [91]. Three kinds of model can be distinguished.

Boundary models, based on variational principles, define the extreme behaviors of composites. The simplest boundary models (first order boundaries) are the serial association (lower limit or Reuss bound) and the parallel association (upper limit also called Voigt bound) of matrix and filler phases. The second and third order boundaries, (called Hashin Shtrikman [92] and Hervé Stoltz Zaoui [93] boundaries) use respectively second order and third order correlation functions. However, in the case of composite materials based on a polymeric matrix, the bounds are generally too distinct to allow reliable predictions. This is due to the large difference between elastic modulus of the components (e.g., Young's modulus of silica ≈70 GPa, glassy polymer ≈3 GPa, rubber ≈1 MPa).

A second set of theoretical predictions corresponds to phenomenological approaches. The description of the elastic behavior of the composite is deduced from empirical or semi-empirical equations, introducing one or more fitting parameters. Although they are not rigorous enough, theses approaches can be very useful as a first step to roughly estimate the effect of the mechanical coupling in a biphasic system. The classical serial-parallel model [94] (mixing law between upper and lower limits) contains for instance one adjustable parameter. It has been extended to the percolation concept ten years ago, determining the adjustable parameter. In this model, the fraction of filler in parallel is the fraction of percolated filler, given by the physical law of percolation:

$$\phi_p = \varphi \cdot \left(\frac{\phi - \phi_c}{1 - \phi_c} \right)^{0.4} \tag{7.17}$$

where ϕ_c is the geometrical percolation threshold [95].

A third kind of mechanical modeling is mean-field approaches, i.e. analytical estimations based on the determination of a homogeneous equivalent material of the heterogeneous composite [96]. First, a *representative volume element* (RVE) of the material is defined considering the phases present (volume fraction, distribution). Then, the local stresses are determined as a function of macroscopic stresses applied at infinity, and the local strains are deduced from the behavior law of each phase. The homogenization step averages the local fields so as to obtain the macroscopic behavior. In the self-consistent approach, the different phases are embedded in the Equivalent Homogeneous Medium, which is obtained by iteration technique. The 2-phase model averages the results obtained from the estimation with each phase embedded in the Equivalent Homogeneous Medium. This model seems well suited to co-continuous morphologies. In contrast, when the RVE displays a single uniform reinforcing phase included in a continuous matrix, an analytical formulation

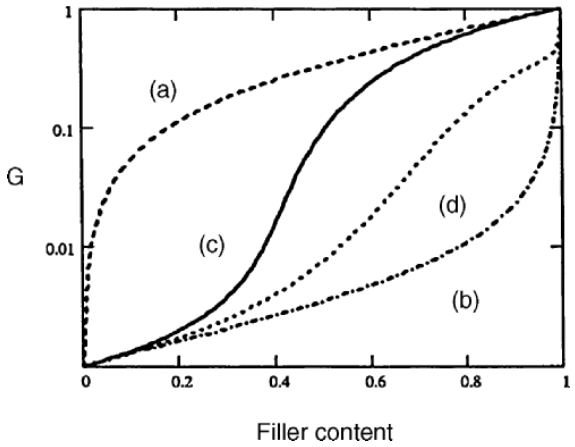


Fig. 7.11. Shear modulus versus filler content (ratio between filler and matrix shear moduli is 1000) for Voigt (**a**) and Reuss (**b**) boundaries, 2 phase (**c**) and 3 phase (**d**) self consistent estimations

is obtained generally referred to as 3-phase model [97]. Different formulations of micromechanical models have been developed for non spherical particles, like platelets [98,99] or rods [100,101]. The 2-phase and 3-phase self-consistent estimations are plotted in Fig. 7.11 with the Voigt and Reuss boundaries. The 3-phase formulation appears to be well suited for homogenization of elastic and viscoelastic modulus when the level of dispersion of the particles into the polymeric matrix is good. However, when particle aggregation occurs and especially when the rubbery plateau modulus is concerned, the 3-phase model fails to fit the data. This has been reported in the case of fillers when the volume fraction of the fillers is high ($\rangle$20 vol%), and even at very low fraction of particles in the case of nanocomposites [102].

It is worth noting that when filler content is above the percolation threshold, it is difficult to define a RVE. Moreover, as calculations assume that the macroscopic stress is applied at infinity, no size parameters are introduced in these models.

Nanocomposites Materials

Nanocomposite materials consist of a nanometer-scale phase in combination with another phase acting as a matrix. Among this class of materials, some of them have been used for a long time, for instance carbon black filled rubber in automotive industry. Work on polymer nanocomposites has exploded over the last few years. Their properties are reported to be different from that of their micro-scale counterparts [103, 104]. The specific features in nanocomposites are (i) the large interfacial area which can reach 100–1000 m^2/g, (ii) the average distance between particles, down to a value comparable with the

macromolecule coils. This can favor the short-distance filler-filler interactions leading, above a threshold fraction, to the formation of a filler network. Moreover, the presence of an interphase polymer layer near the inorganic surface with properties differing from the bulk polymer is often assumed. Due to the large surface area of the nanofillers, the interphase polymer is expected to dominate the properties of the nanocomposites.

Though significant progress has been made in developing nanocomposites with different polymer matrices, a general understanding has yet to emerge. Studying the incidence of the size among the various other parameters already mentioned (shape, interfacial energy, topological distribution, etc.) implies processing model materials by modifying just one of these parameters at a time. Unfortunately, it is really difficult to produce fillers having the same chemical structure with different shapes (rod, platelet, sphere), or even with different sizes and identical surface properties. Thus, the behavior analysis must account for several parameters, and each conclusion must be announced with care.

Processing Aspects

Different routes have been explored, in the literature, to process nanosized filler reinforced polymers (Fig. 7.12).

The first route is the direct incorporation of fillers in the polymer melt. In the case of nano-fillers, a high increase of viscosity is observed even at low amount of filler due to the high interfacial surface and the interactions between particles. Consequently, the bubbles introduced during the process are difficult to remove. The problem appears even more difficult in the case of high aspect ratio fillers, since the viscosity increases also with this parameter. In order to improve the dispersion, the viscosity is generally decreased by mechanical shearing or by the use of additives (processing aids, plasticizers...). The classical industrial processing techniques like extrusion or melt compounding (Brabender) are well known in the case of microsized fillers. These techniques are used for instance to produce silica or carbon black filled elastomers.

The second route consists in dispersing the fillers in the monomer or prepolymer and then activating the polymerization. For example, the polymerization of nylon in the presence of nanoclay platelets has been performed in

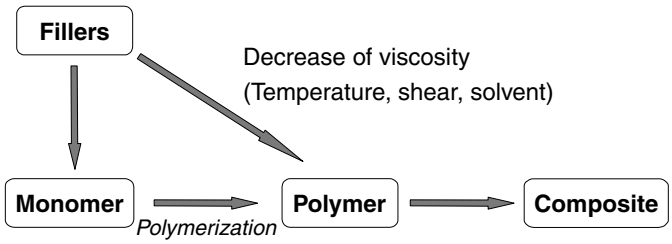


Fig. 7.12. Processing routes for nanocomposites

the early 90's [105]. Montmorillonite clay was exchanged with a quaternary ammonium ion, allowing the clay to mix with e-caprolactam. The caprolactam was then polymerized through ring-opening to form nylon-6. In this case, the issue is to control the polymerization or the curing process, which might be modified by the filler. The in situ polymerization has also been developed to produce organic-inorganic hybrids in which the polymerization of the matrix and the formation of the silica fillers occur at the same time [106].

A third route consists in using a solvent in which fillers and polymer are first dispersed separately and then mixed together. The solvent can be either polar or non polar depending on the polymer chemistry. The main problem is to obtain a stable suspension of the fillers in the chosen solvent: this stabilization depends on the chemical groups on the filler surface. In some cases, the functionalization of the surface of the filler can be an efficient way to solve the problem: for instance, in the case of hydrophilic fillers such as cellulose whiskers, sulfate groups are grafted on the surface in order to create electrostatic repulsion between individualized fillers [107]. In other cases, the stabilization can be achieved by grafting long polymeric chains (steric stabilization). The stabilization of the filler suspension can also be improved by the use of surfactant molecules, either ionic for electrostatic repulsion, or non ionic for steric stabilization. The use of surfactants may have consequences on the final properties of the composite since surfactant molecules can be present at the interface or clustered in the matrix.

Derived from the solvent route, another way to process nanocomposite materials is based on the mixture of various aqueous suspensions (colloids). It is well known that emulsion polymerization provides in a simple way polymer colloidal suspension, and is a flexible tool to produce structured particles by two or more steps of polymerization (having for instance a soft core and a stiff shell, with a significant composition gradient) [108]. The typical size of particles in suspension is about 100 nanometers. A mixture of an aqueous suspension of nanofillers with a colloidal suspension of film forming polymer leads, after water evaporation, to nanocomposite films, for example cellulose whisker-P(S-BuA) matrix composite. The aggregation of particles in the solution can also be reduced thanks to mechanical shear. In the case of carbon nanofibers and cellulose whiskers, sonication appears to be one of the most efficient tools to disperse aggregates [109]. But, the practical conditions of this technique (time, power) have to be controlled in order to avoid degradation of the fibers.

Generally speaking, surface treatments are often known to significantly affect dispersion, whatever the processing route. In the case of silica particles, surface treatments based on silane chemistry are used to produce chemical bonding between the filler and matrix. For nanolayered silicates, use is made of ammonium salts in order to exfoliate the stacks of platelets [110]. For carbon blacks, the modification of the surface properties is usually due to an oxidation treatment [111]. However, surface treatment modifies the surface chemistry and therefore influences the filler matrix interface.

A second issue in the processing of nanosized filled polymers is the stability of the filler dispersion. For instance, in the case of the latex route, the dispersion of the fillers should be stable during film forming, especially during the evaporation of water, to avoid a gradient in the thickness of the sample. The viscosity can play an important role in maintaining the suspension of fillers and avoiding flocculation. Therefore, the optimum viscosity is a compromise between a low value to ensure dispersibility and a high value to maintain stability. Freeze-drying can be used to bypass this problem, as done with cellulose whiskers [109].

With these different techniques, a great number of nanocomposites can be processed, with a polymeric matrix either thermoplastic or thermoset, amorphous or semi-crystalline. Review articles, for instance on the incorporation of layered silicate in different polymers, can be found in the literature [110,112–115]. Although an optimized process can a priori lead to a good dispersion, it is however always necessary to carefully investigate the state of aggregation of the fillers, and their possible orientation in the matrix. Moreover, special attention should be paid to microstructural modification of the polymer due to the presence of the fillers (curing process, modification of the crystallinity: amount, nature, dimension, texture of the crystalline phases). Thus, all studies need the combination of several techniques, including microstructural observations at various scales, physico-chemical measurements for interfacial characterization, mechanical tests at very different scales and stress-strain ranges (from AFM to standard tests up to tear or rupture), and in situ mechanical tests (i.e. where observations are performed during the tests).

Mechanical Behavior of Polymer Based Nanocomposites

For small stress, i.e. within the linear stress-strain domain, it is remarkable that the modulus increase due to nanofillers is much larger above T_g than below. Such an observation has already been reported for microsized composites. The reason for this in the case of microsized fillers is the larger modulus ratio of the components when the polymer is in the rubbery state compared to the rigid glassy state. Less important factors contributing to this effect are the larger Poisson's ratio above T_g and the presence of induced thermal stresses below T_g. However, when the matrix is soft, the reinforcement is most of the time higher for nanosized fillers than for micronic fillers. Several effects can be evoked to explain this difference as detailed in the following: the influence of particle dispersion, polymer-filler and particle-particle interactions.

Influence of Particle Dispersion

In the field of composite materials, it is often assumed that an increase of the interface area allows an optimum mechanical stress transfer between the filler and the matrix. This suggests that an optimum dispersion (uniform

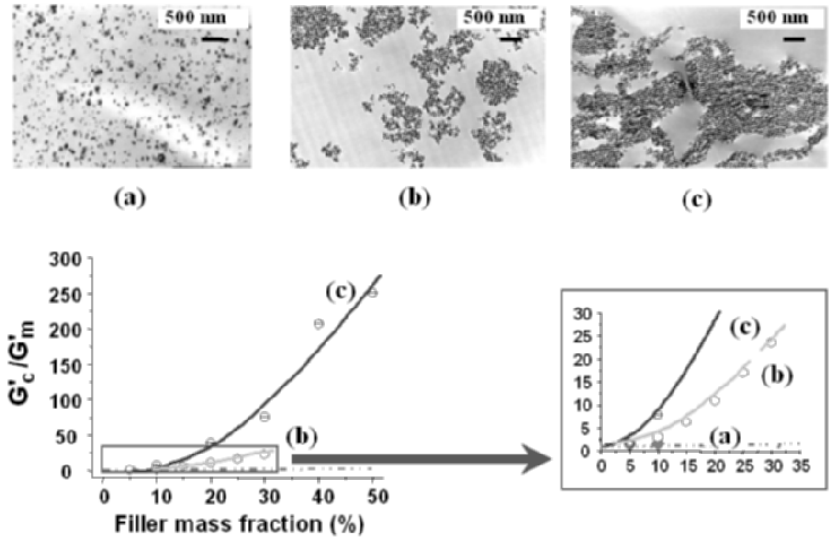


Fig. 7.13. Influence of particle dispersion on reinforcement in the case of silica filled PMMA elaborated through different routes: (**a**) industrial route (extrusion and injection), (**b**) solvent route, (**c**) high energy ball-milling

and without large aggregates) is needed in order to reach the best mechanical behavior. Nevertheless, the presence of a certain amount of aggregates leads to an increase of the elastic properties. This is illustrated in the case of PMMA filled with silica particles (aggregates size around 150 nm) made in three different ways: an industrial route (involving extrusion and injection), a solvent technique requiring the use of acetone and finally high energy ball-milling [104]. The storage modulus in the rubbery plateau appears to be very sensitive to the dispersion state (Fig. 7.13): at a given volume fraction, the worse the dispersion state or the larger the agglomerates, the higher the modulus. The presence of large agglomerates capable of trapping polymer is assumed to increase the apparent volume fraction of filler in the composite, and consequently the modulus. On the other hand, a uniform dispersion of fillers in the matrix is needed to obtain homogeneous properties at a mesoscopic level. Moreover, particle agglomeration tends to reduce the strength of a material: agglomerates are weak points in the material since they break easily when stress is applied. A broken agglomerate acts indeed as a strong stress concentrator.

Effect of Polymer-Filler Interactions

At a given state of dispersion, the modification of interfacial properties influences strongly the modulus in the rubbery plateau, where elasticity is governed by entropy rather than enthalpy. This arises from variations in the degrees of freedom of the polymer chains by interaction with filler particles, which

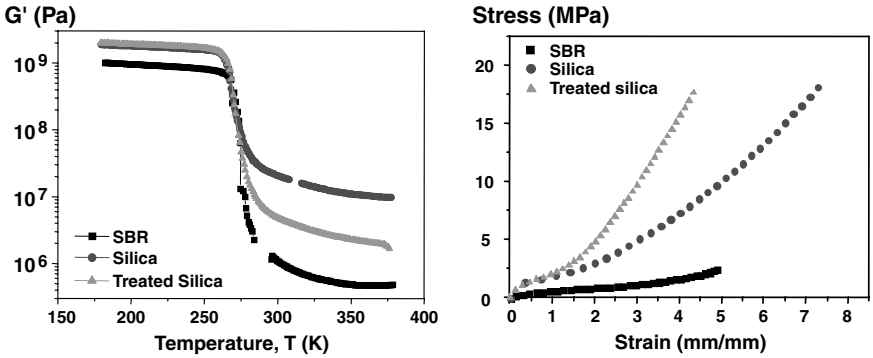


Fig. 7.14. Influence of surface treatment on reinforcement in the case of silica filled SBR (**a**) viscoelastic response (**b**) stress strain curves

depends on the surface chemistry. Experimental evidence is given in Fig. 7.14 for the case of a silica filled rubber (styrene-butadiene rubber). Only the surface treatment of silica was changed leading either to adsorption of macromolecules onto the filler surface (non-treated silica) or to chemical bonding (treated silica). Moreover, it was checked that the same level of dispersion was obtained whatever the surface treatment. The incorporation of silica in the SBR matrix leads to an increase of modulus in both glassy and rubbery plateau. However, there is a strong influence of surface treatment on the reinforcement in the rubbery plateau [116]. The influence of polymer-filler interactions is also clearly visible under large deformation (Fig. 7.14b). It is well established that carbon black or silica act as crosslinking nodes which increase drastically the stiffness of the rubber. This indicates that the fillers together with some macromolecular segments form a flexible network, but also that the properties of this network strongly depend on the interfacial properties. These properties are at the origin of well-known behaviors in rubbery materials, like the Payne and the Mullins effects. They result in an energy loss under cyclic conditions for the former, and in non-recoverable deformations for the latter. Interfacial properties have negligible incidence on the elastic modulus below T_g, when elasticity no more depends on entropy, like in thermosets reinforced by nanotubes.

Effect of Filler-Filler Interactions

The influence of filler-filler interactions are illustrated in the case of cellulose whisker filled polystyrene butyl acrylate latex (P(S-BA)) ($T_g = 0°C$) [107] or in plasticized PVC (hereafter called pPVC, $T_g = -10°C$) [117]. Cellulose whiskers, made from tunicates, are quasi-perfect crystals with $18 \times 9\,nm^2$ lateral dimensions [118] and an aspect ratio of around 100. They have a tensile modulus about 150 GPa and can form hydrogen bonds with their neighbors thanks to the numerous hydroxyl groups on their surface. The whiskers (in

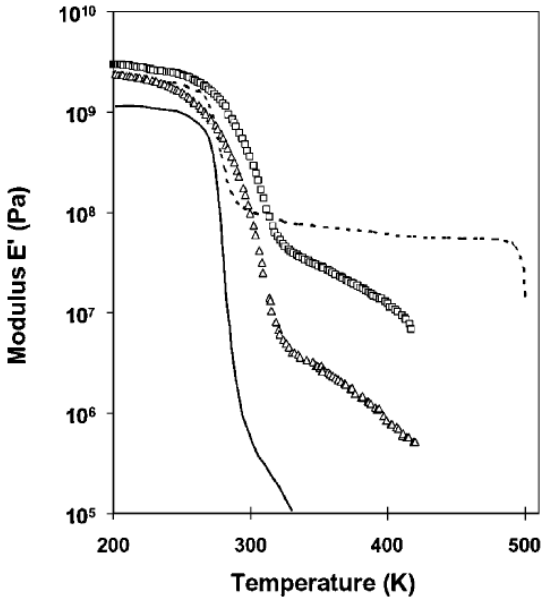


Fig. 7.15. Torsion modulus, E', versus temperature for pPVC matrix (△), pPVC reinforced with 6.6 vol% of whiskers (□), P(S-BA) (*bold line*), P(S-BA) reinforced with 6 vol% of whiskers (*dashed line*)

aqueous suspension) were mixed with the pPVC suspension, freeze-dried, hot mixed in a Brabender (Banburry S.A.), and pressed to form a 2 mm thick sheet. For P(S-BA) matrix, as T_g of P(S-BA) is well below the ambient, the aqueous suspension of whiskers and P(S-BA) droplets is simply dry-cast in a mold and water evaporation leads to film formation. The microstructural characterization of both composites by electron microscopy and small angle neutron scattering shows the homogeneous dispersion of the whiskers inside the matrix and the absence of aggregates. Figure 7.15 shows the shear (or torsion) modulus as a function of temperature of pPVC matrix composite and P(S-BA) latex composite.

The shear modulus of P(S-BA) composite is three times higher than that of pure P(S-BA) for only 6 vol% of whiskers. It is almost constant above T_g, up to the degradation temperature of cellulose (200°C), whereas pure P(S-BA) modulus dramatically decreases in this temperature range. These results suggest that the formation of a cellulose whisker network occurs when the processing allows the formation of strong hydrogen bonds between whiskers. Below the temperature of cellulose degradation, the bonds strength depends weakly on temperature, which leads to a constant network modulus. This latter effect is present in the P(S-BA) composite, for which the evaporation casting process allows whisker contact formation. The existence of a whisker network is confirmed by swelling experiment in toluene. This solvent totally

dissolves non reinforced P(S-BA), but only swells the reinforced sample. The hot mixing process used for PVC composites probably leads to a destruction of the whisker – whisker bonds. This explains the much smaller reinforcement observed with this material, compared to P(S-BA). Moreover, above T_g, the modulus decreases when temperature increases, following a slope close to that observed for the pure matrix. However, even in the case of PVC, the experimental moduli are higher than those calculated with classical model [119]. This indicates the formation of a soft network in which the junctions between whiskers are made of adsorbed PVC chains. These differences of interaction between whiskers inside both composites were confirmed by large deformation experiments. When tensile tests are performed above T_g, the stress-strain curve of P(S-BA) composite with 6 vol% filler content shows a sudden decrease of the stress for deformation above a few %, but not a break of the sample. This indicates the irreversible damage of the whisker-whisker network inside the composites. By contrast, successive tensile tests on PVC composites show a progressive damage of the materials without any critical value of the deformation above which a decrease of the mechanical properties could be observed. To conclude, the existence of a filler network, which is never discussed for micrometer scale composites, is shown to play a strong role in the reinforcement of nanocomposites. However, there is still no direct experimental evidence on the presence of an immobilized layer of polymer at the interphase. This layer, if it exists, may also contribute to the reinforcement as the interphase volume becomes large. There is still lot of debate to determine the exact contribution of each of these two effects, (i), formation of a flexible filler network and (ii) increase of rigid phase volume fraction (immobilized interphase).

7.3.2 Nanotube-Based Composite Materials

Mechanical Coupling in the Cox Model

A model developed by Cox [120] is very handy for demonstrating how reinforcement is related to the shape factor, i.e. the length to radius ratio λ, for the simplest composite: a single filament embedded in a cylindrical matrix (Fig. 7.16).

The Cox model allows calculation of the shear strain (stress) axial component in the matrix and the tensile strain (stress) in the fiber. It cannot totally describe stress and strain fields in specimens which are triaxial (axisymmetric), and neglects: – The influence of radial and orthoradial stresses on interfacial and longitudinal shear – the elasto-visco-plastic behavior of the polymer in polymer matrix composites (PMCs) – the highly anisotropic structure of carbon fibers or nanotube ropes. Nevertheless, the general trend given by the Cox model is not far from more sophisticated analysis.

Load is applied to the matrix cylinder (Fig. 7.16) supposing a perfect interface, so that matrix strain is transferred to the fiber. This ensures continuity

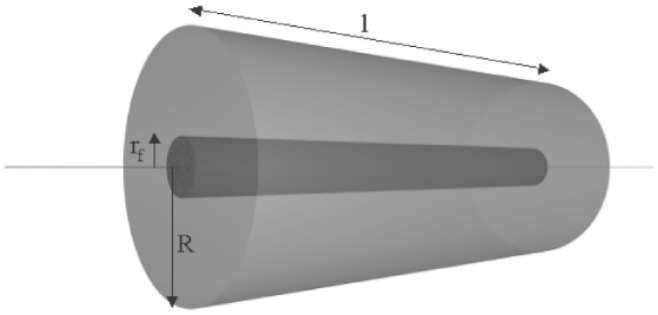


Fig. 7.16. Geometry of the Cox model [120]

of displacement at each point of the interface. The axial strain in the fiber is given by:

$$\epsilon(x) = \epsilon_\infty \left(1 - \cosh\beta\left(\frac{l}{2} - x\right) / \cosh\beta\left(\frac{l}{2}\right)\right) \tag{7.18}$$

with $\beta = [2G_\mathrm{m}/r_\mathrm{f}^2 E_\mathrm{f} \ln(R/r_\mathrm{f})]^{1/2}$. E_f, r_f and l are the fiber axial modulus, radius and length; R and G_m are the radius and the shear modulus of the matrix.

The axial strain at the center of a very long fiber is very close to that of the matrix ϵ_m both being equal to ϵ_∞ for infinite length. Thus $l_0 = 2/\beta$ appears as a characteristic length of the model composite. Figure 7.17 shows ϵ/ϵ_∞ as a function of the reduced length l/l_0.

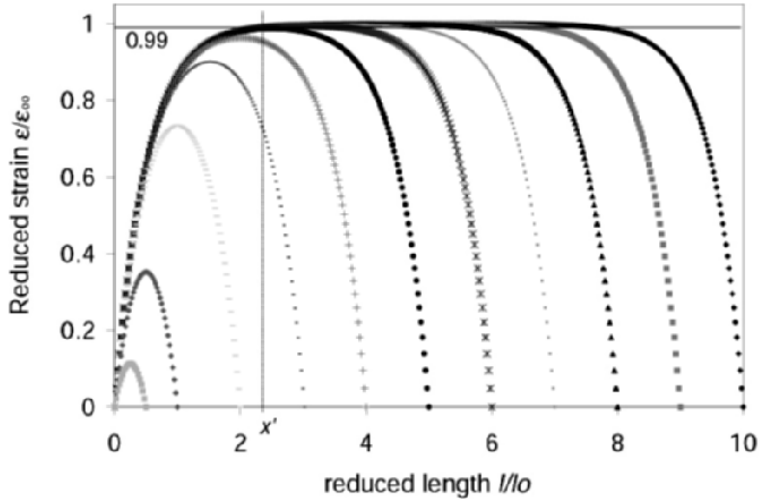


Fig. 7.17. Strain transfer reduced curves in the Cox model. The reduced strain along the fiber is plotted for different values of the reduced length

Strain is maximum at the center of the fiber (and zero at its ends) and depends strongly on l/l_0 for small values of this parameter, i.e. when l/r_f is small. The quantity $\eta = \epsilon_{l/2}/\epsilon_\infty$ reaches 0.99 for $l = 2x'$ where $x' \approx -(\ln 0.01)/\beta$ is a loading length . The strain transfer efficiency ξ can be defined simply as the ratio between the mean strain value $\bar{\epsilon}$ and ϵ_∞.

Purification, Individualization and Functionalization of Nanotubes

SWNT-based composites are often prepared with raw SWNT-containing soots which usually contain a lot of impurities, in particular carbon nanoparticles, which are structurally very close to carbon black. Polymer adhesion on them is expected to be high so they are not considered as a weakening factor in polymer matrix nanocomposites. By contrast, for ceramic and metallic nanocomposites, nanoparticles could generate undesirable phases such as carbides, metallic oxides or clusters, porosity, ... It is thus important to put some effort into purification of raw materials, and to improve synthesis methods.

Some composites could benefit from using individual SWNT's instead of bundles. For that, SWNT's have to be separated from their native bundles. Several papers deal with stabilization of individual carbon nanotubes in solution: For example Bahr et al. [121] achieved bundle dissolution in 1,2-dichlorobenzene, while Bandyopadhyaya et al. [122] used aqueous solutions of gum arabic (a polysaccharide).

Functionalization (see Chap. 8 for details) is expected to increase matrix bonding to nanotube surface, especially for MWNT, which could increase the composite breaking strength. As a side effect, the functionalization treatment (e.g. oxidation in acid solution) may create vacancies at the nanotube surface thus lowering its intrinsic strength, so it should be used with great care. Grafting hydrophilic groups onto the nanotube surface can also improve dispersion in polymers [123].

Nanotube-Polymer Matrix Nanocomposites

The first stage in composite production is to ensure a homogeneous mixture of nanotube and polymer. The second step is to polymerize the gel-like material without creating too much porosity. We describe here a procedure implemented by Vaccarini et al. [124] to prepare homogeneous nanotube polymer composites. SWNT are first sonicated in methanol or dichloromethane (typically, 100 mg in 40 cc leads to a rather stable and consistent pseudo-gel). Bundles unfold and occupy all the liquid volume. Then thermoset resin can be added, with or without hardener, and sonicated. Hardener may also be introduced after solvent evaporation. With thermoplastics, nanotubes are mixed to a powder as fine as possible (ideally submicronic). For instance PEEK (poly ether ether ketone) nanotube blend is molten at 375°C in a pug-mill then molded at this temperature under high pressure (130 bar). Both thermoset and

thermoplastic blends contain 5–40% of SWNT rough products in weight (from arc discharge reactor). With small amounts of nanotubes (≈10 mg) Young's modulus can be measured by Vickers indentation on small pellets. Mechanical tests need larger samples and molding has to be done under high pressure (50–100 bar) to avoid porosity. Figure 7.18 shows two examples of failure surfaces, which suggest that nanotube distribution is indeed homogeneous in the composites thus prepared.

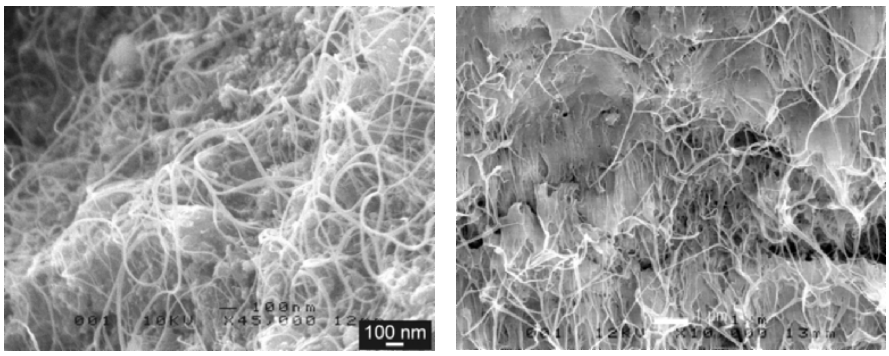


Fig. 7.18. Failure surfaces of SWNT/polymer nanocomposites. *Left*: epoxy matrix contains 30 wt% of rough products. *Right*: PEEK matrix contains 5 wt% [124]

Young's Modulus of Nanotube-Polymer Nanocomposites

Figure 7.19a shows a Vickers Hardness curve. Young's modulus is related to the slope of the unloading curve [125]: the plasticized polymer area under Vickers pyramid viscoelastically returns to its zero load value (the modulus has to be corrected for this effect but values are not reported in Fig. 7.19b). The addition of some 15% by weight of SWNT to an epoxy resin leads to a modulus barely twice that of neat resin [124]. Other authors report similar results.

Such a result can be explained using the Cox model and classical mixture rules. The rule of mixture, valid for long parallel objects, gives the modulus of the composite: $E_\mathrm{c} = E_\mathrm{m}V_\mathrm{m} + E_\mathrm{f}V_\mathrm{f} = 100\,\mathrm{GPa}$ taking $V_\mathrm{f} = 0.15$ and $E_\mathrm{m} = 3.2\,\mathrm{GPa}$ (from a tensile test). If we consider now that nanotubes are long, straight, and randomly oriented, Cox [120] predicts: $E_\mathrm{c} = E_\mathrm{m}V_\mathrm{m} + (1/6)E_\mathrm{f}V_\mathrm{f} = 19\,\mathrm{GPa}$. Figure 7.19b shows we are far below this value. The strain transfer efficiency $\xi = \bar{\epsilon}/\epsilon_\infty$ is reported in Table 7.1 as a function of reduced length l/l_0 (or shape factor $l = l/r_\mathrm{f}$) for isolated SWNT and bundles. To simplify matters, matrix shear modulus was taken as $G_\mathrm{m} = 1.16\,\mathrm{GPa}$ and $R = 10\ r_\mathrm{f}$. With isolated SWNT of length $l = 100\,\mathrm{nm}$, ξ remains noticeable but falls dramatically for bundles when $l < 500\,\mathrm{nm}$. This simple model high-

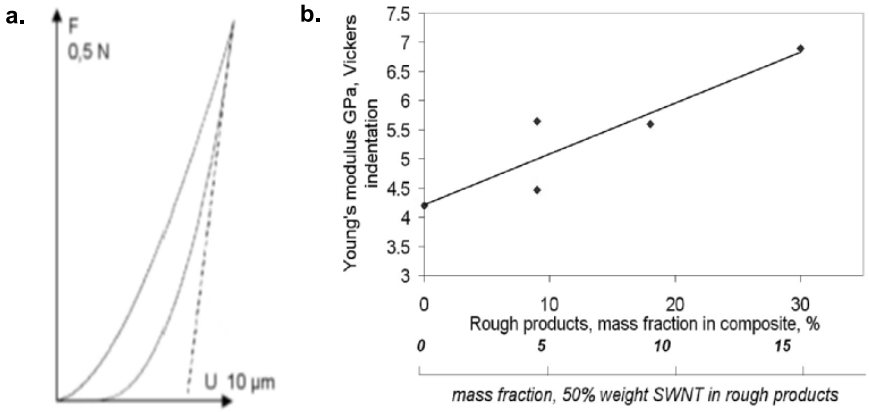


Fig. 7.19. (a) Vickers indentation (hardness) test for Young's modulus measurement. **(b)** Young's modulus vs. weight fraction of rough products (arc) in CIBA LY556/HT972 epoxy resin/SWNT blends (values are not corrected for viscoelasticity effects) [124, 126]

Table 7.1. Cox model strain transfer efficiency

Nanotubes E, D, l_0	Length l	l/l_0	Loading Length x'	Shape Factor $\lambda = l/r_f$	$\eta = \epsilon/\epsilon_0$	Strain Transfer Efficiency ξ
isolated SWNT $E = 1100\,\text{GPa}$	1000 nm	21.6	106.5 nm	1430	1	0.953
$D = 1.4\,\text{nm}$ $l_0 = 46\,\text{nm}$	100 nm	2.2	106.5 nm	143	0.773	0.55
SWNT bundle $E = 650\,\text{GPa}$	1000 nm	1.58	1462 nm	80	0.603	0.417
$D = 25\,\text{nm}$ $l_0 = 635\,\text{nm}$	500 nm	0.79	1462 nm	40	0.246	0.166
	100 nm	0.16	1462 nm	8	0.012	0.008

lights shape ratio effects and gives an approximate expression of the effective Young's modulus: $E_\text{c} = E_\text{m}V_\text{m} + (\xi/6)E_\text{f}V_\text{f}$.

Let us consider Fig. 7.20: SWNT bundles have probably the same configuration in a polymer matrix. During a tensile experiment, it can be seen that only short bundle segments can be considered as parallel to the tensile axis so that both the effective shape ratio and the amount of active parts for reinforcement are small.

Results shown in Fig. 7.19 can be explained if the shape factor, λ, is about 10–40. The behavior is similar to reinforcement in particulate composites. SWNT bundles could also be assimilated to imbricated tori. Mori-Tanaka method for N-phases allows one to model the elastic characteristics of composites containing inclusions versus their geometry. Following Marzani [128]

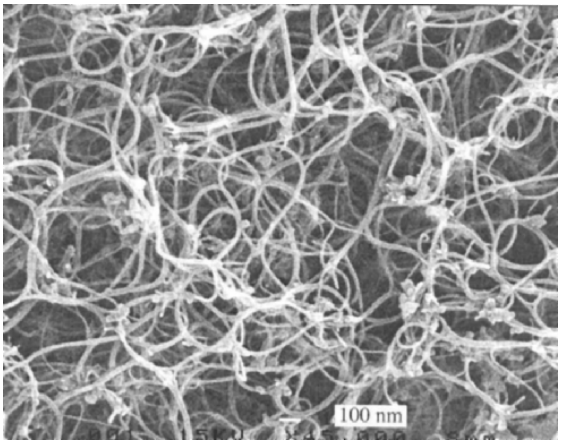


Fig. 7.20. Arc discharge SWNT [124]

and Odegard [129], Kruch [127] has described SWNT as very flat, short ellipsoids: the shape factor values lie in the same order of magnitude as in the Cox model. The straight line fit in Fig. 7.19b is adjusted for $\lambda_{\text{ellipsoid}} = 20$.

Composites with a high nanotube volume fraction are no so frequent in papers: Vaccarini et al. [124] reached 40 wt% of rough products but as V_{f} becomes higher and higher nanocomposites are more and more brittle: this is apparently in opposition with the hypothesis stating nanotubes could render polymers tougher. Porosity and residual stresses (thermal and molding under high pressure) introduce defects and large quantity of elastic energy detrimental to toughness. It could be argued that the low modulus measured on blends comes from a weak polymer/nanotube bonding. Such a statement is false, yet still found in many publications or talks. Consider the model composite in Fig. 7.16 and suppose we are able to compute complete strain and stress fields for a given load. As long as interfaces remain perfect i.e. no debonding occurs, none of the stress/strain field components varies with the adhesion level between the matrix and the fiber. Reinforcement effects only depend on moduli and fiber shape factor. Under loading, for instance in PMC's, interfacial zones debond in the vicinity of broken fibers but the ratio between debonded and undamaged interface is small and the strain transfer makes the composite effective modulus almost unchanged.

Furthermore there is no reason to suspect that SWNT/polymer adhesion is weak: Fig. 7.18b shows SWNT well-embedded in PEEK, qualitatively indicating high levels of adhesion. High resolution TEM micrographs in Fig. 7.21 show large amounts of epoxy resin drawn out along with SWNT bundles by a pull-out process during void or slit edge opening in thin-foil-shaped TEM samples: this could not be possible without a high adhesion level (see also results by Lourie et al. [130]).

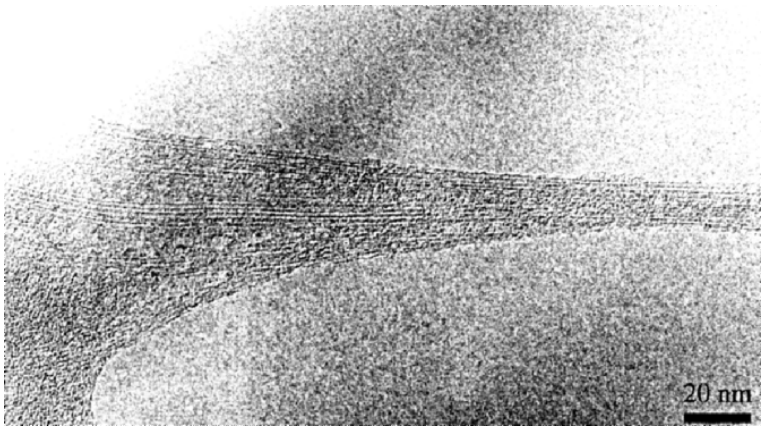


Fig. 7.21. TEM pictures of epoxy resin dragging by SWNT bundles in void tensile opening [124, 126]

Nanotube Alignment

It seems clear that alignment of nanotubes, either during their synthesis or in the composite production stage, is the next step towards high performance nanotube-based composites. Each kind of available nanotubes may pose a specific problem for that, the most difficult cases being SWNT bundles and CVD MWNT. Figure 7.20 illustrates the connectivity of SWNT in a mat. MWNT develop weaker Van der Waals forces because the orthoradial curvature and the surface to volume ratio are both lower than for SWNT. Entanglement may make separation and alignment of bundles very difficult. Plasma enhanced CVD [131] or aerosol pyrolysis [132] produce large arrays of parallel nanotubes which have to be separated prior to making oriented sheets of parallel nanotubes. Fluidized bed CVD techniques [68] slowly produce long strands of parallel nanotubes. All these processes can be greatly improved into continuous and faster processes. Extrusion or spinning of nanotube/polymer melts are probably the best way to produce oriented-oriented preimpregnated sheets or nanocomposite fibers. In both methods, shearing the viscous flow induces nanotube alignment.

Nanocomposite Fibers

Polyvinylic alcohol (PVA)/nanotube composite wires will be treated in the next section. Their Young's modulus may be as high as 50 GPa after 160% stretching of a re-hydrated tow (Vigolo et al. [134,135]). The spinning process of the aqueous nanotube suspension is continuous and possibly implementable with other polymers for particular applications. Kumar et al. [136] have obtained poly(p-phenylenebenzobisoxazole)(PBO)/HipCo SWNT stretched fibers. Young's modulus is 138+/−20 GPa for PBO and reaches 167+/− 15 GPa

for 10 wt% SWNT. Failure strain is also improved. Values are respectively $2.0 \pm 0.2\%$ and $2.8 \pm 0.3\%$. Andrews et al. [137] made SWNT/pitch blends and obtained nanotube reinforced carbon fibers by extrusion and pyrolysis. With 10 wt% of purified nanotubes in pyrolysed fibers the tensile modulus is 78 GPa against 34 GPa for pyrolysed pitch. In both case [136, 137] modulus increase is rather close to that predicted by the ordinary mixture law (taking $E_b = 650$ GPa) indicating effective nanotube bundle alignment.

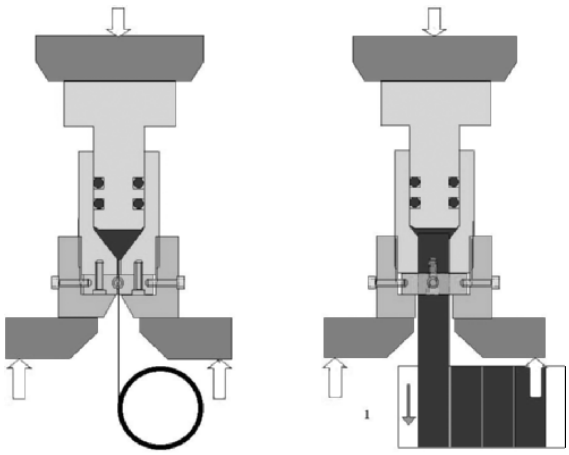


Fig. 7.22. Extrusion of oriented nanotubes/polymer sheets [138]

These results also show that extrusion is probably the simplest process to get oriented nanotubes in polymers. Figure 7.22 is a schema of an extrusion device proposed by Foutel-Richard [138] and designed to obtain preimpregnated nanotubes/polymer sheets. Launois and Poulin published a complete review on aligned carbon nanotubes [139].

Nanotube-Metallic Matrix Nanocomposites

Numerous routes are available to make metal/nanotubes nanocomposites but not all have been explored yet. Three properties at least can be aimed at: reinforcement (with oriented nanotubes), tribology and wear resistance, and creep resistance. For the latter, the underlying hypothesis is that under conditions of high metal/nanotube bonding and good dispersion of isolated SWNT, nanotubes could act as strengthening precipitates, impeding dislocation motion. Such material would be a true nanocomposite because strengthening effects would come with creep reduction (structural hardening alloys are not nanocomposites). Bagsi et al. [140] have computed Al-SWNT interaction using first principle method: they find a maximum Al–C bond energy for semiconducting SWNT, Al forming a continuous layer on SWNT surface. Some

electron beam evaporated metals (Ti, Ni, Pd) also form continuous layers on SWNT but Al and Fe form nanodrops (Zhang et al. [141]). Metal infiltration in fibrous preforms may be obtained by squeeze casting at 1 kbar [138]. The process must be fast enough to prevent metal-carbon reaction. Electrochemical [142] or electroless deposits [143, 144] are also interesting processes but they need further sintering treatment and control of impurity contamination. Mixing nanotubes with ultrafine metallic powders [145] ensures homogeneity and further thermal treatment (hot isostatic pressing) is a means to maintain a nanostructured metallic matrix: the number of atoms belonging to grain boundaries or interfaces is very high. Grain boundaries block dislocation motion and point defect diffusion becomes easier in disturbed zones. Hardness, yield stress and tensile strength of nanostructured materials are enhanced as a consequence of the first effect (Hall-Petch law) if the grain size does not fall below a critical value for which the stress sensibility thus varies as the inverse of grain size. The same phenomena can act favorably or can be detrimental to creep resistance: at medium temperature and stress a finely nanostructured material is more sensitive to creep because boundary slip, point defects and atomic diffusion are easier (Cable creep). But at higher temperature grain boundaries hinder dislocation motion: the nanomaterial becomes less sensitive to creep.

Mechanical alloying (high energy ball milling process) [146, 147] is usable to make nanocomposites by mixing very finely immiscible compounds. Alloying is the result of repeated fracture and cold welding of the component particles. Very high cold working, amorphization, and phase transition give a highly metastable material. This feature is interesting because blends contain energy useful to modify the micro-nano structure in a further thermal treatment. MAFAPAS process [148] adds a second activation to the mechanical activation: under high pressure a very intense electric discharge is released through the blend. Mechanical alloying may be an efficient process to prepare isolated-nanotube/metal composites.

Nanotube-Ceramic Matrix Nanocomposites

Several routes exist to prepare nanotube-containing blends: nanometric powders, sol-gel routes, organosilisic precursors, and ball milling. Expected new properties are less reinforcement than improvement in toughness, tribology, wear and creep resistance, jointly or separately, especially at high temperatures. Improvement in properties could occur whether or not the matrix is nanostructured. Nanotubes are supposed to modify crack initiation at a nanometer or a micrometer level, and could be at the origin of mechanical energy dissipative process by interface debonding. Siegel et al. [149] have obtained toughness increase from 3.4 to 4.2 $\mathrm{MPa\,m^{1/2}}$ with a 10 wt% MWNT-alumina blend. Zhan et al. [150] made α (80%) and γ (20%) alumina- HiPCo nanotubes blend sintered by spark plasma generated by a pulsed discharge between alumina grains which remains nanocrystalline. Toughness changed

from 3.3 to 9.7 MPa $m^{1/2}$. This spectacular result verifies two hypothesis: the beneficial effects of nanotubes and nanometric matrix structure.

Sol-gels offer a large variety of routes for processing advanced ceramic materials and organic/inorganic hybrids: powders, fibers coatings, porous membranes, aerogels, monoliths and composites [151–153]. A sol-gel process often implies the transition from a colloidal solution to a solid state, a gel. Colloid precursors are inorganic metallic salts or organometallic compounds (metal or metalloid atoms surrounded by reactive ligands). Main categories are alkoxides (aluminates, titanates, borates, ...), phenoxides, alkoxisilanes (tetramethoxisilane-TMOS, tetraethoxisilane-TEOS), polyalcools and phenols derivates. Precursors undergo a series of hydrolytic and polymerization reactions to give colloids. Three kinds of reaction describe the sol-gel process: hydrolysis, water condensation, and alcohol condensation:

- Si-OR + HOH $\rightleftharpoons$ SiOH + ROH
- Si-OH + Si-OH $\rightleftharpoons$ Si-O-Si + HOH
- Si-OR + Si-OH $\rightleftharpoons$ Si-O-Si + ROH

The solvent uptake transforms products into a dense gel. Further drying and thermal treatment eliminate volatile fractions. Complex and very pure nanometric formulations are possible but sintering is a general problem of sol-gel routes.

Carbon Fiber Composites with Nanotubes

In PMCs it is generally assumed that compressive failure is due to fiber microbuckling and to low matrix yield stress. Failure arises when an instability is generated by microbuckling under compressive stress or when local weakness induces microbuckling. Nanotubes embedded in the matrix could delay matrix yield or fiber microbuckling. Considered as a reinforcing component, nanotubes have ideal size and shape factor compatible with mean distance between fibers (2 µm). Making a carbon-fiber/polymer-nanotube composite is not a simple task because of SWNT bundle entanglement. It is impossible to force the insertion of an homogeneous polymer/nanotube blend in fibrous preforms [138], since fibers act as a nanotube filter. Nanotube layers have to be deposited between fibers prior to resin impregnation by a liquid polymer [138]. Figure 7.23 shows a carbon fiber-epoxy composite (Toray T800/Hexcel HS 914) containing nanotubes. CVD nanotubes can also be used. An interesting alternative is to make nanotubes grow directly on carbon fiber surface. Thostenson [154] proposed such a process. Perpendicular nanotubes may improve transverse properties of unidirectional plies in structural laminate composites.

What can be expected from nanotubes embedded in a matrix of long fibers PMCs? Foutel-Richard [138] proposed some additional arguments for improved mechanical properties. Leroy [155] has shown the importance of the

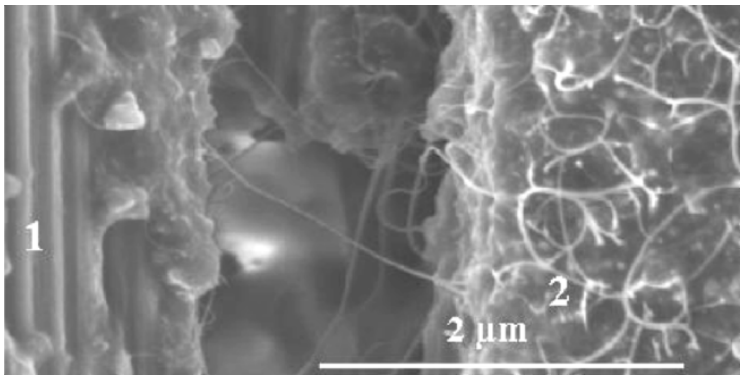


Fig. 7.23. Carbon fiber/epoxy resin-SWNT composite. (1) fiber; (2) matrix and SWNT [138]

dynamics of fiber rupture and crack propagation at a microscopic scale to explain unidirectional composite failure.

When a fiber fails inside the material, mechanical energy is suddenly released which may generate microcracks in the plane of the broken ends. These microcracks may further provoke the failure of neighboring fibers. High stresses and local high volume fraction of fibers enhance the probability of collective fiber failure. Dissipative phenomena such as interface debonding and matrix microcracking result in a threshold shift of collective failure. Nanotube debonding and failure may favorably displace this threshold but it cannot be neglected that nanotubes have a low longitudinal thermal expansion coefficient, which may induce residual thermal stresses. If their level is not too high, mode I and mode II of critical energy release rates (G_{Ic},G_{IIc}) could be enhanced. Elasto-visco-plastic laws of thermoplastic or thermoset polymers are modified by nanotubes (for instance clay/thermoplastic composites): their creep rates could be reduced which is of some importance in the case of heat exposed polymers or thermostable PMC's. Improvement of fatigue behavior is not obvious: expected slowing in crazing and microcracking may be counterbalanced by other effects.

7.3.3 A New Material: The Nanotube Fibers

We describe in this section methods to make fibers of aligned nanotubes and present the structure and physical properties of the resultant systems. As explained in previous sections, mechanical properties of composites or macroscopic assemblies of carbon nanotubes are expected to strongly depend on the alignment of the nanotubes. It is thus of critical importance to develop processes to control and optimize this structural feature. As already well established for polymers, fiber spinning and drawing are efficient approaches to align macromolecules. We show related encouraging results for nanotubes,

even though the degree of alignment in nanotube fibers is still far from the almost perfect alignment commonly achieved in high performance polymer fibers. We only consider fibers that contain a large fraction of carbon nanotubes. We don't review situations where nanotubes are simply used as fillers in polymer fibers to provide some electrical conductivity or mechanical reinforcement without fully exploiting the properties of carbon nanotubes. In materials like nanotube fibers containing a large amount of carbon nanotubes, much higher electrical or thermal conductivities can be expected along with better mechanical properties. The main approaches developed so far to produce nanotube fibers include CVD processes, an electrophoretic method and a particle coagulation spinning (PCS) process. We focus on fibers produced by the PCS process because it is particularly simple and potentially scalable. We describe the principle of each method as well as the structure of the resultant fibers as determined by polarized Raman spectroscopy or X-Ray scattering. These two techniques are of particular interest to characterize nanotube fibers because they allow the nanotube alignment to be quantitatively measured. Advantages and limitations of these techniques are given in the following section.

Nanotube Alignment Characterization

In this part, we briefly discuss the main methods used to quantify the degree of alignment of nanotubes in fibers. For single-walled nanotubes, it can be deduced from X-ray scattering or from polarized Raman spectroscopy. Single-walled nanotubes are usually assembled in bundles, forming a two-dimensional hexagonal array perpendicular to the bundle axis. The crystalline nature of the bundles has been used to quantitatively probe their degree of alignment using X-ray diffraction [156, 157]. Mosaic distributions are obtained from the angular intensity distributions of the first diffraction peak of their hexagonal lattice. In most cases, it can be fitted by a Gaussian function with a full width at half maximum (FWHM) related to the angular distribution of nanotube axes in direct space. The smaller the FWHM, the better the nanotube alignment. For a two-dimensional distribution of nanotube orientations within a plane, the width of the intensity distribution directly gives that of the distribution of orientations in direct space. For a three-dimensional distribution around an axis, the width of the distribution in direct space is equal to that in reciprocal space for FWHM $<40°$, and then becomes slightly smaller: it is for instance equal to 70° for 75° in reciprocal space [159]. For FWHM = 30° (75°), $\approx$50% of the nanotubes axes lie inside a cone of angle 15° (35°). In this section, we refer to widths in reciprocal space, as was done in quoted publications. A two-phase model can be considered with partially aligned nanotubes, characterized by the Gaussian distribution, plus a fraction of non-aligned nanotubes [156–158]. Nanotube alignment can also be deduced from polarized Raman spectroscopy [158, 160–162] (see also Chap. 5). Indeed, Raman line intensities depend on the angles made by the polarization of the

laser excitation and that of the scattered light with the nanotube long axes. This is explained within a resonant model for highly anisotropic tube absorption. All nanotubes, assembled in bundles or not, are probed in the same way with this method. An advantage of the X-ray scattering method with respect to electron scattering or Raman spectroscopy is that the volume investigated is much larger. Moreover, the interpretation of X-ray scattering experiments is more direct than that of Raman experiments. On the other hand, Raman spectroscopy probes all the nanotubes, and not only those preferentially organized in crystalline bundles. Finally, for multiwalled nanotubes, the method used to study their orientation is X-ray (or electron) diffraction, the analysis of the intensity distribution being made on the diffraction peak corresponding to the interwall distance ($\approx$0.34 nm). Other methods are also reported in the literature, but they are not quantitative. Under a scanning electron microscope, the nanotubes can be visualized and thereby their alignment roughly estimated. However, it is a rather local and only two-dimensional probe. If the material is sufficiently transparent (not too thick), it can be placed between crossed vertical and horizontal polarizers: due to nanotube optical anisotropy, the brightest transmitted light is seen when the nanotube axes make an angle of 45° with respect to the polarizer axes.

Approaches for Making Fibers of Aligned Nanotubes

Particle Coagulation Spinning (PCS) Process

Vigolo et al. [134] reported in 2000 a simple method to assemble single-walled carbon nanotubes into long ribbons and fibers. The nanotube bundles are dispersed in water with the help of commercially available surfactant molecules, like sodium dodecyl sulfate (SDS). A detailed study of the phase diagram of the surfactant stabilized nanotube dispersions has been performed to determine the optimized concentrations of surfactant and nanotubes. The aim was to obtain a homogeneous suspension with a relatively high concentration of nanotubes. The SWNT dispersion is injected in the co-flowing stream of a polymer solution that contains between 2 and 6 wt% of polyvinylalcohol (PVA), an amphiphilic polymer. The PVA adsorbs onto the tubes and provides a strong bridging attraction [163] between the bundles. This process leads to the formation of long ribbons that remain stable in the absence of flow. As schematically shown in Fig. 7.24, the nanotubes coagulate when they are in contact with the coagulating polymer solution, and a fiber can be spun.

The nanotubes used in [134] were single-walled nanotubes obtained by the electric arc method. Since then, the same process was successfully applied to single-walled nanotubes obtained from the laser vaporization method or by using the more recent HiPco process [164], and to multiwalled nanotubes [165]. The alignment of nanotubes in the ribbons has been qualitatively studied by Scanning Electron Microscopy and by optical observations between crossed polarizers [134]. The nanotubes exhibit a clear preferential orientation along

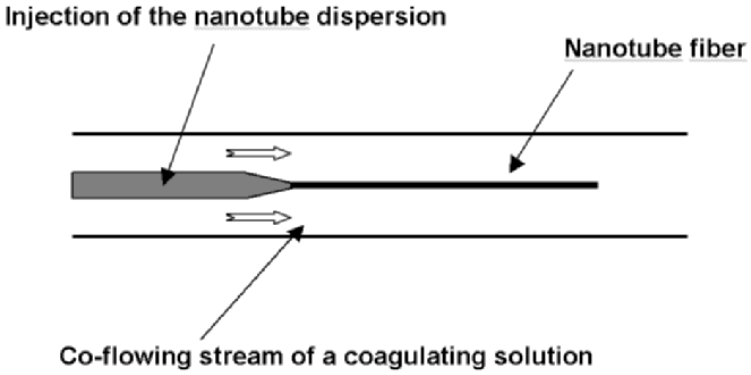


Fig. 7.24. Schematic of the particle coagulation spinning (PCS) process. A nanotube dispersion is injected in the co-flowing stream of a coagulating solution. As a result, the nanotubes stick to each other and form a fiber that can be spun

the main axis of the ribbons. However, no quantitative measurement of this orientation has been published yet.

In order to make more compact systems, rinsed ribbons are vertically drawn out of water [134]. Capillary forces, water drainage and evaporation cause the ribbon to collapse into a dense fiber (density $\approx 1.4 +/- 0.3\,\mathrm{g/cm^3}$ for electric arc raw material) with a diameter ranging from a few micrometers to 100 micrometers when dry. This simple method leads to fibers several tens of centimeters long. Such a fiber is shown in Fig. 7.25.

A knot was intentionally made in the fiber to reveal its high flexibility. The amount of nanotubes with respect to PVA is about 60 wt% as determined by

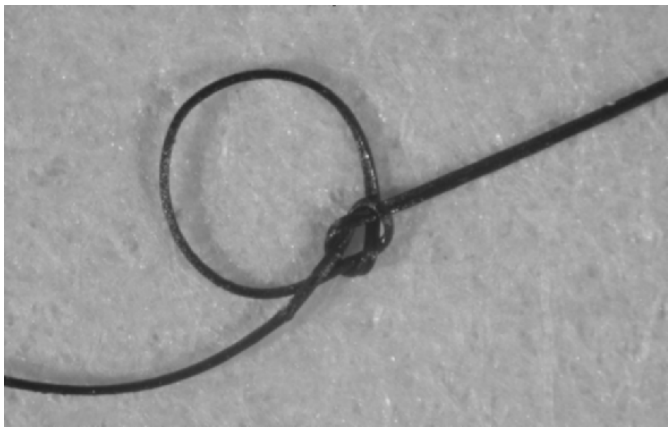


Fig. 7.25. Carbon nanotube fiber. The diameter of the fiber is about 30 microns. The fiber is flexible and can be strongly bent without breaking.

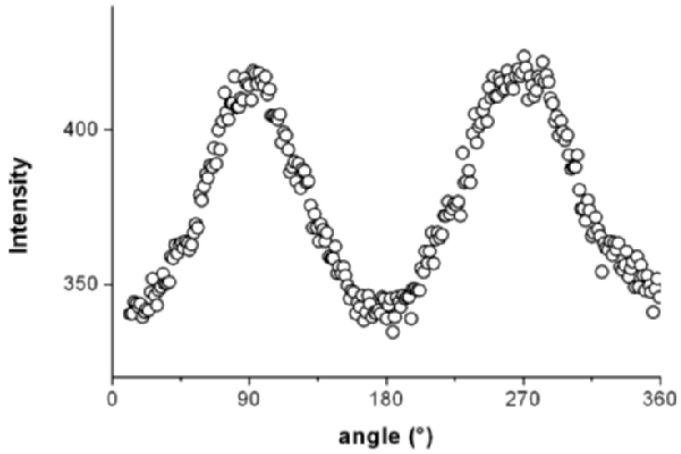


Fig. 7.26. X-ray scattering study of the orientation of the nanotubes along the axis of a fiber obtained by the particle coagulation spinning process described in [134]. The angular distribution of the scattered intensity from a nanotube fiber, at constant Q value of $0.4\,\text{Å}^{-1}$, which corresponds to the (1,0) peak position of nanotube hexagonal array, is reported. The width of the angular distribution measures the orientation of the nanotubes with respect to the fiber axis

thermogravimetric experiments [166]. Moreover, PVA can be completely removed by annealing the fibers at high temperature [156]. Nanotube alignment in electric arc nanotube fibers has been studied using X-ray scattering [156] and polarized Raman spectroscopy [162]. The FWHM within a Gaussian model is found to be $\approx 75 \pm 5^\circ$ using X-ray scattering (Fig. 7.26). It remains the same if PVA is burnt. Surprisingly, Raman measurements [162] indicate a much better alignment; this apparent discrepancy is under study. Note that X-ray scattering and Raman spectroscopy are used in a complementary manner in [158]. The value of FWHM, as determined by X-ray scattering, is strongly dependent upon the raw material used. FWHMs $\approx 45^\circ$ are found for fibers made from HiPco single-walled nanotubes [167].

Different hypotheses can be put forward to account for the better nanotube alignment in HiPco nanotube fibers. The lower amount of carbon impurities in the as-produced material is one of them [164]. Others include the shorter length of HiPco nanotubes and the fact that HiPco nanotubes may be less entangled.

A procedure has been recently developed to improve nanotube alignment in the fibers [135]. The fibers are rewetted, swollen in an appropriate solvent and redried vertically under tensile load, with a weight attached to their end. Even in a solvent in which the polymer is highly soluble, they do not disassemble (this amazing result is attributed to the fact that the networks of nanotubes and adsorbed polymers form cross-linked assemblies). Nevertheless, it was observed that a poor solvent, such as acetone, was necessary to make the

drawing more efficient. In pure water, sliding of polymers and nanotubes make the drawing less efficient to improve nanotube alignment. The fibers can be stretched up to ≈160%, the improvement of the nanotube alignment being significant: FWHMs, determined by X-ray scattering, are reduced by 40%, i.e. to about 45° for arc discharge nanotubes. FWHMs as low as 28° are reached for stretched fibers of HiPco nanotubes [168]. Dalton et al. [169] have used the same spinning process, including drawing in acetone, to make super tough fibers.

Mechanical measurements show that the mixed nanotube-PVA fibers exhibit an elastic behavior followed by a plastic regime before they break (when PVA is removed, the plastic regime disappears and the Young's modulus is slightly reduced). The Young's modulus of non-annealed fibers, deduced from the slope of the stress-strain curve, varies between 10 and 20 GPa for arc discharge nanotube raw fibers. It is one order of magnitude greater than the modulus of high-quality buckypaper [170]. After fiber stretching, Young's modulus can reach ≈40 GPa [135]. Globally, Young's modulus increases when the nanotube alignment improves. A similar trend was found for fibers made of HiPco single-walled nanotubes or of multiwalled nanotubes. Recently, Dalton et al., using the PCS process, have produced fibers that exhibit a mechanical strength of 1.8 GPa and a Young's modulus of about 80 GPa [169]. Energy-to-break is the most spectacular property of the obtained fibers. It reaches 570 J/g, about 17 times that of Kevlar fibers and 5 times that of spider dragline silk, the toughest fibers known so far.

More recently, Ericson et al. [171], using carbon nanotube dispersed in super-acids have produced macroscopic fibers composed solely of SWNTs. The nanotube dispersion was extruded through a small capillary tube into a coagulating bath which does not contain polymer as bridging agent. The solvents of the coagulating bath are chosen so that the nanotubes coagulate quickly. The obtained fibers are comprised of nanotubes and residual sulfuric acids. Because of initial doping and residual acids, such fibers exhibit a very low electrical conductivity of about 0.2 mΩ cm. Without any treatment and post-synthesis stretching fibers spun from super acids exhibit better alignment than fibers spun in polymeric solutions. The FWHMs is 31° with a an unaligned fraction of nanotubes less than 10%. Because of this good alignment, neat SWNT fibers already exhibit promising mechanical properties. Their Young's modulus is about 120 GPa, almost an order of magnitude larger than that of untreated composite fibers [134].

One should note that the modulus and strength of nanotube fibers are still far from those of individual nanotube bundles or from those of carbon fibers. Nevertheless, further improvements can be expected upon better alignment [172]. In principle, Young's modulus up to 700 GPa can be expected along with flexibility, high compression strength and toughness. A significant improvement of the mechanical properties is expected when the disorientation decreases below 20°. The alignment currently achieved is still too low to approach these expected properties. Nevertheless, with improvements of

a few degrees, the PCS process could soon lead to high performance fibers surpassing the best fibers already known.

Finally, we also note that the fibers produced by the PCS process can be used as electromechanical actuators [173, 174]. Stress generation and work per cycle are higher than that of bucky-paper [170]. The stress measured for nanotube fibers can reach 20 MPa, whereas it does not exceed 0.75 MPa for non aligned bucky-paper [170]. This significant improvement in aligned fibers shows again the interest of aligning carbon nanotubes for mechanical or electromechanical properties.

CVD Methods

As described in previous chapters, primary synthesis methods for producing carbon nanotubes include arc-discharge and chemical vapor deposition (CVD). These methods classically lead to the production of entangled and disoriented nanotubes. However, improved CVD methods have allowed the synthesis of large arrays of aligned nanotubes with controlled diameters and lengths. More recently, CVD methods have also been used to grow yarns of aligned nanotubes or to spin fibers from films of aligned nanotubes.

Zhu et al. [175] have optimized a floating catalyst method in a vertical furnace, where n-hexane is catalytically pyrolyzed. The n-hexane solution, which contains some amount of ferrocene and thiophene, was introduced into the reactor at a rate of 0.5 ml/min with hydrogen as the carrier gas flowing at a rate of 250 ml/min. Single-wall nanotubes formed during this continuous process with yields of ≈0.5 g/hour. The formation of very long SWNT strands is a unique characteristic of this vertical floating process.

The resultant strands generally have a diameter of ≈0.3 mm. Scanning electron microscopy images showed the preferential alignment of the tubes. Raman spectroscopy measurements suggest that both metallic and semiconducting single-walled nanotubes coexist with a wide distribution of diameters, ranging from 1.1 to 1.7 nm with a dominant diameter of 1.1 nm. Additional structural characterizations were achieved using X-ray diffraction [68]: the angular distribution is characterized by a FWHM ≈44°. This value is of the same order as that measured on raw HiPco nanotube fibers obtained by a spinning process, but it is larger than that of ≈30° obtained after fiber stretching [167].

The SWNT strands exhibit a metallic behavior above 90 K, with an electrical resistivity of about $7 \times 10^{-6}\,\Omega\,\mathrm{m}$ at room temperature. Such a low value of the resistivity suggests that there are macroscopic lengths of continuous conducting paths in the strands. Young's modulus was measured and found to range from 49 to 77 GPa [175]. This is far from the Young's modulus of individual nanotubes but among the best present results for fibers or ribbons of aligned nanotubes. The synthesis of nanotubes strands by this improved CVD method leads to promising materials with high electrical conductivity and reasonable mechanical strength.

More spectacular results have been even recently obtained by Li et al. [176]. The authors have developed a direct and continuous spinning of nanotube

fibers from a CVD process. By mechanically drawing the carbon nanotubes from the gaseous reaction zone, the authors have found it possible to wind up continuous fibers without apparent limit to the length. Ethanol was selected as the carbon source, in which small fractions of ferrocene and thiophene were dissolved. The solution was injected from the top of the furnace into a hydrogen carrier gas flow. The obtained nanotubes formed an aerogel which was stretched by the gas flow and drawn by winding it onto a rotating rod. Fibers of SWNTs or MWNTs could be spun by varying the reaction conditions. Exceptionally high alignment could be obtained by this process. The FWHM was only 11° for MWNT fibers. As a consequence, these fibers exhibit promising electrical and mechanical properties. The lowest electrical resistivity measured along a fiber was about $10^{-6}\,\Omega$m. Preliminary mechanical measurements indicated that the strength of the fibers could reach 1 GPa and that the strain to failure could exceed 100%.

Jiang et al. [177] have shown that carbon nanotubes can be self-assembled into yarns of up to 30 cm in length simply by drawing out from aligned arrays of carbon nanotubes. While pulling out carbon nanotubes from an array several hundred micrometers high and grown on a silicon substrate, the authors obtained a continuous yarn of pure nanotubes. They estimate that an array of about $1\,\text{cm}^2$ can generate about 10 m of yarn. The authors could make optical polarizers by parallel alignment of their nanotube yarns. When a beam of light passes through the nanotube polarizer, photons having a polarization direction parallel to the axis of the tubes are absorbed, whereas those that are perpendicularly polarized are transmitted. The authors have also submitted their fibers to a strong voltage under vacuum. After 3 h at 70 V, the conductivity of the filament slightly increases and the yarn tensile strength changes from 1 to 6.4 mN (in force unit, as expressed in the text, probably because CNT yarn section cannot be determined with precision). These results indicate that some welding effect may occur at the weak connection points, because these points have a higher resistivity and, as a result, a higher temperature when a current is applied. It seems thus that the properties of the fibers can be improved using this method. Nevertheless, the comparison with the properties of other materials remains difficult because the data reported by Jiang et al. are not normalized with respect to the mass or section of the fibers.

Zhang et al. also recently used nanotubes grown on a substrate to produce spectacular yarns [178]. The authors by introducing twist during spinning of nanotube from MWNT forests to make multi-ply, torque stabilized yarns, achieved yarn strengths greater than 460 MPa. These yarns are nearly as tough as fibers used for bulletproof vests. In addition, they exhibit a high electrical conductivity. The unique combination of good electrical and mechanical properties make these fibers ideal candidates for the fabrication of multifunctional textiles. They could provide functionalities such as the ability to actuate as an artificial muscle and to store energy as a fiber supercapacitor or battery.

Electrophoretic Spinning

Gommans et al. [160] have developed a method for making fibers of SWNTs possessing substantial alignment along the fiber axis. The first step of the method consists in dispersing nanotubes in N,N-dimethylformamide. A commercially available carbon fiber is attached to a conducting wire coupled to a motor-driven translation stage. The carbon fiber is translated along its axis down in the nanotube suspension to a depth of few millimeters. The set-up is designed so that a voltage can be applied between the carbon fiber and the suspension. When a voltage is applied with the carbon fiber as the positive electrode, the nanotubes are attracted and form a cloud around the carbon fiber. Then the carbon fiber is slowly withdrawn from the suspension. As it pulls out of the liquid, another fiber, attached to its end, forms spontaneously from the nanotube cloud. The formation of a SWNT cloud around a positive electrode indicates that nanotubes are negatively charged when dispersed in N,N-dimethylformamide; they migrate electrophoretically towards the positively charged carbon fiber. The fibers are several centimeters long and their diameters typically range between 2 and 10 microns depending on the preparation conditions. Selected area electron diffraction has been used to characterize the structure of the fiber edges. The results qualitatively suggest a substantial alignment of the nanotubes along the fiber axis. More detailed analysis has been achieved using polarized Raman spectroscopy by Gommans et al. and Hwang et al. [160, 161]. The authors have developed a model to interpret the change of the Raman intensities depending on polarization by considering that absorption phenomena induce an angle-dependent resonance enhancement. The intensities have been fitted within a Lorentzian model for the distribution of nanotubes orientations. The FWHM of the distribution was found to be 23°, showing a rather good alignment of nanotubes. The mechanical, electrical and thermal properties of these fibers are still to be analyzed.

Conclusion

Great progress has been recently made in making macroscopic assemblies of aligned nanotubes. Substantial alignments can now be obtained in single-walled and multiwalled nanotube fibers. The obtained materials exhibit anisotropic optical, mechanical, electrical and thermal properties. Even though significant improvements are still expected, their mechanical and electromechanical properties are already promising. Alignment of nanotubes on a macroscopic scale remains of critical importance for the deeper characterization and understanding of their fundamental mechanical properties. It is also of great interest for making materials with improved properties that may find use in industrial applications. In this respect, we underline that spinning processes and CVD methods developed to produce nanotubes fibers could be scaled up for large-scale production.

Acknowledgments

J.P.S. is indebted to P. Lambin for fruitful discussion, critical reading and providing original results to this chapter. G.D. thanks L. Vaccarini, A. Foutel-Richard and A. Mavel for their contribution. We also thank C. Ewels for his help.

References

1. L.E. Nielsen, R.F. Landel: *Mechanical Properties of Polymers and Composites*, 2nd edn (Marcel Dekker, 1994)
2. G.M. Swallowe (ed.): *Mechanical Properties and Testing of Polymers, an A–Z reference* (Kluwer Academic Publishers, 1999)
3. R. Schaller, G. Fantozzi, G. Gremaud (ed.): *Mechanical Spectroscopy Q-1 2001 with applications to Materials Science* (Trans Tech Publications, Switzerland 2001)
4. D. Hull: *An Introduction to Composite Materials* (Cambridge University Press, Cambridge 1981)
5. L.R.G. Treloar: *The Physics of Rubber Elasticity* (Clarendon press, Oxford 1976)
6. R.M. Christensen: *Theory of Viscoelasticity* (Academic Press, New York 1971)
7. R.S. Lakes: *Viscoelastic Solids* (CRC Press, NY 1999)
8. C. Zener: *Elasticity and Anelasticity of Metals* (University of Chicago Press, IL 1948)
9. R. De Batist: *Internal Friction of Structural Defects in Crystalline Solids* (North Holland, Amsterdam 1972)
10. I.M. Ward, D.W. Hadley: *An Introduction to the Mechanical Properties of Solid Polymers* (Wiley, N.Y. 1993)
11. J. Perez: *Physics and Mechanics of Amorphous Polymers* (A.A. Balkema, Rotterdam Brookfield 1998)
12. J.D. Ferry: *Viscoelastic Properties of Polymers* (Wiley, New York 1980)
13. C.A. Angell, K.L. Ngai, G.B. McKenna, P.F. McMillan, S.W. Martin: J. App. Phys. **88** (2000)
14. P.G. de Gennes: *Scaling Concepts in Polymer Physics* (Cornell University Press, Ithaca 1979)
15. C. Gauthier, A. Bonnet, R. Gaertner, H. Sautereau: Polym. Int. **53** (2004)
16. L. David, R. Quinson, C. Gauthier, J. Perez: Polymer Engineering and Science **37**, 1633 (1997)
17. J.A. Roetling: Polymer **6**, 311 (1965)
18. R.E. Robertson: J. Chem. Phys. **6**, 3950 (1966)
19. A.S. Argon: Phil. Mag. **28**, 839 (1973)
20. P.B. Bowden, S. Raha: Phil. Mag. **21**, 149 (1975)
21. P.B. Bowden, S. Raha: J. Mater. Sci. **7**, 52 (1972)
22. C. G'Sell, J.J. Jonas: J. Mat. Sci. **16**, 1956 (1981)
23. J.M. Lefebvre, B. Escaig: J. Mat. Sci. **20**, 438 (1985)
24. J.M.C. Li and J.J. Gilman: J. Appl. Phys. **11**, 42–48 (1970)
25. M.B.M. Mangion, J.Y. Cavaillé, J. Perez: Phil. Mag. **66**, 773 (1992)

26. A. Peterlin: J. Mat. Sci. **6**, 490 (1971)
27. I.M. Ward: J. Mater. Sci. **6**, 1397 (1971)
28. J.M. Haudin: *Plastic Deformation of amorphous and semi-crystalline materials*, ed by B. Escaig and C. Gosell (Les Editions de Physique, Les Ulis 1982)
29. B.I. Yakobson, C.J. Brabec, and J. Bernholc: Phys. Rev. Lett. **76**, 2511 (1996)
30. Zhou Xin, Zhou Jianjun, Ou-Yang Zhong-can: Phys. Rev. B **62**, 13692 (2000)
31. Zhan-chun Tu, Zhong-can Ou-Yang: Phys. Rev. B **65**, 233407 (2002)
32. R.S. Ruoff and D.C. Lorentz: Carbon **33**, 925 (1995)
33. J.P. Lu: J. Phys. Chem. Solids **58**, 1649 (1997)
34. D. Sánchez-Portal, E. Artacho, J.M. Soler, A. Rubio, P. Orderón: Phys. Rev. B **59**, 12678 (1999)
35. G. Van Lier, C. Van Alsenoy, V. Van Doren, P. Geerling: Chem. Phys. Lett. **326**, 181 (2000)
36. G.M. Odegard, T.S. Gates, L.M. Nicholson, K.E. Wise: Composites Science and Technology **62**, 1869 (2002)
37. V.M. Harik: Comp. Mat. Science **24**, 328 (2002)
38. M. Arroyo, T. Belytschko: J. Meca. Phys. Solids **50**, 1941 (2002)
39. P. Zhang, Y. Huang, P.H. Geubelle, P.A. Klein, K.C. Hwang: Int. J. Sol. Struct. **39**, 3893 (2002)
40. C. Li, T.-W. Chou: Int. J. Sol. Struct. **40**, 2487 (2003)
41. L. Landau, E.M. Lifshitz: *Theory of Elasticity*, 3rd ed. (Pergamon, Oxford 1986)
42. S.P. Timoshenko, J.M. Gere: *Mechanics of Materials*, (Van Nostrand Reinhold Company, 1972)
43. A.A. Lucas, P.H. Lambin, R.E. Smalley: J. Phys. Chem. Solids **54**, 587 (1993)
44. D.H. Robertson, D.W. Brenner, J.W. Mintmire: Phys. Rev. B **45**, 12592 (1992)
45. E. Hernández, C. Goze, P. Bernier, A. Rubio: Phys. Rev. Lett. **80**, 4502 (1998)
46. V.N. Popov, V.E. Van Doren, M. Balkanski: Phys. Rev. B **61**, 3078 (2000)
47. D.J. Srolovitz, S.A. Safran, R. Tenne: Phys. Rev. E **49**, 5260 (1994)
48. V.N. Popov, V.E. Van Doren, M. Balkansk: Solid State Comm. **114**, 395 (2000)
49. E. Saether, S.J.V. Frankland, R. Byron Pipes: Composites Science and Technology **63**, 1543 (2003)
50. T. Chang, H. Gao: J. Mech. Phys. Solids **51**, 1059 (2003)
51. S. Zhang, S. Zhao, J. Lü, M. Xia: Phys. Rev. B **61**, 12693 (2000)
52. T. Ozaki, Y. Iwaza, T. Mitani: Phys. Rev. Lett. **84**, 1712 (2000)
53. T. Xiao, K. Liao: Phys. Rev. B **66**, 153407 (2002)
54. K. Shintani, T. Narita: Surface Science, **532–535**, 862 (2003)
55. S. Iijima, C. Brabec, A. Maiti, J. Bernholc: J. Chem. Phys. **104**, 2089 (1996)
56. E.W. Wong, P.E. Sheehan, C.M. Lieber: Science **277**, 1971 (1997)
57. M.R. Falvo, G.J. Clary, R.M. Taylor II, V. Chi, F.P. Brooks Jr, S. Washburn, R. Superfine: Nature **389**, 582 (1997)
58. T. Belytschko, S.P. Xiao, G.C. Schatz, R.S. Ruoff: Phys. Rev. B **65**, 235430 (2002)
59. S. Ogata, Y. Shibutani: Phys. Rev. B **68**, 165409 (2003)
60. T. Dumitrică, T. Belytschko, B.I. Yakobson: J. Chem. Phys. **118**, 9485 (2003)
61. P. Lauginie, J. Conard: J. Phys. Chem. Solids **58**, 1949 (1997)
62. B.I. Yakobson: Appl. Phys. Lett **72**, 918 (1998)
63. M.B. Nardelli, B.I. Yakobson, J. Bernholc: Phys. Rev. B **57**, R4277 (1998)
64. M.B. Nardelli, B.I. Yakobson, J. Bernholc: Phys. Rev. Lett. **81**, 4656 (1998)

65. P. Jensen, J. Gale, X. Blase: Phys. Rev. B **66**, 193403 (2002)
66. C.P. Ewels, M.I. Heggie, P.R. Briddon: Chem. Phys. Lett. **351**, 178 (2002)
67. N. Bernstein, D.W. Hess: Phys. Rev. Lett. **91**, 025501 (2003)
68. C. Wei, K. Cho, D. Srivastava: Phys. Rev. B **67**, 115407 (2003)
69. D. Bozovic, M. Bockrath, J.H. Hafner, C.M. Lieber, H. Park, M. Tinkham: Phys. Rev. B **67**, 033407 (2003)
70. J.R. Neighbours, G.A. Alers: Phys. Rev. **111**, 707 (1958); F.H. Featherston, J.R. Neighbours, Phys. Rev. **130**, 1324 (1963)
71. M. Schanz, H. Antes: Electronic Journal of Boundary Elements, **BETEQ 2001**, 348 (2002)
72. M.M.J. Treacy, T.W. Ebbesen, J.M. Gibson: Nature **381**, 678 (1996)
73. S. Frank, P. Poncharal, Z.L. Wang, W.A. de Heer: Science **280**, 1744 (1998); Z.L. Wang, R.P. Gao, P. Poncharal, W.A. de Heer, Z.R. Dai, Z.W. Pan: Mat. Sc. and Eng. C **16**, 3 (2001)
74. S.T. Purcell, P. Vincent, C. Journet, Vu Thien Binh: Phys. Rev. Lett. **89**, 276103 (2002)
75. N.A. Burnham, X. Chen, C.S. Hodges, G.A. Matei, E.J. Thoreson, C.J. Roberts, M.C. Davies, S.J.B. Tendler: Nanotechnology **14**, 1 (2003)
76. R. Lévy and M. Maaloum: Nanotechnology **13**, 33 (2002)
77. P.A. Williams, S.J. Papadakis, A.M. Patel, M.R. Falvo, S. Washburn, R. Superfine: Phys. Rev. Lett. **89**, 255502 (2002)
78. E. Wong, P.E. Sheehan, C.M. Lieber: Science **277**, 1971 (1997)
79. J.P. Salvetat, A.J. Kulik, J.M. Bonard et al: Adv. Mater. **11**, 161 (1999)
80. J.P. Salvetat, G.A.D. Briggs, J.M. Bonard et al: Phys. Rev. Lett. **82**, 944 (1999)
81. Min-Feng Yu, O. Lourie, M.J. Dyer, K. Moloni, T.F. Kelly, R.S. Ruoff: Science **287**, 637 (2000)
82. Min-Feng Yu, B.S. Files, S. Arepalli, R.S. Ruoff: Phys. Rev. Lett. **84**, 5552 (2000)
83. A. Kis, G. Csányi, J.-P. Salvetat, Thien-Nga Lee, E. Couteau, A.J. Kulik, W. Benoit, J. Brugger, L.Forró: Nature Materials **3**, 153 (2004)
84. R. Daviaud, C. Filliatre: *Introduction aux matériaux composites* (Ed. CNRS, 1985)
85. J.M. Berthelot: *Matériaux composites, comportement mécanique et analyse des structures* (Masson, 1992)
86. A. Einstein: Annalen der Physik **19**, 289 (1906)
87. M. Sumita, T. Shizuma, K. Miyasaka, K. Ishikawa: Macromol. Sci.- Phys. **22**, 601 (1983)
88. M. Shaterzadeh-Yazdi: Etude et Modélisation physique et mécanique du comportement viscoélastique et plastique de composites particulaires à matrice polymère, PhD Thesis, INSA-Lyon, Lyon (1997)
89. S. Ahmed, F.R. Jones: J. Mater. Sci. **25**, 4933 (1990)
90. J. Aboudi: *Mechanics of Composite Materials: a unified Micromechanical Approach* (Elsevier, Amsterdam 1991)
91. Z. Hashin: J. Appl. Mech. **50**, 481 (1983)
92. Z. Hashin, S.J. Shtrikman: Mech. Phys. Solids **11**, 127 (1963)
93. E. Hervé, A. Zaoui: Int. J. Engin. Sci. **31**, 1 (1993); M. Bornert, E. Hervé, C. Stoltz, A. Zaoui: Appl. Mech. Rev. **47**, 1 (1994)
94. M. Takayanagi, S. Uemura, S. Minami: J. Polym. Sci.: Part C **5**, 113 (1964)

95. N. Ouali, J.-Y. Cavaillé, J. Perez: Plast. Rubber and Compos. Process. Appl. **16**, 55 (1991)
96. J.M. Whitney and R.L. McCullough: *Micromechanical Materials Modeling* (Technomic Publishing Co., Lancaster USA 1990)
97. R.M. Christensen, K.H. Lo: J. Mech. Phys. Solids **27**, 315 (1979)
98. S. Van Es: Polymer – Clay Nanocomposites: the importance of particle dimensions. PhD Thesis, Technische Universiteit, Delft (2001)
99. G.P. Tandon, G.J. Weng: Polymer Composites **5**, 327 (1984)
100. J.C. Halpin, S.W. Tsai: AFML-TR **67**, 423 (1969)
101. J.C. Halpin, J.L. Kardos: J. Appl. Phys. **43**, 2235 (1972)
102. P. Hajji, C. Gauthier: Proc. Eurofillers (Lyon, France, September 1999)
103. E.P. Giannelis: Adv. Mater. **8**, 29 (1996)
104. L. Chazeau, C. Gauthier, G. Vigier, J.Y. Cavaillé: in *Handbook of Organic-Inorganic Hybrids Materials and nanocomposites*, ed by H.S. Nalwa (American Scientific Publishers, 2003)
105. A. Okada, M. Kawasumi, A. Usuki, Y. Kojima, T. Kurauchi, O. Kamigaito: Mater. Res. Soc. Proc. **171**, 45 (1990)
106. P. Hajji, L. David, J.F. Gerard, J.P. Pascault, G. Vigier: J. Polym. Sci., part B: Polym. Phys. **37**, 3172 (1999)
107. V. Favier: Etude de nouveaux matériaux composites obtenus à partir de latex filmogènes et de whiskers de cellulose: effets de percolation mécanique. PhD Thesis, INPG, Grenoble (1995)
108. J.C. Daniel: Macromol. Chem Symp. 10/11, 359 (1985)
109. P. Richard, T. Prasse, J.-Y. Cavaillé, L. Chazeau, C. Gauthier, J. Duchet: Materials Science and Engineering A **352**, 344 (2003)
110. T.J. Pinnavaia, G.W. Beall (eds): *Polymer-Clay Nanocomposites* (Wiley, Chichester 2000)
111. J.R. Harbour, M.J. Walzak, W. Limburg, J. Yanus: Carbon **24**, 725 (1986)
112. C. Bonini, L. Heux, J.Y. Cavaillé: Proc. MRS Meeting (San Fransisco, April 2002)
113. E.P. Giannelis, R. Krishnamoorti, E. Manias: Ad. Polym. Sci. **138**, 107 (1999)
114. P.C. LeBaron, Z. Wang, T.J. Pinnavaia: Applied Clay Science **15**, 11 (1999)
115. G. Lagaly: Appl. Clay. Sci. **15**, 1 (1999)
116. J. Ramier, C. Gauthier, L. Chazeau, L. Ladouce, L. David, R. Vassoille: Euro-Fillers 01 Conference (Lodz, Poland, 9–12 July 2001)
117. L. Chazeau, J.Y. Cavaillé, G. Canova, R. Dendievel, B. Boutherin: J. Appl. Polym. Sci. **71**, 1797 (1999)
118. P. Terech, L. Chazeau, J.Y. Cavaillé: Macromolecules **32**, 1872 (1999)
119. Y. Bréchet, J.-Y. Cavaillé, E. Chabert, L. Chazeau, R. Dendievel, L. Flandin, C. Gauthier: Adv. Eng. Mat. **3**, 8 (2001)
120. H.L. Cox: British journal of applied Physics **3**, 72 (1952)
121. J.L. Bahr, E.T. Mickelson, M.J. Bronikowski, R.E. Smalley, J.M. Tour: Chem. Commun., 193–194 (2001).
122. R. Bandyopadhyaya, E. Nativ-Roth, O. Regev, R. Yerushalmi-Rozen: Nanoletters 2002 **2**, 25 (2002)
123. Y. Breton: PhD Thesis, Orléans University, Orléans 2002.
124. L. Vaccarini: PhD Thesis, Montpellier II University, Montpellier France 2000.
125. J.L. Loubet, J.M. Georges, G. Meille: in *Microindentation Technics in materials science and Engineering (ASTM STP 889)*, ed by P.J. Blau, and B.R. Lawn (American Society for Testing and Materials, Philadelphia (PA) 1985)

126. L. Vaccarini, G. Désarmot, R. Almairac, S. Tahir, C. Goze, P. Bernier: *Proceedings of the XIV International Winterschool, Kirchberg, Tyrol* (AIP Conference Proceedings 2000) pp 521–525
127. S. Kruch, unpublished results
128. N. Marzani, M. Ferrari: Journal of Applied Mechanics **59**, 269 (1992)
129. G.M. Odegard, T.S. Gates, K.E. Wise, C. Park and E.J. Siochi: NASA/CR-2002-211760, ICASE Report, 2002.
130. O. Lourie, H.D. Wagner: Appl. Phys. Lett. **73**, 3527 (1998).
131. P.H. Lin, C.R. Lin, K.H. Chen, L.C. Chen: International Journal of Modern Physics B **16**, 853 (2002)
132. M. Mayne, N. Grobert, M. Terrones et al: Chemical Physics Letters **338**, 101 (2001)
133. B. Wei, R. Vajtai, Y.Y. Choi et al: Nano Letters **2**, 1105 (2002)
134. B. Vigolo, A. Pénicaud, C. Coulon et al: Science **290**, 1331 (2000)
135. B. Vigolo, P. Poulin, M. Lucas, P. Launois, P. Bernier: Applied Physics Letters **81**, 1210 (2002)
136. S. Kumar, H. Doshi, M. Srinivasarao, J.O. Park, and D.A. Schiraldi: Polymer **43**, 1701 (2002)
137. R. Andrews, D. Jacques, A.M. Rao, T. Rantell, F. Derbyshire, Y. Chen, J. Chen, and R. Haddon: Appl. Phys. Lett. **75**, 1329 (1999)
138. A. Foutel-Richard: Thesis, Conservatoire National des Arts et Métiers, Paris (2003)
139. P. Launois, P. Poulin: Encyclopedia of Nanoscience and Nanotechnology **4**, 1 (2004)
140. V.M.K. Bagsi, O. Golseren, T. Yildirim, Z. Gedik, S. Ciraci: Phys. Rev. B **66**, 045409 (2002)
141. Y. Zhang, N.W. Franklin, R.J. Chen, H. Dai: Chem. Phys. Lett. **331**, 35 (2000)
142. X.H. Chen, F.Q. Cheng, S.L. Li, L.P. Zhou, D.Y. Li: Surface and Coatings Technology **155**, 274 (2002)
143. X. Chen, J. Xia, J. Peng, W. Li, S. Xie: Comp. Sci. and Technology **60**, 301 (2000)
144. W.X. Chen, J.P. Tu, L.Y. Wang, H.Y. Gan, Z.D.Xu, X.B. Zhang: Carbon **41** 215 (2003)
145. C.L. Xu, B.Q. Wei, R.Z. Ma, J. Liang, X.K. Ma, D.H. Wu: Carbon **37**, 855 (1999)
146. L. Lü, M.O. Lai (Kluwer Academic Publishers, Boston 1997)
147. M.S. El-Eskandarany: *Mechanical Alloying: for Fabrication of Advanced Engineering Materials* (Noyes Publications, 2001)
148. S. Paris, F. Bernard, E. Gaffet, Z. Munir: Matériaux 2002, 21–25 October 2002, Tours
149. R.W. Siegel, S.K. Chang, B.J. Ash et al: Scripta Materialia **44**, 2061 (2001)
150. G-D. Zhan, J.D. Kuntz, J. Wan, A.K. Mukherjee: Nature Materials **2**, 38 (2003)
151. J.D. Wright, A.J.M. Som merdijk: (Gordon and Breach Publishers 2001)
152. N.Y. Turova, E.P. Turevskaya, V.G. Kessler, M. Yanovskaya: *The Chemistry of Metal Alkoxides* (Kluwer Academic Publishers, 2002)
153. L. Sheppard: GB-114U Business Communications Company, Inc., July 2002.
154. E.T. Thostenson, W.Z. Li, D.Z. Wang, Z.F. Ren, T.W. Chou: J. of Appl. Phys. **91**, 6034 (2002)
155. F-H. Leroy: PhD Thesis, Bordeaux I University, Bordeaux (1996)

156. P. Launois, A. Marucci, B. Vigolo, P. Bernier, A. Derré and P. Poulin: Journal of Nanoscience and Nanotechnology **1**, 125 (2001)
157. J.E. Fisher, W. Zhou, J. Vavro et al: J. Appl. Phys. **93**, 2157 (2003)
158. W. Zhou, J. Vavro, C. Guthy et al: J. Appl. Phys. **95**, 649 (2004)
159. P. Launois, private communication
160. H.H. Gommans, J.W. Alldredge, H. Tashiro, J. Park, J. Magnuson, A.G. Rinzler: Journal of Applied Physics **88**, 2509 (2000)
161. J. Hwang, H.H. Gommans, A. Ugawa et al: Phys. Rev. B **62**, R13310 (2000)
162. E. Anglaret, A. Righi, J.L. Sauvajol, P. Bernier, B. Vigolo, P. Poulin: Phys. Rev. B **65**, 165426 (2002)
163. D.H. Everett: *Basic principles of colloid science* (Royal Society of Chemistry, London 1988) pp 138, 139, 191–201
164. P. Nikolaev, M.J. Bronikowski, R.K. Bradley et al: Chem. Phys. Lett. **313**, 91 (1999)
165. S. Delpeux, K. Szostak, E. Frackowiak, S. Bonnamy, F. Béguin: J. Nanosci. Nanotechnol. **2**, 481 (2002)
166. A. Derré, S. Badaire: unpublished results
167. M. Lucas, B. Vigolo, S. Badaire et al: AIP Conf. Proc. **633**, 579 (2002)
168. V. Pichot, S. Badaire, P. Launois, P. Poulin, C. Zakri, M. Maugey: to be published.
169. A.B. Dalton, S. Collins, E. Munoz et al: Nature **423**, 703 (2003)
170. R.H. Baughman, C. Cui, A.A. Zakhidov et al: Science **284**, 1340 (1999)
171. L.M. Ericson, H. Fan, H. Peng et al: Science **305**, 1447 (2004)
172. T. Liu, S. Kumar: Nanoletters **3**, 647 (2003)
173. B. Vigolo, P. Launois, M. Lucas, S. Badaire, P. Bernier, P. Poulin: Mater. Res. Soc. Symp. Proc. **706**, Z1.4.2 (2002)
174. R.H. Baughman, A. Zakhidov, W.A. de Heer: Science **297**, 791 (2002)
175. H.W. Zhu, C.L. Xu, D.H. Wu, B.Q. Wei, R. Vatjai, P.M. Ajayan: Science **296**, 884 (2002)
176. Y. Li, I. A. Kinloch, A. H. Windle: Science **304**, 276 (2004)
177. K. Jiang, Q. Li, S. Fan: Nature **419**, 801 (2002)
178. M. Zhang, K.R. Atkinson, R.H. Baughman: Science **306**, 1358 (2004)

8

Surface Properties, Porosity, Chemical and Electrochemical Applications

F. Béguin, E. Flahaut, A. Linares-Solano and J. Pinson

Abstract. Since their discovery, carbon nanotubes have been proposed for a number of applications, such as gas storage, reinforcement of composites, electrochemical energy storage, catalyst support, where the nanotexture and surface functionality are of fundamental importance. With regard to surface properties, this new form of carbon is not significantly different from the other classical carbon forms (carbon fibers, pyrolytic carbon, graphite, activated carbons, ...) which are also constituted of graphitic carbon layers. Therefore, this chapter aims in its first part at presenting the porous properties and surface functionality of carbon materials and the techniques to control or modify these parameters. However, due to their nanoscale size morphology and inner cavity which can host various species, carbon nanotubes are expected to present specific properties. Mats of highly entangled nanotubes offer an open network of mesopores which favors the access of molecules and ions to the active surface. The second part of this chapter will be focused on the presentation of some specific chemical and electrochemical properties of carbon nanotubes. Filling of nanotubes and in-situ chemistry in the cavity will be documented. Application of carbon nanotubes as lithium battery or supercapacitor electrode materials will be critically discussed by comparison with other kinds of nanostructured carbons.

8.1 Surface Area, Porosity and Reactivity of Porous Carbons

The porous properties of any of the graphite-related materials, including carbon nanotubes, are principally governed by their texture, i.e. the mode and degree of preferred orientation of anisotropic hexagonal carbon layers [1]. Therefore the correct characterization of nanotubes, in term of surface area, porosity and reactivity, fits among other carbon materials. This part, starting with the physical adsorption (physisorption) of gases as a tool to characterize any type of porous carbon, is followed by the analysis of some of the most frequently used adsorption equations, as well as by comments about suitable adsorptives to be used for characterizing microporous carbons. The chemical activation by hydroxides is also included as an example of carbon reactivity.

F. Béguin et al.: *Surface Properties, Porosity, Chemical and Electrochemical Applications*, Lect. Notes Phys. **677**, 495–549 (2006)
www.springerlink.com
© Springer-Verlag Berlin Heidelberg 2006

8.1.1 Physical Adsorption of Gases as a Tool to Characterize Porous Carbons

The carbons involved in many industrial applications present various forms ranging from well-developed crystalline structures, such as graphite and diamond, to other less ordered varieties such as carbon fibers, nanotubes, carbon blacks, cokes, chars, activated carbons, ... [1]. The porous texture of any type of carbon has an immediate relevance (positive or negative) on reactivity and on most of their applications. Therefore knowledge about their porosity, pore size distribution and surface area is essential. A convenient classification of pores according to their average diameter is recommended by the International Union of Pure and Applied Chemistry (IUPAC) [2]:

- micropores, size less than 2 nm
- mesopores, size between 2 nm and 50 nm
- macropores, size more than 50 nm

Because of the various physical forms of carbon, the characterization of porous carbon is complex and, in almost all cases, a combination of methods is necessary. A wide range of pores needs to be covered, from those with visible dimensions – gross cracks – to those with widths of molecular dimensions – micropores – with an interconnected aperture-cavity pore system with pore entrances which are smaller than the pores. There are numerous techniques and methods for analyzing the pore texture and internal surface area, such as microscopy, immersion calorimetry, small angle X-ray and neutron scattering, wide angle scattering, TEM, SEM and STM, mercury porosimetry, adsorption of liquids, vapors and gases. Among them, mercury porosimetry and physical adsorption measurements are the most widely used to obtain a good description of the texture of a porous carbon [3–6]. In a first step, we will give a summary of the essential theoretical background. Thus, the methods mostly used in the characterization of porous carbon solids by physical adsorption techniques (surface area, pore volume and pore size distribution) will be discussed aiming at recognizing their principles, applications and limitations. Special attention will be paid to microporous carbons because the presence of micropores makes the interpretation of gas adsorption data difficult [7–11]. For those requiring further information about the use of physical gas adsorption to characterize porous solids, all the above cited references (and their corresponding literature) should be consulted.

Gas-Solid Interactions

When a gas or vapor (the adsorptive) is confined in a closed space, at a given pressure and temperature, in the presence of an outgassed solid (the adsorbent), an adsorption process begins. The adsorptive molecules are transferred to, and accumulated in, the interfacial layer, as a consequence of an attractive force between the absorbent surface and the adsorptive. In general, two types

of adsorption are distinguished: physisorption and chemisorption [4, 12, 13]. Henceforth we will be concerned mainly with physisorption, that is with systems in which specific chemical interactions between adsorbent and adsorptive are absent, or almost so. Physisorption includes attractive dispersion forces and, at very short distances, repulsive forces, as well as contributions from polarisation and electrostatic forces between permanent electrical moments and the electric field of the solid, if the adsorptive or the adsorbent has a polar nature. Depending on the nature of the molecule and the solid, specific interactions may contribute to the adsorption energy. The overall interaction energy (ϕ_{T}) for a polar adsorbate molecule on a heteropolar surface is given by the equation

$$\phi_{\mathrm{T}} = \phi_{\mathrm{D}} + \phi_{\mathrm{P}} + \phi_{\mathrm{F}} + \phi_{\mathrm{FQ}} + \phi_{\mathrm{R}} \tag{8.1}$$

where

- ϕ_{D} = energy due to dispersion forces
- ϕ_{P} = energy due to polar nature of adsorbent and/or adsorptive
- ϕ_{F} and ϕ_{FQ} = energy due to permanent dipole and quadrupole moments of the adsorptive molecule, respectively
- ϕ_{R} = energy due to repulsion forces

The terms ϕ_{D} and ϕ_{R} are the non-specific contributions which are always present in a physisorption process, whereas the other terms provide specific contribution which may contribute to the overall adsorption energy according to the polar nature of the molecule and the adsorbent. When adsorption on a microporous carbon is considered, the potential energy of adsorption is noticeably enhanced. These specific adsorbate-adsorbent interactions, with microporous carbons, will be dealt with later on.

Adsorption-Desorption Isotherms

The adsorption of a gas or vapor by a solid, among other things, gives important informations about the solid under study (porous texture, surface area, adsorbent-adsorbate interaction energy, ...). Many different procedures have been developed to measure the amount of gas adsorbed on a conveniently outgassed adsorbent. Those which involve the measurement of the amount of gas leaving the gas phase, as occurs in a volumetric system, and those which involve the measurement of the uptake of the gas by the adsorbent, as occurs in a gravimetric system, are in practice the most extensively used procedures [14,15]. The amount of gas adsorbed (n) on the surface of the solid is a function of the mass of the adsorbent, the pressure (P), the temperature (T) and the nature of the gas and of the solid surface.

$$n = f(P, T, gas, solid) \tag{8.2}$$

n may be expressed in different units (moles, grams, cubic centimeters at Standard Temperature and Pressure – STP, or liquid volume). However, recommendations have been made to express it as moles per gram of outgassed

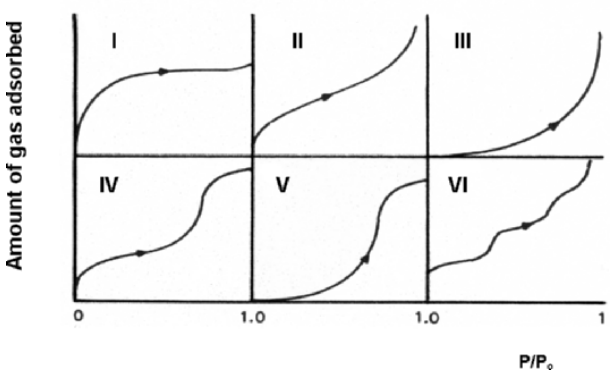


Fig. 8.1. Types of adsorption isotherms. Redrawn from [4]

solid. If pressure and temperature are kept constant, for a given adsorbent-adsorbate system

$$n = f(P)_{T,gas,solid} \tag{8.3}$$

The amount of gas adsorbed at equilibrium is only a function of pressure. The representation of the amount adsorbed versus equilibrium pressure (or relative pressure P/P_0, where P_0 is the saturation vapor pressure at the adsorption temperature) gives the adsorption isotherm. The different types of carbon materials, and the large family of possible adsorptives, give rise to six physical adsorption isotherm groups which often are mixed because different types of pores are present. These adsorption isotherms are schematically represented in Fig. 8.1.

- Type I isotherms are characteristic of microporous carbons. They are widespread (i.e., most gases and vapors on activated carbons)
- Type II isotherms are observed for macroporous and non-porous carbons (i.e., N_2 at 77 K on graphite, nanotubes and carbon blacks)
- Type III isotherms are characteristic of very weak adsorbate-adsorbent interaction and are typical of cooperative adsorption (i.e., adsorption of water vapor on graphitized carbon blacks)
- Type IV isotherms resemble isotherms of type II and are characteristic of carbons which possess a wide proportion of mesopores (i.e., compacted carbon blacks under pressure)
- Type V isotherms are also characteristic of weak adsorbate-adsorbent interactions (i.e., water vapor adsorption on charcoal)
- Type VI isotherms are typical of carbon having a very uniform non-porous surface. Each step represents an adsorbed monolayer (i.e., noble gas adsorption on graphitized carbon blacks)

If the adsorption and desorption branches do not coincide over the whole pressure range, a hysteresis loop is formed. It can exhibit a wide variety of shapes, which have often been associated with specific pore structures of

porous carbon solids. Therefore, looking at the shapes of both the adsorption and desorption branches, interesting information on the porous texture of the adsorbent can be deduced. Thus, from the desorption data, by use of suitable equations (mainly Kelvin based theory), pore size distributions can be obtained [3, 6].

Adsorption-Isotherm Equations

Because carbon forms range from non-porous carbons, such as graphite, to more complex systems, such as activated carbons, which also contain meso and macropores, a brief critical review of the most used adsorption equations developed for non-porous as well as microporous carbons is presented. These equations have mainly been developed to assess the surface area of the solid under study. Knowledge of the starting assumptions used in each equation is important for a good understanding of its limitations and correct use in the characterization of porous carbons.

The Langmuir Equation

By means of molecular-kinetics arguments, Langmuir [16] developed an adsorption equation which describes the shape of type I isotherms very well. The starting point is the dynamic concept of adsorption equilibrium in which the rates of adsorption and desorption are equal. The following simplifying assumptions are made:

1. only one molecule per site can be adsorbed on the free surface of the adsorbent and saturation is reached on completion of the monolayer;
2. the surface of a solid is composed of a two-dimensional array of energetically homogeneous sites;
3. the forces (repulsive or attractive) between the adsorbed molecules are negligible in comparison to adsorbent-adsorptive interactions.

The final equation can be expressed in various forms although, to test it against experimental data, it is preferable to write it in the form:

$$\frac{P}{n} = \frac{1}{Bn_{\mathrm{m}}} + \frac{P}{n_{\mathrm{m}}} \tag{8.4}$$

where n is the amount adsorbed per gram of solid at equilibrium pressure P, n_{m} the amount adsorbed per gram of solid to complete a monolayer, and B an adsorption coefficient of the adsorbate-adsorbent system.

When experimental data fit the Langmuir equation, a linear plot of P/n versus P is obtained, the slope of which gives the value of $1/n_{\mathrm{m}}$, and its intercept with the P/n axis gives $1/Bn_{\mathrm{m}}$. Once the amount adsorbed in the monolayer per gram of solid, n_{m}, is known, the surface area can be assessed (see below).

The BET Equation

The best known theory of physisorption is undoubtedly that of Brunauer, Emmett and Teller [17] who developed the earlier Langmuir's ideas to describe multimolecular adsorption. By introduction of some simplifying assumptions, the BET theory provides an extension of the Langmuir monolayer model. The first adsorbed layer is similar to that of the Langmuir model. Each adsorbed molecule in the monolayer is assumed to be an adsorption site for second layer molecules, and so on for successive layers as the relative pressure increases. When the pressure becomes equal to the saturation vapor pressure, the adsorbate condenses as a liquid, and bulk condensation occurs. The adsorption energy of the second and all higher layers is postulated equal to the heat of liquefaction of the adsorbate at the adsorption temperature. The model for the formation of an infinite number of layers at the saturation pressure, P_0, leads to the well known BET equation:

$$\frac{P}{n(P_0 - P)} = \frac{1}{n_{\mathrm{m}}C} + \frac{C-1}{n_{\mathrm{m}}C} \cdot \frac{P}{P_0} \tag{8.5}$$

where C is a constant, which is related exponentially to the first-layer heat of adsorption by the equation:

$$C = \exp\left|\left(q_1 - q_{\mathrm{L}}\right)/RT\right| \tag{8.6}$$

where q_1 is the heat of adsorption of the first layer, q_{L}, is the heat of adsorption of the second and subsequent layers (equal to the latent heat of vaporisation of the adsorptive). Therefore, $q_1 - q_{\mathrm{L}}$ is the net heat of adsorption. Equation (8.5) gives a linear relation between $P/n(P_0 - P)$ and P/P_0, with a slope equal to $|(C-1)/n_{\mathrm{m}}C|$ and an intercept of $1/n_{\mathrm{m}}C$. The C value affects the shape of the isotherm, in the low relative pressure range, and the stronger the adsorbate-adsorbent interactions, the higher the C value. The C value depends on the relative pressure range used, which should be borne in mind when analyzing microporous carbons. Equation (8.5) gives an adequate description of type II isotherms over a limited P/P_0 range only, usually within $P/P_0 = 0.05$–0.35, due to the limitations of the BET theory. At relative pressures below $P/P_0 = 0.05$, the assumption that the surface is an energetically homogeneous surface does not apply to the great majority of adsorbents. The lack of success at higher relative pressures $P/P_0 \geq 0.35$ is due to failure to take into account lateral interaction between neighboring adsorbed molecules.

The Specific Surface Area of Solids

Once the monolayer capacity is known from (8.4) or (8.5), the specific surface area S (m^2/g) of the adsorbent may be calculated, provided that the area effectively occupied by an adsorbed molecule (A_{m}) in the complete monolayer is known: $S =$ (number of molecules in the monolayer) $\times$ (their cross-sectional area), that is:

$$S = n_{\mathrm{m}} A_{\mathrm{m}} N_{\mathrm{A}} \cdot 10^{-18}\,(\mathrm{m}^2/\mathrm{g}) \tag{8.7}$$

where the monolayer capacity has been expressed in mol/g and N_{A} is Avogadro's constant. The molecular surface area of a given adsorptive may not be constant because it depends somewhat on the nature of the adsorbent. The conventional picture of an A_{m} value for a monolayer completely filled with adsorbate molecules in a liquid-like packing does not correspond to reality. In general, despite limitations and because of its simplicity, (8.5) is still used, even to determine surface area in microporous adsorbents. Its use on these adsorbents is only recommended as a measurement of the monolayer equivalent area (area which would result if the amount of adsorptive required to fill the micropores is spread as a close-packed monolayer of molecules).

Concept and Use of Standard Isotherms

A number of attempts have been made to express adsorption isotherm data in a normalized form. For a large number of non-porous solids, a n/n_{m} plot against P/P_0 can be represented by a single curve, called the 'standard isotherm'. Among these related attempts, the t and α-methods are the most used [3, 4, 6, 15].

The t-plot Method of Lippens and de Boer

This method [18] assumes that a multimolecular layer of adsorbed nitrogen is formed freely on the surface of the solid and the thickness of the layer increases with the relative pressure following the equation (in nm)

$$t = 0.354(n/n_{\mathrm{m}}) = f(P/P_0) \tag{8.8}$$

where 0.354 (nm) corresponds to the thickness of nitrogen, assuming hexagonal close-packing of the molecules in the adsorbed film. By use of this method, valuable information about the porous structure of the adsorbent can be obtained by comparing the nitrogen adsorption isotherm of a given porous solid with the t-curve of a standard non porous solid. In the case of an unhindered adsorption, the t-plot is a straight line passing through the origin, the slope of which is a direct measure of the surface area of the adsorbent. An upward deviation is indicative of capillary condensation taking place in mesopores at high relative pressures thus increasing adsorption much more than in the standard non-porous solid. A downward deviation indicates the presence of micropores in the solid. Because of its simplicity, the t-method has been widely used to analyze microporous carbons, the micropore volume, the external surface area and total surface area, being the most often calculated data by this method.

The α-method of Sing

A different way of comparing an experimental isotherm to a standard one is used by Sing [3]. Instead of the thickness of the adsorbed layer, he used the

ratio $n/n_{0.4}$, called α, where $n_{0.4}$ is the amount adsorbed by a non porous reference solid at $P/P_0 = 0.4$. This P/P_0 value was justified for nitrogen isotherms at 77 K since monolayer coverage and micropore filling, if present, are complete, and capillary condensation has not yet begun. The plot of α versus P/P_0 has much similarity with the t-plot and hence the α-curve is used in an analogous manner. If there is neither capillary condensation nor micropore filling on the test sample, the α-plot is a straight line through the origin. Since the surface of the standard is known (usually, but not necessarily, from the BET nitrogen isotherm) the specific surface (S_α) of the test sample can be obtained by direct comparison to the reference isotherm:

$$S_\alpha(sample) = \frac{Slope(sample)}{Slope(reference)} \times S(reference) \tag{8.9}$$

The use of standard isotherms as a tool to characterize the porosity of solids (even for microporous solids) by means of one of the two methods above may be appropriate. However, it is necessary to keep in mind that all of them are subject to the same limitation; that is, the difficulty of an appropriate choice of a non-porous reference material. In the α-method, one chooses the standard isotherm according to the chemical nature of the sample to be studied, while in the t-method, the choice is independent of the nature of the non-porous adsorbent.

Peculiarities of Adsorption in Microporous Carbons

As was stated earlier, adsorption in microporous solids is not as well understood as in non-porous or mesoporous solids. Pore sizes of the same order of magnitude as the sizes of the adsorbate molecules lead neither to the progressive completion of a monolayer nor to multilayer adsorption but to the filling up of the micropore volume with the adsorbate in a liquid like condition. There are a number of problems associated with adsorption in micropores including the following:

1. BET surface areas are unrealistically high compared with the calculated area for one gram of carbon in the form of an extended graphite layer plane, counting both sides (2630 m^2/g) [19].
2. Adsorption energy within micropores of a given chemical nature is much higher than on a non-porous solid of the same chemical nature.
3. The n_m values obtained by either the BET or Langmuir equation, are similar to the limiting uptake of the type I isotherms, which implies that micropore filling is occurring rather than surface area coverage of the adsorbent.
4. The adsorption of vapors (i.e., benzene or water), expressed as liquid adsorbate per gram of adsorbent, as a function of the relative pressure confirms that the overall adsorption process on microporous carbon is occurring by a volume filling mechanism rather than surface coverage.

5. With some microporous materials, like carbon molecular sieves (CMS) and carbonized chars, where the widths of the pore entrance are comparable to the diameter of the adsorptive molecules, adsorption equilibrium problems might exist. Thus, N_2 adsorption equilibrium (at 77 K) is very difficult to reach, even with very long equilibrium times. In this case, contrary to the exothermic nature of the adsorption process, an increase in the adsorption temperature leads to an increase of the amount adsorbed. In this so-called activated diffusion process, the molecules will have insufficient kinetic energy and the number of molecules entering into the cavity during the adsorption equilibrium time will increase with temperature [10, 21].

Adsorbate-Adsorbent Interactions in Micropores

A marked increase in the dispersion energy is predicted for a molecule which is able to enter into a cavity whose size is similar to the molecular dimensions. Detailed calculations of the potential energy in such narrow micropores indicate that there is an overlap of the force fields of opposite pore walls which will enhance the energy of interaction of an adsorbate molecule compared with that corresponding to adsorption on a plane surface. All the aforementioned points about peculiarities of adsorption in microporous carbons show that special attention is needed when characterizing microporous carbons, such as activated carbons (fibers and nanotubes), CMS, coals, by adsorption methods.

The Polanyi Potential Theory

A major development in understanding adsorption of gases on microporous carbons was provided by the potential theory of adsorption of Polanyi [20]. This theory assumes that on the adsorbent surface, the gas molecules are compressed by attractive forces acting between the surface and the molecules, and these attraction forces decrease with increasing distance from the surface. The attraction force at any given point near the surface is measured by the adsorption potential ϵ, which can be defined as the work of the surface adsorption forces for transferring a molecule from the gaseous phase to the given point above the surface. Polanyi described the adsorption space as a series of equipotential surfaces, each with a given adsorption potential ϵ_i, and each enclosing a volume, W_i. As one moves away from the surface, the value of adsorption potential decreases until it falls to zero and the adsorption space increases up to a limiting value, W_0(zero potential). At the surface, $W = 0$ and $\epsilon_i = \epsilon_\mathrm{max}$. The building of the volume enclosed within the adsorption space is described by a function of the type $\epsilon = f(W)$. Considering that dispersion and electrostatic forces are independent of temperature and assuming that the adsorption potential at constant volume filling is also temperature-independent,

$$\left(\frac{\partial \epsilon_i}{\partial T}\right)_W = 0 \tag{8.10}$$

Equation (8.10) means that the curve $\epsilon = f(W)$ should be the same for a given gas and a given adsorbent at all temperatures. This relationship between ϵ and W is called the characteristic curve. Polanyi expressed the adsorption potential ϵ for a volume filling W as the amount of work necessary to compress the adsorptive from its equilibrium pressure, P_1, to the compressed adsorbate pressure, P_2.

$$\epsilon = \int_{P_1}^{P_2} \frac{RT}{P} dP = RT \ln \frac{P_2}{P_1} \tag{8.11}$$

where $\epsilon = -\Delta \mathrm{G}$, and $\Delta \mathrm{G}$ is the equivalent free energy change. The state of the compressed adsorbate in the adsorption space depends on the temperature. Three cases can be found: (i) when the adsorption temperature is well below the critical temperature, T_c, the adsorbed vapor may be considered as liquid-like; (ii) when the temperature is just below the T_c, most of the adsorbate will be liquid-like and the rest a compressed gas; (iii) when the temperature is above the critical temperature, the adsorbate will be a compressed gas. The first case is, by far, the most used one. Therefore the adsorption potential will take the form

$$\epsilon = RT \ln \left(\frac{P_0}{P} \right) \tag{8.12}$$

Equation (8.12) represents the work needed for compressing the adsorptive from its equilibrium pressure in the gas phase to its saturated vapor pressure, P_0. From this equation, since it is assumed than the liquefied adsorbate is incompressible and has the normal density of the liquid at the given adsorption temperature, it is possible to obtain the volume of filled adsorption space by

$$W = \frac{nM}{\rho} = n v_\mathrm{m} \tag{8.13}$$

where n is the amount adsorbed, expressed in moles; M is the molecular weight of the adsorptive and ρ and v_m are the liquid density and the molar volume of the adsorptive at the adsorption temperature, respectively. The temperature-invariance of the adsorption potential (fundamental postulate of the Polanyi's theory) has been widely proved, especially by the extensive work leaded by Dubinin [7, 8, 22, 23].

The Theory of Volume Filling of Micropores (TVFM)

Dubinin and co-workers [7, 8, 22–25] during the course of their extensive studies of active carbons have developed the so-called Theory of Volume Filling Micropores (TVFM). Among the relevant Dubinin based equations developed over many years, only the Dubinin-Radushkevich will be briefly discussed.

The Dubinin-Radushkevich equation (DR): Based on numerous experimental data, Dubinin and Radushkevich [24] have added a second postulate to the Polanyi theory which complements it. For an identical degree of filling of the volume of adsorption space, the ratio of adsorption potentials for any two vapors is constant.

$$\frac{\epsilon}{\epsilon_0} = \beta \tag{8.14}$$

β, called the affinity (also similarity) coefficient, is obtained experimentally and should be regarded as the relative differential molar work of adsorption of a given vapor (ϵ) relative to the differential molar work of adsorption of the vapor chosen as standard (ϵ_0); for benzene (chosen as standard adsorptive by Dubinin) $\beta = 1$. The affinity coefficient can be approximated by the ratio of the molar polarizabilities, of the molar volumes, or of the parachors for the liquid-like phases of the vapor and benzene [26]. According to experimental data and assuming that the pore size distribution is Gaussian, Dubinin and Radushkevich arrived at an expression which relates the degree of micropore filling, θ, with the differential molar work of adsorption

$$\theta = \frac{W}{W_0} = \exp\left|-K\left(\frac{\epsilon}{\beta}\right)^2\right| \tag{8.15}$$

where K is a constant dependent on the pore structure. By combining (8.12) and (8.15), the well known *DR equation* is obtained:

$$\log W = \log W_0 - D\log^2\left(\frac{P_0}{P}\right) \tag{8.16}$$

where $D = 2.303\ K(RT/\beta)^2$. A plot of $\log W$ against $\log^2(P_0/P)$ will be a straight line from which interception the total micropore volume, W_0 can be assessed. From its slope the value of D is obtained. Because it is related to K and consequently to the microporous structure of the absorbent, D decreases as the size of the pore decreases. Fits to (8.16) are often observed in the literature; different adsorption temperatures with different adsorptive fits give straight lines over a very wide range of relative pressures and all intersect the ordinate axis at one point, indicating the constancy of the limiting volume of adsorption space, W_0. By introducing β into the potential equation, all the characteristic curves of the different adsorptives, on a given adsorbent, should coincide (see example below). Unfortunately deviations of the DR equation from linearity are often observed [3, 4, 10]. These deviations are due to several reasons; among others, to the microporous structure itself, the adsorbent-adsorbate system and the range of P/P_0 studied. It is evident that when deviations occur the extrapolation to the ordinate to obtain W_0 becomes uncertain. To overcome this problem a number of more general equations have been put forward (i.e. the Dubinin-Astakhov and Dubinin-Stoeckli equations [22, 25]). Although the TVMF theory, based on the Polanyi Potential, may be submitted to some criticisms, it is important to note that independent experimental assessments of microporosity support the TVFM theory. Especially, Stoeckli has established a link between the enthalpy of immersion (ΔH_i) and the parameters of the microporous carbon obtained from Dubinin Theory, measuring experimental enthalpies of immersion with a Calvet type calorimeter [11, 27]. Also, the preadsorption method (i.e., n-nonane),

without any previous theoretical assumption and without the need to use any adsorption equation, has confirmed the TVFM.

Adsorptives Other Than N_2: The Usefulness of CO_2 Adsorption at 273 K

Physical adsorption of gases is the most employed technique for the characterization of porous solids. Different adsorptives (N_2, CO_2, Ar, He, CH_4, Kr, Xe, benzene, nonane, ...) can be used for this purpose. Among the gases, N_2 adsorption at 77 K is the most used and, usually, has a special status of recommended adsorptive. The advantage of N_2 adsorption is that it covers relative pressures from 10^{-8} to 1, which results in adsorption in the whole range of porosity. The main disadvantage of N_2 adsorption at 77 K is that when used for the characterization of microporous solids, diffusional problems of the molecules inside the narrow microporosity (size <0.7 nm) occur. To overcome this problem, the use of other adsorptives has been proposed. CO_2 adsorption, either at 273 K or 298 K, is an alternative to N_2 adsorption for the assessment of the narrow microporosity (size <0.7 nm) [10,21]. It requires lower equilibrium times and the amount adsorbed is higher than in the case of N_2 at 77 K. In the case of CO_2 adsorption, though the critical dimension of the CO_2 molecule is similar to that of N_2, the higher temperature of adsorption used for CO_2 results in a larger kinetic energy of the molecules, which are able to enter into the narrow porosity. In this way, the study of CO_2 adsorption has demonstrated that it is an appropriate complementary technique for the analysis of microporosity, where N_2 adsorption can be kinetically restricted.

In the following, the usefulness of CO_2 adsorption at 273 K to achieve a rather complete characterization of the porous texture of microporous carbons will be discussed. To do so, high adsorption pressures of CO_2 (up to 4 MPa) have to be applied to cover the same relative pressure range as with N_2 [21,28, 29]. In order to show the main limitation of N_2 adsorption, and the usefulness of CO_2 for characterizing porous materials, two carbonaceous materials are discussed: (i) an activated carbon prepared by chemical activation with KOH of an anthracite (KUA1GC) and (ii) a carbon molecular sieve (KUA1B8) prepared by blocking the microporosity of KUA1GC by a co-pyrolysis process.

Figure 8.2 presents the N_2 adsorption isotherms at 77 K for both samples. The N_2 adsorption isotherm corresponding to the KUA1B8 is nil because this sample presents a very narrow microporosity which is not accessible to N_2 at 77 K. The kinetics of N_2 adsorption is extremely slow at 77 K, and extremely long times are necessary to reach the equilibrium at each point of the isotherm.

Figure 8.3 shows the CO_2 adsorption isotherms obtained at 273 K for the two samples. It should be mentioned that the sample KUA1B8, which could not be characterized by N_2 adsorption at 77 K, does present adsorption of CO_2 at 273 K and the isotherm can be easily measured with this adsorptive. Each isotherm depicts results obtained from the experiment performed at subatmospheric pressures, which covers a range of pressure from 2×10^{-3} MPa to

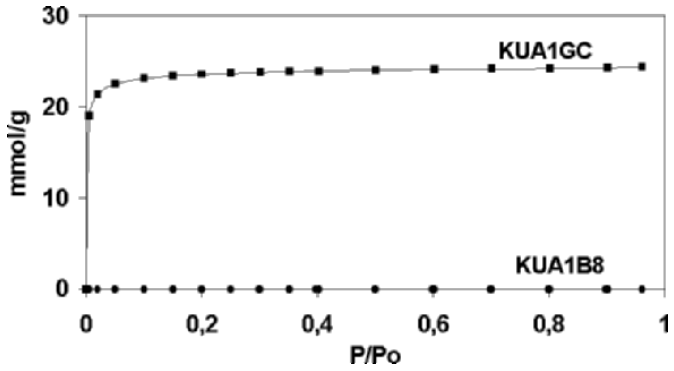


Fig. 8.2. N_2 adsorption isotherm (77 K) for the samples KUA1GC and KUA1B8

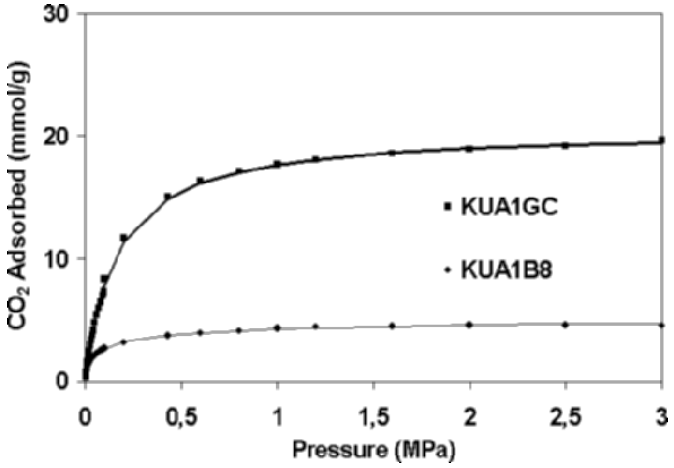


Fig. 8.3. CO_2 adsorption isotherms (273 K) for the samples KUA1GC and KUA1B8

0.1 MPa, and the isotherm done at high pressure, up to 3 MPa, in a gravimetric system.

N_2 and CO_2 adsorption isotherms are of type I, characteristic of microporous materials. It can be seen that all isotherms quickly reach the isotherm plateau. This suggests that these samples present narrow micropore size distribution (MPSD). Figure 8.3 shows that the sample KUA1B8 has a much lower CO_2 adsorption capacity than the sample KUA1GC. This is expected since the former has been prepared by partially blocking the microporosity existing in the latter. After such a process, a sample with a much narrower MPSD and lower micropore volume is obtained. This behavior is quite often observed in samples with molecular sieve properties. Thus Table 1 presents the micropore volume calculated from CO_2 adsorption data, applying the Dubinin-Radushkevich (DR) equation for different materials: a commercial

Table 8.1. Micropore volume calculated from N_2 (77 K) and CO_2 (273 K) adsorption isotherms

Sample	V_{N_2} (cm^3/g)	V_{CO_2} (cm^3/g)
Takeda 3A	–	0.20
Kureha CF	–	0.18
PAN CF	–	0.09
SPF	–	0.11

carbon molecular sieve (Takeda 3A), two commercial carbon fibers (Kureha CF and PAN CF) and a stabilized pitch fiber (SPF), which has been spun and stabilized in our laboratory.

It must be pointed out that the characterization with N_2 at 77 K does not give information, while the characterization with CO_2 at 273 K makes it possible to distinguish between samples, which can be useful for understanding their behavior in a given process. For a proper comparison between adsorption data obtained with different adsorptives and different adsorption temperatures, the experiments have to be corrected considering both the adsorption temperature and the physico-chemical characteristics of the adsorptive. A more suitable comparison of the two experiments is by plotting the so-called Characteristic Curve, applying the Dubinin-Radushkevich (DR) equation. Figures 8.4a and 8.4b present the characteristic curves corresponding to the samples KUA1GC and KUA1B8, respectively. These curves have been obtained by applying the DR equation to the N_2 and CO_2 adsorption isotherms (low and high-pressure) by plotting the logarithm of the volume of liquid adsorbed versus the square of the adsorption potential corrected for the affinity coefficient of the adsorptive ($(RT\ln(P/P_0)/\beta)^2$). Note that the use of high-pressure CO_2 adsorption is important in this study as it allows comparing both N_2 and CO_2 adsorption at similar relative pressures [21, 28, 29].

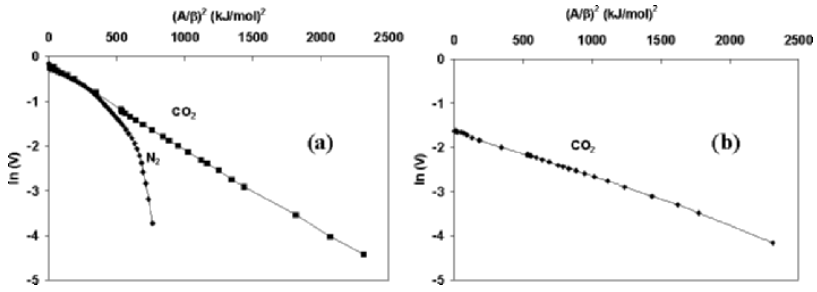


Fig. 8.4. (**a**) Characteristic curve obtained from N_2 (77 K) and CO_2 (273 K) for the sample KUA1GC, (**b**) characteristic curve obtained from CO_2 (273 K) for the sample KUA1B8

Figure 8.4a shows that, at low values of $(A/\beta)^2$, the N_2 characteristic curve superimposes on the CO_2 one. This characteristic curve allows stating that, at low values of $(A/\beta)^2$, CO_2 adsorption at 273 K provides similar information as adsorption of N_2 at 77 K. A common feature of the characteristic curves for N_2 adsorption in microporous carbons is a large downwards deviation for values of $(A/\beta)^2$ higher than about 300 $(kJ/mol)^2$. Note that to 'measure' the narrow microporosity with N_2 at 77 K, low relative pressure must be used with N_2 (i.e. 10^{-4}), that is high adsorption potentials (i.e >300 $(kJ/mol)^2$, in Fig. 8.4).

These low relative pressures are difficult to reach with conventional adsorption equipments. Additionally, as a consequence of the diffusional limitations, N_2 adsorption at 77 K cannot be used to determine the micropore volume of the narrowest porosity. All this necessitates the use of other adsorptive to analyze this range of porosity. CO_2 adsorption at 273 K at sub-atmospheric pressures is very convenient for this purpose, because at this adsorption temperature the saturation pressure for this gas is high, and hence the relative pressures, which can be easily reached with a simple conventional equipment, are low (about 10^{-4}). In addition, with CO_2 adsorption at 273 K any diffusional limitation occurring with N_2 is avoided. Figure 8.4b shows the characteristic curve for CO_2 adsorption corresponding to a sample with very narrow micropores confirming its usefulness.

8.1.2 Reactivity of Carbons

As stated in the introduction, there is a wide variety of carbon materials with different reactivities. This is so, because the parameters which affect the reactivity vary widely (structural order, vacancies, free sites, impurity contents, ...). The reactivity decreases in the order of fullerenes, nanotubes, coals (depending on the rank), fibers (depending on its grade), graphite. As an example of carbon reactivity, the chemical activation process by hydroxides will be analyzed using different carbon materials (including nanotubes). This reaction has been selected because the chemical activation with hydroxides is a process which has been a subject of great interest in recent times, as it allows the preparation of activated carbons with a highly developed porosity [30–33]. The resulting properties of the activated carbons prepared by this activation process depend very much on the experimental variables used, such as the activating agent/carbon ratio, the method of mixing activating agent with carbon, the temperature and flow of gas during the carbonization, the nature of the raw precursor (lignite, sub-bituminous coal, anthracite, lignocellulosic char, nanotubes, ...). As will be discussed later, it also depends on intrinsic variables which affect the carbon reactivity.

The Hydroxide-Carbon Reactions

The main reaction occurring during the activation of a given carbon by hydroxide is a redox process, where carbon is oxidized and the hydroxide is

reduced [33]. Consequently, the reaction products (the metal carbonate, hydrogen and the metal) are formed by the following proposed reactions:

In the case of NaOH:

$$6\ \mathrm{NaOH} + 2\mathrm{C} \rightleftharpoons 2\ \mathrm{Na} + 3\ \mathrm{H_2} + 2\ \mathrm{Na_2CO_3} \tag{8.17}$$

In the case of KOH:

$$6\ \mathrm{KOH} + 2\mathrm{C} \rightleftharpoons 2\ \mathrm{K} + 3\ \mathrm{H_2} + 2\ \mathrm{K_2CO_3} \tag{8.18}$$

Because this is a solid-hydroxide reaction, the reactivity of the solid is a key factor, as we will show further by analyzing carbon precursors of different origins and submitted to different heat-treatment (anthracite (A), anthracite pre heat-treated at different temperatures (A-1000), sub-bituminous coal (SB), lignite (L) and carbonized (LC) lignite). From temperature programmed desorption (TPD) experiments, such as the one shown in Fig. 8.5, the total hydrogen evolved during the activation process, and the beginning of the reaction temperature (T_i), can be assessed. Figure 8.5 demonstrates, as is well-known, that the heat treatment of a given carbon material causes a decrease of its reactivity. The same trend is observed when the anthracite is heat treated.

From this type of TPD experiment, the data of Table 8.2 have been obtained for different carbon precursors. The beginning of chemical activation corresponds to the beginning of the hydrogen appearance. We observe that in all the precursors studied, the starting temperature for the chemical activation is lower for KOH than for NaOH, confirming that KOH is a more reactive chemical agent than NaOH. Table 2 also allows one to see that this activation process depends on the rank/reactivity of the coals and that the higher the reactivity of the coal, the lower the temperature for the beginning of chemical activation both by NaOH and KOH.

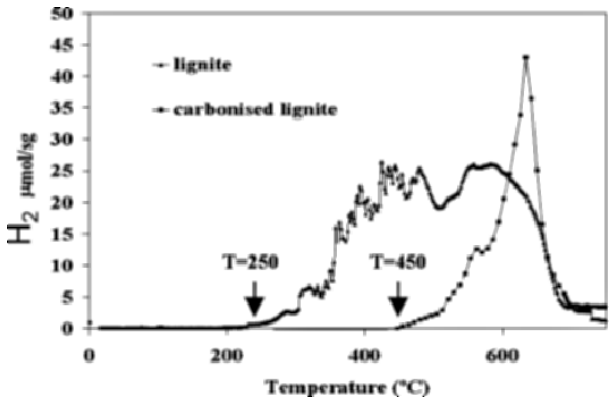


Fig. 8.5. Evolution of hydrogen versus temperature for the lignite and the carbonized lignite

Table 8.2. Temperatures for the beginning of the chemical activation for different precursor-hydroxide mixtures

Precursor	T (°C) NaOH Reaction	T (°C) KOH Reaction
L	250	225
LC	450	250
SB	375	325
A	475	375
A-1000	575	550

From TPD experiments, such as those of Fig. 8.5, the quantification of hydrogen evolved during the activation process can be assessed. Table 8.3 compiles the results obtained in the case of NaOH, for some of the samples studied. If we assume that the hydrogen evolved from the mixtures comes from the conversion of the hydroxides, according to reaction 8.17, the degree of reaction (reacted carbon) can be calculated (Table 8.3). From Table 8.3 we observe that the H_2 evolution and the degree of reaction, for the precursor/NaOH mixtures, decrease as the rank increases. The same trend is observed for KOH activation.

Table 8.3. Hydrogen evolved in the TPD experiments, and degree of activation, carried out over a NaOH-carbon mixture

Precursor	H_2 Evolution (μmol/g)	Reacted Carbon (%)
L	22759	55
SB	13563	33
A	3860	9
A-1000	680	2

Nanotube Activation

It has been seen that for the lower rank coals (the most reactive ones), the chemical activation begins at lower temperatures than for higher rank coals. In addition, the extent of the activation process depends on the reactivity of the starting carbon, decreasing from lignite to anthracite. A heat-treatment prior to the activation reduces considerably the activation easiness, as also happens in the carbon-gas reactions. In the case of nanotubes [34], the behavior against the hydroxide reaction will depend very much on the nanotube preparation conditions. Multiwalled carbon nanotubes (MWNTs) are essentially mesoporous, which is useful for some applications, but it can be a limitation for

others such as gas and energy storage, in which microporosity is required. We have shown that chemical activation with KOH (by a simple physical mixing) is effective in developing micropores in the nanotube walls, while preserving their nanotubular morphology, as has been observed by TEM observations. Figure 8.6 comparing pristine and activated nanotubes shows that the adsorption at low relative pressure is considerably enhanced, which confirms an increase of the micropores volume. The BET specific surface area increases from 222 to 877 m^2/g after activation. The activation of the nanotubes essentially takes place on the defected areas, especially at the nanotubes tips which are opened. This explains the broadening of the hysteresis due to two contributions in the mesoporous character: the entanglement of nanotubes and the inner cavity.

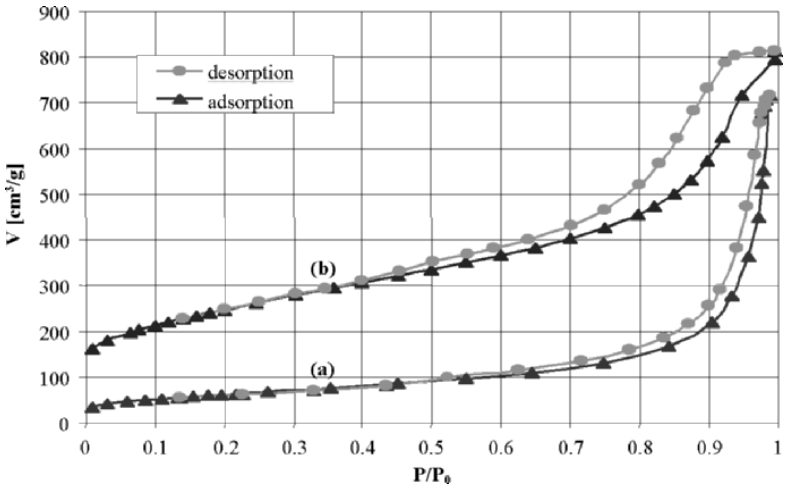


Fig. 8.6. Nitrogen adsorption/desorption isotherms at 77 K on nanotubes from $Co_xMg_{(1-x)}O$ solid solution. (**a**) as prepared; (**b**) activated by KOH

Table 8.4 reports data obtained from chemical activation performed with high purity MWNTs [35] prepared with different structural organization, ranging from well-organized graphitic walls to nanotubes with disorganized layers mixed with some pyrolytic carbon. The results confirm the importance of the intrinsic reactivity of the nanotube material used.

It can be noticed that the BET surface areas and the micropore volumes for the pristine materials increase when the synthesis temperature of the MWNTs decreases. This corresponds to an increase of disorder in the graphitic walls of MWNTs. Table 8.4, which also includes the porous texture characterization for the activated materials, shows that KOH is a very efficient activating agent to generate porosity in MWNTs and that surface area of KOH activated

Table 8.4. Porous texture of pristine nanotubes and KOH activated nanotubes

	S_{BET} (m^2/g)	V_{N_2} (cm^3/g)	V_{CO_2} (cm^3/g)
NT 450°C	345	0.14	0.06
NT 450°C KOH	1670	0.62	0.39
NT 500°C	330	0.13	0.05
NT 500°C KOH	1220	0.46	0.29
NT 600°C	326	0.13	0.03
NT 600°C KOH	868	0.32	0.22

MWNTs increases with decreasing the structural order of the graphitic layers of the pristine materials, reaching $1670\,m^2/g$.

8.2 Surface Functionality, Chemical and Electrochemical Reactivity of Carbons

8.2.1 Surface Functionality of Carbons

All types of carbon materials are essentially composed of carbon atoms. However, because some elements have a tendency to bond to carbon atoms (for instance, oxygen, hydrogen, nitrogen, halogens, ...) they will always be present in small amounts. These foreign elements introduce functionalities which change the surface chemistry of the resulting carbons, in particular their wetting and adsorption behavior and hence their applications. For most carbon materials, including carbon nanotubes, carbon atoms are arranged in aromatic rings which build up lamellae (graphene sheets) of various sizes and stacking heights. These aromatic layers are usually not structurally perfect and several types of defects may be present. Carbon atoms in these defects as well as those present on the edges of the graphene sheets are much more reactive than the atoms in the interior of the graphene sheets. The unique structure of carbon nanotubes does not avoid the existence of reactive unsaturated valences of carbon atoms located at: (a) defects on the outside of the tube, (b) tips in which the carbon atoms have some sp^3 character and (c) edges of the layers, especially in the case of MWNTs. These reactive carbon atoms will chemisorb the above mentioned gases to different extents depending on the temperature and on the type of material, and will build up surface groups or surface complexes which usually are termed surface chemistry. It should be pointed out that because these functional groups affect to a large extent the surface properties of carbon materials, different ways (chemical or thermal) are used to introduce, or to modify, the surface chemistry of a carbon material for a given application. For an up-to-date analysis of the important aspects of carbon surface chemistry we recommend references [36–39].

8.2.2 Oxygen Surface Groups of Carbons

Among the above mentioned gases, oxygen is by far the most common foreign element present on carbon surfaces. Its accumulation takes place even at room temperature and forms different types of organic functionalities, regardless of the nature of the carbon. Much more oxygen is chemisorbed at elevated temperatures (e.g., in the range 300–400°C) by an oxidant gas-solid reaction. Alternatively, surface oxides can be created by treatment with liquid oxidants, controlling concentration and temperature (e.g., aqueous solutions of HNO_3, H_2O_2, NaOCl, $(NH_4)_2S_2O_8$, ...). These oxygen surface groups are stable at room temperature but they decompose when the carbon is heated to higher temperatures giving carbon dioxide, water and carbon monoxide, the two former at much lower temperature than the last. Carbon oxides have been extensively investigated being traditionally split into two families according to their acidic or basic character in aqueous solution. These surface oxides, which have acidic or basic properties, usually coexist on the carbon surface giving an amphoteric character. There are methods available for the characterization of the different types of functional groups, among other, titration methods, specific organic reactions, infrared spectroscopy (FTIR and DRIFTS), X-ray photoelectron spectroscopy (XPS, also ESCA), thermal desorption, potentiometry measurements, ... A recent review of the most frequently used methods for the characterization of surface oxides with discussion about their advantages and problems has been published [40]. Figure 8.7, from [41], illustrates the most probable oxygen functional groups present on carbon surfaces, indicating their acidic or basic character. There is general agreement about the surface functionalities which account for the acidic character (i.e. carboxyl groups, lactones, phenol and lactol groups). However, there is no consensus about basic oxygen-containing functionalities and their strength and relative contributions.

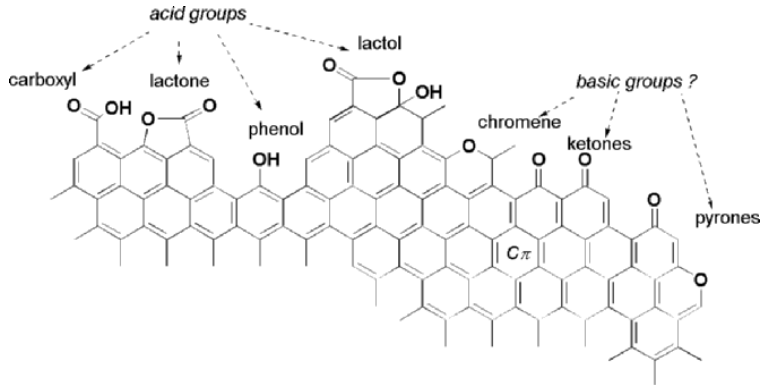


Fig. 8.7. Proposed acidic and basic oxygen functionalities on carbon surfaces [41]

8.2.3 Electrochemical Grafting of Carbon Surfaces

Strong oxidation methods are used to create the variety of oxygenated functions described in the preceding section [42], especially for the modification of carbon fiber surfaces in order to improve their adhesion in composites. However, some milder methods which aim at the derivatization of carbon surfaces with well defined functions are also available. Most of these methods are electrochemical, but we shall discuss several purely chemical methods. Two reviews have been published which partly cover the subject of this section [43, 44].

The Different Methods for the Modification of Carbon Surfaces

Electrochemical Oxidation and Chemical Reaction of Amines (Fig. 8.8)

Amines can be electrochemically oxidized on carbon surfaces (glassy carbon (GC) or carbon fibers), as a result an amino group is bonded to the surface according to the following scheme [45, 46]:

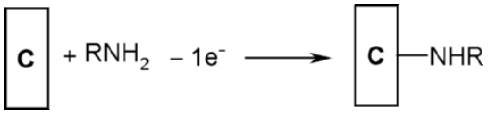


Fig. 8.8. Electrografting of amines

This is achieved very simply by using the carbon to be modified as an anode in acetonitrile (ACN) containing NBu_4BF_4 as the supporting electrolyte and a concentration of the amine from 1 to 10 mM, either by scanning the voltammetric peak of the amine several times or by maintaining the potential equal or negative to the voltammetric peak. A clear indication that grafting of the electrode is occurring is the disappearance of the voltammetric peak of the amine. A large number of amines have been used in this process: primary (*n*-butylamine, ethylenediamine, triethylenetetramine, nitrobenzylamine, aminomethylthiazole, ...), secondary (di-*n*-butyl, di-isobutyl, ...). It was found from voltammetric and XPS data that grafting is easier and leads to a higher surface concentration with primary amine, that the amount of grafting is about half with secondary amines and that tertiary amines hardly lead to any modification of the surface. Amines have been shown to react spontaneously with carbon fibers [47] albeit at high concentration of the amine, high temperature and long reaction times (15 h). Amines also react with C_{60} [48]. Glassy Carbon freshly polished in the presence of ammonia reacts very slowly (≈200 h) with substituted N-hydroxysuccinimide at room temperature [49].

Electrochemical Oxidation of Alcohols (Fig. 8.9)

During the oxidation of n-alkanols containing H_2SO_4 as a supporting electrolyte on a GC electrode a peak appears at $\approx$+1.65 V/SCE, i.e., at a potential close to the background discharge. As with amines, this peak disappears upon repetitive scanning. The following reaction is taking place leading to the attachment of the alkyl chains through an ether linkage [50, 51]:

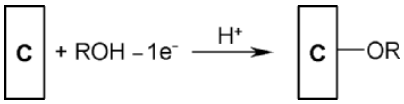


Fig. 8.9. Electrografting of alcohols

Ethanol, n-butanol, n-hexanol, n-octanol were attached in this way to the surface of the electrode as well as ω-diols $HO(CH_2)_nOH$ (n = 2–5) and $HO(CH_2CH_2O)_3$(H or CH_3). The stability of electrodes modified with octyloxy groups was examined as a function of the potential; they were shown to be stable in the potential range: $(-0.5, +1.5)$ V/SCE. It is somewhat surprising that on the cathodic side cleavage occurs at such a low potential, much lower than the reduction potential of ethers.

Electrochemical Oxidation of Carboxylates (Fig. 8.10)

The electrochemical oxidation of carboxylates $RCOO^-$: the Kolbe reaction is one of the oldest electroorganic reactions, it leads to the formation of the RR dimer. If the oxidation of phenylacetate is performed on a GC electrode in ACN + 0.1 NBu_4PF_6 one observes an oxidation peak at 0.98 V/SCE which slowly decreases upon repetitive cycling (in spite of the fact that the solution is stirred between each cycle). The peak completely disappears after 13 cycles (c = 2 mM). This blocking of the electrode corresponds to the following reaction [52]:

It is possible to increase the surface concentration of the R groups by further oxidation of carboxylates on an electrode which has been previously derivatized as above. Conversely, if R is an oxidizable group such as naphthyl-CH_2- or anthryl-CH_2-, scanning upon the oxidation wave leads to the cleavage of the attached group. The reaction has also been performed on Highly Oriented Pyrolytic Graphite (HOPG) [52] and on high specific surface carbon felt [53].

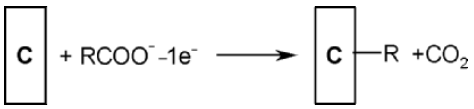


Fig. 8.10. Electrografting of carboxylates

Electrochemical Oxidation of Hydrazides

The electrolysis of hydrazides also leads to the formation of modified carbon surfaces [54, 55]. This reagent has been produced at the tip of a SECM and it was possible to draw very thin (<1 μm) lines of biotin on the surface of GC.

Electrochemical Reduction of Diazonium Salts (Fig. 8.11)

Diazonium salts can be prepared in one very simple chemical step from aromatic amines, with nearly any substituent. They are very easily reduced on carbon electrodes (in the range +0.2 to −0.5 V/SCE) [56]. As shown in Fig. 8.12, they present by cyclic voltammetry on GC, in ACN + NBu_4BF_4, a broad monoelectronic wave; on the second scan this wave completely disappears or at least becomes very small, indicating a blocking of the electrode at least as concerns the charged substrate itself. This corresponds to the following reaction:

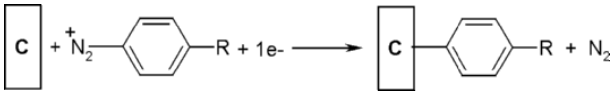


Fig. 8.11. Electrografting of diazoniums

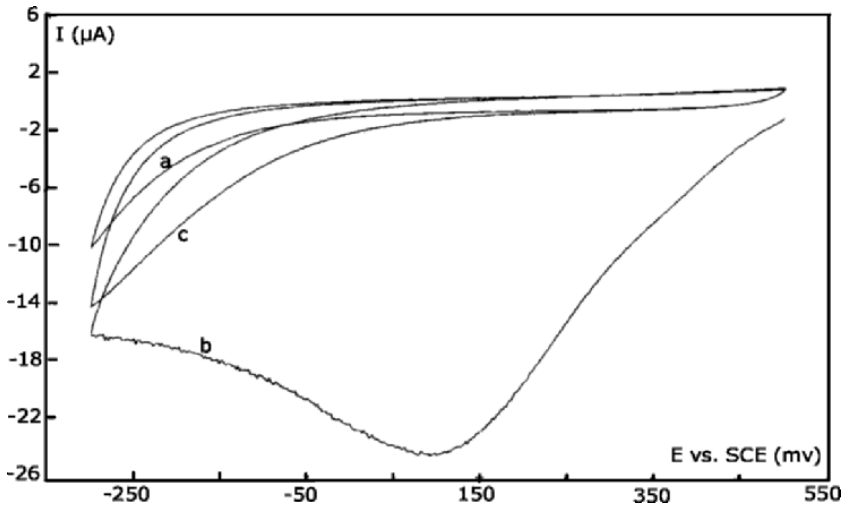


Fig. 8.12. Cyclic voltammetry of (**a**) an ACN + 0.1 mol L^{-1} NBu_4BF_4 solution, (**b**) after addition of 4-nitrobenzenediazonium tetrafluoroborate (c = 5 mmol L^{-1})-first scan, (**c**) second scan. Glassy carbon electrode (d = 3 mm). Reference SCE. Scan rate 0.2 V s^{-1}

This reaction has been performed on GC [56, 57], on carbon fibers [58], on carbon felts [59, 60], on the sp^2 carbons of HOPG [56], on carbon nanotubes, on hydrogen-terminated diamond [61] and on carbon black [62] (without electrochemical induction). The same reaction can also be performed in acidic (pH < 2) aqueous media [57, 58]. The attachment of the organic layer is very strong as it remains unaltered after 6 months at ambient atmosphere, resists sustained ultrasonic cleaning in organic solvents and on HOPG, under ultrahigh vacuum, the layer remains intact up to 700 K [56]. It can be removed by mechanical polishing or by polarization at high positive (ca 1.8 V/Ag-AgCl) or negative (ca −2 V/ag-AgCl) [63]. It should be noted that the modification of conductive surfaces by diazonium salts can be extended beyond carbon to metals such as iron [64] and semiconductors such as Si [65].

Reaction with Hydrogen Radicals

Hydrogen radicals can be generated on a hot filament in a flow of hydrogen gas; they react with the surface of GC to yield a H-terminated surface which is quite resistant to oxidation [66].

Photochemical Functionalization of Diamond Surfaces

Under ultrahigh vacuum conditions, hydrogen-free diamond reacts with alkenes. Fluorine, chlorine, perfluorobutyl, alkyl terminated diamond have been prepared from hydrogen-terminated diamond under photochemical irradiation [67].

Characterization of the Attached Organic Groups

A large variety of techniques have been used to characterize the organic groups attached to the carbon surface; elemental analysis [59, 60, 62], cyclic voltammetry of electroactive reporting groups such as nitrophenyl [45, 46, 49, 50, 52, 53,56], IRRAS [56,59,60,68], Raman [69], XPS [56,57], EDX [59,60], RBS [56], contact angle measurements [44], capacitance measurements [44], STM [52], AFM [68, 70]. Very interestingly, it was possible to observe by Raman spectroscopy the existence of a bond between the carbon and nitroazobenzene attached through the reduction of its diazonium salt. The intensity of the Raman bands varied with the potential implying an electronic interaction between the π system of the graphitic substrate and the attached aromatic molecule [71].

The Reaction Mechanisms and the Structure of the Organic Layers

Reaction Mechanism

The electrochemical reduction of diazonium salts yields an aryl radical through a one electron transfer along with the cleavage of dinitrogen [72]. There is little doubt that this radical is the species responsible for the grafting reaction;

this is confirmed by the fact that the fouling of the electrode observed during the reduction of diazonium salts is also observed in the course of the oxidation of phenyl lithium, i.e., when the same radical is produced by oxidation [73]. As indicated above, it is well known that the oxidation of alkyl carboxylates leads to a radical which binds to the carbon surface [52]. Obviously, gas phase radicals are the reacting intermediates on the way to hydrogen-terminated surfaces. Two species could be responsible for the attachment of amines either the radical-cation obtained after transfer of an electron or the ensuing radical formed after the loss of a proton or an alkyl group. For the moment, it is not clear which of the intermediates binds to the carbon surface. The attachment mechanism of alcohols at negative potentials is different, the carbon itself is oxidized to a radical cation (the oxidation wave at +1.65 V/SCE is observed in the absence of alcohol) which undergoes a nucleophilic attack from the alcohol, in a mechanism similar to the anodic aromatic nucleophilic substitution [44].

Structure of the Grafted Layer

The organic layer obtained through reduction of the diazonium salts has been the most investigated. However, its structure is not yet perfectly clear and there are still contradictions in the literature. The questions of interest are: (i) Is it possible to obtain a homogeneous monolayer? (ii) Is this monolayer organized? (iii) Is it possible to obtain thick layers, how thick? (iv) What are the parameters (potential, electrolysis time, concentration of the diazonium) which influence the thickness of the layer? From the number of aryl groups per unit area of the HOPG surface determined by cyclic voltammetry [56] as well as by the integration of the Raman spectrum [69] of nitrophenyl groups attached to the carbon surface and from RBS measurements on bromophenyl groups the authors concluded to the existence of a homogeneous monolayer. The surface concentration was found in the range 12–18 $\times 10^{-10}$ mol cm^{-2} and the grafting was assumed to be homogeneous based on (100 $\times$ 100 nm) STM images and a simulation of the voltammogram. However, a quite different picture was obtained by AFM [70] on HOPG: nucleation started at the cleavage steps, deposition continued on the basal plane, and after 5 cyclic voltammograms, a quite uniform layer was obtained, but the height of this layer was 7.6 nm, i.e., about 4 layers of aryl groups, and 25 nm thick layers have been deposited in this way. More recently [74] monolayers of biphenyl (obtained after a single voltammetric scan) were observed by AFM on special carbon electrodes prepared by pyrolysis of photoresists. In view of what has been observed by AFM on HOPG one should not expect to find organized monolayers, but such structures have been observed by STM for nitrophenyl [75] and for aryl acetate [52] derivatized HOPG surfaces. It is difficult to reconcile both observation except if the organized structure if formed only on restricted places (on the border of the grafted region?). About the parameters which influence the thickness of the organic layer: (i) on GC (at $E = -0.6$ V/SCE, 400 mV more

negative than the peak potential), the surface concentration (measured by integration of the cyclic voltammogram of 4-nitrophenyl groups) increases with the concentration of the diazonium salt in solution and with time reaching a limit after about 4–10 min ($c = 5$ and $0.2\,\mathrm{mmol\,L^{-1}}$, respectively), there is no difference between electrolysis times of 10–100 min [43, 56, 76] and (ii) with the potential [43, 76] but the values which are obtained always correspond to less than a monolayer. This is in contradiction with what is observed by AFM where the layer continues thickening for 30 min ($c = 5\,\mathrm{mmol\,L^{-1}}$) [68, 70]. One can wonder if there are not some artifacts in the measurements of surface concentration by integration of the voltammograms of nitrophenyl groups. Based on the known chemistry of radicals the structure below (Fig. 8.13) was proposed for the organic layer [68, 70].

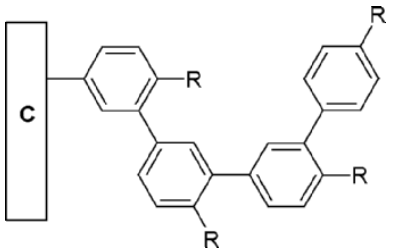


Fig. 8.13. Structure of the organic layer obtained by reduction of diazonium salts

Is it possible to find any sign indicating that the layer is partly due to a reaction of diazenyl radicals ArN_2? The presence of an XPS peak has been assigned to an N = N bond, but its formation is likely due to the reaction of a surface alcohol groups with diazonium salts in solution [77], otherwise, neither Raman nor IR spectroscopy indicated the presence of such bonds [68, 69].

Applications of the Modified Carbon Surfaces

These modified carbon surfaces have been used in many applications: selective electrodes for cationic species [44], for dopamine [78]; suppression of protein adsorption on electrodes allowing direct measurements in biological fluids [44, 79]; electrodes with a catalyst bonded to the surface: dopamine for the catalysis of NAD/NADH [46], Ru(II) bipyridine derivative [53], attachment of biomolecules [49] such as biotin-avidin [54, 55, 80], glucose oxidase [81]; attachment to a carbon electrode of gold nanoparticles [82] as well as polyanions [75]; functionalization of polytetrafluoroethylene after local carbonization [83]; modification of carbon blacks for plastic, paper, textile, ink composition [62]; improvement of carbon-epoxy composites [45, 58], supports for combinatorial chemistry where several chemical steps were performed after the initial grafting of bromobenzyl groups [59, 60]; molecular

electronics with layers of nitrobiphenyl, nitroazobenzene covalently bonded to a flat carbon surface (obtained by pyrolyis of photoresists) acting as a switch for electrical contact by means of conformational and valence isomerizations changes [61, 71, 84].

8.2.4 Functionalization of Carbon Nanotubes

Functionalization can be used to modify the interface between the environment and the outer wall of CNTs. This would for example modify the solubility and facilitate the dispersion in a given medium. Chemical reactivity of CNTs is similar to that of carbon in general, and of graphite in particular, but the unique structure of CNTs confers them some specificities such as the absence of dangling bonds (closed structure) and because of the role played by the curvature of the walls. The curvature leads to a modification of the molecular orbitals of the carbon atoms and a shift of the electronic density towards the outside of the tube, corresponding to an enhanced reactivity of the outer surface. The tips are the more reactive part of the CNTs because it is where the highest strains are located and where the carbon atoms have some sp^3 character. All oxidizing treatments (HNO_3, $KMnO_4 + H_2SO_4$, $K_2Cr_2O_7$, H_2O_2, CO_2, O_2, ...) will attack in priority the tips, but structural defects located on the walls (heptagon-pentagon pairs for example) will be attacked as well to a smaller extent. All these treatments will degrade more or less the CNTs, depending on the strength of the oxidizing agent and the duration of the operation. It is generally admitted that CNTs prepared by arc-discharge are more resistant to oxidation (less structural defects), which in return makes them less chemically reactive. Oxidation of CNTs leads to the formation of chemical groups such as carboxyl functions, lactones, and also ketones, or hydroxyl groups. The important point is that these organic functions can then (theoretically) all be used to graft other functional groups or molecules, opening the door to a very rich chemistry. A priori, one could think that the chemistry of CNTs would be very close to that of fullerenes, but unfortunately the presence of the walls of the CNTs leads to important modifications in terms of chemical reactivity. Thermal Gravimetric Analysis (TGA) is often employed to choose the oxidation temperature when gases are used. Results reported in the literature are difficult to compare because the experimental conditions used are often very different. A very common mistake is to work with a too fast heating ramp, which leads to an overestimation of the temperatures. Other points have to be taken into consideration, such as for example: (a) the presence of traces of catalysts in the samples; (b) the origin and nature of the CNTs (arc-discharge, CCVD; SWNTs or MWNTs); (c) the oxidizing agent used (air, 1% O_2 in an inert gas, CO_2, ...); (d) the flow rate. It is generally agreed that amorphous carbon burns first, followed by CNTs and then by other graphitised compounds but the different steps are often more or less successive, making the interpretation of the data uneasy. The oxidation of remaining catalyst can for example lead to a weight

gain superposed on the weight loss corresponding to the oxidation of some carbon species, leading to an inflexion point on the curve, which could then be misinterpreted as the transition between the combustion of two different carbon species. Functionalization reactions can also concern sp^2 carbon (walls of the CNTs) and this will be illustrated by fluorination reactions (which can then be used in turn as a starting point for further functionalization). Some examples of electrochemical functionalizations will also be described.

Functionalization of Oxidized Carbon Nanotubes

The carboxyl group is the most commonly used starting point for the functionalization of CNTs. The general procedure (Fig. 8.14) consists in generating the acyl chloride by reaction with thionyl chloride, which will then react with the functionality to be added to the CNT.

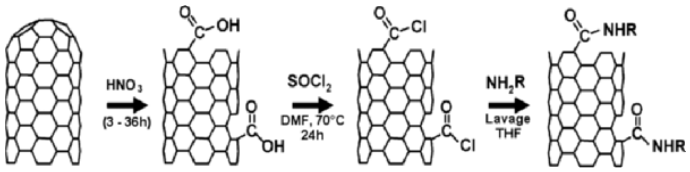


Fig. 8.14. General scheme for the functionalization of oxidized CNTs via acyl chlorides

One example is the functionalization of SWNTs by octadecylamine [85], which brings solubility to the functionalized CNTs in organic solvents such as $CHCl_3$, CH_2Cl_2, aromatic solvents and CS_2. Functionalization by glucosamine can even make the CNTs soluble in water [86]. Direct reaction of an amine (octadecylamine) with the carboxyl group [87] is also possible and leads to a non-covalent functionalization bringing solubility in THF and CH_2Cl_2. Functionalization of CNTs by lipophilic and hydrophilic dendron species (by amidation or esterification) has been reported [88] and brings solubility in hexane, $CHCl_3$ or water. The interesting point is that the functionalization can be removed by modifying the pH, in the case of esters [89]. Direct polymerization of functionalized CNTs [90] has been reported and involves bifunctional molecules such as diamines. Silanization of MWNTs has been described [91]: oxidized MWNTs are first reacted with trimethoxysilane and then hydrolyzed in ethanol to form trisilanol molecules which then react with the surface of the CNTs.

Sidewall Functionalization of Carbon Nanotubes

These functionalization reactions do not involve any structural defect and concern sp^2-hybridized carbon atoms. The first example is that of fluorination reactions. Fluorination of CNTs by F_2 [92, 93] leads to a stoichiometry

close to C_2F. Functionalization is then possible by alkylation (Grignard or alkyl-Li [94]), or reaction with an amine [95], as well as defunctionalization by reaction with hydrazine [92]. Alkylated-CNTs can also be defunctionalized by oxidation in air [94]. Addition of carbenes (electrophilic addition) has been reported [96]; carbenes are prepared by reaction between $CHCl_3$ and a base according to: $CHCl_3 + NaOH \rightarrow :CCl_2$. The question of whether the carbene attacks only the CNTs or not is still open. Cycloaddition of nitrenes (prepared from azides according to $R–N=N^+=N^- \rightarrow R–N: + N_2$) leads to similar results. Reduction of diazonium salts can be achieved either electrochemically or chemically. In the electrochemical process [97], the reduction of the diazonium salt leads to a radical which reacts directly with the walls of the CNTs and the defunctionalization is possible by heating at 450°C in Ar. Surprisingly, only t-butylphenyl groups attached to the surface provided an increased solubility. By applying more negative potentials, it was possible to grow polymeric layers on the surface of CNTs [98], derivatization was observed by XPS and Raman spectroscopy [99] (the evolution of the D-band as a function of the number of the grafted groups supports the formation of a polymeric layer). It was also possible to perform the derivatization by electrochemical oxidation of 4-amino benzylamine in a manner similar to that described above, and by oxidation of amino benzoic acid (however in this case one should expect grafting of the aryl radical obtained by decarboxylation and not of the nitrogen radical as indicated by the authors) [98]. In the chemical process [100], the diazonium cation $R\text{-}N_2^+$ is prepared by reaction between a nitrite $R\text{-}NO_2$ and an amine; the main advantage of this second method is to provide a functionalization process not involving any organic solvent. As far as non-covalent sidewall functionalization is concerned, the affinity of the pyrenyl group for the walls of the CNTs has been used to functionalize SWNTs with ferritin [101], attached to an alkyl chain ended by a succinimid group. The last series of examples of non-covalent sidewall functionalization of CNTs deals with polymer wrapping. Most experiments have been carried out with MWNTs. Polymer wrapping enhances the solubility of the CNTs, without modifying their intrinsic properties. Many polymers have been tested, amongst which are poly(m-phenylenevinylene co-2,5 dioctoxy-p-phenylenevinylene) [102, 103], polystyrene [103, 104], poly(phenylacetylene) [105], and polyvinyl pyrrolidone [106]. In the case of SWNTs, experiments have been reported with polystyrene sulfonate [106] and Arabic gum [107].

Although the chemical functionalization of CNTs has been evidenced, most of the reactions that have been reported are not specific to CNTs; the characterization of the products is thus still problematic when the starting material is not made of 100% pure CNTs. However, this research topic is of prime importance for the future development of the applications of CNTs, such as chemical and biological sensors.

8.3 Filling of CNTs and In-Situ Chemistry

Why fill carbon nanotubes? What is the chemistry of CNTs? The very small inner cavity of CNTs is an amazing tool to prepare and study the properties of confined nanostructures, such as salts, metals, oxides, gases or even discrete molecules like C_{60} for example. Because of the almost 1D structure of CNTs –this is especially true for single-walled CNTs (SWNTs)-, one can expect different physical and chemical properties for the confined foreign materials and even for the composite formed by the filler and the CNT. Indeed, when the volume available inside a CNT is small enough, the foreign material can be made mainly of 'surface atoms' of reduced coordination. This should lead to important modifications of the chemical and physical properties of matter, as proposed by the Nobel prize R. Feynman in a talk he gave on December 29th 1959 at the annual meeting of the American Physical Society at the California Institute of Technology (Caltech) [108]: '*What would the properties of materials be if we could really arrange the atoms the way we want them? They would be very interesting to investigate theoretically. I can't see exactly what would happen, but I can hardly doubt that when we have some control of the arrangement of things on a small scale we will get an enormously greater range of possible properties that substances can have, and of different things that we can do*'. The question of the stability of such structures once the surrounding CNTs are removed is a complex one and will probably depend both on their chemical nature and on the proportion of surface atoms. Applications of filled CNTs may range from superconducting materials (this effect has already been observed in the case of metallofullerenes) to biosensors, catalytic supports and even vectors for therapeutic biomolecules. We will first detail the conditions required for a compound to fill a CNT, before reviewing briefly the different filling processes that have been used until now (during the synthesis of the CNTs, or after their synthesis). We will then focus on the structural modifications occurring because of the confinement of a compound within a CNT. The use of CNTs as nano test-tubes will be illustrated by examples taken from the literature.

8.3.1 Filling Requirements: the Role of Surface Tension

The wetting of a solid by a liquid is described by the Young-Laplace equation (8.19), where ΔP is the pressure difference across the liquid-vapor interface, γ the surface tension, θ the liquid-solid contact angle and r the radius of curvature.

$$\Delta P = \frac{2\gamma \cos\theta}{r} \tag{8.19}$$

One can distinguish two different cases: either ΔP is positive ($\theta \geq 90°$) and the wetting will be bad, indicating that some pressure must be applied to force the liquid inside the CNTs; or ΔP is negative ($\theta < 90°$) and the spontaneous filling by capillary action is possible. Predicting the contact angle (8.20) is

not easy as it depends on the tension at the solid-vapor interface (γ_{SV}) and at the solid-liquid interface (γ_{SL}):

$$\cos\theta = \frac{\gamma_{\mathrm{SV}} - \gamma_{\mathrm{SL}}}{\gamma} \tag{8.20}$$

The question of whether these laws are valid or not at the nanometer scale must be kept in mind. Theoretical calculations [109] indicated that it is possible to confine matter inside a CNT by capillarity, and that this process becomes easier and easier as the diameter of the CNT increases (less and less repulsive energy at the entrance of the CNT). Dujardin and coworkers [110] have shown that elements or compounds which wet graphite well ($\gamma \leq 190\,\mathrm{mN\,m^{-1}}$) are good candidates for the filling of CNTs. The experimental surface tension threshold is around $200\,\mathrm{mN\,m^{-1}}$ and this value depends on the diameter of the CNT because wettability and polarizability are related to each other (in order to get good wetting, the polarizability of the solid has to be higher than that of the liquid). It has been calculated [111] that the polarizability of a convex graphitic surface is lower than that of graphene: the smaller the diameter of the CNT, the more difficult the filling. Experiments carried out with different elements and compounds have shown [112] that the maximum surface tension would be in the 130–$170\,\mathrm{mN\,m^{-1}}$ range. It is interesting to keep in mind that water has a surface tension around $72\,\mathrm{mN\,m^{-1}}$ in normal conditions, and that most organic solvents have a surface tension even lower.

8.3.2 How to Fill Carbon Nanotubes?

There are two very different methods to fill carbon nanotubes: filling can occur during the synthesis of the CNTs (only reported for multiwalled carbon nanotubes, MWNTs) or after their synthesis. This second way has been the most studied one.

Filling During the Synthesis of CNTs

Direct filling during the arc-discharge process has been reported many times. The element or compound to be confined within the CNTs is introduced in the anode (drilled anode containing a mixture of graphite powder and the desired element or compound). This method, used for the first time in 1992 [113] has allowed the filling of MWNTs with carbides (carbides of Cr, Fe, Ni, Pd, Gd, Dy, Yb, La, Ce, Y, Mn) or pure elements (Mn, Co, Cu, Se, Sb, Ge, Cr, Ni, Re, Au, Sm, Gd, Dy, Yb). The interested reader could refer to the review by Ajayan and Ebbesen [114] for more details. The filling can be continuous (up to a few micrometers), or not. Without going into detail, it is interesting to note the role of the addition of sulphur [115], because the presence of a liquid phase is essential and, for most elements, the metal-sulphur phase diagram

shows the existence of an eutectic with a melting point lower than that of the pure element. Moreover, sulphides generally have a surface tension lower than that of the corresponding metal and this can only facilitate even more the filling of the CNTs. It is generally assumed that growth and filling occur simultaneously. Direct filling of CNTs during Catalytic Chemical Vapor Deposition (CCVD) processes, on the other hand, is rare. The CNTs involved have a bamboo-like structure, with irregular walls including numerous structural defects.

Post-Synthesis Filling of CNTs

We will distinguish two different cases: filling by a solution or by a melted phase. Sublimation methods (more limited use) will be described as well.

Filling by Solutions

This process was developed in 1994 by Green and co-workers [116]. It is based on the simultaneous opening and filling of CNTs by a metal nitrate in solution in nitric acid ($\gamma = 43\,\mathrm{mN\,m^{-1}}$ for pure HNO_3). HNO_3 (reflux at 140°C for at least a few hours) attacks in priority where the curvature is the most significant (sp^3 character more pronounced), that is at the tips of the CNTs (as well as on the walls in the case of structural defects such as pentagon-heptagon pairs for example). This leads to the opening of the tips and allows the solution to get inside the CNTs. After settling and washing, the CNTs are calcined (450°C) to form the oxide from the corresponding nitrate. CNTs filled with Ni, Co, Fe and U oxides have been prepared by this method [116]. These oxide-filled CNTs can then be reduced to prepare metal nanowires (detailed later in this chapter). The use of HNO_3 is however not obligatory and solutions in HCl have also been used to fill CNTs with $RuCl_3$ [117] or CrO_3 [118]. CNTs have also been filled by nitrates of Co and Fe in neutral aqueous solution [119] but the CNTs were opened prior to filling. Organic solvents [120] can be used as well: CNTs have been filled by $MoCl_5$ and $FeCl_3$ dissolved in $CHCl_3$. Filling CNTs with solutions has also been successfully tried with biomolecules such as Zn_2Cd_5 metallothionein, β-lactamase I and cytochrom c_3 [121] or DNA oligomers [122]. Generally speaking, the filling rate from solutions is rather low and the filling length is rarely longer than a few micrometers.

Filling of CNTs by a Melted Phase

This method is the first which was used for the filling of CNTs. The historical filling of CNTs by Pb in 1993 [123] was achieved in 2 steps: evaporation of Pb on CNTs, followed by an oxidation in air (400°C) which both opened the tips of the CNTs and allowed Pb to get inside. Repeating the experiment with CNTs already opened was unsuccessful and the identification of the phase inside the CNTs indicated that the formation of an intermediate Pb-O-C compound seemed to be necessary (this compound would have

a lower surface tension compared to that of the metal). Opening and filling seem to have to occur simultaneously. The general procedure for CNT filling by a melted phase is the following: (a) mixing of the CNTs and the chosen element or compound (in a glove-box if necessary); (b) the mixture is placed in an ampoule, sealed in vacuum; (c) the ampoule is heated above the melting point of the chosen element or compound and then slowly cooled down to allow the re-crystallization of the solid. Elements such as S, Cs, Rb, Se [110] or compounds such as V_2O_5 [124] have been tested successfully (all these materials have a surface tension which is less than $100\,\mathrm{mN\,m^{-1}}$). This method has been successfully employed by the Oxford Group [125] to carry out the filling of MWNTs and then SWNTs with a large number of different halides. Most of the time, CNTs are opened prior to filling. This is done by oxidation of the tips of the CNTs and can be realized by different methods involving wet chemistry or gases. Oxidation by HNO_3 has already been described. Air oxidation has been used since 1993 [126] and is reported to be significant for MWNTs only above 700°C (no indication of either heating ramp or flow rate given). This leads to the opening of the CNTs but also to tip degradation. Experimental results seem to indicate that it is difficult if not impossible to fill opened CNTs which would not have been submitted to an annealing treatment. The following hypotheses have been proposed to explain this phenomenon: (a) the presence of bulky carboxyl groups at the tips could obstruct the entrance of the CNTs and thus hinder the filling; (b) remains of the graphitic caps could be sucked inside the CNT during its opening. An annealing treatment at a temperature above 900°C (in vacuum) can get rid of the carboxyl groups and is thus supposed to facilitate the subsequent filling. Sublimation is another way of filling CNTs. Filling by elements or compounds in the gaseous state in the STP conditions (Xe, O_2, N_2, H_2, ...) will not be discussed here. Filling of SWNTs by sublimation of $ZrCl_4$ at 330°C has been described only recently [127]. Filling by fullerenes, leading to the so-called *peapods* (Fig. 8.15), was first reported in 1998 [128] and happened unintentionally during the course of purification of CNT samples prepared by laser ablation. The first intentional fillings by fullerenes were performed in vacuum sealed ampoules with C_{70} [129] at 650°C, with a filling rate of 26%, and C_{60} [130] (50 hours at 400°C, filling rate estimated around 100%). Filling with metallofullerenes [131] has also been reported (example: $Sc_2@C_{84}$ inside SWNTs).

Estimation of the filling rate is a difficult task and is subject to controversy: should the proportion of CNTs containing some filling (whatever the length) be used? Or should it be the ratio of filled length to the total length of CNTs observed? Keeping in mind that this can only be done using a high resolution transmission electron microscope (HRTEM), leading only to (too much) local observation, it seems that neither of these two methods can give a true idea of the filling rate for the whole sample. Global measurements of the filling rate have been proposed in the case of peapods, based on EELS or Raman spectroscopy but apart from that, there is still a need for a method giving

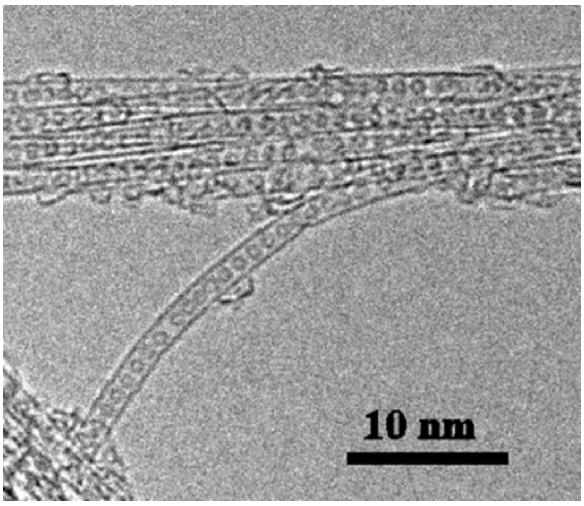


Fig. 8.15. TEM image of C_{60}@SWNTs peapods (by courtesy of M. Monthioux and C. Arrondo)

the global filling rate of filled CNTs samples. Values reported in the literature should thus often be considered with some detachment.

8.3.3 Structural Modifications of Confined Matter

The main effect of confinement inside a CNT of only a few nanometers diameter is to decrease the coordination (Fig. 8.16) of the atoms (or ions). This happens because the inserted material is often reduced to only a few atomic layers when observed in the direction perpendicular to the CNT axis, meaning that complete layers of atoms or ions are lacking when compared to the bulk structure. Confinement thus leads to 1D structures of atoms or ions of reduced coordination, the structure of which can be – or not – related to that of the bulk. We will now describe a series of examples to illustrate the effect of confinement. The effect of the diameter of the CNT will also be discussed.

The first example is that of KI@SWNT [132]. KI has a face-centered cubic structure (a = 3.53 Å). The general methodology employed to determine the structure of confined crystals is the following: (a) HRTEM observation; (b)

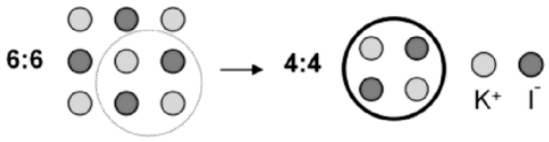


Fig. 8.16. The coordination of the ions decreases from 6:6 in the bulk to 4:4 when confined inside a 1.4 nm diameter CNT

Construction of a rough outline of the structural model from the HRTEM images; (c) Simulation of the HRTEM image from the proposed structural model and comparison with the experimental data. The images are simulated at different focuses in order to match as well as possible the experimental images; (d) correction of the structural model and simulation until the fit with the experimental images is acceptable. In the case of KI@SWNT, the confined KI crystals retain a structure close to that of the bulk but distortions are observed. In the case of two layer 4:4 co-ordinated KI crystals [132] confined within 1.4 nm single-walled carbon nanotubes, lattice distortions were observed perpendicular to the CNT axis: along the axis, the d-spacing is 3.5 Å, as in the bulk; however, this spacing is increased by nearly 0.4 nm across the CNT axis (14% extension). In such a thin crystal where all the ions are indeed 'surface ions' (compared to the bulk), it seems that there is strong interaction between the ions and the CNT inner wall. In the case of CNTs with a larger diameter [133], the situation was a bit more complex and slight distortions were brought to light both parallel and perpendicular to the CNT axis. The measure of such small distortions was made possible by the use of the phase image restoration technique. Another example is that with lead iodide (PbI_2), which was also crystallised inside CNTs of different diameters (see Fig. 8.17) [134]. Bulk PbI_2 has a layered structure, each layer being composed of edge-sharing PbI_6 octahedra. No clear distortions could be observed, however the orientation of the PbI_2 fragments with respect to the CNT axis were found to be strongly dependent on the diameter.

8.3.4 In-situ Chemistry Inside Carbon Nanotubes

In situ chemistry can be employed by choice (will to work in a confined environment) or by obligation (multi-step filling for example). We will now go through a series of examples taken from the available literature. In situ precipitation of SnO inside CNTs [135] has been reported after $SnCl_2$-filled CNTs

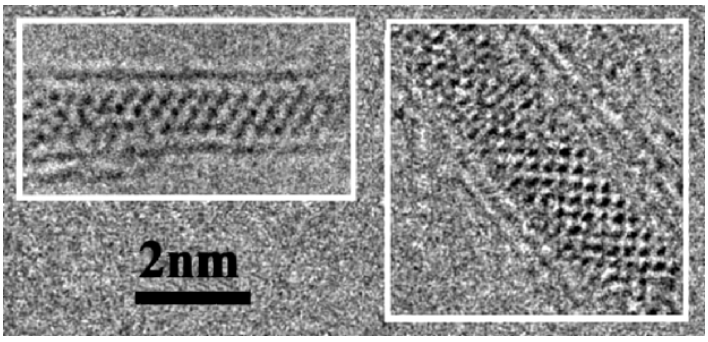


Fig. 8.17. HRTEM images of a single- (on the *left*) and a double-walled CNT filled with lead iodide (by courtesy of E. Flahaut, adapted from [134])

were treated in solution by Na_2CO_3. In situ photolysis (sunlight) of CNTs filled with a $AgCl_{0.2}Br_{0.8}$ solid solution [136] allowed the preparation of Ag (metal) filled CNTs. It was reported that the reactivity increases with the diameter of the CNTs. In situ irradiation [111] of $AgNO_3$ filled CNTs in a transmission electron microscope (TEM) led to the formation of Ag (metal) nanobeads. In situ reduction by H_2 of salt or oxide-filled CNTs has allowed forming the corresponding metals in most cases: Au [137] by reduction of AuCl at 300°C (3h); Ru [117] by reduction of $RuCl_3$ at 45°C (3h); Rh [138] by reduction of $RhCl_3$ at 550°C (6h30); MoO_2 [139] by reduction of MoO_3 at 500°C (8% H_2 in Ar, 6h); Ni, Fe, and Co by reduction of the corresponding oxides [116] at 400°C (2h); Ni metal [140] from NiO by reduction inside a controlled environment TEM (5 mb H_2). Sulphuration reactions have also been achieved by the Oxford group [137] by reacting filled CNTs with H_2S to prepare for example gold sulphides such as Au_2S and Au_2S_3 (from $AuCl_3$) or CdS (reaction at 400°C, from CdO). The last example is the preparation of $CoFe_2O_4$ by air calcination (50°C) of CNTs filled with a mixture of iron and cobalt nitrates [119].

As a conclusion, filling CNTs is possible in certain conditions (surface tension of the compound, diameter of the CNTs, ...). Though filling is possible in situ during the synthesis of the CNTs, a posteriori methods allow a better control. Whatever the method used, the real filling rate is generally difficult to evaluate. The confinement of matter inside CNTs leads to structural modifications more or less significant, depending on both the bulk structure of the confined material and the CNT diameter. These modifications generally occur mainly perpendicularly to the axis of the CNT, where the influence of the interaction with the CNT inner wall is more pronounced. These structural changes are likely to lead to a modification of most of the physical properties (electrical, optical, mechanical, thermal) of the crystal@CNT composites because of the strong interaction between the 1D nanocrystals and the CNTs.

8.4 Electrochemical Energy Storage using Carbon Nanotubes

The exponential growth of the portable electronic devices market has created an ever increasing demand for light-weight and compact electric power sources of high energy and power density. Among the high performance systems which are considered, lithium-ion batteries, nickel/metal hydride batteries, fuel cells and supercapacitors are particularly promising because their technology can still benefit from scientific developments and they have the potential to trigger a cascade of technological breakthroughs. Additionally, the possibility of using battery-supercapacitor hybrid power systems has prompted academic and industrial interest in the field of electric vehicle applications during the

past years. Future developments depend in a decisive way on advanced electrode materials with good electrochemical characteristics. Due to their tunable nanotexture, surface functionality and different forms (powders, fibers, foams, felts, tissues, composites, ...), nanotextured carbons offer a wide range of possibilities for electrochemical energy storage. Additionally, due its amphoteric character, carbon can be doped as well by donor and acceptor species, allowing one to modify the electrochemical properties. An intense research effort is devoted to develop functional carbon materials with optimized electrochemical characteristics and also to use them as a support for enhancing the performance of electrochemically active materials. In this paragraph, electrochemical energy storage properties (lithium storage, supercapacitors) of carbon nanotubes will be discussed and compared with nanotextured carbons, taking into account the nanotexture, and surface functionality. Special attention will be paid to define strategies for an optimization of the electrode materials with some opening to future perspectives.

8.4.1 Lithium Insertion in Carbon Nanotubes

The great interest in lithium insertion into different kinds of carbons is connected with the rapid development of lithium-ion batteries in the world market. Intensive research is still focused on the optimization of anodic carbon materials to attain better performance of this system. Figure 8.18 shows a schematic representation of a lithium-ion battery. The two electrodes are based on intercalation materials between which lithium ions are transferred through the electrolytic medium during charge and discharge [141]. The cathodic (positive electrode) material is a lamellar oxide represented by the general formula Li_yMO_2 ($y \approx 1$), whereas carbon (mostly graphite) is used for the negative electrode (anode).

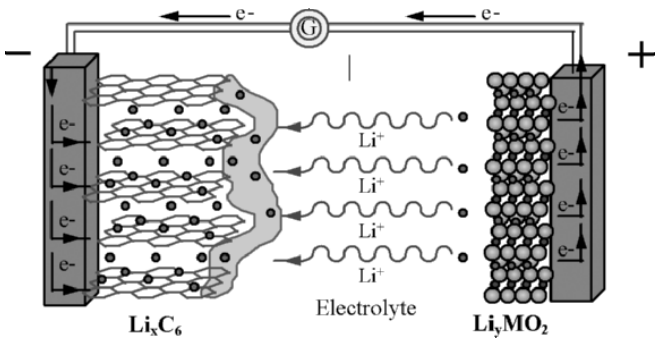


Fig. 8.18. Principle of a lithium-ion battery. This scheme shows the case of charge, i.e. graphite is reduced while the oxide $Li_{1-y}MO_2$ is oxidized

The following equations represent the redox reactions during charging the cell:

$$6\ \mathrm{C} + x\ \mathrm{Li}^+ + x\ \mathrm{e}^- \Leftrightarrow \mathrm{Li}_x\mathrm{C}_6$$
$$\mathrm{Li}_y\mathrm{MO}_2 \Leftrightarrow \mathrm{Li}_{y-x}\mathrm{MO}_2 + x\ \mathrm{Li}^+ + x\ \mathrm{e}^-$$

Using a graphite anode, such a battery operates at almost constant voltage of about 3.5 V during discharge [142], that makes this system very attractive for its high energy density. In the case of graphite, lithium penetrates between the graphene layers through an intercalation process with charge transfer to carbon. The successive formation of stages 3, 2, 1 [143–145] is demonstrated by well-defined plateaus on the galvanostatic curve (Fig. 8.19); the final saturation composition is LiC_6. It is remarkable for graphite that insertion/extraction proceeds very close to the potential of metallic lithium, allowing the lithium-ion battery to discharge at high and almost constant value of voltage. Nevertheless, Fig. 8.19 shows an irreversible capacity which is mainly due to the formation of the Solid Electrolyte Interface (S.E.I.), as LiF, Li_2O, LiOH, Li_2CO_3, $ROCO_2Li$, ... [146–148].

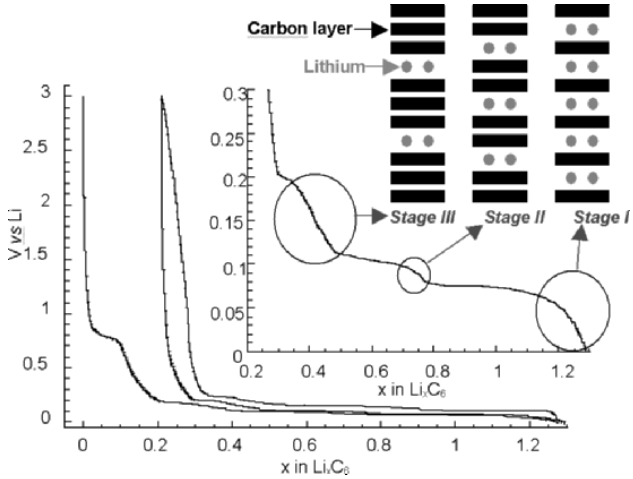


Fig. 8.19. Galvanostatic intercalation/deintercalation of lithium in graphite using a two electrode lithium/graphite cell. The inset is a magnification of the curve at low potential which shows the existence of different stage domains. The potential plateaus represent the transitions from one stage to another

A promising carbon material for a lithium-ion battery should have a higher reversible capacity than graphite, while keeping a small irreversible capacity and a main part of its discharge (oxidation) below 0.5 V vs. Li. During the past years, many efforts have been devoted to develop electrodes based on the use of disordered carbons, especially hard carbons, because of the high reversible

capacity which can be reached with some of these materials, without the inconvenience of exfoliation during insertion-deinsertion processes. However the main drawbacks are a high irreversible capacity and a varying voltage during lithium deinsertion [149]. For microporous carbons, the irreversible capacity is directly related to the active surface area (A.S.A) [150], which corresponds to the cumulated surface area of the different types of defects present on the carbon surface (stacking faults, single and multiple vacancies, dislocations) [151]. It has been shown that the irreversible capacity of the carbon material is noticeably depressed either by coating with coal tar pitch and subsequent carbonisation [152] or by pyrolytic carbon deposition [150]. In both cases, the active sites are blocked by the coating layer. Carbon nanotubes and nanofilaments have been investigated for lithium storage by a few groups [153–156]. Significant values of reversible capacity have been found, up to 780 mAh/g for multiwalled carbon nanotubes [157] and 1000 mAh/g for ball-milled single-walled nanotubes [158]. A typical galvanostatic charge/discharge curve, whatever the kind of nanotube, is shown in Fig. 8.20. Whereas a noticeable value of reversible capacity is indeed observed, the irreversible capacity is rather high, and the voltage continuously increases during lithium deinsertion (oxidation). The latter characteristics should be improved in order to use these materials for the negative electrode of lithium-ion batteries.

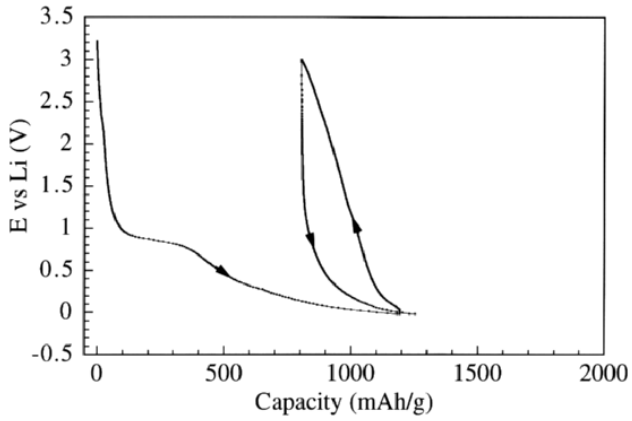


Fig. 8.20. Galvanostatic insertion/extraction of lithium in MWNTs prepared by catalytic decomposition of acetylene on Co supported over silica using a two-electrode lithium/CNTs cell (from [157])

The inset of Fig. 8.21 shows that proportionality which is often observed between the irreversible capacity (C_{irr}) and the BET specific surface area of graphites (graphitic carbons) [159] is not respected for different types of MWNTs. However, if C_{irr} measured after the first discharge/charge cycling is plotted versus the mesopore volume for the different types of nanotubes,

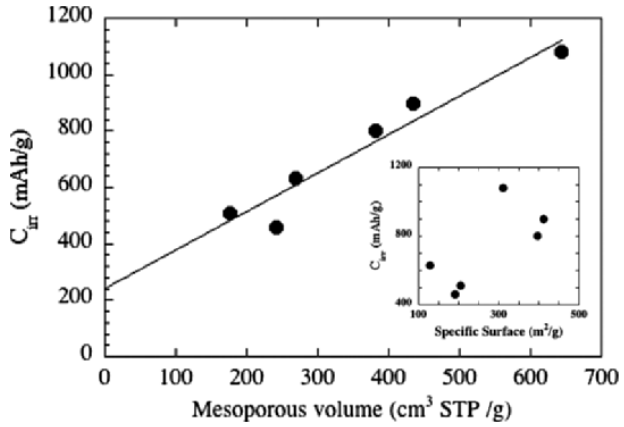


Fig. 8.21. C_{irr} of various MWNTs vs. mesopore volume and BET specific surface area (from [157])

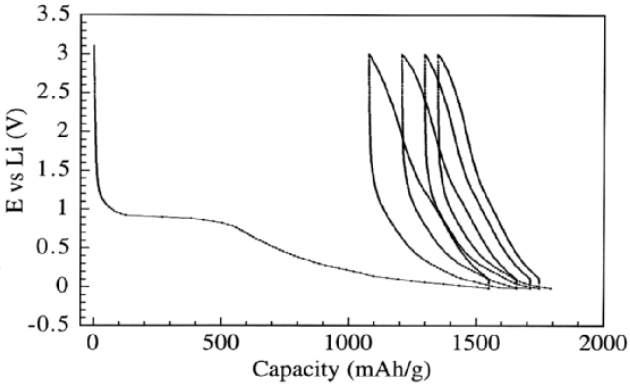


Fig. 8.22. Several galvanostatic reduction/oxidation cycles of MWNTs using a two-electrode lithium/MWNTs cell (from [157])

an almost perfect proportionality is observed (Fig. 8.21). It suggests that the mesopores formed by the nanotube entanglement allow an easy access of the voluminous solvated lithium cations to the active surface where they can be transformed into the decomposition products forming the S.E.I. [157].

During subsequent cycling of nanotube electrodes, an additional passivation layer is formed, as is well demonstrated by the continuous increase of C_{irr} in Fig. 8.22 [157]. It means that in the case of carbon materials with open mesopores, the solvated ions can still have access to the active surface where they are further decomposed. Simultaneously, the reversible capacity also diminishes (Fig. 8.22), and the capacity loss is estimated to ca. 30% after 10 cycles.

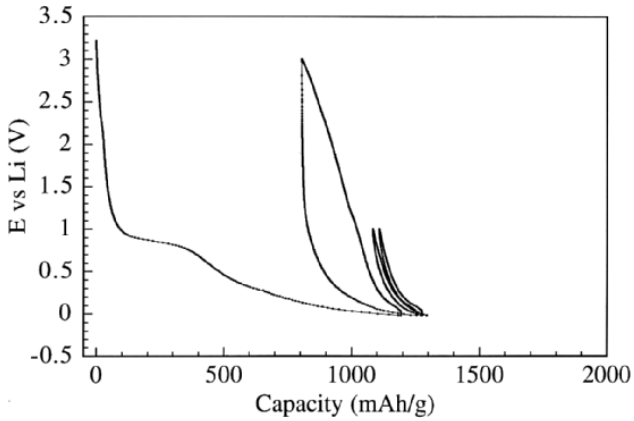


Fig. 8.23. Galvanostatic reduction/oxidation cycles of MWNTs in two different potential ranges using a two-electrode lithium/MWNTs cell (from [160])

For all types of nanotubular materials, a large difference is observed between the values of insertion and extraction potentials [153–155], which is commonly called hysteresis. However, depending on the potential range used for cycling, two regions may be distinguished as shown in Fig. 8.23. When cycling is performed from 0 to 1 V vs. Li, the charge and discharge are perfectly superimposed, as for a true intercalation phenomenon with a charge transfer to carbon, whereas this is not the case for a higher potential range from 0 to 3 V vs. Li [160]. Remarking that the carbon materials which have a high H/C atomic ratio present a high capacity for lithium, Dahn suggested that Li atoms can bind in the vicinity of H atoms, resulting in a corresponding change to the H–C bond. These bonding changes would be activated processes which can lead to hysteresis [161]. Other authors attribute hysteresis to lithium bonding interstitial carbon atoms [162]. In fact, the most pronounced hysteresis, i.e. the most convex character of the oxidation curve is observed for nanotube materials rich in surface oxygenated groups, such as MWNTs after purification by nitric acid [160] or ball-milled SWNTs [158]. Therefore, it has been suggested that hysteresis could be partly attributable to quasi-reversible interactions between oxygenated surface groups and lithium, such as for example $-COO^{-}\ Li^{+}$ [153].

Taking into account the specific surface area of nanotubular materials, which is generally a few hundred m^2/g, the amount of lithium trapped through electrostatic charging/discharging of the electrical double layer should not exceed 5-10% of the total capacity. Therefore, the almost linear dependence of oxidation potential noted for all kinds of nanotubes during the galvanostatic deinsertion above ca. 1 V vs. Li does not have a capacitance effect as its main origin. This linear increase indicates a continuous change of free enthalpy during Li_xC_6 decomposition, i.e. the progressive evacuation of lithium from sites where the interactions with the carbon network are continuously changing.

This so-called pseudocapacitive effect originates from a charge transfer between carbon and $Li_n{}^+$ clusters formed in the mesopores, i.e. either in the meniscus between entangled nanotubes or in the central canal [157]. The high voltage hysteresis, which is also observed for SWNTs and ball-milled SWNTs [158], proves a similar mechanism of lithium storage with a multi-site occupation in the nanotube ropes and different lithium-carbon interactions.

In conclusion, carbon nanotubes are interesting materials for the negative electrode of lithium-ion batteries. They can offer a high reversible capacity, however with more or less noticeable irreversible capacity and hysteresis. The irreversible capacity is principally related to the electrolyte decomposition on the surface active sites of the carbon material. Post-treatments involving the deposition of a thin protecting carbon layer on the carbon substrate are efficient to depress the irreversible capacity without altering the reversible capacity. Regarding the hysteresis, which remains the main drawback, the size of the cavities where the $Li_n{}^+$ clusters are trapped should probably be better controlled in order to get a more uniform distribution.

8.4.2 Use of Nanotubes in Electrochemical Capacitors

Electrochemical capacitors, also called supercapacitors, are an intermediate energy system between the classical dielectric capacitors and batteries. At comparable volume, their storage capacity is roughly one hundred times that of dielectric capacitors, their specific power one hundred times that of batteries, but the specific energy stored is about one hundred times less than in batteries. The high power density of supercapacitors can be adapted for UPS, pulse laser technique and hybrid energy sources for electric vehicles.

When a voltage is imposed between two parallel plates connected to an external circuit, the surfaces become oppositely charged, with a capacitance C_n in farads (F) expressed by:

$$C_\mathrm{n} = \epsilon \frac{S}{d} \tag{8.21}$$

where ϵ is the permittivity or dielectric constant of the material used to separate the plates, S is the area of overlap of the charged plates and d is the separation distance. The capacity of these systems is limited by the surface area of the plates and by their distance. One way of overcoming this dimensionality problem is to use a material with an extremely large surface area, such as an activated carbon, and to take advantage of the electrical double layer which forms at the interface between an electrode and an electrolyte in all electrochemical systems [163, 164]. The electrolyte contains ions which are able to freely move throughout a matrix, such as a liquid or a polymer, and respond to the charge developed on the electrode surface as demonstrated in Fig. 8.24.

The double layer capacitance of each electrode is determined by (8.21), where the distance d is provided by the thickness of the compact layer, which

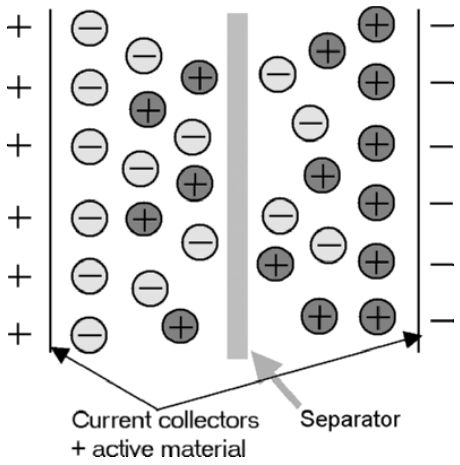


Fig. 8.24. Schematic representation of an electrochemical capacitor. ⊕ cations of the electrolyte; ⊖ anions of the electrolyte

is generally less than one nanometer. This is where the technological advantage of supercapacitors over conventional capacitors lies, as charge storage in the extremely thin compact layer gives rise to specific capacitances of approximately $0.1\,\mathrm{F\,m^{-2}}$. It leads to an increase by several hundred thousand-fold over conventional film capacitors. Taking into account that the specific surface area of activated carbons is in the range of $1000\,\mathrm{m^2/g}$, a capacitance of 100 F per gram of carbon is easily reached. Figure 8.24 shows that an electrochemical capacitor is equivalent to two capacitors in series, therefore the overall capacitance is given by (8.22):

$$\frac{1}{C_\mathrm{n}} = \frac{1}{C_1} + \frac{1}{C_2} \tag{8.22}$$

where $\mathrm{C_1}$ and $\mathrm{C_2}$ denote the capacitance of each electrode. The energy E in Joules stored in an electrochemical capacitor is given by (8.23):

$$E = \frac{1}{2} C V^2 \tag{8.23}$$

where V is the operating voltage. Apart from the size of the supercapacitor, the amount of energy stored is controlled by the electrolyte voltage window. In aqueous medium, this window is generally less than 1 V, whereas it can reach 3 V in organic electrolytes. Hence, the energy stored in supercapacitors working in an organic electrolyte is about one order of magnitude higher than in aqueous media. Another measurement of supercapacitor performance is the ability to store and release the energy rapidly, i.e. the power, P, which is given by (8.24):

$$P = \frac{V^2}{4R} \tag{8.24}$$

where R is the internal resistance of the supercapacitor, i.e. commonly the equivalent series resistance (ESR) R_{S}. The ESR of the entire device is the sum of the resistances of all the materials between the external contacts, i.e. substrate, carbon, binder, separator and electrolyte. The product $R_S C$ determines the rate at which the device can be charged or discharged, and consequently its power. The power can be optimized through an understanding of the nanotexture of the materials and of the processes which dictate the supercapacitor performance. Equation (8.21) indicates that the capacitance value is determined by the surface area S of the electrode/electrolyte interface, which is strongly dependent on the amount of micropores. The dimensions of the latter should be adapted to the size of solvated anions and cations, that is crucial for a high performance of the capacitor. Nevertheless, the presence of mesopores is essential for ions transportation to the active surface of the micropores. A quick transportation of ions in the bulk of the electrodes is certainly the key criterion to lower R_{S} and to reach high power values. Carbon nanotubes are very promising for this function of electrochemical capacitors, because owing to their entanglement they form a well-developed network of open mesopores almost impossible to obtain with activated carbons [165]. Additionally, due to their well-extended graphitic type layers, their intrinsic electric conductivity is quite high, which is also profitable for lowering R_{S}.

Capacitance Properties of Nanotubes

The electrochemical characteristics of supercapacitors built with pellets from various kinds of MWNTs have been investigated in $6\,\mathrm{mol\,L^{-1}}$ KOH medium, and correlated with the nanotexture and elemental composition of the materials [157, 164, 166]. Most of the nanotube based capacitors give a regular box-like shape of the voltammograms, which denotes an entirely electrostatic attraction. In general, the higher the BET specific surface area and oxygen content of the nanotubes, the higher the capacitance values. Values as high as $80\,\mathrm{F/g}$ of carbon have been found with MWNTs prepared by decomposition of acetylene at 700°C on a Co supported catalyst, although the BET specific surface area of these MWNTs is only $411\,\mathrm{m^2/g}$ [157]. Beside the open mesopores which favor the ion access to the active surface, the surface functionality may also contribute to the capacitance value. However, after a few cycles, the capacitance of nanotubular materials rich in surface groups noticeably decreases. Another kind of effect has been demonstrated by Hyperion$^{\mathrm{TM}}$ catalytically grown nanotubes, depending on the electrolytic solution. The capacitance value is $14\,\mathrm{F/g}$ in $6\,\mathrm{mol\,L^{-1}}$ KOH and $78\,\mathrm{F/g}$ in $1\,\mathrm{mol\,L^{-1}}$ H_2SO_4 [167]. A value of $104\,\mathrm{F/g}$ is even measured in 38 wt% H_2SO_4 on a free-standing mat of these nanotubes [165]. Visible humps on the voltammetry curves clearly show that this behavior is not strictly connected with the charging of an electrical double layer. Redox pseudocapacitive reactions, related with iron from the catalyst (1.2 wt%) trapped in the material, contribute noticeably to the observed values [167]. SWNTs prepared by laser ablation (Rice University) or by

the HiPco^{TM} process (Carbon Nanotechnologies) supply capacitance values of 40–45 F/g [167,168]. Taking into account their BET specific surface area of 500 m^2/g, the specific capacitance per unit surface area is around 9 $\mu F\,cm^{-2}$, which is rather less than the value given by activated carbons. After annealing at 1650°C, the capacitance of SWNTs from Rice diminishes to 18 F/g due to a better arrangement of the tubes in the bundles, that hinders the diffusion of solvated ions towards the active surface [167]. Interestingly, the capacitance of the HiPco SWNTs does not decrease at a high current density of 150 $mA\,g^{-1}$. This is attributed to the large external surface area of this material ($\approx$400 m^2/g) on which ion adsorption/desorption proceeds quickly due to the absence of any sieving effect [168]. We already mentioned that the good electrical conductivity of carbon nanotubes, together with the open mesoporous network provided by entanglement, are highly desirable properties for high power capacitors. Supercapacitors built with electrodes from self-standing mats of Hyperion^{TM} MWNTs have been investigated by impedance spectroscopy, showing a frequency 'knee' at about 100 Hz, which suggests that most of the energy stored is accessible at frequencies below 100 Hz [165]. This value, which is much higher than that reported for capacitors from activated carbon electrodes, confirms the advantages of the nanotube backbone to provide a well accessible active surface. As a consequence, a power density as high as 8000 W/kg of total cell weight could be measured [165].

Capacitance Properties of Activated Nanotubes

Although relatively high values of capacitance were claimed for as received nanotubes in some literature reports, often for materials with a high amount of impurities, most of the recent data agree on values in the range of 20–40 F/g during long term cycling. Such values are smaller than those obtained with activated carbons, mainly due to the absence of micropores in carbon nanotubes. Taking into account that a well balanced micro-mesoporosity is always recommended for good performance of supercapacitor electrodes, it has been suggested to use KOH activation of multi-walled nanotubes to produce micropores in the walls, while keeping the mesoporous character provided by the entangled network (see paragraph 8.1.2) [34,169,170]. Such activated MWNTs have been used as electrode material for supercapacitors in various electrolytes. In 6 $mol\,L^{-1}$ KOH medium, the capacitance increased almost 7 times from ca. 15 F/g for non-activated nanotubes to 90 F/g after chemical activation. In organic electrolytes, the capacitance of the activated material reached 65 F/g with a box-like shape of the cyclic voltammograms [169]. Although these values are interesting, they are lower than for the commercial activated carbons used in capacitors. On the other hand, due to the high cost of the pristine material, activated nanotubes cannot be produced at a competitive price. For these reasons, further developments should be oriented to the use of these materials as a component of composites.

Composites with a Nanotube Backbone

The structure of carbon nanotubes is generally characterized by extended graphitic type layers which provide them a high electrical conductivity. On the other hand, the high entanglement of the nanotubes creates an open network of mesopores. Hence, they are a perfect backbone for preparing nanocomposites with various electroactive materials. With nanotubes, the percolation of the active particles is more efficient than with the traditional carbon black which are generally used for the manufacture of electrodes [171]. On the other hand, the open mesoporous network allows the ions to easily diffuse to the active surface of the composite components. The two latter properties are essential to lower the equivalent series resistance (ESR) and consequently increase the power of the device. The active components which are used in these composites are materials with pseudocapacitance properties such as oxides (RuO_2, a-MnO_2) and conducting polymers. Pseudocapacitance is an intermediate situation where a faradaic charge transfer occurs, but the potential changes are a continuous function of the charge passed, $dq = C \times dV$, as in a real capacitor [163]. High values of capacitance can be theoretically obtained with such materials which undergo quick pseudo-faradaic reactions, as illustrated by polypyrrole (PPy) and ruthenium oxide:

$$[PPy^+\ A^-] + e^- \rightleftharpoons [PPy] + A^-$$

$$RuO_a(OH)_b + \delta H^+ + \delta e^- \rightleftharpoons RuO_{a-\delta}(OH)_{b+\delta}$$

However, most of the literature reports are for three-electrode cell constructions and using very thin layers of the active material. Real supercapacitors have been built from novel types of composite electrodes based on MWNTs with deposited conducting polymers. Chemical and electrochemical polymerization of the monomer has been considered in order to get a homogeneous layer of the polymer on the nanotubular materials. The TEM micrograph presented in Fig. 8.25 for a material prepared by electrochemical deposition of polypyrrole (PPy) shows a very uniform polymer coating [172]. When the MWNTS are oxidized, their surface is covered with oxygen-containing groups, which can be used as anionic dopants of a PPy film electrodeposited on the MWNTs [173]. These films are notably less brittle and more adhesive to the electrode than those formed using an aqueous electrolyte as a source of counter ion.

The results reported in the literature about capacitors using these kinds of composites concern mainly the coating by polypyrrole of MWNTs [167, 173–176] and SWNTs [177]. Figure 8.26 shows the voltammogram obtained for such a composite. The square shape of the voltammogram demonstrates a typical capacitor behavior, even if pure PPy usually gives more irregular characteristics, confirming a good synergy between PPy and MWNTs. This kind

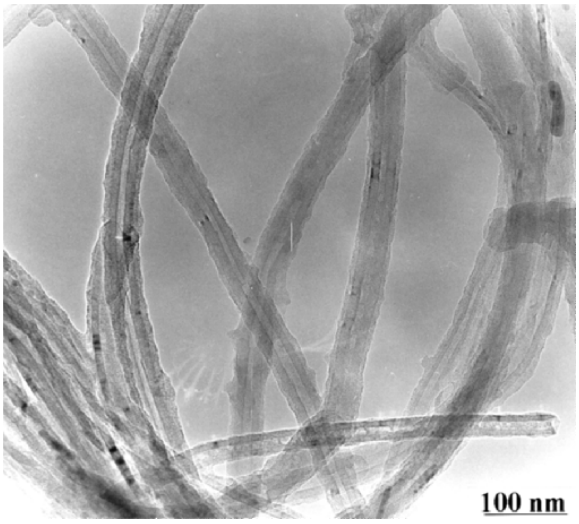


Fig. 8.25. Multiwalled carbon nanotubes electrochemically coated by a thin layer of polypyrrole. The coating thickness is estimated to 5 nm [172]

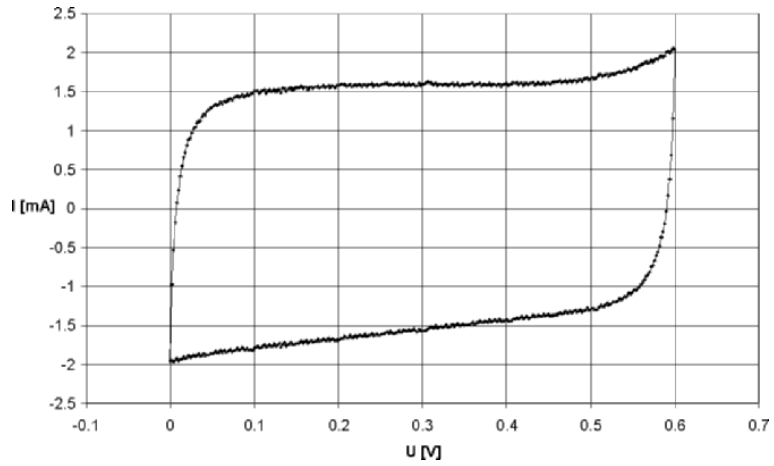


Fig. 8.26. Voltammogram of a two electrode capacitor built with the PPy/MWNTs composite in H_2SO_4 electrolytic medium. Scan rate of potential 2 mV/s [174]

of capacitive behavior is confirmed by the linear discharge on the galvanostatic curve.

The maximum value of capacitance which was reached using a two electrode construction is 190 F/g for the PPy/MWNT composite and 360 F/g for PANI/MWNT (PANI = polyaniline) [178]. In fact, it has been demonstrated that the high values claimed in the literature for very thin layers of pure conducting polymers in three electrode cells are valid only in a given potential

range. For example, the PPy/MWNTs composite investigated in a three electrode cell gives 250 F/g for the range of potential from 0.2 V to −0.3 V and 903 F/g for the negative range from −0.3 V to −0.6 V vs. Hg/Hg_2SO_4. Taking into account these values, and the fact that the overall capacitance for a two electrode cell is given by (8.22) for capacitors in series, the theoretical value cannot be higher than 196 F/g, which fits well with the maximum experimental value of 190 F/g [178]. Hence, it can be concluded that the bulk of the thin PPy layer coating the nanotubes is fully involved in quick pseudofaradaic processes, due to the open network of mesopores formed by the nanotubes, which allows a full doping of the polymer. This open web forms a volumetric electrochemical capacitor where the charge has a three dimensional distribution [157].

8.4.3 Conclusion

The mesoporous character of nanotubular materials strongly influences their electrochemical properties, being somewhat a disadvantage in the case of lithium batteries and profitable for supercapacitors. Nanotubes as active material in lithium-ion batteries lead to a significant irreversibility which is the direct consequence of an easy access of the solvated ions to the carbon surface. Taking into account that intense research is devoted to high-power lithium-ion batteries, especially for electric vehicle applications, the percolating properties of nanotubes should be more extensively investigated, in particular for improving the cathodes. Some other forms derived from nanotubes, such as nanocapsules which are less mesoporous, could also be interesting. Regarding the supercapacitor applications, it is obvious that nanotubes offer an interesting approach to reduce the ESR and increase power. They are especially adapted as a backbone for a material with pseudocapacitance properties. Real capacitors with good electrochemical performance could be built using MWNTs/conducting polymer or MWNTs/a-MnO_2 composites. Taking into account that mainly results in three electrode cells were previously published for these materials, this in an important breakthrough. By using the two-electrode construction, it has been made possible to demonstrate that the performance of such systems is limited due to the impossibility of controlling the potential of both electrodes. Therefore, the developments in progress of hybrid systems, with two different electrodes working in their optimal potential range, are very promising. In these systems, nanotubes are essential for the electrode realization, not only for conductive and mechanical purposes, but also to allow good access of ions to the active surface. Hybrid capacitors, with an activated carbon as negative electrode and MWNTs/a-MnO_2 or a MWNTs/conducting polymer composite as positive electrode, are currently demonstrating high capacitance values while operating at a voltage of 2 V in an aqueous medium [179]. Such systems allow reaching electrochemical performance comparable to that of organic electrolytes, without the environmental drawbacks of these media.

References

1. M. Inagaki: *New Carbons; Control of Structure and Functions* (Elsevier, Amsterdam 2000)
2. K.S.W. Sing, D.H. Everett, R. Haul, L. Moscou, R.A. Pierotti, J. Rouquerol and T. Siemieniewska: Pure and Applied Chemistry **57**, 603 (1985)
3. S.J. Gregg and S.K.W. Sing: *Adsorption, Surface Area and Porosity*, 2nd edn (Academic Press, London 1982)
4. A. Linares-Solano: In *Carbon and Coal Gasification*, ed by J.L. Figuereido and J.A. Moulijn (Martinus Nijhoff, Dordrecht, The Netherlands 1986) p. 137
5. A.W. Adamson: *Physical Chemistry of Surfaces*, 5th edn (J.Wiley Interscience 1990)
6. F. Rouquerol, J. Rouquerol and K. Sing: *Adsortion by Powders and Porous Solids* (Academic Press, San Diego 1999)
7. M.M. Dubinin: In *Chemistry and physics of Carbons*, vol 2, ed by P.L. Walker Jr. (Marcell Dekker Inc., New York 1966) p. 51
8. M.M Dubinin: In *Progress in Surface and Membranes Science*, vol 9, ed by D.A. Cadenhead (Academic Press, New York 1975) p. 1
9. R.Ch. Bansal, J. Donnet and F. Stoeckli: *Active Carbon* (Marcel Dekker, New York 1988)
10. F. Rodriguez-Reinoso and A. Linares-Solano: In *Chemistry and Physics of Carbon*, vol 21, ed by P. Thrower (Marcel Dekker Inc., New York 1998) p. 2
11. F. Stoeckli: In *Porosity in Carbons*, ed by J. Patrick (Edward Arnold, London 1995)
12. D.H. Young and A.O. Crowell: In *Physical Adsorption of Gases* (Butterworth, London 1962)
13. E.A. Flood: In *The Solid Gas Interface*, vol 1 (Marcel Dekker, New York 1967)
14. S. Lowell and J.E. Shields: Powder. In *Surface Area and Porosity*, 3rd edn (Chapman and Hall, 1991)
15. P.A. Webb and C. Orr: *Analytical Methods in Fine Particle Technology* (Micromeritics Instrument Corporation, 1997)
16. I. Langmuir: J. Am. Chem. Soc. **40**, 1361 (1918)
17. S. Brunauer, P.H. Emmett and E. Teller: J. Am. Chem. Soc. **60**, 309 (1938)
18. B.C. Lippens, J.H. de Boer: J. Catal. **4**, 319 (1965)
19. D.H. Everett and J.C. Powl: J. Chem. Soc., Faraday Trans. I. **72**, 619 (1976)
20. M. Polanyi: Trans. Faraday Soc. **28**, 316 (1932)
21. A. Linares-Solano, C. Salinas-Martinez de Lecea, J. Alcañiz-Monge and D. Cazorla-Amorós: Invited paper, Tanso **185**, 316 (1998).
22. M.M. Dubinin and F. Stoeckli: J.Colloid Interface Sci. **75**, 34 (1980)
23. M.M. Dubinin: Carbon **23**, 373 (1985)
24. M.M. Dubinin and L.V. Radushkevich: Proc. Acad. Sci. USSR. **55**, 331 (1947)
25. M.M. Dubinin, V.A. Astakhov: In *Molecular-Sieve Zeolites-II* (American Chemical Society, Washington 1971)
26. G.O. Wood: Carbon **39**, 343 (2001)
27. F. Krehenbuehl, F. Stoeckli, A. Addoum, P. Ehrburger and J.B. Donnet: Carbon **24**, 483 (1986)
28. D. Cazorla Amorós, J. Alcañiz Monge and A. Linares-Solano: Langmuir **12**, 2820 (1996)
29. D. Cazorla Amorós, J. Alcañiz Monge, M.A. De la Casa Lillo and A. Linares-Solano: Langmuir **14**, 4589 (1998)

30. D. Lozano-Castelló, M.A. Lillo-Ródenas, D. Cazorla-Amorós and A. Linares-Solano, Carbon: 39, 741 (2001)
31. D. Lozano-Castelló, J. Alcañiz-Monge, M.A. de la Casa-Lillo, D. Cazorla-Amorós and A. Linares-Solano: Fuel (Review) **81**, 1777 (2002)
32. M.A. Lillo-Ródenas, D. Lozano-Castelló, A. Cazorla-Amorós and A. Linares-Solano: Carbon **39**, 751 (2001)
33. M.A. Lillo-Ródenas, D. Cazorla-Amorós and A. Linares-Solano: Carbon **41**, 267 (2003)
34. E. Raymundo-Piñero, D. Cazorla-Amorós, A. Linares-Solano, S. Delpeux, E. Frackowiak, K. Szostak and F. Béguin: Carbon **40**, 1614 (2002)
35. E. Raymundo-Piñero, P. Azais, D. Cazorla-Amorós, A. Linares-Solano, K. Szostak and F. Béguin: Extended abstracts Carbon 2003, Oviedo (2003)
36. K. Kinoshita: In *Carbon, Electrochemical and Physicochemical Properties* (John Wiley and Sons, New-York 1987) p. 1
37. C.A. Leon y Leon and L.R. Radovic: In *Chemistry and Physics of Carbon*, vol 24, ed by P. Thrower (Marcel Dekker, New York 1994) p. 213
38. H.P. Boehm: Carbon **32**, 759 (1994)
39. E. Raymundo, D. Cazorla, A. Linares, J. Find, U. Wild and R. Schlögl: Carbon **40**, 597 (2002)
40. H.P. Boehm: Carbon **40**, 145 (2002)
41. M.A. Montes-Morán, D. Suárez, J.A. Menéndez and E. Fuentes: Carbon **42**, 1219 (2004)
42. J.C.M. Peng, J.B. Donnet, T.K. Wang, S. Rebouillat: Surface treatment of carbon fibers. In *Carbon Fibers*, 3rd edn, ed by J.B. Donnet, T.K. Wang, S. Rebouillat, J.C M. Peng (Marcel Dekker, New York 1998)
43. A.J. Downard: Langmuir **16**, 9680 (2000); Electroanalysis **12**, 1085 (2000)
44. H. Maeda, Y. Yamauchi and H. Ohmori: Current Topics in Anal. Chem. **2**, 121 (2001)
45. B. Barbier, J. Pinson, G. Désarmot and M. Sanchez: J. Electrochem. Soc. **137**, 1757 (1990)
46. R.S. Deinhammer, M. Ho, J.W. Anderegg and M.D. Porter: Langmuir **10**, 1306 (1994)
47. D.A. Buttry, J.C. Peng, J.-B. Donnet and S. Rebouillat: Carbon **37**, 1929 (1999)
48. F. Wudl, Q. Li and A. Hirsch: Angew. Chem. Int. Ed **30**, 1309 (1991)
49. A. Anne, B. Blanc, J. Moiroux and J.M. Savéant: Langmuir **14**, 2368 (1998)
50. H. Maeda, Y. Yamauchi, M. Hosoe, T.C. Li, E. Yamaguchi, M. Kasamatsu and H. Ohmori: Chem. Pharm. Bull. **42**, 1870 (1994)
51. H. Maeda, K. Katayama, R. Matsui, Y. Yamauchi and H. Ohmori: Anal. Sci. **16**, 293 (2000) and references therein
52. C.P. Andrieux, F. Gonzalez and J-M. Savéant: J. Am. Chem. Soc. **119**, 4292 (1997)
53. F. Geneste, C. Moinet and G. Jezequel: New J. Chem. **26**, 1539 (2000) and references therein
54. W.B. Nowall, D.O. Wipf and W.G. Kuhr: Anal. Chem. **70**, 2601 (1998)
55. M.A. Hayes and W.G. Kuhr: Anal. Chem. **71**, 1720 (1999)
56. P. Allongue, M. Delamar, B. Desbat, O. Fagebaume, R. Hitmi, J. Pinson and J-M Savéant: J. Am. Chem. Soc. **119**, 201 (1997)
57. C. Saby, B. Ortiz, G.Y. Champagne and D. Bélanger: Langmuir **13**, 6805, (1997)

58. M. Delamar, G. Désarmot, O. Fagebaume, R. Hitmi, J. Pinson and J-M. Savéant: Carbon **35**, 801 (1997)
59. E. Coulon, J. Pinson, J.-D. Bourzat, A. Commerçon and J.P. Pulicani: Langmuir **17**, 7102 (2001)
60. E. Coulon, J. Pinson, J.-D. Bourzat, A. Commerçon and J.P. Pulicani: J. Org. Chem. **67**, 8513 (2002)
61. T.C. Kuo and R.L. McCreery, R.L. Swain: Electrochem Solid State Lett. **2**, 288 (1999)
62. J.A. Belmont, R.M. Amici and P. Galloway: Patent PCT Int. Appl. WO 96 18688 A1 (to Cabot Corp)
63. M. D'Amours and D. Bélanger: J. Phys. Chem. B **107**, 4811 (2003)
64. A. Adenier, M.C. Bernard, M.M. Chehimi, E. Cabet-Deliry, B. Desbat, O. Fagebaume, J. Pinson and F. Podvorica: J.Am. Chem. Soc. **123**, 4541 (2001)
65. C. Henry de Villeneuve, J. Pinson, M.C. Bernard and P. Allongue: J. Phys. Chem. B **101**, 2415 (1997)
66. T.-C. Kuo and R.L. McCreery: Anal. Chem. **71**, 1553 (1999)
67. T. Strother, T. Knickerbocker, J.N. Russell, J.E. Butler, L.M. Smith and R.J. Hamers: Langmuir **18**, 968 (2002) and references therein
68. J.M. Kariuki and M.T. McDermott: Langmuir **17**, 5947,(2001)
69. Y.C Liu and R.L. McCreery: J. Am. Chem. Soc. **117**, 11254 (1995)
70. J.M. Kariuki and M.T. McDermott: Langmuir **15**, 6534 (1999)
71. T. Itoh and R.L. McCreery: J.Am. Chem. Soc. **124**, 10894 (2002)
72. C.P. Andrieux and J. Pinson: J.Am. Chem. Soc. **125**, 14801 (2003)
73. B. Jaun, J. Scharwz and R. Breslow: J.Am. Chem. Soc: 102, 5741 (1980)
74. A.O. Solak, L.R. Eichorst, W.J. Clark and R.L. McCreery: Anal. Chem. **75**, 296 (2003)
75. Shaoqin Liu, Zhiyong Tang, Zhong Shi, Li Niu, Erkang Wang and Shaojun Dong: Langmuir **15**, 7268 (1999)
76. A.J. Downard and M.J. Prince: Langmuir **17**, 5581 (2001)
77. B. Ortiz, C. Saby, G.Y. Champagne and D. Bélanger: J. Electroanal. Chem. **455**, 75 (1998)
78. B.D. Bath, H.B. Martin, R.M. Whightman and M.R. Anderson: Langmuir **17**, 7268 (2001) and references therein
79. A.J. Downard and A.D. Roddick: Electroanalysis **7**, 376 (1995)
80. M. Dequaire, C. Degrand and B. Limoges: J.Am. Chem. Soc. **121**, 6946 (1999)
81. C. Bourdillon, M. Delamar, C. Demaille, J. Moiroux and J. Pinson: J. Electroanal. Chem. 336, 5883 (1992)
82. J.A. Harnisch, A.D. Pritt and M.D. Porter: J.Am. Chem. Soc. **123**, 6759 (2001)
83. C. Combellas, F. Kanoufi, D. Mazouzi, A. Thiébault, P. Bertrand and N. Médard: Polymer **44**, 19 (2003)
84. S. Ranganathan, I. Steidel, F. Anariba and R.L. McCreery: Nano Lett. **1**, 491 (2001)
85. J. Chen, M.A. Hamon, H. Hu, Y. Chen, A.M. Rao, P.C. Eklund, R.C. Haddon: Science **282**, 98 (1998)
86. F. Pompeo, D.E. Resasco: Nano Lett. **2**, 369 (2002)
87. J. Chen, A.M. Rao, S. Lyuksyutov, M.E. Itkis, M.A. Hamon, H. Hu, R.W. Cohn, P.C. Eklund, D.T. Colbert, R.E. Smalley, R.C. Haddon: J. Phys. Chem. B **105**, 2525 (2001)
88. Y.P. Sun, W. Huang, Y. Lin, K. Fu, A. Kitaygorodskiy, L.A. Riddle, Y.J. Yu, D.L. Carroll: Chem. Mater. **13**, 2864 (2001)

89. K. Fu, W. Huang, Y. Lin, L.A. Riddle, D.L. Carroll, Y.P. Sun: Nano Lett. **1**, 439 (2001)
90. P.W. Chiu, G.S. Duesberg, U. Dettlaff-Weglikowska, S. Roth: Appl. Phys. Lett. **80**, 3811 (2002)
91. C. Velasco-Santos, A.L Martinez-Hernandez, M. Lozada-Cassou, A. Alvarez-Castillo, V.M Castano: Nanotechnology **13**, 495 (2002)
92. E.T. Mickelson, C.B. Huffman, A.G. Rinzler, R.E. Smalley, R.H. Hauge, J.L. Margrave: Chem. Phys. Lett. **296**, 194 (1998)
93. P.R. Marcoux, J. Schreiber, P. Batail, S. Lefrant, J. Renouard, G. Jacob, D. Albertini, J.Y. Mevelec, Phys. Chem. Chem. Phys. **4**, 2278 (2002)
94. P.J. Boul, J. Liu, E.T. Mickelson, C.B. Huffman, L.M. Ericson, I.W. Chiang, K.A. Smith, D.T. Colbert, R.H. Hauge, J.L. Margrave, R.E. Smalley: Chem. Phys. Lett. **310**, 367 (1999)
95. J.L. Stevens, A.Y. Huang, H. Peng, I.W. Chiang, V.N. Khabashesku, J.L. Margrave: Nano Lett. **3**, 331 (2003)
96. Y. Chen, R.C. Haddon, S. Fang, A.M. Rao, P.C. Eklund, W.H. Lee, E.C. Dickey, E.A. Grulke, J.C. Pendergrass, A. Chavan, B.E. Haley, R.E. Smalley: J. Mater. Res. **13**, 2423 (1998)
97. J.L. Bahr, J. Yang, D.V. Kosynkin, M.J. Bronikowski, R.E. Smalley, J.M. Tour: J. Am. Chem. Soc. **123**, 6536 (2001)
98. S.E. Kooi, U. Schlecht, M. Burghard, K. Kern: Angew. Chem. Int. Ed. **41**, 1353 (2002)
99. P.R. Marcoux, P. Hapiot, P. Batail, J. Pinson: New J. Chem. **28**, 302 (2004)
100. C.A. Dyke, J.M. Tour: J. Am. Chem. Soc. **125**, 1156 (2003)
101. R.J. Chen, Y. Zhang, D. Wang, H. Dai: J. Am. Chem. Soc. **123**, 3838 (2001)
102. S.A. Curran, P.M. Ajayan, W.J. Blau, D.L. Carroll, J.N. Coleman, A.B. Dalton, A.P. Davey, A. Drury, B. McCarthy, S. Maier, A. Strevens: Adv. Mater. **10**, 1091 (1998)
103. J.N. Coleman, A.B. Dalton, S. Curran, A. Rubio, A.P. Davey, A. Drury, B. McCarthy, B. Lahr, P.M. Ajayan, S. Roth, R.C. Barklie, W.J. Blau: Adv. Mater. **12**, 213 (2000)
104. B.Z. Tang, H. Xu: Macromolecules, 32, 2569 (1999)
105. M.J. O'Connell, P. Boul, L.M. Ericson, C. Huffman, Y. Wang, E. Haroz, C. Kuper, J. Tour, K.D Ausman, R.E Smalley: Chem. Phys. Lett., 342, 265 (2001)
106. R. Bandyopadhyaya, E. Nativ-Roth, O. Regev, R. Yerushalmi-Rozen: Nano Lett. **2**, 25 (2002)
107. M.S.P. Shaffer, K. Koziol: Chem. Commun. 2074 (2002)
108. R.P. Feynman: *There's Plenty of Room at the Bottom* (Engineering and Science, Caltech 1960)
109. M.R. Pederson, J.Q. Broughton: Phys. Rev. Lett. **69**, 2689 (1992)
110. E. Dujardin, T.W. Ebbesen, H. Hiura, K. Tanigaki: Science **265**, 1850 (1994)
111. D. Ugarte, A. Chatelain, W.A. de Heer: Science **274**, 1897 (1996)
112. E. Dujardin, T.W. Ebbesen, A. Krishnan, M.J. Treacy: Adv. Mater. **10**, 1472 (1998)
113. R.S. Ruoff, D.C. Lorents, B. Chan, R. Malhotra, S. Subramoney: Science **259**, 346 (1993)
114. P.M. Ajayan, T.W. Ebbesen: Rep. Prog. Phys. **60**, 1025 (1997)
115. A. Loiseau, F. Willaime: Appl. Surf. Sci. **164**, 227 (2000)
116. S.C. Tsang, Y.K. Chen, P.J.F. Harris, M.L.H. Green: Nature **372**, 159 (1994)

117. J. Sloan, J. Hammer, M. Zwiefka-Sibley, M.L.H. Green: Chem. Commun. 347 (1998)
118. J. Mittal, M. Monthioux, H. Allouche, O. Stephan: Chem. Phys. Lett. **339**, 311 (2001)
119. C. Pham-Huu, N. Keller, C. Estournes, G. Ehret, M.J. Ledoux: Chem. Commun., 1882 (2002)
120. J. Mittal, M. Monthioux, H. Allouche: Carbon'01, An International Conference on Carbon, Lexington, KY, United States, July 14–19, 288 (2001)
121. S.C. Tsang, J.J. Davis, M.L.H. Green, H.A. Hill, Y.C. Leung, P.J. Sadler: Chem. Commun. 1803 (1995)
122. S.C. Tsang, Z. Guo, Y.K. Chen, M.L.H. Green, H.A. Hill, T.W. Hambley, P.J. Sadler: Angew. Chem. Int. Ed. **36**, 2198 (1997)
123. P.M. Ajayan, S. Iijima: Nature **361**, 333 (1993)
124. P.M. Ajayan, O. Stephan, Ph. Redlich, C. Colliex: Nature **375**, 564 (1995)
125. J. Sloan, A.I. Kirkland, J.L. Hutchison, M.L.H. Green: Chem. Comm., 1319 (2002)
126. P.M. Ajayan, T.W. Ebbesen, T. Ichihashi, S. Iijimam K. Tanigaki, H. Hiura: Nature **362**, 522 (1993)
127. G. Brown, S.R. Bailey, J. Sloan, C. Xu, S. Friedrichs, E. Flahaut, K.S. Coleman, J.L. Hutchison, R.E. Dunin-Borkowski, M.L.H. Green: Chem. Commun. **9**, 845 (2001)
128. B.W. Smith, M. Monthioux, D.E. Luzzi: Nature **396**, 323 (1998)
129. H. Kataura, Y. Maniwa, T. Kodama, K. Kikuchi, K. Hirahara, K. Suenaga, S. Iijima, S. Suzuki, Y. Achiba, W. Krätschmer: Synth. Met. **121**, 1195 (2001)
130. K. Hirahara, K. Suenaga, S. Bandow, H. Kato, T. Okazaki, H. Shinohara, S. Iijima: Phys. Rev. Lett. **85**, 5384 (2003)
131. K. Suenaga, T. Okazaki, C.-R. Wang, S. Bandow, H. Shinohara, S. Iijima: Phys. Rev. Lett. **90**, 55506.1 (2003)
132. J. Sloan, M.C. Novotny, S.R. Bailey, G. Brown, C. Xu, V.C Williams, S. Friedrichs, E. Flahaut, R.L. Callendar, A.P. York, K.S. Coleman, M.L.H. Green, R.E. Dunin-Borkowski, J.L. Hutchison: Chem. Phys. Lett. **329**, 61 (2000)
133. R.R. Meyer, J. Sloan, R.E. Dunin-Borkowski, A.I. Kirkland, M.C. Novotny, S.R. Bailey, J.L. Hutchison, M.L.H. Green: Science **289**, 1324 (2000)
134. E. Flahaut, J. Sloan, K.S. Coleman, V.C. Williams, S. Friedrichs, N. Hanson and M.L.H. Green: Mat. Res Soc. Symp., Vol. 633, A13.15.1 (2001)
135. J. Sloan, J. Cook, J.R. Heesom, M.L.H. Green, J.L. Hutchison: J. Cryst. Growth **173**, 81 (1997)
136. J. Sloan, D.M. Wright, H.G. Woo, S. Bailey, G. Brown, A.P. York, K.S. Coleman, J.L. Hutchison, M.L.H. Green: Chem. Commun. 699 (1999)
137. Y.K. Chen, A. Chu, J. Cook, M.L.H. Green, P.J.F. Harris, R. Heesom, M. Humphries, J. Sloan, S.C. Tsang, J.F.C. Turner: J. Mater. Chem. **7**, 545 (1997)
138. J. Cook, J. Sloan, R.J. Heesom, J. Hammer, M.L.H. Green: Chem. Commun. 2673 (1996)
139. Y.K. Chen, M.L.H. Green, S.C. Tsang: Chem. Commun. 2489 (1996)
140. E.G. Bithell, A. Rawcliffe, S.C. Tsang, M.J. Goringe, M.L.H. Green: Inst. Phys. Conf. Ser. **147**, 361 (1995)
141. M. Wakihara, O. Yamamoto: *Lithium Ion Batteries – Fundamentals and Performance* (Kodansha Ltd, Tokyo, Wiley-Vch, Weinheim 1998)

142. K. Sawai, Y. Iwakoshi, T. Ohzuku: Solid State Ionics **69**, 273 (1994)
143. D. Guérard, A. Hérold: Carbon **13**, 337 (1975)
144. F. Béguin: Crystallochemistry of intercalation in the crystalline forms of carbon. In *Carbon molecules and materials*, ed by R. Setton, P. Bernier and S. Lefrant (Taylor and Francis, London 2002)
145. M. Winter, J.O. Besenhard, M.E. Spahr, P. Novak: Adv. Mater. **10**, 725 (1998)
146. K. Kanamura, H. Tamura, S. Shiraishi, Z. Takehara: J. Electroanal. Chem. **394**, 49 (1995)
147. A. Naji, J. Ghanbaja, B. Humbert, P. Willmann, D. Billaud: J. Power Sources **63**, 33 (1996)
148. D. Aurbach, A. Zaban, Y. Ein-Eli, I. Weissman, O. Chusid, B. Markovsky, M. Levi, E. Levi, A. Schechter, E. Granot: J. Power Sources **68**, 91 (1997)
149. T. Zheng, J.R. Dahn: Applications of carbon in Lithium-ion batteries. In *Carbon materials for advanced technologies*, ed by T.D. Burchell (Elsevier, Oxford 1999) pp 341–388
150. F. Béguin, F. Chevallier, C. Vix-Guteri, S. Saadallah, V. Bertagna, J.N. Rouzaud, E. Frackowiak: Carbon **43**, 2160 (2005)
151. J. Lahaye, J. Dentzer, P. Soulard, P. Ehrburger: In *Fundamental Issues of Control of Carbon Gasification Reactivity*, ed by J. Lahaye, P. Ehrburger (Academic Publishers, London 1991) pp 143–158
152. S. Yoon, H. Kim, S.M. Oh: J. Power Sources **94**, 68 (2001)
153. E. Frackowiak, S. Gautier, H. Gaucher, S. Bonnamy, F. Béguin: Carbon **37**, 61 (1999)
154. G.T. Wu, C.S. Wang, X.B. Zhang, H.S. Yang, Z.F. Qi, P.M. He, W.Z. Li: J. Electrochem. Soc. **146**, 1696 (1999)
155. B. Gao, A. Kleinhammes, X.P. Tang, C. Bower, L. Fleming, Y. Wu, O. Zhou: Chem. Phys. Lett. **307**, 153 (1999)
156. A.S. Claye, J.E. Fischer, C.B. Huffman, A.G. Rinzler, R.E. Smalley: J. Electrochem. Soc. **147**, 2845 (2000)
157. E. Frackowiak, F. Béguin: Carbon **40**, 1775 (2002)
158. B. Gao, C. Bower, J.D. Lorentzen, L. Fleming, A. Kleinhammes, X.P. Tang, L.E. McNeil, Y. Wu, O. Zhou: Chem. Phys. Lett. **327**, 69 (2000)
159. M. Winter, P. Novak, J. Monnier: J. Electrochem. Soc. **145**, 428 (1998)
160. F. Leroux, K. Méténier, S. Gautier, E. Frackowiak, S. Bonnamy, F. Béguin: J. Power Sources **81–82**, 317 (1999)
161. J.R. Dahn, T. Zheng, Y. Liu, J.S. Xue: Science **270**, 590 (1995)
162. G.T. Wu, M.H. Chen, G.M. Zhu, J.K. You, Z.G. Lin, X.B. Zhang: J. Solid State Electrochem. **7**, 129 (2003)
163. B.E. Conway: *Electrochemical supercapacitors – scientific fundamentals and technological applications* (Kluwer Academic/Plenum, New York 1999)
164. E. Frackowiak, F. Béguin: Carbon **39**, 937 (2001)
165. C. Niu, E.K. Sichel, R. Hoch, D. Moy, H. Tennet: Appl. Phys. Lett. **70**, 1480 (1997)
166. E. Frackowiak, K. Méténier, V. Bertagna, F. Béguin: Appl. Phys. Lett. **77**, 2421 (2000)
167. E. Frackowiak, K. Jurewicz, S. Delpeux, F. Béguin: J. Power Sources **97–98**, 822 (2001)
168. S. Shiraishi, H. Kurihara, K. Okabe, D. Hulicova, A. Oya: Electrochem. Comm. **4**, 593 (2002)

169. E. Frackowiak, S. Delpeux, K. Jurewicz, K. Szostak, D. Cazorla-Amoros, F. Béguin: Chem. Phys. Lett. **361**, 35 (2002)
170. Q. Jiang, M.Z. Qu, G.M. Zhou, B.L. Zhang, Z.L. Yu: Mat. Lett. **57**, 988 (2002)
171. E. Raymundo-Piñero, V. Khomenko, E. Frackowiak, F. Béguin, J. Electrochem. Soc. **152**, A229 (2004)
172. E. Frackowiak, K. Jurewicz, F. Béguin: Polish J. Chem. **78**, 1345 (2004)
173. G.Z. Chen, M.S.P. Shaffer, D. Coleby, G. Dixon, W. Zhou, D.J Fray, A.H. Windle: Advanced Materials **12**, 522 (2000)
174. K. Jurewicz, S. Delpeux, V. Bertagna, F. Béguin, E. Frackowiak: Chem. Phys. Lett. **347**, 36 (2001)
175. J.H. Chen, Z.P. Huang, D.Z. Wang, S.X. Yang, W.Z. Li, J.G. Wen, Z.F. Ren: Synthetic Metals **125**, 289 (2002)
176. Q. Xiao, X. Zhou: Electrochim. Acta **48**, 575 (2003)
177. K.H. An, K.K. Jeon, J.K. Heo, S.C. Lim, D.J. Bae, Y.H. Lee: J. Electrochem. Soc. **149**, A1058 (2002)
178. V. Khomenko, E. Frackowiak, F. Béguin: Electrochim. Acta **50** 2499 (2005)
179. V. Khomenko, E. Raymundo-Pinero, E. Frackowiak, F. Béguin: Appl. Phys. A **82**, 567 (2006)

Index

acoustic phonon 394, 409, 412
activated carbons 538
Aharonov-Bohm flux 368
Aharonov-Bohm oscillations 342, 387, 388
armchair nanotube 165, 182, 193

ballistic conduction 337, 378, 390
BN nanotube 61, 121, 166, 176, 180, 235
boron-doped tubes 234
Bragg diffraction 186, 189, 190
BSU 158, 160, 163

carbon nitrides 39
carbon surface chemistry 513
Catalytic Chemical Vapor Deposition 63
catalytic nanoparticles 76, 85, 88
chemical activation 509, 511
chemical doping 242
chiral angle 182, 184, 194
contact resistance 398
coordination number 5
Coulomb blockade 348
Coulomb gap 421
Coulomb interactions 345, 346, 395, 421

dark-field imaging 160, 163
Debye-Waller factor 189
defected nanotube 223
density of states 204, 213
diamond 3, 7
diffusion constant 208
Drude conductivity 336
Drude formula 208

electric arc discharge technique 51
electrical conductivity 27
electrochemical grafting 515
electron diffraction 133, 185
electron energy-loss spectroscopy 290
electron irradiation 176
electron-electron scattering 336, 410
electron-phonon scattering 336, 393, 408, 410

Fermi golden rule 346, 386, 393, 394
Fermi velocity 213
fiber 19
field emission 268
field-effect transistor 414
Fowler-Nordheim law 253, 255, 266, 267
fullerene 4, 9
functionalization 316, 522, 523

glassy carbon 160
graphene 142, 143, 147, 176
graphene sheet 211
graphite 3, 7, 139, 142, 143, 148, 164, 193
graphitization 19, 20
growth mechanism 75, 95, 106

Haeckelite tubes 225
helicity 165, 170, 171, 182, 185

heterofullerene 41
heteronanotube 41
Hooke's law 440, 442
Hot Filament CVD 254
hybrid orbitals 209
hybridization 5

incoherent scattering 135
incommensurability 389
incommensurate shells 391
intershell coupling 389

Kataura plot 306, 307, 319

Landauer formula 340
Laser Ablation technique 55
Luttinger liquid 354, 395

magnetoresistance 31
mean free path 335–337, 357, 377, 385, 410
mechanical properties 22
metallic nanotube 192, 377
microporous carbons 501, 505
Moiré effect 163

nano-diffraction 182
nanotexture 162
nanotube displays 271
negative magnetoresistance 370, 371, 387, 422
neutron diffraction 134, 186, 188, 189
nitrogen-doping 234
non-crystalline carbon 13

onion 176

pentagon-heptagon pair defects 223
phase object 137, 164
phonon mean free path 426
plasmon modes 293
PMMA/SWNT composite films 420
Poisson's ratio 440, 441, 451, 465
polyaromatic carbon 152, 161
polymorphism 3, 5
powder diffraction 189
pyrolytic carbon 161

quantum interferences 337, 380, 386

Raman scattering 246, 282, 287
Raman spectroscopy 302, 309
Rayleigh scattering 131, 135

rhombohedral graphite 139

scanning tunneling microscope 149, 190
scattering angle 133
scattering structure factor 133, 134, 177, 179, 181
Scherzer focus 146–148, 164, 165, 170, 173
Schottky barrier 408, 414, 416, 418
screened Coulomb interaction 346
screening length 345
semiconductor nanotubes 194
shear modulus 440, 441, 444, 450, 452, 468, 470, 472
Single Electron Tunneling transistor 350
STM current 149, 151, 191
STM image 191, 192, 194
structural defects 157, 176
STS 190, 195

Tersoff-Hamann theory 151, 192
thermal conductivity 424, 427
thermoelectric power 36, 428
thermoelectronic source 269
Thomson scattering 132
tight-binding approximation 203, 206
tight-binding theory 151
topological defects 176, 383
transmission electron microscope 135, 141
turbostratic graphite 152, 154, 163, 186

Universal Conductance Fluctuations 371

van Hove singularities 195, 204, 227, 245

weak localization correction 365, 369, 387
weak phase object 137, 139, 143, 145, 148, 168
work functions 251, 266

X-ray diffraction 132, 186, 189

Young's modulus 440, 441, 449, 457

zigzag nanotube 165, 169, 182, 193

Lecture Notes in Physics

For information about earlier volumes
please contact your bookseller or Springer
LNP Online archive: springerlink.com

Vol.632: A. M. Greco (Ed.), Direct and Inverse Methods in Nonlinear Evolution Equations

Vol.633: H.-T. Elze (Ed.), Decoherence and Entropy in Complex Systems, Based on Selected Lectures from DICE 2002

Vol.634: R. Haberlandt, D. Michel, A. Pöppl, R. Stannarius (Eds.), Molecules in Interaction with Surfaces and Interfaces

Vol.635: D. Alloin, W. Gieren (Eds.), Stellar Candles for the Extragalactic Distance Scale

Vol.636: R. Livi, A. Vulpiani (Eds.), The Kolmogorov Legacy in Physics, A Century of Turbulence and Complexity

Vol.637: I. Müller, P. Strehlow, Rubber and Rubber Balloons, Paradigms of Thermodynamics

Vol.638: Y. Kosmann-Schwarzbach, B. Grammaticos, K. M. Tamizhmani (Eds.), Integrability of Nonlinear Systems

Vol.639: G. Ripka, Dual Superconductor Models of Color Confinement

Vol.640: M. Karttunen, I. Vattulainen, A. Lukkarinen (Eds.), Novel Methods in Soft Matter Simulations

Vol.641: A. Lalazissis, P. Ring, D. Vretenar (Eds.), Extended Density Functionals in Nuclear Structure Physics

Vol.642: W. Hergert, A. Ernst, M. Däne (Eds.), Computational Materials Science

Vol.643: F. Strocchi, Symmetry Breaking

Vol.644: B. Grammaticos, Y. Kosmann-Schwarzbach, T. Tamizhmani (Eds.) Discrete Integrable Systems

Vol.645: U. Schollwöck, J. Richter, D. J. J. Farnell, R. F. Bishop (Eds.), Quantum Magnetism

Vol.646: N. Bretón, J. L. Cervantes-Cota, M. Salgado (Eds.), The Early Universe and Observational Cosmology

Vol.647: D. Blaschke, M. A. Ivanov, T. Mannel (Eds.), Heavy Quark Physics

Vol.648: S. G. Karshenboim, E. Peik (Eds.), Astrophysics, Clocks and Fundamental Constants

Vol.649: M. Paris, J. Rehacek (Eds.), Quantum State Estimation

Vol.650: E. Ben-Naim, H. Frauenfelder, Z. Toroczkai (Eds.), Complex Networks

Vol.651: J. S. Al-Khalili, E. Roeckl (Eds.), The Euroschool Lectures of Physics with Exotic Beams, Vol.I

Vol.652: J. Arias, M. Lozano (Eds.), Exotic Nuclear Physics

Vol.653: E. Papantonoupoulos (Ed.), The Physics of the Early Universe

Vol.654: G. Cassinelli, A. Levrero, E. de Vito, P. J. Lahti (Eds.), Theory and Appplication to the Galileo Group

Vol.655: M. Shillor, M. Sofonea, J. J. Telega, Models and Analysis of Quasistatic Contact

Vol.656: K. Scherer, H. Fichtner, B. Heber, U. Mall (Eds.), Space Weather

Vol.657: J. Gemmer, M. Michel, G. Mahler (Eds.), Quantum Thermodynamics

Vol.658: K. Busch, A. Powell, C. Röthig, G. Schön, J. Weissmüller (Eds.), Functional Nanostructures

Vol.659: E. Bick, F. D. Steffen (Eds.), Topology and Geometry in Physics

Vol.660: A. N. Gorban, I. V. Karlin, Invariant Manifolds for Physical and Chemical Kinetics

Vol.661: N. Akhmediev, A. Ankiewicz (Eds.) Dissipative Solitons

Vol.662: U. Carow-Watamura, Y. Maeda, S. Watamura (Eds.), Quantum Field Theory and Noncommutative Geometry

Vol.663: A. Kalloniatis, D. Leinweber, A. Williams (Eds.), Lattice Hadron Physics

Vol.664: R. Wielebinski, R. Beck (Eds.), Cosmic Magnetic Fields

Vol.665: V. Martinez (Ed.), Data Analysis in Cosmology

Vol.666: D. Britz, Digital Simulation in Electrochemistry

Vol.667: W. D. Heiss (Ed.), Quantum Dots: a Doorway to Nanoscale Physics

Vol.668: H. Ocampo, S. Paycha, A. Vargas (Eds.), Geometric and Topological Methods for Quantum Field Theory

Vol.669: G. Amelino-Camelia, J. Kowalski-Glikman (Eds.), Planck Scale Effects in Astrophysics and Cosmology

Vol.670: A. Dinklage, G. Marx, T. Klinger, L. Schweikhard (Eds.), Plasma Physics

Vol.671: J.-R. Chazottes, B. Fernandez (Eds.), Dynamics of Coupled Map Lattices and of Related Spatially Extended Systems

Vol.672: R. Kh. Zeytounian, Topics in Hyposonic Flow Theory

Vol.673: C. Bona, C. Palenzula-Luque, Elements of Numerical Relativity

Vol.674: A. G. Hunt, Percolation Theory for Flow in Porous Media

Vol.675: M. Kröger, Models for Polymeric and Anisotropic Liquids

Vol.676: I. Galanakis, P. H. Dederichs (Eds.), Half-metallic Alloys

Vol.677: A. Loiseau, P. Launois, P. Petit, S. Roche, J.-P. Salvetat (Eds.), Understanding Carbon Nanotubes